

NATIONAL INSTITUTE FOR FUSION SCIENCE

**Proceedings of the First International Toki Conference
On Plasma Physics and Controlled Nuclear Fusion
— Next Generation Experiments in Helical Systems —**

December 4-7, 1989

NIFS-PROC-3

Mar. 1990

**RESEARCH REPORT
NIFS-PROC Series**

This report was prepared as a preprint of work performed as a collaboration research of the National Institute for Fusion Science (NIFS) of Japan. This document is intended for information only and for future publication in a journal after some rearrangements of its contents.

Inquiries about copyright and reproduction should be addressed to the Research Information Center, National Institute for Fusion Science, Nagoya 464-01, Japan.

NAGOYA, JAPAN

PROCEEDINGS OF THE FIRST INTERNATIONAL TOKI CONFERENCE

ON PLASMA PHYSICS and CONTROLLED NUCLEAR FUSION

— NEXT GENERATION EXPERIMENTS IN HELICAL SYSTEMS —

DECEMBER 4-7, 1989

TOKISHI BUNKA PLAZA, TOKI, JAPAN

CONTENTS

Preface		1
Session I	Next Generation Experiments	
	Present Status of the Large Helical Device Project	
	O. Motojima (NIFS).....	3
	Status of the Wendelstein VII-X Project	
	G. Grieger (Max Planck Inst.).....	7
	Overview of the ATF- II Studies	
	J.F. Lyon (ORNL).....	11
	Review of the TJ- II Flexible Heliac Project	
	A.P. Navarro (CIEMAT)*1).....	16
	The ANU Heliac Program	
	R.L. Dewar (ANU).....	17
	Design of the Compact Auburn Torsatron	
	R. Gandy (Auburn Univ.).....	21
Session II	MHD	
	Optimization of Heliac Configuration	
	J. Nührenberg (Max Planck Inst.).....	29
	Second Stability Studies in a Helical Axis Device : TJ- II	
	C. Alejaldre (CIEMAT).....	33
	3-D Equilibria of Helical Systems : Magnetic Islands and their Control	
	T. Hayashi (NIFS).....	37
	Resistive MHD Stability Studies for ATF Plasmas during Operation in the Second Stability Regime	
	L.A. Charlton (ORNL).....	41
Session III	Transport	
	Drift Optimization of Helical Systems	
	K. Hanatani (PPL, Kyoto Univ.).....	45
	Plasma Transport in Advanced Stellarators	
	H. Wobig (Max Planck Inst.).....	49
Session IV	Special Topics	
	Recent Experiments in JT-60	

H. Kishimoto (JAERI).....	53
Graphites as Plasma Facing Material of a Large Fusion Device	
T. Hino (Hokkaido Univ.).....	57
The main Fusion Activities in Institute of Plasma Physics, Academia Sinica	
Wang Shao-hu (ASIPP).....	61

Session V Edge Physics and Confinement Improvement

Analysis of Scrape off Layer in Toroidal Helical Systems	
K. Nagasaki (PPL, Kyoto Univ.).....	65
Detached Plasma and Density Limit of Tokamaks	
S. Yoshikawa (PPPL).....	69
Confinement Improvement by Edge Control	
N. Ohyabu (NIFS).....	70
Effects of Perturbing Helical Fields on Confinement of Heliotron DR Plasma	
S. Morimoto (NIFS).....	73

Session VI On-going Experiments

Overview of Recent Results from the Advanced Toroidal Facility	
M. Murakami (ORNL).....	77
Status of the WVII-AS Program	
H. Ringler (Max Planck Inst.).....	81
Status of the Torsatron/Stellarator Program	
J. L. Shohet (Univ. of Wisconsin).....	85
Review of Heliotron E Experiment	
T. Obiki (PPL, Kyoto Univ.).....	89
Review of CHS Experiment	
K. Matsuoka (NIFS).....	93
Experimental Studies of a Helical Axis Stellarator (TU-Heliac)	
H. Watanabe (Tohoku Univ.).....	97

Session VII Poster Session

1. Diverted Particle-Flux Studies in the IMS and Proto-Cleo Stellarators	
J.L. Shohet (Univ. of Wisconsin).....	101
2. Pressure and Potential Measurements in IMS during Electron Cyclotron Heating	

J.N. Talmadge (Univ. of Wisconsin).....	105
3. Numerical and Experimental Studies of Simulated Toroidicity Effects in a Linear High-Beta Heliac	
B.A. Nelson (Univ. of Washington).....	109
4. Theory of Electron Cyclotron Heating in the Flexible Heliac TJ- II	
C. Alejaldre (CIEMAT).....	113
5. STORM : A low Aspect Ratio Torsatron for Plasma Stability Studies	
A.P. Navarro (CIEMAT)*1).....	117
6. Dissipative Trapped Electron Modes in $\ell = 2$ Torsatrons	
B.A. Carreras (ORNL).....	118
7. Low-n Stability Calculations for Three Dimensional Stellarator Configurations	
L. Garcia (Universidad Complutense)*1).....	122
8. Destruction of Magnetic Surfaces in Helical Torus	
J. Todoroki (NIFS).....	123
9. Ripple Diffusion and Bootstrap Current in LHD	
T. Amano (NIFS).....	127
10. Numerical Analysis of Temporal Development of RF-Heated Plasma	
T. Watanabe (NIFS).....	130
11. Island Studies for Helias Configurations	
P. Merkel (Max Planck Inst.).....	134
12. On Strong RF Plasma Turbulence	
M.M. Skoric (Boris Kidric Inst.).....	138
13. Structural Design of Large Helical Device	
K. Kitamura (Toshiba Corp.).....	139
14. R&Ds of Forced Flow Superconducting Coil for Large Helical Device	
S. Tsuruga (Toshiba Corp.).....	143
15. Pool-Cooled Superconducting Magnet Design of Large Helical Device	
S. Suzuki (Hitachi Ltd.).....	147
16. Behaviour of Vacuum Vessel Eddy Current in Large Helical Device	
H. Fukumoto (Hitachi Ltd.).....	151
17. Fundamental Design on LHD with Bath Cooling Method	
S. Tado (Mitsubishi Fusion Center).....	155
18. A Compact Helical Device for a Superconducting Large	

Helical Coil	
Y. Tsuda (Mitsubishi Electronic Co.).....	159
19. Optimization of Design Parameters for Large Helical Device	
K. Yamazaki (NIFS).....	163
20. Effect of Multi-Layer Operation of Helical Coil in Large Helical Device	
M. Asao (Kobe Steel Ltd.).....	167
21. ECH System in the Large Helical Device	
K. Ohkubo (NIFS).....	171
22. ICRF Heating Program of the Large Helical Device	
T. Mutoh (NIFS).....	175
23. Motion of Charged Particle in Helical Systems	
M.P. Srivastava (Delhi Univ.).....	179
24. Equilibrium, Stability and Transport in L = 1 Compact Helical Axis Configuration	
H. Kikuchi (Nihon Univ.).....	183
25. Electron Temperature Measurements on ATF Using Electron Cyclotron Emission	
R.F. Gandy (Auburn Univ.).....	188
26. Confinement Studies of Heliotron-E Plasmas in Magnetic Surface Variation Experiments	
F. Sano (PPL, Kyoto Univ.).....	192
27. Profile Measurements in Magnetic Surface Variation Experiments/Multiple Pellet Injection Experiments	
S. Sudo (PPL, Kyoto Univ.).....	196
28. Impurity Behavior in Heliotron E	
K. Kondo (PPL, Kyoto Univ.).....	200
29. Edge Plasma Study in Heliotron E	
T. Mizuuchi (PPL, Kyoto Univ.).....	204
30. Recent Diamagnetic Measurement of Toroidal Coil Experiments on Heliotron E	
S. Besshou (PPL, Kyoto Univ.).....	208
31. Study of Resistive Interchange Mode in Heliotron E	
H. Zushi (PPL, Kyoto Univ.).....	212
32. Measurement of Magnetic Fluctuations in Heliotron E	
M. Harada (PPL, Kyoto Univ.).....	216
33. Transport Study of ECH and NBI Plasmas in CHS	
H. Yamada (NIFS).....	220
34. Effect of Magnetic Axis Shift on CHS Plasma Characteristics	
S. Okamura (NIFS).....	224

35. A Study of Radiation on Collapse in CHS Plasmas	
S. Morita (NIFS).....	228
36. Ion Temperature and Poloidal Rotation Profiles for NBI Heated Plasma in CHS	
K. Ida (NIFS).....	232
37. Driven Currents in Neutral Beam Heated Plasma	
O. Kaneno (NIFS).....	236
38. Power Deposition during ECH in CHS	
S. Kudo (NIFS).....	240
39. A Possible Modification of the FT Tokamak in to a Compact High Field Stellarator with Separatrices.	
F. Crisanti (FRAS)*2).....	244

Session VIII

Engineering

Engineering Design of Large Helical Device

J. Yamamoto (NIFS).....	248
-------------------------	-----

Operation Scenario and Structural Design Analysis of LHD (Large Helical Device) Coils

K. Yamazaki (NIFS).....	252
-------------------------	-----

Engineering Design of LHD Vacuum Vessel

N. Ohyabu (NIFS).....	256
-----------------------	-----

Development of Superconductor for Large Helical Device

T. Mito (NIFS).....	260
---------------------	-----

Overview of Engineering Design of Wendelstein VII-X

J. Sapper (Max Planck inst.).....	264
------------------------------------	-----

100 GHz Half Megawatt Microwave Transmission System Development with Whispering Gallery Mode

M. Sato (PPL, Kyoto Univ.).....	268
----------------------------------	-----

NBI System with Negative Ion Source in Large Helical Device

Y. Takeiri (NIFS).....	272
------------------------	-----

Appendix I	Program of the Conference.....	276
------------	--------------------------------	-----

Appendix II	List of Participants.....	282
-------------	---------------------------	-----

1) presented by C. Alejaldre

2) no presentation at the conference

PREFACE

The First International Toki Conference on Plasma Physics and Controlled Nuclear Fusion was held on 4-7 December 1989, in Tokishi Bunka Plaza. This is in commemoration of the National Institute for Fusion Science to be constructed in the City of Toki, about 30 km north-east of the present site in Nagoya.

The institute, NIFS in short, was established on 29 May 1989 under Ministry of Education, Science and Culture, former Institute of Plasma Physics, Nagoya University being reorganized. Staff at Plasma Physics Laboratory, Kyoto University and Hiroshima Institute for Fusion Theory, Hiroshima University also joined the new institute.

As one of activities to promote nuclear fusion research, NIFS decided to inaugurate a series of international conference with a name of "Toki Conference", annually on the topics of current international interest in fusion research.

The First Toki Conference laid its emphasis on the topics related to "next generation experiments in helical systems", in connection with the Large Helical Device Project which is the major project of NIFS.

About 150 scientists from 10 countries participated in the conference, presented their works and discussed the problems on the topics categorized as follows :

- Next Generation Experiments
- Theories (MHD and Transport)
- Special Topics
- Edge Physics and Confinement Improvement
- On-going Experiments
- Engineering

The program of the conference is attached in the present proceedings. The list of participants is also attached.

The Organizing Committee would like to acknowledge cooperation of all participants and the staff concerned. Special thanks are to Mr. Tsukamoto, Mayor of Toki City and his staff, and to those who are involved in the organization of the conference.

Junji Fujita
Chairman, Organizing Committee
for the Toki Conference

ORGANIZING COMMITTEE

Junji Fujita (Chairman)

Osamu Motojima

Kohnosuke Sato

Keisuke Matsuoka

Yasuhiko Takeiri

Chusei Namba

National Institute for Fusion Science

Furo-cho, Chikusa-ku, Nagoya

Japan 〒464-01

PRESENT STATUS OF THE LARGE HELICAL DEVICE PROJECT

O. MOTOJIMA

LHD Design Group

NATIONAL INSTITUTE FOR FUSION SCIENCE

464-01 FUROCHO, NAGOYA, JAPAN

Abstract

National Institute for Fusion Science is a new large fusion research institute in Japan. It is responsible for joint university researches of plasma physics and fusion technology. The major experimental facility of the institute is Large Helical Device (LHD) which is now in the phase of practical design. This report describes the design study of the Large Helical Device. Our goal is the demonstration of high energy and high β plasma production in the helical device, which is a necessary step toward the realization of the helical reactor system.

1. Introduction

Recently significant progress has been made in the research on helical devices (Heliotron E, CHS, ATF, Wendelstein VII-AS, etc). Both experimental and theoretical studies have revealed that this approach is a very promising fusion reactor concept.

In helical devices, the confining magnetic field is generated by the external coils and thus helical devices are free of tokamak problems, i.e. implementation of the efficient non-ohmic current drive and prevention of the major plasma current disruption, which must be resolved before designing a tokamak reactor system. The inherent advantage of helical system makes helical concept very attractive. It has been demonstrated by small scale helical device experiments that the plasma performance in helical devices is comparable to that of comparable tokamak device. In order to examine whether a helical device is a viable candidate for fusion reactor system, a larger-scale experimental device is needed. For this objective, we have proposed to build superconducting Large Helical Device (Heliotron/torsatron type, $\ell=2$, $m=10$, $\gamma_0=1.2$, $R=4m$, $B=4T$) shown in Fig.1. The budget for the first year of the eight years construction proposal has been approved by the Japanese government April 1989.

Helical system is the representative of the static configuration and can produce the currentless plasma. On the contrary Tokamak is recognized as the dynamic configurations with current. There are many interesting physics issues. We have been primarily concentrating our scientific efforts on the analyses of MHD, transport and edge physics. These issues are listed on Table 1. The analyses on these issues are deeply dependent on the data base of the present experiments and theoretical approaches. We wish new data base of Large Helical Device makes clear the major part of physics origins of these issues.

We report here a summary of our design study of the Large Helical Device. In Section 2, the objectives of the project are depicted. And in Section 3, target plasma and design criteria for magnetic configuration are introduced.

2. OBJECTIVES OF THE PROJECT

The overall objective of this project is to clarify the physics and engineering issues important in designing future helical reactor by studying the behavior of the currentless plasmas in the large-scale experimental helical de-

vice. This research project will be carried out as the major fusion research activity of Japanese Universities.

The most important subjects to be pursued are; (a) To carry out a wide range of research in the transport under high $n \tau T$ plasma conditions extrapolatable to reactor plasmas. (b) To achieve high-beta plasmas with the average beta value of $\bar{\beta} > 5\%$, as needed for reactor, and to understand the related physics. (c) To obtain the basic data necessary to realize steady-state operation through experiments on the quasi-steady plasma control using the divertor. (d) To study the behavior of high-energy particles in the helical magnetic field and to conduct α particle simulation experiments. (e) To increase the comprehensive understanding of toroidal plasmas by carrying out studies complementary to those in tokamaks. The target regime is behind of the present day largest Tokamak data points which are now still improving. However according to our concept definition, this is thought the even and necessary position to extrapolate our data bases of LHD to the reactor regime. Our project is stressed more on the physics development concerned with currentless plasmas in the nonaxisymmetric system. We are also responsible for the comprehensive system, i.e., Tokamak approach.

Characteristics of Large Helical Device is summarized in the followings. 1. Reactor extrapolatable currentless plasma production, 2. Lower aspect ratio ($A \sim 7$), 3. Installation of divertor for edge and particle control (and for confinement improvement), 4. Steady state operation with superconducting coils and divertor, and 5. Utilization of continuous helical coil. Extensive optimization studies have been done during these three years by the design group which was organized as an inter-university active collaboration. Here we also thank for the fruitful international collaborations with especially Oak Ridge, Max-Planck, and Princeton plasma physics groups.

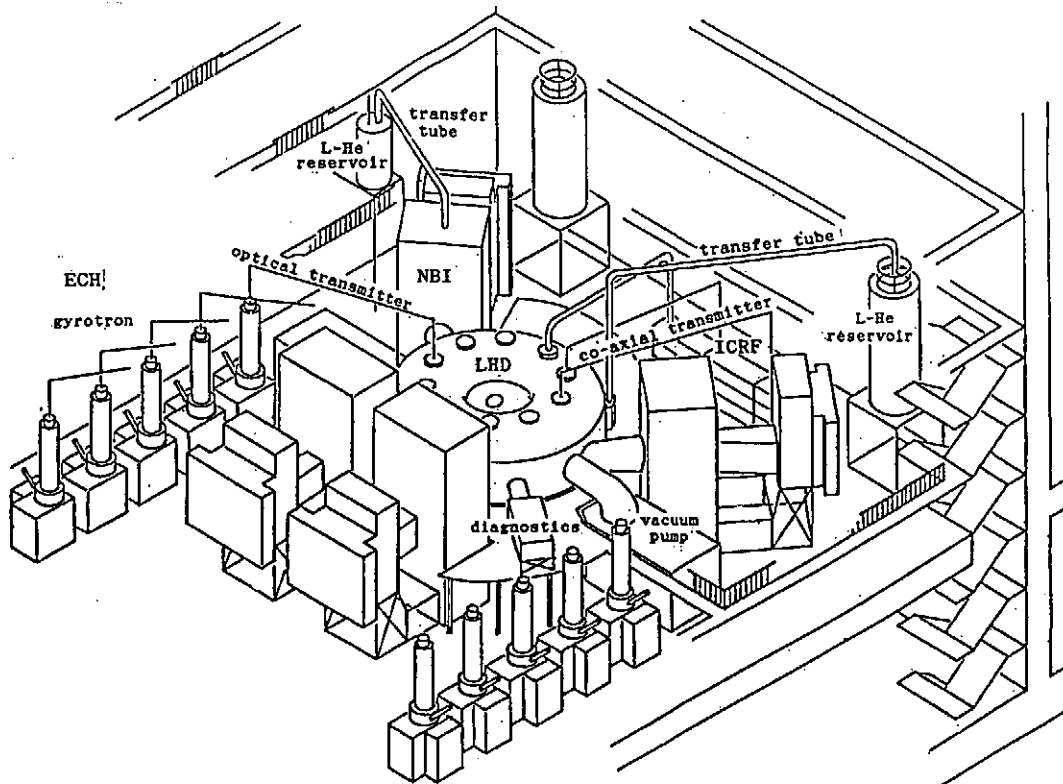


Fig. 1 Bird Eye View of LHD

Table 1 PHYSICS ISSUES OF TOROIDAL CONFINEMENT [by M. Fujiwara]

		MHD	TRANSPORT	EDGE PLASMA
STATIC CONFIGURATION CURRENTLESS ↔ DYNAMIC CONFIGURATION CURRENT	HELICAL HELIOTRON E CHS ATP WENDELSTEIN VIIAS SHATLET-M SHEILA etc.	PRESSURE DRIVEN IDEAL/RESISTIVE MERICER PS CURRENT BS CURRENT THERMAL DISRUPTION	NEOCLASSICAL +ANOMALOUS LHD-EMPIRICAL SCALING ϕ EFFECT β EFFECT HIGH ENERGY PARTICLE ERGODICITY MAGNETIC BRAIDING DRIFT MODE CONVECTIVE CELL	HELICAL DIVERTOR RECYCLING CONTROL (H-MODE)
	TOKAMAK JT-60 JET TFTR TRIAM-1M JIPPT-20 etc.	PRESSURE DRIVEN CURRENT DRIVEN CURRENT/THERMAL DISRUPTION	KAYE-GOLDSTONE L-MODE & H-MODE ANOMALOUS MICRO-INSTABILITY MHD EFFECT	POLOIDAL DIVERTOR RECYCLING CONTROL PUMP LIMITER H-MODE

3. TARGET PLASMA AND DESIGN CRITERIA FOR MAGNETIC CONFIGURATION

The following target values for plasma and device parameters are adopted for conducting the above-mentioned research.

Plasma Parameters:

CASE 1 : (high $n \tau T$)	$T_i = 3 - 4 \text{ keV}$, $\bar{n}_e = 10^{20} \text{ m}^{-3}$ $\tau_E = 0.1 - 0.3 \text{ sec}$, $B = 4 \text{ T}$
CASE 2 : (high T_i)	$T_i(0) = 10 \text{ keV}$, $\bar{n}_e = 2 \times 10^{19} \text{ m}^{-3}$ $\tau_E = \sim 0.1 \text{ sec}$, $B = 4 \text{ T}$
CASE 3 : (high β)	$\beta \geq 5\%$, $B = 1 - 2 \text{ T}$

Device Parameters:

$a_p = (50-60) \text{ cm}$, $R/a_p = 7 \sim 8$
$R = 4 \text{ m}$
$B = 4 \text{ T}$, $P_{abs} = 15-20 \text{ MW}$

The configuration for obtaining high beta is primarily studied with MHD codes (H-APOLLO, H-ERATO) using the stellarator approximation method under the net currentless plasma equilibrium condition. Various parameters reflecting the geometrical shape of coils, $A_0=R/a_0$, m , $\gamma_0 = (m/\ell)(a_0/R)$, are varied widely to find the optimum magnetic configuration, where R , a_0 and m stand for major radius, minor radius and the pitch number of the helical coil, respectively.

The results are; (a) In the case of $m = 10$, $\beta \sim 5\%$ is attainable if $\gamma_0 \geq 1.2$. (b) In the case of $m = 14$, γ_0 should be increased more to attain the high β condition. The inward shift of the plasma improves the equilibrium beta limit because of increase in t and decrease in the axis shift (in vacuum), and the stability beta limit also increases until the sudden loss of the stability for interchange mode due to the loss of the magnetic well. For $m=10/\gamma_0 = 1.20/R=4m$ configuration, the stability beta limit of 5% is achieved when the plasma is shifted about 15cm inwards. If the plasma inward shift is less than this value, the beta limit is restricted by the equilibrium. For $m=14/\gamma_0=1.29$ configuration, beta-limit $\sim 3\%$ is obtained; this value is less than the required equilibrium limit. When the plasma is moved outwards, the beta limit is restricted by the ballooning mode type instability. We have also studied the improvement of the plasma stability caused by the quadrupole, and hexapole magnetic fields.

Confinement studies for evaluating the target values for plasma and device parameters are as follows; a) We used the following empirical scalings obtained from the results of experiments on helical devices,

$$\begin{aligned} \tau_E^{EMP1} &= 0.17 P_{abs}^{-0.58} \bar{n}_e^{0.69} B^{0.84} a^2 R^{0.75} \text{ and} \\ \tau_E^{EMP2} &= 0.21 P_{abs}^{-0.53} \bar{n}_e^{0.66} B^{0.53} a^2 R. \\ (s) \quad (MW) \quad (10^{20} m^{-3}) (T) \quad (m) \quad (m) \end{aligned}$$

b) At the same time we also pursued the confinement scaling based on neo-classical theory and the additional anomalous transport (based on the analysis of ECH and NBI plasmas in Heliotron E). Scaling (b) predicts the following typical properties of plasma energy confinement. (1) In the low-density region ($n_e \leq 3 \times 10^{19} m^{-3}$), it is possible to realize the condition for the electron root (plasma radial electric field $E_r > 0$). As a result, $T_i(0) \geq 10$ keV will be achieved with $P_{abs} \geq 15$ MW and $a_p \geq 50$ cm. (2) The high-density region ($\bar{n}_e \sim 10^{20} m^{-3}$) produces the ion root ($E_r < 0$), and $T_i(0) = 4 - 5$ keV is obtained when $P_{abs} \geq 15$ MW and $a_p \geq 50$ cm. Plasmas with a high $n\tau T$ value are obtained as a result of expected $\tau_E = 0.1 - 0.3$ sec.

Orbit loss of fast ions is a concern for a helical magnetic configuration. Drift orbit calculations have been carried out by using both real coordinates and magnetic coordinates. The drift surface of passing particles can be controlled by the magnetic surface, while the position of drift surfaces for locally-trapped particles are controlled by mod-B structure. The good confinement is realized by adjusting these two structures. The magnetic surface can be moved by vertical field, and mod-B structure. The particle loss fraction can be reduced effectively by the inward shift of the magnetic axis.

In order to study long-pulse, currentless plasmas, various divertor actions are necessary for controlling impurities, particle flux, and heat flux. It may also provide improvement in the energy confinement (H-mode). For $m = 10$, slight pitch modulation of helical coil is desirable for providing a clear separatrix configuration outside the outermost closed magnetic surface.

In 1989, we have developed the basic design phase II and extensively studied $m = 10$ system. We are now starting the detailed design phase I by taking into account the results of Research & Development on super-conducting coils and recent experimental results from Heliotron E, ATF, CHS and Wendelstein VII-AS, etc.

Status of the Wendelstein VII-X Project
G. Grieger and WVII-X Team

Max-Planck-Institut für Plasmaphysik, Euratom Association
D-8046 Garching, FRG

The objectives of the WENDELSTEIN VII-X project are unchanged: to demonstrate the reactor potential of Advanced Stellarators, including the following items:

- to demonstrate plasma build-up by non-ohmic means;
- to prove that plasma confinement is adequate;
- to show that stability can be achieved at high enough beta ($\approx 5\%$);
- to demonstrate stationary operation, controlled by refuelling and exhaust only;
- to prove that the magnet technology is feasible and "simple".

This demonstration may involve some plausible extrapolations to reactor conditions. In particular, there is no need to foresee DT operation because experience with such plasmas can be transferred from Tokamaks. Needless to say that also budget constraints have to be observed.

WENDELSTEIN VII-X Physics

The configuration selected for WENDELSTEIN VII-X was optimized according to the following criteria:

- to ensure good equilibrium properties with limited influence of islands;
- to minimize the influence on the configuration by changing beta which includes the optimization for low bootstrap currents;
- to provide good MHD stability;
- to design the configuration such that the neo-classical losses are in the required range and anomalous losses low enough not to spoil the confinement;
- not to exceed an aspect ratio of 10; and
- to aim at technical simplicity.

The configuration selected is shown in Fig. 1. It has the following parameters:

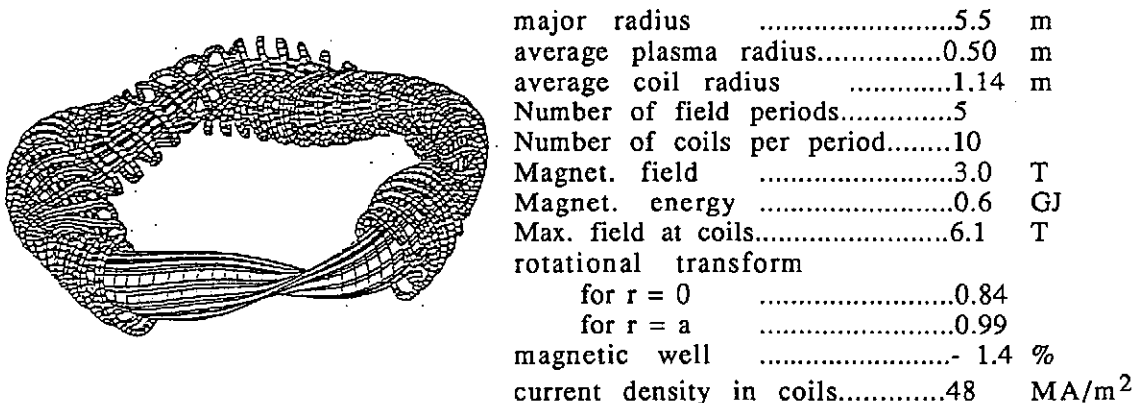


Fig. 1: WENDELSTEIN VII-X (Helias 5 - 10), coil system

Superimposed toroidal field coils - four per field period - allow variation of the rotational transform according to Fig. 2. The magnetic well is displayed in Fig. 3. Fig. 4. shows the geometric helical ripple together with the effective helical ripple which, applied to a configuration being axisymmetric otherwise, would lead to the same transport.

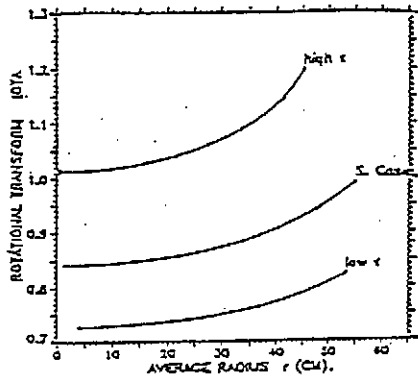


Fig. 2:
WENDELSTEIN VII-X (Helias 5-10)
rotational transform vs. average
radius

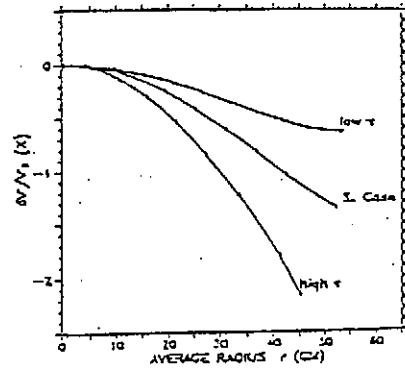


Fig. 3:
WENDELSTEIN VII-X (Helias 5-10)
magnetic well, high rotational
transform: -2 %,
low rotational transform: -0.5 %

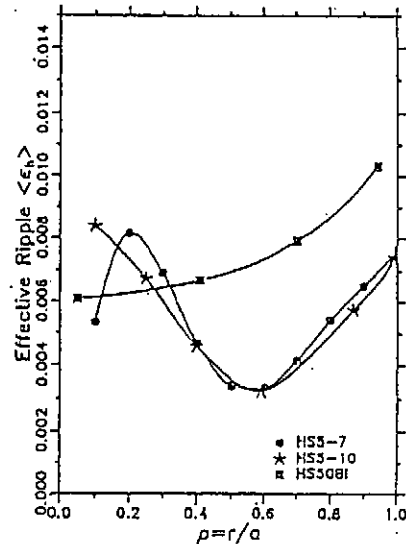
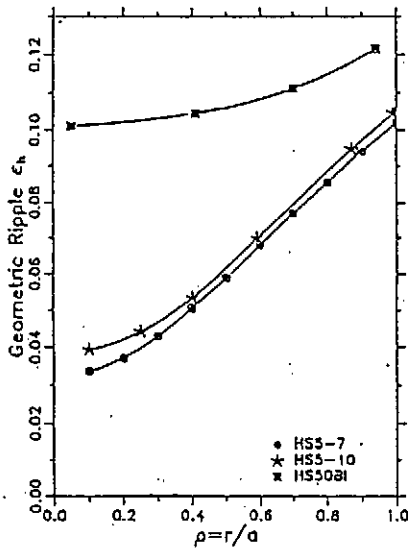


Fig. 4: Helias Configurations: geometric helical ripple (left); effective helical ripple (right). (C. Beidler). WENDELSTEIN VII-X: HS 5-10.

The large ratio between these two quantities shows the large improvement factor achievable by Advanced Stellarators. This can be seen even better in Fig. 5 where the lines of the confinement currents are plotted together with the orthogonal trajectories on B. If both were identical, confinement would be perfect. Fig. 5(a) shows the case for Wendelstein VII-AS which is optimized only to a limited degree and which therefore shows large components of the current flowing parallel to B. Fig. 5(b) is for Wendelstein VII-X where in the critical corners, where the curvature is largest, the parallel component of the confinement current nearly vanishes. Representative magnetic surfaces are shown in Fig. 6. The islands in the boundary region are wanted and can be exploited for exhaust purposes by pumped limiters.

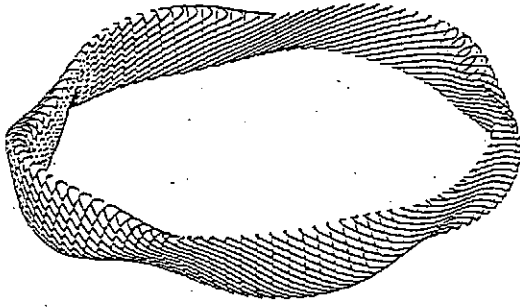


Fig. 5(a): WENDELSTEIN VII-AS, magnetic coordinates and plasma currents

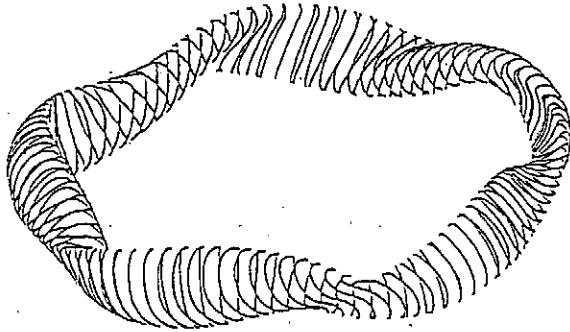


Fig. 5(b): WENDELSTEIN VII-X (Helias 5-10), magnetic coordinates and plasma currents.

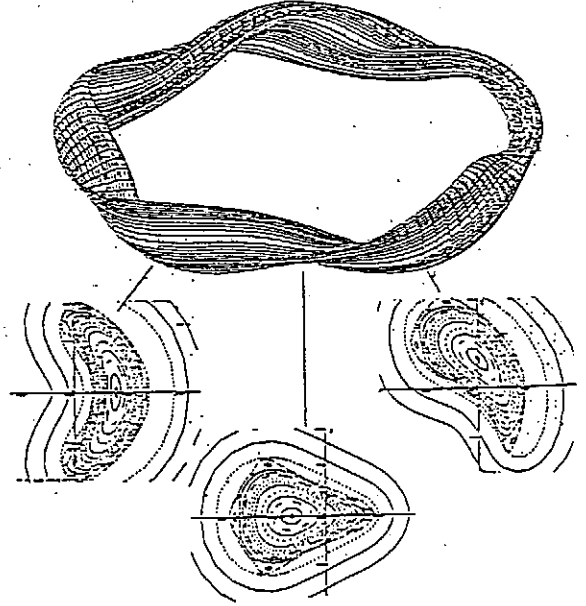


Fig. 6: WENDELSTEIN VII-X (Helias 5-10) magnetic surfaces.

Expected plasma parameters are shown in Tables 1 and 2 for an ECRH scenario with $P_{\max} = 10$ MW and an NBI scenario for $P_{\max} = 20$ MW, respectively. Three cases are assumed for the heat conductivity: $\chi^{(2)}_{e,an}$ is in line with the gross experimental values found in the Wendelstein-VII-plasmas. $\chi^{(3)}_{e,an}$ is a theoretical forecast to result from turbulent diffusion and $\chi^{(4)}_{e,an}$ follows from ASDEX L-mode scaling. For present Wendelstein plasmas these three coefficients lead to very similar results and are thus hardly to distinguish. For the elevated parameters expected for Wendelstein VII-X, however, it would be clearly visible if the transport were not as expected and would rather follow one of the other laws.

	(2)	(3)	(4)		(2)	(3)	(4)
	$\chi_{e,an}$	$\chi_{e,an}$	$\chi_{e,an}$		$\chi_{e,an}$	$\chi_{e,an}$	$\chi_{e,an}$
$n(o)$ [m^{-3}]	1.0×10^{20}	1.0×10^{20}	1.0×10^{20}	$n(o)$ [m^{-3}]	1.5×10^{20}	1.5×10^{20}	1.5×10^{20}
$T_e(o)$ [keV]	7.0	4.5	2.8	$T_e(o)$ [keV]	10.0	5.5	3.0
$T_i(o)$ [keV]	5.0	3.7	2.2	$T_i(o)$ [keV]	11.3	6.5	3.3
$\beta(o)$ [%]	7.7	5.3	3.2	$\beta(o)$ [%]	20.5	11.5	6.1
β [%]	3.1	2.2	1.0	β [%]	8.5	4.8	1.8
E [MJ]	3.82	2.75	1.2	E [MJ]	9.9	5.88	2.2
τ_E [ms]	400	283	124	τ_E [ms]	522	307	113
$n\tau_E$ [sm^{-3}]	2.2×10^{19}	1.6	0.7×10^{19}	$n\tau_E$ [sm^{-3}]	4.5×10^{19}	2.6×10^{19}	0.97×10^{19}
nT_E	7.04×10^{19}	3.8×10^{19}	0.7×10^{19}	nT_E	2.68×10^{20}	9.6×10^{19}	1.16×10^{19}

Table 1:
WENDELSTEIN VII-X (plasma parameters)
($R = 5.5$ m, $a = 0.55$ m, $B = 2.5$ T)

Table 2:
WENDELSTEIN VII-X (plasma parameters)
($R = 5.5$ m, $a = 0.55$ m, $B = 2.5$ T)

WENDELSTEIN VII-X Engineering

Poloidally closed, twisted coils are the natural solution for generating Stellarator configurations because they avoid unnecessary currents, lead to minimum of stray-field energy and thus to a minimum of total field energy for a given configuration, geometrical size and strength of the magnetic field. The flexibility of such modular coils was demonstrated by the technology used for the construction of Wendelstein VII-AS. This technology lends itself directly to larger and even superconducting coils.

Studies on a water-cooled Cu-magnet have shown that the accessible operating parameters are not compatible with the Wendelstein VII-X objectives. On the other hand, study contracts in industry yielded feasible superconducting solutions with NbTi conductors embedded in an aluminium alloy for increasing the mechanical strength. The winding technique will be the same as used for manufacturing the Wendelstein VII-AS coils. After full approval of the project construction would take about six to seven years.

Summary and Conclusions

A configuration for Wendelstein VII-X is now available which satisfies all criteria listed above. It promises good confinement, a negligible loss cone, stability at high enough beta, good prospects for stationary operation, low bootstrap current, moderate shear, a feasible magnet technology and seems to be compatible with present budget constraints. Experiments in Wendelstein VII-AS have demonstrated again the importance of resonances and island formation which yields a strong support for the Wendelstein VII-X concept of avoiding major resonances in the profile.

References:

J. Sapper: Overview of Engineering Design of Wendelstein VII-X.
See also these Proceedings.

H. Wobig: Plasma Transport in Advanced Stellarators.
See also these Proceedings.

"The submitted manuscript has been authored by a contractor of the U.S. Government under contract DE-AC05-84OR21400. Accordingly, the U.S. Government retains a nonexclusive, royalty-free license to publish or reproduce the published form of this contribution, or allow others to do so, for U.S. Government purposes."

OVERVIEW OF THE ATF-II STUDIES*

J.F. Lyon, B.A. Carreras, L. Dresner, S.P. Hirshman, R.N. Morris, S.L. Painter, and J.A. Rome

*Oak Ridge National Laboratory,
P.O. Box 2009, Oak Ridge, Tennessee 37831-8072*

Abstract. Design studies focusing on critical physics and engineering issues for a low-aspect-ratio, large next-generation stellarator ATF-II are described.

*Research sponsored by the Office of Fusion Energy, U.S. Department of Energy, under contract DE-AC05-84OR21400 with Martin Marietta Energy Systems, Inc.

Overview of the ATF-II Studies

*J. F. Lyon, B. A. Carreras, L. Dresner, S. P. Hirshman, R. N. Morris,
S. L. Painter, and J. A. Rome*

*Oak Ridge National Laboratory, P.O. Box 2009,
Oak Ridge, Tennessee 37831-8072, U.S.A.*

Abstract: Design studies focusing on critical physics and engineering issues for a low-aspect-ratio, large next-generation stellarator ATF-II are described.

1. Introduction

Design studies for a next-step, low-aspect-ratio stellarator (ATF-II) have been carried out over the past few years. Although it is not an approved project, the time from initial studies to start of operation for a device with the scope of ATF-II is sufficiently long (~ 10 years) that scoping studies need to be conducted as early as possible. ATF-II studies (Ref. 1) have focused on critical physics and engineering issues.

The primary goal of a next-step device should be to study some of the key issues relating to the feasibility of steady-state stellarator reactors: high beta, steady-state operation; confinement at low collisionality; loss of energetic helically trapped particles; particle and impurity control; plasma heating and heat removal; testing of wall materials and in-vessel components; and use of superconducting windings in an experimental facility. The distinguishing features of ATF-II are an average plasma radius \bar{a} similar to those of LHD and W VII-X and a low plasma aspect ratio A similar to those of most present tokamaks. The major motivation for this approach is to minimize the cost of the stellarator D-T ignition device that would follow a successful next-generation hydrogen plasma experiment.

To meet these needs, some reference parameters have been chosen for ATF-II based on operational experience from the present ATF device.² To further reduce edge effects and to give adequate energy confinement time τ_E , $\bar{a} \simeq 0.5$ m is chosen. The low $A = R_0/\bar{a} = 3-5$ assumed for ATF-II gives a major radius $R_0 \simeq 2$ m, similar to that of ATF, which lowers the cost and maximizes compatibility with the ATF site. An on-axis field $B_0 = 4-5$ T is chosen to increase τ_E and allow use of electron cyclotron heating at densities $n > 10^{20}$ m⁻³. A heating power $P = 10-15$ MW is chosen to obtain more relevant plasma parameters. Superconducting NbTi/Cu windings are chosen to allow steady-state operation at maximum field. Finally, hydrogen plasma operation is selected to avoid the problems and cost associated with neutron shielding, activation, and remote maintenance. The device cost assumed is \$50 million to \$100 million, which is consistent with our component cost scaling studies.²

2. Compact Torsatron Approach

The most-developed concept is the Compact Torsatron³ with a helical winding trajectory $\phi = \phi_0 + \ell [\theta - \sum \alpha_n \sin(n\theta)]/M$, where the set of α_n values is chosen to maximize the rotational transform $\iota(\bar{a})$ subject to the constraints $\iota(0) \sim 0.3$ (to provide shear) and $V''(0) < 0$ (a central magnetic well). The resulting helical windings are shown in Fig. 1 for $M = 6, 9,$ and 12 . The winding pitch modulation, access to the plasma, and plasma size increase as M decreases. The magnetic configurations have $\iota(\bar{a}) \simeq 1$, high edge shear, a magnetic well usually out to $\iota \simeq \frac{1}{2}$, $A \propto M$, a second stability regime ($\beta_{stab} > \beta_{equil}$), and $\beta_{equil} \propto 1/A$ that increases with decreasing M .

The $M = 6$ Compact Torsatron shown in Fig. 2 has been chosen as the ATF-II reference case. It has half the aspect ratio of ATF, $A = 3.9$, approximately the same $\iota(r)$, and better access for heating and diagnostics. The choice of the device parameters ($B_0 = 4-5$ T,

$R_0 = 2$ m) is determined by constraints on the distance between the plasma edge and the center of the helical winding, on the maximum field on the superconductor, and on cost.

Use of an optimized, forced-flow, cable-in-conduit NbTi/Cu superconductor allows high-current-density (j) operation at high field on the conductor (B_{\max}) with a high stability margin (100 mJ/cm^3) and moderate maximum quench pressures ($<500 \text{ atm}$).⁴ With reasonable assumptions for the thickness of the coil case, cryostat, first wall, etc., a transverse winding elongation $K = 2$ allows $j_{\max} = 7.4 \text{ kA/cm}^2$, $B_{\max} = 8.7 \text{ T}$, a radial coil depth of 21 cm, and a minimum plasma-wall distance of 15 cm. Reducing the liquid helium coolant temperature from 4.2 K to 2.5 K allows operation at $B_0 = 5 \text{ T}$ with $j = 9.3 \text{ kA/cm}^2$ and $B_{\max} = 11 \text{ T}$ for the same helical windings.

The $M = 6$ ATF-II would occupy roughly the same space as ATF. Its major radius ($R_0 = 2$ m) would be 5% smaller than that of ATF, and the outer diameter of the vacuum vessel (6.1 m) would be only 13% larger. ATF-II would have 1.9 times the plasma radius ($\bar{a} = 0.52$ m) and 3.5 times the plasma volume (10.6 m^3) of ATF, and the large outer ports ($2.1 \text{ m} \times 1 \text{ m}$) would have 3.9 times the area of those on ATF. The maximum field would be 5 T steady state, compared with a 5-s limit at the maximum field of 2 T for the copper-coil ATF. The maximum force on the helical winding is 25 MN/m at $B_0 = 5 \text{ T}$, and the length of the helical winding (and the cooling path) is 16 m.

Studies of Compact Torsatrons show that they could be attractive steady-state reactors.⁵ Figure 3 shows a side view of an $M = 9$ reactor. This reactor would have $R_0 = 10.54$ m, $\bar{a} = 2.26$ m, 72% of the surface area available for tritium breeding, a total weight of 11,040 tonnes, an average neutron wall loading $\Gamma_n = 2.7 \text{ MW/m}^2$, a total thermal power of 5.27 GW (including energy multiplication in the Be-rich blanket), and a mass utilization of 172 kW/tonne assuming a net electrical efficiency of 36%. WHIST 1-D transport code calculations for stellarators give $T_i(0) = 10.4 \text{ keV}$, $T_e(0) = 11.1 \text{ keV}$, and $\langle\beta\rangle = 6.3\%$ at $\langle n_e \rangle = 2 \times 10^{20} \text{ m}^{-3}$ with ≈ 30 MW required for ignition. An $M = 6$ reactor would be smaller ($R_0 = 8.37$ m and 9,386 tonnes total weight) and have higher mass utilization (206 kW/tonne), but it would have higher plasma parameters [$\Gamma_n = 3.4 \text{ MW/m}^2$, $T_i(0) = 11.9 \text{ keV}$, $T_e(0) = 12.7 \text{ keV}$, $\langle\beta\rangle = 7.2\%$] and require more power (≈ 33 MW) for ignition.

3. Confinement Studies

Estimates of the plasma parameters expected in ATF-II are obtained from the LHD scaling law⁶ $\tau_E = 0.17P^{-0.58}\bar{n}_e^{0.68}B_0^{0.84}\bar{a}^{2.0}R_0^{0.75}$, coupled with a density limit scaling⁶ $\bar{n}_{e,\max} = 0.25(PB_0/\bar{a}^2R_0)^{1/2}$, and from our new 1-D steady-state transport code.⁷ Plasma parameters from the scaling laws are given in Table 1 for cases with $P = 10$ MW and parabolic profiles for n and T . The last row of Table 1 shows the effect of a factor of 2 improvement in τ_E . For more peaked (parabolic-squared) profiles for n and T , these values are multiplied by 1.25 for $n_0\tau_E$, 1.33 for T_0 , and 1.67 for β_0 .

A fast and efficient 1-D steady-state transport code that uses a Chebyshev collocation method and that includes alpha-particle losses and ∇p -limiting terms in addition to the usual transport terms has been developed. Code results for the base ATF-II case are shown in Fig. 4. This figure shows contours of constant auxiliary heating power (solid lines) and central ion temperature (dashed lines) in a volume-averaged density versus density-averaged temperature ($\langle n \rangle$ vs $\langle T \rangle$) plane. The results depend sensitively on the assumed electrostatic potential profile $\Phi(r)$. In general, the results are comparable to or better than those obtained from the LHD scaling. For reactors, a negative potential, which could be maintained until thermal runaway to ignition by energetic (~ 50 -kV) perpendicular neutral beam injection, looks more attractive than a positive potential. It allows lower temperature operation at higher density and some degree of burn control, and it is less sensitive to the density profile. Although higher heating power (~ 100 MW) and some modest power to

the sacrificial perpendicular neutral beam are required for ignition, the total power is still smaller than that required (continuously) for tokamaks.

A possible limitation of Compact Torsatrons is larger loss of energetic helically trapped ions at lower aspect ratio. Calculation of energetic ion orbits indicates that typically more than half of the helically trapped alpha particles in a reactor are born in a loss region; this is $\simeq 15\text{--}30\%$ of the total alpha-particle population. More alpha-particle energy can be lost by pitch-angle scattering into the loss region during slowing down and by outward shifts of magnetic surfaces as beta increases. These effects have been evaluated using our 1-D transport code, as shown in Fig. 5. The reduced heating by alpha particles increases the temperature (and auxiliary heating power) required for ignition, although only modest startup power (50–100 MW) is needed if a low-density route to ignition is followed. After thermal runaway to ignition, increased alpha-particle losses are beneficial: easier burn control, an effective helium ash removal mechanism, less dilution of the fuel ions, reduced impact on MHD stability, and less sputtering of vacuum vessel walls and divertor plates.

If the energetic particle losses are too severe, they can be reduced significantly through modification of the magnetic field,^{8,9} but this must be done in such a way that the MHD properties are not adversely affected. A seven-parameter specification of the plasma surface is used in an optimization procedure that includes both MHD stability and orbit confinement as well as weak constraints on the central and edge values of τ (for adequate shear). The Mercier criterion is used to evaluate MHD stability and the width of the last closed B_{\min} contour is used to evaluate energetic orbit confinement. Only preliminary, but encouraging, results have been obtained thus far.² Configurations have been found at $\langle\beta\rangle = 2\%$ that have no loss of alpha particles, whereas Compact Torsatrons lose up to $\sim 50\%$ of the alpha-particle energy at this value of beta. Configurations that are Mercier stable at $\langle\beta\rangle = 5\%$ have also been found, but improvement is still needed in their confinement properties. Studies of the windings needed to create these magnetic configurations have started. Some interesting (quasi-helical and modular) winding configurations look possible, but more study is needed to see if they are practical for ATF-II.

In summary, our studies have focused on key physics and engineering issues for a low-aspect-ratio ATF-II. The Compact Torsatron approach is the most developed, but there are concerns about energetic orbit confinement. An integrated (MHD plus orbit) optimization may lead to a better magnetic configuration.

Acknowledgments

This research was sponsored by the Office of Fusion Energy, U.S. Department of Energy, under contract DE-AC05-84OR21400 with Martin Marietta Energy systems, Inc.

References

1. J.F. LYON et al., *Fusion Technol.*, **17**, 188 (1990).
2. J.F. LYON et al., *Fusion Technol.*, **10**, 179 (1986).
3. B.A. CARRERAS et al., *Nucl. Fusion*, **28**, 1195 (1988).
4. J.W. LUE et al., *Proc. 7th Int. Workshop on Stellarators* (IAEA, Vienna, in press).
5. J.F. LYON et al., *Fusion Technol.*, **15**, 1401 (1989).
6. S. SUDO et al., *Nucl. Fusion*, accepted for publication (1989).
7. S.L. PAINTER and J.F. LYON, *Proc. 13th Symp. Fusion Engineering* (IEEE, New York, in press).
8. B.A. CARRERAS et al., ORNL/TM-11101, Oak Ridge National Laboratory (1989).
9. S.L. PAINTER and J.F. LYON, *Fusion Technol.*, **16**, 157 (1989).

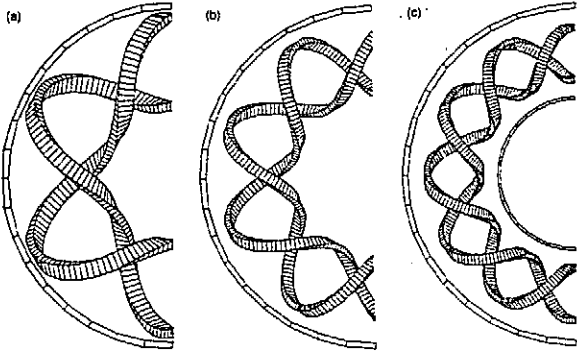


Fig. 1. Compact Torsatrons: (a) $M = 6$, (b) $M = 9$, (c) $M = 12$.

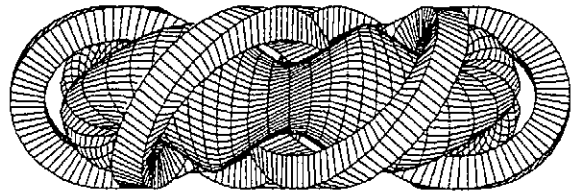
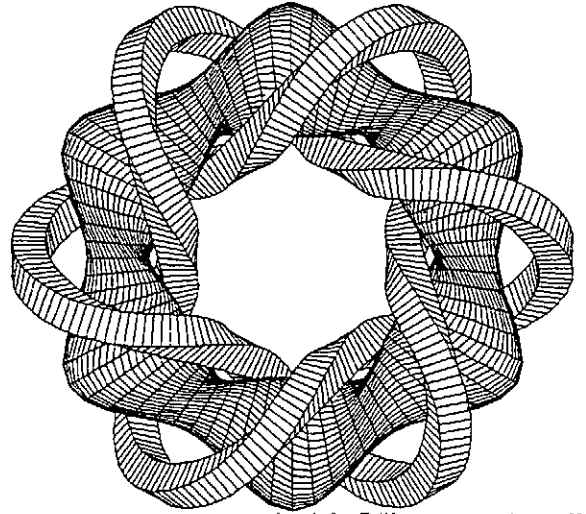


Fig. 2. Top and side views of an $M = 6$ ATF-II.

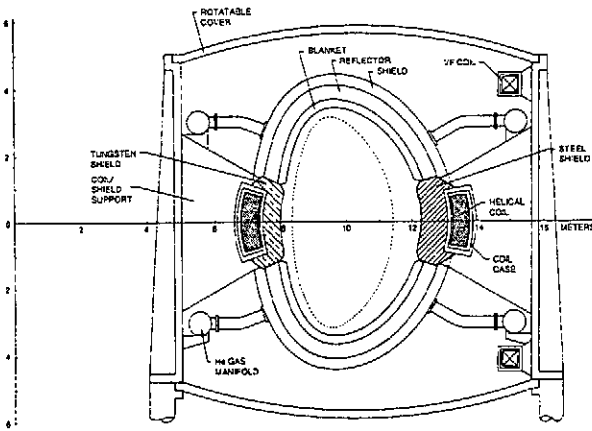


Fig. 3. Cross section of an $M = 9$ reactor.

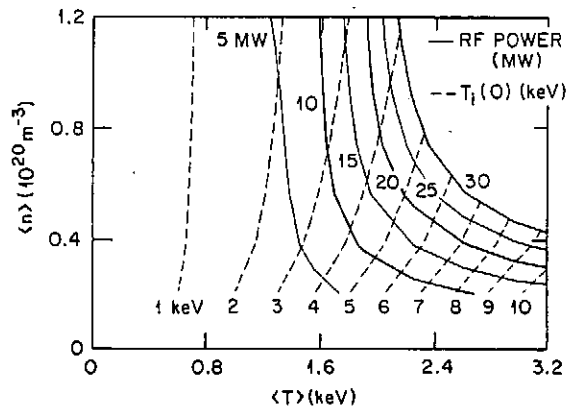


Fig. 4. 1-D transport code results for ATF-II.

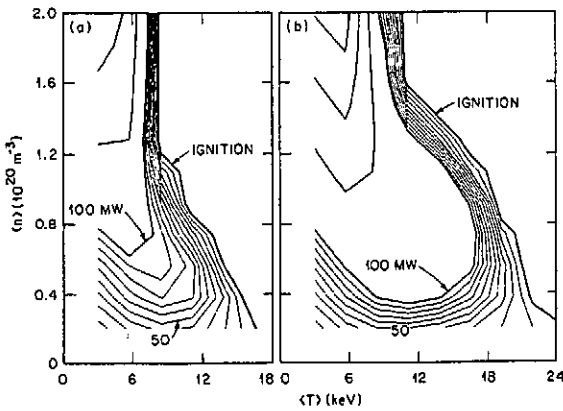


Fig. 5. Heating contours for reactor (a) without and (b) with α -particle losses.

Table 1. Plasma Parameters from LHD Scaling

\bar{n}_e (10^{20} m^{-3})	τ_E (ms)	$n_0 \tau_E$ (10^{19} $m^{-3}s$)	T_0 (keV)	$\langle \beta \rangle$ (%)	β_0 (%)	B_0 (T)
0.25	25	0.094	3.91	0.25	0.74	4
0.5	40	0.30	3.16	0.40	1.19	4
1.0	65	0.98	2.55	0.64	1.92	4
2.15 ^a	110	3.55	2.01	1.08	3.25	4
1.08 ^a	21	0.34	0.78	3.4	10.1	1
2.4 ^a	144	5.2	2.34	0.9	2.7	5
$\bar{n}_{e,max}$	220 ^b	7.1 ^b	7.8 ^b	7 ^c	21 ^c	

^a $\bar{n}_e = \bar{n}_{e,max}$; ^b At $B_0 = 4$ T; ^c At $B_0 = 1$ T

REVIEW OF THE TJ-II FLEXIBLE HELIAC PROJECT

TJ-II Team¹, presented by A.P. Navarro

Asociación EURATOM / CIEMAT para Fusión

28040 Madrid, SPAIN

ABSTRACT

TJ-II is a device oriented to the study of the properties of helical magnetic axis plasmas in a wide range of configurations. Design of the device, to be built at CIEMAT site, has been oriented to provide as much flexibility as possible in the magnetic structure. Design parameters are $R_0 = 1.5$ m and $B_0 = 1$ T in a 4 periods symmetry. A central core composed by two different coils enables to obtain, by adequate setting of the current in each coil, different magnetic configurations with the following flexibility ranges: $t/M \approx 0.24$ to 0.62 , plasma radius $\approx 0.2 - 0.1$ m, shear $\approx -1\%$ to $+10\%$ and magnetic well ≈ 0 to 6% . Plasma startup and heating will be based on ECH, by using 2 gyrotrons 200 kw each, cw at 53.2 GHz.

In this paper, we review the physics studies for such configurations in different areas: Equilibrium, deducing the operational space for TJ-II; Stability, with special emphasis on β limits and access to second stability regime; Heating, discussing the optimization of absorption and the adopted ECH scheme; and Transport, deducing confinement properties for the different heating scenarios. In addition, the experimental programme to develop in this device and the engineering solutions found for the most critical elements of the TJ-II heliac during its detailed design will be discussed.

1. C. Alejaldre, L. Almoguera, J. Alonso, E. Anabitarte, E. Ascasibar, M. Blaumoser¹, J. Botija, B. G. Castañer, F. Castejón, J. R. Cepero, A. Cucchiaro², T. Estrada, J. Guasp, A. L. Fraguas, J. B. Galván, L. García³, A. Grau, C. Hidalgo, V. Krivenski, M. Liniers, R. Martín, J. Moreno, A. P. Navarro, M.A. Ochando, C. Pardo, M. A. Pedrosa, A. Perea, A. Pizzuto², L. Rodríguez, A. Rodríguez-Yunta, A. Salas, J. Sanchez, J. Sentfés⁴, M. Sorolla, F. Tabarés, V. Tribaldos, A. Varias, J. Vega, B. Zurro.

1 IPP-Garching

2 ENEA - Frascati

3 Univ. Complutense, Madrid

4 Univ. Cantabria, Santander

The ANU Heliac Program

R.L. Dewar, H.J. Gardner, G.J. Cooper,
Department of Theoretical Physics
S.M. Hamberger, L.E. Sharp, B.D. Blackwell, T.Y. Tou,
G.D. Conway, X.-H. Shi, D.-F. Zhou, J. Howard,
Plasma Physics Laboratory
Research School of Physical Sciences
The Australian National University

B.A. Carreras, N. Dominguez, V.E. Lynch,
Oak Ridge National Laboratory, U.S.A.

Abstract

The history and current status of experimental and theoretical work on heliacs at the Australian National University is reviewed.

Introduction

The need for a plasma containment device which is suitable, in reproducibility of conditions, ease of operation, and cost, for basic plasma physics experiments and yet can come close to the confinement, density and temperature parameters of medium sized fusion experiments has led to the adoption at the Australian National University (ANU) of the flexible heliac concept [1,2]. A table-top sized apparatus, SHEILA, was built in 1984 as a first prototype, with the limited aims of demonstrating the existence of closed magnetic surfaces in a heliac configuration and of comparing the magnetic field geometry actually produced with that predicted by numerical calculation. Despite the small size of the apparatus, it has also been possible to perform several experiments on the properties of the plasma produced in and confined by its magnetic fields. The initial experimental results verifying the existence of a low-pressure equilibrium in this apparatus were reported briefly in 1985 [3]. A helical control winding was added to SHEILA during 1986, and the results of its effect on plasma formation and confinement reported to the IAEA plasma physics conference later that year [4], and in more detail in [5]. Breakdown has been achieved by low amplitude, low frequency oscillation of the current in the central conductor and by electron cyclotron heating at the fundamental and second harmonic [6]. A detailed description of the machine may be found in [7].

A much larger device, H-1, capable of operating under conditions relevant to fusion is under construction [8]. Its design largely follows the successful experience on SHEILA in adopting the same three-field period ($N = 3$) configuration, and thus complements the $N = 4$ design adopted by CIEMAT for the TJ-II Heliac, roughly comparable in size, optimized mainly for high- β studies. The H-1 magnetic configuration has been optimized for low aspect ratio (≈ 5), minimum $|B|$ ripple by modulation of the toroidal field coils and by optimization of the vertical field magnitude and index [9]. Heating is planned initially to rely on fast wave ion cyclotron heating [10], with ion Bernstein, whistler wave and electron heating to be investigated later.

Table I
Parameters of Canberra Heliacs

	SHEILA	H-1
No. of field periods	3	3
No. of toroidal coils	24	36
Mean radius of toroidal coils (m)	0.065	0.383
Swing radius of toroidal coils (m)	0.025	0.22
Major radius (m)	0.19	1.0
Typical mean minor plasma radius (m)	0.03	0.20
Plasma volume (m ³)	0.004	0.91
Max. field (T)	0.4	0.25/1.0
Duration (s)	0.04	∞/1
Max. ring current (kA)	28	500
Mean radius of control helix (mm)	1.4	96
Dia. of vacuum enclosure (m)	0.6	3.9
RF heating power (kW)	0.4	200

One of the main contributions of university scale research in plasma physics is the development of novel diagnostic methods. Diagnostics being developed include a novel multi-view scanning interferometer [11].

Magnetic surface studies on SHEILA

Magnetic surfaces have been computed by field line tracing and show the expected sensitivity to the changing rotational transform profile as the current in the helical winding is varied. The electric field required for breakdown and the central plasma density achieved for otherwise constant conditions have been measured as the configuration was changed in the range $0.7 < \iota < 1.86$ [5]. The 'worst' conditions for plasma formation, characterized by sharp dips or gaps in the density or sharp peaks in the breakdown field, clearly corresponded to the presence of the low order resonances $\iota = 1$ and $\iota = 3/2$. The case, $\iota = 3/2$ corresponds to the breaking up of the confinement region into two main islands, while loss of confinement when $\iota \sim 1$ is related to the complete absence of closed flux surfaces, found when symmetry breaking errors are included in the computation. Results from both RF and ECR produced plasmas are essentially the same. Plasma isobars obtained from local measurements agree closely with computed magnetic flux surfaces [7]. Measured pressure profiles [5] also showed distinctly a flattening in regions which the computations showed to have chaotic field lines. Surfaces have also been mapped using an electron beam [12], showing excellent agreement with the computations.

Drift wave studies on SHEILA

By an appropriate choice of experimental conditions the fluctuation spectrum in SHEILA can be reduced to a single, coherent mode whose eigenstructure has been studied [13] using a set of Langmuir probes in the form of fixed arrays which can be pre-set to sample around a given flux surface, or as a pair of one fixed and one articulated probe which can sample throughout a given cross-section.

Detailed studies have been made for three configurations characterised by quite different ι profiles. Fluctuation data is Fourier analysed in the form

$$\tilde{n}_e = \sum_{m,n} \tilde{n}_e(r) \exp i(m\vartheta - n\phi)$$

where m and n are the poloidal and toroidal mode numbers, and the flux coordinates are defined as follows: r is the mean radius of a flux-surface, ϕ is the usual toroidal coordinate and ϑ is a poloidal coordinate chosen to keep the field lines straight.

A simplified two-fluid drift wave model, in periodic cylindrical geometry, has been used to analyse the results by making the simple assumption that the magnetic coordinates r and ϑ can be identified with their cylindrical counterparts. The predicted real part of the frequency for the mode with m and n chosen for maximum growth rate agrees remarkably well with the measurements when plotted against collision frequency. The dependence of the saturated amplitude on field and collision frequency correlates qualitatively with that of the predicted linear growth rate, though the theory predicts a lower threshold, indicating a stabilization mechanism not included in this simple theory.

Confinement degradation, as evidenced by a turnover in the curve of density vs. magnetic field, shows a clear correlation with the onset of these fluctuations.

The fact that a reasonable understanding of this important plasma instability can be obtained with a simple theory confirms the appropriateness of the heliac for basic plasma physics studies, which are needed for an understanding of anomalous transport mechanisms in fusion devices. A more detailed theoretical understanding, requiring a fully three dimensional calculation, would be a major computational challenge.

Computational Equilibrium and Stability Studies

A free boundary equilibrium code FEQ2.5 to compute helically invariant ('straight') models of heliac and other stellarator equilibria has been developed at ANU [14,15]. More recently [16] a Green's function method for calculating the vacuum energy for straight helical equilibria has been implemented in the Princeton/ANU PEST2.5 [17] stability code and validated by comparison studies with the Lausanne/Garching HERA code.

The Oak Ridge DESCUR (plasma boundary fitting) and VMEC [18] (three dimensional equilibrium) codes have been installed on the ANU Fujitsu VP-100. Attempts to use them for Mercier and ballooning instability studies of optimized pressure profiles have been so far frustrated by the inability of VMEC to converge on a sufficiently accurate equilibrium when using the large numbers of Fourier modes necessitated by H-1's relatively low aspect ratio. A new version of VMEC using a preconditioning method to accelerate convergence has recently been developed at Oak Ridge and has been used successfully to compute fixed boundary equilibria (Fig. 1) which should be adequate for stability studies. Using 113 Fourier modes and 31 radial mesh points, a zero pressure equilibrium with mean square force residuals $< 10^{-11}$, and a case with peak β of 7% and residuals $< 10^{-9}$ have been generated. Preliminary Oak Ridge work has indicated that the β limit for Mercier instabilities in H-1 may be less than 1% in some configurations due to large pressure driven currents, although further work with the new accurate equilibria, optimized pressure profiles and a sequence of equilibria resulting from systematic changes in coil currents needs to be undertaken to determine the actual limit. Low

limits are necessary for the purposes of basic research with modest heating powers to make the thresholds accessible for study.

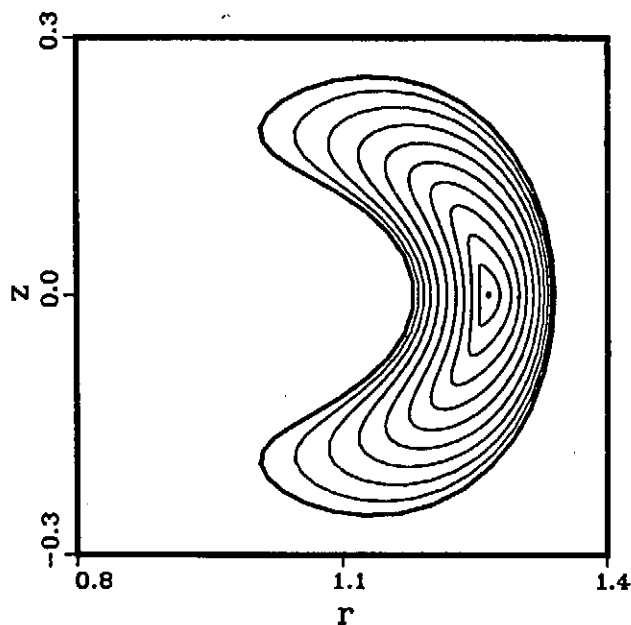


Fig. 1 VMEC plot of contours of $\sqrt{\psi}$ for a central β of 7%. Hard core current 444 kA, TF current 138.89 kA, helical current 150 kA.

Acknowledgments

It is a pleasure to acknowledge helpful discussions with Dr J.L. Johnson. We also wish to thank Dr A.B. Ehrhardt for her Heliac field line tracing code and Dr S.P. Hirshman for his VMEC code. We also acknowledge the ANU Supercomputer Facility for providing time on the ANU Fujitsu VP-100.

References

- [1] Boozer, A.H., Chu, T.-K., Dewar, R.L., Furth, H.P., *et al.* in Plasma Physics and Controlled Fusion Research (Proc. 9th Int. Conf., Baltimore 1982) **III** IAEA, Vienna (1983) 129; Yoshikawa, S., *Nucl. Fusion* **23**(1983) 667.
- [2] Harris, J.H., Cantrell, J.L., Hender, T.C., Carreras, B.A., Morris, R.N., *Nucl. Fus.*, **25**(1985) 623.
- [3] Blackwell, B.D., Hamberger, S.M., Sharp, L.E., Shi, X.-H. *Nucl. Fusion* **25**(1985) 1485.
- [4] Blackwell, B.D., Dewar, R.L., Gardner, H.J., Hamberger, S.M., Sharp, L.E., Shi, X.-H., Vance, C.F., Zhou, D.-F. in Plasma Physics and Controlled Fusion Research (Proc. 11th Int. Conf. Kyoto, 1986) **II**, 511, IAEA, Vienna (1987)
- [5] Shi, X.-H., Hamberger, S.M., Blackwell, B.D., *Nucl. Fusion* **28**(1988) 859.
- [6] Conway, G.D., Blackwell, B.D., Proceedings of the 7th International Workshop on Stellarators & IAEA Tech. Meeting, Oak Ridge, Apr. 10-14, 1989 (SW89).
- [7] Blackwell, B.D., Hamberger, S.M., Sharp, L.E., Shi, X.-H., *Aust. J. Phys.* **42**(1989) 75.
- [8] Hamberger, S.M., Blackwell, B.D., Sharp, L.E., Shenton, D.B., SW89.
- [9] Sharp, L.E., Blackwell, B.D., Tou, T.Y., SW89.
- [10] Blackwell, B.D., Conway, G.D., SW89.
- [11] Howard, J., Sharp, L.E., SW89.
- [12] Blackwell, B.D., Tou, T.Y., SW89.
- [13] Shi, X.-H., Blackwell, B.D. and Hamberger, S.M., *Plasma Phys. Contr. Fusion*, **31** in press.
- [14] Gardner, H.J., Dewar, R.L., Sy, W.N.-C., *J. Comp. Phys.* **74**(1988) 477.
- [15] Dewar, R.L., Gardner, H.J., *J. Comp. Phys.* **77**(1988) 485.
- [16] Cooper, G.J., *Stability of Helical Plasmas* (ANU Ph.D. thesis, submitted 1989).
- [17] Dewar, R.L., Monticello, D.M., Sy, W.N.-C., *Phys. Fluids* **27**(1984) 1723.
- [18] Hirshman, S.P., van Rij, W.I., Merkel, P. *Comput. Phys. Commun.* **43**(1986) 143.

DESIGN OF THE COMPACT AUBURN TORSATRON

R.F. Gandy, M.A. Henderson, J.D. Hanson, T. Schneider, D.G. Swanson
Physics Department

Auburn University, Ala., USA 36830

J.R. Cary

Department of Astrophysical, Planetary, and Atmospheric Sciences
University of Colorado
Boulder, Colo., USA 80309

Abstract

The Compact Auburn Torsatron (CAT) is a low-aspect ratio, continuous coil, toroidal magnetic fusion device. CAT has two main helical coils : an $\ell=2, m=5$ coil, and an $\ell=1, m=5$ coil. The machine has a major radius of 56 cm, an average plasma radius of 11 cm, and a steady-state magnetic field of 1 kG. CAT was designed using an optimization scheme which employs the coil positions and coil winding laws as parameters. Once CAT is operational, the research program will focus on the study of magnetic flux surfaces and ion cyclotron heating.

I. INTRODUCTION

The Compact Auburn Torsatron (CAT) is a low-aspect-ratio torsatron currently under construction at Auburn University and scheduled for completion in spring 1990. The machine will replace the Auburn Torsatron ¹ which has been operating since 1984. The design of CAT was done using the Cary-Hanson Optimization technique²⁻⁴. This procedure minimizes the islands which form at rational magnetic surfaces by varying the placement and winding law parameters of the coils. The reduction of the island size effectively increases the plasma volume. In the optimization process the helical field coils are modulated from a straight winding law by the addition of $\alpha_n \sin(n\theta)$ terms, (where θ is the poloidal angle and n is an integer). As well as verifying the Cary-Hanson Optimization technique, CAT will be used to study various magnetic configurations, island sizing and reduction, island effects on the plasma, and the physics of ion cyclotron heating.

The design of CAT is unique among stellarator devices in that it will have two helical field (HF) coils. It will also have the standard set of outer vertical field (VF) coils, and a set of inner VF coils. The main component of the HF is provided by the $\ell=2, m=5$ coil which has an aspect ratio $A_c=1.9$. Here ℓ and m refer to the toroidal and poloidal periodicity of the magnetic field, respectively. An additional component of the HF is provided by $\ell=1, m=5$ coil with an aspect ratio $A_c=2.6$. This second coil is required to keep the magnetic axis circular. The outer VF coils have a radius of 85 cm and are located at $z = \pm 19$ cm. An inner set of VF coils will also be used in the various configuration studies, the location is currently undecided. All of the coils will be water cooled to provide steady state operation at 1 kG field strength.

The machine is compact with a vacuum vessel aspect ratio $A_v=3$ and a plasma aspect ratio $A_p \approx 5$. CAT will have rotational transform ($\tau \equiv 1/q$), $\tau_0 \approx 0.3$ on axis, $\tau \approx 0.6$ at the edge, moderate shear, and a magnetic well. Each coil (VF and HF) is designed to allow adjustments to the current centers to optimize the magnetic surfaces. CAT also has the flexibility of adding various helical and toroidal trim coils to further optimize the vacuum magnetic surfaces.

In stellarator construction a great deal of effort is taken in accurately positioning the coils. This effort increases the cost of the device. The previously mentioned trim coils can be used to make adjustments to the current centers and account for small winding errors⁵. Therefore the precision requirements can be relaxed in the building phase of the device. The control of the plasma boundary, which is crucial for impurity control and divertor action, can also be optimized using these trim coils. The CAT vacuum vessel is simple in design and therefore economical. The vessel has a circular cross section and is made of commercially available SS pipe. These design

features of CAT, coupled with its relatively low-aspect-ratio, make the machine interesting from a torsatron reactor design perspective.

II. DESIGN & OPTIMIZATION PROCEDURE

Recently, considerable effort has been given to the detection of islands that occur at rational surfaces ^{7,8} through investigating the vacuum magnetic flux surfaces. Recent work on the Auburn Torsatron ⁵ has demonstrated the capability to optimize the magnetic surfaces using trim coils. This procedure should lead to a corresponding increase in the plasma confinement time and density. The process of minimizing the island size is uncertain. One purpose of CAT is to provide a test-bed for the reduction of magnetic islands through modifications in the magnetic configuration using trim coils. This investigation requires a significant amount of machine time devoted to vacuum surface mapping. This would be impractical on larger machines, where plasma operation is the main goal. However a small research device such as CAT is ideally suited to thoroughly investigate an important reactor issue such as this.

The general design goal of CAT was to design a low-aspect-ratio torsatron. The Cary-Hanson optimization technique was used to accomplish this goal. The pre-conditions of the design were : (1) design a $\ell=2$ torsatron, (2) keep the m number as low as possible to maximize access, (3) have moderate shear with $\tau_0 \approx 0.3$, (4) have a near circular magnetic axis, and (5) have an plasma aspect ratio ≤ 5 . Since the CAT research program focuses on magnetic island studies, care was taken to insure that the rotational transform profile had as many relevant rational surfaces as possible. Another constraint on the machine design was to insure the presence of the $\tau = 1/2$ surface in the rotational transform profile. The $\tau = 1/2$ surface, being a low order rational surface, will characteristically display a large island compared to most other rational surfaces, since island size typically decreases as order number increases.

The Cary-Hanson optimization technique²⁻⁴ was used to design the machine. The technique minimizes the stochasticity of the field line flow and thereby maximizes the enclosed plasma volume. This process calculates the residuals associated with selected rational field lines. The magnitude of the residuals of a rational are directly related to the size of the magnetic island formed at that particular rational. The magnetic field modeling was done with the Integrable Field Stellarator (IFS) code³. The coils are represented as a collection of connected straight line filaments. The filament endpoints lie on a continuous curve called the winding law. A convenient parameterization for the helical coil winding law is

$$\phi = \frac{\ell \theta}{m} \pm \sum \alpha_n \sin(n\theta)$$

where $\phi(\theta)$ is the toroidal (poloidal) angle, and the \pm refer to the two components of the main helical coil.

Several configurations were investigated to yield the optimal machine. Ultimately the $\ell=2$, $m=5$ torsatron with an inner $\ell=1$, $m=5$ minor coil was chosen as the best candidate in view of construction limitations and machine parameters. The parameters of the machine were systematically modified to minimize chaotic field lines, yet keep the rotational transform on axis at the required value. The list of parameters includes the currents in each coil, coil aspect ratios, coil locations, the α_1 term of the $\ell=1$ coil, and the $\alpha_1, \alpha_2, \alpha_3$ terms of the $\ell=2$ coil (all other α_n values were set = 0). The procedure also kept the magnetic axis locked to the vacuum vessel axis (within 2 mm) at every field period and also at every half field period.

CAT was designed using a multi-filament model for each coil. Due to the low-aspect-ratio of CAT several filaments per helical coil (typically 16) were required to closely model the real coil situation. The final winding law obtained for the $\ell=2$ coil is:

$$\phi = \frac{2\theta}{5} - 0.21 \sin(\theta) + 0.04 \sin(2\theta) - 0.02 \sin(3\theta)$$

and for the $\ell=1$ coil:

$$\phi = \frac{\theta}{5} - 0.1 \sin(\theta)$$

III. MACHINE DESIGN

A. Vacuum Vessel

The vacuum vessel for CAT was designed to be approximately the same size as the existing Auburn Torsatron. A simple design was chosen to minimize machining costs. As mentioned earlier, the major part of the vacuum vessel is formed by welding four 90° bends together to form the torus. The wall thickness of the bends are 0.48 cm and made of 306 stainless steel. The tolerances on the machining of the torus are somewhat relaxed to further reduce costs, ± 0.48 cm over the 53.3 cm major diameter. A layer of epoxy on the vacuum vessel is used to form the actual winding surface for the coil pack. The width of the epoxy is ~ 1.0 cm. This allows 0.5 cm tolerance on both the major and minor radius of the torus and still preserve the capability of forming the correct size toroidal surface with epoxy.

The horizontal ports were designed with a square cross section. This shape allows adequate access while still maintaining a fairly simple machine design. The optimum size of the port was 30 x 30 cm. This specific port size permits a circular screen having the diameter of the vacuum vessel cross section to be passed through the port. This proves convenient for the extensive surface mapping to be performed on CAT. In summary, the low-aspect-ratio feature of CAT allows for good access for plasma diagnostic and heating applications.

B. Winding Process

As previously mentioned, epoxy is placed on the vacuum vessel to define the toroidal surface which the coils will rest on. The purpose of the epoxy is two fold. First, the epoxy provides an extra insulation break between the coils and the vacuum vessel. Second, the epoxy can be shaped and sanded to form a near perfect toroidal surface. This relaxes the machining precision requirements on the torus. The epoxy was chosen for its pliability while curing, machineability, strength and insulation properties. The epoxy is placed on the vacuum vessel (~ 1 cm thick) and sanded to obtain a near toroidal surface (within 1 mm).

Once the epoxy has been shaped and the location of a given coil has been identified on the surface of the epoxy, the vacuum vessel is ready for coil winding. The wire that is wound on CAT is made of soft tempered copper with a dimensions of 0.89 cm x 0.89 cm, and a 0.02 cm coating of Dacron glass insulation. This copper wire has a 0.64 cm diameter hole running along its length. This allows water cooling of the coil pack and steady state operation with a 1.0 kG field (500 Amperes of HF coil current). The cross sectional size of the conductor was determined by the existing power supplies (two 180 Volt, 200 Ampere, DC supplies). Since the length of the CAT coils is similar to the length for the existing Auburn Torsatron, the cross section of the copper was kept approximately the same.

The $\ell=1$ helical coil is wound first and is supported by epoxy on the vacuum vessel. The $\ell=2$ coil is wound next, outside of the $\ell=1$ coil. The $\ell=2$ coil is supported by the $\ell=1$ helical coil and a bridge made of aluminum sheets. The bridge is held in place by standoffs from the vacuum vessel or rests directly on the $\ell=1$ coil pack. The standoffs are again attached by studs welded directly to the vacuum vessel. The aluminum sheets are mounted onto the standoffs and form rigid surfaces on which to apply the epoxy. The epoxy is then shaped to provide a toroidal winding surface for the $\ell=2$ coil. During this process a winding jig is again used to measure the toroidicity of the epoxy as well as to mark the $\ell=2$ coil location.

IV. SURFACE MAPPING SETUP

The research emphasis of CAT will be magnetic island studies. Therefore, extensive work will be done in the field of vacuum magnetic surface mapping. The experimental setup for the surface mapping is modeled after previous experiments ^{1,6}. The phosphor screen technique ^{6,9} will be the primary method of magnetic surface mapping. To a lesser extent the diode technique ^{1,10} of surface mapping will be used. With the phosphor screen method a high transparency screen is coated with sodium salicylate. The sodium salicylate is applied by dissolving it in ethyl alcohol then spraying on the screen with an atomizer. Typically, 5-10 coatings are applied. The screen is then placed in a poloidal plane of the machine. A CCD camera is placed on a horizontal plane with

a view of the screen. An electron beam gun is placed on the opposite side of the machine. The gun is mounted on a probe with two degrees of freedom. The probe allows the positioning of the gun anywhere in the poloidal cross section. Our particular probe has been used for surface mapping on the Auburn Torsatron¹ and has been adapted for use on CAT.

The resulting image formed by the electron beam interacting with the phosphor screen is read from the CCD camera and recorded on a ED-Beta VCR. The VCR provides high resolution (500 horizontal lines) and insures no degradation in the picture quality. Lower resolution VCRs (such as standard VHS recorders) tend to diminish the contrast of the picture. The recorded image from the VCR is displayed on an Apple Macintosh II using an image capture board (Scion Image Capture 2). The image then can be analyzed to determine volume, island size, rotational transform, etc. Software has been written to remove distortion and enhance the image. The sources of distortion include : (1) non-normal viewing angle, (2) camera lens distortion, (3) image capture distortion, and (4) computer monitor display distortion. The overall distortion was measured by viewing a calibration grid with the CCD camera. The distortion of the calibration grid was measured and recorded. The transformation used to remove the distortion from the calibration grid is then used in subsequent surface mapping with the phosphor screen technique.

V. Conclusions

We have presented details of the design of a low-aspect-ratio torsatron, an attractive candidate for a future fusion reactor. The attractive features of low-aspect-ratio torsatrons include: plasma current free operation, good diagnostic and heating access, and flexible magnetic configuration. The first use of the Cary-Hanson optimization technique to design a machine has been demonstrated. CAT will have trim coils to allow detailed studies of the important question of magnetic islands.

ACKNOWLEDGEMENTS

This work was supported under U.S. Department of Energy grant DEFG605-85ER53192C. Jim Hanson was also supported by the United States National Science Foundation, grant NSF-PHY-8451275 with matching grants from Maxwell Laboratories, Inc., TRW Corporation, and Allied Signal Corporation. John Cary was also supported by U.S. Department of Energy grant DEFG02-85ER53207.

REFERENCES

1. Gandy, Henderson, Hanson, Hartwell, and Swanson; "Magnetic Surface Mapping with an Emissive Filament Technique on the Auburn Torsatron", *Review of Scientific Instruments*, **58** (4), p. 509, April 1987.
2. Hanson and Cary, " Elimination of Stochasticity in Stellarators", *Phys. of Fluids*, **27** (4), p. 767, Apr. 1984.
3. Cary and Hanson, " Stochasticity Reduction", *Phys. of Fluids*, **29** (8), p. 2464, Aug. 1986.
4. Cary, *Phys. Rev. Letts.*, "Vacuum Magnetic Fields with Dense Flux Surfaces", **49** (4), p. 276, 1982.
5. Henderson, Gandy, Hanson, Hartwell, and Swanson; " Magnetic Surface Optimization on the Auburn Torsatron", *Nuclear Fusion*, Volume 28, No.6, (1988).
6. Hartwell, Gandy, Henderson, Hanson, and Swanson; "Magnetic Surface Mapping with Highly Transparent Screens on the Auburn Torsatron", *Review of Scientific Instruments*, **59** (3), p. 460, March 1988.
7. Hailer, Massig, Schuler, Schoworer and Zwicker, "Studies of the Magnetic Surfaces in the Stellarator Wega"; *Proc. of the 14th Eur. Conf. on Contrl. Fusion and Plasma Physics*, June 1987.
8. Colchin, Anderson, England, Gandy, Harris, Henderson, Hillis, Kindsfather, Lee, Million, Murakami, Neilson, Saltmarsh and Simpson; "Electron Beam and Magnetic Field Mapping Techniques Used to Determine Field Errors in the ATF Torsatron", *Review of Scientific Instruments*, August 1989.
9. A. V. Georgievskij, Y. V. Gutarev, A. G. Dikij *et al.*, "Proceedings of the 12th European Conference on Controlled Fusion and Plasma Physics," supplement to *Proceedings of the 12th European Conference on Plasma Physics and Controlled Nuclear Fusion Research*, Budapest, Vol. 9F, Part 1 (1985).
10. R. Takahashi, et al., "Measurements of Magnetic Surfaces on Heliotron-E", in *Proc. of Int. Stellarator/Heliotron Workshop, IAEA Tech. Comm. Meeting*, Vol.II, p.220, (1986).

DESIGN OF THE COMPACT AUBURN TORSATRON

R.F. Gandy, M.A. Henderson, J.D. Hanson, T. Schneider, D.G. Swanson

Physics Department

Auburn University, Ala., USA 36830

J.R. Cary

Department of Astrophysical, Planetary, and Atmospheric Sciences

University of Colorado

Boulder, Colo., USA 80309

Abstract

The Compact Auburn Torsatron (CAT) is a low-aspect ratio, continuous coil, toroidal magnetic fusion device. CAT has two main helical coils : an $\ell=2, m=5$ coil, and an $\ell=1, m=5$ coil. The machine has a major radius of 56 cm, an average plasma radius of 11 cm, and a steady-state magnetic field of 1 kG. CAT was designed using an optimization scheme which employs the coil positions and coil winding laws as parameters. Once CAT is operational, the research program will focus on the study of magnetic flux surfaces and ion cyclotron heating.

I. INTRODUCTION

The Compact Auburn Torsatron (CAT) is a low-aspect-ratio torsatron currently under construction at Auburn University and scheduled for completion in spring 1990. The machine will replace the Auburn Torsatron ¹ which has been operating since 1984. The design of CAT was done using the Cary-Hanson Optimization technique²⁻⁴. This procedure minimizes the islands which form at rational magnetic surfaces by varying the placement and winding law parameters of the coils. The reduction of the island size effectively increases the plasma volume. In the optimization process the helical field coils are modulated from a straight winding law by the addition of $\alpha_n \sin(n\theta)$ terms, (where θ is the poloidal angle and n is an integer). As well as verifying the Cary-Hanson Optimization technique, CAT will be used to study various magnetic configurations, island sizing and reduction, island effects on the plasma, and the physics of ion cyclotron heating.

The design of CAT is unique among stellarator devices in that it will have two helical field (HF) coils. It will also have the standard set of outer vertical field (VF) coils, and a set of inner VF coils. The main component of the HF is provided by the $\ell=2, m=5$ coil which has an aspect ratio $A_c=1.9$. Here ℓ and m refer to the toroidal and poloidal periodicity of the magnetic field, respectively. An additional component of the HF is provided by $\ell=1, m=5$ coil with an aspect ratio $A_c=2.6$. This second coil is required to keep the magnetic axis circular. The outer VF coils have a radius of 85 cm and are located at $z = \pm 19$ cm. An inner set of VF coils will also be used in the various configuration studies, the location is currently undecided. All of the coils will be water cooled to provide steady state operation at 1 kG field strength.

The machine is compact with a vacuum vessel aspect ratio $A_v=3$ and a plasma aspect ratio $A_p=5$. CAT will have rotational transform ($\tau \equiv 1/q$), $\tau_0 \approx 0.3$ on axis, $\tau \approx 0.6$ at the edge, moderate shear, and a magnetic well. Each coil (VF and HF) is designed to allow adjustments to the current centers to optimize the magnetic surfaces. CAT also has the flexibility of adding various helical and toroidal trim coils to further optimize the vacuum magnetic surfaces.

In stellarator construction a great deal of effort is taken in accurately positioning the coils. This effort increases the cost of the device. The previously mentioned trim coils can be used to make adjustments to the current centers and account for small winding errors⁵. Therefore the precision requirements can be relaxed in the building phase of the device. The control of the plasma boundary, which is crucial for impurity control and divertor action, can also be optimized using these trim coils. The CAT vacuum vessel is simple in design and therefore economical. The vessel has a circular cross section and is made of commercially available SS pipe. These design

features of CAT, coupled with its relatively low-aspect-ratio, make the machine interesting from a torsatron reactor design perspective.

II. DESIGN & OPTIMIZATION PROCEDURE

Recently, considerable effort has been given to the detection of islands that occur at rational surfaces $7/8$ through investigating the vacuum magnetic flux surfaces. Recent work on the Auburn Torsatron ⁵ has demonstrated the capability to optimize the magnetic surfaces using trim coils. This procedure should lead to a corresponding increase in the plasma confinement time and density. The process of minimizing the island size is uncertain. One purpose of CAT is to provide a test-bed for the reduction of magnetic islands through modifications in the magnetic configuration using trim coils. This investigation requires a significant amount of machine time devoted to vacuum surface mapping. This would be impractical on larger machines, where plasma operation is the main goal. However a small research device such as CAT is ideally suited to thoroughly investigate an important reactor issue such as this.

The general design goal of CAT was to design a low-aspect-ratio torsatron. The Cary-Hanson optimization technique was used to accomplish this goal. The pre-conditions of the design were : (1) design a $l=2$ torsatron, (2) keep the m number as low as possible to maximize access, (3) have moderate shear with $\tau_0 \approx 0.3$, (4) have a near circular magnetic axis, and (5) have an plasma aspect ratio ≤ 5 . Since the CAT research program focuses on magnetic island studies, care was taken to insure that the rotational transform profile had as many relevant rational surfaces as possible. Another constraint on the machine design was to insure the presence of the $\tau = 1/2$ surface in the rotational transform profile. The $\tau = 1/2$ surface, being a low order rational surface, will characteristically display a large island compared to most other rational surfaces, since island size typically decreases as order number increases.

The Cary-Hanson optimization technique²⁻⁴ was used to design the machine. The technique minimizes the stochasticity of the field line flow and thereby maximizes the enclosed plasma volume. This process calculates the residuals associated with selected rational field lines. The magnitude of the residuals of a rational are directly related to the size of the magnetic island formed at that particular rational. The magnetic field modeling was done with the Integrable Field Stellarator (IFS) code³. The coils are represented as a collection of connected straight line filaments. The filament endpoints lie on a continuous curve called the winding law. A convenient parameterization for the helical coil winding law is

$$\phi = \frac{l\theta}{m} \pm \sum \alpha_n \sin(n\theta)$$

where $\phi(\theta)$ is the toroidal (poloidal) angle, and the \pm refer to the two components of the main helical coil.

Several configurations were investigated to yield the optimal machine. Ultimately the $l=2$, $m=5$ torsatron with an inner $l=1$, $m=5$ minor coil was chosen as the best candidate in view of construction limitations and machine parameters. The parameters of the machine were systematically modified to minimize chaotic field lines, yet keep the rotational transform on axis at the required value. The list of parameters includes the currents in each coil, coil aspect ratios, coil locations, the α_1 term of the $l=1$ coil, and the $\alpha_1, \alpha_2, \alpha_3$ terms of the $l=2$ coil (all other α_n values were set = 0). The procedure also kept the magnetic axis locked to the vacuum vessel axis (within 2 mm) at every field period and also at every half field period.

CAT was designed using a multi-filament model for each coil. Due to the low-aspect-ratio of CAT several filaments per helical coil (typically 16) were required to closely model the real coil situation. The final winding law obtained for the $l=2$ coil is:

$$\phi = \frac{2\theta}{5} - 0.21 \sin(\theta) + 0.04 \sin(2\theta) - 0.02 \sin(3\theta)$$

and for the $l=1$ coil:

$$\phi = \frac{\theta}{5} - 0.1 \sin(\theta)$$

III. MACHINE DESIGN

A. Vacuum Vessel

The vacuum vessel for CAT was designed to be approximately the same size as the existing Auburn Torsatron. A simple design was chosen to minimize machining costs. As mentioned earlier, the major part of the vacuum vessel is formed by welding four 90° bends together to form the torus. The wall thickness of the bends are 0.48 cm and made of 306 stainless steel. The tolerances on the machining of the torus are somewhat relaxed to further reduce costs, ± 0.48 cm over the 53.3 cm major diameter. A layer of epoxy on the vacuum vessel is used to form the actual winding surface for the coil pack. The width of the epoxy is ~ 1.0 cm. This allows 0.5 cm tolerance on both the major and minor radius of the torus and still preserve the capability of forming the correct size toroidal surface with epoxy.

The horizontal ports were designed with a square cross section. This shape allows adequate access while still maintaining a fairly simple machine design. The optimum size of the port was 30 x 30 cm. This specific port size permits a circular screen having the diameter of the vacuum vessel cross section to be passed through the port. This proves convenient for the extensive surface mapping to be performed on CAT. In summary, the low-aspect-ratio feature of CAT allows for good access for plasma diagnostic and heating applications.

B. Winding Process

As previously mentioned, epoxy is placed on the vacuum vessel to define the toroidal surface which the coils will rest on. The purpose of the epoxy is two fold. First, the epoxy provides an extra insulation break between the coils and the vacuum vessel. Second, the epoxy can be shaped and sanded to form a near perfect toroidal surface. This relaxes the machining precision requirements on the torus. The epoxy was chosen for its pliability while curing, machineability, strength and insulation properties. The epoxy is placed on the vacuum vessel (~ 1 cm thick) and sanded to obtain a near toroidal surface (within 1 mm).

Once the epoxy has been shaped and the location of a given coil has been identified on the surface of the epoxy, the vacuum vessel is ready for coil winding. The wire that is wound on CAT is made of soft tempered copper with a dimensions of 0.89 cm x 0.89 cm, and a 0.02 cm coating of Dacron glass insulation. This copper wire has a 0.64 cm diameter hole running along its length. This allows water cooling of the coil pack and steady state operation with a 1.0 kG field (500 Amperes of HF coil current). The cross sectional size of the conductor was determined by the existing power supplies (two 180 Volt, 200 Ampere, DC supplies). Since the length of the CAT coils is similar to the length for the existing Auburn Torsatron, the cross section of the copper was kept approximately the same.

The $\ell=1$ helical coil is wound first and is supported by epoxy on the vacuum vessel. The $\ell=2$ coil is wound next, outside of the $\ell=1$ coil. The $\ell=2$ coil is supported by the $\ell=1$ helical coil and a bridge made of aluminum sheets. The bridge is held in place by standoffs from the vacuum vessel or rests directly on the $\ell=1$ coil pack. The standoffs are again attached by studs welded directly to the vacuum vessel. The aluminum sheets are mounted onto the standoffs and form rigid surfaces on which to apply the epoxy. The epoxy is then shaped to provide a toroidal winding surface for the $\ell=2$ coil. During this process a winding jig is again used to measure the toroidicity of the epoxy as well as to mark the $\ell=2$ coil location.

IV. SURFACE MAPPING SETUP

The research emphasis of CAT will be magnetic island studies. Therefore, extensive work will be done in the field of vacuum magnetic surface mapping. The experimental setup for the surface mapping is modeled after previous experiments 1-6. The phosphor screen technique 6,9 will be the primary method of magnetic surface mapping. To a lesser extent the diode technique 1-10 of surface mapping will be used. With the phosphor screen method a high transparency screen is coated with sodium salicylate. The sodium salicylate is applied by dissolving it in ethyl alcohol then spraying on the screen with an atomizer. Typically, 5-10 coatings are applied. The screen is then placed in a poloidal plane of the machine. A CCD camera is placed on a horizontal plane with

a view of the screen. An electron beam gun is placed on the opposite side of the machine. The gun is mounted on a probe with two degrees of freedom. The probe allows the positioning of the gun anywhere in the poloidal cross section. Our particular probe has been used for surface mapping on the Auburn Torsatron¹ and has been adapted for use on CAT.

The resulting image formed by the electron beam interacting with the phosphor screen is read from the CCD camera and recorded on a ED-Beta VCR. The VCR provides high resolution (500 horizontal lines) and insures no degradation in the picture quality. Lower resolution VCRs (such as standard VHS recorders) tend to diminish the contrast of the picture. The recorded image from the VCR is displayed on an Apple Macintosh II using an image capture board (Scion Image Capture 2). The image then can be analyzed to determine volume, island size, rotational transform, etc. Software has been written to remove distortion and enhance the image. The sources of distortion include : (1) non-normal viewing angle, (2) camera lens distortion, (3) image capture distortion, and (4) computer monitor display distortion. The overall distortion was measured by viewing a calibration grid with the CCD camera. The distortion of the calibration grid was measured and recorded. The transformation used to remove the distortion from the calibration grid is then used in subsequent surface mapping with the phosphor screen technique.

V. Conclusions

We have presented details of the design of a low-aspect-ratio torsatron, an attractive candidate for a future fusion reactor. The attractive features of low-aspect-ratio torsatrons include: plasma current free operation, good diagnostic and heating access, and flexible magnetic configuration. The first use of the Cary-Hanson optimization technique to design a machine has been demonstrated. CAT will have trim coils to allow detailed studies of the important question of magnetic islands.

ACKNOWLEDGEMENTS

This work was supported under U.S. Department of Energy grant DEFG605-85ER53192C. Jim Hanson was also supported by the United States National Science Foundation, grant NSF-PHY-8451275 with matching grants from Maxwell Laboratories, Inc., TRW Corporation, and Allied Signal Corporation. John Cary was also supported by U.S. Department of Energy grant DEFG02-85ER53207.

REFERENCES

1. Gandy, Henderson, Hanson, Hartwell, and Swanson; "Magnetic Surface Mapping with an Emissive Filament Technique on the Auburn Torsatron", *Review of Scientific Instruments*, **58** (4), p. 509, April 1987.
2. Hanson and Cary, "Elimination of Stochasticity in Stellarators", *Phys. of Fluids*, **27** (4), p. 767, Apr. 1984.
3. Cary and Hanson, "Stochasticity Reduction", *Phys. of Fluids*, **29** (8), p. 2464, Aug. 1986.
4. Cary, *Phys. Rev. Letts.*, "Vacuum Magnetic Fields with Dense Flux Surfaces", **49** (4), p. 276, 1982.
5. Henderson, Gandy, Hanson, Hartwell, and Swanson; "Magnetic Surface Optimization on the Auburn Torsatron", *Nuclear Fusion*, Volume 28, No.6, (1988).
6. Hartwell, Gandy, Henderson, Hanson, and Swanson; "Magnetic Surface Mapping with Highly Transparent Screens on the Auburn Torsatron", *Review of Scientific Instruments*, **59** (3), p. 460, March 1988.
7. Hailer, Massig, Schuler, Schoworer and Zwicker, "Studies of the Magnetic Surfaces in the Stellarator Wega"; *Proc. of the 14th Eur. Conf. on Contrl. Fusion and Plasma Physics*, June 1987.
8. Colchin, Anderson, England, Gandy, Harris, Henderson, Hillis, Kindsfather, Lee, Million, Murakami, Neilson, Saltmarsh and Simpson; "Electron Beam and Magnetic Field Mapping Techniques Used to Determine Field Errors in the ATF Torsatron", *Review of Scientific Instruments*, August 1989.
9. A. V. Georgievskij, Y. V. Gutarev, A. G. Dikij *et al.*, "Proceedings of the 12th European Conference on Controlled Fusion and Plasma Physics," supplement to *Proceedings of the 12th European Conference on Plasma Physics and Controlled Nuclear Fusion Research*, Budapest, Vol. 9F, Part 1 (1985).
10. R. Takahashi, et al., "Measurements of Magnetic Surfaces on Heliotron-E", in *Proc. of Int. Stellarator/Heliotron Workshop, IAEA Tech. Comm. Meeting*, Vol. II, p.220, (1986).

First International Toki Conference
December 4-7, 1989
Toki, Japan

Optimization of Helias Configurations

J. NÜHRENBERG

*Max-Planck-Institut für Plasmaphysik
IPP-EURATOM Association
D-8046 Garching bei München
Federal Republic of Germany*

Abstract

The Helias optimization procedure is outlined. Evidence for the convergence behaviour in stellarator configurational space is presented. The hierarchy of optimization is described. Details of the optimization of Helias configurations for W VII-X, i.e. the attainability and compatibility of seven stellarator-specific goodness criteria, are given in the subsequent IEA workshop.

1. Introduction

The plasma behaviour in the confinement region can be optimized by noting that the geometry of the confinement boundary which may be described by the last closed flux surface completely determines the properties of the confinement region. Thus, boundary value problems may be solved during optimization, the parameters of the boundary being the optimization variables. Here, examples of optimizations are used to study the convergence behaviour in this parameter space.

2. Examples for Optimizations

The structure of the optimization space has been described earlier [1, 2, 3]. Details of the choice of variables have been examined to address the question which variables have to be used to obtain complete convergence of an optimization. Here, examples are presented.

A structurally simple and particularly convincing example is the construction of quasi-helically symmetric configurations [2, 3]. For given aspect ratio A and number of periods N , the symmetry of the strength of the magnetic field $B = B(s, \theta - \phi)$ in magnetic coordinates s, θ, ϕ is established by optimization in a 22-dimensional space of variables. For the example $A = 14, N = 7$, the space of variables and their resulting values are shown in Table I. The fact that the computational proof of quasi-helical symmetry is essentially complete is demonstrated in Table II, which shows the Fourier components of B at half radius and at the boundary. Across the entire cross-section the Fourier coefficients with $m \neq n$ are $\mathcal{O}(10^{-3})$. Flux surface cross-sections of this example are shown in the middle row of Fig. 1.

A significant degree of freedom in the boundary parameter space is found for quasi-helically symmetric equilibria [3]. Here, this freedom is used in the form, that $R_{m,m}, Z_{m,m}, m \geq 1$ may be specified. Top and bottom of Fig. 1 show examples for $R_{1,1} = -Z_{1,1} = 0.3$ and 0.1 , respectively.

Other examples of optimization of the structure of B in magnetic coordinates are suggested by considering various other physics goals, see next section. The question whether the same space of variables is essentially complete is being investigated.

	0	1	2	3	4
-2		0.002			
-1		0.001	-0.021		
0	14.0	1.012	0.045	0.008	
1	1.431	-0.225	0.229	-0.011	
2	0.119	-0.049	0.000	0.032	
3	0.003	-0.004	0.019	0.000	0.006
4			0.005	-0.007	

Table I: Boundary coefficients $R_{m,n}$ for the configuration shown in the middle row of Fig. 1; $R = \sum R_{m,n} \cos(mU - nV)$, $m \geq 0$, $-2 \leq n \leq 4$.

	0	1	2	3	4
-2		0.002			
-1		0.001	-0.021		
0	0.000	0.988	0.028	0.008	
1	-1.335	0.225	0.264	0.011	
2	-0.119	0.049	0.000	0.032	0.000
3	-0.003	0.004	-0.018	0.000	-0.006
4			-0.005	0.007	

Same as above, but $Z_{m,n}$; $Z = \sum Z_{m,n} \sin(mU - nV)$.

	0	1	2	3	4	5
-2	0.	0.	0.	0.	0.	0.
-1	0.	0.	0.	0.	0.	0.
0	1.214	0.	0.001	0.	0.	0.
1	-0.001	-0.128	0.	0.	0.	0.
2	0.	0.	0.	0.	0.	0.
3	0.	0.	0.	0.	0.	0.
4	0.	0.	0.	0.	0.	0.
5	0.	0.	0.	0.	0.	0.

Table II: Fourier coefficients $B_{m,n}$; $B = \sum B_{m,n} \cos 2\pi(m\theta - n\phi)$, $m \geq 0$, $-2 \leq n \leq 5$ at $s \approx \frac{1}{2}$ of the configuration shown in row 2 of Fig. 1. Coefficients whose absolute value is smaller than 0.0005 are indicated by 0.

	0	1	2	3	4	5
-2	0.	0.	0.	0.	0.	0.
-1	0.	0.001	0.	0.	0.	0.
0	1.225	0.	0.001	0.001	-0.001	0.
1	-0.004	-0.268	0.001	-0.001	-0.001	0.
2	0.002	0.	0.	0.001	-0.001	0.
3	0.	0.	-0.002	0.	0.001	0.001
4	0.	0.	0.001	0.001	0.001	-0.001
5	0.	0.	0.	0.	-0.002	0.

Same as above, but at $s \approx 1$. Coefficients whose absolute value is smaller than 0.0005 are indicated by 0.

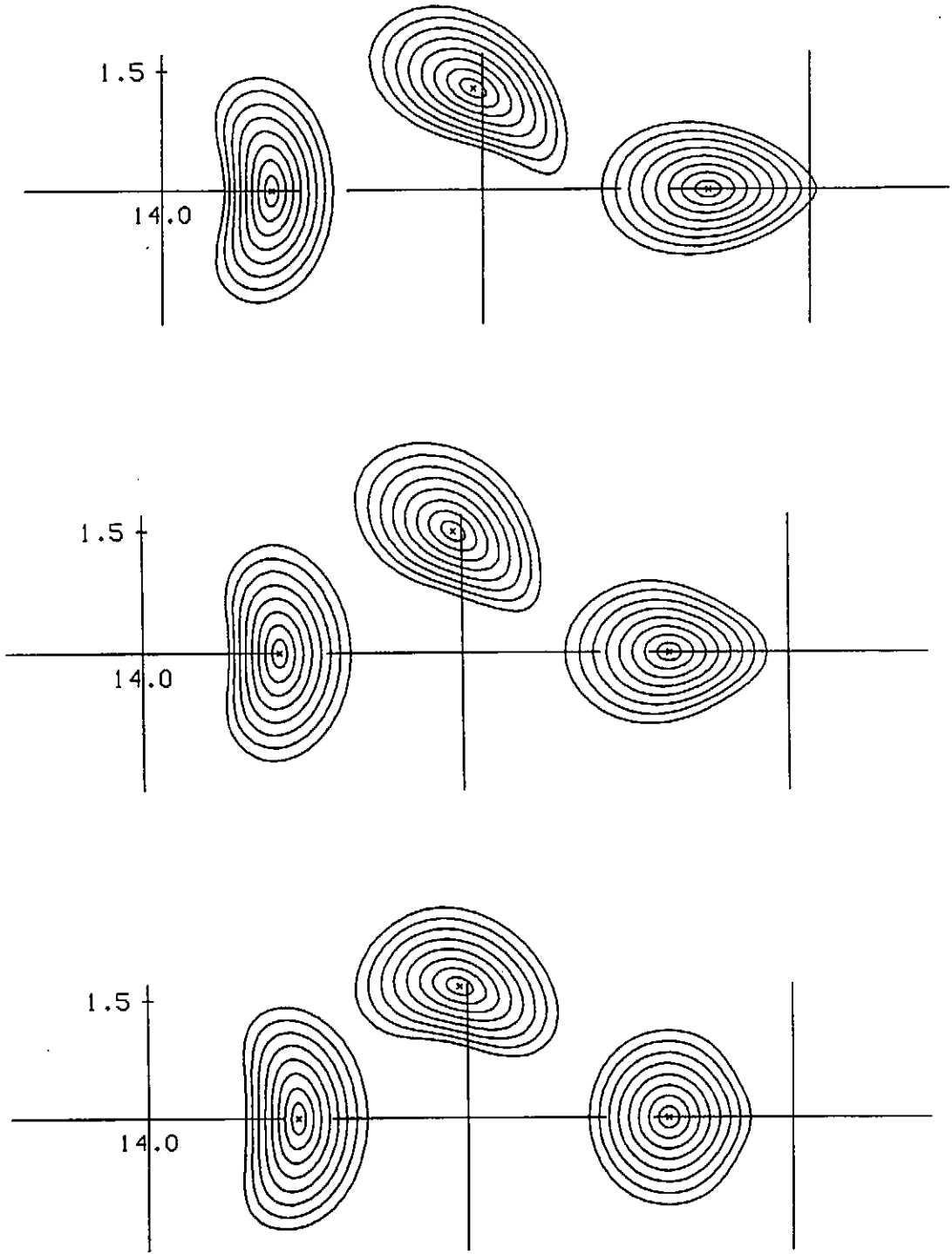


Fig. 1: Flux surface cross-sections of quasi-helically symmetric stellarators with $N = 7$, $R_{0,0} = 14$. The boundary of the middle row is given by Table I. The boundaries of the first row and the last row are obtained by analogous optimizations with $R_{1,1} = -Z_{1,1} = 0.3$ and 0.1 , respectively.

3. Structure of the Optimization

For the optimization of Helias configurations for W VII-X the following set of criteria has been used:

1. high quality of vacuum field magnetic surfaces (sufficiently small thickness Δ_{is} of islands),
2. good finite- β equilibrium properties (sufficiently high β_{eq}),
3. good MHD stability properties (sufficiently high β_{stab}),
4. small neoclassical transport in the $\frac{1}{\nu}$ -regime (small equivalent ripple δ_e),
5. small bootstrap current in the $lmfp$ -regime ($J_{BS,stell}/J_{BS,tok}$ sufficiently small),
6. good collisionless α -particle containment (fraction of prompt loss f_α sufficiently small),
7. good modular coil feasibility (sufficiently large distances Δ_c and radii of curvature R_c of the coils).

Criteria 1 and 7 are taken into account by solving Helias boundary value problems with side conditions on the shaping parameters. Criteria 2 and 3 are satisfied by maintaining resistive-interchange and ballooning stability at $\langle\beta\rangle \approx 0.05$ for configurations with 5 periods and aspect ratio of approximately 10. While maintaining resistive-interchange stability is directly incorporated into the optimization, ballooning stability is taken into account through its driving terms [4]. Criteria 4, 5, and 6 are taken into account by optimizing the structure of $B(\theta, \phi)$ in magnetic coordinates. This optimization procedure constitutes an inner optimization loop.

The evaluation of ballooning stability and of the three neoclassical properties 4, 5, and 6 leads to an iteration of this inner loop until satisfactory properties are found. Goodness parameters Δ_{is} , β_{eq} , β_{stab} , δ_e , $J_{BS,stell}/J_{BS,tok}$, f_α which can simultaneously be achieved appear to be 0.1, 0.05, 0.05, 0.01, 0.1, 0.1 (Helias50B).

The construction of modular coils [5] leads to a further iteration of results until satisfactory properties 1 - 7 are found. Goodness parameters Δ_c , R_c which can simultaneously with the above numbers be achieved appear to be 0.27 m, 0.2 m at a torus radius of 6.5 m and a magnetic field of 3 T [6].

4. Conclusion

Considering the above physics issues one may conclude that stellarators should be treated threedimensionally in real space and fivedimensionally in phase space. Therefore, the theoretical evaluation of stellarator physics properties will to a significant extent have to be based on large codes. The above computable physics properties, as opposed to as of now not computable physics properties (for example, anomalous behaviour), seriously limit stellarator performance. The number of stellarator optimization variables is large, but, as the above examples show, not discouragingly large. So, large scale computing will be continuing to be necessary for the progress of stellarators.

5. References

- 1 Nührenberg, J., R. Zille, Phys. Letters A 114A (1986) 129
- 2 Nührenberg, J., R. Zille, Phys. Letters A 129 (1988) 113
- 3 Nührenberg, J., Zille, R., Proc. Workshop on Theory of Fusion Plasmas, Chexbres, Switzerland, 1988, Eds. J. Vaclavik, F. Troyon, E. Sindoni, EUR 12149 EN (1989) 3
- 4 Nührenberg, J., R. Zille, Sherwood Theory Conf. 1989, San Antonio
- 5 Merkel, P., Nucl. Fusion 27 (1987) 867
- 6 Merkel, P., Third Workshop on W VII-X, Schloss Ringberg (1989)

Second Stability Studies in a Helical Axis Device:TJ-II

C. Alejaldre, A. Varias and A. López-Fraguas
Asociación EURATOM/CIEMAT para Fusión
28040 Madrid, Spain

B.A. Carreras, N. Dominguez and V. Lynch
Oak Ridge National Laboratory
Oak Ridge, U.S.A.

Abstract

The helical hard core in the four period TJ-II heliac permits to access a variety of magnetic configurations with very different MHD properties. In this paper a particular set of shearless configurations is presented with similar rotational transform at the magnetic axis, ≈ 1.20 , and slightly different values of the magnetic well, that exhibit self-stabilization behavior to Mercier modes characteristic of a second stability regime.

1. Introduction

Heliacs [1] in the helically symmetric limit have been proven to have excellent stability properties to low- n and high- n modes [2,3], with β -limits reaching the 30%. Recently a

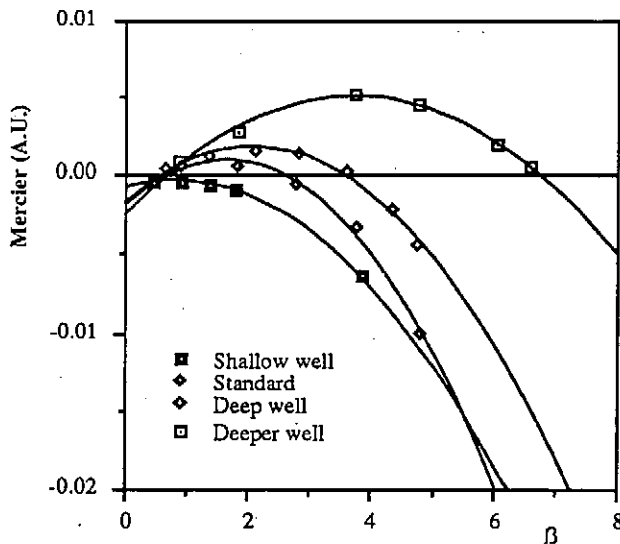


Figure 1
The Mercier criterion in arbitrary units for four configurations with the same rotational transform.

set of configurations in the finite aspect ratio realization of the heliac TJ-II to be built in Madrid, Spain [4], have been analyzed and found to have β -limit in excess of 6% to Mercier modes [5]. Results from this study are summarized in figure 1, where the Mercier criterion in arbitrary units is

shown versus $\langle\beta\rangle$ at a specific normalized radius, $r=0.95$, for four configurations labeled, Shallow, Standard, Deep and Deeper for the magnitudes of their magnetic well depths: $\approx 1\%$, 2% , 3% , 4% , respectively. All of them have a rotational transform per period at the magnetic axis of 0.36 and a practically flat iota profile. For finite β TJ-II equilibria, instabilities start appearing at the boundary, therefore if the configuration is stable to Mercier modes at this radius, it is also stable at the inner flux surfaces.

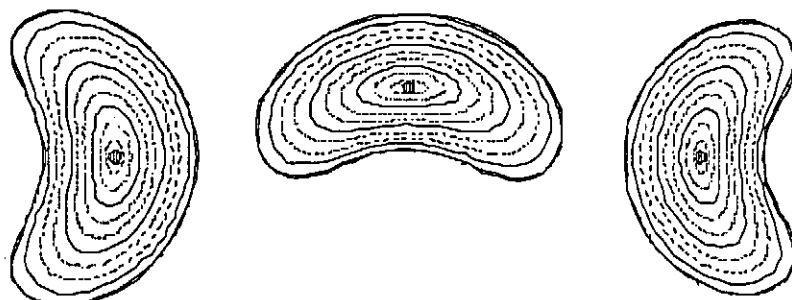


Figure 2
Flux surfaces at three toroidal locations for configuration B

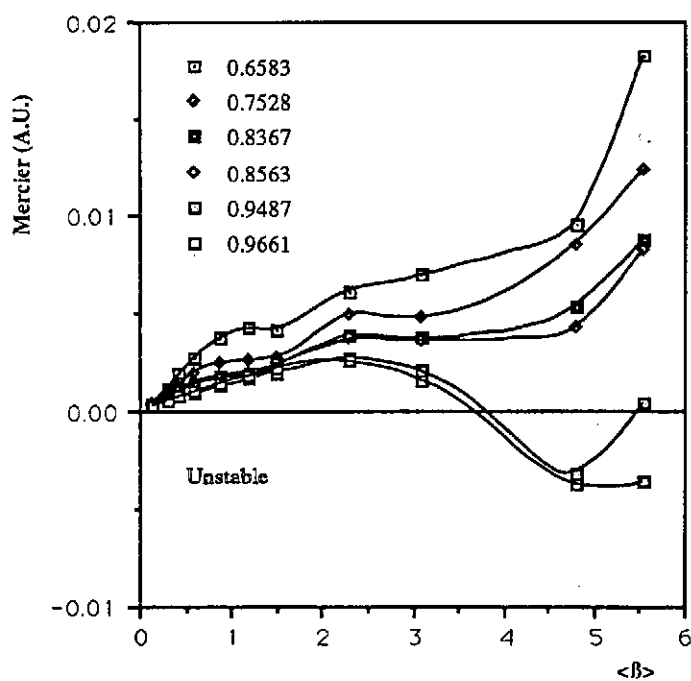


Figure 3

Equilibrium

The three dimensional code VMEC [6] in its fixed boundary version has been used to obtain a set of equilibria with increasing value of the pressure for the configurations chosen. VMEC finds the equilibria by minimizing the MHD energy over a toroidal domain Ω_p using an inverse representation for the cylindrical coordinates R, Z . The pressure profile considered was:

$$P(r) = P_0 (1-r^2).$$

We concentrated the study in two configurations labeled A and B close to each other in the flexibility diagram that shows the accessible configurations as the currents in the circular and helical conductors are varied[4]. These configurations are characterized for having a smaller average radius, (8 cm. for configuration B and 11 cm. for configuration A), and therefore an effective aspect ratio higher than the configurations considered in fig. 1. Figure 2 shows the flux surfaces at three toroidal positions for configuration B having a rotational transform per period at the axis of 0.30. The depth of the magnetic well in both configurations is similar, and equal to $\approx 1.3\%$.

Stability

For planar axis, zero-current stellarators, the stability beta limits given by the Mercier criterion agrees or is more pessimistic than the low-n stability limits [7]. Having a negative shear, ballooning modes in stellarators should impose a higher limit in the stability limit. We have then analyzed the stability properties of TJ-II with the 3-D Mercier criterion. Nevertheless a study has already been started to see what limits, if any, ballooning modes impose to results presented here.

The Mercier criterion can be written for closed magnetic flux surfaces as:

$$D_M = D_S + D_I + D_W + D_G > 0 \quad (1)$$

where the contributions due to the shear, D_S , and the net currents, D_I are negligible since the equilibria considered are essentially shearless, zero-current equilibria. The stability properties of TJ-II are then given by the competitive effect between the positive contribution of the magnetic well,

$$D_w = \left\langle \frac{gB^2}{g^{ss}} \right\rangle P' V' - (P')^2 \left\langle \frac{g}{B^2} \right\rangle \left\langle \frac{B^2 g}{g^{ss}} \right\rangle \approx a\beta + b\beta^2 \quad (2)$$

and the negative contribution of the geodesic curvature,

$$D_G = - \left\langle \frac{(\vec{J} \cdot \vec{B})^2}{B^2} \frac{g}{g^{ss}} \right\rangle \left\langle \frac{gB^2}{g^{ss}} \right\rangle + \left\langle \frac{g\vec{J} \cdot \vec{B}}{g^{ss}} \right\rangle^2 \approx -c\beta^2 \quad (3)$$

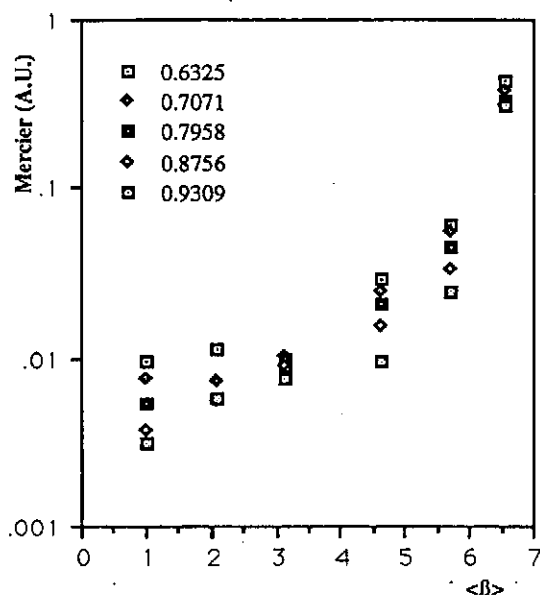


Figure 4
Mercier criterion vs. $\langle \beta \rangle$ for configuration B

Results

Figure 3 shows the result of applying the Mercier criterion to configuration A. In the figure the result of applying (1) is plotted at different radii for increasing values of $\langle \beta \rangle$. It is seen that as β increases, the Mercier criterion becomes more positive for most of the configuration and even changes sign at the most external part of the radius. This self-stabilization behavior characteristic of a second stability regime is more clearly seen in figure

4 where the same criterion is applied to configuration B, and continuously goes to more positive values indicating that the configuration is in a second stability regime to Mercier modes.

References

- 1.- Yoshikawa, S., Nucl. Fusion **23** (1983) 667
- 2.- Merkel, P., Nühremberg, J., Gruber, R., Troyon, F., Nucl. Fusion **23** (1983) 1061
- 3.- Monticello, D.A., Dewar, R. L., Furth, H.P., Carreras, B.A., Reiman, A., Phys. Fluids **27** (1985) 1248
- 4.- Review of the TJ-II Flexible Helic Project. A. P. Navarro and the TJ-II Team. This conference
- 5.- Ideal Mercier stability for the TJ-II flexible Helic. Varias, A., Alejaldre, C., López-Fraguas, García, L., Carreras, B., Dominguez, N., Lynch, V. Submitted for publication.
- 6.- Hirshman, S.P., Van Rij, W. I., and Merkel, P., Comput. Phys. Com., **43** (1986) 143.
- 7.- Dominguez, N., et al. 1989 IAEA Workshop in Stellarators, Oak Ridge, U.S.A.

3-D Equilibria of Helical systems: Magnetic Islands and Their Control

Takaya Hayashi

National Institute for Fusion Science, Nagoya 464-01

Abstract

Three dimensional equilibrium and breaking of magnetic surfaces due to the finite beta effect in a $l=2$ heliotron configuration are studied by using a newly developed three-dimensional equilibrium code. Several methods to suppress the breaking are discussed.

The equilibrium beta limit of a helical system is conventionally defined by the amount of the Shafranov shift, such as $\Delta_s(\beta) < \frac{\alpha_p}{2}$. However, we should also be careful on the breaking of magnetic surfaces due to the finite pressure effect, since it is well known that a non-axisymmetric toroidal finite beta equilibrium does not necessarily regularly nest magnetic surfaces. The boundary region of a helical system is ergodic even in a vacuum field. Therefore, the physical issue in this paper is to investigate how large the boundary ergodic region expands in a finite beta equilibrium.

The mechanism of the appearance of magnetic islands in a finite beta equilibrium is that when a finite pressure is given onto a vacuum field, the plasma current is induced to satisfy the equilibrium force balance condition $\mathbf{j} \times \mathbf{B} = \nabla p$. Then, the plasma current could be a source of error poloidal fields which resonate with rational surfaces. The resonant field causes the appearance of magnetic islands. When an island is induced, the pressure profile is significantly modified near the island. Thus, a consistent analysis between the $\mathbf{j} \times \mathbf{B} = \nabla p$ condition and the island formation is required.

Several excellent 3-D codes to solve helical equilibria have been developed so far, and are actively used to study magnetohydrodynamic properties of helical systems. One problem with these codes, however, is that they assume the existence of clearly nested magnetic surfaces, explicitly or implicitly. Therefore, a new approach is required to analyze consistently the island formation in a finite pressure equilibrium. Several efforts have been addressed to solve this problem. In this paper we show results on this matter which were obtained by newly developed 3-D equilibrium code (HINT).

HINT is a 3-D equilibrium code to obtain currentless helical equilibria by a relaxation method using free boundary conditions.[1] We adopt an Eulerian coordinate system which rotates with the same pitch as the helical coil. The calculation scheme has fourth order accuracy both in space and time. The amount of the Shafranov shift vs. β for a $l=2/M=10$ heliotron configuration which was obtained by the HINT code is plotted in Fig. 1, and is compared with the result obtained by the VMEC code. The agreement between these codes is fairly good as far as the occurrence of the breaking is not significant.

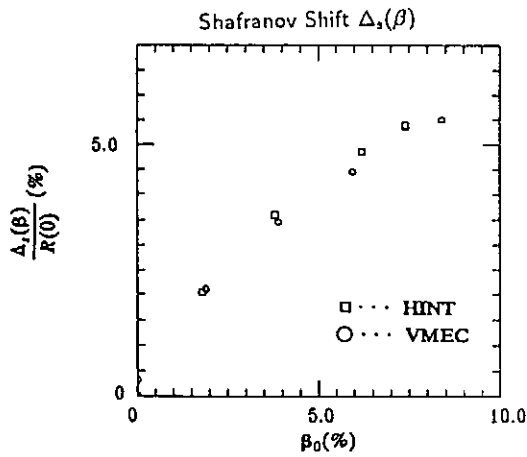


Fig.1

Fig.2

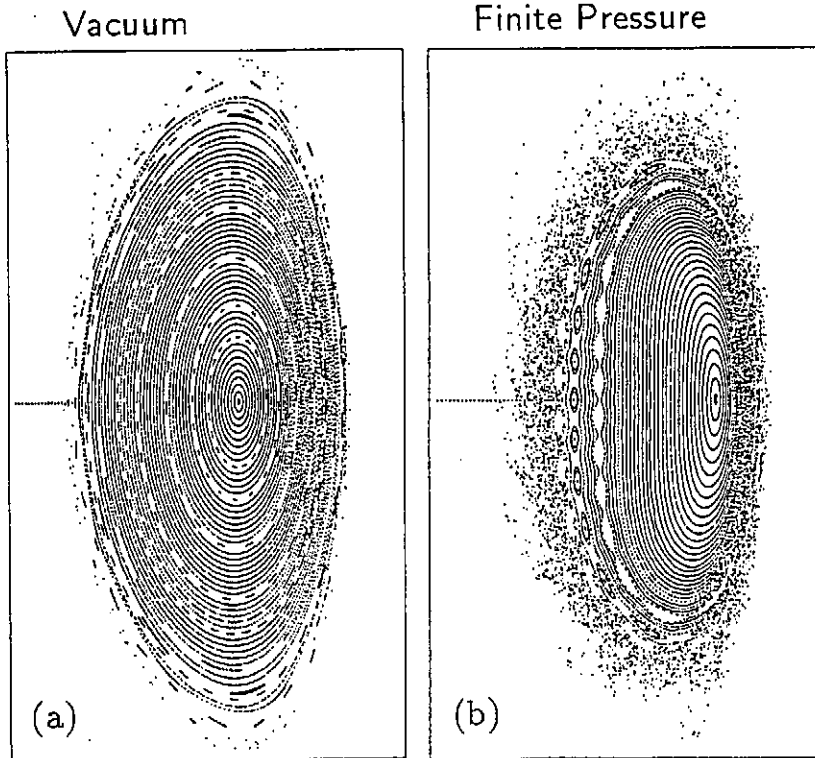
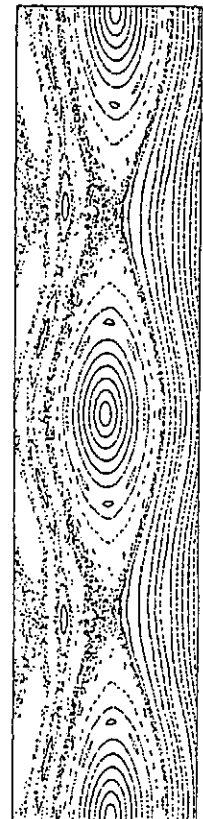


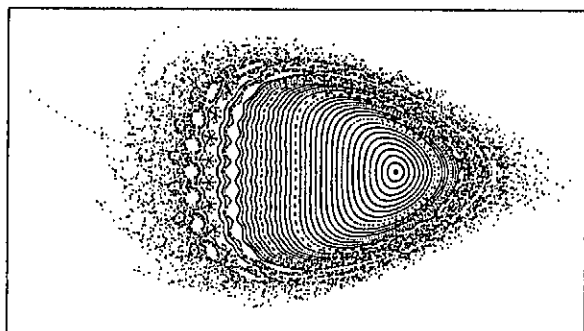
Fig.3



The state of the appearance of islands and ergodic region on the plasma boundary is plotted in Fig. 2 for $M=10$ heliotron configuration, where Fig.2(a) is for the vacuum field and (b) is for the $\bar{\beta} = 3.6\%$ case. The boundary ergodic region is observed to expand when β is increased. Figure 3 shows the expanded plot of the island which appeared in Fig.2(b). In order to confirm that the observed appearance of islands is not due to numerical artifact but due to some physical mechanism, we executed a mesh convergence check, where the same equilibrium is calculated using several different mesh numbers. The result is shown in Fig.4 for two different mesh sizes. The agreement for the island width as well as the overall width of the ergodic region between these calculations is fairly good. When we extrapolate the width of the island shown in Fig.3 down to the null mesh-interval case, we conclude that there must be finite width island, for which the width is very similar to the one shown in Fig.4.

Mesh Convergence Check

49x49x21



97x97x29

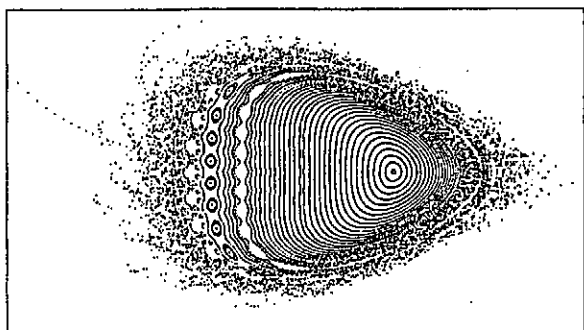


Fig.4

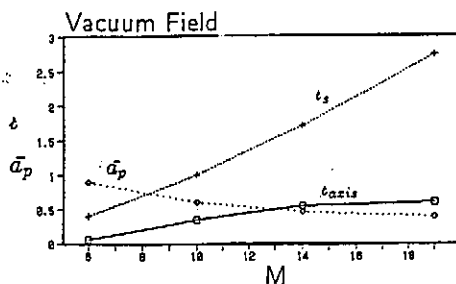
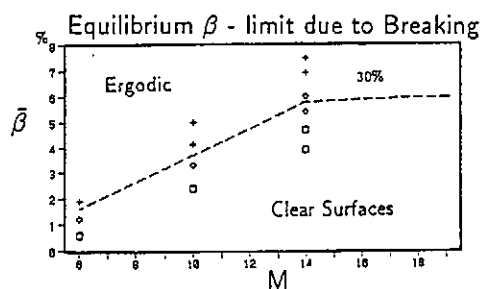


Fig.5

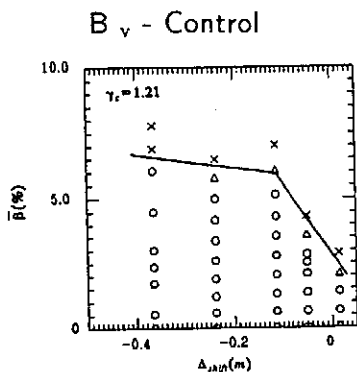


Fig.6

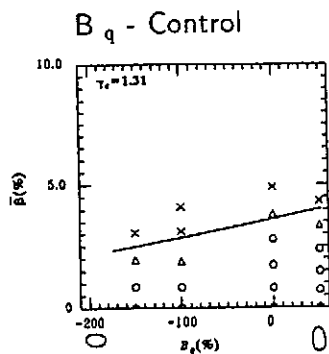


Fig.7

In order to understand the general tendency of the "fragility" of magnetic surfaces in a finite beta equilibrium, we have executed parameter survey for several kinds of parameters. The M (pitch period number) dependency of the breaking of magnetic surfaces is shown in Fig.5 for the $l=2$ heliotron configuration. This survey was made under conditions that the pitch parameter γ_c is fixed to be 1.3, the vacuum magnetic axis is at the helical coil center, external quadrupole component $B_q = 0$, and the helical coil has no modulation. The broken line in Fig.5 indicates a tentative beta limit at which the outer region of about 30 % of the minor radius becomes ergodic.

In the plot of Fig.5, it looks as if the equilibrium beta limit defined by the amount of the breaking for $M=10$ heliotron configuration is at most 3 or 4 %. However, we have several free parameters to control the situation.[2] Figure 6 shows the effect of the external vertical field B_v , which controls the radial position of the vacuum magnetic axis. As is shown in Fig.6, the inward shift of the magnetic axis is favorable to suppress the breaking, and in fact, we can obtain the high beta equilibrium (such as $\bar{\beta} \geq 5\%$) keeping clearly nested surfaces by a small inward shift for the $M=10$ configuration. As for the effect of B_q , as is shown in Fig.7, vertically elliptic shaping of the surfaces is favorable to suppress the breaking.

Summary

1. We need to analyze the breaking of boundary magnetic surfaces due to the finite beta effect in evaluating the equilibrium beta limit of a helical system, in addition to the usual standard of the Shafranov shift.
2. We have found several methods to suppress the breaking of magnetic surfaces by a control of M , γ_c , B_v , and B_q .
3. High beta equilibrium ($\bar{\beta} \geq 5\%$) keeping clearly nested surfaces can be obtained for $M=10$ heliotron configuration, especially by a control of B_v .

References

- [1] K.Harafuji, T.Hayashi and T.Sato, J.Comput.Phys., 81, 169 (1989).
- [2] T.Hayashi, T.Sato and A.Takei, Phys. Fluids B, in press (1990).

Resistive MHD Stability Studies for ATF Plasmas During Operation in the Second Stability Regime*

*L. A. Charlton, J. N. Leboeuf, B. A. Carreras, N. Dominguez, and V. E. Lynch
Oak Ridge National Laboratory, Oak Ridge, Tennessee 37831-8058, U.S.A.*

Abstract: Self-stabilization effects were experimentally observed in the first period of operation of the ATF device. These effects are reproduced by nonlinear calculations.

1. Introduction

In the initial period of operation of the ATF device, the β self-stabilization effect on fluctuations was observed. The measured magnetic fluctuations increased with β up to $\beta_0 \sim 1.5\%$ and decreased for higher β values.¹ This indicated that ATF was operating in a regime where β self-stabilization effects were dominant. ATF was designed to operate in the second stability regime with respect to ideal MHD.² It was shown that resistive instabilities remain in the second stability regime, but they can be affected by β self-stabilization effects.³ We present the results of detailed nonlinear studies of these instabilities for equilibrium parameters corresponding to those of ATF. The results show a reduction in the ($m = 2, 3; n = 1$) magnetic perturbations at high β , as observed in the experiment. The β self-stabilization effect is also seen in the simulations from a sharp reduction in the turbulence inside the plasma core at high β and a decrease in the saturation level of the kinetic energy.

2. Equilibria

The approach followed in generating the equilibria was the stellarator expansion,⁴ whereby a two-dimensional equilibrium is generated by performing a toroidal angle average. This results in an equilibrium equation very similar to the Grad-Shafranov equation that is solved by standard techniques.⁵ Four equilibria, with β_0 values of 0.26%, 0.80%, 1.5%, and 2.3% and with profiles closely matching those seen experimentally, were used for the study. Two features of these profiles affect the stability in ATF as β is increased. The first is the formation of a magnetic well, as shown in Fig. 1(a). At the lowest value of β , there is a magnetic hill throughout the plasma, but a magnetic well develops and becomes deeper and broader as β increases. The second feature is the change in the ι profile near the magnetic axis induced by the requirement of zero net current. As β increases, the shear decreases, resulting in fewer lower-order rational surfaces. This is illustrated in Fig. 1(b), where the ι profiles are shown in the plasma interior (the plasma edge is at $r = 29$ cm) for the four values of β . The relevant low- m rational surfaces are indicated. At the lowest β , both the ($m = 10; n = 3$) and the ($m = 7; n = 2$) surfaces are present inside $r = 10$ cm. At the highest β , there are no included rational surfaces to support the instability near the plasma magnetic axis. Both of these effects are present in the nonlinear stability results presented in Sect. 3.

3. Results

The nonlinear evolution of the resistive instability (resistive ballooning in the plasma core and resistive interchange near the plasma edge) is studied with the reduced MHD equations derived by

Strauss.⁶ We use as input the ATF equilibria described in Sect. 2. The pressure profiles have a gradient in the region $0.35 < \tau < 0.40$. The lowest- m rational surfaces in this region are $(m = 2; n = 5)$, $(m = 3; n = 8)$, $(m = 4; n = 11)$, $(m = 5; n = 13)$, The corresponding modes have the largest linear growth rates in the cylindrical limit, while the $n = 1$ modes $(m = 2, 3; n = 1)$ have growth rates close to zero. When the steady state in the nonlinear evolution is reached these two components are the largest, and they dominate the magnetic energy spectrum, as expected from the resistive pressure-gradient-driven turbulence theory.³ The saturated levels of the $(m = 2, 3; n = 1)$ fluctuations as a function of β_0 have the same features as the experimental data, as shown in Fig. 2.

The β self-stabilization effect is also seen in the saturated pressure contours (Fig. 3). The radial extent of the turbulence is from the edge to about one-fourth of the minor radius at the lowest β (0.26%) and increases at the next higher β (0.80%). Some healing of the contours is seen, however, at $\beta_0 = 1.5\%$, and at the highest β equilibrium flux surfaces are unaffected in the plasma core. Two effects are responsible for the change of the radial extent of the turbulence with β : the broadening of the magnetic well with increasing β and the flattening of the τ profile in the interior. The flatness excludes lower-order rational surfaces that can support an instability.

Focusing on the results of the nonlinear evolutions, we observe three salient features: (1) the development of fine-scale turbulence about halfway out in plasma radius, (2) an $m = 1$ bulk displacement of the plasma, and (3) a central pressure flattening. The turbulence is driven by the large pressure gradient. The outward displacement and pressure flattening are $(m = 1; n = 0)$ and $(m = 0; n = 0)$ effects, respectively. Toroidal effects strongly couple modes that have the same toroidal mode number (n) and poloidal mode numbers (m) that differ by 1. Since nonlinearly modes with $n = n_1 + n_2$, $n_1 - n_2$ and $m = m_1 + m_2$, $m_1 - m_2$ are driven by modes with toroidal mode numbers n_1 and n_2 and poloidal mode numbers m_1 and m_2 , the toroidal effects drive the $(m = 1; n = 0)$. This gives rise to the displacement. At the magnetic axis, the pressure perturbation can be driven only by an $m = 1$ mode. Since the only $m = 1$ mode with appreciable strength near the axis is the $(m = 1; n = 0)$ mode, the $(m = 0; n = 0)$ pressure flattening results from $(m = 1; n = 0)$ self-coupling. This could be the cause of the flatness of the core profiles measured in ATF.

For comparison, calculations in cylindrical geometry were also done. The mid-radius turbulence was very similar to that seen with toroidal geometry. However, the displacement and the central pressure flattening were not seen since, as described earlier, they are due to toroidal coupling.

References

- ¹J. H. Harris et al., Phys. Rev. Lett. **63**, 1249 (1989).
- ²J. F. Lyon et al., Fusion Technol. **10**, 179 (1986).
- ³B. A. Carreras, Comments Plasma Phys. Controlled Fusion **12**, 35 (1988).
- ⁴J. M. Greene and J. L. Johnson, Phys. Fluids **4**, 875 (1961).
- ⁵J. A. Holmes, Y-K. M. Peng, and V. E. Lynch, J. Comput. Phys. **36**, 35 (1980).
- ⁶H. R. Strauss, Plasma Phys. **22**, 733 (1980).

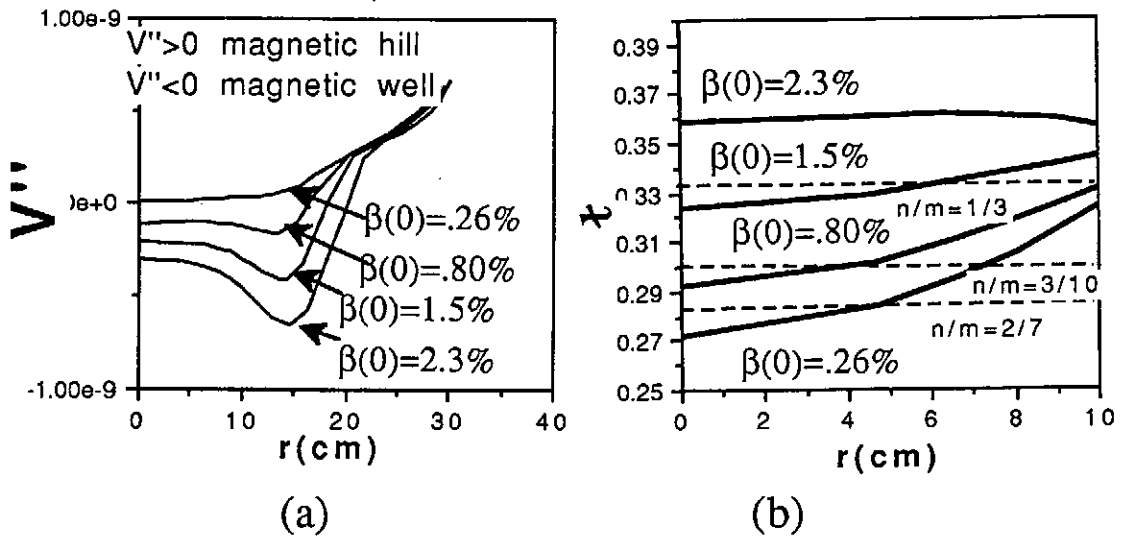


Fig. 1. (a) Magnetic wells and (b) q profiles for the equilibria used in this study.

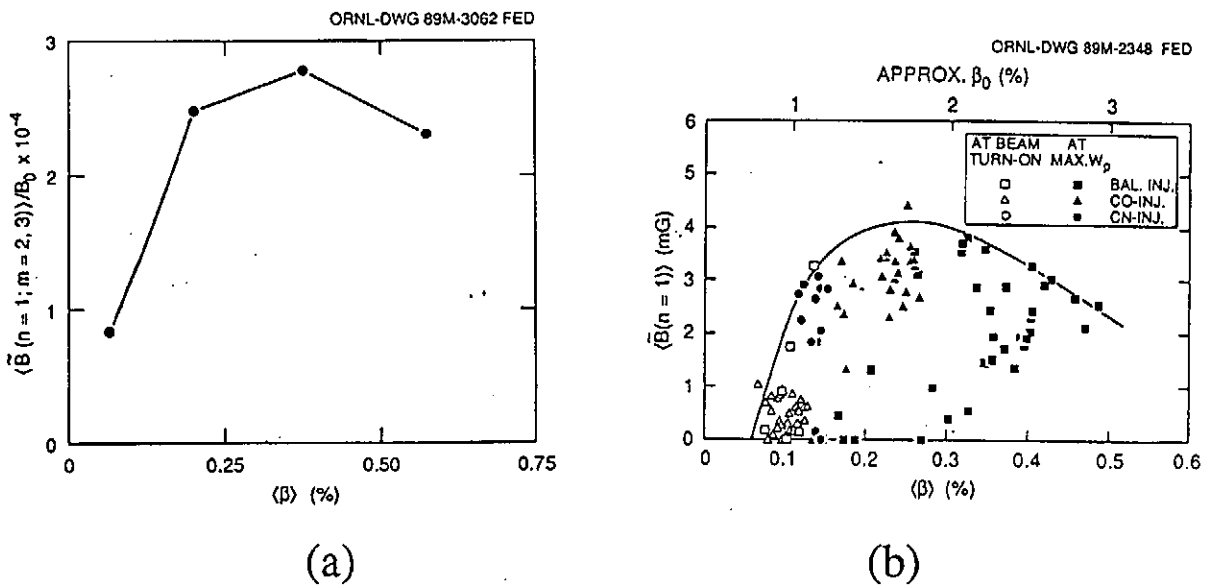
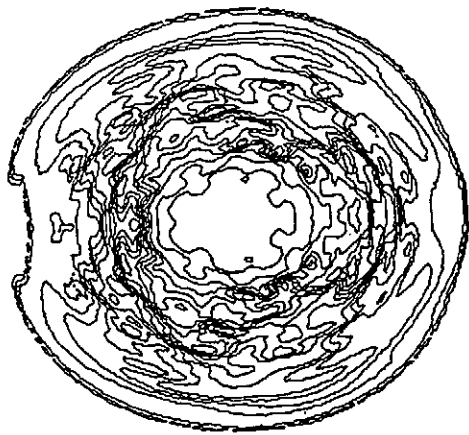
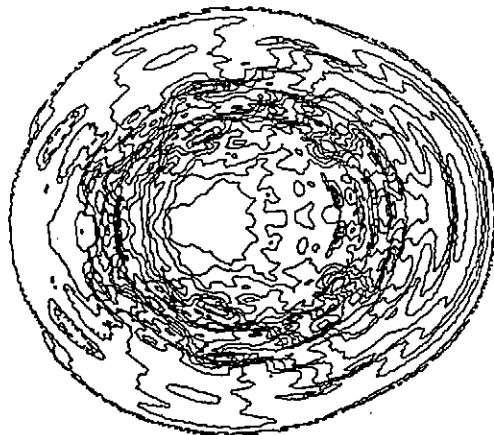


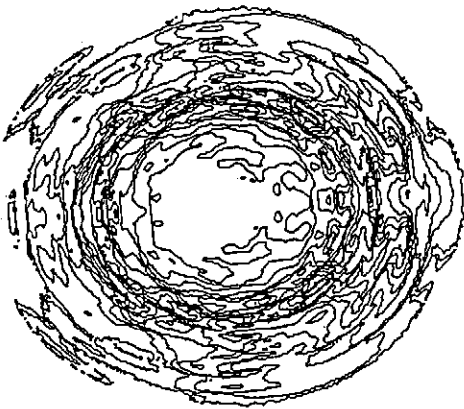
Fig. 2. Saturated levels of the $(m = 2, 3; n = 1)$ fluctuations from (a) theory and (b) experiment.



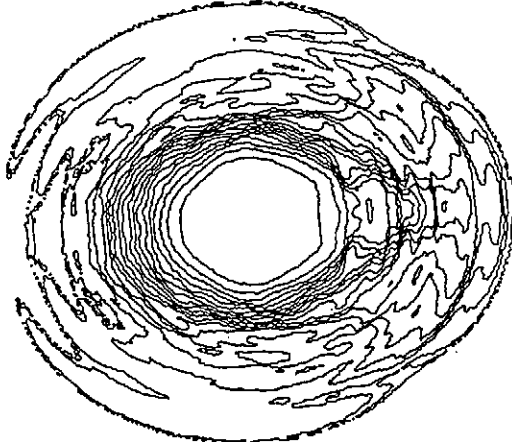
(a)



(b)



(c)



(d)

Fig. 3. Saturated pressure contours at (a) $\beta_0 = 0.26\%$, (b) $\beta_0 = 0.80\%$, (c) $\beta_0 = 1.5\%$, (d) $\beta_0 = 2.3\%$.

DRIFT OPTIMIZATION OF HELICAL SYSTEMS

K. Hanatani

*Plasma Physics Laboratory, Kyoto University
Gokasho, Uji, Kyoto JAPAN*

ABSTRACT

The minimization of particle loss region of heliotron/torsatron configurations is considered. Both Heliotron E (high aspect ratio) and Large Helical Device (low aspect ratio) configurations are examined and compared. In the drift optimization of Heliotron E, vertical field B_v is used to minimize the loss region. The optimum shift of magnetic axis Δ_v^{opt} and "operation window" with respect to B_v are predicted and compared with Heliotron E experiments; correlations between the theoretical prediction and experimental observations are discussed. As for LHD configuration, modulations of HF (helical field) coil and multipole moments from PF (poloidal field) coil set are used to minimize the loss region. It is shown that loss region of a LHD configuration can be reduced as narrow as that of the standard Heliotron E configuration by simultaneous control of vertical and quadrupole field.

INTRODUCTION

In finite aspect ratio helical systems, toroidal perturbation distorts both mod- B and flux surfaces. These distortions, which can be large in low aspect ratio devices, enhance radial drift of helically trapped particles and create collisionless particle loss region in the velocity space. Since large loss region is harmful to efficient heating and confinement of plasmas, we wish to minimize the extent of loss region by optimizing free parameters of external coils. The optimization can be achieved by appropriate flux-surface positioning and shaping that effectively remove the unfavorable distortions. We have used realistic magnetic field configurations produced by finite size HF coils and PF coils. The use of realistic magnetic fields—rather than simplified model fields—is necessary to make precise prediction about the existing experiment and to give practical feedback to the design of the next generation device.

In order for the theoretical optimization about future experiments has credibility, it must succeed to interpret existing experiments. Recent kinetic and diamagnetic measurements [1, 2] carried out in Heliotron E showed that sustainable plasma energy W_p depends sensitively on the position of magnetic axis Δ_v : W_p decreases rapidly with outward shift ($\Delta_v > 0$) although magnetic well exists, increases slightly with small inward shift ($\Delta_v = -2 \sim -3$ cm), and decreases again with large inward shift ($\Delta_v < -5$ cm). One hypothesis to explain these observations is change in shear which may affect anomalous transport of the bulk plasma. An alternative hypothesis [3] is that observed variations of W_p may be correlated to the particle loss region.

QUALITATIVE OPTIMIZATION

In the drift optimization of helical systems—like in any other optimization—one must distinguish free parameters from constraints. For existing devices such as Heliotron E, the HF coil parameters are the constraints, whereas auxiliary VF coil field (dipole moment) is the free parameter that can be used to improve confinement properties. In the present drift optimization of LHD, basic HF coil parameters of the reference design ($M = 10$, $\gamma = 1.2$, $R = 4\text{m}$, $B = 4\text{T}$) were fixed as constraints, which were imposed to keep the advantages of original LHD design. Remaining free parameters (modulations of the winding law of HF coils and multipole moments of PF coils) can be used to reduce the loss region. (Hexa-pole and higher multipole moments are not controlled in this study.)

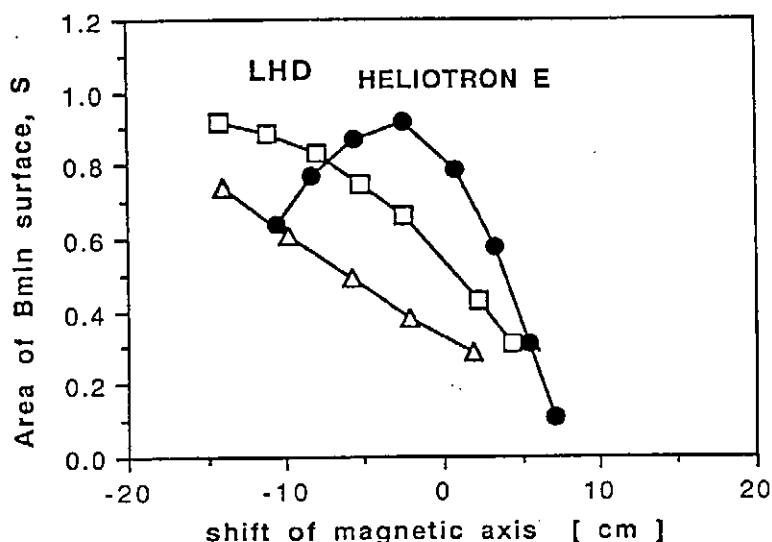


Figure 1 Dependence of area of B_{\min} surface on the position of magnetic axis. SYMBOL Δ for LHD with $B_Q(\text{PF})=0$, \square for LHD with $B_Q(\text{HF}) + B_Q(\text{PF}) = 0$, \bullet for Heliotron E.

Because of large number of freedoms of HF and PF coils, it is often useful to obtain rough trend of confinement quality before carrying out Monte Carlo simulation. As a convenient measure of the confinement quality, one can use the area enclosed by the largest B_{\min} surface [4] within the last closed flux surface. We define normalize area, S , as follows

$$S = \frac{\text{(area enclosed by largest } B_{\min} \text{ contour)}}{\text{(the area of last closed flux surface)}}$$

Figure 1 shows the output from HELIOS code, showing the effects of magnetic axis shift in Heliotron E and LHD configurations; values of S are plotted against the shift of magnetic axis.

Closed circles in Fig. 1 show the value of S for Heliotron E. With the outward shift ($\Delta v > 0$), outside-loss region grows and the confinement of helically trapped particles strongly degrades. Minimum-loss-region configuration is realized in

Heliotron E by a slight inward shift ($\Delta v^{\text{opt}} = -2.6$ cm). At this optimal shift, the radial drift of deeply trapped ($v_{\parallel} \approx 0$) particles approximately vanishes. This can be understood by the mod- B contour on the last closed surface, which becomes nearly “helically symmetric” around the bottom of the ripple. However with large inward shift ($\Delta v < -5$ cm), new *inside*-loss region appears on the inner side of the torus. Drift orbits of barely trapped particles were, as expected, found to deviate from the B_{min} contour. When the confinement of $v_{\parallel} \approx 0$ particles are improved, confinement of barely trapped particles are confirmed to be improved. As a criterion for optimization, $S \geq 80 \sim 90\%$ may be required because this is the condition for good plasma production in Heliotron E experiments. Configurations with $S \leq 50\%$ are dominated by loss of helically trapped particles.

In the pre-optimized LHD configuration (i.e. $B_Q^{\text{PF}} = 0$, $\Delta v = 0$), S is so small (about 30%) that even $v_{\parallel} \approx 0$ particles are lost from the core of the plasma. Two optimization steps for LHD are noted. The first step (moderate improvement) is to remove the vertical elongation of flux surface, which is caused by toroidal effect of HF coil, by applying B_Q field from PF coil set. The second step (more efficient than the first) is to compensate the toroidal distortion of mod- B surface by shifting magnetic axis inward by about 10 cm. With the simultaneous optimization of B_Q and B_v , S value of above 80%, which is comparable to the standard Heliotron E configuration, is obtained. Favorable MHD properties are predicted for this configuration [5]. Detail parameter survey including the dependence of various types of modulations of HF coil was reported elsewhere [6].

MONTE CARLO SIMULATION

At first sight, the variation of W_p observed in Heliotron E looks very similar to the normalized area of B_{min} contour shown in Fig. 1. This qualitative similarity is not enough to conclude that the change in the extent of loss region is responsible for the observed variation of W_p . This is because the estimate based on collisionless $v_{\parallel} \approx 0$ particles (Fig.1) ignores important physics issues such as :

- (1) effects of barely-trapped particles,
- (2) effects of Coulomb collision,
- (3) effects of charge exchange and re-ionization,
- (4) effects of radial electric field.

Effect that influences the loss rate most is the position of loss boundary: Helically trapped particles which go out of the last closed surface can re-enter the confining region. To evaluate the orbit loss correctly one has to specify the vacuum vessel wall as the loss boundary [7].

Monte Carlo calculations of perpendicular neutral injection was carried out by using HELIOS code, which can include all the above effects, to investigate the role of trapped particle loss in the variation of W_p in Heliotron E. In Figure 2, calculated heating power P_{heat} multiplied by a^2 is plotted against Δv . The factor a^2 is multiplied to take account possible size scaling of bulk plasma confinement. The rapid decrease of W_p with $\Delta v > 0$ can be explained by the outside loss region. It must be emphasized, however, that largest fraction of loss is not orbit loss but the charge exchange loss which occur peripheral and outside of the confining region. In the simulation, re-

ionization of fast ions was included to avoid overestimate of charge exchange loss. The agreement between observed W_p and calculated a^2P_{heat} is good except for large inward shift; The former drops more steeply than the simulation curve in Fig. 2. This difference suggests the deterioration of bulk particle confinement at large inward shift. Candidates for this are enhance transport due to the presence of (1) inside loss region and (2) fluctuation induced by magnetic hill. However (3) deterioration of plasma caused by increased plasma-wall interaction can not be excluded.

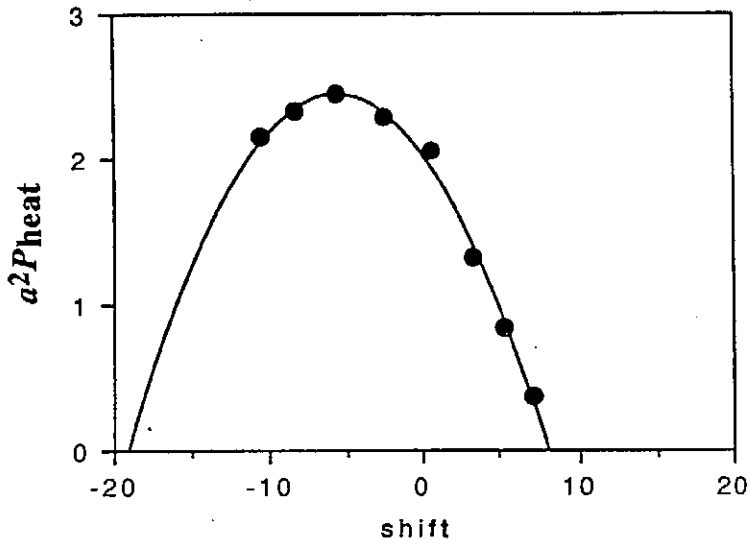


Figure 2. Dependence of a^2P_{heat} on the position of magnetic axis [cm]. Monte Carlo simulation (HELIOS code) of confinement of perpendicularly injected fast ions in Heliotron E. Line averaged $n_e = 5.6 \times 10^{13} \text{ cm}^{-3}$

acknowledgements

A part of this work was carried out in collaboration with T. Kamimura, H. Sanuki, and K. Itoh (National Institute for Fusion Science) as a design team activity of Large Helical Device.

references

- [1] T. Obiki et al., *Overview of recent Heliotron E experiments*, International Stellarator Workshop, (Oak Ridge, April, 1989).
- [2] S. Besshou et al., *Recent Diamagnetic Measurements of Heliotron E Toroidal Coil Experiments*, this conference
- [3] K. Hanatani, *Fast ion confinement in Heliotron E—effects of magnetic axis shift—* JPS-28aTE10, (1989, March)
- [4] B. Carreras et al., *Physics Study Strategy for ATF II, Proc US-Japan Workshop on new generation experiments and reactors (joined by EC) (PPLK-10) p109* (1988, July)
- [5] J. Todoroki, et al., IAEA-CN-50/C-5-4, (Nice, October, 1988)
- [6] K. Hanatani, H. Sanuki, T. Kamimura, *Drift optimization of low aspect ratio helical configurations* JPS-3pJ13 (1989, October)
- [7] R. H. Fowler, et al., *Neutral Beam Injection Benchmark Studies for Stellarators/Heliotrons*, submitted to Nuclear Fusion.

Plasma Transport in Advanced Stellarators

H. Wobig

(Max-Planck-Institut für Plasmaphysik, D-8046 Garching, EURATOM-Association)

Abstract. The present paper reformulates the neoclassical theory of general toroidal equilibria. The relevant geometrical parameters are identified and it is shown how the reduction of Pfirsch-Schlüter currents affects neoclassical transport and bootstrap effects. The influence of turbulent electromagnetic fluctuations is also discussed. Since a toroidal loop voltage is included, the theory is valid for all toroidal systems.

Introduction: In the present paper a formulation of neoclassical transport theory valid for general toroidal equilibria will be given. In advanced stellarators with reduced Pfirsch-Schlüter currents [1], the radial drift of trapped particles can also be reduced to a certain extent leading to a small neoclassical transport level, although the number of trapped particles is not small. In particular, Helias-configurations [2] exhibit small Pfirsch-Schlüter currents and small neoclassical losses. As introduced by Shaing and Callen [3] in their pioneering paper on neoclassical transport in non-axisymmetric equilibria, the Hamada coordinate system (V, θ, φ) is the appropriate system to describe toroidal equilibria. It exists if a solution of the ideal equilibrium condition $\mathbf{j} \times \mathbf{B} = \nabla p$ exists. With \mathbf{e}_p and \mathbf{e}_t being the poloidal and toroidal base vectors on the magnetic surface, the magnetic field is $\mathbf{B} = \psi'(V)\mathbf{e}_t + \chi'(V)\mathbf{e}_p$ and the plasma current $\mathbf{j} = I'(V)\mathbf{e}_t + J'(V)\mathbf{e}_p$. $\psi(V)$ and $\chi(V)$ are the toroidal and poloidal magnetic fluxes and $I(V)$, $J(V)$ the corresponding currents. Using the equilibrium condition the plasma current can also be written in the form: $\psi'(V)\mathbf{j} = p'(V)\mathbf{e}_p + I'(V)\mathbf{B}$. The poloidal current $p'(V)\mathbf{e}_p$ consists of the diamagnetic current perpendicular to \mathbf{B} and the Pfirsch-Schlüter current $p'(\mathbf{e}_p \cdot \mathbf{B})\mathbf{B}/B^2$, however there is no need to separate these terms.

In deriving the flux-friction relationships on magnetic surfaces the latter representation of the plasma currents turns out to be more convenient than the former one. A simple form of the flux-friction relations can be derived from Ohm's law $\nabla\Phi + \mathbf{v} \times \mathbf{B} = \eta\mathbf{j}$. The average over the magnetic surface is defined by $\langle g \rangle = \int g df / |\nabla V|$ and some useful relations of the base vectors are: $\langle \mathbf{e}_p \cdot \mathbf{B} \rangle = I(V)$, $\langle \mathbf{e}_t \cdot \mathbf{B} \rangle = J(V)$ and $\mathbf{e}_p \times \mathbf{B} = \psi'(V)\nabla V$. Application of the averaging procedure $\langle \mathbf{e}_p \cdot \dots \rangle$ and $\langle \mathbf{B} \cdot \dots \rangle$ to Ohm's law yields the following system

$$\begin{aligned} -(\psi'(V))^2 \Gamma &= \eta \langle \mathbf{e}_p \cdot \mathbf{e}_p \rangle p'(V) + \eta I I'(V) \\ (\psi'(V))^2 U_L &= \eta I p'(V) + \eta \langle B^2 \rangle I'(V) \end{aligned} \quad (1)$$

$\Gamma = \langle \mathbf{v} \cdot \nabla V \rangle$ is the radial flux of \mathbf{v} . The electric potential is single-valued in the poloidal direction, however, with toroidal loop voltage we find $\langle \mathbf{B} \cdot \nabla \Phi \rangle = \psi'(V) U_L$. The transport matrix L in (1) is positive definite and symmetric. The non-diagonal terms in L describe the classical bootstrap effect and its conjugate, the pinch effect. The coefficient $D_{ps} = \langle \mathbf{e}_p \cdot \mathbf{e}_p \rangle$ is the Pfirsch-Schlüter factor. The aim of the present paper is to extend eq. (1) to neoclassical plasmas including turbulent effects.

The Fokker-Planck equation. We consider a fluctuating plasma with turbulent electromagnetic fields $\mathbf{B} = \overline{\mathbf{B}}_0 + \delta\mathbf{B}(t)$, $\mathbf{E} = \mathbf{E}_0 + \delta\mathbf{E}(t)$, where similar to the procedure of K.C Shaing [4] and R.Balescu [5], the electromagnetic fields are given. $\mathbf{E}_0, \mathbf{B}_0$ are the time averaged fields and \mathbf{B}_0 is assumed to satisfy the equation of ideal equilibrium. In velocity space we separate the space of all square integrable distribution functions $f(\mathbf{v})$ in two orthogonal subspaces H^s and H^a containing all symmetric distributions $\{f^s : f^s(-\mathbf{v}) = f^s(\mathbf{v})\}$ and antisymmetric distributions $\{f^a : f^a(-\mathbf{v}) = -f^a(\mathbf{v})\}$. The scalar product in \mathbf{v} -space is $(f, g) = \int fg d^3\mathbf{v}$. A further orthogonal partition of H^s is $H^s = H_0^s + H_1^s$, with H_0^s containing all spherically symmetric distributions $f_0^s(v^2)$. P^s, P_0^s, P_1^s and P^a are the projection operators onto these subspaces. After introducing the abbreviations $\mathbf{v} \cdot \nabla_x f = V f$, $q_\alpha/m_\alpha \mathbf{E} \cdot \nabla_v f = E f$, $q_\alpha/m_\alpha (\mathbf{v} \times \mathbf{B}) \cdot \nabla_v f = B f$ the Fokker-Planck equation of each particle species is

$$\frac{\partial f^s}{\partial t} + (V + E) f^s + B f^s = C(f^s, f^s) + C(f^a, f^a) + S^s \quad (2)$$

$$\frac{\partial f^a}{\partial t} + (V + E) f^s + B f^a = C(f^s, f^a) + C(f^a, f^s) + S^a \quad (3)$$

C is the collision operator $C(f, f) = \sum C^{\alpha, \beta}$ in the Landau form. S is the source term (heating, refuelling, current drive etc.) and S^s, S^a its projection onto H^s and H^a . $C_l f^a =: C(f^s, f^a) + C(f^a, f^s)$ The generalised macroscopic flow vector is defined by $\mathbf{u}(x) = \int f^a g(v^2) \mathbf{v} d^3\mathbf{v}$ and the generalised density by $n(x) = \int f_0^s g(v^2) d^3\mathbf{v}$. The generalised viscous tensor $\pi = \int g(v^2) (\mathbf{v} : \mathbf{v} - v^2/3\mathbf{I}) f_1^s d^3\mathbf{v}$ with $f_1^s \in H_1^s$ is of particular importance in neoclassical effects. $g(v^2) \in H_0^s$ is an arbitrary weight function, however in the application we follow the procedure of Hirshman and Sigmar [6] and use the Laguerre-Sonine polynomials $L_k^{3/2}(v^2), k = 0, 1, 2, \dots$ for $g(v^2)$.

Following the same surface averaging procedure as in the introduction we obtain the generalised flux $\Gamma = \langle \mathbf{u} \cdot \nabla V \rangle$ from taking the $\langle (\mathbf{e}_p \cdot \mathbf{v} g(v^2), \dots) \rangle$ -average of eq. (3): $\langle (\mathbf{e}_p \cdot \mathbf{v} g(v^2), \mathbf{B}_0 f^a) \rangle = \psi'(V) q_\alpha/m_\alpha \Gamma$. Collecting all terms in eq.(3) and averaging over time yields

$$\begin{aligned} \psi'(V) (q_\alpha/m_\alpha) \Gamma &= \langle (\mathbf{e}_p \cdot \mathbf{v} g(v^2), C_l \bar{f}^a) \rangle - \langle (\mathbf{e}_p \cdot \mathbf{v} g(v^2), V \bar{f}_1^s) \rangle \\ &\quad - \langle (\mathbf{e}_p \cdot \mathbf{v} g(v^2), E_0 \bar{f}^s) \rangle + \langle (\mathbf{e}_p \cdot \mathbf{v} g(v^2), S^a) \rangle \\ &\quad - \langle (\mathbf{e}_p \cdot \mathbf{v} g(v^2), \overline{\delta E \delta f^s}) \rangle - \langle (\mathbf{e}_p \cdot \mathbf{v} g(v^2), \overline{\delta B \delta f^a}) \rangle \end{aligned} \quad (4)$$

The first term on the right-hand side contains the classical losses, which have been analysed in ref.[6] by expanding \bar{f}^a in a series of Laguerre polynomials: $\bar{f}^a = \sum f_M(v^2) g_k(v^2) \mathbf{v} \cdot \mathbf{u}_k(x)$ ($f_M = \exp(-mv^2/2T)$ is the Maxwellian). The lowest approximation to the flow vector \mathbf{u}_k is the dissipationless flow in the magnetic surface with $\mathbf{U}_k \times \mathbf{B}_0 = A_k(V) \psi'(V) \nabla V$ and $\nabla \cdot \mathbf{U}_k = 0$, which can be written in the form $\psi'(V) \mathbf{U}_k = A_k(V) \mathbf{e}_p + \Lambda_k(V) \mathbf{B}_0$. The symmetric distribution \bar{f}^s in this order is $F^s = \sum f_M g_k(v^2) P_k(V)$. The condition of equilibrium links the generalised pressure $P_k(V)$ to the thermodynamic force A_k by

$$A_k(V) \psi'(V) = P_k'(V) - (q/T) \Phi'_0(V) P_k(V) + (q/m) 2 \Phi'_0 \hat{P}_k \quad (5)$$

with $\hat{P}_k = \sum (v^2/3) f_M g_k g'_k d^3 v P_k$. $\Phi_o(V)$ is the potential of the lowest-order E-field. $\Lambda_k(V)$ describes the toroidal integral flux of \mathbf{U}_k . $k = 1$ yields the toroidal particle flux and the toroidal electric current $I'(V) = \sum q_\alpha N_{1,\alpha}(V) \Lambda_{1,\alpha}(V)$. With $\bar{f}^a \rightarrow F^a = \sum f_M g_k (v^2) \mathbf{v} \cdot \mathbf{U}_k$, the vector $\Gamma =: \{(q_\alpha/m_\alpha) \Gamma^{k,\alpha}\}$ of classical radial fluxes can be written in the form

$$\psi'(V)\Gamma = -l \{ \langle \mathbf{e}_p \cdot \mathbf{e}_p \rangle \mathbf{A} + I(V)\Delta \} \quad (6)$$

The matrix l is the matrix of classical transport coefficients [6] and $\mathbf{A} =: \{A_{k,\alpha}\}$ the vector of thermodynamic forces. \mathbf{A} is the vector of toroidal differential fluxes. The same averaging process can be made with $\mathbf{B}_o \cdot \mathbf{v}g(v^2)$ and eq.(3). We separate the inductive part $U_L \nabla \varphi$ from \mathbf{E}_o and find

$$\begin{aligned} (q_\alpha/m_\alpha)U_L \langle ((\mathbf{B}_o \cdot \mathbf{v}g(v^2)) \nabla \varphi \cdot \nabla_v \bar{f}^s) \rangle = & \\ \langle (\mathbf{B}_o \cdot \mathbf{v}g(v^2), C_l \bar{f}^a) \rangle - \langle (\mathbf{B}_o \cdot \mathbf{v}g(v^2), V \bar{f}_1^s) \rangle & \\ - \langle (\mathbf{B}_o \cdot \mathbf{v}g(v^2), E_o \bar{f}^s) \rangle + \langle (\mathbf{B}_o \cdot \mathbf{v}g(v^2), S^a) \rangle & \\ - \langle (\mathbf{B}_o \cdot \mathbf{v}g(v^2), \overline{\delta E \delta f^s}) \rangle - \langle (\mathbf{B}_o \cdot \mathbf{v}g(v^2), \overline{\delta B \delta f^a}) \rangle & \end{aligned} \quad (7)$$

Eqs. (4) and (7) are the generalisation of eq. (1) to a multispecies plasma.

Neoclassical losses. Neoclassical effects are described by the second term in eq.(4) and (6) which can also be written in the form $\langle \mathbf{e}_p \cdot \nabla \cdot \pi \rangle$ and $\langle \mathbf{B}_o \cdot \nabla \cdot \pi \rangle$. In the guiding center approach only the gyro-angle average of \bar{f}_1^s is retained leading to the Chew-Goldberger-Low form of π . The equation for \bar{f}_1^s is derived from the time averaged Fokker-Planck equation (2) and (3).

$$L \bar{f}_1^s = (V + E_o) F^a - \bar{S}_1^s - P_1^s (\overline{\delta E \delta f^a} + \overline{\delta B \delta f_1^s}) \quad (8)$$

The operator L is $L = (V + E_o)[C_l - B_o]^{-1}(V + E_o) - (C_l - B_o)$ and $V F^a = \sum g_k(v^2) f_M (\mathbf{v} : \mathbf{v} - 1/3 \mathbf{I}) \nabla : \mathbf{U}_k$. $\nabla : \mathbf{U}_k$ is the rate of strain tensor of \mathbf{U}_k . Eq. (8) holds in all regimes of collisionality. The inhomogeneous term consists of 3 parts: The first one, $(V + E_o) F^a$, is the relevant term of neoclassical transport, the second one, S_1^s , is the term of ECR-current drive and the third one the influence of turbulence on the distribution function \bar{f}_1^s . In a collision dominated plasma L is approximately equal to $B_o - C_l$, which is a differential operator in \mathbf{v} -space. Its inverse, L^{-1} , is an integral operator and therefore the viscous stress tensor in \mathbf{x} -space is locally proportional to the rate of strain tensor $\nabla : \mathbf{U}_k$. However, in the long-mean-free-path regime L^{-1} is an integral operator in \mathbf{v} -space and \mathbf{x} -space and the linear relation between π and $\nabla : \mathbf{U}_k$ is non-local.

Guiding center average. The standard guiding center approach is obtained by averaging eq.(8) over the gyro-angle. The important term on the right hand side of eq.(8) is $V F^a$ which after averaging over the gyro-angle is:

$$(V F^a)_{av} = \sum g_k(v^2) f_M (v_{\parallel}^2 - v_{\perp}^2/2) \mathbf{U}_k \cdot \frac{\nabla B}{B}, \quad (E_o F^a)_{av} = 0 \quad (9)$$

Since \mathbf{U}_k is linear in $A_k(V)$ and $\Lambda_k(V)$ the solution \bar{f}_1^s is also linear in $A_k(V)$ and $\Lambda_k(V)$ and therefore the tensor π and the neoclassical terms $\langle \mathbf{e}_p \cdot \nabla \cdot \pi \rangle$ and $\langle \mathbf{B}_o \cdot \nabla \cdot \pi \rangle$

are also linear in A_k and Λ_k . Summarising the results yields the neoclassical terms in the form

$$\langle \mathbf{e}_p \cdot \nabla \cdot \pi \rangle = L_1 \mathbf{A} + L_2 \mathbf{\Lambda} \quad , \quad \langle \mathbf{B}_o \cdot \nabla \cdot \pi \rangle = L_2 \mathbf{A} + L_4 \mathbf{\Lambda} \quad (10)$$

The matrices L_i are the neoclassical transport matrices; explicitly they are:

$$L_1 = \langle ((\mathbf{e}_p \cdot \frac{\nabla B}{B}), H_{k,k'}^{\alpha,\beta}(\mathbf{e}_p \cdot \frac{\nabla B}{B})) \rangle \quad L_2 = \langle ((\mathbf{e}_p \cdot \frac{\nabla B}{B}), H_{k,k'}^{\alpha,\beta}(\mathbf{B}_o \cdot \frac{\nabla B}{B})) \rangle \quad (11)$$

$$L_3 = \langle ((\mathbf{B}_o \cdot \frac{\nabla B}{B}), H_{k,k'}^{\alpha,\beta}(\mathbf{e}_p \cdot \frac{\nabla B}{B})) \rangle \quad L_4 = \langle ((\mathbf{B}_o \cdot \frac{\nabla B}{B}), H_{k,k'}^{\alpha,\beta}(\mathbf{B}_o \cdot \frac{\nabla B}{B})) \rangle \quad (12)$$

with $H_{k,k'}^{\alpha,\beta} = (v_{\parallel}^2 - v_{\perp}^2/2) g_k(v^2) L^{-1} f_M g_{k'}(v^2) (v_{\parallel}^2 - v_{\perp}^2/2)$. L_1 describes the neoclassical transport, L_2 the pinch effect, L_3 the neoclassical bootstrap effect and L_4 the neoclassical resistivity. An immediate conclusion is that neoclassical losses and bootstrap effects become small or zero if $\mathbf{e}_p \cdot \nabla B/B \rightarrow 0$. Because of $\mathbf{e}_p \cdot \mathbf{B}_o \rightarrow 0$ > $\mathbf{e}_p \cdot \nabla B \rightarrow 0$ the minimisation of Pfirsch-Schlüter currents minimises neoclassical effects. By proper choice of $\mathbf{e}_p \cdot \nabla B/B$ and $\mathbf{B}_o \cdot \nabla B/B$ the bootstrap and pinch effects can be made small even if the L_1 -matrix is not small.

Source terms and turbulent effects. The antisymmetric part of S adds an extra term to the plasma loss; this may for example occur via momentum input by neutral beam injection. The symmetric part S_1^s occurs during ECRH-current drive which adds an extra term to π and therefore to $\langle \mathbf{e}_p \cdot \nabla \cdot \pi \rangle$ and $\langle \mathbf{B}_o \cdot \nabla \cdot \pi \rangle$. Turbulence also modifies the viscous tensor π via the driving term $P_1^s(\delta E \delta f^s + \delta B \delta f_1^s)$ which can compete with the neoclassical effects. Besides these modifications of the tensor π the turbulence gives rise to the last two fluxes in eq.(4), which are those conventionally discussed as anomalous losses. Without computing the plasma response δf to the fluctuating fields a precise analysis of turbulent losses is not possible. In the special case of electrostatic fluctuations, however, the driving term for plasma instabilities (see linearised version of eq.(2)) is the term $\delta E F^s$ which is linear in the lowest order flow \mathbf{U}_k . The symmetric distribution $F^s(v^2)$ which occurs in the form $\delta E F^s$ drives instabilities if F^s is non-monotonic in v^2 . In contrast to neoclassical effects which are driven by the rate of strain tensor $\nabla : \mathbf{U}_k$, the electrostatic instabilities depend on \mathbf{U}_k directly. With fixed thermodynamic forces A_k the flow vector \mathbf{U}_k can be minimised by minimisation of its parallel components $\Lambda_k \mathbf{B}_o$ and $A_k (\mathbf{e}_p \cdot \mathbf{B}_o) \mathbf{B}_o$. In conclusion, reducing the integral toroidal fluxes and the Pfirsch-Schlüter currents in toroidal equilibria reduces also the driving terms of electrostatic turbulence.

References

- [1] G.Grieger et al. *Proc. 12th Int. Conf. Plasma Phys. and Contr. Fusion Res.* Nice, 1988
- [2] J. Nührenberg, R. Zille, *Phys. Letters A* **114** (1986), 129
- [3] K.C. Shaing, J.D. Callen, *Phys. Fluids* **26** (1983), 3315
- [4] K.C. Shaing, *Phys. Fluids* **31** (1988), 8
- [5] R. Balescu, to be published
- [6] S.P. Hirshman, D.J. Sigmar, *Nucl. Fusion* **21**,1079 (1981)

RECENT EXPERIMENTS IN JT-60

JT-60 Team presented by H. Kishimoto
 Naka Fusion Research Establishment, Japan Atomic Energy Research
 Institute, Naka-Machi, Naka-Gun, Ibaraki, Japan

Recent experiments in JT-60 have been conducted mainly on the plasma parameter improvement and the current drive optimization. Energy confinement can be improved by pellet injection. High $\beta_p (\geq 3)$ discharges are obtained with high power NB heating and then the bootstrap current becomes dominant in the plasma current. LH current drive efficiency is improved up to $3.4 \times 10^{19} \text{ m}^{-2} \text{ MA/MW}$ with a multijunction launcher. Sawtooth activity is suppressed successfully by the LH wave.

1. Introduction

The advanced experiment of JT-60 has been made progress since 1987 in the investigation of confinement improvement and steady state operation. In the first phase of the advanced experiment from April 1987 to October 1989, the major efforts have been concentrated on the pellet injection experiment, the lower single null divertor study with high heating power and the current drive optimization with an improved lower hybrid (LH) launcher. Experiments have been done in discharges with ohmic, neutral beam (NB), LH and ion cyclotron (IC) heatings over a range of parameters: toroidal field $B_T \leq 4.8\text{T}$, plasma current $I_p \leq 3.2\text{MA}$, NB power $P_{NB} \leq 25\text{MW}$, LH power $P_{LH} \leq 7\text{MW}$, and IC heating power $P_{IC} \leq 3\text{MW}$. In addition to the results described in this paper, LH electron and ion heating, LH limiter H-mode, IC harmonic heating, improved divertor confinement, and helium ash exhaust have been studied experimentally.

2. Pellet Injection Experiments

Hydrogen pellets (two of 3.0mm and other two of 4.0mm in both diameter and length) were injected into high current limiter discharges with the maximum velocity of 2.3km/s. The pellet-fueled plasmas were heated by NB and IC. Peaked density profiles are formed by the pellet injection. The peaking factor $n_e(0)/\langle n_e \rangle$ becomes up to 5. The sawtooth activity observed in the SX signal is suppressed during the formation of a highly peaked density profile and the plasma stored energy increases in the sawtooth-free phase/1/, as shown in Fig. 1. According as the peaking factor decreases, sawtooth oscillations appear and the stored energy is saturated. It is found from the peaked pressure profiles

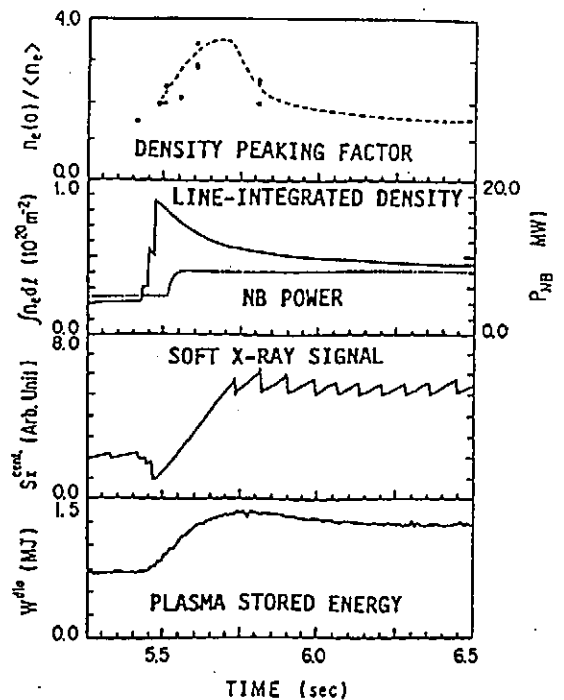


Fig. 1. Time evolution of pellet injected 2.1MA limiter discharge.

in pellet injection discharges that the major increase of the stored energy comes from the plasma region inside the sawtooth inversion radii. Improvement of the energy confinement time τ_E is closely related to the density profiles and τ_E increases with the density peaking factor as shown in Fig. 2. The increase in the energy confinement time amounts up to 40 percents as compared to the gas puffing discharges.

According to stability analyses the maximum pressure gradient in the pellet injection discharges is determined by the ideal ballooning mode. Another favorable aspect of pellet injection is the high fueling rate up to 100 percents, while the fueling rate is significantly low as 10 percents (divertor) to 20 percents (limiter) in gas puffing discharges.

3. High- β_p /High- T_i Discharges and Bootstrap Current

High β_p discharges have been attempted by high power NB injection into low I_p plasmas/2/. High β_p values exceeding 3 have been achieved during a heating phase for 2-3 sec. Both ion and electron temperatures have peaked profiles with the peaking factors around 2.5. The central temperatures are $T_i=5-12\text{keV}$ and $T_e=3-6\text{keV}$. The ion temperature and the electron density have a close correlation in the radial profiles. MHD analyses imply that the pressure profiles of high β_p discharges are determined by the ideal ballooning limit. Ion temperature gradient turbulence model is likely appropriate for understanding the observed ion temperature profiles of these high β_p discharges.

It is found that the MHD activities have correlations with the energy confinement characteristics as well as the ion temperature. Figure 3 indicates that the improved energy confinement and an increase in ion temperature are associated with the disappearance of the sawtooth activity at $I_p \leq 1\text{MA}$. In the plasma current range of $I_p=0.5-1\text{MA}$, the stored energy is sustained at a nearly constant value and the ion temperature

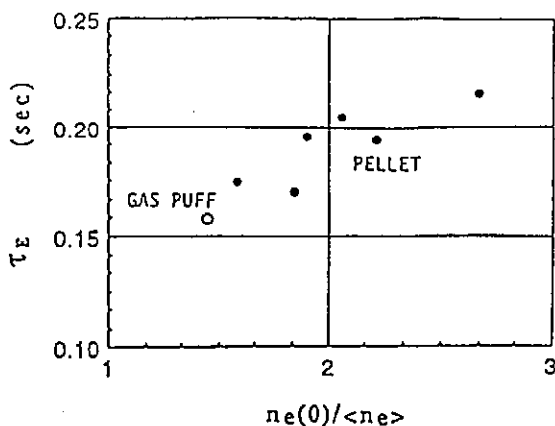


Fig. 2. Energy confinement time versus density peaking factor for pellet injection and gas puffing discharges.

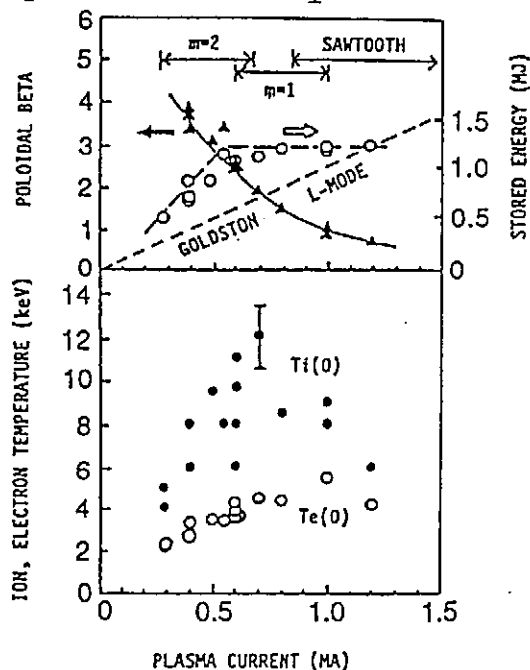


Fig. 3. High- β_p /high- T_i discharge characteristics at $B_T=4.5\text{T}$ and $P_{NB}=21\text{MW}$.

reaches its maximum. Continuous $m=1$ ($I_p=0.7-1\text{MA}$) and $m=2$ ($I_p=0.5-0.7\text{MA}$) activities are observed in this high T_i mode. The stored energy in the sawtooth-free discharges exceeds the Goldston L-mode scaling by a factor of 1.7. When I_p is less than 0.5MA , β_p becomes larger than 3 and $m=2$ oscillations induce periodic β_p collapses which degrade the energy confinement.

NB injection in JT-60 is nearly perpendicular to the toroidal plasma. Consequently it can drive a merely small plasma current. This situation reveals clearly the existence of a bootstrap current at high β_p as illustrated in Fig. 4. The vertical axis of this figure is given by the resistive voltage ratio of measured values to calculated ones based on the neoclassical theory without bootstrap current. The theoretical line from the neoclassical theory including bootstrap current fits well the experimental β_p dependence. The bootstrap current reaches 80 percents of the net plasma current at $\beta_p \sim 3$.

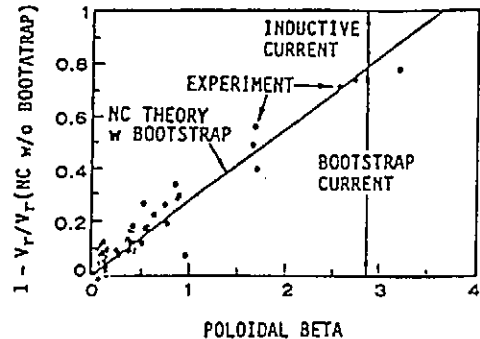


Fig. 4. Bootstrap current contribution in resistive loop voltate at various poloidal beta values.

A new concept of a steady state tokamak power reactor has been derived from the high β_p bootstrap current experiments on JT-60/3/. Design bases are the followings; the beta limit by Troyon scaling, bootstrap current constituting 70 percents of the plasma current, negative ion NB current drive at the plasma center for the residual 30 percents of the plasma current, confinement time twice the L-mode scaling, and the superconducting magnet technology constraint about 12T in the maximum field strength. Such a power reactor concept which has a larger aspect ratio and a smaller plasma current, illustrated in Fig. 5, provides a high Q and small circulating power system. Thus it is feasible as a steady state power reactor with a high plant efficiency.

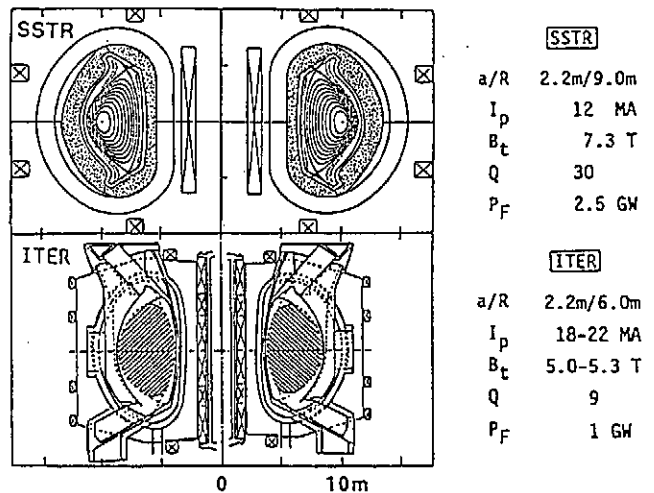


Fig. 5. Steady state tokamak power reactor concept.

4. Lower Hybrid Current Drive and Sawtooth Suppression

A new type wave launcher consisting of multijunction modules has been introduced in JT-60 to optimize the current drive efficiency. This launcher has characteristics of sharp power spectra and good wave directivity. These features have favorable effects on the improvement of LH current drive efficiency. The maximum current drive efficiency (averaged electron density \times plasma major radius \times driven current / injected power) reaches $3.4 \times 10^3 \text{m}^{-2} \text{MA/MW}$, which corresponds to 70 percents of the ITER design base.

LH current profile control and sawtooth suppression have been made successfully by changing the refractive index N_{\parallel} from 1 to 4. The LH wave with $N_{\parallel} \sim 1.3$ was utilized for an effective sawtooth suppression of beam heated plasmas as shown in Fig. 6. In the sawtooth-free phase large increases were observed in the soft X-ray signal and the ion temperature at the plasma center.

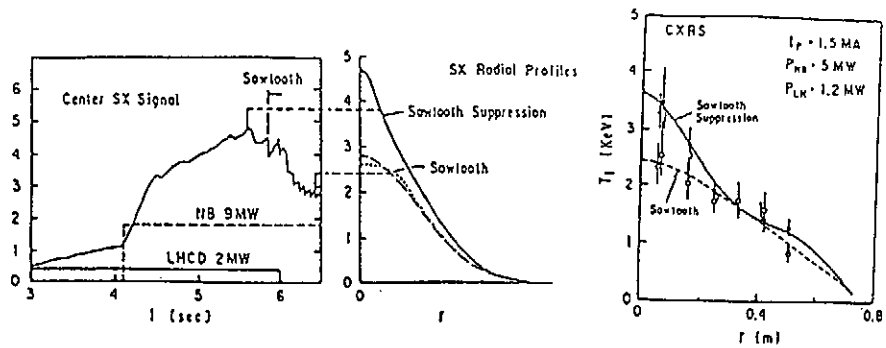


Fig. 6. LH sawtooth suppression with improved central plasma parameters.

5. Future Programs

JT-60 was shut-down in the end of October 1989 for the upgrade modification. The cross-sectional view of JT-60 is shown in Fig. 7. JT-60 after modification has a noncircular cross-section of divertor plasma with the maximum plasma current of 6MA. In the later phase of the upgrade experiments application of a high energy (500keV) negative ion NB is envisaged to demonstrate the physical and technological feasibility of steady state tokamak operation at reactor-grade plasma parameters.

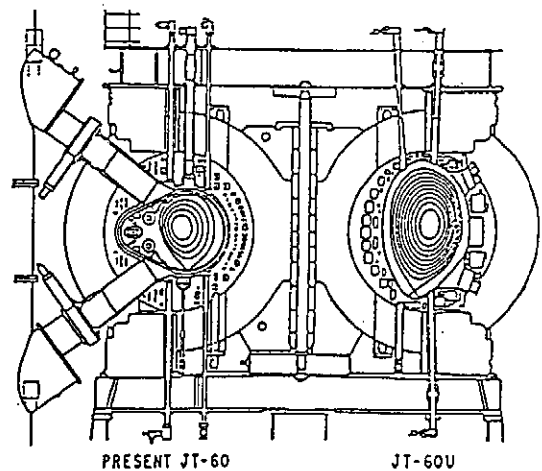


Fig. 7. Cross-sectional view of JT-60 before and after upgrade modification.

6. Summary

- (1) Improved confinement has been achieved in pellet injection experiments by suppressing the sawtooth activity.
- (2) High β_p beyond 3 and high T_i mode of operation has been obtained. Correlation between MHD activities and confinement property has become evident at high β_p .
- (3) Clear evidence of bootstrap current has been achieved in high β_p discharges, in which the major part of the plasma current is contributed by the bootstrap current.
- (4) High efficiency current drive has been demonstrated with a multijunction LH launcher. LH sawtooth suppression has improved the central plasma parameters.

References

- /1/ R. Yoshino and Y. Kamada, JAERI-M 89-134 (1989).
- /2/ S. Ishida, et al., to be submitted to Phys. Rev. Lett..
- /3/ M. Kikuchi, JAERI-M 89-164 (1989), to be published in Nuclear Fusion.
- /4/ M. Naito, et al., submitted to Nuclear Fusion.

GRAPHITES AS PLASMA FACING MATERIAL OF A LARGE FUSION DEVICE

T.Hino and T.Yamashina
Department of Nuclear Engineering,
Hokkaido University, Sapporo 060, Japan

ABSTRACT

Several graphites, as the first wall materials of Large Helical System, are evaluated in terms of erosion, thermal shock resistance and the recycling. Adequate graphites are suggested, and the required conditions such as baking, cooling and the discharge cleaning are discussed.

1. INTRODUCTION

As the helical fusion device has been scaled to larger size with substantially increased stored energy densities and longer pulse operations, the engineering tasks of first wall materials to handle high heat fluxes becomes increasingly important. In large tokamaks, the energy confinements time has been considerably improved by use of graphite first walls. In the Large Helical System, the heat load of the first wall has been estimated to be considerably high, especially in a case of long pulse operation. Graphite material, thus, has to be used at least in the divertor region, in order to protect the metal vacuum chamber and to suppress the metal impurity emission. For the graphite, as the first wall, both high thermal shock resistance and low recycling rate are required to avoid cracking of graphite tile and to enhance the energy confinement time, respectively.

The overall properties of the graphite, however, had not been examined in detail so far for the fusion application. Recently, the properties of several graphite materials have been studied by the Graphite Project Team organized in 1986 [1,2]. We here discuss the graphite material adequate for the first wall in the divertor region of the Large Helical System, based upon the results obtained in this project study. The required conditions for the graphite first wall are also described.

2. PROPERTIES OF GRAPHITE AND REQUIRED CONDITIONS AS FIRST WALL MATERIAL

Several graphite materials such as isotropic graphite, pyrolytic carbon and C/C composite have been characterized with respect to

- (1) vacuum engineering properties
(gas desorption, micro surface area, hydrogen permeation),
- (2) interactions with hydrogen ions/plasmas
(chemical sputtering, radiation enhanced sublimation,
retention of hydrogen ion, change of surface morphology),
- (3) thermal-mechanical properties
(heat load test, fracture toughness).

From the point of the vacuum engineering properties, the pre-baked graphite with relatively lower density would be adequate since both the gas desorption and the micro surface area are lower. The gas species desorbed from the graphite are H_2 , H_2O , CO , CO_2 and hydrocarbons. The gas desorption amount has a tendency to have peaks around the graphite temperature of $\sim 300^\circ C$ and $500-700^\circ C$. In order to eliminate these gas species up to the first peak region, the baking with temperature of approximately $350^\circ C$ is needed. As an example, Fig.1 shows the gas desorption amount from felt type C/C composite, CX-2002U. By the bakings with temperatures of $350^\circ C$ and $600^\circ C$ during 30min, the gas amount of $\sim 40\%$ and $\sim 70\%$ can be eliminated, respectively. Since the graphite is extremely porous, the effective surface area is at least several hundreds larger than the geometrical area. The capacity of the absorbed gas is also very large. Thus, the suppression of the recycling becomes difficult without the baking with adequate temperature.

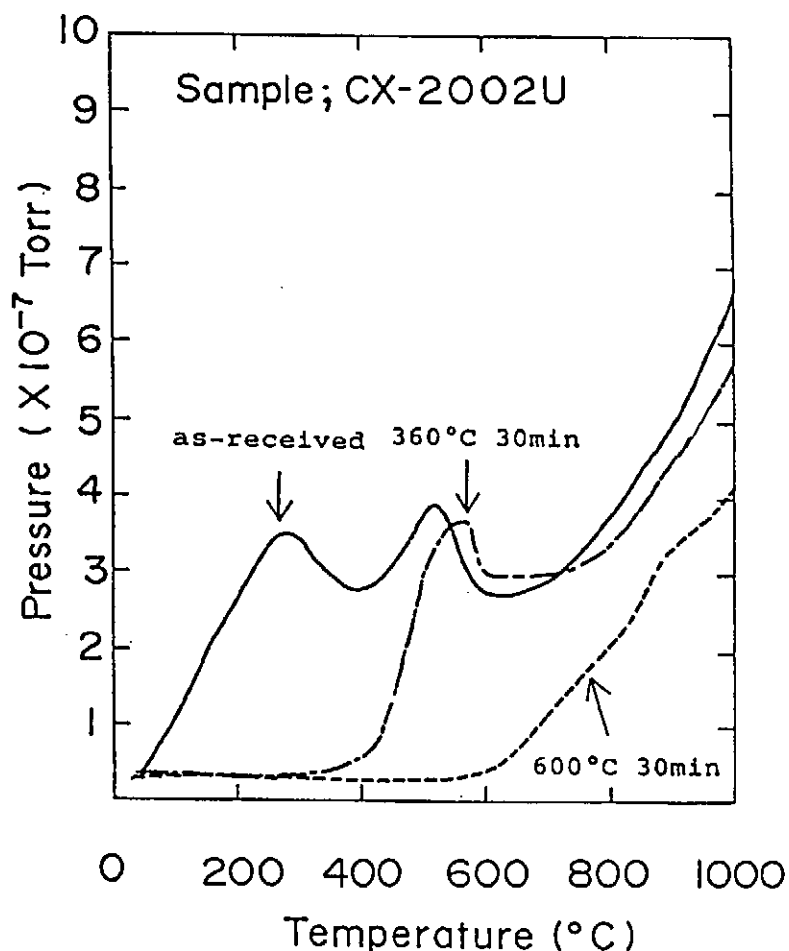


Fig.1 Thermal desorption spectra of felt type C/C composite, CX2002U.

The graphite material is extremely eroded by chemical sputtering and the radiation enhanced sublimation when the temperature is about 500 °C and over 1000 °C, respectively. So the graphite tiles have to be cooled for the temperature to be kept less than ~500 °C. This requirement is important, especially for the long pulse operation. In addition to above sputterings, the graphite evaporates or sublimates when the temperature exceeds ~2000 °C. The weight loss due to this sublimation is roughly expressed by the product of heat load and square of the pulse time [3]. For the case of isotropic graphite, the region in which the sublimation becomes dominant, is shown in Fig.2. If the weight loss factor is less than (25-32) [MW/m².√s], the sublimation may not occur. For the Large Helical System, the weight loss factor does not exceed this limit, when the pulse length is 10 sec and the heat load is 5 MW/m². Thus, the erosion of this type is not serious.

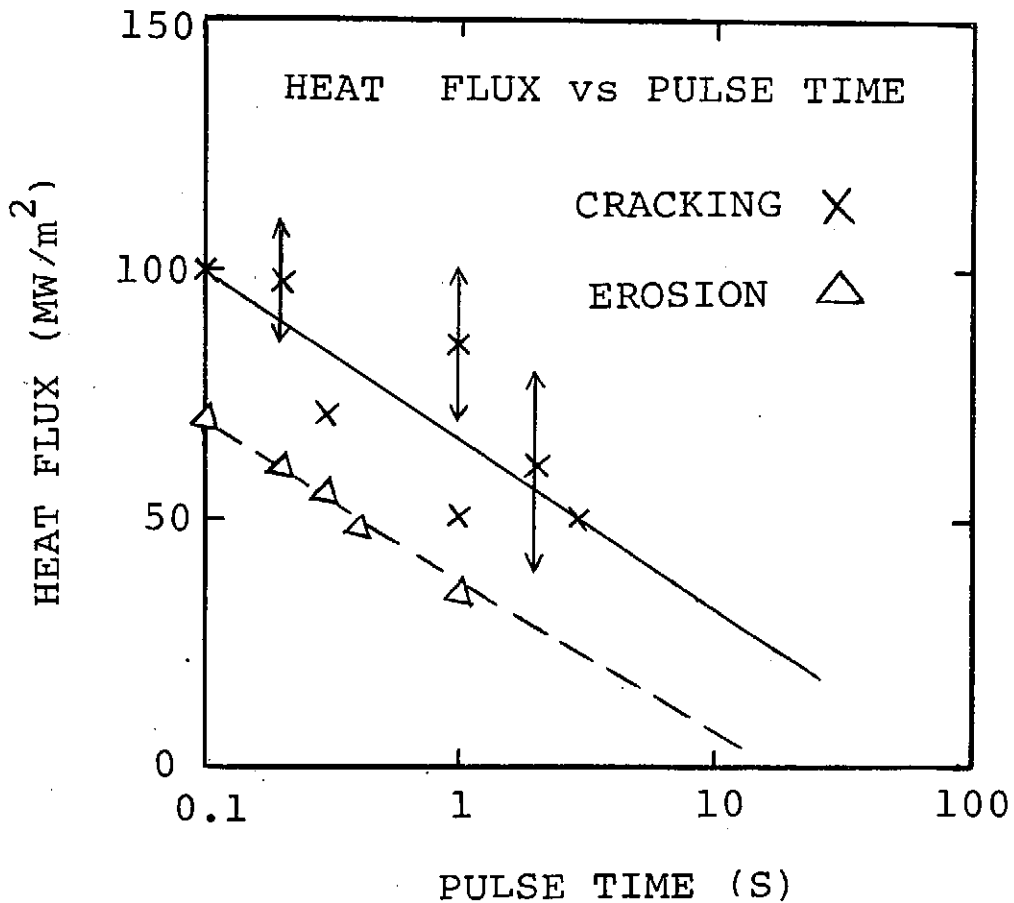


Fig.2 Limit of isotropic graphites for erosion and cracking.

The serious problem may be cracking of the graphite tile due to the thermal shock. Figure 2 also shows the region for the isotropic graphite to be cracked. The experimental data are referred from the heat load tests [4]. If we extrapolate the experimental data to the pulse length of 10 sec, the limit value of the heat flux is approximately 25 MW/m^2 . The heat flux of 5 MW/m^2 in the Large Helical System, then, may not cause the cracking of the graphite tile. This result is valid only in the case that the heat load is uniform in the divertor region. If the heat load is very localized, the tile made by the isotropic graphite might be cracked.

It is known that felt type C/C composite material has excellent thermal-mechanical properties, large fracture toughness and large thermal shock resistivity. Thus, the C/C composite may have to be used in the divertor region with very high heat load. The isotropic graphite materials with high thermal shock resistivity, on the other hand, has been recently developed. The isotropic graphites also should be used for the region with relatively lower heat load.

3. SUMMARY

The graphite materials such as isotropic graphite and C/C composite, which can be used as the divertor tile, are evaluated in terms of erosion, thermal shock resistance and recyclings. It is also suggested that the baking with temperature of $\sim 350^\circ\text{C}$ and the cooling for the chemical sputtering to be suppressed are required. For the first wall region not covered graphite tile, i.e. side metal walls, the discharge cleaning has to be applied. It is important to perform the discharge cleanings without the sputterings, for the graphite surface not to be covered by metals.

REFERENCES

- [1] T.Yamashina and T.Hino, J.Nucl.Mater.,162-164,p.841-850,1989.
- [2] T.Yamashina, "Overall Characterizations of Graphites as Fusion First Wall Material and Evaluation of the Stability Against Plasmas", published in Jan.,1989.
- [3] H.Takatsu and T.Oku, Tanso, No.135,p.286(1988).
- [4] H.Bolt, Proc. US-Japan Workshop Q86,SAND 88-1072,p.392(1988).

The Main Fusion Activities in Institute of Plasma Physics,
Academia Sinica
Wang Shao-hu
Institute of Plasma Physics, Academia Sinica
Hefei, P.R.China

Abstract

ASIPP was established in 1978. It is one of important fusion research center in China. Two tokamak devices have been put into operation. Resonant Helical Field can significantly suppress the MHD modes and improve the confinement of plasma. A middle size tokamak device, HTU will be put into operation in 1991. Since 1987, ASIPP began to carry out a National High Technology Program---Fusion-Fission Hybrid Reactor Program.

A. Basic Situation of ASIPP

1. ASIPP was established in 1978. It develops very fast and has become a medium size laboratory and a very important fusion research center in China.

2. 557 staff include 63 senior researchers
127 graduate students

3. Division, Centers and main Facilities:

* Power Supply Division:

a 200MJ inductor

design and construct all of the power supply system for tokamak and ICRH system.

* High Magnetic Field Division

a 20 Tesla hybrid steady-state magnet

Theory Division

MHD

Transport

RF-plasma interaction

Numerical simulation

Tokamak Division

two tokamaks:

HT-6B: $R=45\text{cm}$; $a=12.5\text{cm}$; $B_t=1\text{T}$; $I_p=50\text{KA}$

HT-6M: $R=65\text{cm}$; $a=20\text{cm}$; $B_t=1.5\text{T}$; $I_p=150\text{KA}$

more than 30 diagnostics

Vacuum Technology Division

pump limiter and pellet injector are under construction

plasma-wall interaction

Computer/Data Acquisition and Processing Division

two PDP 11/24 computers with 100-channel CAMAC system

RF Heating and Current Drive Division

1MW ICRH system available

100 KW LHCD system under construction

two 40KW ECRH systems in operation

Alternative Approach Division

a simple mirror HER (hot electron ring)

MPT-X tokamak/octopole configuration, another simple mirror TAT is under construction.

Technical Center

4 sets of d.c. flywheel generators, total 80MW

1 set a.c. flywheel generator 120MW

deionized water station with ability of 60 tons/hour

cryogenic system with 30 liters/hour LHe and LN

Engineering and Technology Center

a large workshop

the ability and the experience in design and fabrication of medium size tokamaks, diagnostic equipments and some important components of accelerators.

B. Scientific Research in ASIPP

1. Resonant Helical Field (RHF) experiments on HT-6B:

* It can suppress the MHD modes (1984)

* All of different resistive MHD modes, including $m=1$ mode, are coupled so strongly that it seems to be only one global mode (1986)

* RHF can significantly improve the confinement of plasma (1988)

2. Super-low density discharge experiment on HT-6M:

get more peak profile of $T_e(r)$; get good confinement of plasma.

3. The slow compression along plasma minor radius experiment on HT-6B:

The results showed that plasma confinement was improved effeciently and the plasma parameters were increased apparently.

4. Studies of fine structure of discharge region on HT-6B:

It is found that in a operation diagram of n_p vs $q(a)$ there exist a transition region. In that region and its vicinity, the external helical field (RHF) has many intense effects, such as suppression of MHD oscillation, amplification of sawtooth fluctuation and improvement of discharges and so on.

5. Hot electron ring experiments on small simple mirror:

HER can stabilize instabilities

C. International cooperation and exchange:

1. we have received fusion journals, preprints from almost all the main fusion centers over the world. Each year we send our scientists and engineers to attend the important international conferences and meetings.

2. In ASIPP, there are about 50 scientists and engineers who have experiences working in main fusion labs abroad for at least 2 years and there are still about 40 persons working or learning abroad. In average, there are about 40 scientists from Europe, USA and Japan visiting ASIPP each year.

3. We have begun some collaboration program with other fusion labs such as: a collaboration program for the construction of TEXT UP-Grade between ASIPP and Fusion Research Center in Texas has been carried out and will be further developed into a scientific collaboration program on TEXT Up-Grade. Since this summer a Chinese scientist group have been working at Julich fusion institute in West Germany. They will work there for two years.

4. We have also emphasized to develop the relation with the plasma physics labs in developing countries. The collaboration agreement between ASIPP and Plasma Physics Lab of San Paulo University has already been carried out. We have contacted with Iranian Plasma Lab and the Fusion Center in India.

D. Further research Programs:

1. We will continue the experiments of helical field to study the mechanism of improvement of the plasma confinement and will use more ways to change the plasma boundary condition, such as the local ECRH heating and the slow compression in the minor-radial direction. Our theoretical group will work on this research project.

The detailed study of the properties of super-low-density discharge and the effects of helical field on the collapse process of sawtooth will also be continued. We attempt to find some simple way to control the sawtooth oscillation.

2. We have already prepared 1MW ICRH system for HT-6M, so the heating power density will reach nearly $2\text{MW}/\text{M}^3$. Another 1.5MW ICRH system is under construction now. One of our main aim of plasma research is to study the plasma behaviour under very high ICRH power density. We think that such study will become more significant in the future. In addition we will prepare 0.5MW low-hybrid wave system (2.54GHz) for current drive.

We began to design and build a new tokamak HTU. The main parameters are $R=125\text{cm}$, $a=35\text{cm}$, $B_t=3\text{T}$, $I_p=500\text{KA}$, with 3MW ICRH and 1MW LHCD. It will be put into operation in 1991.

E. Fusion-Fission Hybrid Reactor

---A Chinese National High Technology Program

Since 1987, we began to carry out a National Fusion-Fission Hybrid Reactor program which has been directly under the National Commission of Sciences and Technology. ASIPP is in charge of this program.

1. The purpose is to produce fission fuel
From U^{238} to Pu^{239} or From Th^{232} to U^{233}

The neutrons from the fusion core would react with fissile material and lithium in a blanket surrounding the core. So it will create fission fuel and tritium also some heat.

2. The necessity and feasibility of a Fusion-Fission Fuel Factory for supporting PWR nuclear power station in China.

China is developing PWR program for middle size nuclear power stations now. However, because of only limited uranium resource, it is necessary to consider developing breeder type reactors.

We can make a fusion core based on the technology less challenging than that required for a pure fusion reactor. The plasma physics knowledges and fusion technologies, needed for a hybrid reactor mainly producing fuel, seems to be well developed.

3. The blanket could be a passive system.

The fission part of the hybrid reactor is blanket. It could always be sub-critical, and thus, a passive system. The power density in the blanket can be designed as low as the existing heat transfer technology. The blanket can easily be fission-suppressed or partial fast-fissional.

4. In recent years the main aim is studying the feasibility of such kind of hybrid system and developing some key technologies, including high power density ICRH; high power LHCD; material, tritium technology and so on.

The main Chinese Fusion Institute and some nuclear institutes have been involved in the Hybrid national Program. ASIPP has not only organized this program, but also proceeded the conceptual design, high power ICRH and LHCD experiments.

Analysis of Scrape-off Layer in Toroidal Helical Systems

K. Nagasaki, K. Itoh[†], S.-I. Itoh[†] and A. Fukuyama[‡]

Plasma Physics Laboratory, Kyoto University, Uji, Kyoto, Japan

[†] *National Institute for Fusion Science Chikusaku, Nagoya, Japan*

[‡] *Faculty of Electric Engineering Okayama University, Okayama, Japan*

Abstract

Magnetic field structure of the scrape-off layer region in toroidal helical systems is analyzed by using toroidal harmonic functions. The connection length of the field line to the wall, L , is calculated for various configurations. It is found that L has a logarithmic dependence on the distance from the outermost magnetic surface or from the residual magnetic islands, δ . The effect of the axisymmetric fields on the field structure is also discussed.

1. Introduction

In straight helical systems and in axisymmetric toroidal systems like tokamaks, the magnetic surfaces are perfectly closed within the separatrix, provided that there are no perturbations. In toroidal helical systems, the closed magnetic surfaces can be partly destroyed so that a stochastic region appears in the scrape off layer (SOL) region. When the field is stochastic, it is necessary to analyze its statistical properties.

Divertor function has an important role in controlling particles and heat in toroidal plasmas. It also improves the confinement of the core plasma. The separatrix has a divertor function in axisymmetric systems. The question of whether the stochastic region plays the role of the divertor function or not merits further study, because the separatrix disappears in toroidal helical systems. We study the magnetic field structure of the SOL region in $\ell = 2$ toroidal helical systems. The connection length of the magnetic field is used to determine the field structure in toroidal helical systems. We use a simple toroidal harmonic function to construct a model of vacuum magnetic fields.

2. Model

The vacuum magnetic field of toroidal helical systems can be expressed by the magnetic scalar potential as $\mathbf{B} = -\nabla\Phi$. The potential, Φ , is represented in terms of the toroidal harmonic functions as

$$\Phi = \sum_{\ell, m} \alpha_{\ell m} f_{\ell m}(y) \sqrt{1 - y \cos \psi} \cos(\ell\psi + m\zeta) \quad (1)$$

where ℓ and m are the poloidal and toroidal pitch numbers, respectively, $\alpha_{\ell m}$ is a numerical coefficient, and (y, ψ, ζ) are the toroidal coordinates.

By taking a simple (ℓ, m) -Fourier component and superimposing the axisymmetric toroidal and vertical fields, \mathbf{B}_ζ and \mathbf{B}_v , the total magnetic field is expressed as

$$\mathbf{B} = -\nabla\{\alpha_{\ell m} f_{\ell m}(y) \sqrt{1 - y \cos \psi} \cos(\ell\psi + m\zeta)\} + \mathbf{B}_\zeta + \mathbf{B}_v. \quad (2)$$

For these reasons, the connection length near the OMS can be written as

$$L_{\pm}(\delta, \theta, \zeta) \sim L(\delta) + \frac{\ell}{m} \left\{ \frac{\pi}{\ell} \mp \left(\theta + \frac{m\zeta}{\ell} \right) \right\} R \quad (3)$$

where $L(\delta)$ is a logarithmic function of δ ,

$$L(\delta) = \frac{\ell R}{m \lambda_1} \ln \frac{b-a}{\delta \lambda_2} \quad (4)$$

where a is a plasma radius and b is an wall radius. The coefficients, λ_1 and λ_2 are order of unity.

The value of λ_1 is a key parameter which determines the absolute value of the connection length. It is confirmed that λ_1 is weakly dependent on both m and the wall radius. The toroidal field changes λ_1 . From the numerical result, we find that λ_1 is proportional to $(a/R)^{1/2}$ as shown in Fig. 4. The inverse aspect ratio a/R is proportional to $(B_{\zeta} - B_{\zeta}^*)^{1/2}$, where B_{ζ}^* is the critical toroidal field at which the confinement region disappears. Therefore, the dependence of λ_1 on the toroidal field is weak. The logarithmic property in straight systems are also studied. The value of λ_1 in straight systems is proportional to $(a/R)^{1/2}$ and is close to the value in toroidal systems. That is, helical systems have a logarithmic property regardless of the existence of the separatrix with similar value of the connection length.

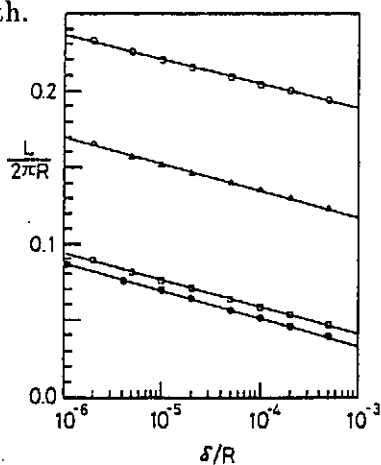


Fig. 3

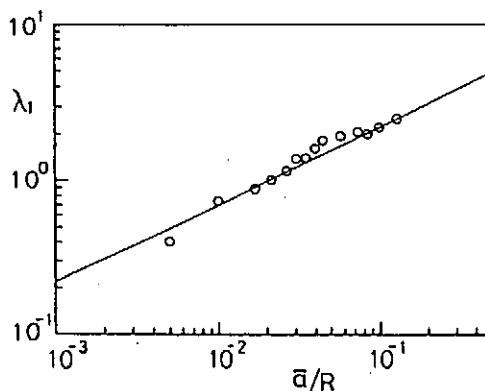


Fig. 4

The dependence of the connection length on δ is similar to that of divertor tokamaks. In axisymmetric systems, the OMS coincides with the separatrix and there exists an X-point where the relative poloidal field disappears. In toroidal helical systems, however, since the separatrix disappears, the logarithmic dependence is caused by other characteristics. This is related to the Kolmogorov-Sinai entropy [1]. When two field lines start from a small distance apart, the distance between them grows exponentially. By taking the initial distance to be δ and the final distance $b - a$, the connection length is found to have a logarithmic

The equation of field line is solved to analyze the structure of the field.

An example of closed magnetic surfaces ($z = 0, \zeta = \pi/2m$) is shown in Fig.1, simulating Heliotron-E device ($\ell = 2, m = 19$). Values of characteristic quantities of the magnetic surface are $\iota(0) = 0.5, \iota(a) = 2.44, a/R = 0.07$, where a is average minor radius.

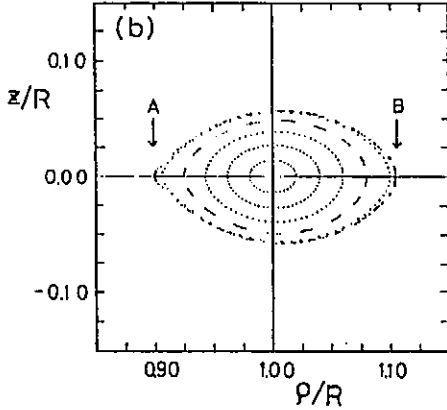


Fig.1

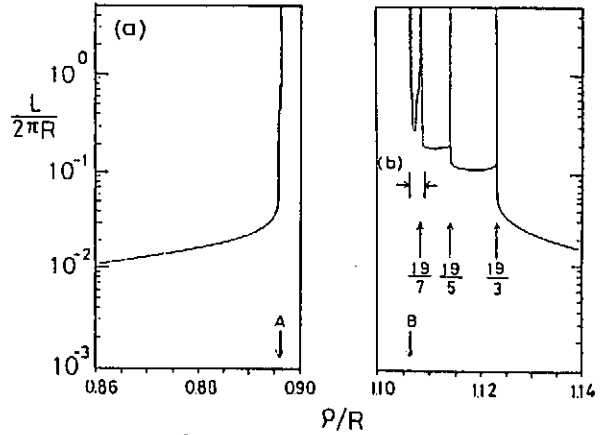


Fig.2

3. Connection Length in Stochastic Region

We follow the field line in the direction of increasing ζ until it reaches the wall. The connection length, L_+ , is defined as the distance along the field line from the initial point to the wall. L_- is also given by following the field line in the opposite direction. L_{\pm} is a function of the initial point coordinate.

Figure 2 shows the example of the radial profile of connection length L_+ . Parameters are the same as in Fig.1. Initial points of the field line are $(r, \theta, \zeta) = (r, 0, \pi/2m)$. Since magnetic surfaces are perfectly closed within the OMS, the connection length has an infinite value within it. Away from it, the connection length decreases rapidly. Magnetic islands exist on rational surfaces and still remain even in the SOL region. In the SOL region, islands are isolated and self-enclosed and have their own inner structure; they have similarly small islands around them. The connection length has an infinite value on the islands and decreases away from the islands' surfaces. Figure 3 shows the asymptotic behavior near the OMS and the surface of residual islands. It is found that L_{\pm} has a logarithmic dependence on δ , where δ is the distance from the OMS or from the surfaces of residual islands. This dependence holds up to a range, $\delta/R \sim 10^{-3}$.

It is also found that the connection length for different values of (θ, ζ) has the same dependence except for a constant term. The distance that the field line travels to reach the low field sides is approximated by $\pi/m \mp (\ell\theta/m + \zeta)$, because the rotational transform near the OMS is much smaller than the geometrical pitch, m/ℓ . This means that the field line moves in a laminar manner and obeys the stochastic law in radial directions near the X-point.

dependence on δ . Though the logarithmic dependence on δ is similar to that in divertor tokamaks, the absolute values are quite different. The connection length in tokamaks is given as ^[2] $L_t \simeq \pi R q_I \ln a/\delta$, where q_I is effective q value. The ratio of L for helical systems (L_h) and tokamaks (L_t) can be obtained as

$$\frac{L_h}{L_t} \simeq \frac{\ell}{m} \frac{1}{q_I}. \quad (5)$$

This ratio is less than 1/10 for typical value ($\ell = 2, m = 12, q_I = 3$). Therefore particles and heat would reach the wall faster in toroidal helical systems than in tokamaks with similar major radius.

4. Conclusion

Field structure of the SOL region in toroidal helical systems was analyzed by calculating the connection length of the field line to the wall. The value of λ_1 increases according to the formula, $\lambda_1 \propto (B_\zeta - B_\zeta^*)^{1/4}$. Increasing B_ζ results in an incremental increase in the inverse aspect ratio, but also brings about an undesirable reduction in the connection length. The plasma volume is also affected by B_v , but λ_1 is nearly independent of B_v . Adjustment in the vertical field can increase the volume without a reduction in the connection length. Therefore, optimization of the plasma volume by B_v is better than optimization by B_ζ from the viewpoint of the SOL plasma confinement.

The value of λ_1 would be modified in real devices, because the single harmonic model field is too simple to describe the fields generated by winding currents. The logarithmic dependence has been verified in a real coil system, Heliotron-E.^[3] and λ_1 is nearly 1.1. This value differs from that of the simple model field by less than a factor of two.

Since this dependence of L on δ is similar to that of tokamaks, analysis of the SOL plasma in tokamaks using the fluid model is applicable. Edge temperature and width of the heat channel have been estimated.^[2] The edge temperature scales as $P^{0.364}$ and the half width of the temperature profile scales as $P^{-0.273}$, where P is the total heat flux out of the plasma surface. These dependencies are the same as in tokamaks. It is noted, however, that the edge temperature is lower than in tokamaks because the connection length is shorter by one order of magnitude, resulting in a set of conditions that make a divertor operation difficult.

References

- [1] B. V. Chirikov, Phys. Rep. **52** (1979) 263
- [2] K. Itoh, et. al, Nucl. Fusion **29** (1989) 1299
- [3] T. Mizuuchi, et. al, J. Nucl. Mat. **121** (1984) 3

DETACHED PLASMA AND DENSITY LIMIT OF TOKAMAKS

Shoichi Yoshikawa
Princeton University, Plasma Physics Laboratory
P.O. Box 451
Princeton, NJ 08543 USA

An analytical solution of detached plasmas in a tokamak is presented. The plasma radius is determined, if the impurity density of a tokamak plasma is assumed at the plasma edge. The additional condition that the safety factor, q , of the plasma must be over 2, leads to the density limit. Thus a tokamak plasma can be classified into (i) limiter or divertor limited, (ii) detached plasmas, and (iii) disruptive plasmas, as the plasma density increases from (i) to (iii).

Confinement Improvement by Edge Control

N. Ohyabu
National Institute for Fusion Science
Furo-cho, Chikusa-ku, Nagoya 464-01, Japan

Abstract: Three types of the divertor operation mode have been considered to improve the plasma performance, particularly the energy confinement in the LHD device.

i) High density, cold divertor plasma operation for reducing the impurity sputtering, ii) H-mode type operation for minimizing the deterioration of the energy confinement at high input power, iii) High temperature divertor plasma operation for further enhancement of the energy confinement.

Deterioration of the energy confinement with added input power is the major concern in designing a large toroidal device such as LHD. Our approach to this problem is to incorporate the τ_E improvement schemes successfully demonstrated in the tokamak discharges into our design as well as to develop our own approaches. Depositing the input power in the central region and reducing the impurity radiation loss are important to achieve good energy confinement, but they are not ones which improve the heat transport. τ_E improvement schemes successfully demonstrated in the tokamak discharges involve particle fuelling and recycling control. It is probably true that some kinds of particle fuelling or recycling control are the only practical scheme to improve the heat transport for a given magnetic configuration and a given average density. For our plan, pellet and neutral beam injections are utilized to make the core density profile steep for improvement of τ_E , seen in the pellet injection discharges and the supershot discharges. Recycling control by the divertor action is believed to be the most effective τ_E improvement scheme. For this reason, one of the LHD design goals is to install a closed helical divertor which is close to ASDEX tokamak divertor in terms of particle control.

We consider three types of the divertor operation mode.

1) High Density, Cold Divertor Plasma Operation.

With such a operation mode, sputtering of the impurity from the divertor plate is minimized and thus the radiative loss can be kept low. Unfortunately, the energy confinement in the tokamak discharge with such a operation tends to be poor.

2) H-mode Type Operation:

From the various tokamak experiments, achieving H-mode discharge requires localization of the particle recycling in the divertor region. For this reason, the divertor is designed to be a tight, closed one, similar to that of ASDEX. An example of the divertor configuration is shown in Fig. 1. High shear seems to be a key ingredient to achieve a good H-mode discharge because the high temperature and density gradients exist in the high shear region just inside the separatrix. Note that "H-mode" has been observed in the circular tokamak discharges without high shear, but the improvement in Σ_E is very minimal. For the LHD configuration (when $\alpha=0.1$), Shear in the edge region within ~ 5cm from the outermost flux surface is ~ three times higher than that in the edge region of the circular tokamak. Thus effective recycling control by the divertor, combined with high shear in the edge region may lead to an H-mode helical discharge.

3) High Temperature Divertor Plasma Operation: If the neutral particles recycled at the divertor plate are pumped by the getter pump in the divertor chamber with pumping efficiency (ζ_{pump}) of > 50%, then the edge plasma temperature will increase up to a few keV. the diverter temperature (T_{div}) is estimated to be

$$T_{\text{div}} = \frac{\zeta_{\text{pump}} (Q_{\text{ex}} / P_{\text{ex}})}{\gamma} \dots\dots\dots (1)$$

where Q_{ex} and P_{ex} are the external power and neutral particle fluxes into the core plasma respectively. Here we assume Bohm sheath theory and γ is the heat transfer coefficient (~8). We neglect the radiative loss and C.X loss for simplicity. For a case in which neutral beam with input power (Q_{ex}) and particle flux (P_{ex}) are injected into the core plasma, $Q_{\text{ex}}/P_{\text{ex}}$ is the beam energy. (100keV for LHD). Assuming that $\zeta_{\text{pump}} \sim 0.5$ and ~ 8 , T_{div} becomes as high as 5keV. In such a operation, the energy confinement is determined by the core particle transport and the wall-plasma interaction.

Achieving high temperature divertor plasma requires minimization of the particle source from the divertor plate. Selection of the divertor plate material is important. Sputtering rate of carbon becomes low at high incident energy of D^+ ion and the self sputtering rate is ~0.4 at the incident energy above 1 keV. Therefore impurity sputtering will not be a problem. If the massive particle source is created e.g. by unipolar ark, the achievable temperature will be limited. The heat transfer coefficient (γ) increases with the electron secondary emission rate, but is limited to ~ 20 because the electron emission then becomes space charge limited. In such a case, T_{div} becomes ~ 2 keV for LHD parameters. However the edge

temperature will still be raised significantly above the H-mode threshold temperature seen in the tokamak and thus a good energy and particle transports are expected in the core region.

In summary, three types of the divertor operation mode have been considered to improve the energy confinement. They are i) High density, cold divertor plasma operation for reducing the impurity sputtering, ii) H-mode type operation for minimizing the deterioration of the energy confinement at high input power and iii) High temperature divertor plasma operation for further enhancement of the energy confinement. The major design goal of the LHD divertor system is that a wide range of divertor operation modes or scenarios can be attempted to optimize overall plasma performance.

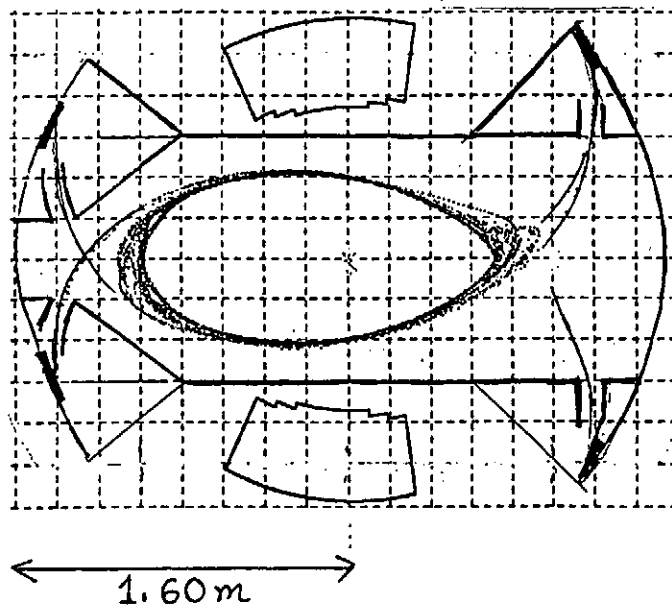


Fig.1 A design of LHD helical divertor

Effects of perturbing helical fields on confinement
of Heliotron DR plasma

S.Morimoto^{*,**}, M.Nakasuga^{**}, N.Yanagi^{*}, M.Sato^{**}, T.Obiki^{**}

^{*} National Institute for Fusion Science, Nagoya 464-01, Japan

^{**} Plasma Physics Laboratory, Kyoto University, Uji 611, Japan

Abstract: Two types of perturbing helical fields have been applied to Heliotron DR plasma ; type A makes a large $m=n=1$ magnetic island at $r/a_p \sim 0.5$ whereas type B makes a set of many islands with high mode numbers ($m=5,4,3$ $n=5,6,7,8,9,10$) at $0.5 \lesssim r/a_p \lesssim 1$. Deterioration of plasma confinement due to the type A perturbation has been observed at $B_{1,1}/B_t \sim 3 \times 10^{-4}$, where $B_{1,1}$ and B_t are the Fourier component of $m=n=1$ and the confining toroidal field, respectively. The plasma performance is less sensitive to the type B perturbation and the confinement deterioration has not been found even at $\zeta > 1$, where ζ is the overlapping parameters of the magnetic islands.

1. Introduction

Many plasma confinement studies in Stellarator/Heliotron devices have shown that anomalous energy transport is dominant particularly in peripheral region of the plasmas. Magnetic field errors and fluctuations have been considered as candidates for this anomalous transport. We have externally applied perturbing helical fields to Heliotron DR plasmas ($R=0.9m$, $a_p \sim 0.07m$, $B_t \lesssim 0.6T$, $t(0)=0.8$, $t(a_p)=2.2$, $\bar{n}_e \lesssim 3 \times 10^{19} m^{-3}$, $T_e(0) \lesssim 400eV$, $\langle \beta \rangle \lesssim 0.5\%$) and examined their responses to the plasma confinement.

2. The perturbing helical fields

Two perturbing helical windings are used in the present experiments as shown in Fig.1. They have poloidal (M) and toroidal (N) pitch numbers of $M/N=1/1$ (type A) and $M/N=5/5$ (type B) and perturb the magnetic surfaces in different manners; the type A produces a large magnetic island of $m=n=1$ at $r/a_p \sim 0.5$ (m and n are poloidal and toroidal mode numbers of the islands) whereas the type B produces a set of many islands of $m=5,4,3$ and $n=5,6,7,8,9,10$ at $0.5 \lesssim r/a_p \lesssim 1$. Figure 2 shows the radial distribution of the rotational transform $t(r)$ and the magnitudes of Fourier

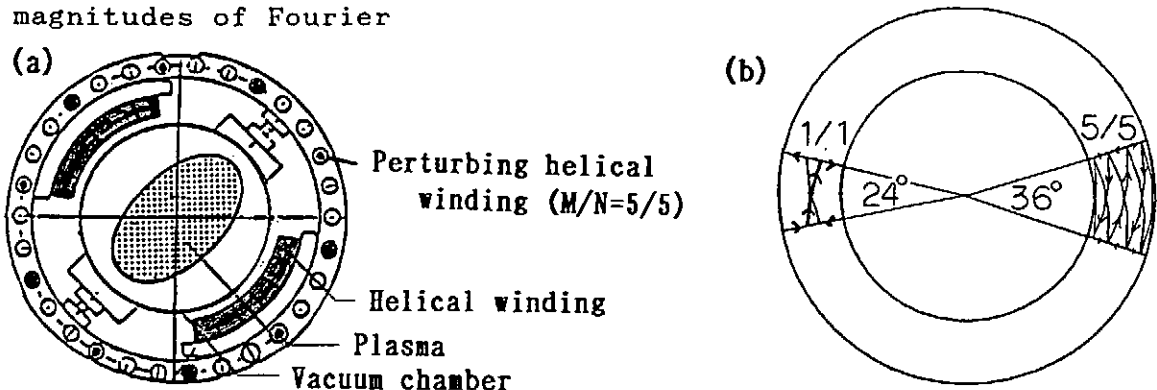


Fig.1 Arrangement of the perturbing helical windings.
(a) poloidal cross section, (b) plan view.

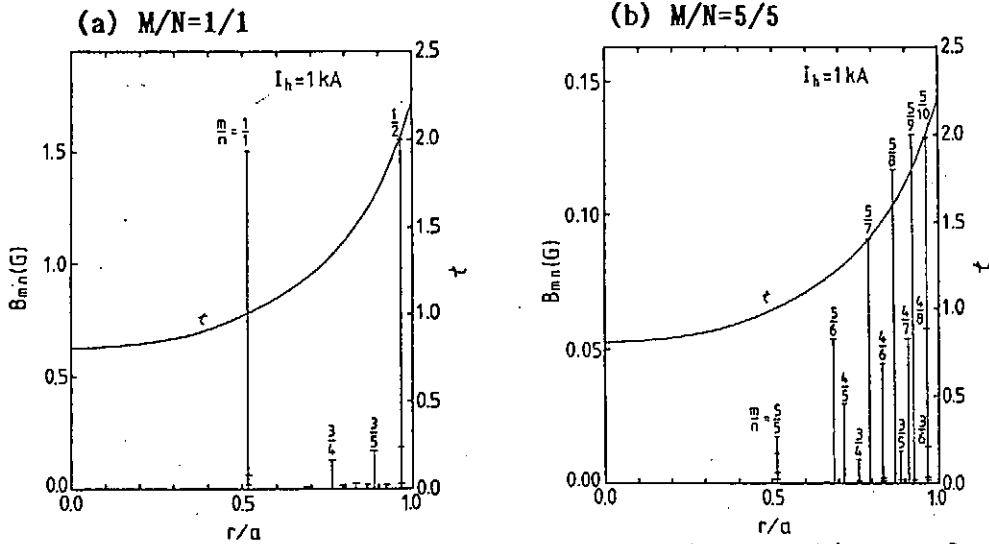


Fig. 2 Fourier components at each resonant magnetic surface.

components, $B_{m,n}$, at the resonant surfaces with $t(r)=n/m$. Since the windings do not cover the full torus, the components with different toroidal mode numbers are excited besides the fundamental one. In case of strong type B perturbations, deterioration of confinement due to overlapping of the magnetic islands is expected [1,2]. The overlapping parameter, ζ , is defined by $(d_{m,n}+d_{m',n'})/2D_{m,n-m',n'}$, where the numerator is sum of the widths of two adjacent islands and $D_{m,n-m',n'}$ is the distance between two rational magnetic surfaces with $t=n/m$ and n'/m' . It is reported that overlapping of magnetic islands starts at $\zeta \sim 0.8$ and full ergodization occurs at ~ 1.5 [2]. In Table I, normalized widths of the magnetic islands and the overlapping parameters for each pair of islands are summarized for typical perturbing coil currents, I_{hel} , in the present experiments. The island width is calculated by using the well known formula; $d_{m,n}=4r(B_{m,n}/m\Theta B_t)^{0.5}$, where Θ is shear parameter. It is expected that a large $m/n=1/1$ island is produced by the type A

Table I Normalized magnetic island width, $d_{m,n}$ and overlapping parameter ζ ($B_t=0.5T$)

Type A winding ($I_{hel}=1kA$)			Type B winding ($I_{hel}=9kA$)		
$m/n - m'/n'$	$d_{m,n}/a_p$	ζ	$m/n - m'/n'$	$d_{m,n}/a_p$	ζ
1/1 - 3/4	0.23	0.52	5/5 - 5/6	0.033	0.23
3/4 - 3/5	0.027	0.20	5/6 - 4/5	0.046	1.30
3/5 - 1/2	0.023	0.61	4/5 - 3/4	0.035	0.64
1/2	0.073		3/4 - 5/7	0.021	1.16
			5/7 - 4/6	0.048	1.10
			4/6 - 5/8	0.035	1.25
			5/8 - 3/5	0.046	1.64
			3/5 - 4/7	0.018	1.14
			4/7 - 5/9	0.033	2.95
			5/9 - 5/10	0.044	1.00
			5/10	0.040	

perturbation whereas under the type B perturbation of $I_{hel} \geq 5kA$ ($B_t = 0.5T$), the islands are small but they overlap to each other and the magnetic field becomes stochastic except for the narrow region between $t = 5/4$ and $4/3$ surfaces.

The influence of these perturbations have been studied by numerical calculations. Examples of the perturbed magnetic surfaces are shown in Fig.3 for the same coil currents as those in Table I. In case of the type A perturbation, an $m/n=1/1$ island exists around the $t=1$ surface whose size agrees well with analytically calculated one. Closed magnetic surfaces exist outside the $m/n=1/1$ island, however, at the periphery, magnetic field lines show radial excursions. This ergodization of magnetic surfaces is enhanced with increase of I_{hel} . Under the type B perturbation, nested magnetic surfaces can be seen inside the $t=1$ surface (even at the strong perturbation of $I_{hel} = 18kA$), however, in the outer region of $t > 1$, the magnetic field lines show large radial excursions which also increase with increase of I_{hel} .

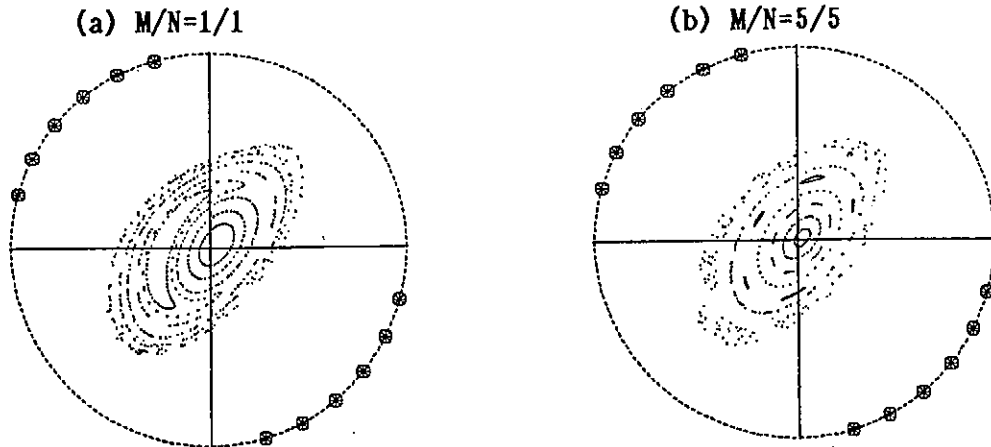


Fig.3 Magnetic surfaces under type A (a) and B (b) perturbations

3. Experimental results

The perturbation fields are applied to the overdense ECH plasmas heated by a 28GHz, 200kW gyrotron [3]. During the ECH pulse, the electron density is gradually increased above the cut-off value of $1 \times 10^{19} m^{-3}$. The stored plasma energy is also increased along with the density. The collisionality of such overdense plasmas is in plateau regime. An regression analysis of the decay time of the stored energy after the turn-off of ECH pulse shows that it agrees well with the LHD scaling law indicating dominant anomalous energy transport. Figure 4(a) shows the effect of the type A perturbation on the averaged electron density, \bar{n}_e , the stored plasma energy (diamagnetic), W_p , and conductivity electron temperature, $T_{e\sigma}$, measured at the end of the ECH pulse. The small plasma currents, $I_p \leq 0.8kA$, are induced to suppress pressure driven MHD instability [4]. The experimental conditions such as the gas flow rate and one-turn loop voltage are fixed in this series of discharges. Although the density is almost unchanged, $T_{e\sigma}$ and W_p start to drop at $I_{hel} \sim 1kA$ which corresponds to $B_{1,1}/B_t \sim 3 \times 10^{-4}$ and also to $d_{1,1} \sim a_p/4$. Callen et al. discussed confinement deterioration due to $m=2$ Mirnov oscillation-induced magnetic island in tokamak discharges [5]. They derived the equation of $\tau_E/\tau_{E0} = 1 - (d/a)(4r_s^3/a_p^3)$, where d

is island width and r_s is radius of the singular surface. According to this model, the deterioration occurs much more gradually with increase of I_{hel} as is shown in Fig. 4(a). The ergodization of peripheral magnetic surfaces may be responsible for the experimentally observed confinement deterioration but detail is not clear now.

Plasma performance is less sensitive to the type B perturbation compared with the type A perturbation. We have not found an appreciable reduction of W_p up to $I_{hel}=11\text{kA}$ at $B_t=0.5\text{T}$ although the overlapping parameters mostly exceed 1 (Table I). The level of the perturbation can be raised by operating at lower confining magnetic field. Figure 4(b) shows W_p versus I_{hel} at $B_t=0.25\text{T}$ and also the representative overlapping parameters. The reduction of W_p is seen at $\{ \sim 2$. One possible reason that the confinement deterioration is not found up to such a high perturbation level might be existence of more strong magnetic fluctuations in the plasma. Analyses of magnetic probe data suggest that the fluctuation level attains to the order of 10^{-4}T in the plasma which is higher than the externally applied perturbations. We have observed the confinement is deteriorated at lower $\{$ values of ~ 1 for lower beta plasmas (lower fluctuation level).

Summarizing, an $m=n=1$ perturbation with $B_{1,1}/B_t \sim 3 \times 10^{-4}$ has been observed to be dangerous for plasma confinement. Confinement deterioration due to high m, n perturbations (type B) has not been found even at high overlapping parameters of ≥ 1 . There is a possibility that magnetic fluctuations due to plasma turbulence invalidate the effect of externally applied perturbations.

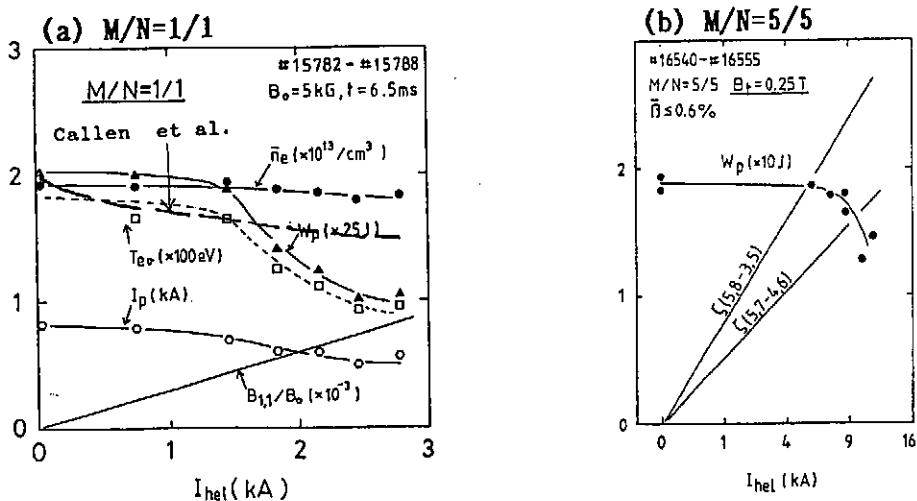


Fig.4 Effects of (a) type A and (b) type B perturbations.

References

- [1] R.B.White et al., Plasma Phys. and Contr. Nucl. Fusion Research, Baltimore 1982, IAEA, Vienna 1983, Vol. III, p.391
- [2] M.Hugon et al., 1987 Int. Conf. on Plasma Phys., Kiev 1987, Vol. I, p.432.
- [3] S.Morimoto et al., Nucl. Fusion 29, 1697 (1989).
- [4] S.Morimoto et al., Jap. J. of Appl. Phys. 28L, 1470 (1989).
- [5] J.D.Callen et al., Plasma Phys. and Contr. Nucl. Fusion Research, Innsbruch 1978, IAEA, Vienna 1979, Vol. I, p.415

Overview of Recent Results from The Advanced Toroidal Facility

M. Murakami, E. Anabitarte,¹ F. S. B. Anderson,² G. L. Bell,³ J. D. Bell,⁴
T. S. Bigelow, B. A. Carreras, L. A. Charlton,⁴ T. L. Clark,⁵ R. J. Colchin,
E. C. Crume, N. Dominguez, J. L. Dunlap, G. R. Dyer, A. C. England, P. W. Fisher,
R. F. Gandy,³ J. C. Glowienka, R. H. Goulding, G. R. Hanson,⁶ J. H. Harris,
G. R. Haste, C. Hidalgo-Vera,¹ D. L. Hillis, S. Hiroe, L. D. Horton, H. C. Howe,
D. E. Hutchinson, R. C. Isler, T. C. Jernigan, K. L. Kannan, H. Kaneko,⁷ M. Kwon,⁶
R. A. Langley, J. G. Leboeuf, D. K. Lee,⁴ J. W. Lue, V. E. Lynch,⁴ J. F. Lyon,
C. H. Ma, M. M. Menon, P. K. Mioduszewski, R. N. Morris,⁴ G. H. Neilson,
A. L. Qualls,⁵ D. A. Rasmussen, Ch. P. Ritz,⁸ P. S. Rogers,⁶ S. W. Schwenterly,
K. C. Shaing, P. L. Shaw,⁶ T. D. Shepard, J. E. Simpkins, K. A. Stewart, S. Sudo,⁷
C. E. Thomas,⁶ J. S. Tolliver,⁴ T. Uckan, M. R. Wade,⁶ J. B. Wilgen, W. R. Wing,
H. Yamada,⁹ and J. J. Zielinski¹⁰

*Oak Ridge National Laboratory
Oak Ridge, Tennessee 37831-8072, U. S. A.*

Abstract: An overview of recent experimental results from the Advanced Toroidal Facility (ATF) is presented. Beam-heated plasmas with n_e of 10^{20} m^{-3} and τ_E^* of ≈ 20 ms have been achieved. Thermal collapse of the plasmas is mitigated by wall conditioning and particle fueling. Confinement time scales positively with density and magnetic field, offsetting deterioration with power. Results fit the LHD scaling and the drift wave turbulence scaling. Bootstrap currents observed during ECH agree with neoclassical theory in magnitude and parameter dependences. Fast reciprocating Langmuir probe measurements show that edge fluctuations in ATF have many similarities to those in the TEXT tokamak. The location of \tilde{B} instabilities has shifted outward in radius, consistent with the broader pressure profiles.

1. Introduction

In the past year, significant progress has been made in extending the research capabilities of ATF.¹ After verification of the successful repair of the error field, the maximum magnetic field was increased from 0.95 T to 1.9 T, a power supply was added for the mid-VF coils, six getter sources and a second 53-GHz gyrotron were installed, and profile diagnostics were improved (two-dimensional Thomson scattering, scanning neutral particle analyzer, FIR interferometer, etc.). Recent experiments² have concentrated on (1) plasma performance improvement and confinement scaling (2) bootstrap current and (3) fluctuation studies.

2. Improvement of Plasma Performance and Confinement Scaling

Recent improvements in plasma performance are the result of improved impurity and particle control. Previously, glow discharge cleaning with vacuum vessel baking (at 150°C) was used for wall conditioning. Although quasi-stationary ECH discharges lasting for up to 1s were obtained at 0.95 T, NBI discharges suffered thermal collapse in spite of low impurity density and low radiative power fractions ($Z_{\text{eff}} \leq 2$ and $P_{\text{rad}}/P_{\text{input}} < 40\%$ until the time of the collapse).^{3,4} The low radiation levels suggested that impurities might not be the sole culprit.

¹CIEMAT, Madrid, Spain.

²University of Wisconsin, Madison, WI.

³Auburn University, Auburn, AL.

⁴Computing and Telecommunications Division, Martin Marietta Energy Systems, Inc.

⁵University of Tennessee, Knoxville, TN.

⁶Georgia Institute of Technology, Atlanta, GA.

⁷Plasma Physics Laboratory, Kyoto University, Uji, Japan.

⁸University of Texas at Austin, Austin, TX.

⁹National Institute for Fusion Science, Nagoya, Japan.

¹⁰Rensselaer Polytechnic Institute, Troy, NY.

The collapse has not been eliminated, but extensive gettering ($\approx 60\%$ wall coverage) and better gas programming have led to extended longevity (up to 0.27 s) for NBI discharges.

Figure 1 shows the time evolution of several plasma parameters for a typical recent discharge with NBI (H^0 into D^+ , 1.4 MW total from co- and counter-injecting beams, 1.9 T, Ti gettering). "Reheating" occurs after cessation of the strong gas puff at the beginning of the beam pulse. At the peak of the soft x-ray signal, the line-average density $\bar{n}_e \approx 6.1 \times 10^{19} \text{ m}^{-3}$, the diamagnetically measured plasma stored energy $W_p = 19 \text{ kJ}$, the global energy confinement time $\tau_E^* = W_p/P_{in} = 12 \text{ ms}$, and the "apparent" ion temperature obtained from neutral particle analysis is 0.28 keV. Profile analysis based on Thomson scattering profiles taken at this time indicates that the "apparent" ion temperature is approximately consistent with neoclassical ion conductivity. The analysis yields a stored energy of 17 kJ (with a 5% contribution from the fast ion component), and a (thermal) gross energy confinement time, $(W_e + W_i)/(P_{be} + P_{bi}) = 12 \text{ ms} \approx \tau_E^*$. The optimal gas puffing (a strong, short fueling which results in reheating) is reminiscent of successful pellet injection and of the Improved Ohmic Confinement (IOC) mode in ASDEX.⁵

The maximum value obtained for W_p (27 kJ at $B_0 = 1.9 \text{ T}$) is an increase by factor of 3.5 over the level achieved in 1988.³ Global confinement times of 20 ms have been obtained with injected power $> 1 \text{ MW}$; confinement times as high as those in ISX-B even including the operations with impurity-enhanced confinement (the Z-mode).⁶ The highest volume-average β ($\langle\beta\rangle = 0.84\%$ at $B_0 = 0.95 \text{ T}$) was achieved with NBI and fueling with two 0.5-mm pellets at 1.0 km/s.

Higher densities are possible with NBI, and the positive density dependence offsets the degradation with power. Global confinement in ATF is consistent with the LHD scaling,⁷

$$\tau_E^{\text{LHD}} = 0.17 P^{-0.58} n^{0.69} B^{0.84} a^{2.0} R^{0.75} \quad (\text{s}; \text{MW}, 10^{20} \text{m}^{-3}, \text{T}, \text{m}, \text{m})$$

as shown in Fig. 2. ATF (and other stellarator) data also fit well the drift wave turbulence (gyro-reduced Bohm) scaling,^{8,9}

$$\tau_E^{\text{dw}} = (1 \times 10^{-9}) \cdot P^{-0.6} n^{0.6} B^{0.8} a^{2.4} R^{0.6} \kappa_A^{-0.2} \quad (\text{SI units})$$

as shown in Fig. 3. This suggests that drift waves, in particular trapped-electron instabilities, may be important in stellarator (and tokamak) plasmas. ATF can make a significant contribution here because the fraction of confined trapped-particles and the magnetic shear can be externally controlled, thereby directly influencing the instabilities.

3. Bootstrap Current

The present ATF experiment is aimed at verifying neoclassical theory on bootstrap current through direct measurements (in the absence of other current) and parametric scans (in particular, with magnetic configuration). Neoclassical theory¹⁰ predicts that, in the low-collisionality limit, the bootstrap current is given by $j_b = -3(f_i/f_e) G_b B_0^{-1} \nabla p$, where G_b is a magnetic geometry factor that depends on the $|B|$ spectrum on a flux surface and changes with the quadrupole (shaping) or dipole (vacuum axis) component of the vertical field.

The toroidal current observed during ECH in ATF is predominantly bootstrap current. There is negligible OH loop voltage ($V \leq 0.003 \text{ V}$). ECH current drive is negligible, because: (1) the microwave power is launched perpendicular to the magnetic field, and (2) the observed current responds to reversal of the helical coil current and to changes in n_e , in contradiction to the expectations for an ECH-driven current. More importantly, the following results confirm the parametric dependences on vertical field that are predicted by neoclassical theory.

Figure 4 shows the currents observed as a function of the mid-VF coil current ratio, the parameter that changes the quadrupole component of the vertical field. Also shown are the bootstrap currents calculated with neoclassical theory. The agreement is good in both magnitude and dependence on the quadrupole field. The bootstrap current decreases as the plasma is vertically elongated (as the coil current ratio increases). Figure 5 shows that the bootstrap current observed in the dipole field scan is also consistent with the theory. The current increases as the vacuum axis is shifted inward ($\Delta_v < 0$), until it eventually decreases owing to reduction of plasma pressure by confinement deterioration. We also observe that the current normalized to the stored energy (or total pressure) for operation at 1.9 T is lower by about a factor of 2 than that at 0.95 T, supporting the assertion that I_p is inversely proportional to B_0 .

The results show that the neoclassical theory of the bootstrap current describes the current flow in ATF even in the presence of anomalies in particle and heat flows. In addition, the results demonstrate the ability to reduce the toroidal current down to zero, as is desirable for stellarator operation. The directions of the vertical field components to minimize the current are the same as those needed for high- β plasmas (which optimize with outside shift and elongation).¹

4. Fluctuation Studies

There are three general classifications of fluctuation studies in ATF: (1) plasma edge turbulence; (2) high- β stability; and (3) the low-collisionality regime. We have initial results in the first two areas, and are starting investigation of the third with the recent installation of a second gyrotron.

In the edge fluctuation studies we use a fast reciprocating Langmuir probe (like that used on the TEXT tokamak¹²) to measure density (\bar{n}) and potential (Φ) fluctuations in the plasma edge ($0.95 < r/a < 1.13$) of ATF and then compare the results with those from TEXT. The general features of the fluctuations are the same on both devices. In particular, the data show a departure from the Boltzmann relationship; experimentally, $\langle e\Phi/kT_e \rangle > \langle \bar{n}/n \rangle$, as shown in Fig. 6(a). These features are generally consistent with a model of radiative thermal instability coupled with resistive instabilities.¹³ The calculated fluctuation-induced particle flux [Fig. 6(b)] is comparable to the total particle flux estimated from H_α measurements, assuming that particle flux is constant on a magnetic flux surface.

In recent work, instabilities seen by magnetic fluctuation (\bar{B}) probes have shifted outward in radius. We interpret this shift as a consequence of pressure profile broadening brought on by the field error repair and performance improvement. A clear change in the edge density fluctuation spectrum measured by the microwave reflectometry occurs during the "reheating" phase described in Section 2 and appears to have a $\langle \beta \rangle$ threshold. Part of its spectrum is then correlated with \bar{B} .

ACKNOWLEDGMENTS

We acknowledge with appreciation the efforts of our technical support group (G. H. Henkel, L. A. Massengill, C. R. Schaich, T. F. Rayburn, W. L. Redmond, and J. L. Yarber), of our engineering group (R. D. Benson, W. R. DeVan, W. A. Gabbard, J. W. Halliwell, R. L. Johnson, J. A. White, C. T. Wilson, and R. E. Wright), and of our data handling group (C. A. Giles, D. C. Giles, D. E. Greenwood, D. L. Million, D. R. Overbey, T. C. Patrick, and K. G. Young). We are grateful for the encouragement and support of Drs. M. J. Saltmarsh and J. Sheffield. This research was sponsored by the Office of Fusion Energy, U.S. Department of Energy, under contract DE-AC05-84OR21400 with Martin Marietta Energy Systems, Inc.

REFERENCES

- [1] J. F. Lyon et al., *Fusion Technol.* **10** (1986) 179.
- [2] R. J. Colchin and the ATF Group, to be published in *Phys. Fluids* (1990).
- [3] M. Murakami et al., in Proc. 16th Eur. Conf. on Controlled Fusion and Plasma Physics, Venice, 13–17 March, 1989, Europhys. Conf. Abstr., **13B** (1989) Part II, 575.
- [4] R. C. Isler et al., *Nucl. Fusion* **29** (1989) 1381.
- [5] F. X. Soldner et al., *Phys. Rev. Lett.* **61** (1988) 1105.
- [6] E. A. Lazarus et al., *Nucl. Fusion* **25** (1985) 135.
- [7] S. Sudo et al., to be published in *Nucl. Fusion* (1989).
- [8] F. W. Perkins, in Heating in Toroidal Plasmas: Proc. 4th Int. Symp. Rome, 1984, Vol. 2 (1984) 977.
- [9] R. Goldston, *Bull. Am. Phys. Soc.* **34** (1989) 1964.
- [10] K. C. Shaing et al., *Phys. Fluids B* **B**, 1 (1989) 163, and references therein.
- [11] J. H. Harris and the ATF Group, to be published in *Phys. Fluids B* (1990).
- [12] Ch. P. Ritz et al., *Nucl. Fusion* **27** (1987) 1125.
- [13] D. R. Thayer and P. H. Diamond, *Phys. Fluids* **30** (1987) 3724.
- [14] J. H. Harris et al., *Phys. Rev. Lett.* **63** (1989) 1249.

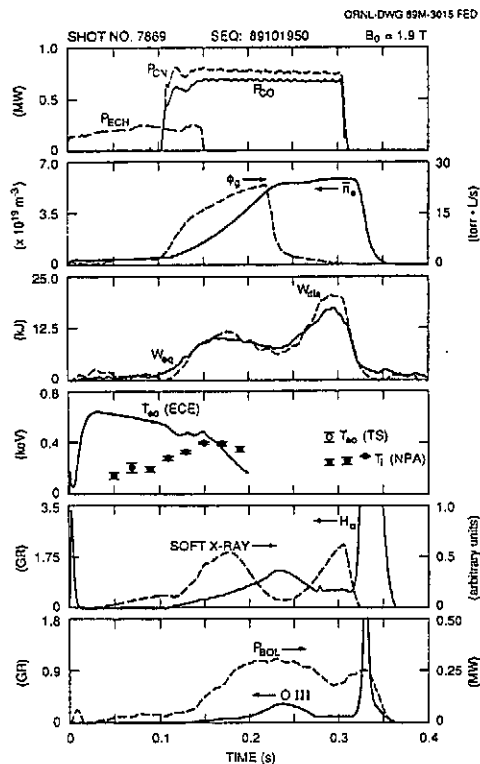


Fig. 1 Time evolution of a typical NBI discharge.

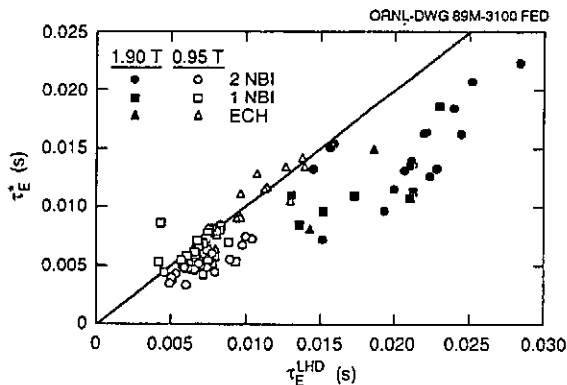


Fig. 2 Global energy confinement vs LHD scaling.

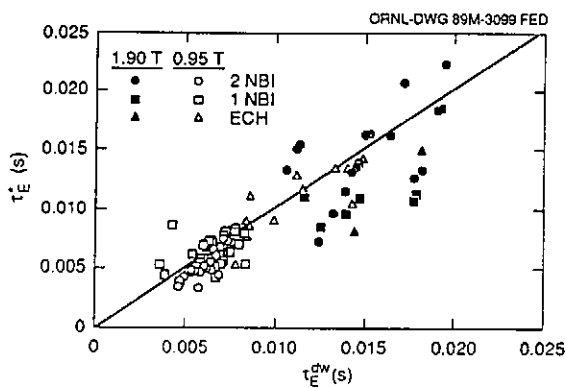


Fig. 3 Global energy confinement vs drift wave turbulence scaling.

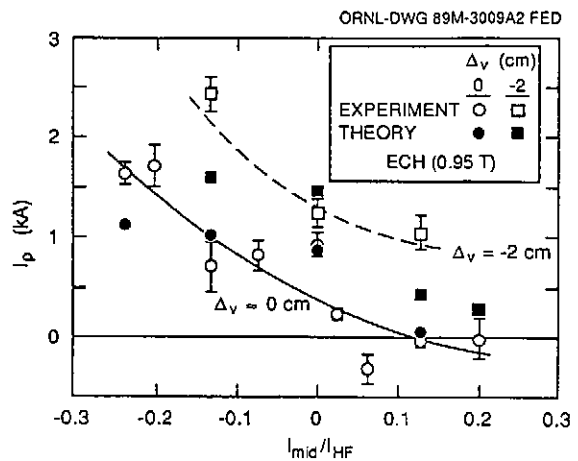


Fig. 4 Bootstrap current vs mid-VF current ratio in the quadrupole field scan: experiment and theory.

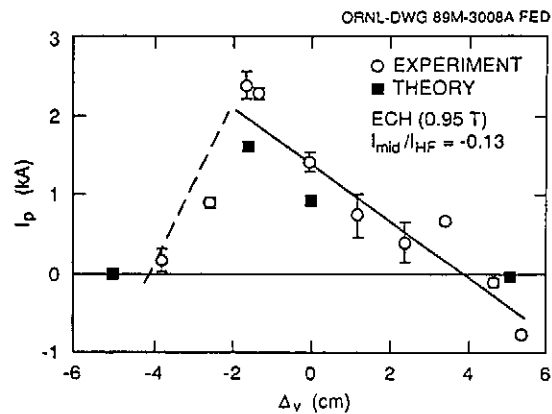


Fig. 5 Bootstrap current vs vacuum axis shift in the dipole field scan: experiment and theory.

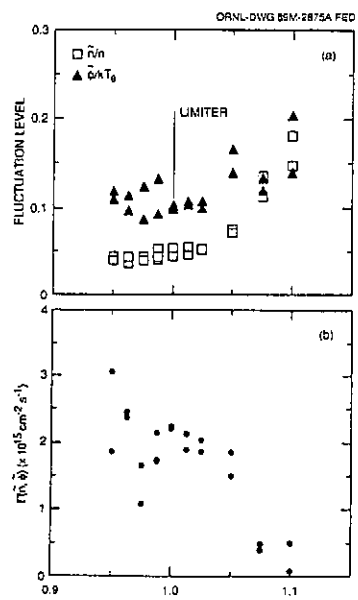


Fig. 6 Radial dependences of (a) edge density and potential fluctuations and (b) calculated induced particle flux.

Toki-Conference, December 1989

Status of the WVII-AS Program
H. Ringler, WVII-AS Team, NBI-Group
ICF-Group, ECRH-Group

Max Planck Institut für Plasmaphysik, Euratom Association,
D-8046 Garching, FRG
Institut für Plasmaforschung der Universität Stuttgart
D-7000 Stuttgart, FRG

WVIL-AS E. Anabitarte¹⁾, E. Ascasibar¹⁾, S. Besshou²⁾, R. Brakel, R. Burhenn, G. Cattanei, A. Dohy, D. Dorst, A. Elsner, K. Engelhardt, V. Erckmann, D. Evans, U. Gasparino, G. Grieger, P. Grigull, H. Hacker, H. Hailer⁶⁾, H.J. Hartfuss, H. Jäckel, R. Jaenicke, S. Jiang³⁾, J. Junker, M. Kick, H. Kroiss, G. Kühner, I. Lakicevic, H. Maaßberg, C. Mahn, R. Martin¹⁾, G. Müller, H. Münch, A. Navarro¹⁾, M. Ochando¹⁾, W. Ohlendorf, M. Petrov⁴⁾, F. Rau, H. Renner, H. Ringler, J. Saffert, J. Sanchez¹⁾, J. Sapper, A.V. Saposhnikov⁵⁾, F. Sardei, I.S. Sbitnikova⁵⁾, I. Schönewolf, K. Schwörer⁶⁾, F. Tabares¹⁾, M. Tutter, A. Weller, H. Wobig, E. Würsching, N. Zippe.

NBI J.H. Feist, K. Freudenberger, R. C. Kunze, W. Ott, F.P. Penningsfeld, E. Speth, W. Melkus.

ECRH W. Kasperek, G.A. Müller, P.G. Schüller, M. Thumm, R. Wienecke (IPF Stuttgart).

ICF J. Bäumlner, W. Becker, F. Braun, R. Fritsch, F. Hofmeister, A. Murphy, J.M. Noterdaeme, S. Puri, F. Ryter, H. Wedler, F. Wesner.

- 1) Guest from CIEMAT Madrid
- 2) Guest from Kyoto University
- 3) Guest from Southwestern Institute of Physics, Leshan, China
- 4) Guest from Ioffe Institute, Leningrad
- 5) Guest from General Physics Institute, Moscow
- 6) Guest from IPF, University of Stuttgart

The first experimental campaign aimed at plasma production and confinement studies was successfully finished on August 2. 1989. All standard diagnostics, the data-aquisition and -handling system were available from the start up phase. During Sept./Oct. 89 the support of the modular field coils MF3 and MF4 has been completed, to reduce the deformation of the coils, which has been observed during the 2.5 T runs. Most experiments have therefore been done at 1.25 T. After some technical tests, the machine is expected to be ready for 2.5 T operation in Dec. 89.

Plasma production and heating was routinely performed with up to 4 gyrotrons (≤ 800 kW) at 70 GHz and the 2nd harmonic with pulse durations up to 0.8 s.

Combined heating with NBI was difficult due to the low cut off density. A fast density rise by pellet injection improved the production of NBI sustained discharges. Plasma parameters with $n_e \leq 6 \times 10^{19} \text{ m}^{-3}$, $T_e \approx T_i = 0.3$ keV, were obtained with NBI heating.

In first tests of the ICRH antenna system, up to 700 kW HF power were launched without significant density and impurity increase. The application at higher field (2.5 T) envisaged for the coming campaign seems to be very promising.

First experimental investigations were focused on:

- Plasma generation using ECF.
- Plasma processing by variation of power deposition and density programming.
- Optimization of heating efficiency and current drive.
- Confinement studies depending on the magnetic configuration: rotational transform, shear, remaining plasma current, modifications by current control.
- First analysis of electron energy transport.
- Evaluation of the particle balance.
- Radiation and impurity content.

Different physical models were adapted to WVII-AS conditions. On the basis of the corresponding numerical codes first comparisons of theoretical predictions and experimental data were possible.

Preliminary results are available for the following topics:

- Transformation of spatial coordinates to magnetic coordinates, including finite β .
- Transport analysis using calculations from the DKES code: heat transport, particle transport, bootstrap current.
- Ray tracing and ECF power deposition, current drive.
- Particle generation and profiles of neutral particles on the basis of the Degas code.
- Impurity sources, radiation.

The first results are based on 6000 discharges, about 5000 at 1.25 T and 300 at 2.5 T.

Details can be found in various publications [1,2,3,4].

Parameter range

Plasma production and heating of a "currentless" plasma over a wide range of parameters with $\beta (o) \leq 0.8 \%$ by ECF ($P_{HF} \leq 800$ kW, 4 Gyrotrons).

X-mode at 1.25 T rotational transform 0.25 - 0.65
 $n_{e0} \leq 2 \times 10^{19} \text{ m}^{-3}$, $T_{e0} \leq 2.8$ keV, $T_i \approx 0.2$ keV

O-mode at 2.5 T ($P_{HF} \leq 400$ kW) rotational transform < 0.35
 $n_{e0} \leq 4 \times 10^{19} \text{ m}^{-3}$, $T_{e0} \leq 2$ keV, $T_i \approx 0.4$ keV.

Configurational effects

- Similar to WVII-A the global confinement in WVII-AS depends on the rotational transform. A degradation of the confinement is found with $\iota(a) = 1/4, 1/3, 2/2, 2/3, \dots$, whereas optimal confinement can be established close to these "resonances".
- Small shear seems to be favourable as long as rational surfaces can be avoided across the plasma. With resonant magnetic surfaces in the confinement region a flattening of the T-profiles has been documented around the position of these surfaces. To avoid strong degradations of the confinement, the edge value of the rotational transform has to be kept at a non rational number, the plasma current has to be controlled.
- This can be done by application of small loop voltages $U_L < 0.2$ Volt from the OH-transformer.
- It has also very successfully been done by ECF current drive with k_{\parallel} components. For plasma parameters $n_{e0} = 1.2 \times 10^{19} \text{ m}^{-3}$, $T_{e0} = 1.5$ keV, the maximum efficiency of 20 A/kW was achieved with a launching angle of 10° off the perpendicular with respect to the magnetic field.
- NBI current drive with balanced beams (co/counter). Ohkawa currents up to 5 kA with $P_{NI} \leq 750$ kW have been observed with unbalanced injection.

Transport

- In almost all discharges that have been investigated the electron heat conduction χ_e is between 0.5 and 2 m²s⁻¹ at half-radius. Towards the plasma center a small increase is observed whereas χ_e increases very strongly at the plasma edge. Significant deviations from calculations with the DKES code are found there in particular.
- Neutral gas transport simulations with the 3D-Degas Code were applied. H_α-signals were used to scale the 3D-distributions of the neutrals and the radial profile of the ion sources. The calculated total particle fluxes from the integrated ion sources are consistent with neoclassical predictions in the temperature gradient region, near the plasma edge however, the fluxes are strongly anomalous. The diffusion coefficient estimated from fluxes and the measured gradients is about 1/10 - 1/20 of the heat conductivity.
- Radiation losses from ECE discharges are less than 50kW. The main impurities are C, T_i and O. Contributions from Fe and T_i play only a role at high temperatures.
- Plasma currents up to 3 kA have been found in ECF-discharges. Their contribution to the rotational transform adds to the external transform. Parameter studies have shown a behaviour expected for the bootstrap current. Comparisons with results based on DKES Code simulations lead to the same conclusion.

ECF - Heating

The development of the 140 GHz system at KfK is on schedule. At the end of the year power supplies and a quasioptical transmission line will be supplied by IPP/IPF (Stuttgart). KfK is testing a prototype at 140 GHz (TE₀₃ Mode, 200 kW, < 100 ms).

The complete system is expected to be operational summer 1990.

References

- [1] Gasparino, U. et. al., 16th Europ. Conf. on Controlled Fusion on Plasma Physics, Venice (1989) P8 B4
- [2] Maaßberg, H. et. al. 16th Europ. Conf. on Controlled Fusion on Plasma Physics, Venice (1989) P8 B5
- [3] Sardei, F. et. al., 16th Europ. Conf. on Controlled Fusion on Plasma Physics, Venice (1989) P8 B6
- [4] Renner, H. Plasma Physics and Controlled Fusion Vol. 31 No. 10 pp. (579-1596) (1989).

Status of the Torsatron/Stellarator Program

J.L. Shohet and the TSL Group

Torsatron/Stellarator Laboratory
University of Wisconsin-Madison
Madison, Wisconsin 53706 U.S.A.

Abstract

Experimental research in the Torsatron/Stellarator Laboratory has concentrated on two main areas: transport and divertor operation. Measurements were made in the Interchangeable Module Stellarator with Langmuir probes to ascertain the extent to which the plasma pressure and potential varies on a magnetic surface. The degree to which the divertor flow could be altered in IMS was investigated by means of electron injection into the divertor region. Also, the flux of particles streaming into the continuous coil Proto-Cleo Stellarator divertor was measured as a function of poloidal angle along the helical divertor path.

1. Introduction

The Torsatron/Stellarator Laboratory operates two stellarators for experimental research, the Proto-Cleo Stellarator and the Interchangeable Module Stellarator (IMS). Proto-Cleo is a conventional continuous coil $l=3$, seven field-period stellarator with a major radius of 40 cm and a coil minor radius of 9 cm. The average plasma radius is 4.5 cm. The rotational transform is zero on axis and peaks at 0.6 on the edge.

IMS is also a seven field period, $l=3$ stellarator with roughly the same parameters as Proto-Cleo. The confining fields, however, are produced by currents flowing in a modular coil set based upon the twisted coil [1] and ultimate stellarator concepts [2]. Each field period in IMS is made up of three individual coil modules called, according to their shape, the 'S', '8' and 'Z' coils. Figure 1 shows the IMS coil set.

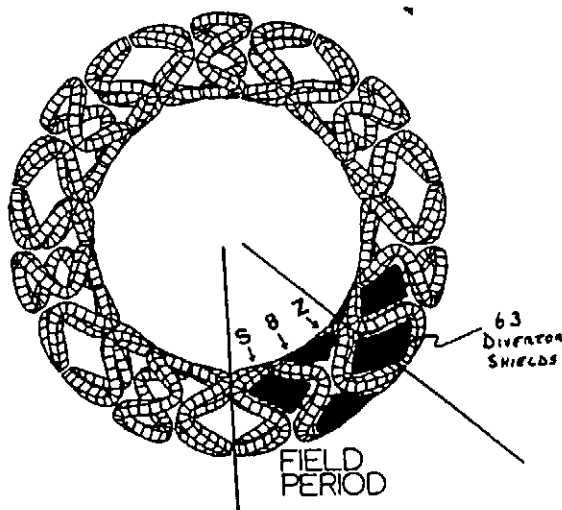


Fig. 1 The IMS coil set

A consequence of the modular nature of the IMS coil set is the existence of a set of discrete modular 'bundle' divertors [3]. Within each field period there are nine divertors for a total of 63 throughout the seven field period device. Electrically-isolated strike-plates, mounted on the coil support rings, are located at each of the divertors. The strike-plates can be individually biased by applying a potential to the connections at the vacuum feed-throughs. At three of the divertors an array of Langmuir probes is embedded into the shields, which allows detailed measurements of the structure in the diverted plasma flow.

Plasmas are currently produced in both devices with a 7.28 GHz microwave source which has a power output of up to 2 kW for 10 msec. Plans are now underway for the installation of an antenna into IMS that would allow for low-frequency RF plasma production at a greater density than the $1-3 \times 10^{11} \text{ cm}^{-3}$ produced with the ECRH.

2. IMS

ECRH plasmas in IMS have hollow density profiles, with the degree of hollowness varying as the resonant layer moves from the inboard side of the torus to the outboard side [4]. The ratio of the edge peak density to the central density can vary from 1.2 to about 10.0. Measurements were made with Langmuir probes of the electron density and temperature throughout the cross-section of the plasma at two separate toroidal locations. A comparison of the plasma pressure with the vacuum magnetic flux surfaces indicates that the pressure peaks at the vertices of the triangular-shaped surfaces. The pressure profile itself is hollow during the ECRH, however, when the heating source is shut off the plasma profile fills in on a time scale of about 100 μsec . Figure 2 is a surface plot of the pressure during the ECRH and the ion saturation current about 125 μsec after the ECRH is turned off. The scale for the two figures is not the same.

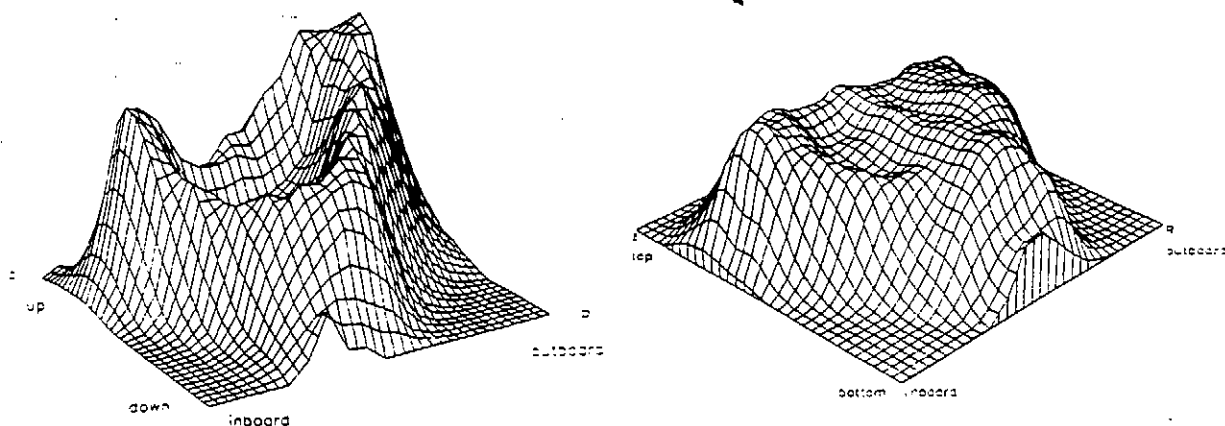


Fig. 2 Surface plot of the pressure during ECRH and ion saturation current 125 μsec after pulse turn-off

A new method is being developed to measure the space potential variation along a magnetic field line. Two emissive probes are aligned on a magnetic field line in vacuum by using one of the probes to collect the current emitted by the other. The probes are aligned when the collecting probe records a maximum in the current. Initial results have shown that the space potential is a maximum on the outboard side of the torus and the variation of the potential on a magnetic surface has the appearance of an $m=1$ mode.

Previously it was shown that the distribution of diverted particle flux between the 63 divertors in IMS could be altered by applying a bias to the divertor strike-plates [5]. At present, preliminary measurements are being made to determine whether the injection of electrons into the divertor region can alter the flow to the strike-plates. The electron source is a thoria-coated iridium filament enclosed by a transparent screen.

The source was located close to one of the divertors and about 5 mA of 100 eV electrons were injected in vacuum. An initial set of measurements were made to map the connections from the source divertor to the other divertors. By monitoring the current to the other strike-plates, approximately 92% of the injected electrons could be accounted for. The results agreed qualitatively with numerical calculations of magnetic field lines launched at the location of the source divertor.

The net flow to each of the strike-plates was then monitored in the presence of the ECRH plasma, but without the electron injection. It was observed that the ion or electron dominated flow was consistent with the grad-B drift direction. However, the net divertor flows were not toroidally symmetric. A large electron dominated flow was observed very close to the ECH antenna. Approximately 180° toroidally and poloidally from the antenna, a large ion dominated flux was observed.

The last sequence of measurements made was in the presence of the plasma and with the electron injection. It was demonstrated that electron injection could in fact alter the distribution of flow to the divertors. Many of the strike-plates that were shown to be simply connected to the source divertor from the vacuum measurements did have a change in the current in the presence of the plasma. However, some strike-plates showed changes in the plasma flow that were not expected.

3. Proto-Cleo

Previous experiments in IMS showed that the particle flux to the strike-plates could be modified with a vertical magnetic field that shifted the plasma to the inboard or outboard side of the torus [6]. To determine whether a similar effect could be observed in a continuous coil stellarator, two arrays with a total of 52 Langmuir probes were installed along a helical winding, in the 'fish-tail' region of the diverted flux.

As seen in Figure 3, the flux of particles to the probes shows a strong dependence on location along the helix. The greatest flux was seen on the inboard and outboard sides of the torus, with somewhat greater flux on the inboard side. It was observed that a small vertical magnetic field which shifted the magnetic axis ap-

proximately 1.5 cm inward and outward had only a marginal effect on the divertor pattern. The observation of concentrated flux in the continuous coil stellarator allows for the possibility of differential biasing to introduce electric fields into the scrape-off layer.

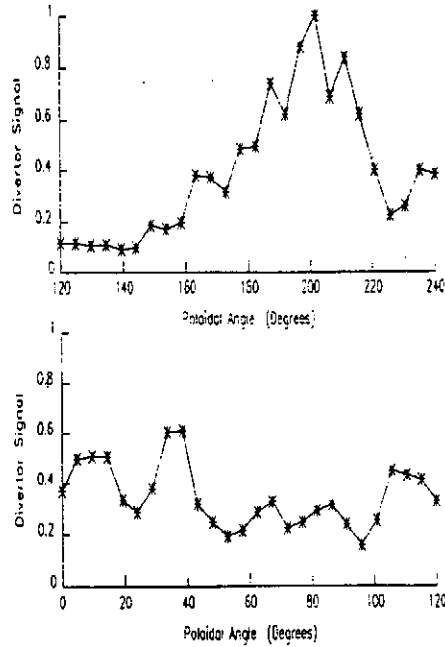


Fig. 3 Divertor flux versus poloidal angle in the Proto-Cleo Stellarator

4. Acknowledgement

This work was supported by the U.S. Department of Energy Grant No. DE-FG02-86-ER53216.A004 and Oak Ridge National Laboratory Contract No. 19X-3591-C.

5. References

1. S. Rehker and H. Wobig, IPP2/215, (1974).
2. D.T. Anderson, J.A. Derr and J.L. Shohet, IEEE Trans. Plasma Sci., PS-9 212.
3. J.A. Derr and J.L. Shohet, IEEE Trans. Plasma Sci., PS-9 (1981) 234.
4. J.N. Talmadge, C.A. Storlie, D.T. Anderson et al., Nucl. Fusion 29 (1989) 1806.
5. R.P. Doerner, D.T. Anderson, W.N.G. Hitchon, P.G. Matthews and J.L. Shohet, Phys. Rev. Lett. 62 (1989) 159.
6. R.P. Doerner et al., Nucl. Fusion 28 (1988) 1901.

Review of Heliotron E Experiment

T. Obiki, H. Zushi, F. Sano, S. Sudo, K. Kondo, M. Sato, M. Nakasuga,
T. Mizuuchi, S. Besshou, H. Okada, K. Hanatani, Y. Nakamura, M. Wakatani,
K. Muraoka*, K. Uchino*, K. Matsuo*, T. Kajiwara*, A. Komori*,
T. Yamashina**, H. Minagawa** H. Matsuura***, N. Noda****, H. Kaneko*****

Plasma Physics Laboratory, Kyoto University

* Interdisciplinary Graduate School of Engineering Sciences, Kyushu University

** Department of Nuclear Engineering, Hokkaido University

*** College of Engineering, University of Osaka Prefecture

**** National Institute for Fusion Science

§1. Introduction

The effects of the magnetic configuration on edge plasma parameters, plasma-wall interaction, transport improvement, MHD activities, and fast ion confinement are studied by varying the vertical field B_v and toroidal field B_t . The role of B_v is a change in the magnetic well/hill formation and the helical ripple localization by the axis shift Δ_v . With B_t , the shape and size of the plasma cross section, the rotational transform and as a consequence shear are changed. The parameter range in ECH/NBI plasmas is as follows: $1 < \bar{n}_e < 10 \times 10^{13} \text{ cm}^{-3}$, $0.3 \lesssim T_e \lesssim 1 \text{ keV}$, $0.2 \lesssim T_i \lesssim 0.9 \text{ keV}$, $\langle \beta \rangle \lesssim 1\%$, $P_{NBI} \leq 2.5 \text{ MW}$, $P_{ECH} < 0.6 \text{ MW}$, $0.94 \leq B \leq 1.9 \text{ T}$, $-0.1 \leq \alpha^* \equiv B_t/B_h \leq 0.15$ and $-6 \lesssim \Delta_v(\alpha B_v) \lesssim 4 \text{ cm}$.

§2. Experimental results

2-1. Change in the magnetic configuration^[1,2]

The change in the magnetic limiter configuration was studied by measuring the edge density profile and diverted particle/heat fluxes with movable Langmuir probes, neutral L_i beam probe, and calorimeter arrays. It was observed that the density profile decayed exponentially with a scale length $\lambda_1 \sim 3 \text{ cm}$ near the outermost surface, and then with $\lambda_2 \sim 1 \text{ cm}$ at about 3 cm from the outermost surface. It was found that the structure of this density profile followed the change in the position of the outermost surface by varying B_t , as shown in Fig.1. The poloidal distribution of calorimeter showed the particle/heat fluxes were flowed to the chamber wall in the narrow width of channel of $\lesssim 3 \text{ cm}^{[3]}$. The change in the poloidal distribution by varying B_t agreed with the result of field line tracing. The vacuum magnetic limiter configuration was also studied at $B_h=4\text{kG}$ by measuring the leakage current from an electron gun biased at $\sim -15\text{V}$ with respect to the chamber. The high current means that the magnetic surface is destroyed or that the field line starting from the gun position connects to the wall. The current was almost constant for $R_c \leq R \leq R_{wall}$, and then decreased gradually for $R_{OM} \leq R \leq R_c$, here R , R_{wall} , R_c and R_{OM} are the gun position, the wall position, the critical point where the connection length becomes very short, and the outermost magnetic surface position, respectively. This structure changed reasonably when the magnetic limiter configuration was varied by $B_t(-0.1 \leq \alpha^* \leq 0.1)$ as is shown in Fig.2.

The enhanced plasma-wall interaction was observed spectroscopically. When the plasma

size was large by B_t , the F_e XV intensity was drastically increased. OV line intensity and bolometric power, however, were not so much changed.

2-2. Profile change and transport analysis^[4,5,6]

It was observed that the density profile in NBI plasmas became peaked when α^* ($\equiv B_t/B_h$) was negative. The peaking factor $\eta_m \equiv n_e(r \sim 0)/n_e(r \sim 0.5a)$ increased from 2 ($\alpha^* = 0$) to 3 ($\alpha^* = -0.1$), but decreased to ~ 1.3 ($\alpha^* = 0.15$), as is shown in Fig.3.

Under the same gas puffing, \bar{n}_e (H_α emission) decreased (increased) little for $\alpha^* < 0$, but increased (decreased) for $\alpha^* > 0$. A relation between the global particle confinement and the density profile peakedness is under study. On the other hand, the electron temperature profile did not change, especially in the half radius, as B_t was varied. In ECRH plasmas, it was observed that the electron density profile was changed by varying the magnetic configuration. When $\alpha^* = +0.05$ and $\Delta_v = -2\text{cm}$, the density profile was changed from hollow ($\alpha^* = 0$ and $\Delta_v = -2\text{cm}$) to bell-shaped, and the line averaged density could be increased up to $\sim 4 \times 10^{13}\text{cm}^{-3}$ by additional gas puffing.

The transport optimization was done by varying B_t and B_v . It has been found that τ_E was improved by $\sim 20\%$ when the magnetic axis was shifted by -2cm ^[7]. By adding small B_t field the maximum stored energy of 26kJ was obtained at $P_{NBI} \sim 2.5\text{MW}$ for $\Delta_v = -2\text{cm}$. The minor radius a_p dependence of τ_E was studied by varying B_t . τ_E changed with the a_p^2 dependence, as is shown in Fig.4. However, when a_p was varied by B_v , τ_E did not follow the a_p^2 dependence. The discrepancy may be due to a drastic change in the shear and particle orbit by B_v .

2-3. MHD activities^[8,9]

Although the transport was improved by the axis shift, MHD activities were enhanced due to the magnetic hill much below the ideal interchange beta limit. The internal disruptions were driven by the $m=2/n=1$ mode for $\Delta_v = -2\text{cm}$ and $\alpha^* = 0$, in which the location of the $\iota = 1/2$ surface in vacuum is $\sim 3\text{cm}$ from the axis. This mode was found to be stabilized by adding small B_t , as shown in Fig.5. This condition corresponds to the maximum stored energy condition. Since $\iota(0)$ is decreased from 0.47 to 0.41, the Shafranov shift ($\propto \iota(0)^{-2}$) is increased by 30%. This finite beta effect on stabilization is now under study. On the other hand, when $\alpha^* < 0$, the plasma became more unstable because of the magnetic hill formation and decrease in shear. Magnetic fluctuations were investigated in the frequency range of 4-20kHz. It was observed that \tilde{B}_θ with the $m=1/n=1$ mode became easily unstable even when the plasma seemed to be macroscopically stable. The FFT analysis showed a good correlation between $\tilde{B}_\theta(1/1)$ and $\tilde{n}l$ measured by FIR. Although the change in shear at $\iota = 1$ is little as α^* becomes negative (-0.1) to positive (+0.15), a clear stabilization effect of B_t on $\tilde{B}_\theta(1/1)$ was also found around at $\alpha^* = 0.05$.

2-4. Fast ion confinement

Confinement of fast ions with $V_{||} \sim 0$ was studied by a vertically viewing neutral particle energy analyzer (NPA). This analyzer can be moved fan-like along the major radius direction with a pivot point at R_0 . Test particles with $V_{||} \sim 0$ are injected into a low density ECRH plasma for 20 ms. The angular distribution of neutral particles at injected energy $E_{inj} \sim 22\text{keV}$ was measured by varying the magnetic configuration. It was

observed that the angular distribution was shifted inwardly by ~ 3 degree, which agreed well with the shift of the trapped particle orbit $\Delta \sim \frac{eI_0}{2c h_0} \cdot a$. When the magnetic axis was shifted outward by +7.5 cm, the angular distribution was also shifted inwardly. This indicates that the trapped particle orbit is rather insensitive to the change in magnetic surfaces by B_v , which agrees with the orbit theory^[10]. In this case, although the size of the magnetic surface was small, the flux was clearly observed along the viewing chord which did not cross the plasma. This results suggests that the fast ions travel outside the last closed magnetic surface.

§3 Conclusions

The conclusions are summarized as follows;

- Results of edge diagnostics qualitatively agree with the change in the magnetic limiter configuration by the toroidal field.
- The transport improvement is found in the inward shift case ($\Delta_v \sim -2$ cm) with a small toroidal field ($B_t/B_h \sim 0.05$).
- The stabilization effect of B_t on the $m=2/n=1$ and $m=1/n=1$ modes is found.
- Observed inward shifted CX flux distribution agrees well with the trapped particle orbit theory.

References

- T. Mizuuchi, H. Matsuura, et al., This conference.
- K. Kondo, et al., This conference.
- T. Obiki, et al., 12th IAEA Conf. (1988).
- S. Sudo et al., This conference.
- S. Besshou et al., This conference.
- F. Sano et al., This conference.
- H. Zushi, et al., 7th Int. Workshop on Stellarators, Oak Ridge Apr. 1989; 03-3.
- H. Zushi, et al., This conference.
- M. Harada, et al., This conference.
- K. Hanatani, et al., This conference.

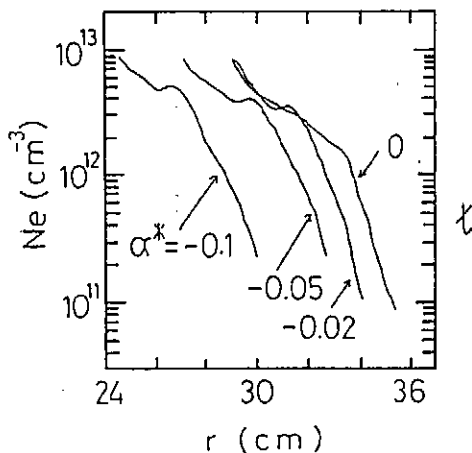


Fig. 1. Density profile along the major radius measured by L_i beam for various α^* values.

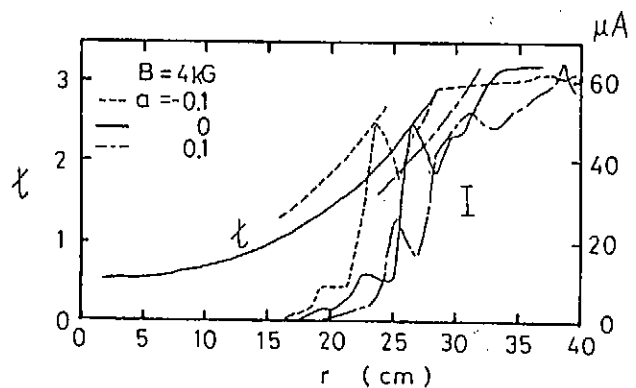


Fig. 2. Leakage current distribution for $\alpha^* = -0.1, 0$ and $+0.1$.

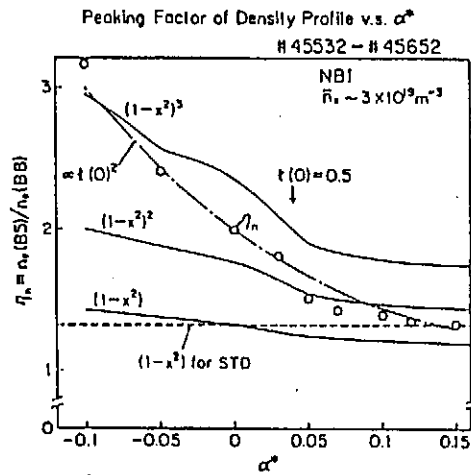


Fig. 3. Density profile peaking factor η_n versus α^* .

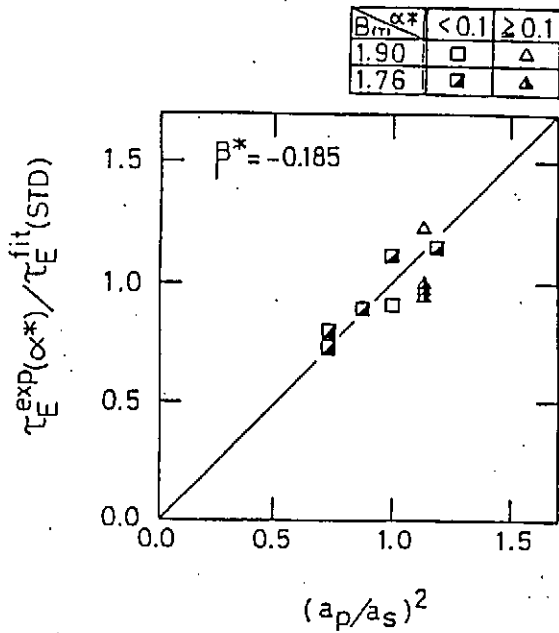


Fig. 4. Gross energy confinement time as a function of plasma radius at $\Delta_e \sim 2$ cm ($a_s = 21.5$ cm for standard configuration)

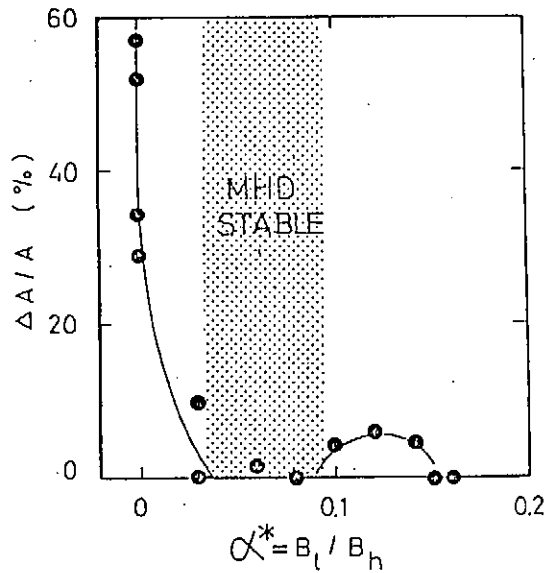


Fig. 5. Stabilization effect by B_t ($\Delta A/A$ is the change of the soft X ray intensity at the sawtooth crash)

Review of CHS Experiment

K.Matsuoka, M.Fujiwara, J.H.Harris^{a)}, M.Hosokawa, K.Ida, H.Idei,
H.Iguchi, O.Kaneko, S.Kubo, K.Masai^{b)}, S.Morita, K.Nishimura,
N.Noda, S.Okamura, T.Ozaki, L.Peranich^{c)}, A.Sagara, H.Sanuki,
T.Shoji^{b)}, S.Sobhanian^{d)}, C.Takahashi, Y.Takeiri,
Y.Takita, K.Tsuzuki, H.Yamada

National Institute for Fusion Science
Nagoya 464-01, Japan

Abstract

Heating experiments with 28GHz/53GHz ECH and NBI have been done under the following conditions: the field strength B_t from 0.46T to 1.5T, heating powers up to 150kW and 1.1MW for ECH and NBI respectively. The line averaged electron density \bar{n}_e is $0.1 \sim 10 \times 10^{13} \text{cm}^{-3}$, electron and ion temperatures are up to about 1.1keV and 600eV respectively; the collisionality ranges from the plateau to $1/\nu$ regime. Magnetic field configuration study, where the magnetic axis position is scanned from the viewpoint of loss cone, shows that the confinement characteristics improve at an inward shifted axis position. Global energy confinement time is found to follow the LHD scaling and to be improved compared with the scaling in some discharges.

1. Introduction

Following the previous fiscal year's experiment i.e., the preliminary transport study in a low density ECR plasma¹⁾ by the use of 28GHz gyrotron and the NBI-target-plasma production experiment²⁾ using Nagoya type-III antenna with the frequency range of 7.5~13MHz, transport studies of ECH and NBI heated plasmas have started since July 1989 in the Compact Helical System(CHS) where the multipolarity $l=2$, the field period number $m=8$, the major and minor radii are 1m and 0.2m respectively, the maximum field strength is 1.5Tesla.

Main parameters of heating equipments are as follows: 40kV, 1.2MW, 1sec for NBI and 28GHz, 200kW, 75msec and 53GHz, 200kW, 100msec for ECH, and 7.5~13MHz, 800kW, 100msec, 9~28MHz, 500kW, 10msec and 40MHz, 1.2MW, 30msec for ICRF. Major efforts of heating experiments have been concentrated on NBI and ECH; ion Bernstein wave heating experiments are now under way, besides RF plasma production for NBI target. The maximum NBI power through the port is 1.1MW and the maximum pulse length so far is limited to be 250ms. This is because of no armor tile for the protection against shine-through bombardment of the vacuum vessel on which the helical coil is wound directly. The maximum ECH powers through the port are 120kW(28GHz) and 150kW(53GHz) and the pulse lengths in the usual experiment are about 40ms.

Electron temperature and density profiles are obtained by scanning the Thomson scattering system shot by shot. The ion temperature profile is obtained with charge-exchange recombination spectroscopy³⁾ and VUV spectroscopy, which can also measure the poloidal and toroidal rotations, and the toroidal rotation of the plasma, respectively. The plasma stored energy W_{dia} is obtained with a diamagnetic loop. Comparison between W_{dia} and the kinetic energy from the profile measurements gives reasonable agreement. Radiation loss profiles are measured with 10 channel bolometer array: 2π pyroelectric detector monitors radiation loss level.

Titanium gettering is applied to suppress oxygen which is the dominant impurity. Plasmas are limited by the stainless steel vacuum vessel or by a movable graphite limiter in inward shifted configurations.

2. Parameters of heated plasmas

NBI heated plasmas have been realized in a wide range of B_t from 0.46T to 1.5T. Target plasmas are produced with various methods: 2nd and fundamental resonances of 28GHz ECH($B_t \sim 0.46T$ and $\sim 0.95T$, respectively), 7.5MHz and 13MHz RF production($B_t = 0.6T$ and $1.05T$, respectively), 2nd and fundamental resonances of 53GHz ECH($B_t \sim 0.9T$ and $1.5T$, respectively). The 53GHz ECH at B_t of 1.5T uses off-axis resonance heating.

Parameters of heated plasmas are the followings: $\bar{n}_e = 0.1 \sim 2 \times 10^{13} \text{cm}^{-3}$, $T_e(0) < 1.1 \text{keV}$, $T_i(0) < 120 \text{eV}$ for ECH and $\bar{n}_e = 2 \sim 10 \times 10^{13} \text{cm}^{-3}$, $T_e(0) < 600 \text{eV}$, $T_i(0) < 400 \text{eV}$ for NBI plasmas. Central electron temperatures as a function of the central electron density are shown in Fig.1 under various experimental conditions such as heating method, the field strength and the magnetic field configuration. The collisionality of electrons enters into the $1/\nu$ regime in the high temperature ECH plasma.

Radiation loss plays an important role in the power balance of NBI plasmas as the electron density increases. The radiation loss level is typically 20~50% of the NBI input power⁴⁾, while the wall condition, i.e. freshness of Ti gettering has substantial effect on the level. The maximum electron density is limited by oxygen impurity radiation, above which density W_{dia} begins to deteriorate as is shown in Fig.2. The critical density is about $10 \times 10^{13} \text{cm}^{-3}$ at B_t of 1.5T. The absolute value of the critical density and its dependence on B_t are consistent with the analytic estimate based on the detached plasma⁵⁾. There may be some ambiguities in the power balance of NBI plasma. The power deposited on the graphite limiter inserted inside the outermost magnetic surface, which should measure conduction/convection loss power experimentally, shows the small level of a few tens of kW; the estimate of charge exchange loss and orbit loss in the course of thermalization remain as a future task.

The maximum volume averaged β value of NBI plasma is 1.4~1.5% at B_t of 0.46~0.6T. MHD activities appear on W_{dia} and Mirnov coil signals when the magnetic axis is shifted inward. The electron and ion temperature profiles show that their peak positions shift outward by a few centimeters from the vacuum magnetic axis.

Induced currents are observed in ECH and NBI plasmas⁶⁾. Beam induced current is $> 10 \text{kA}$ in low density ($\bar{n}_e \sim 1 \times 10^{13} \text{cm}^{-3}$) plasmas and the dependence of induced current on T_e , \bar{n}_e and the absorbed power is similar to that in tokamaks. When \bar{n}_e is high the bootstrap current increases its importance.

3. Energy confinement characteristics

Confinement characteristics have been studied under various conditions. Besides the dependence of global energy confinement time τ_E^{exp} on B_t , \bar{n}_e and the absorbed power P_{in} , the magnetic configuration has been surveyed from the viewpoint of loss cone⁷⁾. The loss cone in a low-aspect-ratio helical system can be reduced by shifting the magnetic axis inward. In CHS, the magnetic axis position R_{axis} is scanned from 88.8cm to 101.6cm by controlling the dipole field from the poloidal field coil system keeping the quadrupole field component constant. The central electron temperature of NBI plasmas increases as R_{axis} is shifted inward.

The confinement time τ_E^{exp} is estimated from W_{dia} and P_{in} which is estimated analytically in ECH⁸⁾ and NBI⁹⁾ plasmas. In NBI plasmas, the absorbed power P_{in} used here is the following: (the port-through power)-(shine-through power)-(direct orbit loss). In ECH plasmas, the maximum absorption power is estimated to be about 80% of the port-through power. Dependence of W_{dia} on \bar{n}_e is shown in Fig.3 for NBI plasmas as a parameter of B_t under various magnetic axis positions. The stored energy is nearly proportional to B_t in the range from 0.6T to 1.5T, which shows stronger dependence than LHD scaling. The

confinement time τ_E^{exp} improves as R_{axis} shifts inward; W_{dia} does not decrease in spite of smaller plasma volume. Comparison of τ_E^{exp} with the LHD scaling is shown in Fig.4. Plasmas with low to medium density ($\bar{n}_e < 4 \times 10^{13} \text{cm}^{-3}$) and inward axis position show improvement from the scaling, however, data with high density ($\bar{n}_e > 5 \times 10^{13} \text{cm}^{-3}$) are scattered below the scaling at present. Transport analysis based on ORNL PROCTR-mod is under way by the use of the profile measurement results⁹⁾.

- a) Oak Ridge National Laboratory, Oak Ridge, USA. b) Plasma Science Center, Nagoya University, Nagoya 464-01, Japan. c) General Atomics, San Diego, USA. d) On sabbatical leave from University of Tabriz, Tabriz, Iran.

references

- 1) K.Matsuoka et al., in Plasma Physics and Controlled Nuclear Fusion Research(Proc. 12th IAEA Conf. Nice,1988) IEAE-CN-50/I-I-3.
- 2) S.Okamura et al., 16th Europ. Conf. on Controlled Fusion and Plasma Physics, Venice(1989).
- 3) K.Ida, S.Hidekuma and CHS group, this conference.
- 4) S.Morita and CHS group, this conference.
- 5) K.Itoh and S.-I.Itoh, Journal of the Physical Society of Japan vol.57(1988) 1269.
- 6) O.Kaneko et al., this conference.
- 7) S.Okamura, H.Iguchi and CHS group, this conference.
- 8) S.Kubo et al., this conference.
- 9) H.Yamada et al., this conference.

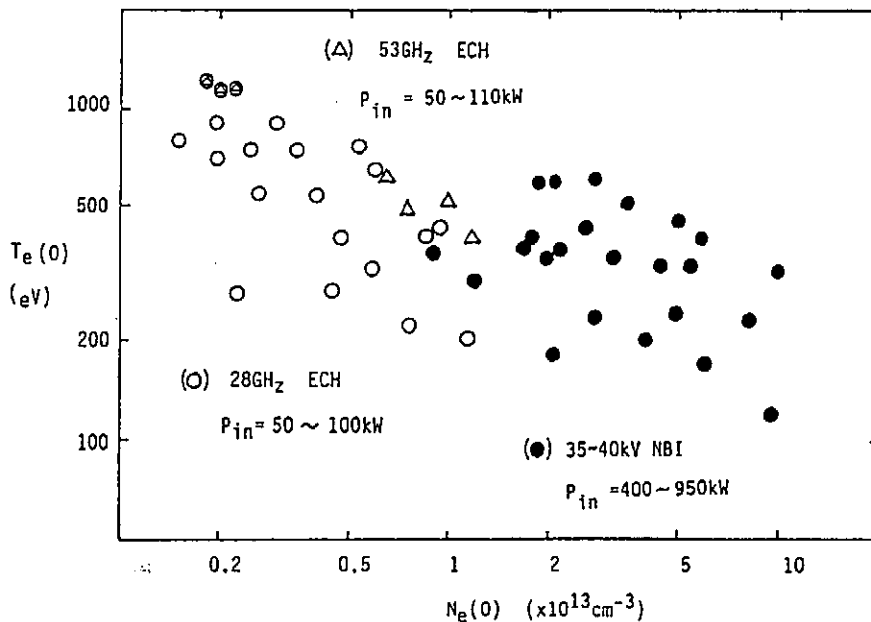


Fig.1. Central electron temperature as a function of central electron density under various experimental conditions. Data with $T_e(0) > 1100 \text{eV}$ refer to the combined operation of 28GHz and 53GHz gyrotrons.

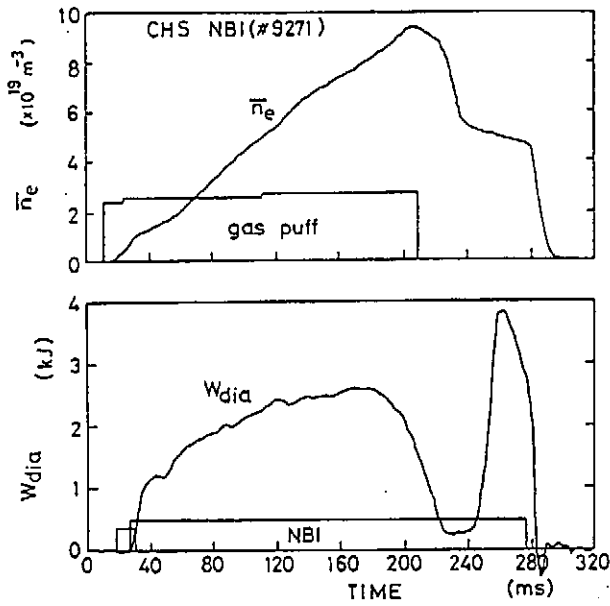


Fig.2. Temporal evolution of \bar{n}_e and W_{dia} when strong gas puff is applied. W_{dia} begins to deteriorate as the density increases. Plasma is reheated after gas puff turn-off.

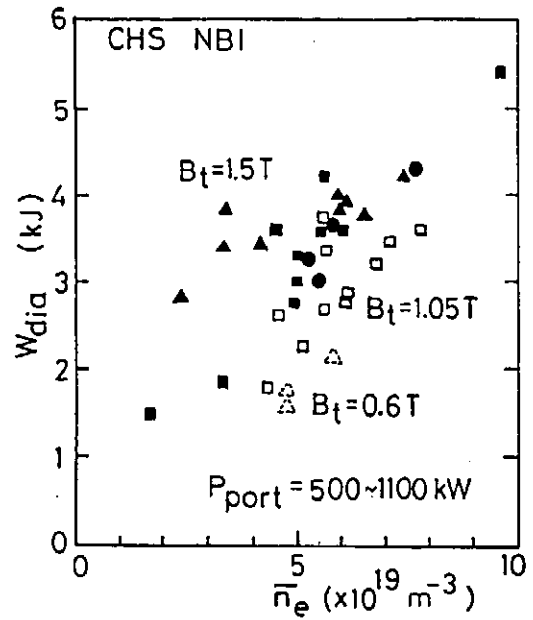


Fig.3. W_{dia} as a function of \bar{n}_e for NBI plasmas. Solid, open and dotted symbols refer to B_t of 1.5, 1.05 and 0.6T, respectively. Triangles, squares and circles refer to R_{axis} of 92.1, 94.9 and 97.4cm, respectively.

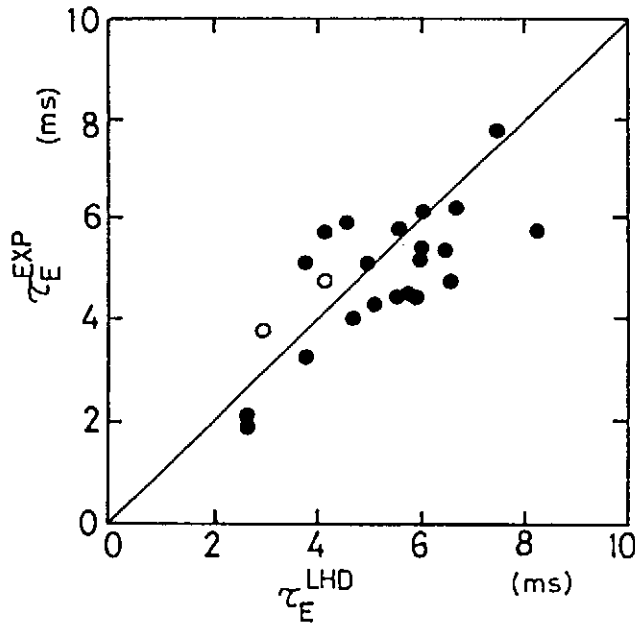


Fig.4. Comparison between τ_E^{exp} and τ_E^{LHD} . Open and solid circles refer to ECH with $\bar{n}_e > 1 \times 10^{13} \text{cm}^{-3}$ and NBI plasmas, respectively.

Experimental Studies of a Helical Axis Stellarator (TU-Heliac)

S. Kitajima, M. Takayama, T. Zama, M. Takahashi
N. Takeuchi and H. Watanabe

Department of Nuclear Engineering,
Faculty of Engineering, Tohoku University
Sendai 980, Japan

1. Introduction

We present here the recent experimental results on TU-Heliac . TU-Heliac is a helical axis stellarator of heliac type to have been built at Sendai in July 1988. The device description has been already done in Ref.1. As explained there, TU-Heliac has 4 periods, 48 cm of major radius, maximum toroidal field of 3.5 kG and an average plasma radius of 6-8 cm. The swing radius of TF coil is 8 cm. The topics which we present here will be dealt with measurements of the vacuum magnetic surfaces of TU-Heliac by three different kinds of electron beam methods, and measurements of 2D contour of the plasma pressure to ensure the existence of the plasma equilibrium in a heliac and brief analytical calculation of the toroidal heliac equilibria.

2. Measurements of Magnetic Surfaces

It is an important and necessary step, in the stellarator-type magnetic confinement devices, to confirm actually existence of the vacuum magnetic surfaces which are expected in advance.

Three kinds of methods for mapping magnetic surfaces in TU-Heliac were used and compared with the broad numerical predictions. The first method is the usual electron beam mapping one with an electron energy of 7.5 eV and a pulse length of 10 μ s. The second is the resistance-capacitance method (R-C method) with an electron energy of 15 eV, 2 ms pulse. The third is so-called fluorescent mesh method with a 700 eV energy, 10 ms pulse duration. We mention below the results of the R-C method and the fluorescent mesh method.

a. R-C Method

The principle for measurement and experimental procedure of the R-C method are as follows. The injected electrons accumulate on some surface. There appears capacitance C between electron cloud and the chamber wall and also there is a leakage resistance R between them illustrated in Fig.1.

By moving the electron gun two-dimensionally in the poloidal cross section of the torus, one can get C and R corresponding to the location of the gun. Plotting the contour lines of equi-resistance or equi-capacitance, we can get the approximate shape of the magnetic surfaces. An example of the surfaces measured by this method is shown in Fig.2.

b. Fluorescent Mesh Method^{2), 3)}

Fluorescent mesh is made of 0.1 mm stainless steel wire and the space of the mesh of a net is 2.5 mm. The fluorescent paint is P 15 (ZnO₂:Zn). The mesh is coated by spraying the suspension of P 15 in polyvinyl alcohol with an atomizer. Transmission coefficient of the mesh was arranged in the range of more than 90 %.

Four LEDs as the marks were put on the frame of the mesh for providing vertical and horizontal reference points. As the angle that the fluorescent screen makes with the film is 15° , it is necessary to transform the recorded position of the electron beams from the film to the actual positions by computer program. We show a photograph of the magnetic surface by this method in Fig.3.

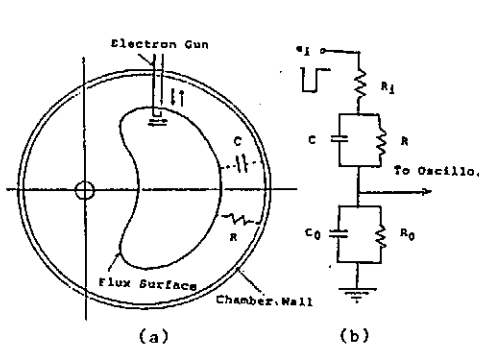


Fig.1 (a): The injected electrons by the gun form C and R to chamber wall. (b): Equivalent circuits of the R-C method: R_i : internal resistance of the gun, R_0, C_0 : external resistance and Capacitance.

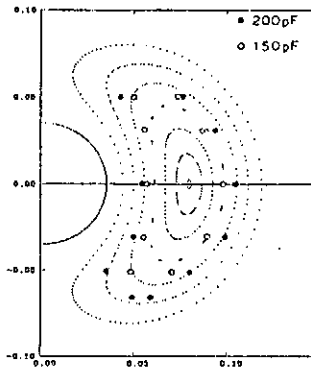


Fig.2 Plots of constant equivalent capacitance which is measured by R-C method. The computed magnetic surfaces are shown corresponding to the experimental results.

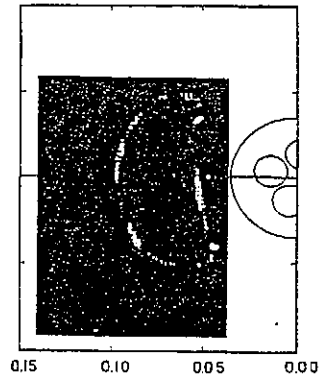


Fig.3 The experimental results of fluorescent mesh method for the case of $I_e/RH_0=0.39$. The electron gun position is $R=9.8\text{cm}$ and $Z=0.0\text{cm}$. The electron beam energy is 700eV.

3. Plasma Production and Plasma Equilibrium

The vacuum system is evacuated to the base pressure $< 2 \times 10^{-6}$ Pa by 3 turbo-molecular pumps. Plasma is produced using ECRH of 2.45 GHz microwave source with 3-6 ms pulse of 3 kW peak power. Working gas is argon at a pressure of 5×10^{-3} Pa.

Plasmas produced by ECRH typically have electron densities n_e and temperature T_e in the ranges of $1 \times 10^9 < n_e < 3 \times 10^{10} \text{ cm}^{-3}$ and $T_e \leq 10 \text{ eV}$ respectively. Local plasma density and temperature are measured by Langmuir probe. The probe tip consists of 3 mm diameter disk of SUS 304. The probe can be placed anywhere in a poloidal cross section of the torus. The probe position is known to within $\pm 0.5 \text{ mm}$. The local electron density n_e can be derived from the ion saturation current if the electron temperature is known, and the local plasma pressure is taken as can be estimated as the product $n_e T_e$ by assuming the ions to be cold.^{4), 5)}

The magnetic surface Ψ can be, in general, defined as a surface on which a line of magnetic field lies, so $\mathbf{B} \cdot \nabla \Psi = 0$ is to be satisfied. On the other hand, we have the relation of $\mathbf{B} \cdot \nabla p = 0$ from one of the equations of MHD equilibrium. From these relations, the plasmas confined in torus by the magnetic field must have constant pressure on the magnetic surfaces.

Hence an experimental demonstration that $p = \sum n_i T_i \sim n_e T_e$ is the same at all points on a predicted magnetic surface may be taken as evidence that the plasma equilibria do exist as calculated.

In Fig.4, the existence of the heliac plasma is shown at the simplest level by photographs: the luminous region by plasma

on the fluorescent mesh which we used to map the magnetic surfaces is clearly restricted to inside the outermost magnetic surface.

More precise information about the plasma equilibria can be obtained by drawing the contour maps of the electron density and temperature and relating their product $p = n_e T_e$.

Figures 5 and 6 show examples of the contour maps of $P = n_e T_e = \text{const.}$ in the afterglow plasma after 2 ms of microwave turned off for the cases of $I_c/RH_0 = 0.39$ and 0.25 respectively.

It is very interesting to see that the plasma is limited to inside the $1/3$ island for the case of $I_c/RH_0 = 0.25$ in Fig.6. The observed contours clearly reflect the shapes of the numerical predicted magnetic surfaces.

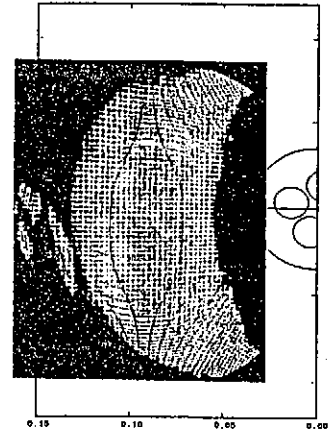
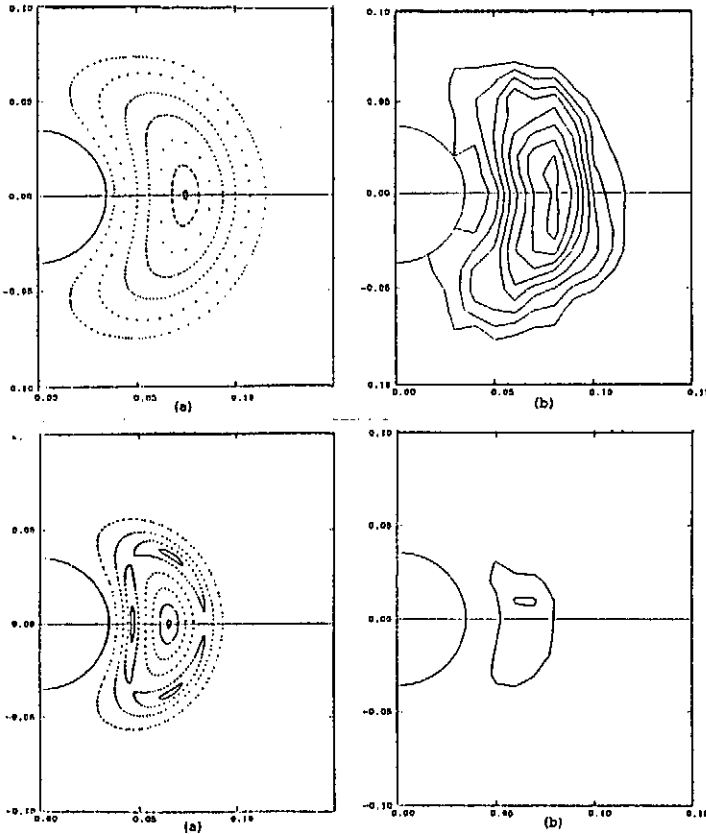


Fig.4 The luminous region by plasma on the fluorescent mesh. $I_c/RH_0 = 0.59$.

Fig.5 (a); The computed magnetic surfaces for the case of $I_c/RH_0 = 0.39$. (b); The contour maps of $p = n_e T_e = \text{const.}$

Fig.6 (a); The computed magnetic surfaces for the case of $I_c/RH_0 = 0.25$. (b); The contour maps of $p = n_e T_e = \text{const.}$

4. Currentless Equilibria of Toroidal Heliacs

The purpose of this section is to try to calculate analytically toroidal heliac equilibria. Procedure of calculation is as follows. At first, we get an equilibrium solution for the straight heliac which has the helical symmetry. Next, we bend it into torus. In our calculation, we employ the stellarator expansion ordering:

$$\left(\frac{B^\delta}{B_0}\right)^2 \sim \frac{B^k}{B_0} \sim \frac{B^\beta}{B_0} \sim \frac{B^\sigma}{B_0} \sim \frac{B^{\delta\delta}}{B_0} \sim \frac{a}{R} = \epsilon \ll 1. \quad (1)$$

a. Straight Heliac Equilibrium Solution

Flux function of the vacuum magnetic field for the straight with the helical symmetry is given by

$$\psi_v(r, \phi) = \frac{1}{2} B_0 h r^2 - \frac{\mu_0 I_C}{2\pi} \ln r - C_1 h r I_1(hr) \cos \phi + C_2 \quad (2)$$

In the presence of plasma, we have the flux function from Grad-Shafranov equation with $I(\psi) = I_0 + \sigma(\psi - \psi_a)$, $p = p_0(1 - \psi/\psi_a)$ as

$$\begin{aligned} \psi(r, \phi) = & -\frac{I_0 - \sigma\psi_a}{\sigma} + \frac{\mu_0 p_0}{\psi_a \sigma^2} (1 + h^2 r^2 + 2h/\sigma) \\ & + a_0 \{ \sigma r J_0(\sigma r) - \frac{\sigma}{h} J_0(\sigma r) \} + b_0 \{ \sigma r N_0(\sigma r) - \frac{\sigma}{h} N_0(\sigma r) \} \\ & + a_1 \{ \lambda r I_1(\lambda r) - \frac{\sigma}{h} I_1(\lambda r) \} \cos \phi + b_1 \{ \lambda r K_1(\lambda r) - \frac{\sigma}{h} K_1(\lambda r) \} \cos \phi \end{aligned}$$

where $\lambda = (h^2 - \sigma^2)^{1/2}$. (3)

We choose the integral constants a_0 , b_0 , a_1 and b_1 so as to make $\psi(r, \phi)$ equal to the vacuum flux function $\psi_v(r, \phi)$ in the limit of $\sigma \rightarrow 0$ and $p_0 \rightarrow 0$. This gives

$$\begin{aligned} a_0 = & - \left\{ \frac{hB}{\sigma^2} + \frac{\mu_0 p_0}{\psi_a \sigma^2} \left(\frac{\sigma}{h} \right) \left(1 + \frac{2h}{\sigma} \right) - \frac{h}{\sigma} \psi_a \right\}, \quad b_0 = \frac{\mu_0 I_C}{4} \frac{h}{\sigma}, \\ a = & -C_1 \quad \text{and} \quad b_1 = 0. \end{aligned} \quad (4)$$

Currentless condition gives a relation between σ and p_0 . This is $\sigma = \mu_0 p_0 / B_0 \psi_a$.

b. Flux Function for Toroidal Helic

Here we use the quasi-toroidal coordinate (ρ, ω, ζ) with the metric of $h_\rho = 1$, $h_\omega = \rho$ and $h_\zeta = 1 + k\rho \cos \omega$.

In equilibrium, we have the relation: $\mathbf{B} \cdot \nabla \psi = 0$.

Magnetic field and the flux function of the toroidal heliacs can be divided into two parts, the straight components and the components due to the curvature effect like,

$$\mathbf{B} = \mathbf{B}^{st} + \mathbf{B}^k, \quad \psi = \psi^{st} + \psi^k \quad \text{and} \quad \nabla = \nabla_0 + \nabla_{k^*} \quad (5)$$

Substituting these in $\mathbf{B} \cdot \nabla \psi = 0$, we can get ψ^k as

$$\psi^k = \frac{1}{2} (B_0 h \rho^2 - A) \left(\ln \frac{k\rho}{8} + 1 + \frac{4\pi B_1'}{\mu_0 I_C} \right) k\rho \cos(\phi + h\zeta),$$

where $k = 1/R$, $\phi = -(\omega + h\zeta)$ and $h = \frac{\mu_0 I_C}{h/R}$. (6)

Thus we can get the flux function $\psi = \psi^{st} + \psi^k$ for toroidal heliacs

5. Conclusions

Measurements of the magnetic surfaces have been done by three different kinds of electron beam methods in a heliac magnetic configurations. Results are in good agreement with the broad numerical calculations of the magnetic surfaces within measurement accuracy. We have also done the experimental evidence of low β plasma equilibria in a heliac by comparing the contours of the plasma pressure with the predicted magnetic surfaces.

References

- 1). H.Watanabe et al., Proc.Inter.Stellarators Workshop(Oak Ridge), IAEA Tech.Comm.Meeting,1989 (to be published).
- 2). R.Takahashi et al., Proc.Inter.Stellarator/Heliotron Workshop (Kyoto),IAEA Tech.Comm.Meeting, Vol.II p.220,1986.
- 3). G.J.Hartwell et al., Rev.Sci.Instrum. 59 (1988) 460.
- 4). B.D.Blackwell et al., Nucl.Fusion 25 (1985) 1485.
- 5). X.H.Shi et al., Nucl.Fusion 28 (1988) 859.

Diverted Particle-Flux Studies in the IMS and Proto-Cleo Stellarators

J.L. Shohet, D.T. Anderson, F.S.B. Anderson, P.G. Matthews and J.N. Talmadge

Torsatron/Stellarator Laboratory
University of Wisconsin-Madison
Madison, Wisconsin 53706 U.S.A.

Abstract

Diverted particle-fluxes have been measured under varying conditions in electron cyclotron resonance produced and heated plasmas in both the Interchangeable Module Stellarator (IMS) and the Proto-Cleo $l=3$, seven field period conventional stellarator. Flow patterns are observed to be dependent upon magnetic field strength in IMS, with abrupt changes observed as the central field strength passes through resonance with the microwaves. Electron injection into the IMS diverted-flux areas, using a strongly emissive filament, has been used to map connections between various diverted flux areas and to the scrape-off layer. Electron injection can also significantly alter observed divertor flows, in a fashion similar to previous results with divertor strike-plate biasing¹. Scoping studies of the diverted particle-flux pattern have been made in the Proto-Cleo Stellarator. Asymmetries are observed in the strength of the diverted flux along the path of the helical coil. These asymmetries are not strongly dependent upon moderate levels of applied external vertical magnetic fields.

1. Introduction

Divertors in stellarators are a natural consequence of having all of the confining magnetic geometry produced by various sets of external coils. Free-streaming particles which escape from within the separatrix tend to follow non-confined field lines until intersecting a material object. Control over the locations of the plasma/material interactions and heat deposition is highly desired. In a conventional stellarator, the diverted flux tends to emerge from the confinement volume near one current-sense of helical coils as shown in Figure 1. In the IMS, the modular nature of the coil set results in a segmentation of this continuous pattern into a set of 63 (nine/period x seven periods) 'modular' divertors². These individual divertors are identified by the poloidal angle of their centers, as illustrated in Figure 2, and their toroidal angle.

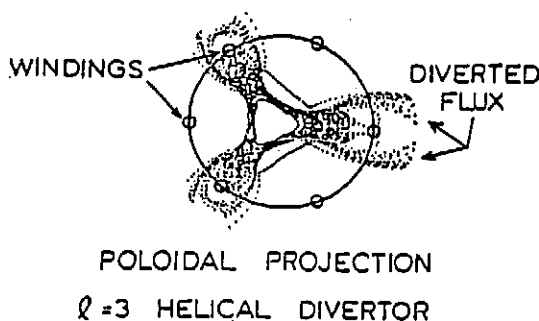


Figure 1. Diverted magnetic flux in a conventional stellarator.

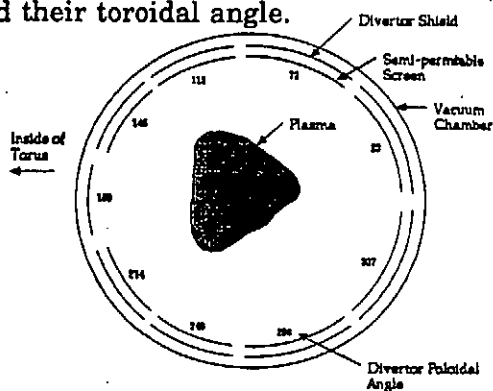


Figure 2. IMS divertor identification.

The distribution of diverted particle flux between the 63 divertors in IMS can be altered through the use of externally applied potentials to the divertor strike plates¹. During the course of these studies, it was noticed that the distribution without biasing was sensitive to the magnetic field strength.

2. Dependence of Diverted Fluxes on Magnetic Field Strength

By monitoring fluxes to all nine types of divertor strike plates at once, a poloidal distribution of flux can be obtained within a single discharge. This distribution has been studied as a function of the electron-cyclotron resonance location by small variations in magnet current. Data reproducibility as a function of field strength is good, and independent of position within the time-history of the discharge (not a discharge-dynamics phenomenon). Figure 3 shows the collected data for six of the divertor types. There is an abrupt change in the distribution around a central field strength of 2.5 kG. Symmetry of stellarators in poloidal angle with respect to toroidal angle of both magnetic surfaces and field strength result in equal numbers of magnetic flux lines connecting to 'mirror' pairs of divertors, i.e. (23,337), (72,288), and (112,248). It can be seen from the figure that increasing (decreasing) fluxes to one divertor is accompanied by decreasing (increasing) fluxes to its mirror companion.

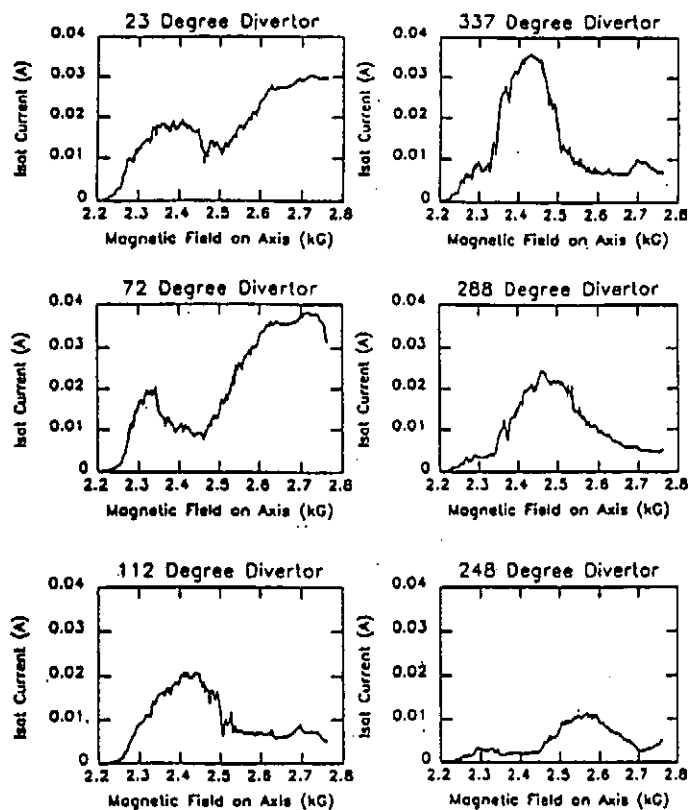


Figure 3. Distribution of diverted particle flux to six of the IMS divertors as a function of central field strength

As seen in Figure 4, the overall line-density and total divertor current do not change dramatically over this range of interest.

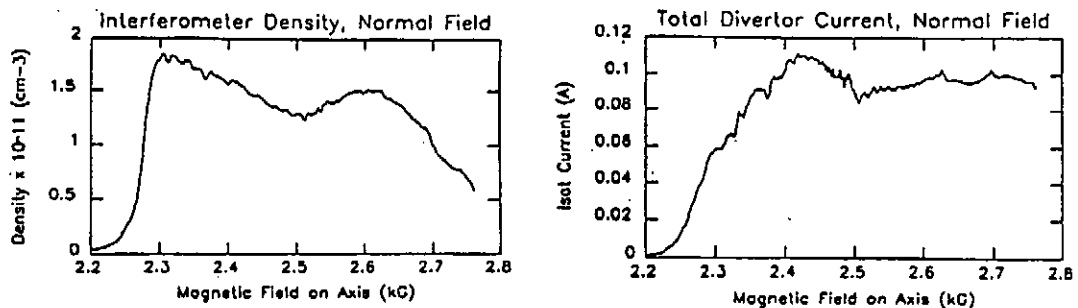


Figure 4. Line-average density and total divertor current for data presented in Figure 3.

To assess whether particle drifts play an important role in this redistribution of flux, the same measurements were made with the magnetic field reversed. The direction of change in flow for the individual divertors does not change with field reversal, indicative that field-dependent directional drifts are not playing a dominant role in the observed flow changes, and that the effects are more closely tied to the resonance layer location.

3. Divertor Electron Injection Experiments

With all of the 63 divertor strike plates acting as monitors, IMS offers the capability of measuring electron flows through each and all of the diverted field-line bundles and therefore diagnosing the whole divertor topology. Experiments using electron injection through the divertors can provide information on divertor connections, the possibility of influencing flows and edge potentials without plasma contact with a divertor strike plate, and a method for altering central potentials and transport.

As an initial study, electrons have been injected using a highly-emissive filament at two symmetric divertor locations in IMS (the 23° and 337° divertor bundles). Each of the divertor strike plates was used as an electron collector. Data has been compared to a field-line model which launches field lines at the injection site and follows them until reaching another divertor strike plate. The majority of these field lines emerge within two field periods of the injection site in agreement with the detection of strong electron signals. As the launch distance is moved inward minor-radially, both the code and data show increased toroidal connection distances.

Electron injection through the divertors in the presence of plasma has shown the ability to redistribute diverted particle flows. Only seventeen of the divertor locations are fitted with screens to permit measurement of individual electron and ion flows without perturbing potentials in the plasma and divertor regions. Within these constraints, the changes in electron and ion flow have been measured under the conditions of both positive and negative bias to an individual strike plate and with electron injection at the same location, as shown in Table I. Significant changes to some flows have been measured under both scenarios, but differences are seen in the redistribution between the two methods.

Divertor Monitored	Field Periods Away from Launch	Pos. Bias		Neg. Bias		Electron Injection	
		% Δ_{ion}	% Δ_{elec}	% Δ_{ion}	% Δ_{elec}	% Δ_{ion}	% Δ_{elec}
72	1/3	+60	+70	-10	-10	0	+10
337	2/3	-25	-50	0	0	+20	0
23	1	-35	-10	0	+10	+30	+10
288	1 1/3	0	-40	0	0	-5	+180

Table I. Comparisons of flow changes with strike-plate biasing and electron injection.

4. Diverted Flux Pattern in the Proto-Cleo Stellarator

Experiments in IMS³ have shown that diverted particle flows can be concentrated to the inboard or outboard side of the torus with an external vertical magnetic field. To examine if a similar effect can occur in a continuous-coil device, allowing the possibility of differential biasing of groups of field lines, a preliminary scoping study has been made of the distribution of diverted particle flux along the helical 'stripe' in the Proto-Cleo Stellarator divertor region. Two arrays, with a total of 52 Langmuir probes, follow the helix for 2/3 of a wire period at the minor radius of the coil. An additional array of 14 probes is located perpendicular to the helical coils. The perpendicular array shows the flux localized around one sense of helical coil as expected. The arrays which follow the helical coils showed that there was a helical stripe, but that there was significant peaking on the inboard and outboard sides of the torus, with the strongest peak on the inboard side. Small external vertical magnetic fields were applied (which shifted the magnetic axis approximately 1.5 cm inward and outward, respectively) to see the effects on the divertor pattern. Similar fields in IMS had significant effects on the diverted flux pattern. On Proto-Cleo, however, the flux patterns were observed to be relatively insensitive to these fields.

5. References

- 1) R.P. Doerner, D.T. Anderson, W.N.G. Hitchon, P.G. Matthews and J.L. Shohet, Phys. Rev. Letters, **62**, 159 (1989).
- 2) R.P. Doerner, D.T. Anderson, F.S.B. Anderson, P.H. Probert, J.L. Shohet and J.N. Talmadge, Phys. Fluids, **29**, 3807 (1986).
- 3) R.P. Doerner, D.T. Anderson, F.S.B. Anderson, P.G. Matthews and J.L. Shohet, Nucl. Fus., **28**, 1879 (1988).

Pressure and Potential Measurements in IMS
During Electron Cyclotron Heating

J.N. Talmadge, D.T. Anderson, F.S.B. Anderson,
B.J. Peterson and J.L. Shohet

Torsatron/Stellarator Laboratory
University of Wisconsin-Madison
Madison, Wisconsin 53706 U.S.A.

Abstract: Two-dimensional measurements of the plasma pressure have been made in the Interchangeable Module Stellarator (IMS) at two separate toroidal locations. The results indicate that the profile is hollow during Electron Cyclotron Heating (ECH) and that there is a significant variation of the plasma pressure on the magnetic surfaces towards the plasma edge. Also, two emissive probes are aligned along a magnetic field line in vacuum by using one probe to detect the emitted electrons from the other. The locus of detected peaks in the current agree well with the numerical calculation of the magnetic surface. Measurements of the space potential on a flux surface indicate a maximum on the outboard side of the torus and a possible $m=1$ structure.

1. Introduction

Experiments in IMS during ECH have shown that the steady-state density profiles are hollow and that the addition of a convective term in the particle balance equation is necessary to explain the profile [1]. The hollowness of the profile increased as the resonant layer was moved from the inboard side of the torus to the outboard side. Shot-to-shot measurements of the space potential across the plasma cross-section indicated that the poloidal electric fields increased as the profiles became more hollow. Based on indications that the potential varied on a magnetic surface, measurements were made to explore whether the plasma pressure was a constant on a magnetic surface. Similarly, experiments were conducted to determine whether plasma parameters could be measured directly from probes aligned along a magnetic field line, rather than relying on interpolation onto a magnetic surface from shot-to-shot measurements made on a uniform grid.

2. ECH Plasmas and Probes

The plasma is produced by a 7.28 GHz microwave source which is resonant with 2.6 kG. The maximum power available is 2 kW for a pulse length of 10 ms. Plasma densities are in the range of $0.5-3.0 \times 10^{21} \text{ cm}^{-3}$, and electron temperatures are 4-10 eV. IMS, which consists of 21 discrete twisted coils, has 7 field periods with 3 coils per field period. These are labeled the 'Z', 'S' and 'B' coil according to their shape when viewed from above. Horizontal ports are located at only the 'Z' and 'S' coils. The vacuum magnetic surfaces at these locations are mirror images of each other with respect to the midplane.

The pressure profiles are measured with Langmuir probes which can be moved in two dimensions to access the plasma cross-section. Measurements of the plasma density and temperature were made at 5

mm intervals at one 'Z' port and also at one 'S' port, separated by 124° toroidally. About 250 shots were needed to obtain the data. The space potential measurements were made with two emissive probes that are also located at a 'Z' and an 'S' port. The emissive probe at the 'S' port was fixed at $r = 2$ cm, while the emissive probe at the 'Z' port could access the entire plasma cross-section.

The probes could then be run cold to obtain the ion saturation current or the electron temperature between two positions on a field line. To obtain the space potential, the probes were used as standard emissive probes, utilizing the inflection point technique [2]. Data for the plasma parameters along a magnetic field line were taken for each probe on alternate discharges, to minimize the possibility that sweeping the voltage on one probe would affect the other.

3. Pressure Profiles

Figure 1 shows contours of constant plasma pressure for the two toroidal locations. Also shown in the figure are the numerical calculations of the vacuum magnetic surfaces. It can be seen that the relationship between the pressure profiles and the magnetic surfaces is fairly good. However, the pressure on a surface can vary significantly, especially in the regions towards the plasma edge where the density peaks. Up to a 40% variation on a surface has been detected. Also it can be observed that at small minor radii, the pressure profiles are slightly shifted inward with respect to the magnetic surfaces.

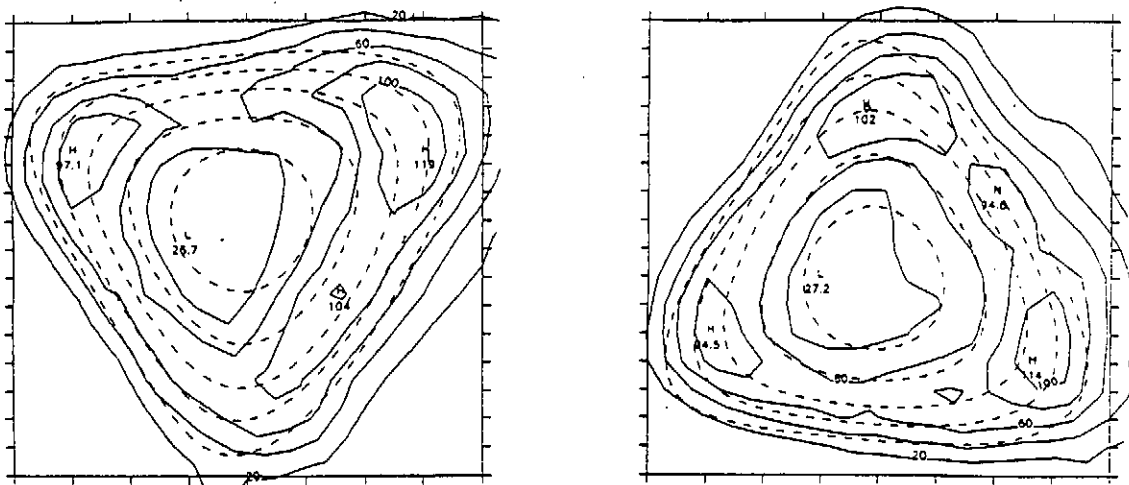


Fig 1. Constant pressure contours and vacuum magnetic surfaces for the 'Z' and 'S' ports

Figure 2 shows the pressure plotted as a surface plot. From this figure one can see that the pressure profile is hollow throughout the plasma cross-section. At the 'Z' port, however it can be seen that the pressure peaks on the inboard and outboard side of the torus and is a minimum at the top and bottom. At the 'S' port the pressure peaks at the vertices of the triangular-shaped magnetic surfaces.

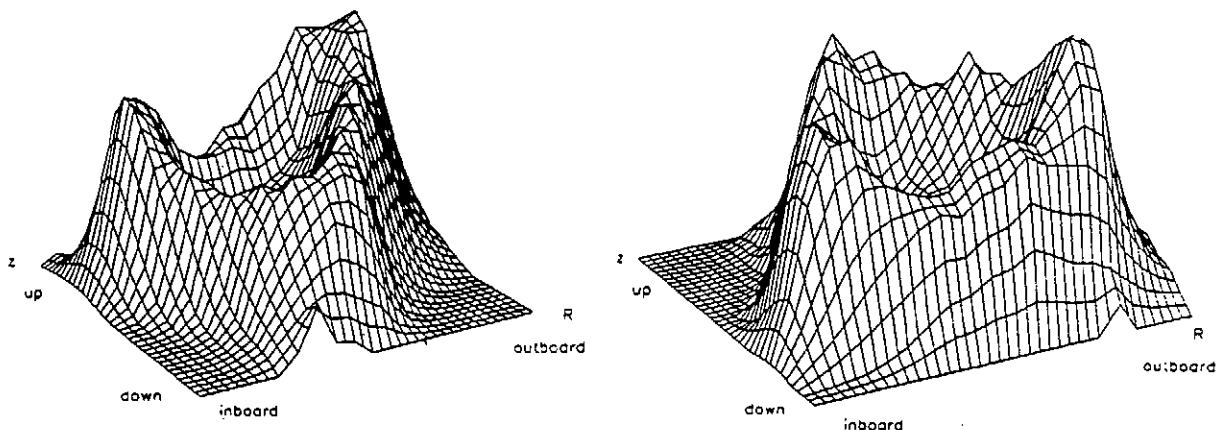


Fig 2. Surface plots of the pressure at the 'Z' and 'S' ports

4. Probe Measurements Along a Magnetic Field Line

To align the emissive probes along a magnetic field line, the fixed probe located at the 'S' port was heated to emission and 100 V negative bias was applied between the filament and ground. The movable probe at the 'Z' port was then used to detect the emitted electrons in vacuum in the presence of the magnetic field. As the probe was moved in 1-2 mm increments, the current to the probe was recorded and the peak in the detected signal was interpreted as alignment along a magnetic field line. In Figure 3 is shown the locus of detected peaks in the current to the probe, which compares well to the numerical calculation of the flux surface.

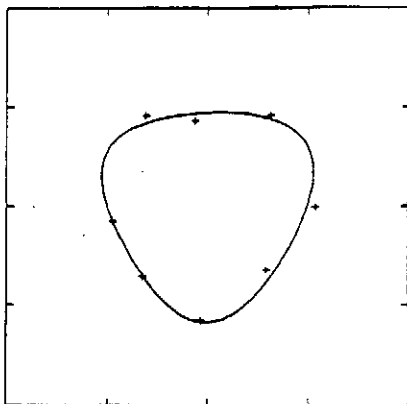


Fig. 3 Location of peaks

The alignment of the probes based on the peak in the detected signal should still result in alignment in the presence of plasma. Numerical calculations of the drift of 100 eV electrons for different pitch angles indicates that the drift of the electrons off the flux surfaces is approximately 1 mm, which is smaller than the 2-3 mm size of the probes. Also the shift of the magnetic surfaces in the presence of the plasma is still smaller than the probe size since the plasma β is on the order of 10^{-6} .

Only in the region about the magnetic axis where the rotational transform approaches zero will there be substantial error involved.

Figure 4 shows the ion saturation signal on a magnetic field line as a function of poloidal angle for the movable probe. Also shown is the data for the fixed probe which indicates the degree of reproducibility of the data. It can be observed that the ion

saturation for the 'Z' port peaks on the inboard and outboard side of the torus. An $m=2$ or possibly $m=3$ structure can be seen. Figure 5 shows the space potential for the movable and fixed probes as a function of poloidal angle. From the figure it can be seen that the space potential peaks on the outboard side of the torus and that the variation of the potential as a function of poloidal angle has the appearance of an $m=1$ mode.

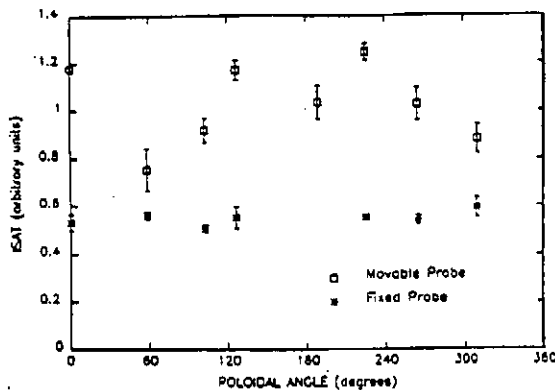


Fig. 4 Ion saturation current

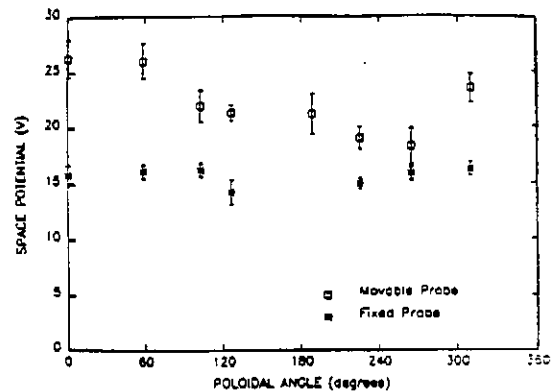


Fig. 5 Space potential

5. Conclusion

Measurements of the plasma pressure over the cross-section of the plasma at two probe positions indicate that in general the pressure surfaces agree with the vacuum flux surfaces, however regions of greater pressure can be detected at the vertices of the triangular surfaces. Measurements of the ion saturation current on a magnetic field line, using two emissive probes to insure alignment, confirm the localized regions of greater pressure. Measurements of space potential on a magnetic surface indicates that the potential peaks on the outboard side of the torus, a result that was first detected on a shot-to-shot basis by an emissive probe that was moved in equal increments across the plasma area [1]. A recent improvement in the method of measuring electron temperature, density and potential on a magnetic field line during the same discharge has been made with the use of a timing circuit which allows the alternate sweeping and floating of two emissive probes, thereby minimizing the interaction between the two probes.

6. Acknowledgement

This research was supported by the Department of Energy under contract number DE-FG02-86ER53216.A004.

7. References

1. J.N. Talmadge, C.A. Storlie, D.T. Anderson et al., Nucl. Fusion 29 (1989) 1806.
2. J.R. Smith, N. Hershkowitz and P. Coakley, Rev. Sci. Instrum. 50 (1979) 210.

Numerical and Experimental Studies of Simulated Toroidicity
Effects in a Linear High-Beta Heliac

B.A. Nelson, G. Spanjers, F.L. Ribe, D.C. Barnes⁺, and R. Bishop⁺⁺

University of Washington, Seattle, WA 98195 USA

Abstract

Formation and equilibrium studies of a linear high-beta heliac have been performed, showing an axial current is induced. Vacuum field numerical studies have shown that when the hardcore center conductor is shifted, the magnetic field structure is similar to a large aspect-ratio toroidal heliac. An experiment in a hardcore theta-pinch has shown that programming of the hardcore current can significantly reduce the induced axial current. Finite-beta effects have been incorporated into a code to study the evolution of plasma on a shifted hardcore heliac. These results will be used in an experimental study of simulated toroidicity in a shifted hardcore linear heliac.

Previous Heliac Results

Previous formation studies of a linear high-beta heliac^[1] in the High-Beta Q Machine (HBQM) show that a fast-rising current in the hardcore center conductor is necessary to avoid forming plasma pressure around the hardcore. The equilibrium was formed with $n_e \sim 10^{21} \text{m}^{-3}$, $T_e + T_i \sim 100 \text{ eV}$, and $\langle B \rangle \sim 25\text{-}30\%$ for plasma lifetimes of 10-20 μs . This fast-rising hardcore current was found to induce an oppositely directed net parallel plasma current in the heliac bean. Miniature three-dimensional internal magnetic field probes (6 mm OD quartz jacket protruding radially 4 - 6 cm into the plasma) were used to locally measure B. Global plasma parameters were provided by axial heterodyne quadrature laser interferometry, flux loops, and external magnetic field probes.

Basis for Simulated Toroidicity

A vacuum magnetic field line solving program, HELIK^[2], found that both the field line structure and Boozer harmonic structure are quite similar between a large aspect ratio toroidal heliac, $R=1.86 \text{ m}$, and a linear heliac with a "shifted" hardcore, (i.e., the hardcore translated off center from but parallel to the $\ell=1$ coil geometrical axis). The similarity of loss of helical symmetry for the toroidal and shifted hardcore cases was seen from the

⁺ Los Alamos National Laboratory, Los Alamos NM, USA

⁺⁺ University of Texas, Austin TX, USA

partial recovery of flux surfaces by an inward shift of a toroidal hardcore. The empirical relationship between the major radius, R , of the toroidal heliac and the shift, δ , of the hardcore in the linear heliac is $R \delta = 0.371 \text{ m}^2$, so that a $\delta = 2 \text{ cm}$ shift corresponds to a $R = 1.86 \text{ m}$ toroidal heliac.

It is proposed to study magnetic island formation and evolution in a toroidal heliac by simulating the toroidicity in a shifted-hardcore experiment on the HBQM. A hardcore shifting end box capable of up to 2 cm shifts under vacuum has been implemented and tested. It will be possible to perform a series of discharges without a shift, shift under vacuum, then take another series with the shifted hardcore for comparison.

Induced Current Studies

The characterization and elimination of the induced plasma currents are deemed crucial for the simulated toroidicity experiments on the HBQM. It is desired to produce islands in the heliac plasma by the helical symmetry breaking, but these islands are predicted to be sensitive to small axial currents and grow^[3], thus we wish to study them in an initially currentless heliac.

An induced current experiment was performed on the HBQM configured as a hardcore theta-pinch. A hardcore current programming circuit was developed using a slow-rising ($\tau_{1/4} \sim 15 \mu\text{s}$) ignitron-switched bank and a fast-rising ($\tau_{1/4} \sim 1.1 \mu\text{s}$) bank switched by spark gaps through a 5:1 turn bitter plate transformer. The slow circuit is initiated, then the fill gas is preionized with a ringing capacitor bank, Fig. 1. (A slow "positive bias" B_z field was added for protection of the hardcore during the notch.) Immediately prior to the main bank current firing, the fast hardcore current bank is initiated to either increase or decrease the hardcore current. This induces a plasma current in either the opposite or the same direction (respectively) as the slow-rising hardcore current. Results show that the increasing fast current ("notch up") configuration significantly reduces the residual induced current after the main bank implosion field. This is attributed to the direction of $\mathbf{J}_{\text{induced}} \times \mathbf{B}_{\text{hardcore}}$. In the notch down case, $\mathbf{J} \times \mathbf{B}$ is toward the hardcore and away in the notch up case. The notch up case induces a current in the same direction as the induced current found in the heliac formation, but this induced current is removed when the notched hardcore current returns to the slow hardcore current value. We feel that the notch up configuration will allow the formation of a current free heliac.

Numerical Results with Finite Beta

The ISLE code was developed to study the build-up of plasma pressure in the shifted hardcore heliac experiment^[4]. To specifically study island formation, a helically symmetric pressure distribution is loaded onto helically symmetric field lines near the hardcore which

are interpolated onto a non-helically symmetric grid near the $\ell=1$ coils. ISLE evolves plasma pressure using finite-pressure resistive MHD equations, with a pressure source term (on a resistive time scale) inside the separatrix, and a pressure sink outside the separatrix. The profiles are Fourier analyzed in θ and z , and finite differenced in r . The vector potential \mathbf{A} is advanced using a semi-implicit time difference method.

Initial results show the evolution of constant pressure contours from the symmetrically loaded pressure at time $t = 0$, (Fig. 2-a), to quasi-equilibria 100 Alfvén times (t_A) later, for no hardcore shift, (Fig 2-b), and a 2 cm hardcore shift, (Fig. 2-c). Note the asymmetry in Fig. 2-c, resulting from helical symmetry breaking. Magnetic field line puncture plots for the same conditions as Fig. 2 are given in Fig. 3, viz., (a) $t = 0$, no shift, (b) $t = 100 t_A$, no shift, and (c) $t = 100 t_A$, 2 cm shift. These results will be used to guide magnetic probed data taking strategies, as the previous method of using helical symmetry to map data at several axial locations to one plane cannot be used.

References

- ¹C.M. Greenfield, M.E. Koepke, and F.L. Ribe, *Physics of Fluids* (in publication).
- ²D.C. Barnes, SAIC Report APPAT-88, Austin, TX 78746, USA.
- ³A.H. Reiman and A.H. Boozer. *Physics of Fluids*, 27(10):2446-2454, October 1984.
- ⁴D.C. Barnes, SAIC Report SAIC-89/1577:APPAT-117 San Diego, California 92121 USA.

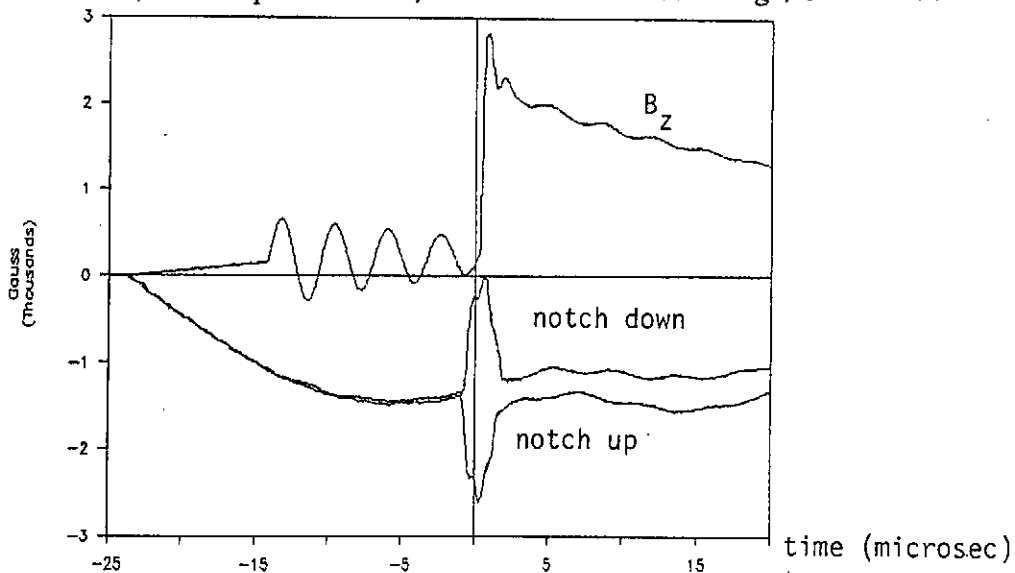


Figure 1. Vacuum B_z and B_θ for the notch down and notch up hardcore currents.

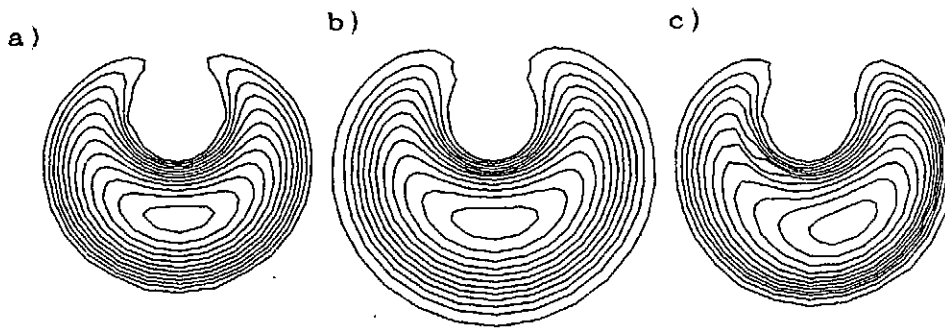


Figure 2. Plasma pressure profiles from the ISLE code for (a) $t = 0$, (b) $t = 100 t_A$, no shift, and (c) $t = 100 t_A$, 2 cm hardcore shift.

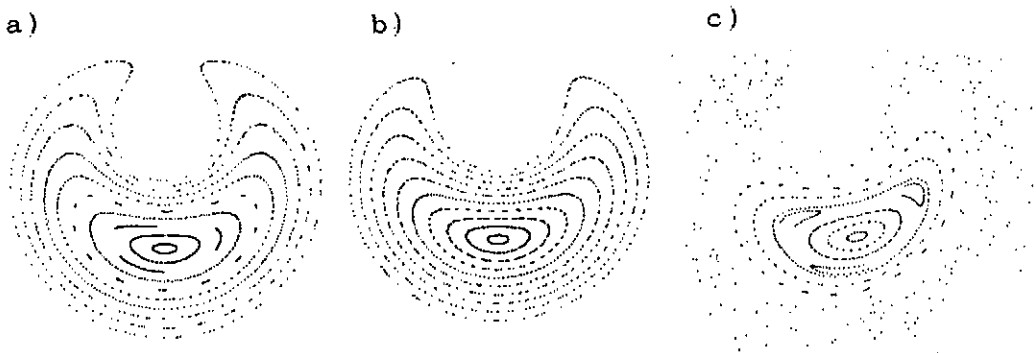


Figure 3. Magnetic field line puncture plots from the ISLE code for (a) $t = 0$, (b) $t = 100 t_A$, no shift, and (c) $t = 100 t_A$, 2 cm hardcore shift.

Theory of Electron Cyclotron Heating in the Flexible Helic TJ-II

C. Alejandre, F. Castejón, V. Krivenski and V. Tribaldos

Asociación EURATOM/CIEMAT para Fusión

28040 Madrid, Spain

Abstract

A theoretical model has been developed to study microwave absorption in the presence of non-Maxwellian electron distribution functions, that can easily be incorporated in existing ray-tracing codes. A TJ-II and a CHS/ATF magnetic configuration are used to illustrate the results obtained with the model. To fully understand ECH in TJ-II, quasilinear effects are taken into account by means of a flux-averaged quasilinear Fokker-Planck code. The modification of the electron distribution function will be presented for central and off-axis heating in the second harmonic.

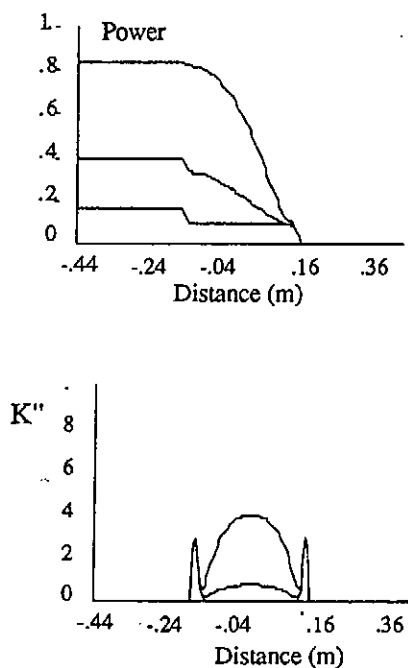


Figure 1

CHS/ATF-like magnetic configuration, with its typical saddle-point structure, from the low-field side in the X-mode at 53.2 GHz (second harmonic). In the figure it can be clearly seen

Linear Theory

To examine the effect of the superthermal electrons on the absorption we have developed a weakly relativistic non-maxwellian model valid for oblique propagation. We have simulated the electron distribution function by a drifting maxwellian added to a bulk maxwellian. In this conditions it is possible to simulate the experimentally measured suprathreshold populations and to calculate analytically the dielectric tensor [1]. We have found qualitative and quantitative differences in the plasma absorption properties with respect to the deposition profile and the power absorbed when we take into account the presence of a suprathreshold tail. Figure 1 shows the imaginary part of the wave vector and the power absorbed for a wave propagating into a

that the absorption profile broadens considerably and depending on the amount of suprathermals, the total power absorbed can go from 20% to 80%.

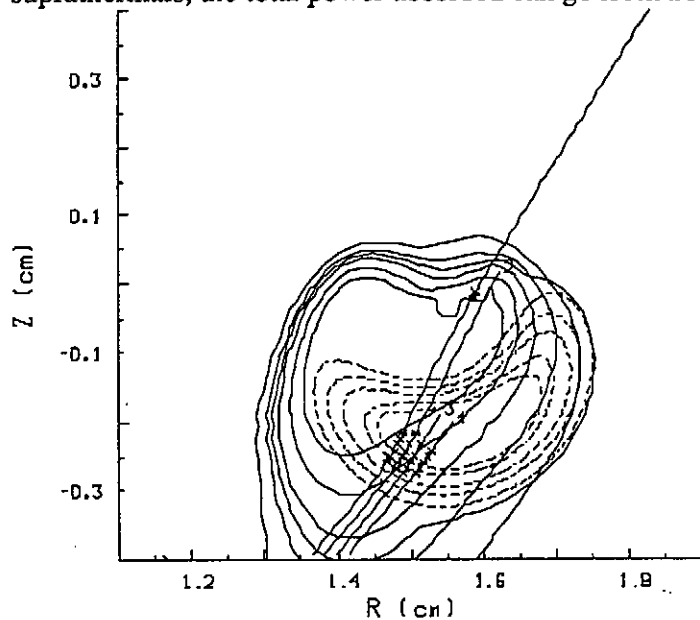


Figure 2

The absorption model has been introduced into the ray-tracing code RAYS developed at the Oak Ridge National Laboratory [2] to study microwave absorption in TJ-II in the presence of a suprathermal tail. Figure 3 shows the importance that suprathermals can have when the rays follow a path for which the resonant electrons are mainly the superthermal ones. Since these electrons resonate at higher values of the magnetic field, it is

possible to have absorption in places of the plasma in which it would not happen for a Maxwellian distribution. In figure 3, two cases are compared, in a) the distribution function is assumed Maxwellian, in figure 3 b) a tail is assumed in the electron distribution function. The microwave characteristics are kept constant in both cases. The power absorption rises considerably in the non-Maxwellian case.

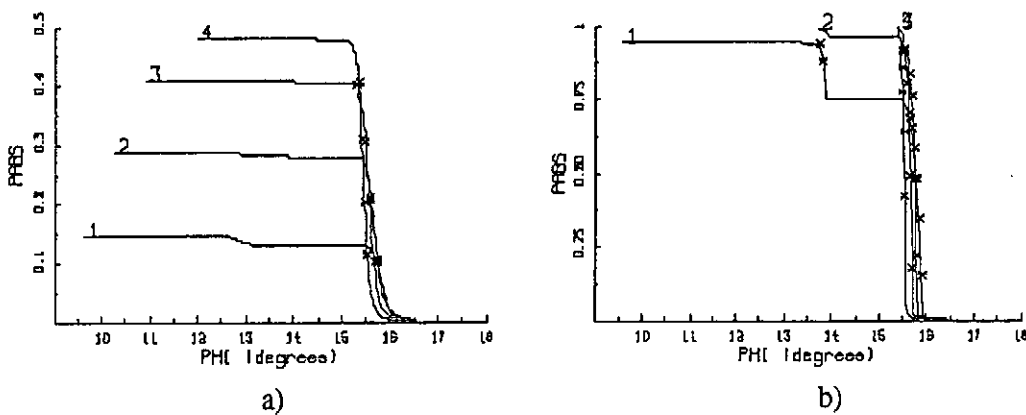


Figure 3

Quasilinear Theory

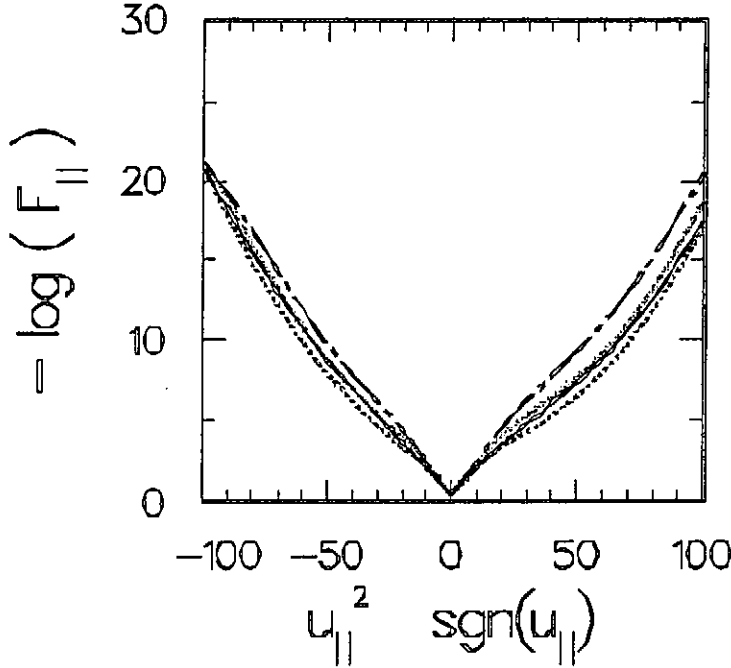


Figure 4
The parallel distribution function for four radial positions: $\langle r \rangle = 6.5, 6.0, 5.0,$ and 5.5 cm.

Electron cyclotron heating results in the increase of the perpendicular energy of the resonant electrons, the collisional thermalization of this energy then causes bulk heating. If the amount of energy absorbed per single resonant electron is large, collisions may not be able to thermalize this energy and a non-thermal distribution of energy can appear. This situation can appear even for modest levels of wave power if the

plasma density is low or the coupling between the wave and the electrons is strong, i.e., the wave damping is large. Both these conditions are met in TJ-II for X-mode, 2nd harmonic heating.

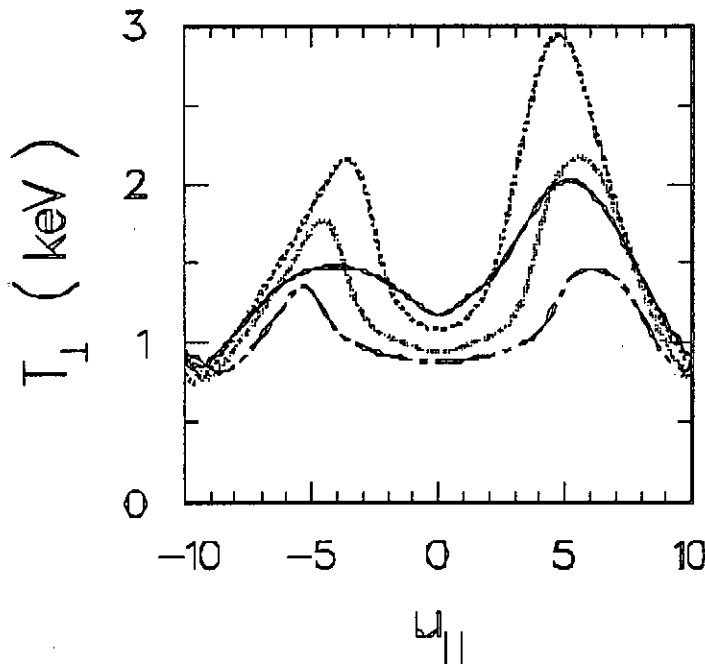
In order to study this process we have solved the kinetic equation containing the two relevant terms: the collision term, describing the collisions of the suprathermal population with a thermal bath, and the quasilinear term, describing the heating process as a diffusion process in momentum space. The complete integral linearized collision operator [3] has been used to describe correctly the modification of the low energy part of the distribution function, as it occurs during bulk heating. The relativistic diffusion coefficient [4] has been bounce averaged taking into account the magnetic field geometry of TJ-II. The resulting equation is 2D in momentum space, 2D in wave vector space and 1D in real space.

The kinetic equation has been solved numerically for typical TJ-II parameters, $T_e(0) = 1$ keV, $n(0) = 1.5 \times 10^{13}$ cm⁻³, $Z_{\text{eff}} = 2$, $f = 53.2$ GHz and $P_{\text{EC}} = 360$ kW. The resonance layer is located near $\langle r \rangle = 5$ cm for perpendicular injection.

The parallel function and the perpendicular temperature,

$$F_{\parallel}(u_{\parallel}) = 2\pi \int_0^{\infty} du_{\perp} u_{\perp} f(u_{\parallel}, u_{\perp}), \quad T_{\perp}(u_{\parallel}) = 2\pi T_e \int_0^{\infty} du_{\perp} u_{\perp}^3 f(u_{\parallel}, u_{\perp}) / F(u_{\parallel}),$$

($\mathbf{u} = \mathbf{p} / p_{th}$), are presented in Fig. 4 and 5 , after 50 collision times (1.2 ms) evolution of the distribution function, when a nearly steady-state is attained. We observe a large deformation of the distribution function at high energies, however the deformation at low energies, even if smaller, is much more important because it involves a much larger number of electrons. The distribution is slightly asymmetric due to the non symmetric deformation of the wave packet caused by the magnetic configuration of TJ-II.



The wave damping, which is determined by the perpendicular slope of the distribution function, greatly differs from the Maxwellian one [5,6] and the optical depth decreases from $\tau = 6.1$ to $\tau = 4.3$. The plasma remains optically thick, but since the wave absorption is in a regime of strong variation, the result is sensitive to the exact plasma parameters.

Figure 5

References

- [1] C. Alejaldre and F. Castejón. Phys. Fluids Nov. 1989[
- [2] RAYS
- [3] M. N. Rosebluth, W. M. MacDonald, and D. L. Judd, Phys. Rev. **107**,1 (1957).
- [4] I. Fidone, G. Granata, and R. L. Meyer, Phys. Fluids **25**, 2249 (1982).
- [5] Fidone, R.L. Meyer, and G. Granata, Phys. Fluids **26**, 3292 (1983).
- [6] V. Krivenski, I. Fidone, G. Giruzzi, R. L. Meyer, L. F. Ziebell, Phys. Fluids **30**, 438 (1987).

STORM : A LOW ASPECT RATIO TORSATRON FOR PLASMA STABILITY STUDIES

A.P. Navarro, J. Guasp, C. Alejaldre, J. Alonso, E. Ascasibar, J. Botija, F. Castejón, J. R. Cepero, A. L. Fraguas, L. García, M. Liniers, R. Martín, M.A. Ochando, A. Perea, A. Rodríguez-Yunta, M. Sorolla, F. Tabarés and A. Varias.

Asociación EURATOM / CIEMAT para Fusión
28040 Madrid, SPAIN

ABSTRACT

STORM is a low aspect ratio torsatron ($R_0 = 0.6$ m, $\langle a \rangle = 0.1$ m, $B_0 = .5$ T, $\ell = 1$ and $M=6$), currently under construction at CIEMAT and to be in operation next year. Main configuration parameters are $\iota(0) = 0.3$, shearless, magnetic well depth $\approx 7\%$ and helical axis elongation ≈ 0.025 m. Plasma start-up and heating is based on ECH using a 2nd harmonic heating scheme, with a 200 kw gyrotron at 28 GHz.

In this paper we describe in detail this device and discuss the configuration studies made for the selection of the configuration. Predictions from stability and transport analysis for the plasma behaviour in the device will be also presented together with microwave absorption studies, made with ray tracing codes to optimize the heating scheme.

Changing currents in the vertical field coils, some flexibility in the configuration parameters is obtained ($\iota(0) : 0.14$ to 0.4 , shear : -5% to $+37\%$, magnetic well : 0 to 7% , average plasma radius is almost constant in all this range, magnetic axis shifts from 6 cm inside to 3 cm outside). This device flexibility allows to study stability properties with and without magnetic well. In the case of the configuration without magnetic well, a high fraction of the energetic particles, generated by injection of ECH, could be trapped in the plasma. So, the effect of these particles on stability could be also experimentally studied in STORM. Theoretical estimations made for all these experiments will be presented in this paper.

"The submitted manuscript has been authored by a contractor of the U.S. Government under contract DE-AC05-84OR21400. Accordingly, the U.S. Government retains a nonexclusive, royalty-free license to publish or reproduce the published form of this contribution, or allow others to do so, for U.S. Government purposes."

Dissipative Trapped Electron Modes in $\ell = 2$ Torsatrons*

*B. A. Carreras, N. Dominguez, V. E. Lynch
Oak Ridge National Laboratory, Oak Ridge, Tennessee, U.S.A.*

*P. H. Diamond
University of California, San Diego, California, U.S.A.*

Abstract: Trapped electron modes in stellarators can be more unstable than those in tokamaks. They could be easier to detect in a stellarator and may be responsible for anomalous losses in the low collisionality regime.

1. Introduction

Trapped electron modes¹ can play an important role in enhancing losses in a toroidal confinement device. They could be one of the causes for the deterioration of confinement with increasing beta in tokamaks and stellarators. For straight stellarators and for a model field, it has been shown² that the helical ripple and short connection lengths allow for strongly localized solutions to the drift wave equation. Therefore, it appears that trapped electron modes can be more unstable in stellarators than in tokamaks. This is particularly the case for low shear configurations.

In contrast to tokamaks, stellarators have the advantage that the magnetic field can be changed substantially by modifying the currents in the vertical field (VF) coils. In ATF,³ for example, changing the quadrupolar moment of the VF coils changes the rotational transform at the magnetic axis and, as a consequence, the shear. The change of the quadrupole field also changes $|\mathbf{B}|$ along the field lines, allowing change of the trapping regions independent of the average curvature. This presents the opportunity to substantially change the parameters that control the trapped particle instabilities. Experiments can be carried out in ATF to study trapped electron modes and evaluate their role in plasma confinement.

2. Stellarator Drift Waves

Bhattacharjee et al.² derived the drift wave equation along a magnetic field line, assuming that the electrons are adiabatic and the ions are a fluid. Their result is

$$\frac{c_s^2}{\omega^2} \frac{d^2 \Phi}{ds^2} = - \left[m^2 |\nabla \beta|^2 \rho_s - \frac{m(\vec{v}_* + \vec{v}_d) \cdot \vec{\nabla} \beta}{\omega} + 1 \right] \Phi, \quad (1)$$

* Research sponsored by the Office of Fusion Energy, U.S. Department of Energy, under contract DE-AC05-84OR21400 with Martin Marietta Energy Systems, Inc.

where c_s is the sound velocity, s is the length along a field line, v_* is the diamagnetic drift velocity, and v_d is the magnetic drift velocity. The perpendicular wave number k_\perp is equal to $m|\nabla\beta|$. This equation is analogous to the tokamak drift wave equation in the ballooning representation, but the eikonal phase β has an important oscillatory component along the field line.

With regard to trapped electron modes, the main differences between tokamaks and stellarators are the connection length L_\parallel , the shear length L_s , and the $|\mathbf{B}|$ structure along the magnetic field lines.

The connection length in a stellarator is given by $L_\parallel \approx R_0/M$, while in a tokamak it is $L_\parallel \approx R_0q$. Here R_0 is the major radius, M is the number of toroidal field periods, and q is the safety factor. Therefore, L_\parallel can be smaller by an order of magnitude in a stellarator. As $\nu_* = L_\parallel\nu/v_T$, it is easier to achieve $\nu_* < 1$ in a stellarator than in a tokamak.

Another important difference between tokamaks and stellarators is the characteristic shear length L_s . For similar parameters and at the plasma core, L_s/L_n can be larger by a factor of 2 to 10 in a stellarator than in a tokamak. Here L_n is the density scale length.

The third main difference is in the φ dependence of $|\mathbf{B}|$ along a magnetic field line. The helical ripple in a stellarator causes a multiplicity of magnetic wells where the eigenfunction can be localized.

It is useful to examine the case of a straight stellarator. Its main difference from the tokamak comes through the eikonal phase:

$$\begin{aligned} |\vec{\nabla}\beta|^2 = & \frac{1}{\rho^2} \{1 + \delta \cos[(\ell\tau - M)\varphi] - (\rho\tau'\varphi)\delta \sin[(\ell\tau - M)\varphi] \\ & + (\rho\tau'\varphi)^2 \{1 - \delta \cos[(\ell\tau - M)\varphi]\} \} , \end{aligned} \quad (3)$$

where ℓ is the multipolarity, ρ is a radius-like flux surface label, and δ is the ripple field parameter. The oscillatory terms can cause the localization of the eigenfunction in a single field ripple. Depending on the shear, radial position, and wave number, the solutions of the straight stellarator drift wave equation are mainly of two types:

- Modes localized inside a helical ripple. The width of these modes in ballooning space, Δ_φ , is less than one field period, $2\pi/M$.
- Extended modes. Their width along the field lines is 2π or larger.

For the localized solutions with $M\Delta_\varphi \ll 1$, we can expand the oscillatory functions in φ and analytically solve the eigenvalue problem, Eq. (1). The solutions are of the form $\Phi \approx \Phi_0 \exp(-\varphi^2/2\Delta_\varphi^2)$, with the mode width given by

$$\Delta_\varphi \approx \frac{1}{M^{1/2}} \left(\frac{2}{\delta}\right)^{1/4} \frac{1}{k_\theta \rho_s} \left(\frac{L_n \omega_*}{R_0 \omega}\right)^{1/2} \quad (4)$$

and the frequency by

$$\omega = \omega_* \frac{1 + (\delta/2)^{1/2} M(L_n/R_0) + \delta M^2(\rho L_n/R_0^2)}{1 + k_\theta^2 \rho_s^2 (1 + \delta)^2} \quad (5)$$

For a stellarator, the relation between Δ_φ and the radial width of the eigenfunction Δ_r is analogous to that for the tokamak case, $\Delta_r = 1/(k_\theta \tau \hat{S} \Delta_\varphi)$. Here \hat{S} is the shear parameter. Therefore, for modes localized in a single field ripple,

$$\Delta_r \approx \rho_s \sqrt{\left(\frac{\delta}{2}\right)^{1/2} M \frac{L_s^2 \omega}{L_n R_0 \omega_*}} \quad (6)$$

The radial width can be significantly larger than the width of the tokamak-slab eigenfunction, $\Delta_r \approx \rho_s (L_s/L_n)^{1/2}$.

Equation (1) has been solved for 3-D stellarator equilibria that were obtained with the VMEC code.⁴ Details of the numerical calculations are given in Ref. 5.

3. Dissipative Trapped Electron Modes in a Stellarator

Including the non-adiabatic response and assuming that only helically trapped particles contribute to the instability and that $\nu_{eff} \gg \omega_{*e} \gg \nu_{ei}$, we obtain an integro-differential equation for the dissipative trapped electron modes in a stellarator,

$$\frac{c_s^2}{\omega^2} \frac{d^2 \Phi}{ds^2} - U(s)\Phi = -i \frac{\omega \langle \Phi \rangle - \langle \omega_{*e} \Phi \rangle}{\bar{\nu}_{eff}} \quad (7)$$

where the angle brackets $\langle \rangle$ indicate bounce average over each helical ripple well. For localized solutions, the eigenvalue equation can be solved perturbatively, and the change in frequency is

$$\delta\omega = \frac{-1}{\bar{\nu}_{eff}} \left[\int ds \Phi^* (\omega_0 \langle \Phi \rangle - \langle \omega_{*e} \Phi \rangle) \right] \left(\int ds \frac{\partial U}{\partial \omega} \Big|_{\omega_0} |\Phi|^2 \right)^{-1}, \quad (8)$$

where ω_0 is the frequency of the adiabatic electron mode.

When the eigenfunction of the drift wave equation is localized in the first ripple well of $|\mathbf{B}|$ (Fig. 1a), the bounce average of Φ , $\langle \Phi \rangle$, has a value close to 1. Thus, for localized solutions, the non-adiabatic contribution to the dispersion relation gives a strong destabilizing contribution.

When the eigenfunction of the drift wave equation is extended along the field lines, its periodicity is different from the periodicity of $|\mathbf{B}|$ (Fig. 1b). Therefore, its net contribution to $\langle \Phi \rangle$ is small. Thus, for extended solutions, the non-adiabatic contribution to the dispersion relation is small and can be of either sign.

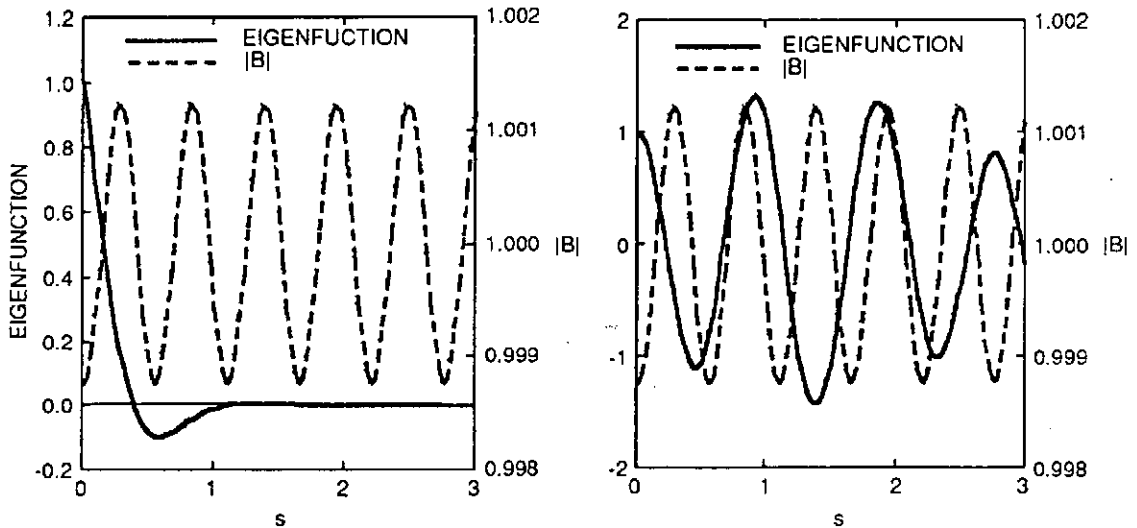


Fig. 1. (a) Localized and (b) extended eigenfunction along field lines of straight stellarator drift wave compared with the variation of $|\mathbf{B}|$.

4. Dissipative Trapped Electron Modes in ATF

The VF coil system in ATF permits the independent control of (1) the flux swing, (2) the dipole component, and (3) the quadrupole component of the poloidal field. These external controls allow change of $|\mathbf{B}|$ on a flux surface. This implies changes in the magnetic field line curvature, the $|\mathbf{B}|$ spectrum, and the trapped particle population.

For trapped electron mode studies, the important parameters to control are the shear and the trapped particle population. Both parameters can be varied simultaneously by changing the quadrupole moment of the VF coils. Using ATF equilibrium parameters, we have solved Eq. (10) for several values of the VF quadrupole moment. We find that by increasing the shear at the plasma core, the highly localized (in ballooning space) trapped electron modes can be eliminated.

To carry out the experimental test in ATF, the most favorable experimental conditions are obtained in ECH plasmas because the $\nu_* < 1$ regime is relatively easy to reach. The diagnostics required are (1) the ECE diagnostic for measuring the temperature fluctuations (as a consequence of the enhancement of the radial width for the helically localized modes, the resolution constraints are less severe than for a tokamak); (2) the heavy-ion beam probe to measure \tilde{n} and $\tilde{\Phi}$ fluctuations; and (3) the VF coils to change shear and trapped particle population.

References

1. B. B. Kadomtsev and O. P. Pogutse, *Sov. Phys. Dokl.* **14**, 420 (1979).
2. A. Bhattacharjee et al., *Phys. Fluids* **26**, 880 (1983).
3. J. F. Lyon et al., *Fusion Technol.* **10**, 179 (1986).
4. S. P. Hirshman, W. I. van Rij, and P. Merkel, *Comput. Phys. Comm.* **43** (1986) 143.
5. B. A. Carreras et al., in *Proceedings of the 7th International Stellarator Workshop*, Oak Ridge, 1989 (IAEA, Vienna, in press).

LOW- n STABILITY CALCULATIONS FOR THREE DIMENSIONAL STELLARATOR CONFIGURATIONS

L. Garcia

Universidad Complutense and Asociacion EURATOMCIEMAT. 28040 Madrid. SPAIN.

B.A. Carreras, N. Dominguez, J.N. Leboeuf, V.E. Lynch.

Oak Ridge National Laboratory. Oak Ridge, Tennessee 37831. USA.

The MHD equilibrium and stability stellarator calculations are complex because of the intrinsic three-dimensional (3-D) character of these configurations. The stellarator expansion [Greene and Johnson, *Phys. Fluids* 4 (1961) 875] can be applied to low- n stability for modes which variation along field lines is slow compared with the variation of the stellarator terms. A reduced set of MHD stellarator equations was derived by Strauss [*Plasma Phys.* 22 (1980) 733], and has been implemented in different stability codes. The accuracy of the method has been tested and demonstrated by comparing with 3-D stability results.

Here, we apply the averaging method to an equilibrium represented in a straight field line coordinate system. This will allow the extension of the low- n linear stability calculations to helical axis systems and hopefully improve the accuracy of the low- n stability for any type of configuration. We take the exact 3-D equilibrium as the lowest order of the expansion, and assume that this equilibrium is given in Boozer coordinates. Numerical solutions are shown to agree well with marginal stability boundaries given by the classical stellarator expansion in the planar magnetic axis case.

Destruction of Magnetic Surfaces in Helical Torus

Jiro TODOROKI

National Institute for Fusion Science, Nagoya 464-01

Abstract. The toroidal magnetic field is decomposed into two parts, the field consisting the magnetic surfaces, and the field part destroying the magnetic surfaces. The structure of the surface destroying part is determined only by the helical coils, and determines the bound of the magnetic surface, as well as the structure of the divertor magnetic field lines.

1. Introduction.

Although the position and shape of the vacuum magnetic surfaces in the helical torus can be controlled by external vertical and quadrupole field, the range of existence of magnetic surfaces is bounded. This boundary can be well understood with the concept of surface destroying part of the magnetic field (SDF), introduced in connection with the magnetic coordinates.¹⁾ In this paper, we will see that SDF has the spatial structure independent to the actual magnetic surfaces, and it poses essential boundary to the existence of magnetic surfaces as well as the other kind of structure of the magnetic field lines observed in the divertor layer. The position of the SDF is calculated for the various coil configurations, and the dependence to the pitch parameter γ_c , pitch number M , and pitch modulation α is discussed.

We decompose the magnetic field in a helical torus into two part:

$$B = B^{(S)} + B^{(D)}, \quad (1)$$

where $B^{(S)}$ is the part which composes nested magnetic surfaces: $B^{(S)} \cdot \nabla \Psi = 0$, and $B^{(D)}$ is the part which can not be represented in the form of such nested magnetic surfaces.

2. Coordinate Transformation.

The decomposition can be made by introducing the coordinate transformation from the cylindrical coordinates (r, z, ϕ) to a curvilinear coordinates (X, Y, ζ)

$$r = R(X, Y, \zeta), \quad z = Z(X, Y, \zeta), \quad \phi = \zeta, \quad (2)$$

under the assumption that the quantities (induction densities) $H^X = \sqrt{g} B^X$, $H^Y = \sqrt{g} B^Y$, and $H^\zeta = \sqrt{g} B^\zeta$ do not depend on the toroidal angle ζ , where B^X, B^Y, B^ζ are contravariant component of the magnetic field, and

$$\sqrt{g} = R \left\{ \frac{\partial R}{\partial X} \frac{\partial Z}{\partial Y} - \frac{\partial R}{\partial Y} \frac{\partial Z}{\partial X} \right\}, \quad (3)$$

is the Jacobian of the transformation.

If such coordinate transformation is obtained, there is a function $\Psi(X, Y)$, such that

$$H^X = \frac{\partial \Psi}{\partial Y}, \quad H^Y = -\frac{\partial \Psi}{\partial X}. \quad (4)$$

The surface $\Psi(X, Y) = \text{const.}$ is the magnetic surfaces. The magnetic field can be expressed as $B = B^{(S)}$, where

$$B^{(S)} = \nabla\psi(X,Y) \times \nabla\zeta + H^{\zeta}(X,Y) \nabla X \times \nabla Y. \quad (5)$$

The coordinate transformation is determined by the equations

$$H^{\zeta} \frac{\partial R}{\partial \zeta} + H^X \frac{\partial R}{\partial X} + H^Y \frac{\partial R}{\partial Y} = \sqrt{g} B_r, \quad H^{\zeta} \frac{\partial Z}{\partial \zeta} + H^X \frac{\partial Z}{\partial X} + H^Y \frac{\partial Z}{\partial Y} = \sqrt{g} B_z, \quad H^{\zeta} R = \sqrt{g} B_{\phi}, \quad (6)$$

with $X=\langle R \rangle, Y=\langle Z \rangle, \langle \dots \rangle$ being the average with respect to ζ . Since three equations in eqs.(6) are not independent because of the condition $\text{div} B=0$, eliminating \sqrt{g} , we can rewrite them in the following form

$$\frac{\partial R}{\partial \zeta} + h^X \frac{\partial R}{\partial X} + h^Y \frac{\partial R}{\partial Y} = \frac{RB_r}{B_{\phi}}, \quad \frac{\partial Z}{\partial \zeta} + h^X \frac{\partial Z}{\partial X} + h^Y \frac{\partial Z}{\partial Y} = \frac{RB_z}{B_{\phi}}, \quad (7)$$

with $h^X = H^X/H^{\zeta}, h^Y = H^Y/H^{\zeta}$, which are determined as "eigen values", in order that R and Z are periodic with respect to ζ .

Since the magnetic surfaces can exist only in the limited region and the magnetic islands may also exist in that region, such coordinate transformation can be obtained only in a certain region and only in the asymptotic sense. When the nonlinear eigenvalue equations (7) are solved by using an iteration procedure, the procedure converges to give the sought transformation in a certain region; but in the other region the solution cannot be obtained because the procedure diverges or the Jacobian becomes negative. In the region where the transformation can not be obtained the smooth extension from the obtained region is adopted.

3. Surface Destroying Field.

From such transformation we can introduce the residual field

$$B^{(D)} = B - B^{(S)}, \quad (8)$$

with $B^{(S)}$ defined by eq.(5).

The residual field (8) is very small in the region where the good magnetic surface exists and it grows rapidly near the boundary of the existence of the solution of eq.(7) up to the order of B_0 , the typical magnetic field strength. The residual field can be regarded as the component which destroys the magnetic surfaces (SDF).

An example of the structure of the poloidal component of SDF is shown in Fig.1. The magnetic surfaces with the poloidal field such that the magnetic axis is at the coil center are also superposed in the figure. From this figure we can see the envelope as shown in Fig.2. The envelope restricts the region where the magnetic surface can exist, and it also determines the region of divertor magnetic lines of force.

Calculations show that SDF $B^{(D)}$ is essentially determined by the helical coils; it changes little by the vertical and quadrupole component. This is because axisymmetric poloidal field can be essentially included into the flux function ψ . In the low m heliotron/torsatron configuration, the region is shifted inside of torus.

Since the growth of SDF is very fast, we can practically determine the boundary of the global structure of the magnetic lines of force from the envelope of the amplitude of $B^{(D)}$. Calculating SDF to various helical coil configurations, we can see the global structure of the helical magnetic field. The envelope of SDF moves outside (inside) of torus when the positive (negative) pitch modulation is applied (Fig.3). The envelope shrinks as the pitch parameter $\gamma_c = (m a_c / l R_c)$ decreases. The position of the envelope is plotted in Fig.4, for various pitch number M . The influence of the current density in the helical coil to the position of the envelope can be practically ignored, because its change is smaller

than the change of coil thickness (in the LHS parameters).

4. Discussion

Even if SDF is small in the region where good surfaces are observed, the magnetic island may be formed as the result of its resonant Fourier components. The analysis of Fourier component of SDF can predict the island formation.

The breaking of the magnetic surfaces is related to the island formation due to the resonant component $n=ml$. The precise position of the outermost magnetic surface can be determined by taking into account such resonance; but since SDF grows very fast near the envelope discussed above, its Fourier component also grows fast near the envelope, envelope giving the upper bound for the existence of the magnetic surfaces.

The spatial structure of the surface destroying field (SDF) can interpret the boundary of the magnetic surfaces as well as the local structure of the divertor magnetic lines of force. Although the present analysis is restricted to the vacuum magnetic field, the same structure may be expected in the finite beta magnetic field.

In the plasma equilibrium calculations the determination of the plasma surface is the unsolved problem. It is expected that the construction of SDF may give the means to determine plasma surface as the outermost magnetic surface.

This work is supported by Grant-in-Aid for Fusion Research of Ministry of Education, Science and Culture.

References

- 1) J.Todoroki, J.Phys.Soc. Japan, 58 (1989) 3979

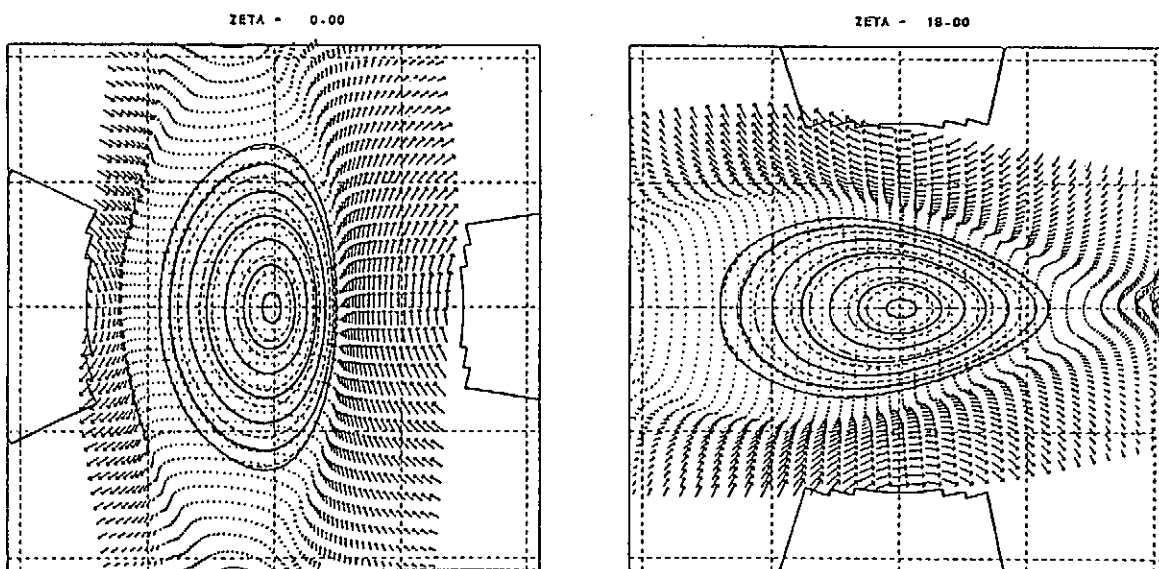


Fig.1 The poloidal component of the surface destroying magnetic field. The magnetic surfaces for $\Delta=0$ $B_q=100\%$ are also shown.

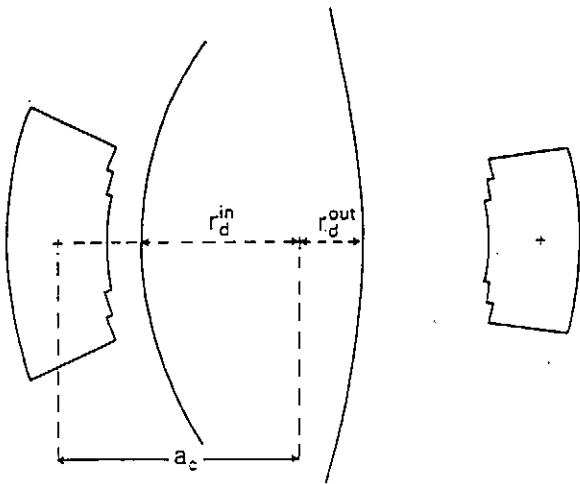


Fig.2 The envelope of the surface destroying magnetic field. The definitions of r_d^{in} and r_d^{out} are also shown.

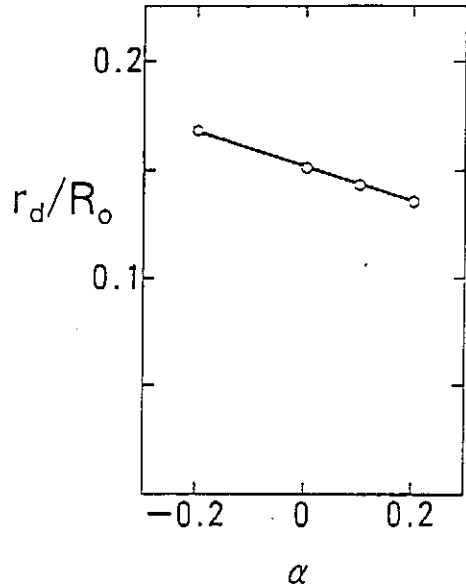


Fig.3 Dependence to the pitch modulation parameter α for $M=10$, $\gamma_c=1.20$. The winding law is $\theta=\kappa\varphi-\alpha\sin(\kappa\varphi)$, $\kappa=M/l$, θ being 0 inside of the torus.

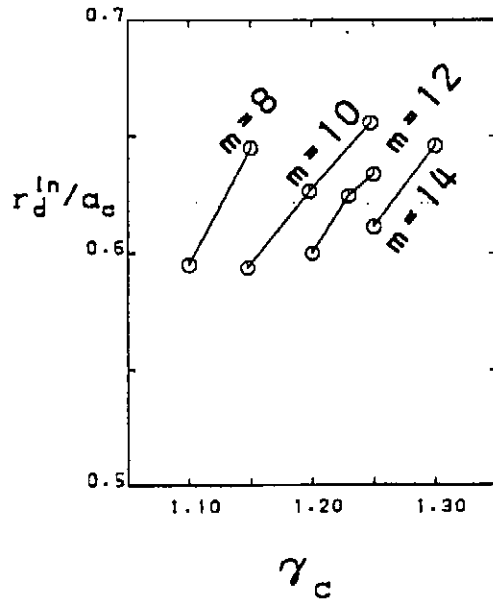
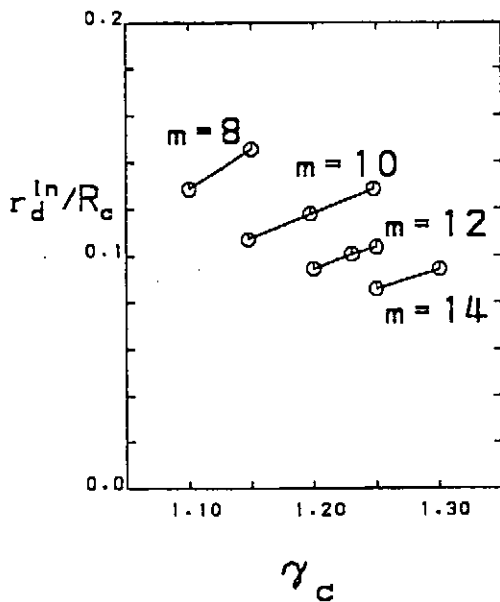


Fig.4 Dependence to the pitch parameter γ_c and pitch number M .

Ripple Diffusion and Bootstrap Current in LHD

T.Amano, M.Okamoto, N.Nakajima, Y.Ogawa, K.Yamazaki

National Institute for Fusion Science

Chikusa-ku, Nagoya 464-01

and

S.P.Hirshman, W.I.van Rij

Fusion Energy Division, Oak Ridge National Laboratory

Oak Ridge, Tennessee, USA

Ripple diffusion and bootstrap current are calculated for the plasma of Large Helical Device(LHD) with $L=2$, $M=10$, $R=4\text{m}$, and $B=4\text{T}$. The ripple diffusion is calculated by using GIOTA code and DKES code[1,2]. GIOTA code calculates the diffusion coefficient in $1/\nu$ regime very quickly and DKES calculates the neoclassical transport coefficients in all collisionality regime by solving drift kinetic equation. Bootstrap current is evaluated by using the formulation in Ref.(3) and (4).

The DKES calculation shows that the energy convoluted ion thermal conductivity χ_i at the minor radius of $r/a=0.5$ for $T_i=5\text{keV}$ is less than $1.0\text{m}^2/\text{s}$ for $e\phi/T_i > 1.0$. We have examined the effects of the magnetic axis shift Δ , pitch modulation of helical coils α , and the plasma $\beta(0)$ on the neoclassical transport. Comparison has been made only for effective flux of mono-energy particles with $v/\nu=10^{-4}/\text{m}$, where ν is collision frequency and v is velocity of particles. In the case of weak electric field ($E_r/\nu=10^{-6}\text{Vsec}/\text{m}^2$), the improvement of the diffusion coefficient by a factor of 2-3 has been observed when the magnetic axis is shifted inward ($\Delta=-0.1\text{m}$). While, the diffusion coefficient deteriorates by a factor of 2-3, when the positive pitch modulation $\alpha=0.1$ is applied, or when the central beta value is raised to $\beta(0)=5\%$. The VMEC[5] code is used

to obtain equilibria. In the $1/\nu$ regime, the neoclassical diffusion has been also evaluated with GIOTA code. It is found that the results of DKES code in $1/\nu$ regime agree well with those of GIOTA code.

When the radial electric field is increased ($E_r/\nu=3 \times 10^{-3} \text{Vsec/m}^2$), it is found that the deterioration of the diffusion coefficients due to the positive pitch modulation and the finite beta effect has been overcome, keeping the improvement due to the inward shift of the plasma column.

Various vacuum magnetic field configurations have been considered to reduce the neoclassical bootstrap current in the LHD. In the banana regime, it is clarified that the geometric factor of the bootstrap current depends strongly on the vertical field and still more strongly on the quadrupole field, but the dependence on M value is weak. The small outward shift of the magnetic axis and the vertically elongated poloidal cross section of magnetic surfaces can reduce the bootstrap current significantly. By controlling the applied vertical field to shift the magnetic axis outward the bootstrap current can be reduced to $1/2$ - $1/4$, and to $1/10$ - $1/40$ by controlling the external quadrupole field to elongate the cross section of magnetic surfaces vertically. On the contrary, the bootstrap current in the plateau regime is sensitive to the M number and insensitive to vertical and quadrupole fields. The magnitude and profile of helical ripples in the radial direction are crucial in the plateau regime and we have observed negative bootstrap current. Their absolute values increase as M increases. When compared with tokamaks, the bootstrap current may be driven appreciably in the plateau regime in helical systems and it seems difficult to suppress or reduce it by the control of poloidal fields. It should be remarked that the bootstrap currents in both banana and plateau regimes are inversely proportional to the magnetic field strength B_0 , since $\langle J_{bs} B \rangle$ is independent of B_0 , hence J_{bs} becomes proportional to $1/B_0$.

It is concluded that the poloidal field control may optimize the equilibrium to reduce the bootstrap current in the banana regime small enough so as not to change the vacuum rotational transform. However, It should be emphasized that the compatibility

of the optimized configuration for the bootstrap current with MHD stabilities and ripple transports is important for the LHD. In the above bootstrap current calculations, we have considered vacuum magnetic field configurations. The finite beta effect causes the shift of the magnetic axis, which will affect the bootstrap current significantly. If the magnitude of the bootstrap current is so large to alter the rotational transform appreciably, the equilibrium, bootstrap geometric factor, and transport fluxes should be solved simultaneously to obtain the self-consistent bootstrap current. The anomalous transport and island formation are also important for determining the bootstrap current. These problems are under investigation.

In order to assess the effects of change of configurations due to finite beta, the magnetic axis shift and helical coil ripple modulation on the neoclassical transport of the LHD, a transport code EQ-TRANS is now being developed. In the EQ-TRANS, 1-D transport code and 3-D equilibrium code VMEC are solved simultaneously as in 1-1/2D tokamak transport codes. From the output of the VMEC code, Boozer coordinates are constructed which are used to calculate $1/\nu$ regime neoclassical transport coefficients by use of the GIOTA code and also to calculate bootstrap current. Neutral beam heating is calculated by using HFREYA code which traces ionizations of injected neutral particles in the VMEC coordinates. Thermalization of the fast ion beams is treated with a Fokker-Planck code. The anomalous transport can be taken into account by assuming the LHD scaling. The current diffusion equation for the FCT current due to heating and bootstrap current will be also implemented.

References

- 1) S.P. Hirshman et al., *Phys. Fluids* **29**(1986) 2951.
- 2) W. van Rij and S.P. Hirshman., *Phys. Fluids* **B1**(1989)563.
- 3) K.C. Shaing and J.D. Callen, *Phys. Fluids* **26**(1983)3315.
- 4) N. Nakajima et al., *Nucl. Fusion* **29**(1989) 605.
- 5) S.P. Hirshman and J.C. Whitson, *Phys. Fluids* **26**(1983)3553.

Numerical Analysis of Temporal Development of RF-Heated Plasma

Tsuguhiro Watanabe

National Institute for Fusion Science
Chikusa-ku, Nagoya, 464-01, Japan

Abstract: Numerical calculation of an overall temporal development of an rf-heated straight plasma cylinder is tried by new numerical method HIDM (higher order implicit difference method). The plasma is described by electron, ion, and neutral-atom fluids(3-fluid model), with ionization, recombination, and charge exchange processes being taken into account.

The radial electric field plays an important role for plasma confinement in helical systems. The structure of the radial electric field is affected drastically by plasma production, transport, and heating processes. Hence, a comprehensive analysis is required to study the global structure of the electrostatic potential. Purpose of the present study is construction of the computer code to analyze the global temporal development of rf-heated plasma.

We analyze the temporal development of an rf-heated plasma numerically, assuming a straight cylindrical model (Fig.1).

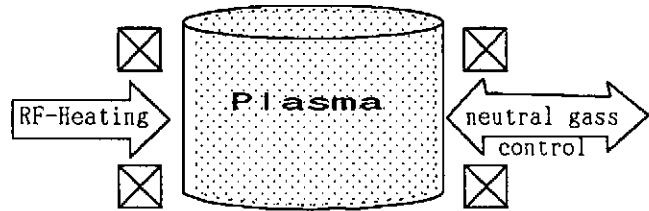


Fig.1 Model of rf-heating plasma column

The plasma is described by electron, ion, and neutral-atom fluids(3-fluid model), with ionization, recombination, and charge exchange processes being taken into account, as follows:

$$\frac{\partial n}{\partial t} + \frac{\partial (rnu_r)}{r \partial r} = \alpha n_0 n - \beta n^2, \quad (1)$$

$$\frac{\partial n_0}{\partial t} - \frac{D_0}{r} \frac{\partial}{\partial r} \left(r \frac{\partial n_0}{\partial r} \right) = -\alpha n_0 n + \beta n^2, \quad (2)$$

$$\frac{\partial u_r}{\partial t} + u_r \frac{\partial u_r}{\partial r} - \frac{u_{e\theta}^2}{r} = -\frac{e}{m} \left[E_r + \frac{u_{e\theta} B_z - u_{ez} B_\theta}{c} \right] - \frac{1}{mn} \frac{\partial (nT_e)}{\partial r} - \alpha n_0 u_r, \quad (3)$$

$$\frac{\partial u_{e\theta}}{\partial t} + \frac{u_r}{r} \frac{\partial (ru_{e\theta})}{\partial r} = -\frac{e}{m} \left[E_\theta - \frac{u_r B_z}{c} \right] - \alpha n_0 u_{e\theta}, \quad (4)$$

$$\frac{\partial u_{ez}}{\partial t} + u_r \frac{\partial u_{ez}}{\partial r} = -\frac{e}{m} \left[E_z + \frac{u_r B_\theta}{c} \right] - \alpha n_0 u_{ez}, \quad (5)$$

$$\frac{\partial u_r}{\partial t} + u_r \frac{\partial u_r}{\partial r} - \frac{u_{i\theta}^2}{r} = \frac{e}{M} \left[E_r + \frac{u_{i\theta} B_z - u_{iz} B_\theta}{c} \right] - \frac{1}{Mn} \frac{\partial (nT_i)}{\partial r} - \alpha n_0 u_r - \gamma n_0 u_r, \quad (6)$$

$$\frac{\partial u_{i\theta}}{\partial t} + \frac{u_r}{r} \frac{\partial (ru_{i\theta})}{\partial r} = \frac{e}{M} \left[E_\theta - \frac{u_r B_z}{c} \right] - \alpha n_0 u_{i\theta} - \gamma n_0 u_{i\theta}, \quad (7)$$

$$\frac{\partial u_{iz}}{\partial t} + u_r \frac{\partial u_{iz}}{\partial r} = \frac{e}{M} \left[E_z + \frac{u_r B_\theta}{c} \right] - \alpha n_0 u_{iz} - \alpha n_0 u_{iz}, \quad (8)$$

$$\frac{\partial T_e}{\partial t} + u_r \frac{\partial T_e}{\partial r} + \frac{2T_e}{3r} \frac{\partial (ru_r)}{\partial r} = -\alpha n_0 \left[T_e - \frac{m}{3} \vec{u}_e^2 + \frac{2}{3} W_i \right] - \chi (T_e - T_i) + \frac{\partial}{r \partial r} \left[r q_e \frac{\partial T_e}{\partial r} \right] + \frac{2P_{eH}}{3n}, \quad (9)$$

$$\left[\vec{u}_e^2 = u_r^2 + u_{e\theta}^2 + u_{ez}^2 \right],$$

$$\frac{\partial T_i}{\partial t} + u_r \frac{\partial T_i}{\partial r} + \frac{2T_i}{3r} \frac{\partial (ru_r)}{\partial r} = -(\alpha + \gamma) n_0 \left[T_i - \frac{M}{3} \vec{u}_i^2 \right] - \chi (T_i - T_e) + \frac{\partial}{r \partial r} \left[r q_i \frac{\partial T_i}{\partial r} \right] + \frac{2P_{iH}}{3n}, \quad (10)$$

$$\left[\vec{u}_i^2 = u_r^2 + u_{i\theta}^2 + u_{iz}^2 \right],$$

$$\frac{\partial B_z}{\partial r} = -\frac{4\pi e}{c} n(u_{i\theta} - u_{e\theta}), \quad (11), \quad \frac{\partial B_\theta}{\partial t} = c \frac{\partial E_z}{\partial r}, \quad (13)$$

$$\frac{1}{r} \frac{\partial (rB_\theta)}{\partial r} = \frac{4\pi e}{c} n(u_{iz} - u_{ez}), \quad (12), \quad \frac{\partial B_z}{\partial t} = -c \frac{\partial (rE_\theta)}{r \partial r}, \quad (14)$$

where α , β , γ , and χ represent ionization, recombination, charge exchange, and temperature relaxation rates, being assumed as follows:

$$\alpha = 10^{-5} \frac{\sqrt{T_e}}{W_i (6W_i + T_e)} \exp\left(-\frac{W_i}{T_e}\right) \left[\frac{\text{cm}^3}{\text{sec}} \right], \quad \beta = 5.2 \times 10^{-14} \sqrt{\frac{W_i}{T_e}} \left[\frac{\text{cm}^3}{\text{sec}} \right],$$

$$\gamma = 0.2 \times 10^{-8} \sqrt{T_i} \left[\frac{\text{cm}^3}{\text{sec}} \right], \quad \chi = 3.2 \times 10^{-3} \log_e \Lambda \frac{n}{10^{12}} T_e^{-3/2} \left[\frac{1}{\text{sec}} \right].$$

$$\left[W_i \text{ (eV : ionization potential), } T_e \text{ (eV), } n \text{ (cm}^{-3}\text{)} \right]$$

To solve the equations (1)~(14), we have applied a new numerical method HIDM (higher order implicit difference method)(ref.1), which can solve time evolution of boundary value problems described by sets of partial differential equations and boundary conditions:

$$\begin{aligned}
 L_1 \left[\overrightarrow{\phi}, \overrightarrow{\phi_t}, \overrightarrow{\phi_x}, \overrightarrow{\lambda}, \overrightarrow{\lambda_t}, t, x \right] &= 0, & \overrightarrow{\phi} &= \left[\phi_1(t, x), \dots, \phi_N(t, x) \right], \\
 & \dots & \overrightarrow{\phi_t} &= \left[\frac{\partial \phi_1(t, x)}{\partial t}, \dots, \frac{\partial \phi_N(t, x)}{\partial t} \right], \\
 L_N \left[\overrightarrow{\phi}, \overrightarrow{\phi_t}, \overrightarrow{\phi_x}, \overrightarrow{\lambda}, \overrightarrow{\lambda_t}, t, x \right] &= 0, & \overrightarrow{\phi_x} &= \left[\frac{\partial \phi_1(t, x)}{\partial x}, \dots, \frac{\partial \phi_N(t, x)}{\partial x} \right], \\
 & \left(x_0 \leq x \leq x_1 \right) & \overrightarrow{\lambda} &= \left[\lambda_1(t), \dots, \lambda_M(t) \right], \\
 & & \overrightarrow{\lambda_t} &= \left[\frac{\partial \lambda_1(t)}{\partial t}, \dots, \frac{\partial \lambda_M(t)}{\partial t} \right], \\
 Q_1 \left[\overrightarrow{\phi}(t, x_0), \overrightarrow{\phi}(t, x_1), \overrightarrow{\phi_t}(t, x_0), \overrightarrow{\phi_t}(t, x_1), \overrightarrow{\lambda}, \overrightarrow{\lambda_t}, t \right] &= 0, \\
 & \dots & & \\
 Q_K \left[\overrightarrow{\phi}(t, x_0), \overrightarrow{\phi}(t, x_1), \overrightarrow{\phi_t}(t, x_0), \overrightarrow{\phi_t}(t, x_1), \overrightarrow{\lambda}, \overrightarrow{\lambda_t}, t \right] &= 0, \\
 & (K=N+M) & &
 \end{aligned}$$

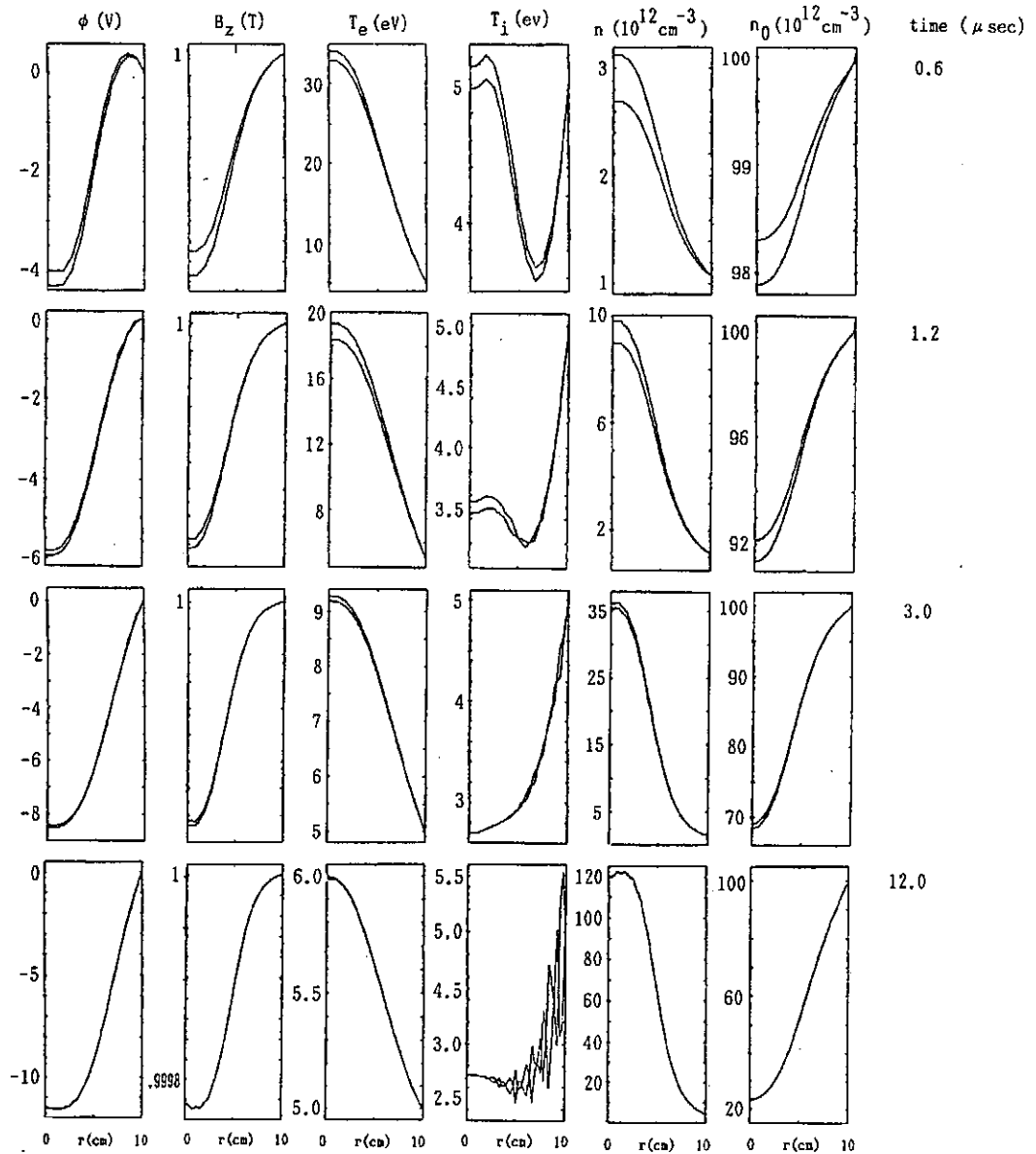
with a high degree of accuracy and numerical stability (ϕ is unknown variables and λ is unknown eigenvalues). The performance of HIDM has been proved in many applications, for example, the analysis of plasma transport by an electric field, the analysis of the ion acoustic wave instability driven by an ion beam, and the analysis of the penetration of an rf field into a magnetized plasma.

An example of an numerical analysis of temporal development of rf-heated plasma is shown in Fig.2. Present results is still in a preliminary stage, but overall calculation of rf-heating process of a plasma is carried out by HIDM. Most important key issue for the computation of the time evolution of heating process was the choice of the appropriate boundary conditions. Next step of the study is the refinement of the model of the transport coefficients and comparison with the actual heating experiments.

reference

1. T.watanabe, K.Abe, A.Ishida, Y.Kanada and K.Nishikawa: *Kakuyugo Kenkyu*(in Japanese), 58 (1987) 265.

Fig.2 Example of the numerical computation of rf-heating process of plasma. Time evolution of plasma density(n), neutral gas density(n_0), electron and ion temperature (T_e and T_i), electrostatic potential ϕ are shown. Initially, plasma (density: 10^{11}cm^{-3} , electron and ion temperature: 5eV, neutral gas density: 10^{13}cm^{-3}) and magnetic field(1 Tesla in z-direction) is assumed to be uniform. No electric field is assumed. Energy input to electron P_{eH} turn on at time 0 with time constant $\sim 0.5\mu\text{sec}$ to the level of $\sim 5.9\text{ kW/cm}$ and energy input for ion is assumed to be in the level of $1/20$ of P_{eH} . Electron heat conduction coefficients is assumed to be constant and corresponding energy confinement time is $\sim 0.1\text{ msec}$. Ion heat conduction coefficient is assumed to be in the range of $1/10$ of electrons one. Neutral gas density diffusion coefficient is also assumed to be constant and corresponding diffusion time is $\sim 10\text{ msec}$.



First International Toki Conference
on Plasma Physics and Controlled Nuclear Fusion
December 4 - 7, 1989
Toki, Japan

Island Studies for Helias Configurations

P. MERKEL

*Max-Planck-Institut für Plasmaphysik
IPP-EURATOM Association
D-8046 Garching bei München
Federal Republic of Germany*

1. Abstract

In the framework of the NESCOIL code a method analogous to the procedure of Cary and Hanson has been developed to eliminate islands and more generally to control the size and phase of islands. The method has been applied to Helias stellarator vacuum fields in order to determine configurations with a dense set of flux surfaces in the plasma region and an island chain at the boundary which may serve as a basis for a divertor concept.

2. Introduction

In stellarator research it has proved to be useful to separate the discussion of the magnetic properties of a configuration from its realization by coils. The properties of the plasma equilibria are completely determined by the geometry of the boundary. Therefore, it is reasonable to optimize stellarator configurations by considering the plasma region only. This approach has led to the Helias class of optimized stellarators [1]. The NESCOIL [2, 3, 4] code was then developed to compute external currents (coils) generating the appropriate vacuum field: On a closed surface surrounding the plasma boundary a surface current distribution

$$\vec{j} = \vec{n} \times \text{Grad } \Phi(u, v),$$

$$\Phi(u, v) = \sum_{m=0, n=-N}^{M, N} \Phi_{mn} \sin 2\pi(mu + nv) - \frac{I_p}{n_p} v - I_t u$$

is determined in such a way that the field \vec{B} approximates the vacuum field by solving approximately a Neumann boundary value problem, which is achieved by requiring that the normal component of \vec{B} be minimized on the plasma boundary (\vec{n} = normal unit vector on the outer surface, v = toroidal angle, u = poloidal-like angle, I_p = net poloidal current, I_t = net toroidal current, n_p = number of field periods). The surface current can be expressed in terms of a potential $\Phi(u, v)$. The net currents I_p, I_t are prescribed and the minimization procedure determines the Fourier harmonics Φ_{mn} . The coils are obtained by discretizing the surface currents into a finite number of infinitely thin filaments. They are modular (poloidally closed) if the longitudinal current is $I_t = 0$.

The NESCOIL code was applied to the Helias50B configuration ($n_p = 5$ field periods). The Helias50B stellarator is an example of the Helias class of optimized equilibria [5]. The realization of the Helias50B vacuum field with 10 filaments per period yields an iota profile in the range of $0.76 < \iota < 1.0$ with islands of $\iota = \frac{5}{6}$ and $\iota = \frac{5}{5}$, shown in Fig. 1.

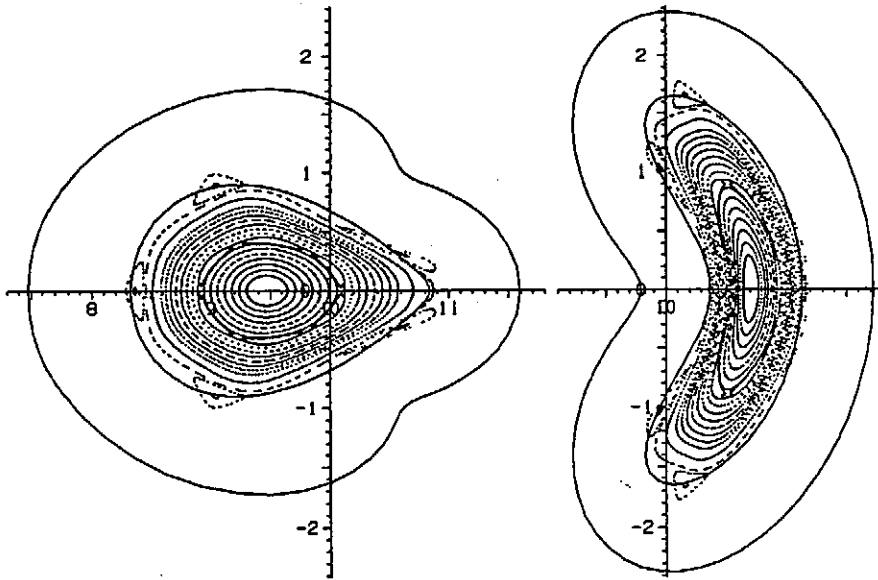


Fig. 1 Poincaré plots of the Helias50B vacuum field generated by 10 current filaments per period. Number of periods $n_p = 5$. The filaments are obtained by discretizing the surface current on the outer boundary. Iota profile $0.76 < \iota < 1.0$. Islands appear at $\iota = \frac{5}{6}$ and $\iota = \frac{5}{5}$.

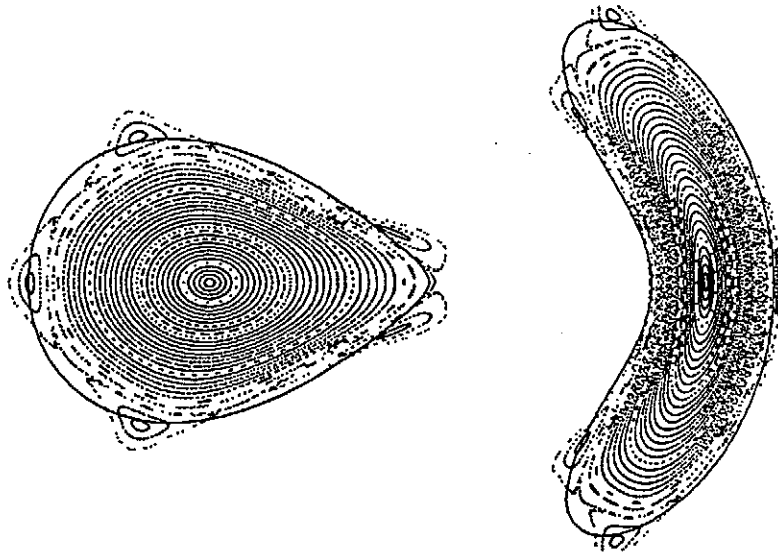


Fig. 2 Poincaré plots of the Helias50B vacuum field generated by 10 current filaments per period where the islands at $\iota = \frac{5}{6}$ are eliminated by adding a resonant correction field which is generated by adding Fourier amplitudes $\Phi_{6,0} = 5 \cdot 10^{-4}$ and $\Phi_{11,-1} = -1.6 \cdot 10^{-4}$ to the surface current potential.

One concept of controlling the plasma edge is to utilize a “separatrix and islands” region for a divertor. Optimal vacuum fields should therefore consist of a dense set of flux surfaces in the inner region bounded by a separatrix surrounded by a

chain of islands. For this purpose it is necessary to describe a method which allows one to eliminate and, more generally, to control the size and phase of islands.

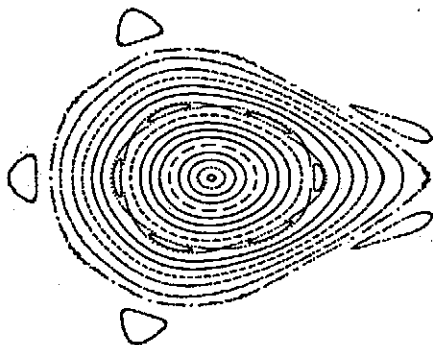


Fig. 3a

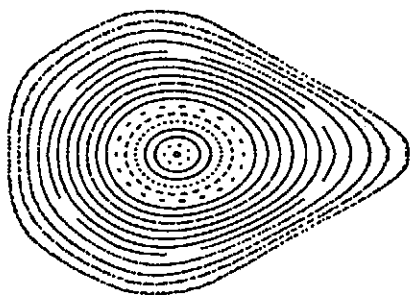


Fig. 3b

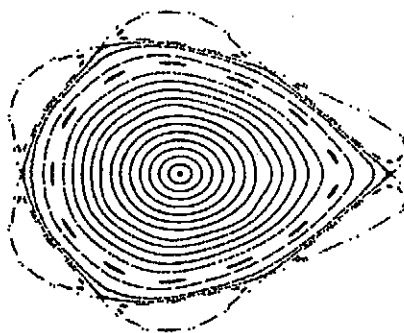


Fig. 3c

Fig. 3a-c Poincaré plots of the Helias50B vacuum field where the rotational transform is shifted by applying a longitudinal field produced by a current I_c of an additional coil set (see Fig. 4). a) $0.76 < \iota < 1$, $I_c = 0$, b) $0.72 < \iota < 0.95$, $I_c = 0.05I_p$, c) $0.7 < \iota < \frac{5}{6}$, $I_c = 0.12I_p$ (I_p = total modular coil current).

In the present paper it is shown that this can be achieved by a procedure analogous to the method of Cary and Hanson [6]: Small resonant correction fields are generated by modifying the coil geometry. In the framework of the NESCOIL code it is reasonable to generate the resonant fields by adding appropriately chosen Fourier harmonics Φ_{mn} to the surface current potential.

To provide sufficient flexibility, it has been proposed that an additional set of planar coils (see Fig. 4) be applied in order to vary the iota profile. With regard to the divertor island chain it has also been investigated whether reasonably sized divertor islands at the boundary are compatible with a sufficiently small size of these islands in the plasma interior on variation of ι .

3. Results

In Fig. 1 Poincaré plots of the Helias50B stellarator configuration are shown. The surface current is determined on the outer surface. The surface current is discretized into 10 filaments per period. A chain of 5 islands ($\iota = \frac{5}{5}$) forms the boundary. However, the size of the island at $\iota = \frac{5}{6}$ should be diminished. This is achieved by adding the potential harmonics $\Phi_{6,0}$ and $\Phi_{11,-1}$ (see Fig. 2). The term $\Phi_{11,-1}$ is directly resonant to a chain of 11 islands

understood as a nonlinear coupling of $\Phi_{6,0}$ with the geometry of the current-carrying surface:
 $\Phi_{6,0} \xrightarrow{m=0, n=-1} 6, -1.$

Figure 4 shows a period of the modular coils with an additional coil set which allows variation of ι . In Fig. 3a-c Poincaré plots for different values of additional current I_c are shown: $I_c = 0$, $I_c = 0.05I_p$, $I_c = 0.12I_p$ ($I_p =$ total modular coil current). The values of iota at the boundary decrease from $\iota = 1$ to $\iota = 0.95$ and $\iota = \frac{5}{6}$, respectively.

The main modular coil set slightly differs from the coils producing the field in Fig. 1. In order to minimize the thickness of the island at $\iota = \frac{5}{6}$ for the case $I_c = 0.05I_p$, a correction potential $\Phi_{6,0} = 1.1 \cdot 10^{-3}$ has been added. Comparison of Fig. 1 and Fig. 3a ($I_c = 0$) shows that the phase of the islands at $\iota = \frac{5}{6}$ is changed by this correction field. Figure 3b shows a configuration with a dense set of flux surfaces, and in Fig. 3c the chain of 6 islands appears at the boundary. This example demonstrates that the variation of iota and the concept of a suitable "separatrix and islands" region bounding the plasma seem to be compatible.

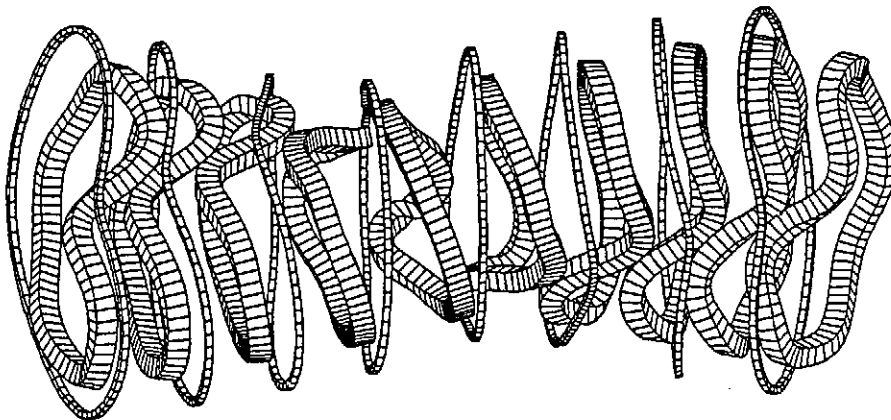


Fig. 4 One period of the modular coils for the case shown in Fig. 3 and the extra coil set producing an additional longitudinal field. For purely computational convenience the coils of this extra set have here not been taken as planar coils.

4. References

- 1 J. Nührenberg, R. Zille, Phys.Lett.A 114 (1986) 129
 J. Nührenberg, R. Zille, Phys.Lett.A 129 (1988) 113
- 2 P. Merkel, Nucl. Fusion 27 (1987) 867
- 3 P. Merkel, In: Theory of Fusion Plasmas, Eds. A. Bondeson, E. Sindoni, and F. Troyon, Varenna, Italy, EUR1136EN, 25-46
- 4 P.Merkel, In: Proc. 2nd Workshop on Wendelstein VII-X, Schloss Ringberg, Eds. F. Rau, G.G. Leotta, CEC Brussels 1988, EUR11705EN, 231-243
- 5 W. Lotz, P. Merkel, J. Nührenberg, A. Schlüter, R. Zille, Seventh Int. Workshop on Stellarators, 1989, Oak Ridge/USA
- 6 J.D. Hanson, J.R. Cary, Phys.Fluids 27 (1984) 767

ON STRONG RF PLASMA TURBULENCE

Miloš M. Škorić

The Boris Kidrič Institute of Nuclear Sciences, Vinča, P.O.B. 522,
11001 Belgrade, Yugoslavia

There is a sound theoretical and experimental evidence of strong nonlinear effects associated with RF heating of toroidal plasmas. In particular, concerning high power lower-hybrid heating schemes it is expected that nonlinear, strongly turbulent effects can become important. We discuss basic features of strong RF plasma turbulence of upper-hybrid and lower-hybrid waves. We present model equations, having a Hamiltonian structure, and show that in those nonlinear systems, the nonexistence of three-dimensional soliton wave solutions is superseded by wave collapse phenomena, governed by strong ponderomotive nonlinearity. Collapse of RF waves as a unique self-focusing type phenomena plays a role of an effective dissipation, determining basic microfeatures of emerging strong plasma turbulence. Moreover, it is shown that there exists a hierarchy of wave-collapse regimes, starting from a weak-collapse case which formally preserves zero energy into the final collapse stage and concluding with strong-collapse, where the trapped RF energy remains finite. In this way, collapse classification appears significant concerning the plasma heating efficiency.

Further, we have performed direct numerical simulations in two-dimensions of nonlinear evolution of upper-hybrid waves. In the highly nonlinear stage we have observed a collapse process. Moreover, for all considered cases, close to collapse singularity results show a self-similar behaviour consistent with a weak-collapse regime. Finally we note that lower-hybrid wave simulations appear to be a complex problem, due to its inherent three-dimensional nature, a task planned for near future.

STRUCTURAL DESIGN OF LARGE HELICAL DEVICE

K. Kitamura, M. Shibui, K. Yamamoto, S. Nakamoto, S. Mizumaki, H. Takano,
Y. Wachi, T. Hamajima and T. Sasaki
Toshiba Corporation, 2-4, Suehiro, Tsurumi, Yokohama, 230 Japan

O. Motojima, J. Yamamoto, K. Yamazaki and Large Helical Design Team
National Institute for Fusion Science, Furo-cho, Chikusa-ku,
Nagoya, 464 Japan

ABSTRACT

A structural design of the Large Helical Device (LHD) has been performed with proposals of: (1) application of forced flow superconductor to helical and poloidal coils, (2) toroidal shell for support structure of the coils and (3) corrugated vacuum vessel with high temperature difference between inner and outer skins^[1]. Structural analyses of these components have also been carried out to understand their mechanical behaviors including load transmission and to assess the structural reliabilities of the LHD.

INTRODUCTION

The LHD is now being developed and will be a next major experimental fusion device for National Institute for Fusion Science^[2]. The preliminary design of the LHD has been performed with particular emphasis on feasibility of the LHD. Major parameters of the LHD are given in Table 1. The key engineering issues of the LHD are: (1) reliable large superconducting coils with a stored energy of over 2 GJ, (2) in-situ winding technique of a pair of helical coils with a field accuracy of 5×10^{-4} , (3) effective support for the coils against large electromagnetic forces of over 1000 tons/m, (4) complex dumbbell-shaped vacuum vessel with a thickness smaller than 30 mm and (5) reliable divertor structure for long pulse operation ($t \geq 5$ sec).

COIL DESIGN

Helical Field Coil (HFC)

The HFC uses a cable-in-conduit type forced flow superconductor having a rectangular cross section of 29.0×25.8 mm² with subchannel for SHE. The conductor consists of 1.5 mm thick 316L conduit, 1.0 mm insulation and 486 NbTi/Cu strands of 0.7 mm diameter stabilized with pure Al. Major parameters of HFC are given in Table 2. The HFC conductor bundles are encased in a 316LN coil case to suppress the conductor deformation.

Poloidal Field Coils (PFCs)

The poloidal field coils consist of 2 outer vertical coils (OV coils), 2 inner shaping coils (IS coils) and 2 inner vertical coils (IV coils). The PFCs also use cable-in-conduit type conductors consisting of 243 to 486 NbTi/Cu/CuNi strands, compacted in 1 mm thick 316L conduit (first conduit), further encased 2.0 mm to 4.0 mm thick 316LN conduit (second conduit) and 1.0 mm thick insulation. Major parameters of PFCs are given in Table 2. The PFC conductor bundles are not encased in the coil case.

Table 1 Major Parameters of LHD

Major Radius	4 m
Average Plasma Minor Radius	0.6 m
Minor Radius of Helical Coil	0.96 m
Magnetic Field Strength	4 T at Plasma Center 8.4 T at Coil
Helical Field Period (l/m)	2/10
Magnetic Field Accuracy	5×10^{-4}
Magnetic Energy	2 GJ
Heating Power	20 MW

Table 2 Major Parameters of HF and PF Coils

	Magnetic Motive Force (MA)	Coil Cross Section (mm ²)	Rated Current (kA)	Number of Turns	Conductor Cross Section (mm ²)	Conductor Current Density (A/mm ²)	
HFC	8	522x429	34.8	230	29x25.8	46.5	
DVC	-5.02	396x504	32.6	154	36x36	25.4	
PFC	ISC	-3.22	288x312	22.4	144	24x26	35.8
	IVC	6.11	432x416	21.2	288	24x26	34.0

Coil Support Structure

A concept of the LHD support structure is illustrated in Fig. 1.

A 100 mm thick toroidal shell has been employed to effectively support the HFCs against large electromagnetic forces. Toroidal and poloidal ribs of 100 mm thickness are attached to the toroidal shell to reinforce the shell without increase in total weight of support structure. They are made of 316LN stainless steel. The toroidal shell is divided into 5 sectors in toroidal direction and each sector is also divided into upper and lower segments in the poloidal cross section for easy maintainability. They are mechanically connected by bolts and shearing keys. The HFC coil case is fixed to the toroidal shell by bolts and shearing keys. The 6 PFCs are supported by support frames mounted on poloidal reinforcing ribs. The toroidal shell is sustained by 10 thermally insulated support legs, which consist of FRP cylinders and stainless steel thermal anchors.

Structural Analyses

An overall analysis has been performed with a FEM model for a whole helical device shown in Fig. 2. A 72° sector of full torus was chosen as an analytical region because of geometric symmetry. Two kinds of coil operations are considered here: forces by HFC operation (L1) and forces by both HFC and PFC operations (L2).

The HFCs and their support structure expand in major radius direction in the case of L1 load, but in the case of L2 load, they shrink toward machine center. Table 3 summarizes analytical results on the displacements and stresses of structure components under L1 and L2 loads. PFC vertical displacements are estimated to be -0.5 to -0.8 mm including deformations of toroidal shell and support legs of about -0.3mm, with maximum conduit stresses of 20 to 40 MPa against their vertical forces.

A detailed stress analysis of PFC conduits has been performed to investigate the load transmission between conductors and detailed stress distribution of 1st and 2nd conduits and insulation under hoop force and assumed quench internal pressure of 80 atms. Figure 3 shows hoop stress and radial displacement distribution of OV coil conductors in the radial direction. Maximum hoop stress is induced in the 2nd conduit and estimated to be 360 MPa for OV coil and 430 MPa for IV coil.

Optimum HFC conduit thickness is set to be 1.5 mm from an elasto-plastic analysis of the conductor conduit under assumed quench pressure of 80 atms^[3].

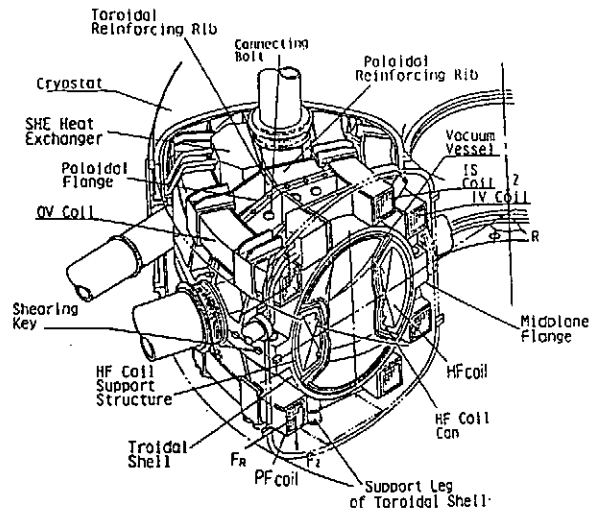


Fig. 1 Concept of LHD support structure

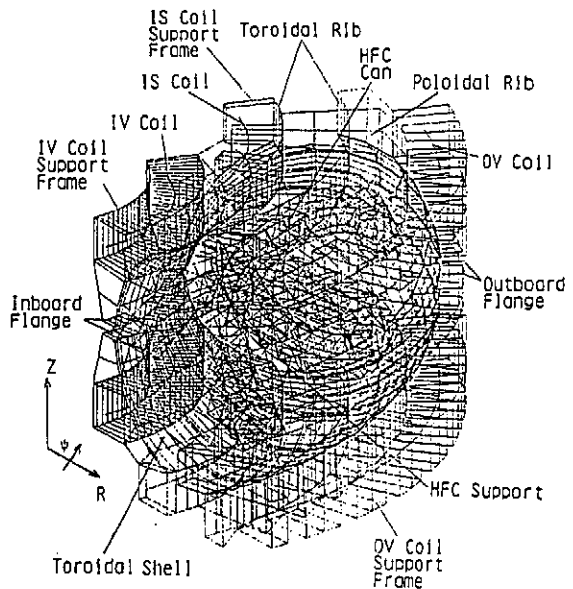


Fig. 2 FEM model on a whole helical device

Table 3 Summary of overall analysis results

		Load L1		Load L2	
		Displacement (mm)	Stress (MPa)	Displacement (mm)	Stress (MPa)
HFC	Conduits	1.34	110	-1.08	80
	Coil Case	1.29	123	-0.94	93
Toroidal Shell	Reinforcing ribs	0.99	88	-0.72	106
	Poloidal		55		44
Midplane joint bolts of flange	Inboard	---	35	---	-15
	Outboard	---	33	---	61
Toroidal joint bolts or flange		---	123	---	-9

VACUUM VESSEL DESIGN

The vacuum vessel has a complex and twisted configuration with a dumbbell-shaped cross section and is an all-welded structure made of Inconel 625, with 30 mm thick walls, mostly of sandwich construction with corrugated core. The high strength and high resistivity of the Inconel 625 material and the low cross sectional area of the corrugated wall allow the structure to be continuous without electrical break or bellows and achieve an acceptably high toroidal resistance ($\sim 0.5 \text{ m}\Omega$). To accommodate its numerous large port openings and still maintain structural strength, the corner sections of the dumbbell-shaped vessel are solid Inconel 625 with 30 mm thickness, as shown in Fig. 4. The corrugated walls consist of an inner skin (3.2 mm), outer skin (3.2 mm) and a corrugation (1.6 mm) and the passage of corrugation is used for cooling and heated gas path during operation and baking, respectively. The vessel is supported with 20 tranion supports at inboard and outboard sides on the machine midplane.

The FEM model of the vessel and the typical results are shown in Fig. 5 and Fig. 6, respectively.

Figure 6 shows the Von Mises stress distribution along the vessel perimeter in the poloidal cross section in the case of load combination of internal atmospheric pressure of 1 atm and dead weight including weight of first wall. Maximum stress is induced on inner surface at outboard corner and is estimated to be 70 MPa with maximum vertical displacement of $\sim 4 \text{ mm}$.

DIVERTOR AND FIRST WALL DESIGN

The divertor consists of an armor block with 8 mm thick graphite armor metallurgically joined to 8 mm thick OFCu (or M_0) plate and an OFCu base plate with cooling tube. The armor block is mechanically attached to the cooling base plate by bolts. The cooling base plate is bolted to vacuum vessel inner surface through thermal insulation.

The first wall also has almost the same structure as the divertor except the thickness of graphite armor (6 mm). Coolant for the first wall is considered to be N_2 or CO_2 gas because of low heat flux of $0.1 \text{ kW/cm}^2 - 10 \text{ sec}$. For the divertor, water has been used as coolant because of its relatively high heat flux of $0.5 \text{ kW/cm}^2 - 10 \text{ sec}$.

Figure 7 shows temperature time variation of typical component points on the divertor. The temperatures on the divertor saturate

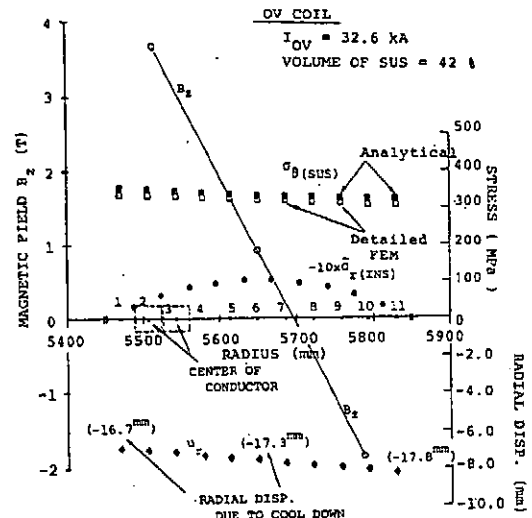


Fig. 3 Hoop Stress and Radial Displacement on OV Coil

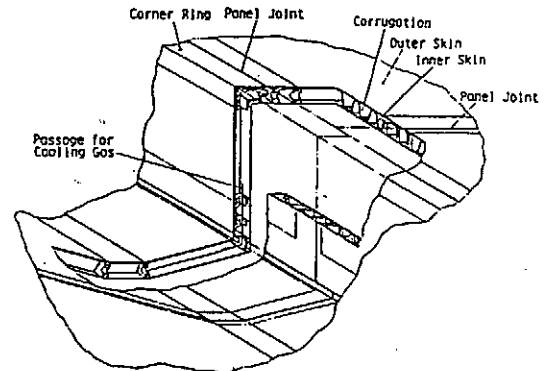


Fig. 4 Concept of Vacuum Vessel Structure

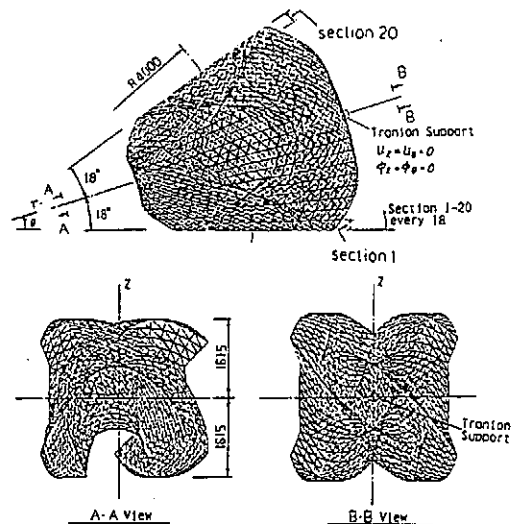


Fig. 5 Stress Analysis Model of Vacuum Vessel

within 2 or 3 operating cycles resulting in a maximum surface temperature of 1260°C , which is sufficiently below a sublimation temperature of the graphite.

The analytical result indicates that when the thermal conductance between the armor block and the base plate is greater than $0.1 \text{ W/cm}^2\text{C}$, the divertor is well cooled down to the initial temperature. However, since the temperature between graphite and molybdenum substrate exceeds 900°C , direct brazing method by precipitation of M_2O_3 will be required.

CONCLUSION

The structural design and analyses of the LHD has been performed. From the design work, following proposals have been made: (1) cable-in-conduit type forced flow superconductor for both HF and PF coils, (2) toroidal shell for support structure of the coils and (3) corrugated vacuum vessel with high temperature difference between inner and outer skins.

Analytical results show that both displacements and stresses on the structure components are successfully below the allowable values and our design concept is confirmed to have enough structural integrity.

REFERENCES

- [1] S. Ioka et al., "Forced-Flow Design for SC Magnets on the Large Helical Device", US/Japan Workshop on High Accuracy Large Superconducting Magnet for Helical Devices, Jan. 12 -13, 1988 at MIT
- [2] O. Motojima et al., "ENGINEERING DESIGN STUDY OF THE LARGE SUPERCONDUCTING HELICAL DEVICE", Proceedings of 15th SOFT, Sep. 1988 (P402)
- [3] K. Kitamura et al., "STRUCTURAL ANALYSIS OF FORCED-COOLED SUPERCONDUCTING HELICAL COIL FOR LARGE HELICAL DEVICE", to be published in 11th International Conference on Magnet Technology, Aug. 28 - Sep. 1, 1989

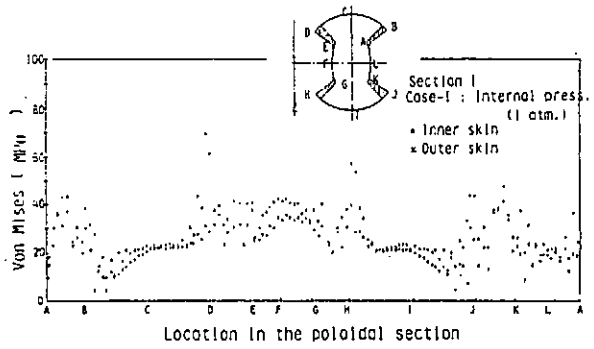


Fig. 6 Von Mises Stress Distribution on Vacuum Vessel

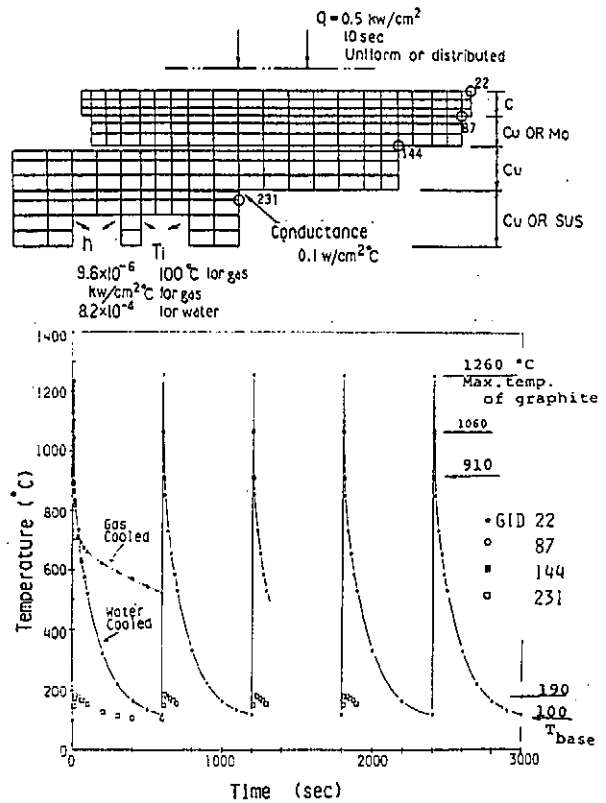


Fig. 7 Thermal Analytical Model and Temperature Time Variation on Divertor Plate

R&Ds OF FORCED FLOW SUPERCONDUCTING COILS FOR LARGE HELICAL DEVICE

S. Tsuruga, K. Yamamoto, K. Nakamoto, S. Mizumaki, H. Takano,
M. Shibui, K. Kitamura, T. Uchida, Y. Wachi, and S. Ioka
Toshiba Corporation, Suehiro-cho,
Tsurumi-ku, Yokohama, 230 Japan

O. Motojima, J. Yamamoto, T. Mito, and K. Takahata
National Institute For Fusion Science,
Furo-cho, Chikusa-ku, Nagoya, 464 Japan

ABSTRACT

A forced flow superconducting coil has been proposed for application to coils of the Large Helical Device (LHD). Main objectives of R&Ds are to study characteristics of a forced flow superconducting coil and to examine fabricability of large helical coil for the LHD. A R&D facility consists of a cryostat with 30 kA power leads and two types of R&D coils. Cable-in-conduit type superconductors using NbTi/Cu are adopted for the coils. A computer controlled winding machine has been developed in order to fabricate the TOKI-TF (helical coil). The design features of the R&D facility are presented.

INTRODUCTION

The Large Helical Device (LHD) is a large scaled heliotron/torsatron-type fusion experimental machine with all superconducting coils, and is now planning as a main experimental apparatus of National Institute for Fusion Science [1]. Major parameters of the current design are given in Table 1. A forced flow superconducting coil has been proposed for application to helical field coils and poloidal field coils of the LHD [2].

Main objectives of R&Ds are to study characteristics of forced-cooled superconducting coil and to examine fabricability of large helical coil for the LHD using forced-cooled superconductors. The R&D facility consists of a cryostat with 30 kA power leads and two types of R&D coils, TOKI-TF and TOKI-PF. The TOKI-TF is the 1/4 scaled model coil of the helical field

coil with a field period, $l/m=1/4$. The TOKI-PF is the model coil of the poloidal field coil. Cable-in-conduit type superconductors using NbTi/Cu are adopted for the coils. This facility is now under construction and will be completed in March next year. This paper describes the design and fabrication features of the R&D facility, the TOKI-TF and the TOKI-PF.

Table 1 Major parameters of LHD

Major Radius	4 m
Average Plasma Minor Radius	0.6 m
Minor Radius of Helical Coil	0.96 m
Magnetic Field Strength	4 T at Plasma Center 8.4 T at Coil
Helical Field Period [l/m]	2/10
Magnetic Field Accuracy	5×10^{-4}
Magnetic Energy	2 GJ
Heating Power	20 MW

COIL DESIGN

Elevation view of the R&D facility is shown in Fig. 1. The

cryostat is composed of the vacuum vessel, LN₂ shield, 30 kA power leads, SHE (supercritical helium) heat exchanger, etc. The vacuum vessel has a diameter of 2.8 m, height of 6.0 m and weight of 15 tons, and is evacuated with the turbo molecular pumping system. The vacuum vessel is divided into two parts for easy exchange of the R&D coil. The R&D coil is set in the lower part of the vacuum vessel. The power leads, SHE heat exchanger, and valves for SHE are set in the upper part of the vacuum vessel. A gas-cooled current lead is adopted, and its heat load at the cold terminal is less than 40 W at 30 kA.

The TOKI-TF consists of the coil winding and a 316 coil case to suppress the conductor deformation. The conductor has a rectangular cross section of 11x11 mm² and consists of 1.0 mm thick 316L conduit, 1.0 mm insulation and NbTi/Cu strands of 0.428 mm diameter. The void fraction is designed to be 40 %. The cables wound in a 3 x2x6 configuration. Major parameters of the TOKI-TF and its conductor specifications are shown in Table 2 and Table 3, respectively. Operating current is 8.0 kA, magnetomotive force is 800 kAT, and central magnetic field is 0.78 T at R=0.9 m. Electromagnetic forces are supported with the coil case and toroidal beams joining the coil case in toroidal direction. Support structures are examined using 3D FEM. The maximum deformation of the coil is calculated to be less than 0.3 mm.

Number of cooling paths is 10, and design mass flow rate is 1 g/s for each path. Electrically all conductors are connected in series by means of 9 joints. The average length of a turn is 8.453 m. The coil winding contains 837 m of

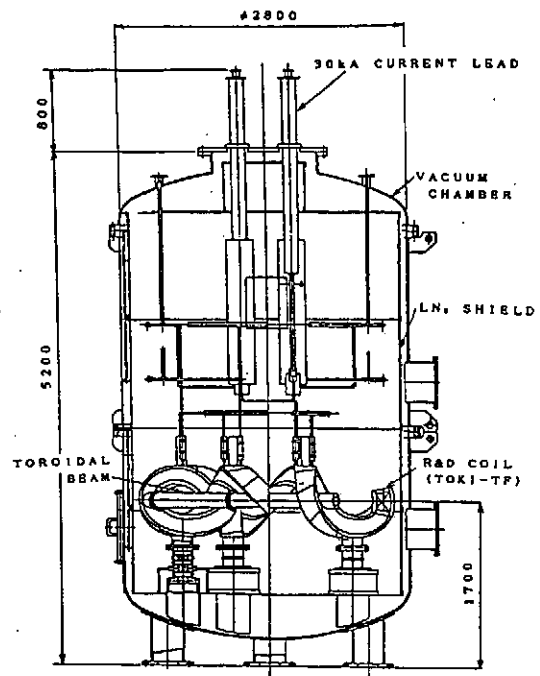


Fig. 1 Elevation view of the R&D coil

Table 2 Major parameters of TOKI-TF and TOKI-PF

Parameter	Unit	TOKI-TF	TOKI-PF
Major radius	mm	900	-
Minor radius	mm	250	-
Inner radius	mm	-	600
Outer radius	mm	-	820
Field periods: n		4	-
Multipolarity: l		1	-
Operating current	kA	8.0	25
Average current density	A/mm ²	41.1	41.3
Max. field	T	2.77	2.76
Inductance	mH	41.1	3.35
Stored energy	HJ	1.34	1.05

Table 3 Major parameters of superconductors

Parameter	Unit	TOKI-TF	TOKI-PF
Type of conductor		Cable-in-conduit, Forced-flow	
Material		NbTi	NbTi
Critical current	kA	16 at 4T	50 at 7T
Conduit dimension	mm ²	11x11	17x22.5
thickness	mm	1.0	1.0
Void fraction		0.4	0.4
Strand diameter	mm	0.428	0.67
Number of strands		324	480
NbTi:Cu:Cu-Ni ratio		1:4.8	1:1.6:0.5
Stability margin	nJ/cc	699	449

conductor. The exterior surface of conductor is completely insulated by a layer of half-lapped Glass-Kapton-Glass tapes, which allows a dump voltage of 1 kV.

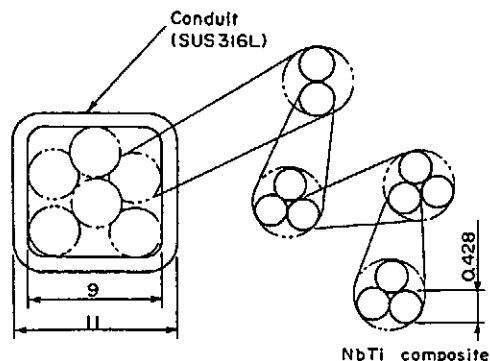
The TOKI-PF also uses cable-in-conduit type conductors consisting of 486 NbTi/Cu/CuNi strands and 1.0 mm thick 316L conduit, and having a rectangular cross section of 17×22.5 mm². AC losses are estimated in the condition that field changing rate is assumed to be 0.5 T/s in according to the current LHD coil design parameters. The TOKI-PF coil winding is not encased in the coil case. Therefore a detailed stress analysis of conduits has been performed to investigate the load transmission between conductors and detailed stress distribution of conduit and insulation under hoop force and assumed quench internal pressure of 30 atms. A maximum stress is estimated to be 400 MPa, and this value is nearly equal to that induced in the conduit of the poloidal field coil of LHD [3]. Major parameters of the TOKI-PF and its conductor specifications are shown in Table 2 and Table 3, respectively.

Cable layouts of the TOKI-TF and TOKI-PF are shown in fig.2 along with conductor dimensions.

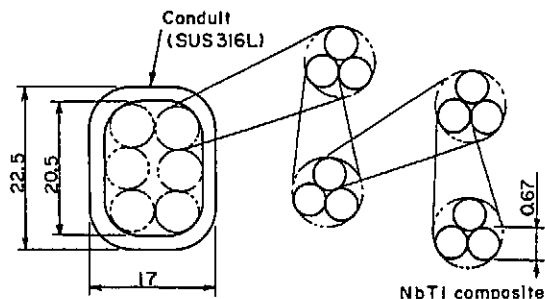
COIL WINDING

The helical machine is also developed with special attention to the winding accuracy. Unlike a ring coil, the geodesic line and the twisting angle of the conductor of the helical coil depend on spacial point along the helical axis. Thus the roller bending method with twisting capability is employed in the winding machine shown in Fig.3.

The winding machine consists of: (1) a conductor supply drum with a supply capacity of one



(a) TOKI-TF



(b) TOKI-PF

Fig.2 Cable layouts of the superconductor

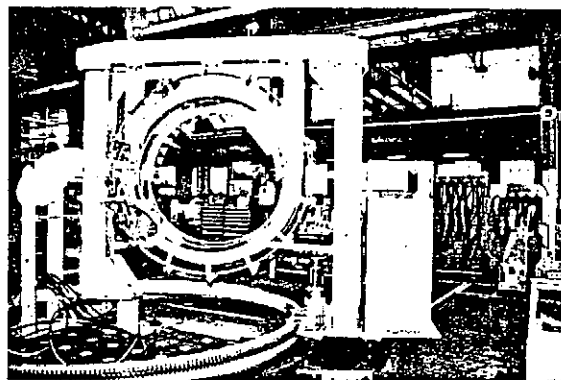


Fig.3 Winding machine

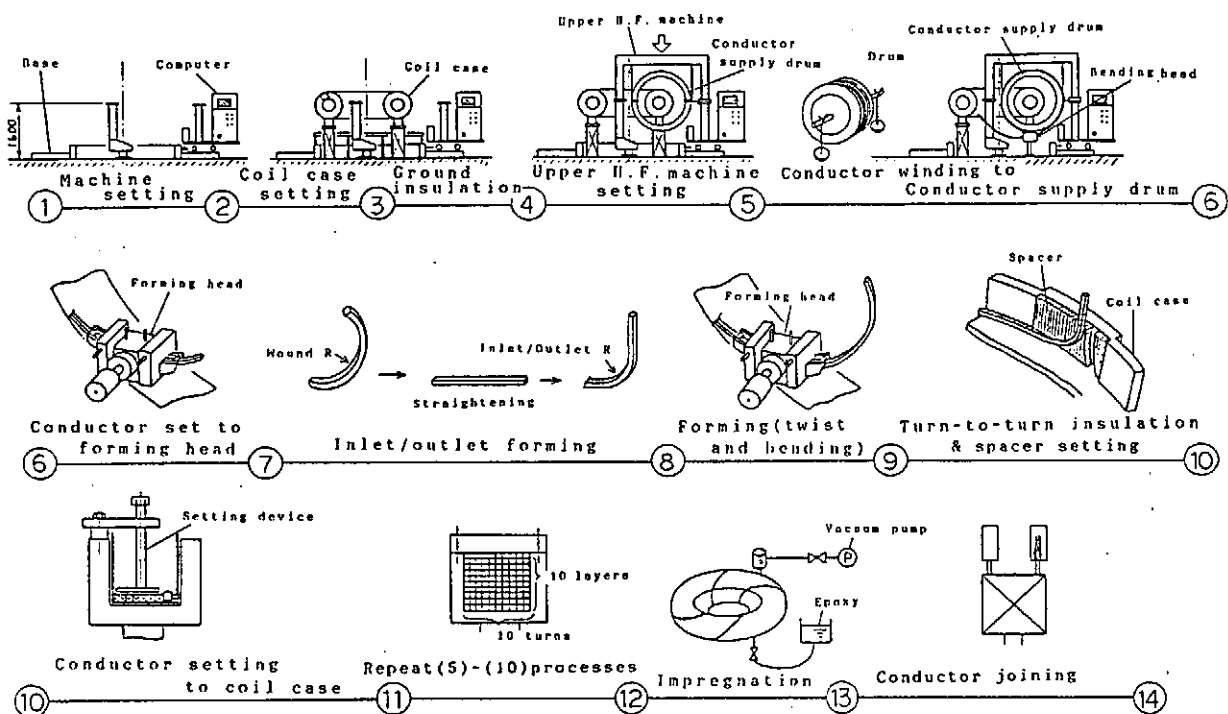


Fig.4 Winding procedure

layer conductor length, (2) forming head to draw out and form the conductor, (3) toroidal rotation device to give winding motion in toroidal direction, (4) poloidal rotation device to make winding motion in poloidal direction and (5) a computer system to control spacial and angular parameters required for helical winding.

The winding procedure is shown in Fig.4.

REFERENCES

- [1] O. Motojima et al., "Large Helical Device Status", US/Japan Workshop on High Accuracy Large Superconducting Magnet for Helical Devices, Jan. 12-13, 1988 at MIT.
- [2] S. Ioka et al., "Forced-flow Design for SC Magnets on the Large Helical Device", US/Japan Workshop on High Accuracy Large Superconducting Magnet for Helical Devices, Jan. 12-13, 1988 at MIT.
- [3] K. Kitamura et al., "Structural Design of Large Helical Device", presented in this conference.

POOL-COOLED SUPERCONDUCTING MAGNET DESIGN OF LARGE HELICAL DEVICE

S. Suzuki, H. Miyazawa, R. Saito, Hitachi Works, Hitachi, Ltd.
1-1, Saiwaicho 3-chome, Hitachi-shi, Ibaraki-ken, 317 JAPAN

F. Iida

Hitachi Research Laboratory, Hitachi, Ltd.

5-2-1 Omikacho, Hitachi-shi, Ibaraki-ken, 319-12 JAPAN

H. Ogata

Mechanical Engineering Research Laboratory, Hitachi, Ltd.

502 Kandatucho, Tsuchiura-shi, Ibaraki-ken, 300 JAPAN

Y. Yamazaki, O. Motojima, J. Yamamoto, M. Fujiwara

National Institute for Fusion Science

Furocho, Chikusa-ku, Nagoya, 464-01 JAPAN

M. Takeo

Kyushu University

Hakozaki, Fukuoka, 812 JAPAN

ABSTRACT

The Large Helical Device is a next generation helical equipment for nuclear fusion. The large scale superconducting magnets are going to be applied for these coils. The major and minor radius of helical coil system are 4 m and 0.96 m respectively and the magnetic field is 4T at plasma center and 8T at the coil surface. The coil system stores about 2GJ of total energy. Superconductor of helical coil is pure aluminum stabilized Nb-Ti compacted strand cable with copper housing. The coils have the helium can made of stainless-steel and this can is filled by liquid helium. This pool-cooled superconducting helical coil system satisfies the fully stabilized condition.

The superconducting poloidal coils are composed of six (three pairs) circular coils and use forced-cooled superconductor to reduce the eddy current losses by the field changing operation.

The helical and poloidal coil systems are built in the large bell-jar (Vacuum vessel for thermal insulation) with outer diameter of 13m.

This paper describes conductor design and stability of superconducting magnet for helical and poloidal coil systems.

INTRODUCTION

The Large Helical Device (LHD) Project is the major project of the National Institute for Fusion Science. LHD has large scale superconducting magnets such as the total stored energy of about 2GJ. The magnets are consist of helical coil and poloidal coils.

The superconducting helical coil is excited in steady state operation. In this design, we chose the pool-cooling concept for helical coil to keep the cryogenic stability. On the other hand, the superconducting poloidal coils varies their current to keep the equilibrium of plasma during plasma heating. We chose the forced-cooled magnet for poloidal coils to reduce the a.c. losses.

The major design parameters of LHD are shown in TABLE 1.

HELICAL COIL

The requirements of helical coil are (1) Long pulse operation, (2) High current density and (3) Flexible magnetic configuration for plasma confinement. From these requirements, the design concepts of helical coil are:

- (1) Superconductor is Nb-Ti ($B_{max} \leq 8T$: given value)
- (2) Fully stabilized magnet (Stored energy $\sim 2GJ$)
- (3) At site winding (Transportation limit)
- (4) Medium operating current ($I_d \sim 30kA$)

TABLE 1
MAJOR DESIGN PARAMETERS OF LHD

Item	Parameter
Major radius	4.0 m
Plasma minor radius	0.6 m
Helical coil system	
Helical field	4.0T at plasma axis
ℓ	2
m	10
Coil minor radius	0.96 m
Magneto-motive force	8MAT \times 2
Poloidal coil system	
Number of coils	6 blocks
Magneto-motive force	\sim 6MAT/each block
Core components	Vacuum vessel with divertor space Graphite first wall and divertor plate

- (5) Individual supports for coil and vacuum vessel. (Different temperature between coil and vessel)
- (6) Large vacuum tank (bell-jar) containing major components.
- Cross section of helical winding is shown in FIGURE 1 and design parameters of helical coil is shown in TABLE 2.

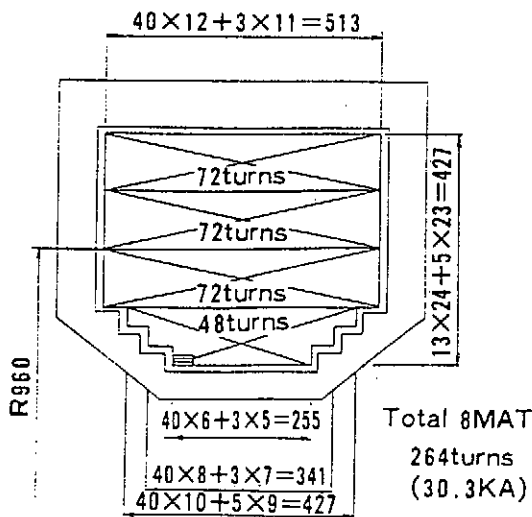


TABLE 2
DESIGN PARAMETERS OF HELICAL COIL

Item	Parameter
Major radius	4 m
Minor radius	0.96 m
Winding rule	$\ell=2$ m=10
Magnetomotive force	8 MAT / coil \times 2 coils
Operating current	30.3 kA
Number of turns	264 turns
Self inductance	4 H
Stored energy	1.84 GJ
Maximum field on winding	8 T
Size of winding	513 \times 427 mm
Average current density	39.1 A/mm ²
Number of units	4 units / coil

FIGURE 1 CROSS SECTION OF
HELICAL WINDING

Superconductor for helical coil is a Aluminum stabilized Nb-Ti fine-multi strand cable with Copper housing. Cross section of the superconductor is shown in FIGURE 2 and design parameters of the superconductor is shown in TABLE 3.

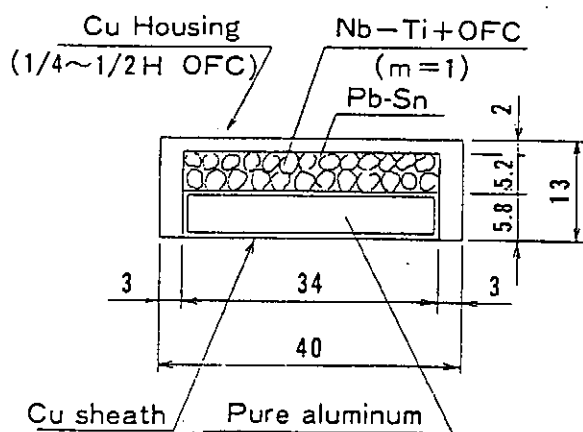


FIGURE 2 CROSS SECTION OF HELICAL COIL CONDUCTOR

TABLE 3 DESIGN PARAMETERS OF HELICAL COIL CONDUCTOR

Item	Parameter
Size of conductor	40 mm width 13 mm height
Area of conductor	520 mm ²
Area of Cu Housing	146 mm ²
Area of Pure Al	157.8 mm ²
Area of Cu sheath	39.4 mm ²
Area of strands	148.8 mm ²
Number of stands	26
Strand diameter	2.7 mm
Number of filaments	1750/st.
Filament diameter	0.046 mm
Maximum Field	8 T
Critical current	60480 A
Operation current	30300 A
Equal area Heat flux	0.3 W/cm ²
Conductor Perimeter	10.6 cm
Spacer area ratio	0.5
Stability parameter	0.97

In the helical coil, the angle of the heat conduction plane varies torsionally. The measured average equal area heat flux (q_e) of various plane angle is 0.3 W/cm². The rough surface was not adopted because of the damage in winding procedure. This conductor satisfies fully stabilized criteria at the current of 30.3 kA at the field of 8T and at the temperature of 4.2 K. The load line of helical coil conductor is shown in FIGURE 3 and result of stability simulation is shown in FIGURE 4.

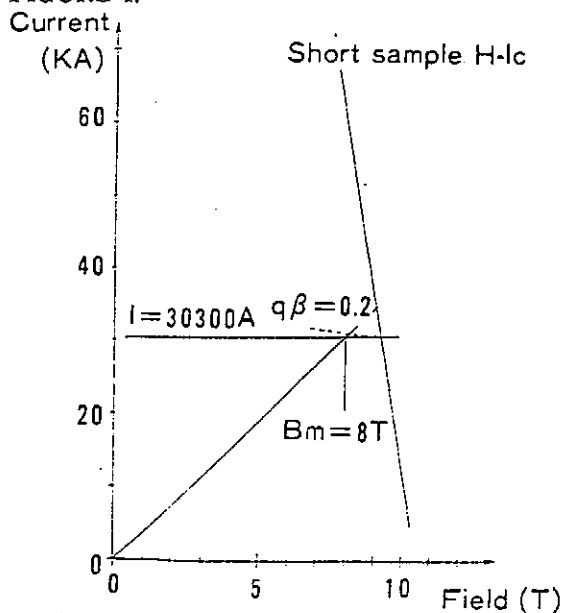


FIGURE 3 LOAD LINE OF HELICAL COIL CONDUCTOR

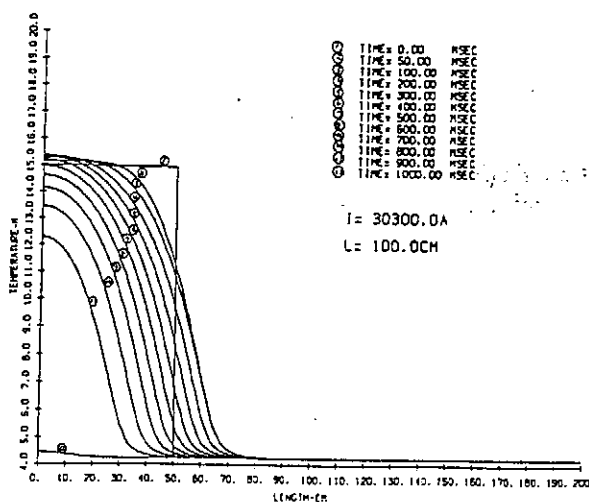


FIGURE 4 RESULT OF STABILITY SIMULATION

POLOIDAL COILS

In the LHD poloidal coils we introduced the forced-cooled superconducting magnet with bundle type cable-in-conduit superconductor. Poloidal coils are consist of outer vertical (OV) coils, inner shapin (IS) coils, and inner vertical (IV) coils. Each coils have two coil blocks coaxially located upper and lower. The arrangement of poloidal coils is shown in FIGURE 5. FIGURE 6 shows the cross section of poloidal coil conductor.

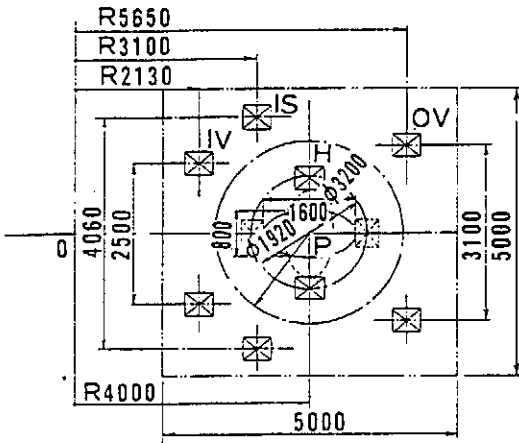


FIGURE 5 ARRANGEMENT OF POLOIDAL COILS

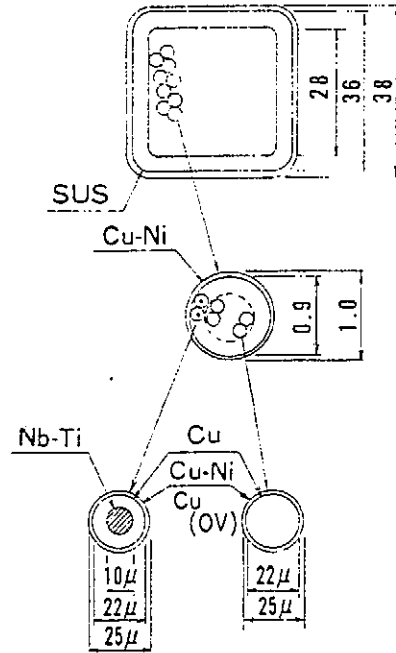


FIGURE 6 CROSS SECTION OF POLOIDAL COIL CONDUCTOR

CONCLUSIONS

Superconducting helical coil and poloidal coils are designed. The helical coil satisfied the fully stabilized condition. the poloidal coils have enough limiting current to operation.

REFERENCES

I. Motojima, O. Yamamoto, J. Yamazaki, K. Ohyabu, N. Mito, T. Fujiwara, M. Iiyoshi, A. Project of Large Helical Device for Currentless Steady Experiment, 11th international conference on magnet technology, 28 August-1 September, 1989.

Behavior of Vacuum Vessel Eddy Current in Large Helical Device

Hideshi FUKUMOTO, Shigeyoshi KINOSHITA, Michio OTSUKA,
Nobuyoshi OHYABU†, Nobuaki NODA†,
Kozo YAMZAKI†, Osamu MOTOJIMA†

Energy Research Laboratory, Hitachi, Ltd.,
1168 Moriyama-cho, Hitachi, Ibaraki 316, Japan

† National Institute for Fusion Science,
Nagoya 464-01, Japan

Abstract: Eddy current has been analysed on Large Helical Device to understand its flow pattern on the vacuum vessel with helical structure in the existence of helical field or poloidal field change. Magnetic field in plasma region and electromagnetic force which are induced by eddy current have also been evaluated.

1. Introduction

Eddy current has not been calculated in helical devices because there exist no major eddy current sources such as plasma disruption in tokamak. However, eddy current even under normal operation condition may disturb plasma equilibrium by creating undesired magnetic field. In devices with superconducting coils, current quench of the coils may induce large eddy current and so large electromagnetic force in structural materials. Eddy current analysis, therefore, has become important in design study of the next generation helical devices. In the present paper eddy current on vacuum vessel of LHD is analysed using shell approximation to show the characteristics of its distribution. The results of magnetic field and electromagnetic force evaluation are also shown.

2. Eddy current calculation

Eddy current has been calculated by a computer code 'ECTAS' which is based on finite element circuit method¹⁾ and is able to treat arbitrary shaped coils as eddy current sources. Two different vacuum vessel models are used for comparison. One is vacuum vessel with circular cross section and the other is that with helical structure which is shown in Fig.1. In both models vacuum vessel is represented by a conducting shell of finite elements. The effect of port structures on vacuum vessel is also evaluated using the latter model. Structures other than vacuum vessel have not been considered for simplicity.

External field conditions considered are helical coil current quench and poloidal coil current change (quadrupole field mode). In both cases external field is assumed to change linearly in time because of long time constant of superconducting coils.

3. Behavior of eddy current

Eddy current becomes to steady state after several times of vacuum vessel time constant because of the constant field change. Shown in Fig.2 are eddy current flow patterns for three cases in the steady state.

Eddy current by helical field change exhibits different flows depending on vessel shapes. On circular vacuum vessel eddy current has strong toroidal component which corresponds to the direction of electrical field generated by helical coil. It shows helical flow with the same pitch as helical coil on vacuum vessel with helical structure. This distribution is mainly determined by geometrical effect.

Eddy current by poloidal field change is dominated by toroidal component which reflects the direction of external electrical field. In the case of Fig.2 it can be explained by quadrupole toroidal flow with saddle-like flow in weak electrical field regions.

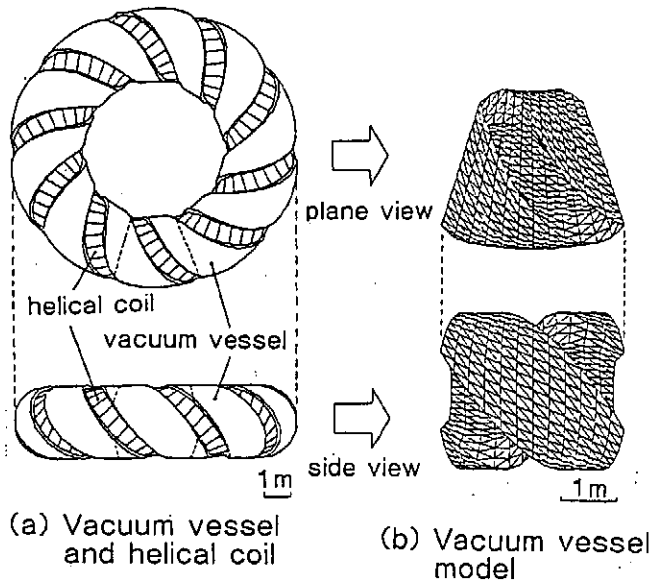


Fig.1 LHD and its vacuum vessel model

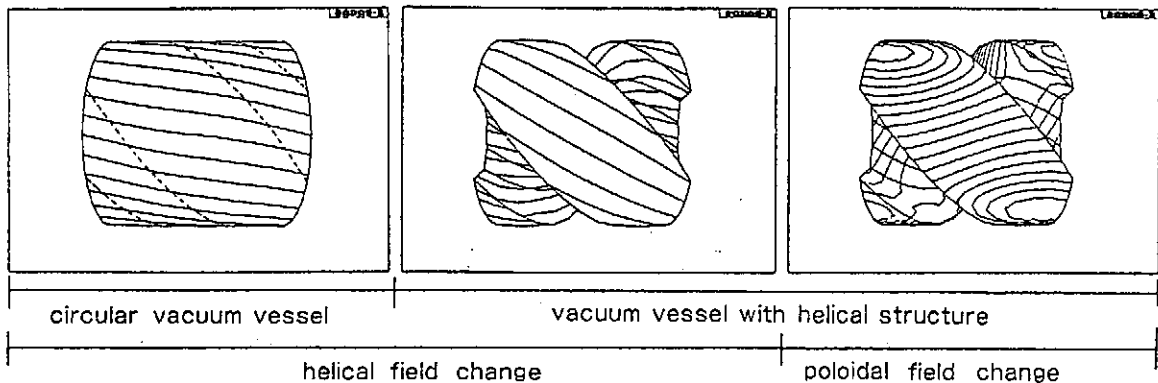


Fig.2 Eddy current distribution in steady state

4. Evaluation of magnetic field and electromagnetic force

Magnetic field by eddy current and the time constant of field penetration are calculated for quadrupole poloidal field change. Poloidal distribution of magnetic field for different toroidal angles is shown in Fig.3. In this calculation port structures are included in the vacuum vessel model. Magnetic field in plasma region shows little toroidal angle dependence in spite of the helical structure of the vacuum vessel. It has the characteristics of quadrupole field and the toroidal component is almost negligible. This fact means that the effect of poloidal eddy current due to helical structure is cancelled each other. Disturbance of magnetic field due to the existence of port structures is also very small (<10%). Typical value of magnetic field strength is about 4 gauss in the plasma peripheral. Estimated time constant of field penetration is about 50ms (SUS30mm²).

Electromagnetic force by eddy current and helical field is shown in Fig.4 for the case of helical coil current quench. Large force is generated along the helical structure. But the maximum pressure is about 1.4×10^4 Pa which is well below the atmospheric pressure.

5. Conclusion

Vacuum vessel eddy current on LHD has been calculated. The results are summarized as follows.

(1) Eddy current distribution due to helical coil current quench on circular vacuum vessel has large toroidal component which agrees with the direction of external electrical field, while that on vacuum vessel with helical structure is determined by geometrical effect. Electromagnetic force in this case is about 1.4×10^4 Pa at maximum.

(2) Eddy current distribution due to poloidal coil current change is dominated by toroidal component which reflects the direction of external electrical field. The resulted magnetic field in plasma region shows little toroidal angle dependence and has very small toroidal component. Magnetic field strength in the plasma peripheral is about 4 gauss.

References

1) Kameari, A., Transient Eddy Current Analysis on Thin Conductors with Arbitrary Connections and Shapes, J. Comput. Phys, 42, 124(1981)

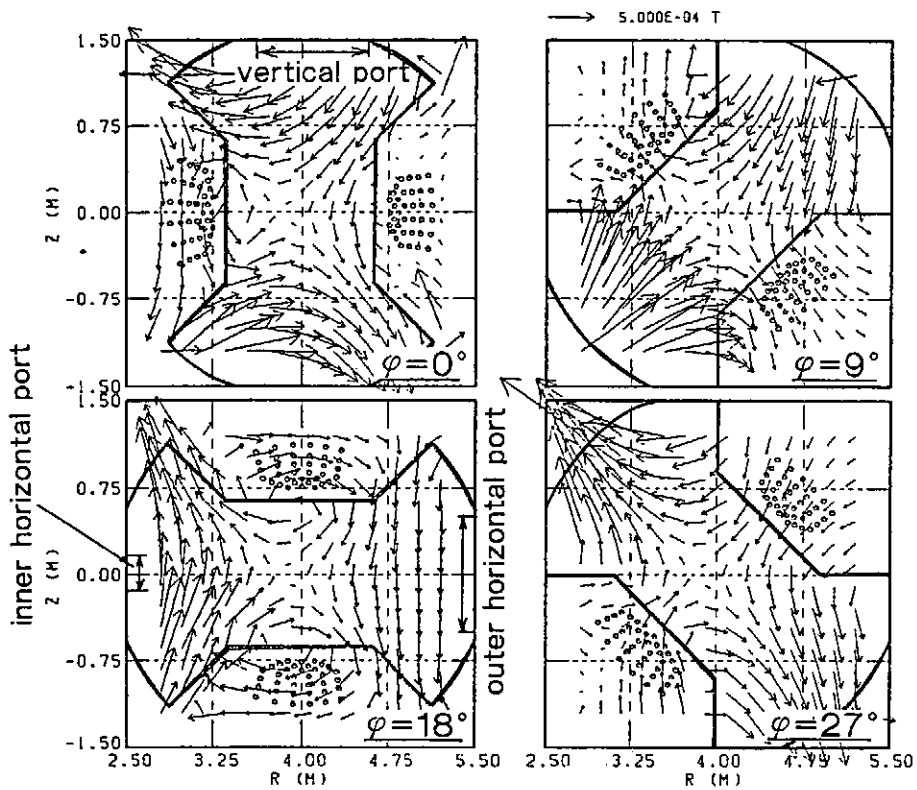


Fig.3 Magnetic field distribution induced by eddy current in poloidal coil current change

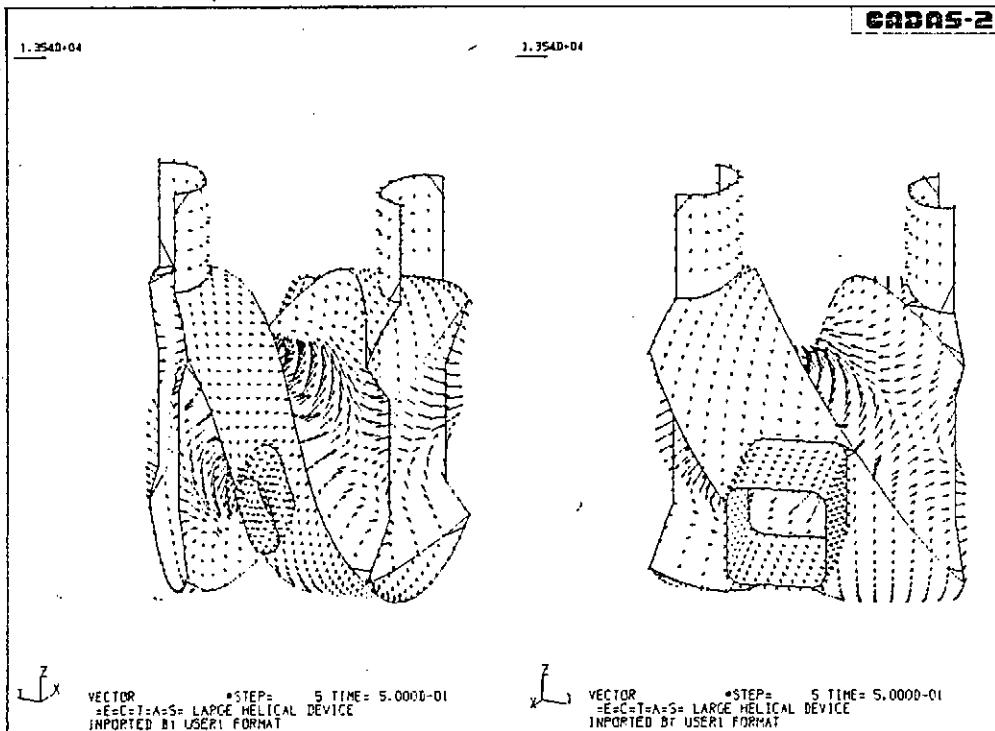


Fig.4 Electromagnetic force distribution in helical coil current quench

FUNDAMENTAL DESIGN ON LHD WITH BATH COOLING METHOD

S.Tado, K.Shimizu, B.Ikeda, A.Kameari, R.Saito,
M.Tomita, T.Tsukamoto
Mitsubishi Fusion Center, 2-2-3 Marunouchi Chiyoda-ku
Tokyo, 100, Japan

K.Kuno, K.Toyota, T.Satow
Mitsubishi Electric Corporation Kobe Works,
Wadasaki-cho, Kobe, 652, Japan

O.Motojima, J.Yamamoto, K.Yamazaki, T.Mito, N.Oyabu, N.Noda
National Institute for Fusion Science,
Furo-cho, Chikusa-ku, Nagoya, 464, Japan

1. Introduction

The Large Helical Device (LHD) is a fusion experimental device of heliotron type. It has been designed by the design team organized of the members of National Institute for Fusion Science and the others. LHD has a major radius of 4m and a minor radius of 0.96m. The design specifications of LHD are shown in Table 1.

Major components of LHD include the helical coils, the poloidal coils, the vacuum vessel, and the structural support system. All the coils (two helical coils and three pairs of poloidal coils) are superconducting coils. These components must be feasibly designed in consideration of the requirements of plasma physics and manufacturing. The superconducting coils and their supporting structure must be set up with high accuracy and have high stiffness against the large electromagnetic load in order to suppress the error field which disturbs the magnetic field configuration. Then, it is important to estimate the deformation of the coils, especially the helical coils, which is caused by the electromagnetic load. On the other hand, the vacuum vessel is constructed of shell and has a complicated shape. Besides atmospheric pressure and electromagnetic load caused by eddy current, the vacuum vessel receives a severe thermal load during long pulse operations. Then, it is necessary to estimate the mechanical strength of the vacuum vessel against these loads.

This paper mainly describes the results of the structural analyses which have been made on the coil supporting structure and the vacuum vessel as a preliminary design study of LHD.

2. Electromagnetic Analysis

The typical operation scenarios of LHD are as follows ; (1) Mode #1 Long Pulse, (2) Mode #2 Displacement of Magnetic Axis and High β , (3) Mode #3 Displacement of Plasma Cross Section, (4) Mode #4 Current Drive. In addition to these modes, the independent excitation of the helical coils is included as Mode #5. Figure 1 shows the distributions of the electromagnetic force along the winding of the helical coil for Mode #3 and Mode #5. The maximum electromagnetic force is ~1000 ton/m. The maximum intensity of the magnetic field, which the helical coil winding experiences, is about 8.4 T.

3. Helical Coil and Coil Supporting Structure

3.1 Conductor and Coil Configuration

Figure 2 shows the configuration of the conductor and the cross section of the helical coil.

3.2 Concept of the Coil Supporting Structure

Figure 3 shows the supporting structure of the coil system. The supporting structure is constructed of four supporting rings, poloidal coil supporting structure and reinforcing ribs. The helical coils are supported by these four rings through highly rigid supports. The supporting rings and the poloidal coil supporting structure form a closed ring in the toroidal direction. The reinforcing ribs are set up at 18° intervals along the toroidal direction. The material of the supporting structures is austenitic stainless steel.

3.3 Structural Analysis of the Coil Supporting Structure

The structural analysis has been made by using NASTRAN. The modeling is made for the 72° sector. The model is shown in Fig. 4. The calculations have been made for typical two electromagnetic loading (Mode #3 and Mode #5).

Figure 5 shows the deformation and the stress distribution of the coil supporting structure in Mode #3. The maximum values of the displacements are $\delta_r = 0.72\text{mm}$, $\delta_\phi = 0.27\text{mm}$, $\delta_z = 1.72\text{mm}$. In view of the requirements from the magnetic field configuration, it must be judged whether these values of the displacements are acceptable or not. The maximum stress value (von Mises stress) is 176MPa. High stresses are set up in the inner supporting ring but they are lower than the allowable stress. Then, it can be considered that there are no problems in regard to the stresses set up in the members of the supporting structure.

4. Vacuum Vessel

The vacuum vessel has a dumbbell-shaped cross section as shown in Fig.6, where each part has been named A (arc), B (straight) and C (arc) on the cross section.

We have supposed basic concepts for the vessel structure as follows ;

(1) the vessel is composed of thick shell structures, (2) supporting structures are arranged at the lower part every 72 degrees, (3) cooling channels are mounted only outside of the part-A and (4) for baking the vessel up to 120°C, high temperature and pressurized water and/or electric heater are used, and so on.

In this section, we have studied feasibility of the vessel structure using a simple model against atmospheric and heat loads.

4.1 Atmospheric Loads

We have parametrically studied on thickness of the vessel using an axisymmetric model as shown in Fig.7. Obtained Results are as follows ; (1) CASE #1 (A,B,C :15mm thick) ; the maximum stress 244MPa (2) CASE #2 (A,C : 15mm thick B : 30mm thick) the maximum stress 200MPa (3) CASE #3 (A : 15mm thick B,C : 30mm thick) the maximum stress 112MPa (deformation and stress distribution are shown in Fig.7.)

4.2 Heat Loads

Thermal and stress analysis have been performed using a partial model as shown in Fig.8 on the following assumptions ; (1) thickness of wall is 15mm. (2) heat load of 0.2MW/m² during operation of 10 seconds (3) water cooling (1m/sec, 0.1MPa, 30°C).

Typical results are shown in Figs.8 and 9. The maximum temperature difference between inner and outer surface is about 90°C at time = 10sec, and at that time, the maximum stress intensity is 195MPa.

We will proceed to the investigations on the vacuum vessel with the detailed model including the various ports, and the analyses on buckling, earthquake shocks and electromagnetic loads induced at the helical coil

current quench and plasma current quench will be performed.

5. Conclusion

We have had some prospect of the engineering feasibility of LHD by the design study of the coil system and the vacuum vessel. However, at the same time, it has been clarified that there are some engineering problems to be solved and investigated in the LHD design study. Then, we will proceed to the detailed design of the components and the total system in the next stage of the LHD design.

Table 1 Device Parameters of the LHD

(Helical Coil)		(Vacuum Vessel)	
Major Radius (R_C)	4 m	Major Radius (R_V)	4 m
Major Radius (a_C)	0.96 m	Outer Radius	1.6 m
Magnetic Field (plasma center)	4 T	Inner Radius	0.625 m
(maximum)	-8	Shape of Cross Section	Dumbbell
Coil Current	8 MAT/coil	One Turn Resistance	>0.1 m Ω
Current Density	-40 A/mm ²	Baking Temp.	
Stored Energy	-2 GJ	Vacuum Vessel	100 °C
Toroidal Field Period	10	First Wall	300 °C
Cooling Method	Bath Cooling	Heat Load	0.2 MW/m ²
Winding Section	429 mm x 514 mm		

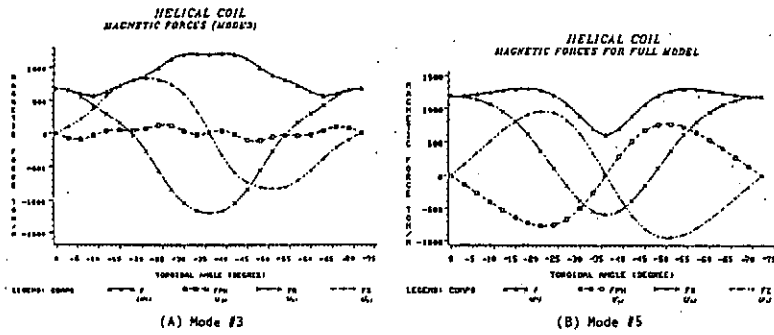


Fig.1 Distribution of Electromagnetic Force

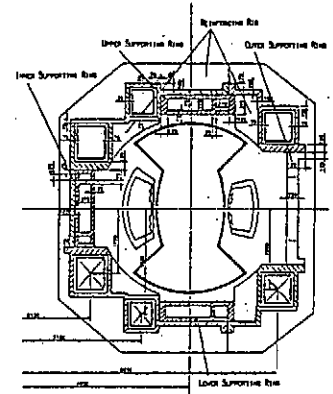


Fig.3 Supporting Structure of Coil System

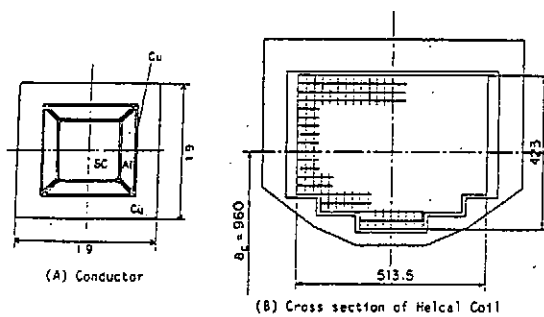


Fig.2 Configuration of Conductor and Helical Coil

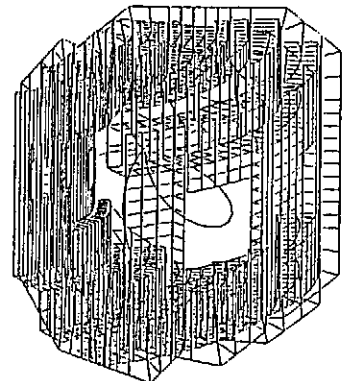
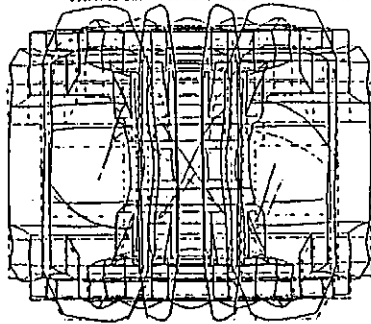


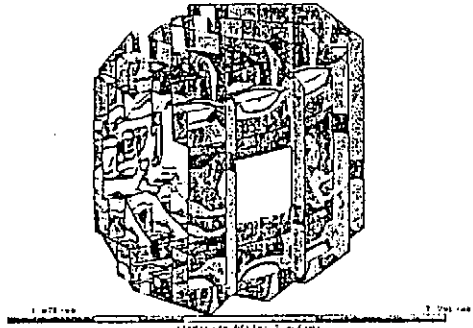
Fig.4 Model for Structural Analysis

273 LOWE MEDICAL SYSTEM -- M1173 -- 001
DISPLACEMENT - AND SHELL E.O.C. OF PWA 2.201-00



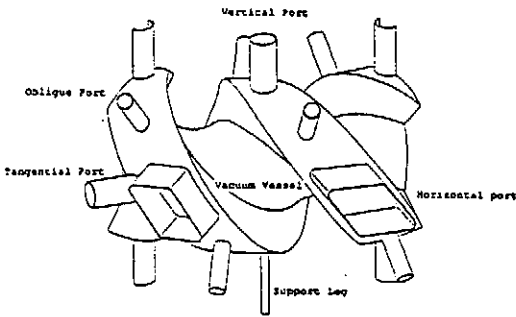
(A) Deformation

DISPLACEMENT - AND SHELL E.O.C. OF PWA 2.201-00 SHELL STRESS

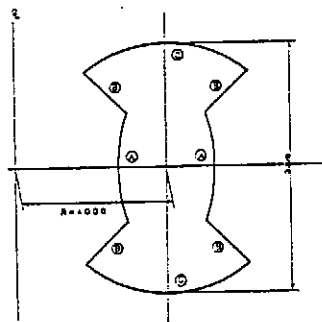


(B) von Mises Stress

Fig.5 Deformation and Stress Contour of Supporting Structure (Mode #3)



(a) Outer View of Vacuum Vessel



(b) Polaroid Cross Section of Vacuum Vessel

Fig.6 Schematic Structure of Vacuum Vessel

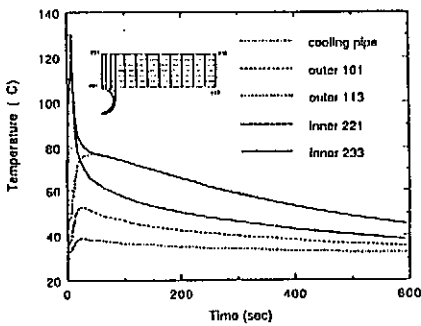


Fig.8 Time Evolution of Temperature

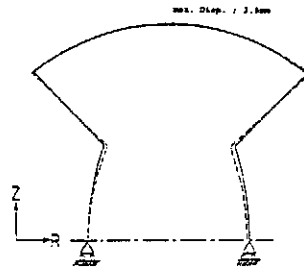
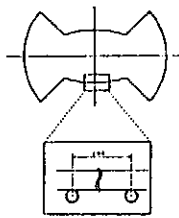


Fig.7 (a) Deformation

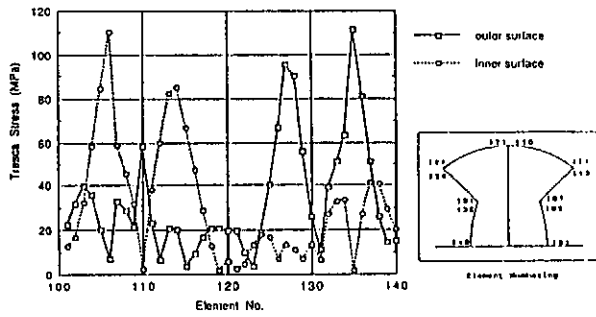


Fig.7 (b) Distribution of Tresca Stress

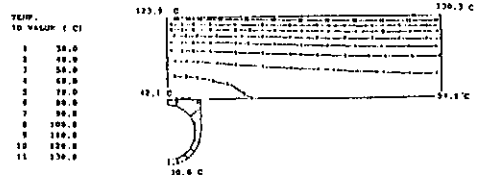


Fig.9 (a) Temperature Distribution at time = 10sec.

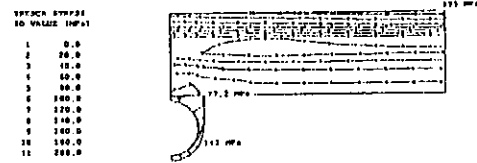


Fig.9 (b) Stress Distribution (Tresca Stress) at time = 10sec.

A COMPACT HELICAL DEVICE FOR A SUPERCONDUCTING LARGE HELICAL COIL

Y. Tsuda¹⁾, K. Toyoda¹⁾, T. Hirayama¹⁾, S. Kida¹⁾, K. Kuno¹⁾
T. Mito^{2), 4)}, J. Yamamoto⁴⁾, K. Takahata⁴⁾, M. Takeo³⁾,
I. Ohtake⁴⁾, Y. Takeiri⁴⁾, O. Motojima⁴⁾, A. Iiyosi⁴⁾

- 1) MITSUBISHI ELECTRIC CORPORATION KOBE WORKS , Hyogo, Kobe, 652, Japan
- 2) PLASMA PHYSICS LABORATORY, KYOTO UNIVERSITY , Uji, Kyoto, 611, Japan
- 3) KYUSYU UNIVERSITY , Fukuoka, 812, Japan
- 4) NATIONAL INSTITUTE FOR FUSION SCIENCE, Chikusa, Nagoya, 464-01, Japan

ABSTRACT

We constructed the first superconducting helical coil. The fabricated coil has the major radius of 300 mm, the minor radius of 62.7 mm. In order to simulate the construction technique of Large Helical Coil, the small-scale coil was wound with the computer controlled winding machine which was developed for the automatic helical winding. We gained useful technical data about the fabrication of a superconducting helical coil and confirmed a feasibility of fabricating Large Helical Coil.

INTRODUCTION

A necessity of continuous winding method of superconducting wires or cables had been pointed out in feasibility study for Large Helical Coil, which is planned to be constructed as a main experimental apparatus of National Institute for Fusion Science. In order to demonstrate the superconducting helical coil to be essentially feasible, in both of fabrication and stability of performance, we developed a continuous helical winding method and constructed a compact helical device (KYOTO-SC), as the first step of following R&D programs of Large Helical Coil.

DESIGN

SUPERCONDUCTING WIRE

A Cu/NbTi rectangular monolithic wire was used. Its cross sectional dimension was $1.6 \times 3.2 \text{ mm}^2$, Cu ratio to NbTi was 4, critical current was 2710 A at 4.2 K @ 3T, and coated with PVF (polyvinyl formal) as turn to turn insulation.

COIL CONFIGURATION

The superconducting helical coil is shown in Photo.1 , and main parameters of the coil are summarized in Table.1 . The definition of the coordinate system (ψ , θ , r) in this helical coil is shown in Fig.1 .

The coil was wound along a geodesic line , which is a shortest line on the doughnut shape mandrel . This shape allows for tension winding (the preferable method of fabrication) and the winding is stable . The superconducting wire locus of the geodesic method is approximated by the following modified winding equation .

$$\psi = (1/\kappa) \cdot (\theta - \alpha \cdot \sin \theta) \quad (1)$$

ψ , θ : toroidal, and poloidal angle [radian]
 α : coefficient of modification (= 0.4795)
 κ : number of the pitch (=8)

Equation (1) express a line ,but real coil has a volume . Therefore we calculate the coordinates of the coil surface by applying the equation (1) to a center line of the coil, and shifting points by half coil width .The coordinates are expressed by (X_a, Y_a, Z_a), as the following equations.

$$X_a = (R+r \cdot \cos \theta) \cdot \cos \psi - d \cdot \cos \beta \cdot \sin \theta \cdot \cos \psi + d \cdot \sin \beta \cdot \sin \psi \quad (2)$$

$$Y_a = (R+r \cdot \cos \theta) \cdot \sin \psi - d \cdot \cos \beta \cdot \sin \theta \cdot \sin \psi + d \cdot \sin \beta \cdot \cos \psi \quad (3)$$

$$Z_a = r \cdot \sin \theta - d \cdot \cos \beta \cdot \cos \theta \quad (4)$$

where $\beta = \tan^{-1} \{ r \cdot \kappa / (R+r \cdot \cos \theta) \cdot (1 - \alpha \cdot \cos \theta) \}$,

$R = 300$ mm , $2 \cdot d$: the coil width

SECTIONAL STRUCTURE

The two identical coils are on the ground insulated mandrel, separated by a half pitch along the torus center line . Support blocks were fixed on the mandrel between the two coils. These prevent the winding from getting out of shape , from winding process through the cool-down and excitation . The support blocks had to have smooth curved surfaces, which were numerical control machined.

The cooling channel between layers consists of G10 spacers, which were 0.45 mm thick , 5mm wide ,and arranged with 10 mmpitch along the winding . Each turn, layer, and cooling spacer are adhered to others with pre-preg epoxy. One layer of $\phi 1.6$ mm stainless steel wire was wound over the spacers (G10, 3mm thickness) on the outermost layers of the winding.

WINDING PROCESS

WINDING MACHINE

The continuous helical winding machine was developed for KYOTO-SC .

The configuration is shown in Fig.2 . The winding head consists of ① a wire supply drum , ② a tension brakedrum , ③ a twist and positioning head .

Especially, the tension brake drum is designed not to lose its winding tension, in the case of temporary stop or reverse drive. One of the four posts falls down automatically , when the poloidal rotation table passes ,while the other three support the mandrel .

WINDING METHOD

In order to wind the rectangular superconducting wire helically, it is required to twist the wire continuously. At first trial, the wire often induced some under-twists especially at the inner region of torus, in where the largest twist was required, and hence it is difficult to line up the wire. This is explained by the position of the winding head which was always located forward of the point of contact of the winding^[1]; more over the rocking motion of the winding head which was resisted by a spring but not controlled. This problem will be solved by controlling of the winding head to change its twist angle corresponding to its position, but this positive angular change has not been adopted this time.

In the result we succeed to complete the continuous helical winding with a teaching method. The epoxy-fiber glass mixture was beforehand molded on the side surfaces of support blocks. Coil-shape gauges which had been machined by means of numerical control, and the support blocks with the mixture were assembled on the mandrel, and then cured together.

We practiced the teaching at the first turn of every layer with manual control. This process was carried out by winding the wire along side surfaces of the support blocks. Therefore the final shape of the winding was formed by the shape of cured mixture on the side surfaces of support blocks.

CONCLUSION

We succeeded to construct the first superconducting helical coil, using the continuous helical winding machine, which was specially designed and developed for this time. Furthermore, excitation result^[2] shows the coil is mechanically stable despite its unusual winding structure, that means possible with the similar technique to advance to the next step for the construction of Large Helical coil.

REFERENCES

1. Y.Tuda, K.Toyoda, T.Hirayama, S.Kida, K.Kuno, T.Mito, J.Yamamoto, K.Takahata, M.Takeo, I.Ohtake, Y.Takeiri, O.Motojima, A.Iiyosi, "FIRST CONSTRUCTION OF A SUPERCONDUCTING HELICAL COIL FOR FEASIBILITY STUDY OF LARGE HELICAL COIL", presented MT-11, NC-16.
2. T.Mito, J.Yamamoto, O. Motojima, K.Takahata, M.Takeo, Y.Tuda, T. Obiki, A.Iiyosi, " EXCITATION TESTS OF THE FIRST SUPERCONDUCTING HELICAL COIL AS AN R&D PROGRAM OF LARGE HELICAL DEVICE", presented MT-11, MD-05.

TABLE. 1
Main parameters of the coil

THE NUMBER OF COIL	2
THE POLOIDAL PITCH NUMBER	16
MAJOR RADIUS	300 mm
MINOR RADIUS	62.7mm
NOMINAL CURRENT	775 A
/ UPPER CURRENT	/1530 A
NOMINAL CENTRAL FIELD	2.1 Tesla
/ UPPER CENTRAL FIELD	/4.1 Tesla
THE NUMBER OF TURNS (1 coil)	
ψ DIRECTION	8 PITCHES \times 11 LINES
r DIRECTION	22 LAYERS

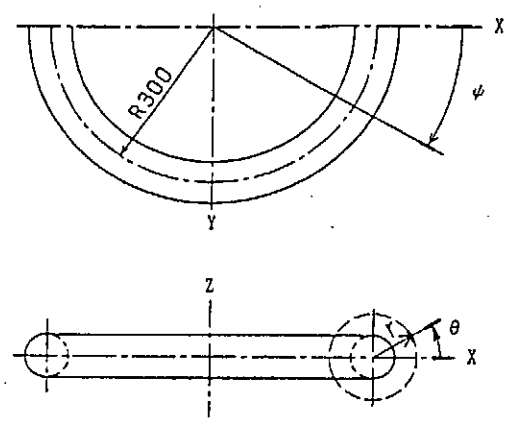


Fig. 1 the coordinate system

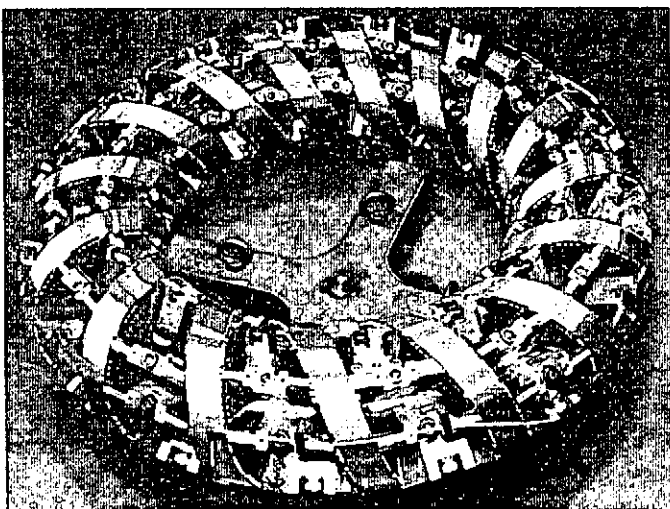


Photo. 1 the superconducting helical coil

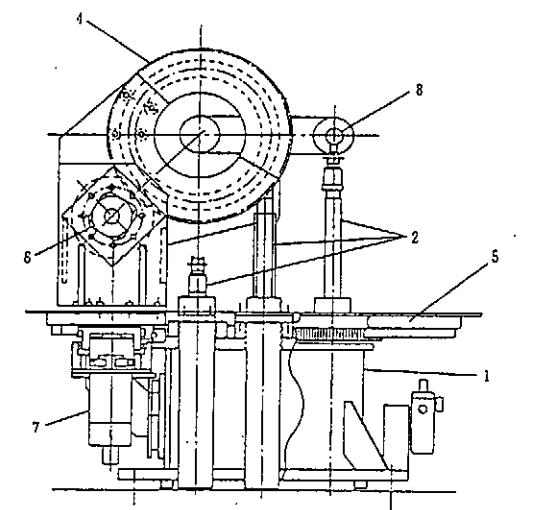
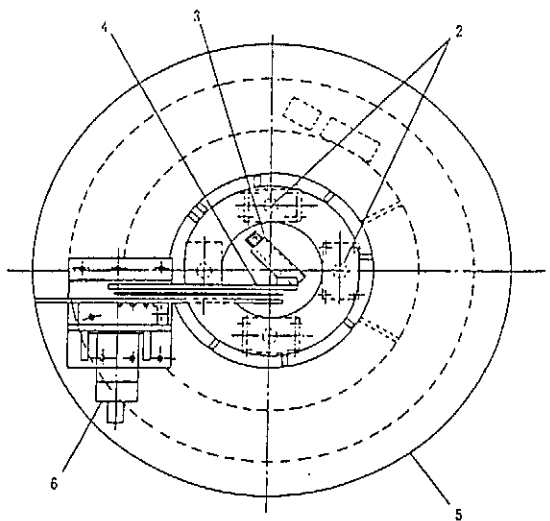


Fig. 2 the configuration of the winding machine

- 1. Base , 2. Posts, 3. Winding head ,
- 4. Poloidal rotation table ,
- 5. Toroidal rotation table ,
- 6. Poloidal motor , 7. Poloidal motor
- 8. Mandrel

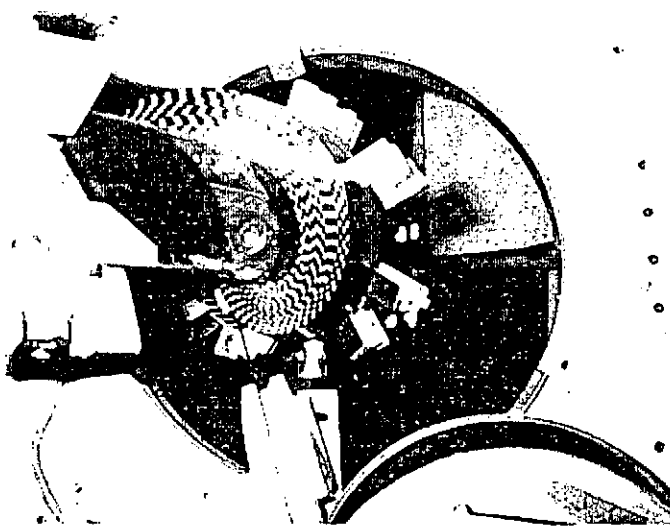


Photo. 2 the close-up of the winding

Optimization of Design Parameters for Large Helical Device

Kozo YAMAZAKI, Makoto ASAO⁺, Osamu MOTOJIMA and LHD Design Group
*National Institute for Fusion Science,
Chikusa-ku, Nagoya 464-01, JAPAN*

Abstract

The convenient scaling formula for plasma configurations and engineering design parameters of $\ell=2$ helical systems are derived from wide range of computations. Using these formula, optimized designs of heliotron / torsatron experimental devices with NbTi superconducting coils are surveyed for the next generation machines (with major radius of ~ 4 m and magnetic field of ~ 4 Tesla). An $\ell=2 / m=10 / \gamma \sim 1.2$ system with coil current density of ~ 40 A/mm² is found as a optimized higher-beta better-confinement configuration with respect to the clean divertor installation, the coil engineering requirement and the cost optimization.

1. Introduction

The design study has been carried out to optimize the design of NbTi superconducting large heliotron/torsatron systems as next-generation devices, focusing on confinement characteristics, divertor clearance, SC coil engineering (stress, stability and safety) and cost consideration. For this purpose, simple scaling formula are derived.

2. Optimization Model

The design consideration of LHD system is focused on three physics points:

- (i) estimation of beta limit,
- (ii) theoretical/empirical confinement scalings, and
- (iii) clearance between the divertor layer and the wall,

and on three engineering items:

- (i) the electromagnetic stress limit
- (ii) the maximum magnetic field and allowable SC current density, and,
- (iii) cost scaling of the helical device.

The following design criteria are adopted:

$$\beta_{eq} = \frac{\epsilon^2}{A_p} \geq 5\% \quad (1)$$

$$A_p \lesssim 8 \quad (2)$$

$$\Delta_{d-c} \geq 12 - 15 \text{ cm} \quad (3)$$

$$\sigma \propto BRj \geq 4T \cdot 4m \cdot (40 - 44) A / \text{mm}^2 \quad (4)$$

$$\text{Cost} \propto W_{HFC} \sim \text{const.} \quad (5)$$

Here, Eqs (1) and (2) are related to the 5 % equilibrium and stability beta limits respectively. Within these constraints, the fusion products $n\tau T$ or temperature T should be maximized, where empirical or neoclassical transport scaling is utilized. As for magnetic configuration properties, simple formula are used, which are obtained by using magnetic field tracing code HSD with multi-filament coil models and by minimizing standard derivatives based on various configurations for

$$\ell = 2, \quad 8 \leq m \leq 12, \quad 1.1 \leq \gamma \leq 1.4,$$

$$R_c = 4m, \quad -0.1m \leq \Delta_{ax} \leq 0m$$

The details of these scalings will be published somewhere.

3. Optimization Results

Figure 1 shows three physics configuration constraints, and Fig.2 shows three engineering boundaries, where shaded area is allowable. Within these boundaries, maximum $n\tau T$ or maximum T (empirical) is obtained for $m=10$, $\gamma=1.2$. On the other hand, maximum T (Neoclassical) is given for $m=12$, as shown in Fig.3.

Using more strict MHD computations, we obtained the schematic m - γ plot (Fig.4) showing favorable regime for a next generation device. The present LHD design ($m=10$, $\gamma=1.2$) was chosen as a optimized configuration shown here.

4. Conclusions

These analyses clarified the following points:

(1) m - γ optimization

Higher γ (helical pitch parameter > 1.3) configurations with larger plasma minor radius are prohibited from the clearance between divertor layer and the wall. Rather compact lower- m ($m < 8$) system is bounded by the equilibrium beta limit and the coil current stability limit related to higher maximum magnetic field strength on the SC coil.

Larger-aspect-ratio larger- m ($m > 12$) system with good neoclassical confinement is not acceptable because of lower stability beta and narrow divertor clearance.

(2) B - R optimization

A higher-field smaller-scale system does not have clean divertor configuration and the sufficient SC coil instability. On the other hand, a lower-field larger-scale device is not acceptable due to low plasma temperature, the stress limit and the cost constraint.

(3) Optimized configuration

A $\ell=2 / m=10 / \gamma \sim 1.2$ system with coil current density of 40 A/mm² is found as a optimized higher-beta better-confinement configuration for the next generation device having major radius of about 4 m and field strength of about 4 T, with respect to divertor installation, coil engineering requirement and cost optimization.

+ on leave from Kobe Steel, LTD. Nada-ku, Kobe 657, Japan

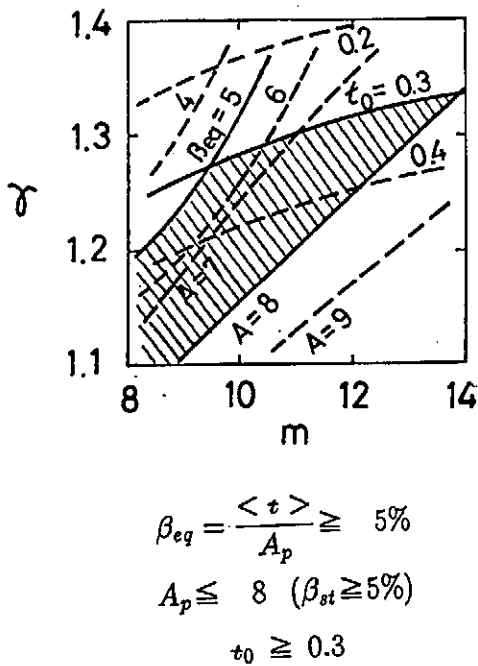


Fig. 1 m - γ plot showing physics configuration constraints

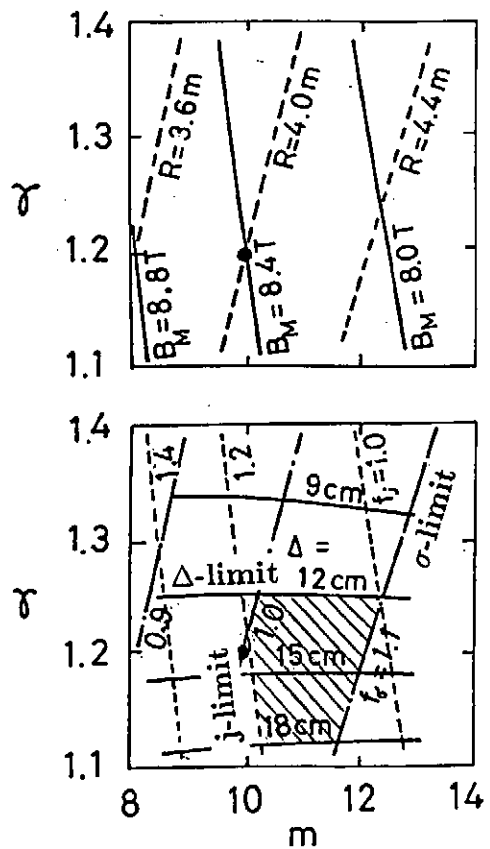


Fig. 2 m - γ plot showing engineering constraints.

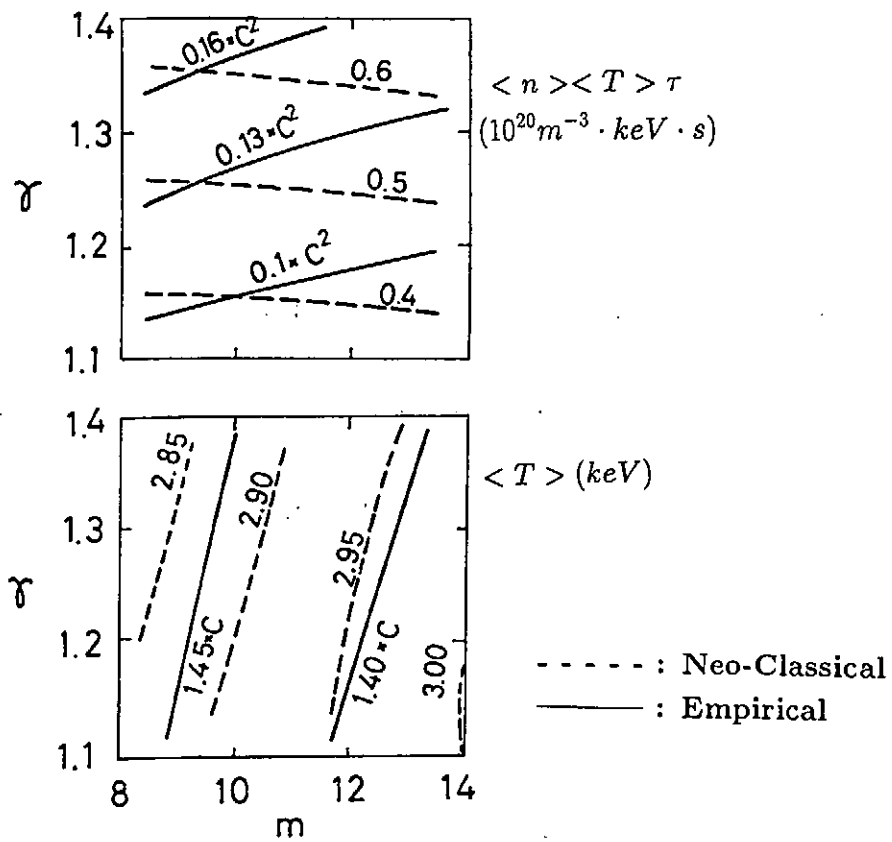


Fig. 3 Plasma parameter variations on m - γ plot

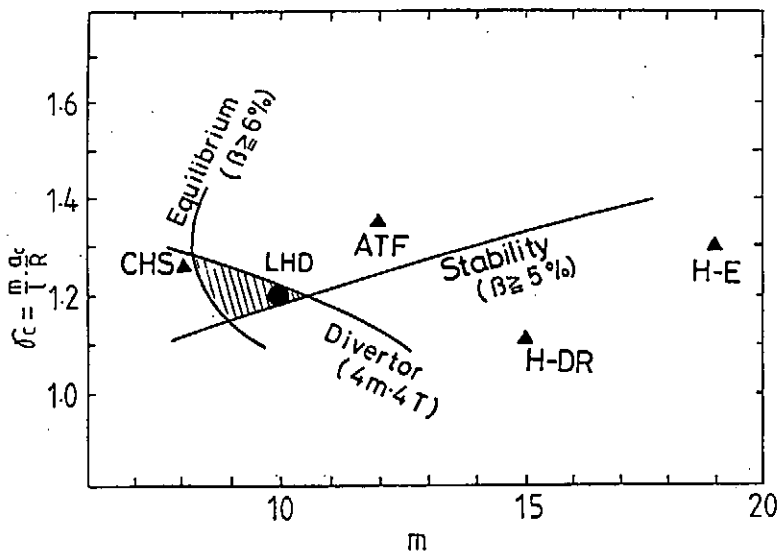


Fig. 4 Schematic m - γ plot

Effect of Multi-Layer Operation of Helical Coil in Large Helical Device

Makoto ASAO⁺, Kozo YAMAZAKI, Osamu MOTOJIMA and LHD Design Group
*National Institute for Fusion Science,
Chikusa-ku, Nagoya 464-01, Japan*

Abstract

One of main objectives in Large Helical Device Project is to investigate the fundamental properties of helical torus system in wide plasma parameter range. Therefore it is necessary to design the flexible coil system to obtain various magnetic field configurations. For this purpose, helical coil is divided into multi-layers to change helical pitch parameter (τ). A variety of configurations with different rotational transform and minor radius are obtained by this multi-layer operation of the helical coil.

1. INTRODUCTION

To keep experimental flexibility, two flexible coil systems are planned:

- (1) 3-pair poloidal coil system
 - (a) to move the magnetic axis
 - (b) to change the shape of plasma cross-section
 - (c) to minimize leakage field, and
- (2) multi-layer helical coil system
 - (a) to obtain various magnetic characteristics
(i.e. ι , a_p , well, etc.)
 - (b) to control divertor layer

After the installation of helical coil, it is ordinarily impossible to change magnetic field structure of helical coil. However, multi-layer coil system of this design is available for modifying magnetic field components of helical coil.

2. COIL CROSS-SECTION

The standard coil parameters are shown in Table 1. The size of helical coil is 514 mm \times 429 mm with width-height ratio of 1.2. This coil is divided into three equal parts (radially). Then the coil minor radius of outer layer (I-layer) is 1110 mm, that of center layer (II-layer) is 981 mm, and that of inner layer (III-layer) is 844 mm. The helical pitch parameters (τ) of each layer coil are 1.38, 1.22, and 1.06, respectively (Fig.1).

⁺: on leave from Kobe Steel LTD. Nada-Ku, Kobe 657, JAPAN

3. MAGNETIC SURFACES

The change of magnetic surface properties are shown in Fig.2 and Fig.3 . At I-layer operation ($\gamma = 1.38$), the plasma contacts the vacuum vessel and the limiter configuration is obtained with low central rotational transform and magnetic well. On the other hand, at III-layer operation ($\gamma = 1.06$), it takes divertor configuration with high rotational transform and magnetic hill.

In addition to single layer operation, by controlling the current of three layers, it is possible to change γ continuously from 1.06 to 1.38. The plasma minor radius (a_p) and rotational transform (ϵ) as function of γ are shown in Fig.4 and Fig.5 .

4. DIVERTOR LAYER CONTROL

The divertor layers in the operation of each layer are shown in Fig.6 . According to change the current of each layer, the location of divertor layer can be moved. Then plasma heat load can be controlled to adjust to divertor plate.

5. ATTAINABLE MAGNETIC FIELD

The operation to change γ is not full-current operation of helical coil, and maximum magnetic field is limited. The relation between γ and the attainable magnetic field in plasma center is shown in Fig.7. In more than 3 Tesla operation, γ can be varied from 1.15 to 1.25. A wide range of operation (from 1.05 to 1.4) is possible for 1-Tesla high-beta experiments.

6. CONCLUSION

According to make helical coil divided into 3 layers (radially), γ can be varied from 1.06 to 1.38. Therefore, in addition to change vertical field by controlling 3-pair poloidal coil currents, following experimental flexibility can be obtained.

(1) Various magnetic configurations can be formed with ϵ of $0.29 \sim 0.92$ at center and $0.71 \sim 1.49$ at surface. plasma minor radius is changed from 0.36 m to 0.73 m in case of magnetic axis inward shift of 10cm.

(2) Control of divertor layer position is feasible and particle and heat flux to the wall can be controlled.

This approach is limited to rather low field operation (1 T operation for wide range γ -control), however it is specially helpful to get flexible configurations in high β experiment. Moreover, fine adjustment of divertor layer is feasible by this multi-layer system even in high-field operation.

Table 1.

ℓ	2	
m	10	
MAJOR RADIUS	4.0	m
γ (m/ $\ell \cdot ac/R$)	1.2	
COIL MINOR RADIUS	0.96	m
MAGNETIC FIELD (CENTER)	4.0	T
COIL CURRENT DENSITY	40	A/mm ²

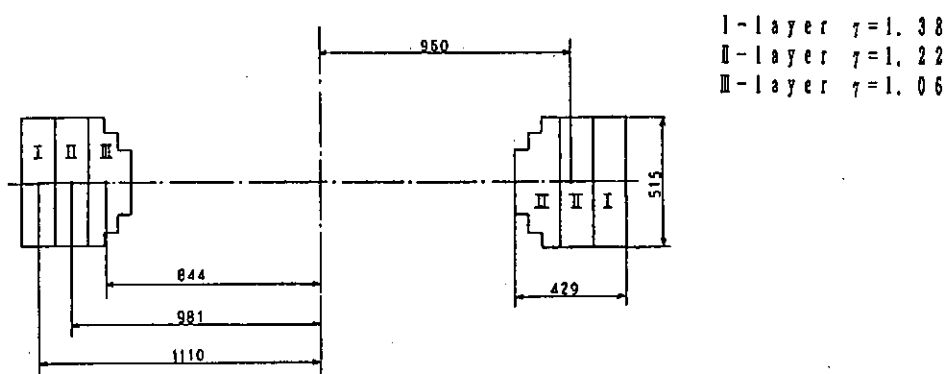


Fig.1 Cross-section of 3-layer helical coil system

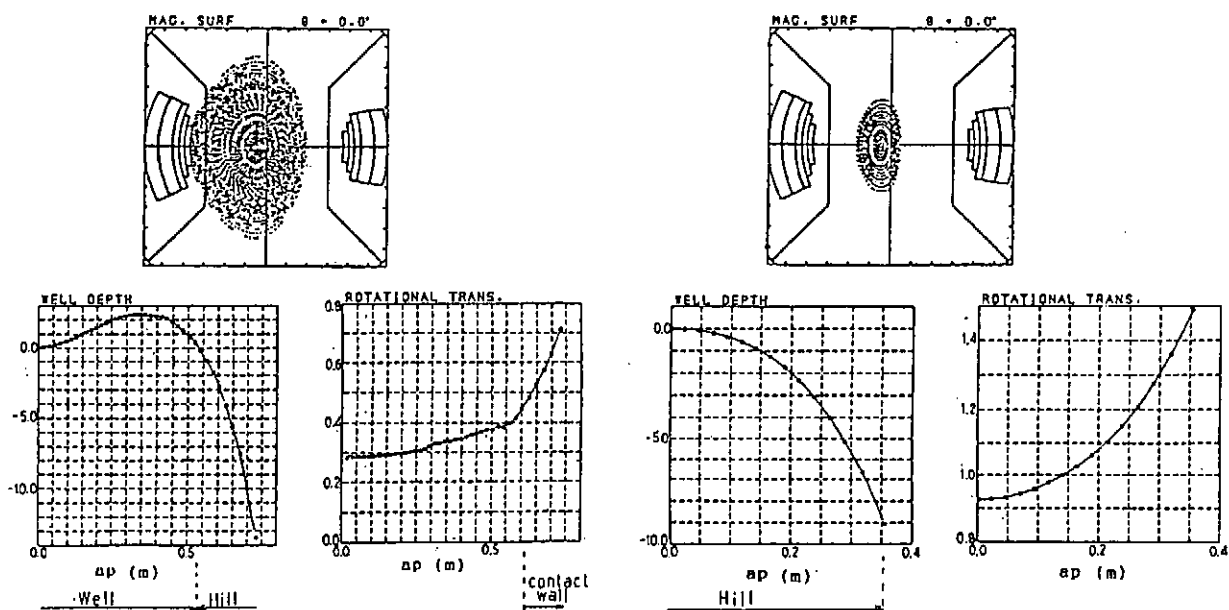


Fig.2 Magnetic surface properties (I-layer operation)

Fig.3 Magnetic surface properties (III-layer operation)

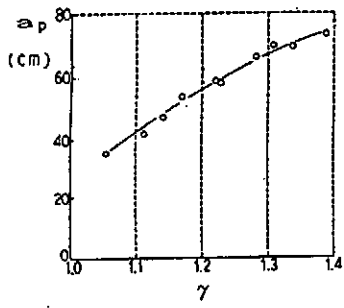


Fig. 4 Plasma minor radius a_p VS. γ (pitch parameter)

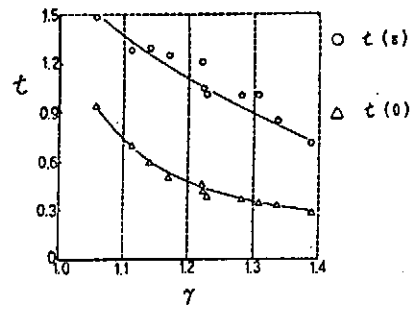


Fig. 5 t profiles VS. γ (pitch parameter)

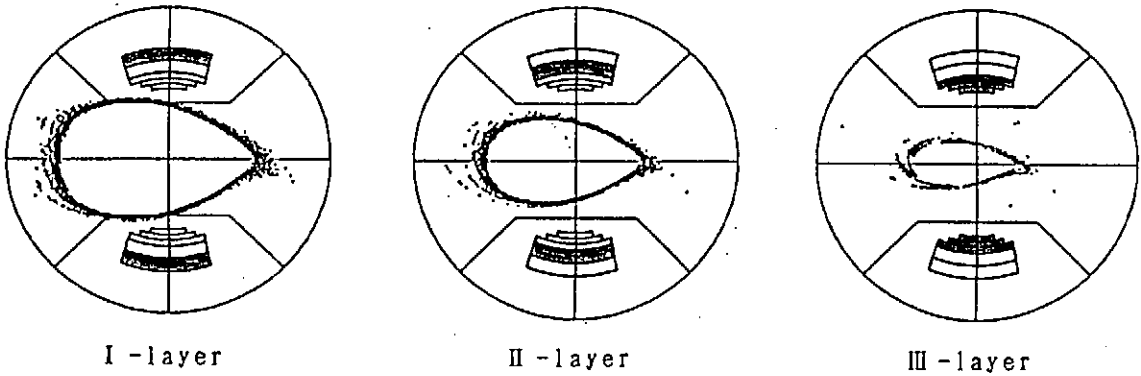


Fig. 6 Change of divertor layer as function of coil current position

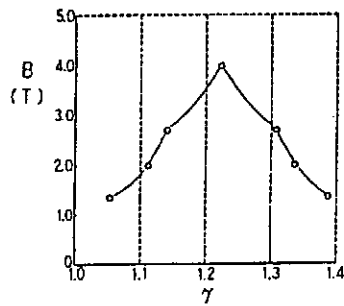


Fig. 7 γ dependence of B

ECH System in the Large Helical Device

Kunizo OHKUBO, Minolu HOSOKAWA, Shin KUBO, Takashi MUTOH,
Motoyasu SATO*, Ryuhei KUMAZAWA, Tetsuo WATARI, Tutomu KURODA

National Institute for Fusion Science, Nagoya, 464-01

**Plasma Physics Laboratory, Kyoto University, Uji, 611*

Abstract

The electron cyclotron heating system will provide 10 MW of rf power for the large helical device. The rf power will be generated by ten 1 MW gyrotrons and transmitted via the mirror system and/or the corrugated waveguide. High voltage dc power to the ECH equipment will be supplied from -80 kV power supplies with CW and 10 sec pulse width. A control system will interface to the supervisory control system for the large helical device.

Introduction

The goal of this investigation is to define an electron cyclotron heating (ECH) system for the large helical device (LHD) on the grounds of the state of the art from the experimental and theoretical points of view. The ECH system should have the performance of 10 MW/10 sec as well as 3 MW/CW in the frequency range of around 100 GHz, taking into account the experimental objects for the LHD. The objects are as follows: target plasma production, transport analysis, potential control, electron root confinement and steady state heating in connection with the superconducting LHD. Those result in necessities of R&D for (1) the CW gyrotron with high power and (2) transmission line for high power including the component such as the dummy load and window with low loss and high mode purity. For this purpose, R&D for ECH system started from June 1989.

Operation Mode

The operation of the ECH system will have three operation modes: (1) the normal operating mode, (2) the alignment adjusting mode and (3) the gyrotron tune-up mode. The gyrotron tune-up mode for aging will be operated by a slight increase in the beam voltage and pulse width, until normal rate is achieved. The various parameter setting of this mode will be carried out by the manual or software. The alignment adjusting mode will be required for checking or readjusting the deviation from the optimal position in the axis of transmission line to the LHD. The normal operating mode will be necessary for the physics experiments such as the plasma production and heating. The parameters (e.g. timing, waveform, power and selection of the gyrotrons required for the operation) of this mode are set by the programmed software.

Power Supply System

The power supply system with the high dc voltage (-80 kV) will be connected to both the commercial power line (for R&D phase and CW operation with 3 MW for the LHD) and the flywheel generator (< 10 sec). The system will consist of the down-transformer, the SCR, the up-transformer, the

rectifier, the filter bank, the crowbar and the regulator tube. The output of the beam power supply necessary for driving a gyrotron is around 50 amps and -80 kV and 7MVA of ac power input is consumed. At present, we are discussing how many gyrotrons can a regulator tube drive and how many gyrotrons can the crowbar system protect. The beam and anode voltages should be regulated within 0.2% over the full operating range. The rise and fall times for waveform of both voltages and the time for the operation of the crowbar are being discussed from the viewpoint of the cost and performance.

Gyrotrons

As described in Introduction, total output power of the ECH system is planned to be 10 MW/10 sec. Because the present state of the art of gyrotron may give the expectation for developing the megawatt gyrotron with high efficiency (around 30 %) during R&D phase, ten gyrotrons will be able to serve as the rf generator of ECH system. The magnetic field strength leaked from the LHD is not small (< 50 gauss) near the gyrotron cabinets positioned at the torus hall. Therefore, it is necessary to shield the leakage field. Since the cavity and electron beam near the collector are decoupled, it is possible for an electrically depressed collector to be used to recover the beam unused energy. Because the advantage will serve the decrease in the cost of the beam power supply, the possibility of R&D is also being discussed in relation to the schedule of developing the megawatt gyrotron and to the withstanding voltage of the body or the collector.

Transmission Line

As the transmission mode of rf power, three candidates are considered: (1) TE_{01} mode in the waveguide with the smooth wall, (2) HE_{11} mode in the corrugated or the dielectric lined waveguide and (3) TEM_{00} gaussian beam mode in the relay of the mirrors. By considering that the output of the gyrotron converted by the mode convertor is of linear polarization, main transmission using the TE_{01} mode is not suitable. The method of (3) is of fascinating from following points of view: application to the second EC harmonic heating experiment, simplification of the rf components and installation with the rf shielding duct with rough accuracy. In the final choice of the transmission line, the combination of the above-mentioned candidates will be adopted. For instance, in the mirror relay system of 50 m transmission using 45 degrees-incidence and 7 m of distance between aluminum mirrors, it is estimated that seven mirrors with the diameter of 32 cm are required and is calculated that total loss (including a diffraction loss, an ohmic loss, a scattering loss by the surface roughness in the machining of the mirror, an absorption loss by air and an alignment loss) is around 5 %. In Fig. 1 (a) and (b), attenuation constant for TE_{11} , TE_{01} and HE_{11} modes is shown. The corrugated waveguide with the diameter of 63.5 mm (corrugation height and width of a quarter wavelength) has an attenuation constant 3×10^{-4} db/m at 93 GHz. The electric field at this corrugated guide, which is inversely proportional to the radius, is estimated to be around 9 kV/cm at the transmission of 1 MW and the waveguide may withstands for arcing. To estimate the coupling of the gaussian beam reflected by the mirror to HE_{1m} , TE_{1m} and TM_{1m} modes in the waveguide, the coupling constants for each m are calculated by the

orthogonal mode expansion when the beam waist locates at the inlet of the (corrugated) waveguide. The coupling to HE_{11} has a maximum value when the ratio of waist radius (r_0) to waveguide radius (a) is 0.455. At this condition, 98% of the injected power couples to the HE_{11} -mode and 1.2% of injected power excites higher modes. The remain power of 0.8% does not enter the waveguide (Fig. 2). For TE_{11} mode, the coupling power has a maximum value of 86.6% when the ratio of r_0/a is 0.543. Here, the coupling power for TE_{11} , TE_{12} , TE_{13} TM_{11} , TM_{12} and TM_{13} is 86.6, 0.5, 2.4, 8.8, 0.9 and 0.2% respectively (Fig. 3). Therefore, the combination of candidates (2) and (3) is preferable. In connection with the incidence into the dummy load, plasmas and the window, the radiation patterns for HE_{11} mode from the waveguide (Fig. 4) and for the gaussian beam truncated by the circular aperture are calculated (Fig. 5). At the same time, the power along an axis normalized by both the wavelength and the waveguide radius (i.e. $D\lambda/a^2$) is examined. In both cases, Fresnel diffraction is in $D\lambda/a^2 < 1 \sim 3$ (Fig. 6) and the radiation of HE_{11} mode can be approximated as the gaussian beam with the ratio r_0/a of around 0.4 (Fig. 7 (a)). For the truncated gaussian beam, if the size of aperture is more than 3 times as large as the waist size, the effect on truncation by the aperture is negligible (Fig.7 (b)).

Control System

In normal operation mode, the system will be controlled remotely by the LHD central control computer and the ECH subcomputer. The control and instrumentation interface between the control system and ECH equipment will be implemented with the CAMAC crates which can communicate with the ECH subcomputer through the highways. The signals from the timing control system driven by supervisory timing system will be sent to the ECH equipment.

Figure Captions

- Fig.1: Attenuation constant for (a) various smooth-wall waveguides and (b) the different corrugated waveguides as a function the waveguide radius R for the frequency of 93 GHz. Here, H - T and H are the width and period of corrugation, and the depth of corrugation is $\lambda/4$.
- Fig.2: Coupled power with HE_{11} and higher modes (HE_{12} , HE_{13}) as a function of r_0/a .
- Fig.3: Coupling constant of gaussian beam with the waveguide mode: (a) HE_{1n} , (b) TE_{1n} and (c) TM_{1n} . Here, a is the radius of the waveguide.
- Fig.4: Radiation patterns for the HE_{11} mode as a parameter of the distance D .
- Fig.5: Radiation patterns for truncated gaussian beam by the aperture of radius a as a parameter of the distance D . (a) $r_0/a=0.3$ and (b) $r_0/a=0.5$.
- Fig.6: Radiation power along the axis for (a) HE_{11} and (b) truncated gaussian beam with $r_0/a=0.3$, 0.4 and 0.5.
- Fig.7: Equivalent waist $(r_0/a)_{cal}$ for gaussian beam approximation calculated from the radiation patterns for (a) HE_{11} mode and (b) truncated gaussian beam.

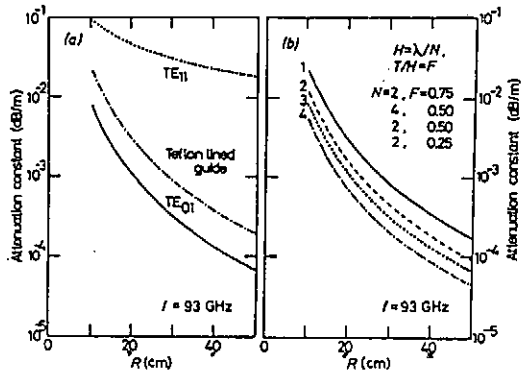


Fig. 1

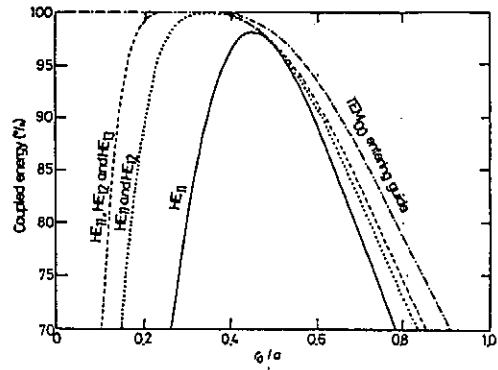


Fig. 2

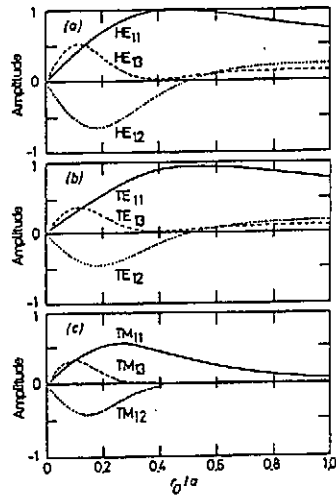


Fig. 3

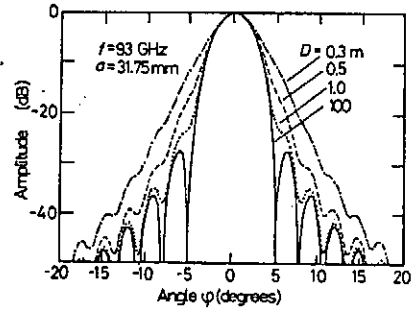


Fig. 4

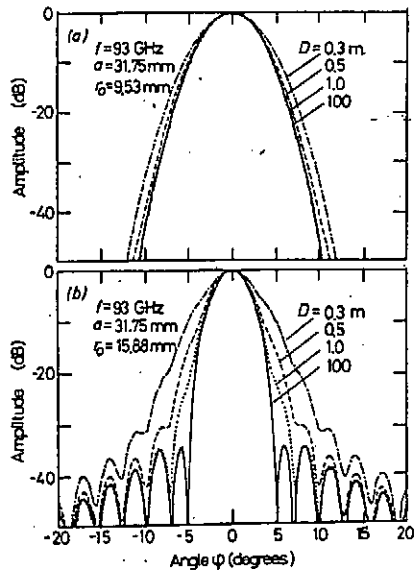


Fig. 5

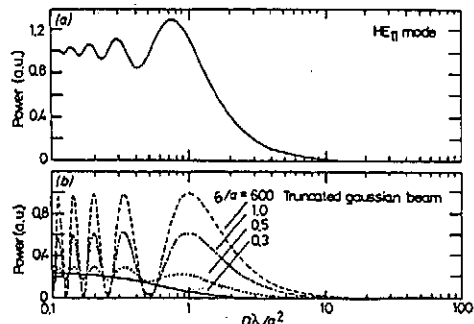


Fig. 6

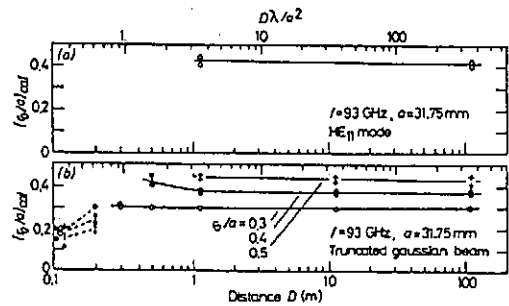


Fig. 7

ICRF Heating Program of the Large Helical Device

Takashi MUTOH, Atsusi FUKUYAMA¹⁾, Tetsuo WATARI, Ryuhei KUMAZAWA,
Hiroyuki OKADA²⁾, Masashi OHNISHI²⁾, Masao OKAMOTO,
Kiyohiko NISHIMURA, Tutomu KURODA

National Institute for Fusion Science, Furo-Cho, Nagoya, Japan

1) *Okayama University, Okayama, Japan*

2) *Kyoto University, Uji, Kyoto, Japan*

Abstract: ICRF heating programs of the Large Helical Device (LHD) have been discussed. The ICRF heating is considered as the one of the additional heating methods to achieve the objective plasma parameters and as the useful tool to study the various physics subjects. Theoretical analysis methods have been developed and parameter surveys have been carried out to find out optimum heating conditions. Wave propagation and Fokker-Planck analyses are used to evaluate the heating deposition profiles and direct orbit loss effect. Monte-Carlo calculation is also used to confirm above results. Alpha particle simulation program using ICRF is studied and it is possible to examine to a certain extent by forming a similar distribution function in ion velocity space. From these analyses, it becomes clear that the ICRF heating has high potentiality as useful heating tool, even if the loss cone exists at the radial range of $r/a_p \geq 0.4$.

§1. Objectives and Basic Design Concepts

An ICRF heating method has been established as the one of the most reliable high power heating methods in large tokamaks. Recent successful experiments in JET and other large tokamaks confirmed the effectiveness of this method to obtain the high ion temperature and high effective Q value. The ICRF heating method had become successfully done as improving the confinement of the high energy ions. In this sense, the efficiency of ICRF heating in the LHD is considered to become higher than that of the former experiments in helical devices. In tokamaks, theoretical analysis and hardware construction techniques are well developed. Some of these knowledge and experiences can be applied to our works. However, there are still many problems to apply the ICRF heating of 10MW level in the LHD which is designed to use superconducting magnets. The ICRF system has to be designed for continuous operation which is longer than 10 minutes.

The main objectives of the ICRF heating are followings. 1) To achieve the objective plasma parameters as a part of the additional heating system. Especially, at the low \bar{n}_e and high T_i operation condition, the ICRF heating has advantages. 2) To control the power deposition profile and the velocity space distribution function which offer the useful tools to solve the plentiful physics subjects. 3) To study the high energy particle behavior in the helical system. (α -particle simulation) 4) To supply the heating power for steady state operation. 5) To enlarge the effective Q value by making the high energy ion tail.

To design the ICRF heating system, the data base of the former experiments in helical systems is important. In Heliotron E, efficient ion heating was observed on the fast wave heating mode.¹⁾ Ion temperature was increased from 200 eV to 1000 eV on minority heating. ³He minority mode had better efficiency than the H minority mode. And in the H minority mode, high energy protons, which energy range reach up to 100 keV, were produced and observed to be confined in the plasma. On the other hand, CHS experiments have shown that the plasma production at the wide range of $|B|$ strength is available by using the Nagoya Type-III antenna. From the data base of these helical devices and many tokamaks, it is worth to consider the high power ICRF heating in the LHD. Both fast-wave and ion-Bernstein wave (IBW) heatings may be useful. In this report, we report the analytical results of only fast-wave mode. The IBW heating mode is now intensively investigated in CHS, JIPP TII-U and Heliotron E experimentally.

At present stage, main specifications of ICRF system design are followings; frequency is tunable at 30 ~ 90 MHz, total power is ~ 9MW and pulse length is 10sec (CW for 3MW).

§2. Theoretical Analysis of Fast-wave Heating in the LHD

Wave propagation and damping profiles are analyzed by analytical method by Fukuyama and et al.²⁾ on the straight heliotron model. From these calculations, we can optimize the launched parallel wave number k_{\parallel} and the position of antenna loops to heat the central region of the plasma column. Figure 1 shows some examples of wave analysis in the low field launch case. The spatial distribution of the fast-wave electric fields and the absorbed powers to majority and minority ions and electrons are shown. To achieve the core heating, relatively small k_{\parallel} value is necessary. In the figure, two cases of minority ions of H and ^3He are analyzed. In both cases, almost all power goes to the minority ions. These minority ions have high energy tail components on the distribution functions, which are decided from the balance of heating power, orbit loss and relaxation processes.

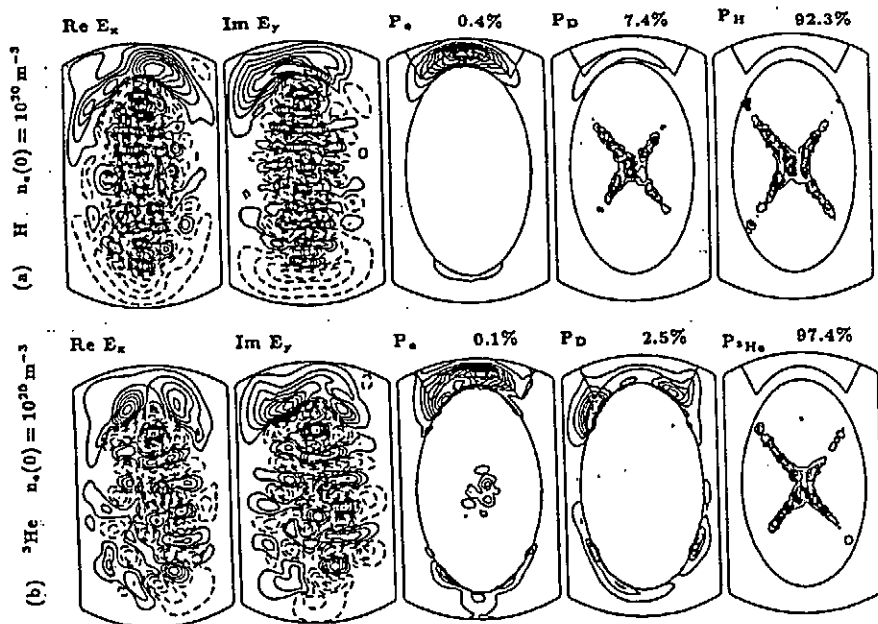


Fig. 1 Spatial distribution of fast-wave electric field and absorbed power.
($n_{eo} = 10^{20} \text{ m}^{-3}$, $B = 4T$, minority ratio 5%)

To estimate the heat transfer to bulk particles, Fokker-Planck analysis code was combined with the wave analysis code. In the Fokker-Planck code, the effect of the loss cone in the velocity space is included.³⁾ Figure 2 shows the radial profiles of orbit loss power and heating powers to majority ions and electrons. In these calculations, loss cone angle θ in velocity space has dependence of $\sin \theta = \sqrt{\epsilon_h}$ and loss time is decided by the toroidal drift motion. In this calculation, finite loss-cone angle exists at all radial point. Power loss portion due to particle loss is large when heating power density is high and the minority ion specie is proton. In the case of ^3He minority heating, we can expect about 70% thermalized power from antenna loops. These profiles are well peaked, but the real thermalized power deposition profiles are broader than that of the figures due to the large shift of the helically trapped ions from the magnetic surfaces. In the design work of the Large Helical Device, one of the main criteria is to eliminate the loss-cone inside the one third of the plasma radius. The percentages of the orbit loss power are shown in Fig.3 versus the minimum radius at which loss-cone exists. From these calculations, it becomes clear that the thermalized heating power efficiency of over 70% is available if the deposition profile is well peaked.

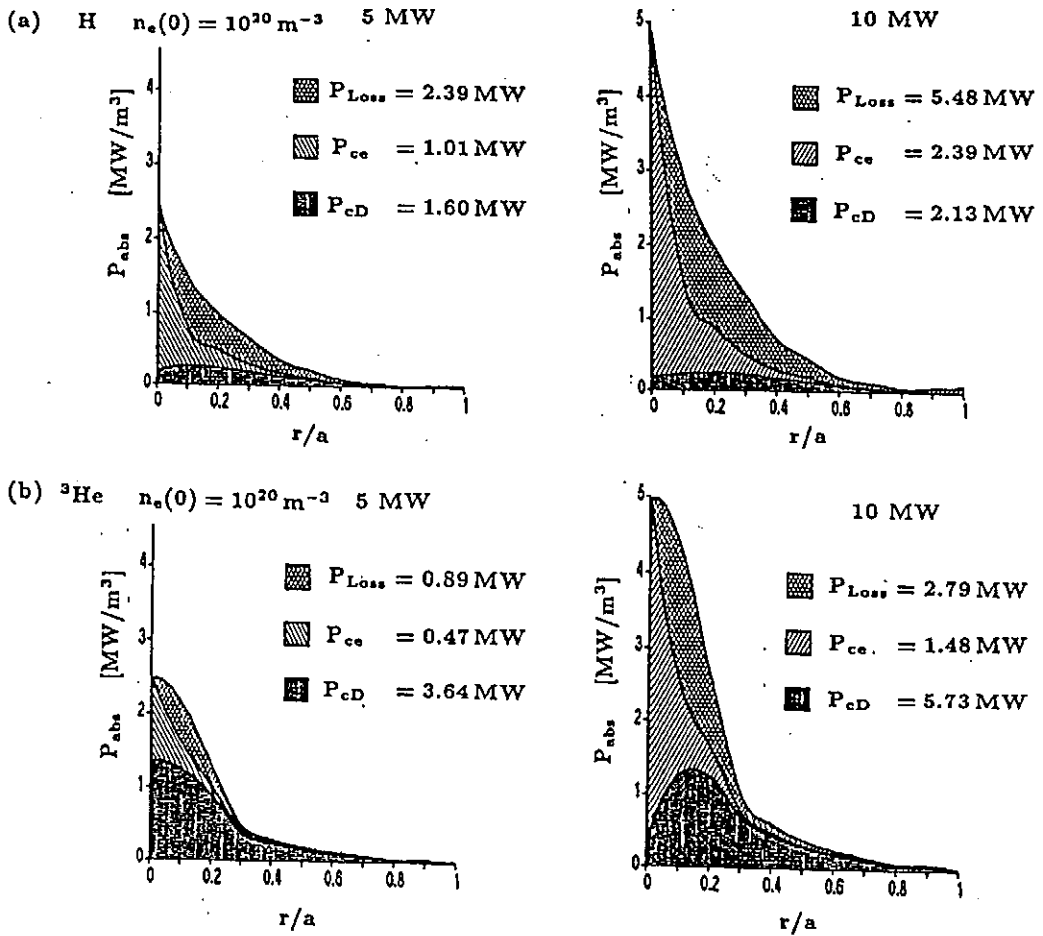


Fig. 2 Radial profiles of direct orbit loss power and thermalized powers. (Real thermalized power profiles are different due to the inward shift of trapped particles.)

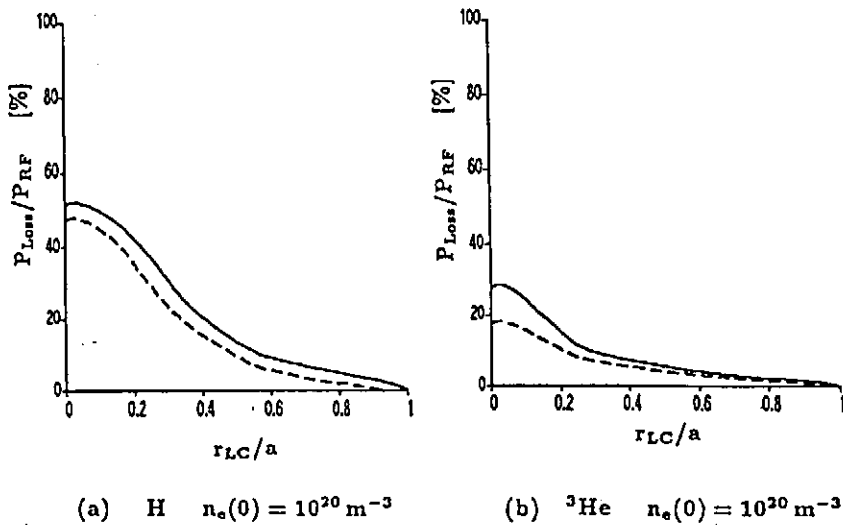


Fig.3 Ratios of the direct loss to the RF input power versus minimum radius which has a finite loss cone angle. (solid lines correspond to the 10MW input power, and the dotted lines correspond to the 5MW.)

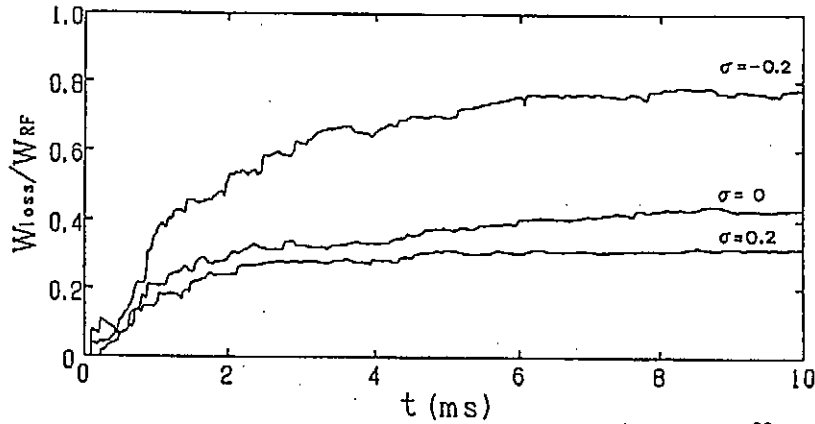


Fig.4 An example of Monte-Carlo simulation analysis. ($n_{eo} = 10^{20} m^{-3}$, $T_{eo} = 2.5 keV$)

In these calculations, toroidal effects are considered as the existence of the loss cone in the velocity space. Monte-Carlo simulation code, which includes more realistic 3-D configuration, can examine the effect of the orbit shifts from the magnetic surfaces⁴). An example of the Monte-Carlo calculation is shown in Fig.4. All heating power is given to the test particles (minority ions). Power ratios of the particle loss to the thermalization, which are time integrated, are shown versus time from the start of the test particles (1000 ions). Minority test particles get energy at the resonant regions ($\omega \simeq \omega_{cH}$) and transfer the energy to the bulk deuterons and electrons. The three lines in the figure correspond to the pitch modulations of the helical windings of the LHD. This result shows clearly that the confinement ability of high energy ions strongly relates to the efficiency of the minority heating mode. Further optimization of LHD is desirable to minimize the particle loss power.

§3. α -particle Simulation Experiment

One of the main objectives of the ICRF heating in the LHD is an α -particle simulation experiment. For this subject, we are planning two different scenarios. One is the 3He minority heating mode and another one is the 3rd or 4th harmonic heatings³) of injected ions by NBI. By these methods, we can produce large high energy tails in velocity space to examine the confinement properties of both high energy ions and bulk plasma. In Fig. 5, the velocity distribution functions of minority 3He ions are shown. The functions of α -particles in a D-T reactor are also shown. The similar high energy tails are obtained by high power ICRF heatings of 10 MW level.

[References]

- 1) O.Motojima, T.Mutoh, M.Sato, et al. IAEA-CN-50/E-1-4, Nice, 1988
- 2) A.Fukuyama, et al., 26 Nuclear Fusion, (1986) 151
- 3) LHD design team reports, 1988 and 1989, NIFS-report (in Japanese)
- 4) M.Ohnishi, M.Okamoto, et al. IPPJ-884, Nagoya Univ. 1988

Ref. ** (A.Nocentini et al.)

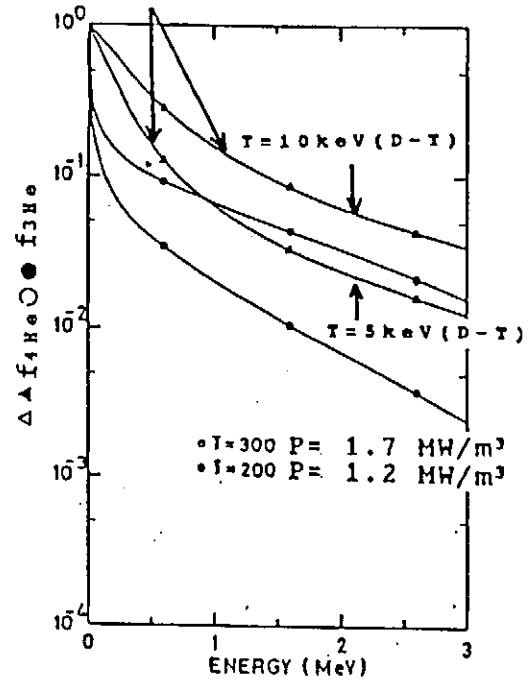


Fig.5 Velocity distribution functions of 3He particles of ICRF heating and α -particles of D-T self-sustained reactor. (ξ is a Stix's parameter)

MOTION OF CHARGED PARTICLE IN HELICAL SYSTEMS

M.P.SRIVASTAVA

Department of Physics and Astrophysics,
University of Delhi
Delhi-110007, INDIA

Abstract: We have studied the motion of a charged particle in an axially symmetric magnetic field such as found in straight helical systems. We reduce the three dimensional motion of a charged particle into a two dimensional one by introducing an effective potential. It has been possible to classify the motion into an offaxis motion and an encircling motion in the r-z plane.

1. Introduction :

The motion of charged particle in various magnetic field configurations such as mirror machine, cusp stellarators, heliotrons and toroidal devices have been investigated by many authors. In a straight helical system, the helical configuration is bounded by a separatrix magnetic surface which is expected to operate as divertor. However, in actual toroidal helical system such as torsatron or helical heliotron the separatrix disappears because of the violation of pure helical symmetry. The model vacuum magnetic field may be used as toroidal harmonic function.

In the present paper we consider the motion of a charged particle in the presence of straight helical system described by cylindrical coordinates. In section 2 we have discussed the motion in presence of a typical magnetic field in helical systems. We have reduced a three dimensional motion into a two dimensional one in the presence of a fictitious potential.

2. Motion in Helical magnetic field :

We consider the motion of a charged particle moving in a magnetic field typical of straight helical system. The Lagrangian of the system is given by

$$L = (p_r^2 + p_\theta^2 + p_z^2) + p_\theta A_\theta \quad (1)$$

where p_r , p_θ and p_z are components of momentum of the particle in r, θ , z directions respectively. A_θ is the θ component of vector potential determining the magnetic field. The magnetic field \vec{B} in cylindrical coordinate for a typical straight helical system is given by

$$\vec{B} = (B_r, 0, B_z) \quad (2)$$

$$B_r = \beta [kr - I_1(kr) \sin kz] \text{ and } B_z = \beta [-2kz - I_0(kr) \cos kz] \quad (3)$$

where β is the measure of the strength of the field. K is a dimensional constant occurring in helical system. $I_0(kr)$ and $I_1(kr)$ are modified Bessel's function of zeroth and first order respectively. We nondimensionalize the parameters as

$$r' = kr, \quad \theta' = \theta, \quad z' = kz, \quad t' = \omega t, \quad (4)$$

where $w = qB/m$ is the characteristic frequency of the system. We replace the dashed quantities by undashed ones. The magnetic lines of force are given by

$$\psi = r^2 z + r I_1(r) \cos z = \text{constant} \quad (5)$$

The magnetic lines of force are symmetrical about z axis and $r=0$ is the asymptote for the family of magnetic lines of force. The vector potential \vec{A} for the field (3) is given by

$$\vec{A} = [0, -(rz + I_1(r)\cos z), 0] \quad (6)$$

From (5) and (6), we note that $\psi = -rA_\theta$ which is the flux of magnetic lines of force. We note that the Lagrangian is independent of θ coordinate. Therefore the canonical angular momentum, say M , will be a constant of the motion i.e.,

$$\frac{\partial L}{\partial \dot{\theta}} = [r p_\theta + r A_\theta] = M \quad (7)$$

The Hamiltonian of the particle is given by

$$H = p_r^2 + p_z^2 + \left(\frac{M}{r} - A_\theta\right)^2 = p_r^2 + p_z^2 + \phi \quad (8)$$

Where

$$\phi = \left(\frac{M}{r} - A_\theta\right)^2 \quad (9)$$

ϕ is called the fictitious potential. Consequently equation (8) gives the Hamiltonian of the particle in two dimension i.e. $(r-z)$ plane and the particle is also subjected to potential. As $r \rightarrow 0$, $\phi \rightarrow \infty$. If we are interested in confined particles, it is necessary that the potential function has at least one minimum. The points of extremum of $\phi(r)$ are given by $\partial\phi/\partial r = 0$ i.e.

$$\left(\frac{M}{r} - A_\theta\right) = 0 \quad (10)$$

$$\text{or } \frac{M}{r^2} + \frac{\partial A_\theta}{\partial r} = 0 \quad (11)$$

For $\phi(r)$ to have a minimum, it is necessary to see the sign of second order derivative of $\phi(r)$ at those points. We have

$$\frac{\partial^2 \phi}{\partial r^2} = 2 \left[\left(-\frac{M}{r^2} - \frac{\partial A_\theta}{\partial r}\right)^2 + \left(\frac{M}{r} - A_\theta\right) \left(\frac{2M}{r^3} - \frac{\partial^2 A_\theta}{\partial r^2}\right) \right] \quad (12)$$

From (12) we note that $\partial^2 \phi / \partial r^2 > 0$ if (10) is satisfied which shows that $\phi(r)$ has a minimum. But if (11) is satisfied then $\phi(r)$ to have a minimum, it is necessary that

$$\left(\frac{M}{r} - A_\theta\right) \left(\frac{2M}{r^3} - \frac{\partial^2 A_\theta}{\partial r^2}\right) > 0 \quad (13)$$

Therefore ϕ form a potential trough about the minimum and the particle oscillates between the turning points of the trough when injected from a point close to the minimum.

The motion in the two cases are different. Since we know that $M - rA_\theta = \eta r$ is the angular momentum of the particle; equation (10) would imply that $\eta = 0$. The particle in such a potential trough performs an offaxis motion. But if equation (13) satisfies the condition of minima for $\phi(r)$ there is no point where $\eta = 0$. This motion is called an encircling motion.

We now determine the ranges of M and z in which the particle

will perform off axis and encircling motion. We consider following cases.

Case 1 $0 \leq z \leq \pi/2$

(a) $M > 0$: so that

$$f(r) = \frac{M}{r} - A_{\theta} = \frac{M}{r} + rz + I_1(r) \cos z \quad (14)$$

$$\text{and } g(r) = \frac{M}{r^2} + \frac{\partial A_{\theta}}{\partial r} = \frac{1}{r^2} [M - r^2 z + (rI_1(r) - r^2 I_0(r)) \cos z] \quad (15)$$

we note that $f(r)$ is nonzero for all values of r in this domain of z and M . But $g(r)$ will become zero for at least one value of r . The particles injected with this value of r will make an encircling motion.

(b) $M < 0$: In this case the equation $f(r) = 0$ will give at least one real root whereas $g(r) = 0$ will not give any real root. Thus we can say that when the particle entering at the point when $f(r) = 0$, it will describe an off axis motion.

(c) $M = 0$: In this case neither $f(r) = 0$ nor $g(r) = 0$ will have any real root.

Case 2. $-\pi/2 < z < 0$

(d) $M > 0$. $f(r) = 0$ will have at least one real root and $g(r) = 0$ will also give at least one real root. Hence we can conclude that as soon as the particle goes to second quadrant for a particular value of z , the particle will have an off axis motion for some value of r and an encircling motion for some other value of r .

(e) $M < 0$: Here again we note that $f(r) = 0$ is satisfied for some value of r and $g(r) = 0$ is satisfied for some other value of r . So we will have off axis type of motion at some r and encircling motion for some other value of r .

(f) $M = 0$: For this case also we note that for some value of r $f(r) = 0$ and for some other value of r $g(r) = 0$ so that the particle will have off axis motion for some value of r and encircling motion for some other value of r .

Conclusion : We note that the particle motion is either an off axis motion or an encircling motion depending on which region it is located and the values of physical parameters. The motion will be complicated when we investigate the motion of charged particle in model vacuum magnetic field described by toroidal harmonic function which are more appropriate to toroidal system. This motion in toroidal coordinates will be investigated subsequently.

References :

A. Garren, et al., Proc. IInd UN Conf Peaceful uses of Atomic Energy 31, (1958) 65.

G. Schmidt Phys. Fluids 5 (1962) 994.

T. Amano, Jour. Phys. Soc. Japan 16, (1961) 2517.

T. Amano, Murakami M & Outi A., Jour. Phys. Soc. Japan 20 (1965) 1239.

K. Itoh et al., Jour. Phys. Soc. Japan 55 (1986) 3101.

K. Itoh et al., Nuclear Fusion 29 (1989) 1299.

Equilibrium, Stability and Transport in L=1 Compact Helical Axis Configuration

Hitoshi Kikuchi, Hikaru Ueno, Masamitsu Aizawa, Kiyomitsu Suzuki, Hirokazu Gesso, Katsunori Saito, Ichiro Kawakami, Shoichi Shiina

Atomic Energy Research Institute
College of Science and Technology, Nihon University
1-8 Kanda Surugadai, Tokyo 101

Abstract

The L=1 torsatron is modified by two methods to improve the plasma stability. First one is the negative pitch modulation of coil winding. Second is the superposition of a relatively weak L=-1 torsatron field. These modifications give rise to a local magnetic well keeping a positive magnetic shear. The equilibrium, stability and transport of plasma in these modified L=1 torsatrons are described and discussed.

1. Introduction

Helical magnetic axis configurations as Heliac are known to be suitable for high β plasma confinement because of the high rotational transform and the deep magnetic well. However there are the problems of magnetic island formation and surface destruction, which result from the resonant and non-resonant vacuum field Fourier components. These islands make the equilibrium limit unacceptably low.[1] In this paper, the L=1 compact helical magnetic axis torsatron having a excursion of magnetic axis smaller than the plasma radius is studied. The axis twist in the L=1 torsatron provides a rotational transform sufficient for the equilibrium and a high positive magnetic shear. However it has a large magnetic hill. The modified L=1 torsatron by both the negative pitch modulation of coil winding and the superposition of a relatively weak L=-1 torsatron field have a local magnetic well keeping moderate positive magnetic shear.[2,3] The finite beta effects on the equilibrium and the stability of these modified L=1 torsatrons are examined with the use of BETA code.[4] The particle drift and transport have been calculated from the Fourier components of the field strength in magnetic coordinates.

2. Vacuum Magnetic Configuration

The L=1 torsatron, which has the simplest coil structure among many other toroidal devices, is composed of a single helical coil and vertical field coil. The pitch-modulated L=1 torsatron has the helical coil with a winding law $\theta = N\phi + \alpha^* \sin(N\phi)$, where θ and ϕ are poloidal and toroidal angles, respectively, N the number of field periods and α^* the modulation parameter. The coil aspect ratio A_c (R_0/r_c , R_0 is the major radius and r_c the minor radius), N and α^* are optimized into a good compromise of the plasma size, the rotational transform, the magnetic shear and well, and the transport. The magnetic surfaces, which are calculated by Biot-Savart's law using a filamentary representation of the helical coil, are shown in Fig.1 for the optimized coil parameters indicated, where B_0 is the toroidal field at the minor axis produced by helical coil. The magnetic axis excurses helically with much smaller amplitude than the average radius of the

outermost magnetic surface (a). The plasma aspect ratio R_0/a is 9.5. Fig.2 shows the dependence of the rotational transform $\iota(r)$ and the specific volume $V'(r)$ profiles on the pitch modulation parameter α^* . For $\alpha^* < 0$, $\iota(r)$ profile does not straddle the dangerous rational surface $\iota = 1$. The local magnetic well is formed near $a/2$ for the negative α^* , while the magnetic shear decrease. Furthermore, the negative pitch modulation reduces the field ripple at magnetic axis and makes $\iota(0)$ increase. The superposition of a weak $L=-1$ torsatron field on the $L=1$ torsatron ($\alpha^*=0$) reduces the magnetic hill near $a/2$, keeping the high positive magnetic shear, as shown in Fig. 3, which means the improvement of the plasma stability. The weak $L=-1$ field, in turn, makes the increase of both the Pfirsh-Schlüter current and the field ripple and the decrease of ι . The plasma aspect ratio R_0/a is 6.9 when $I_{-1}/I_{+1} = -0.3$, where I_{\pm} is each coil current and minus sign means opposite coil current direction each other.

3. Finite Beta Effect on Equilibrium and Stability

The finite beta equilibrium is examined for the fixed boundary plasma and for the stellarator/torsatron equilibrium without net toroidal current. There appears to be no difficulty with the existence of equilibrium in the beta range of 10% for both pitch-modulated $L=1$ and $L=\pm 1$ torsatrons, because the shift of the magnetic axis to the outer flux surface is smaller than $a/2$ in this beta range. The magnetic island widths near the magnetic axis evaluated by the low beta analytical theory [1] are much smaller than those in Helicac because of the higher toroidal mode number of magnetic axis periodicity. This result is contrast to that of Helicac, where the equilibrium beta limit is determined from the magnetic island. The numerical calculation on island formation is being carried using Hiroshima code. Fig. 4 shows the dependence of $\iota(r)$ and $V'(r)$ profiles on beta value for pitch-modulated $L=1$ torsatron, which is calculated using BETA code. As β value increases, the local magnetic well is formed in a wider region while the distribution of ι flattens out with the value at the edge of the plasma falling of significantly. The self-magnetic well beta value, β_{well} , at which the magnetic well is formed in whole plasma region, and the shearless beta value, β_{sh} , at which the magnetic shear becomes zero, are $\sim 5\%$. These critical beta values are 10% for $L=\pm 1$ torsatron and 12% for $L=1$ torsatron. The stability beta limit for $m=1, n=1$ global mode is 2.7% for $L=1$ torsatron. For $L=\pm 1$ torsatron, there is not the tendency for the presence of the stability beta limit within the calculated beta range of 3.5% as shown in Fig.5. This enhancement of the stability beta limit is due to the improvement of magnetic hill formed without changing the magnetic shear. However, the growth rate of localized modes, which is assessed via the Mercier criterion, has the tendency to increase with $L=-1$ field strength. This increase comes mainly from the increase of Pfirsh-Schlüter current. The stability beta limit for pitch-modulated $L=1$ torsatron is being examined. The Mercier criterion does not change compared with that for $L=1$ torsatron.

4. Particle Drift Orbits

We have studied the particle transport properties of this system. Recently, it has become well known that the magnetic coor-

ordinates has made the particle orbit physical and readily interpretable. We have used the magnetic coordinates, so-called Boozer coordinates (ψ, θ_0, χ) . Boozer's coordinates system has straight field lines and a Jacobian that depends only on the strength of the magnetic field. The curl-free field is represented by $\mathbb{B} = \nabla \psi \times \nabla \theta_0 = \nabla \chi$. Here $2\pi \psi$ is the toroidal magnetic flux, and θ_0 is angle variable which labels the field line. In these coordinates, one of the appropriately normalized drift equations is, $d\psi/dt = -[\mu + B\rho^2] \partial B / \partial \theta_0$, where B is the magnetic field strength, μ is the magnetic moment and ρ is the parallel Larmor radius. The relations among the usual toroidal angle ϕ and poloidal angle θ and the magnetic coordinates are, $\theta = \theta_0 + \iota(\psi) \cdot \phi$, $\chi = g\phi$, where ι and g are the rotational transform and poloidal current outside a flux surface ψ , respectively. At first, the magnetic field strength is calculated along the field line. The number of field period is 17. Utilizing the periodicities in θ and ϕ in a torus, the Fourier decomposition technique [5] tell us the following relation, $B = \sum_{nm} B_{nm} \cdot \exp[i((n-m)\iota(\psi))g^{-1}\chi - m\theta_0]$. The original method [5] had difficulty in determining the harmonics when the rotational transform is rational and when the transform is large near the outermost magnetic surface. We have decided the correct harmonics automatically, as shown in Fig. 6. Here, we used some improved methods, one of them is the use of the anti-symmetry character of magnetic field strength along the field line which is started from the half-symmetry plane^[6], and another is the correction for Fourier amplitude and frequency by theoretically expected values. Substituting above equation to the drift equations, then we can obtain the trajectories of particles. The equations for the drift orbits are integrated by the Adams-Bashforth method with variable step and order. Fig. 7 shows the typical transition particle drift orbit for L=1 torsatron. The starting point is $\theta_0 = \pi$, $\chi = 0$, and $\psi = \psi_0/4$, where ψ_0 is the outermost magnetic surface, and cosine pitch to the parallel velocity is $2\pi/5$.

5. Conclusion

The plasma stability in L=1 torsatron is improved by two types of modification; the negative pitch modulation of coil winding and the superposition of a weak L=-1 torsatron field. The former modification makes a local magnetic well keeping a positive magnetic shear. The latter enhances the stability β limit but makes localized(Mercier) made more unstable. The particle drift orbits are also obtained by utilizing the magnetic coordinate which is automatically transformed from the Cartesian coordinates.

References

- [1] A. H. Reiman and A. H. Boozer: Phys. Fluid 27 (1984) 2446
- [2] H. Kikuchi, H. Ueno, K. Saito and S. Shiina:
J. Phys. Soc. Japan. 58 (1989) 231
- [3] H. Kikuchi, K. Saito, H. Gesso and S. Shiina:
J. Phys. Soc. Japan. 58 (1989) 511
- [4] F. Bauer, O. Betancourt and P. Garabedian: MHD Equilibrium
and Stability of Stellarators(Springer-Verlag, New York, 1984)
- [5] G.Kuo-Petravic, A. H. Boozer: J. Comput. Phys. 261 51 (1983)
- [6] J. A. Romé : J. Comput. Phys. 348 82 (1989)

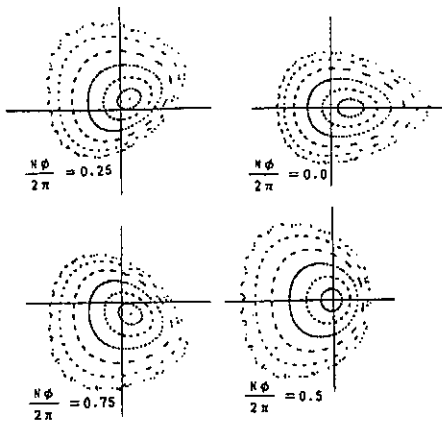


Fig. 1. Magnetic surfaces over one field period (at toroidal angles $\phi=0.0, 0.25, 0.5, 0.75 \times 2\pi/N$) in the case of major radius $R_0=2.1$ m, the minor radius of the $l=1$ helical coil $r_c=0.3$ m, field periodic number $N=17$, pitch modulation factor $\alpha^*=-0.4$ and vertical field $B_z=0.156B_0$.

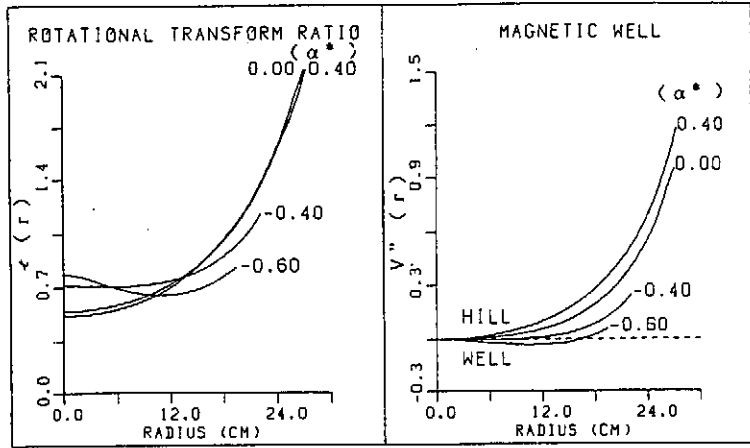


Fig. 2. Dependence of $t(r)$ and $V''(r)$ profiles on the pitch modulation factor α^* in the case of $R_0=2.1$ m, $r_c=0.3$ m, $N=17$ and $\Delta X=0$.

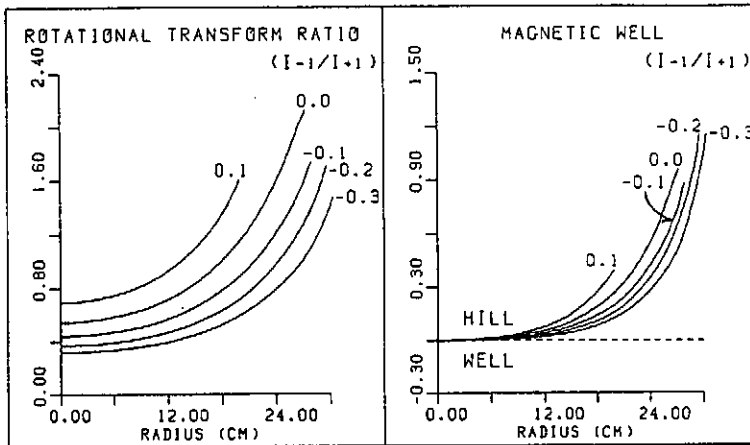


Fig. 3. Dependence of $t(r)$ and $V''(r)$ profiles on current ratio I_{-1}/I_{+1} , in the case of $R_0=2.1$ m, $N=17$, $B_0=0$ and $\Delta X=0$.

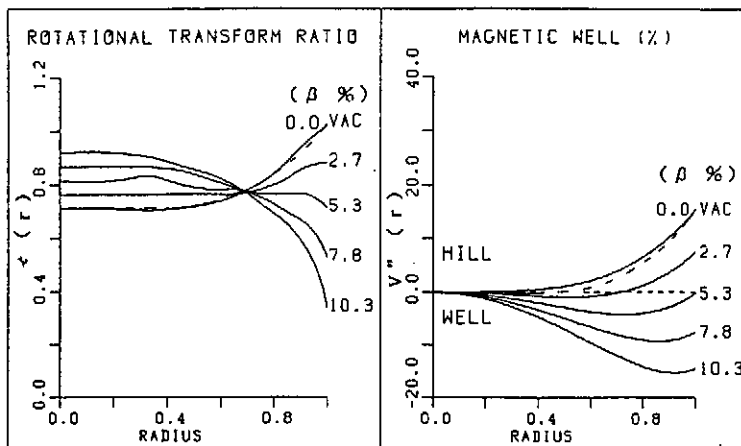


Fig. 4. Dependence of $t(r)$ and $V''(r)$ profiles on β in the case of $\alpha^*=-0.4$, $R_0=2.1$ m, $r_c=0.3$ m and $N=17$.

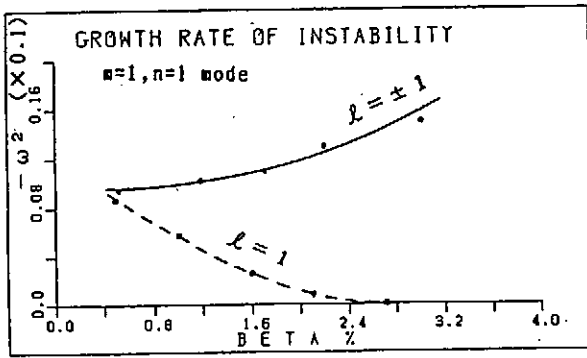


Fig. 5. Global stability of $L=\pm 1$ torsatron

($R = 2.1$ m, $r_{c+1} = 0.3$ m, $r_{c-1} = 0.4$ m, $I_{-1}/I_{+1} = -0.3$, $N=17$, $B_V = 0.044 B_0$)
 Note that $-\omega^2 > 0$ corresponds to a stable mode.

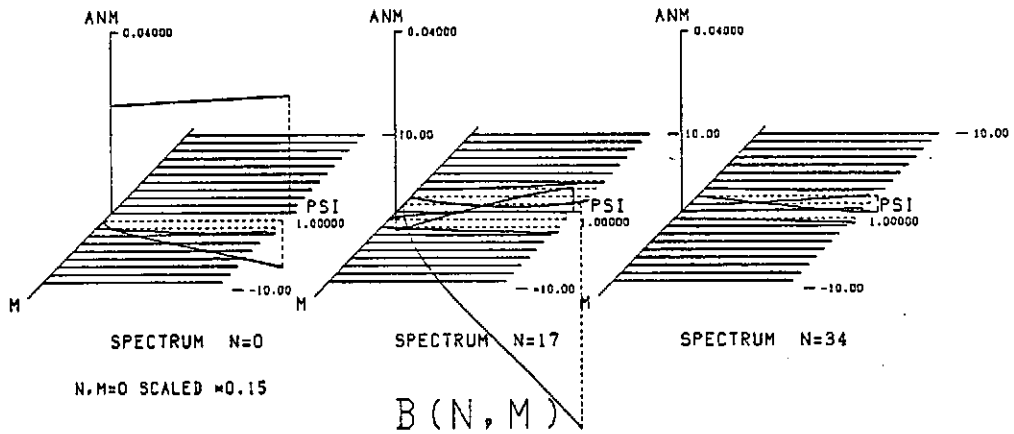


Fig. 6. Automatically assigned Fourier amplitude of magnetic field strength.

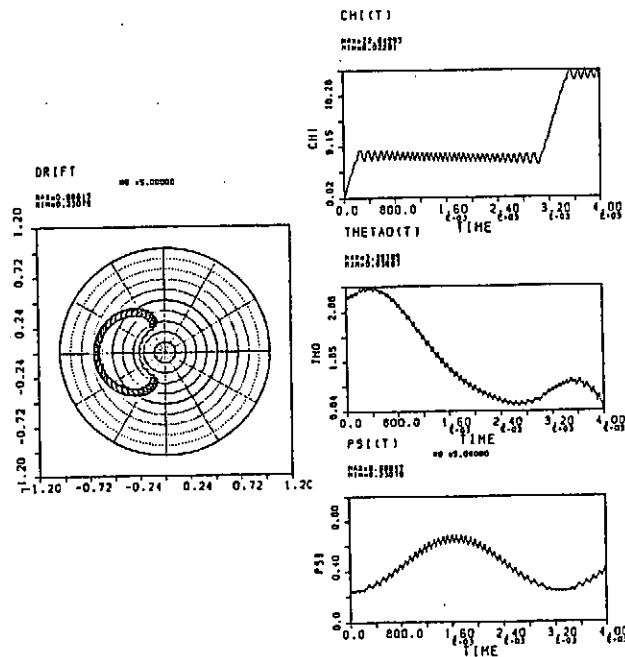


Fig. 7. Drift orbit projected onto the $\psi - \theta$ plane and time evolution of particle position (ψ, θ, χ) .

ELECTRON TEMPERATURE MEASUREMENTS ON ATF USING ELECTRON CYCLOTRON EMISSION

R.F. Gandy, G.L. Bell
Physics Department
Auburn University, Ala., USA 36830
J.B. Wilgen, T.S. Bigelow and D.A. Rasmussen
Oak Ridge National Laboratory
Fusion Energy Division, PO Box 2009
Oak Ridge, Tenn., USA 80309

Abstract : Second and third harmonic electron cyclotron emission measurements have been carried out on the Advanced Toroidal Facility (ATF) at Oak Ridge National Laboratory. ATF is a $l=2$, $m=12$ torsatron with a major radius of 2.1m and an average plasma radius of 0.3m. At the standard magnetic field values of 1T and 2T, we have used heterodyne receivers with fixed frequency Gunn local oscillators. The optically thick second harmonic emission has been used to monitor the electron temperature profile as a function of time. The optically thin third harmonic emission has been used to measure the central electron temperature during ECH and Neutral Beam Injection. Results from both harmonics agree well with the Thomson Scattering data. Calculations of the width of the resonance zones indicate values from 1 cm at the edge to 5 cm centrally. An in-situ absolute calibration of the system using a liquid Nitrogen source has been performed. The beam pattern of the system has also been measured in-situ and agrees well with theoretical calculations. A beam viewing dump has been installed to reduce the wall reflection problem for the optically thin emission.

I. Introduction.

The Advanced Toroidal Facility(ATF) is a $l=2$, $m=12$ torsatron located at Oak Ridge National Laboratory. ATF has a major radius of 2.1 m and an average plasma minor radius of 0.3 m. The magnitude of the magnetic field on axis lies in the range 1-2 Tesla. Electron cyclotron emission (ECE) from ATF provides a means of measuring the time evolution of the electron temperature. To obtain electron temperature profiles a 16 channel filter bank radiometer has been designed and implemented. Using a waveguide mixer to attain an intermediate frequency (IF) range of 2 - 18 GHz, the signal is passed through a divider network into a filterbank consisting of 16 bandpass filters, each having a 3 dB bandwidth of 1 GHz. A Gaussian beam horn-lens system with a vertical view perpendicular to the major axis provides spatial resolution on the order of 5 cm within the emitting plasma volume. The complete system has been absolutely calibrated in-situ using a liquid Nitrogen cooled source. For the optically thick second harmonic ECE at 2T operation, the calibrated ECE system gives direct temperature information up to the cutoff density of $n_{e0}=2 \times 10^{13} \text{cm}^{-3}$. We have used the approach of Talmadge¹ to obtain electron temperature measurements from third harmonic ECE at 1 Tesla operation. For the optically thin third harmonic ECE at 1T operation, the calibrated ECE system gives direct temperature information up to the cutoff density of $n_{e0}=5 \times 10^{13} \text{cm}^{-3}$. The results agree well with independent electron temperature measurements made by Thomson scattering.

II. Calculated Emission

In order to predict and analyze the ECE from ATF, emission codes have been developed. Using the expressions for the absorption coefficient, α , as developed by Bornatici², and assuming parabolic density and temperature profiles, and the vacuum B-field, we calculated the optical depth ($\tau = \int \alpha ds$) for straight line propagation through the plasma. Using a slab model and the equation of radiative transport the specific intensity emission profiles were calculated³. Due to the density cutoff restriction of the second harmonic at low field operation, the third harmonic was selected to provide electron temperature information. However, density cutoff still remains a concern. For the expected range of central electron temperatures (1-3 keV) and densities ($1-5 \times 10^{13} \text{cm}^{-3}$), the second harmonic for high field operation (2 T) is optically thick and emission will be in the 80 - 112 GHz range while the third harmonic for low field operation (1 T) is optically thin with emission falling in the 67 - 83 GHz range. At present a ray tracing code is being developed to investigate the role of refraction.

III. Diagnostic System

A. Viewing Beam

The selection of a horn to couple the free space radiation to the waveguide for transport to the heterodyne receiver required a design which provides adequate spatial resolution inside the emitting plasma volume. The radiation pattern of a horn usually subtends a large solid angle making interpretation of the data more complicated for both optically thick and thin plasmas. Utilizing Gaussian Optics⁴ a horn-lens system is used to form a viewing beam with a waist at the plasma center, defining the viewing geometry. Only radiation originating within the beam contours enters the horn. A vertical view of the saddle point geometry of the ATF mod B spatial contours provides a line of sight along which the mod B contours are symmetric about the horizontal midplane. For the situation where the ATF plasma is optically thin, the beam waist should be located on the horizontal midplane. For this waist location the plasma exhibits nearly identical behavior at each of the two locations where the beam intersects the emitting flux surfaces. Beam, mod B and flux surface symmetry about the midplane guarantees the uniqueness of the ECE spectrum and preserves space-frequency mapping. The selection of the beam parameters was governed by the desire to maintain Gaussian purity, maximize power flow through the 5.78" vacuum port, and attain acceptable spot size at center of the plasma. A corrugated conical horn (axial length 18.0cm and aperture diameter of 4.47 cm) and a 32 cm focal length TPX lens were designed to couple efficiently to the viewing beam while providing broadband 67-114 GHz performance by matching the frequency scaling of the horn with that of the beam. The circumferential corrugations are designed to produce identical E and B field boundary conditions in order to launch a linearly polarized axially symmetric beam with the majority of power channelled into the fundamental Gaussian mode^{4,5,6,7}. Beam measurements indicate the symmetric sidelobes are typically 30 dB down at the location of the beam waist.

The horn views the plasma through a wedged (2 degree) quartz vacuum window located on an upper vertical port. In order to compensate for beam deflection due to the quartz vacuum window, an oppositely-oriented, 4.5 degree wedged Teflon piece was added. Initially a pyrex window served as a beam dump on the bottom port by providing an exit for the beam. This was improved by employing two pyrex pieces having an inverted V-shape above the bottom port. In-situ measurements of the radiation pattern of the viewing beam revealed a spatial resolution better than the initial design due to over illumination of the lens used to focus the beam.

B. Transmission Line

The ECE cabinet housing the receiver and digitizers is located outside the containment wall. Delivery of the radiation to the receiver is accomplished by a 34 ft run of C-band waveguide. Fundamental waveguide sections immediately after the horn provide polarization selection prior to transmission by the oversized section. Two H-plane quasi-optical 90 degree C-band bends give necessary direction changes with minimal loss. A waveguide high pass filter is provided to eliminate the lower mixer sideband. Total insertion loss from plasma to mixer is approximately 10 dB.

C. Receiver

The configuration for 1 Tesla operation consists of a mixer with an intermediate frequency (IF) output of 2-18 GHz (67-83 GHz). The configuration for 2 Tesla operation is very similar except that two mixers are used in order to cover the required range of frequencies (83-114 GHz). During the system design, swept frequency systems were considered but due to the required large bandwidth and maximum sweep rates on the order of 1 GHz/ms, their temporal resolution were deemed unacceptable. Systems using switched fast sources were rejected due to their complexity. The filter bank system offers simultaneous information at all frequencies of interest, thus a spectrum is available with each sampling. Temporally unfolding the ECE spectra with its inherent loss of time resolution is not a factor in the data analysis. Sampling rates up to 20 KHz are possible, allowing fluctuation studies. Using fixed frequency Gunn LOs makes for a quieter receiver easily calibrated with LN₂. Simplicity, reliability and cost were also attractive features.

For 1T operation a Millitech balanced mixer with an integrated 65 GHz Gunn local oscillator (LO) covers the radio frequency (RF) range from 67-83 GHz. The coaxial IF system consists of two Avantek low noise amplifiers each with 30 dB gain, providing input to a 16 way power division network (15 dB loss per channel). Frequency resolution is provided by a filter bank consisting of 16 bandpass filters, each having a 3 dB width of 1 GHz. Krytar crystal

detectors with a sensitivity of 0.5 mV/ μ W and video amplifiers provide signals to the data acquisition. Additional frequency resolution can be achieved by using narrower band filters in the regime of interest. The 2 T systems are identical to the 1T system except that LO frequencies of 81 GHz and 96 GHz are used. For 2 T operation a power divider is used to divide the signal into the two mixers.

D. System Calibration

Calibration of the ECE radiometer on ATF was carried out using a chopped, liquid Nitrogen cooled blackbody source. In order to get an instrument response calibration curve that describes the output voltage of the radiometer in response to an emitting plasma (i.e. eV/volt) a known temperature source with well known emission characteristics is required. A convenient and often used method is known as the Dicke switching technique.⁸ This involves switching the source being viewed by the radiometer between two loads of different temperatures so as to obtain the change in the radiometer output voltage resulting from a change in the input temperature. This was done for the three Mixer/LO front ends covering the frequency range 67-114 GHz, where 67-83 GHz represents the 3rd harmonic for 1 T operation, while 83-114 GHz is the range for 2nd harmonic at 2T.

It is essential that the radiation from the calibration source pass through all the components of the viewing system so that all system losses and frequency responses are included in the calibration. In addition, one must take care to insure that the viewing beam is completely filled by the calibration source. A 7 inch diameter glass vacuum dewar was mounted on a fixture and placed inside the ATF vacuum vessel at R=2.10 m. A three inch thick, seven inch diameter circular piece of Eccosorb CV was placed in the bottom of the dewar and submerged in liquid Nitrogen. The large diameter of the dewar is required because the 3 dB beamwidth of the viewing beam at the horizontal midplane can be as large as 8 cm in diameter. To get a change in voltage corresponding to a change in temperature we chop the viewing beam with a mechanical chopper wheel. So that the beam is effectively switched from a source at a known temperature to a source at a hotter known temperature the top surface of the chopper wheel was coated with the microwave absorber Eccosorb AN-72. By rotating the chopper wheel the viewing system was exposed to alternating hot/cold loads.

A black body source at liquid nitrogen temperature radiates with a peak temperature of about 7×10^{-3} eV, some three orders of magnitude below the design temperature resolution and six orders of magnitude below typical plasma operation. Switching from liquid Nitrogen to room temperature is a temperature change of 1.92×10^{-2} eV. Voltage changes resulting from temperature changes on this order are well below the DC level resulting from the noise power of the IF system. Therefore synchronous detection methods are required. We use a chopper wheel equipped with a wheel position detector which feeds our standard data acquisition system (Camac). This generated a square wave voltage waveform that served not only as a record of the chopper wheel position but provided the modulation frequency used in the Fourier analysis of the voltage-time records. The amount of time and effort required to perform a liquid Nitrogen calibration of a radiometer makes it desirable to have a secondary calibration standard. Toward this end we carried out the cross calibration of noise tubes with respect to liquid Nitrogen. The chopper frequency was typically about 12 Hz, such that about 130 complete hot/cold cycles were recorded during each shot. About 30 shots were recorded per session. The frequency was varied to check for any chopper frequency dependence in the n=1 amplitudes but no dependence was found.

Initially the n=1 amplitudes for cosine and sine components at the averaged chop frequency were calculated using an integral number of periods. The calculated phase ($\tan^{-1}(A_{\sin}/A_{\cos})$) was used to help determine the IF gain necessary to observe adequate voltage output response to the chopped loads. If the IF gain was not sufficiently high then the calculated phase plotted as a function of channel number showed a random distribution. The gains were adjusted until a flat phase response was observed. The gain could not be set arbitrarily high (upper bound=70 dB) due to the need to keep the point contact diode microwave detectors in the square law regime for both the liquid Nitrogen and noise tube signals. The n=1,2,3,4,5 sine and cosine Fourier coefficients were extracted from the raw data and averaged to recreate the average waveform. Twice the amplitude of the wave was taken to be the radiometer response to the chopped liquid Nitrogen load.

III. Results

For 2 T operation with ECH only (approximately 200 kW), the optically thick second harmonic emission is quiescent, decreasing with increasing density. Typical central T_e values of 500 eV are seen at $n_{e0}=10^{13}\text{cm}^{-3}$. Characteristics are similar for NBI discharges. For the NBI discharges heavy gas puffing results in a rapid density rise. The central X-mode cutoff is typically reached within 80 ms of beam turn-on. As the beam power couples to the plasma, the measured emission falls, then rises again.

The ECE system viewing third harmonic emission at 1 Tesla on ATF now operates routinely. Since the emission is optically thin, the approach successfully used by Talmadge¹ on Heliotron E is used in the data analysis. Basically the approach consists of unfolding the third harmonic ECE, which depends on T_e and n_e , to find T_e . To accomplish this we use the electron density as measured by the microwave interferometer. When this is done with the system absolutely calibrated as described above, a measurement of T_e results which can then be compared with Thomson Scattering measurements. To date the technique has primarily been applied to emission from near the center of the plasma. For 1 T operation with ECH only (approximately 200 kW), the optically thin third harmonic emission is quiescent, decreasing with increasing density. Typical central T_e values of 600 eV are seen at $n_{e0}=10^{13}\text{cm}^{-3}$. For NBI operation, the electron temperature again decreases as the electron density increases. As the central electron density exceeds $1.5 \times 10^{13}\text{cm}^{-3}$ refractive effects result in the coupling of the viewing beam to the isotropic background and localization of temperature information becomes suspect. For operation with two neutral beams, the density exceeds the X-mode cutoff of $n_{e0}=5 \times 10^{13}\text{cm}^{-3}$ and the viewing beam is coupled to the mod-B averaged emission.

IV. Summary

Second and third harmonic electron cyclotron emission measurements have been carried out on the Advanced Toroidal Facility (ATF) at Oak Ridge National Laboratory. The ECE from both harmonics has been used to measure the central electron temperature during ECH and Neutral Beam Injection. Partial electron temperature profiles have been obtained using the optically thick second harmonic emission at 2 T. The results agree well with the Thomson Scattering data. An in-situ absolute calibration of the system using a liquid Nitrogen source has been performed. The beam pattern of the system has also been measured in-situ and agrees well with theoretical calculations. A beam dump has been installed to reduce the effects of wall reflections.

* Research sponsored by the Office of Fusion Energy, U.S. Department of Energy, under contract DE-AC05-84OR21400 with Martin Marietta Energy Systems, Inc.

References

1. J.N. Talmadge et al., "Central Electron Temperature Measurements by Third-Harmonic Electron-Cyclotron Emission from the Heliotron-E Currentless Plasma," *Phys. Rev. Letts.*, **52**, No. 1 (1984).
2. M. Bornatici, R. Cano, O. De Barbieri, F. Engelmann, "Electron Cyclotron Emission and Absorption in Fusion Plasmas," *Nuclear Fusion*, Vol. 23, No. 9, pp. 1153-1257, September 1983.
3. G. Bekefi, *Radiation Processes in Plasmas*, (John Wiley and Sons, NY, 1966), pp. 318-321.
4. V. H. Rumsey, "Horn Antennas with Uniform Power Patterns Around Their Axes," *IEEE Trans. Antennas and Propagation*, Vol AP-14, pp. 656-658, September 1966.
5. H. C. Minnett and B. M. Thomas, "A Method of Synthesizing Radiation Patterns with Axial Symmetry," *IEEE Trans. Antennas and Propagation*, Vol AP-14, pp. 654-650, September 1966.
6. S. K. Buchmeyer, "Corrugations Lock Horns With Poor Beamshapes," *Microwaves*, pp. 44-49, January 1973.
7. P. J. B. Clarricoats and A. D. Olver, *Corrugated Horns for Microwave Antennas*, (Peter Peregrinus Ltd., London, 1984), pp.97,162.
- 8) R.H. Dicke, "The Measurement of Thermal Radiation at Microwave Frequencies," *Rev. Sci. Instr.* **17** 268 (1946).

Confinement Studies of Heliotron-E Plasmas in Magnetic Surface Variation Experiments

F. Sano and Heliotron E Group

Plasma Physics Laboratory, Kyoto University Gokasho, Uji, Kyoto, Japan

§1. Introduction

Confinement studies of Heliotron-E neutral beam heated plasmas were carried out with reference to magnetic surface variation by using additional toroidal field, B_t , as well as additional vertical field, B_v . The variation of α^* ($= B_t/B_h$; B_h helical field on axis) causes mainly a change in mean plasma radius a_p and in rotational transform $\iota(r)$, while that of β^* ($= B_v/B_h$) causes a shift of magnetic axis (Δ_v) and a variation of shear parameter (Θ). In the standard configuration (α^*, β^*) = (0, -0.185), the gross energy confinement time τ_E^G is given empirically as $\tau_E^G[ms] = 13 \cdot \bar{n}_e^{0.53} [10^{14} cm^{-3}] \cdot P_{heat}^{-0.71} [MW] \cdot B^{0.35} [T]$ for NBI plasmas¹⁾ and then the anomalous electron thermal diffusivity χ_e^{an} associated with the above power-degradation scaling is now the crucial problem to be settled urgently. From the viewpoint of confinement improvement in the helical system, therefore, the investigation of confinement properties as functions of magnetic surface quantities such as a_p , Δ_v or Θ is of special importance in order to find out the physical mechanism of anomalous diffusivity. This paper describes mainly the experimental studies of the effects of a_p on transport with special regard to NBI plasmas.

§2. Experimental and Results

Measurements of τ_E^G were made in the (α^*, β^*) map by utilizing a 1-D profile analysis/transport-code (Proctr-Mod) with laser Thomson scattering $T_e(r)$, FIR $\bar{n}_e(r)$, $T_i(0)$ (CXRS:OVIII), and other diagnostics. Figure 1 shows typical time evolutions of \bar{n}_e , P_{bol} and P_{inj} and the laser timing profiles $\bar{n}_e(r)$, $T_e(r)$ at the magnetic configuration of (α^*, β^*) = (0.05, -0.192).

When we assume the confinement scaling of the standard configuration as the general reference, it was found from the α^* -scan databases that when $\Delta_v \sim 0$ ($\beta^* = -0.185$) or $\Delta_v \sim -2[cm]$ ($\beta^* = -0.192$), the size scaling of τ_E^G is not contradictory with the a_p^2 dependence within experimental error bars despite the very limited variation range of a_p .

In addition, the values of τ_E^G generally increase by $\sim 20\%$ when Δ_v moves from 0 to $-2[cm]$. See Fig.2-(a) and -(b). Here, it should be noted that at large values of α^* (e.g., $\alpha^* \gtrsim 0.1$ at $\beta^* = -0.185$ or $\alpha^* \gtrsim 0.05$ at $\beta^* = -0.192$) the increase in a_p is suppressed by the carbon protector rods of the vacuum vessel, leading to a decrease in a_p with increasing α^* accompanied by a limiter discharge.

On the other hand, it was found from the β^* -scan databases that the a_p dependence of τ_E^G , accompanied by the magnetic-axis shift, deviates to a large extent from the a_p^2 scaling (Fig.3). When $\tau \propto a_p^2/\chi$ is assumed, the above findings reveal that the effective χ_e^{an} is insensitive to the α^* -scan variations of magnetic-surface quantities while that is sensitive to the β^* -scan variations of magnetic-surface quantities. From drift-orbit theory, the confinement of deeply-trapped particles in Heliotron E is expected to degrade with the outside shift of the magnetic axis, leading to a possible interpretation as of the β^* -scan dependence. Concerning the loss-cone variation for the deeply-trapped particles, the dynamics of the fast ions injected perpendicularly has been measured using the neutral particle energy analyzer. The observed time-dependent neutral particle flux was compared with the calculated Laplace-transform solution of Fokken-Planck equation, which shows a good agreement on the basis of classical nature of fast ions. The effective confinement time of the injection-energy fast ions can be deduced experimentally both from the steady-state energy spectrum shape and from the beam trun-off decay time of the neutral flux, which suggests a direct indication of loss-cone variation. As shown in Fig.4, the experiment confirms the theoretical expectation.²⁾

In addition to the loss-cone variation, the variation of shear parameter can not be ignored as another important factor affecting the bulk transport. The shear parameter Θ at the plasma periphery ($r \sim 2a/3$) is sustained to be relatively high ($0.15 \sim 0.2$) for the present α^* -scan variation whereas Θ drastically decreases with decreasing $|\beta^*|$. In this connection, the fluctuation-induced transport ($\bar{n}_e, \tilde{B}_\theta$, etc.) is now under study.

§3. Summary

In conclusion, the present experimental data are consistent with the a_p^2 scaling at conditions where "good heating" is sustained with regard to beam orbits.

[Reference]

- 1) F. Sano et al., to be published in Nuclear Fusion Vol.30(1990), No.1.
- 2) K. Hanatani, 44th Meeting of P. S. J., 28a TE10, March 1989, Japan.

$\alpha^* = 0.05$, $\beta^* = -0.192$, $P_{inj} = 2.2$ MW

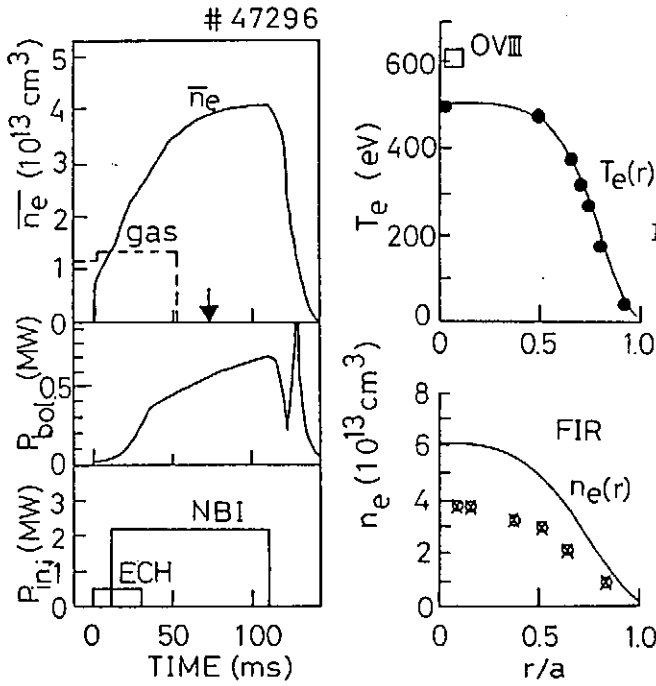


Fig.1 Typical time evolutions of electron density \bar{n}_e , bolometric power loss P_{bol} , injection power P_{inj} , and laser timing profiles $n_e(r)$ and $T_e(r)$. Ion temperature near plasma center was estimated from CXRS (OVIII).

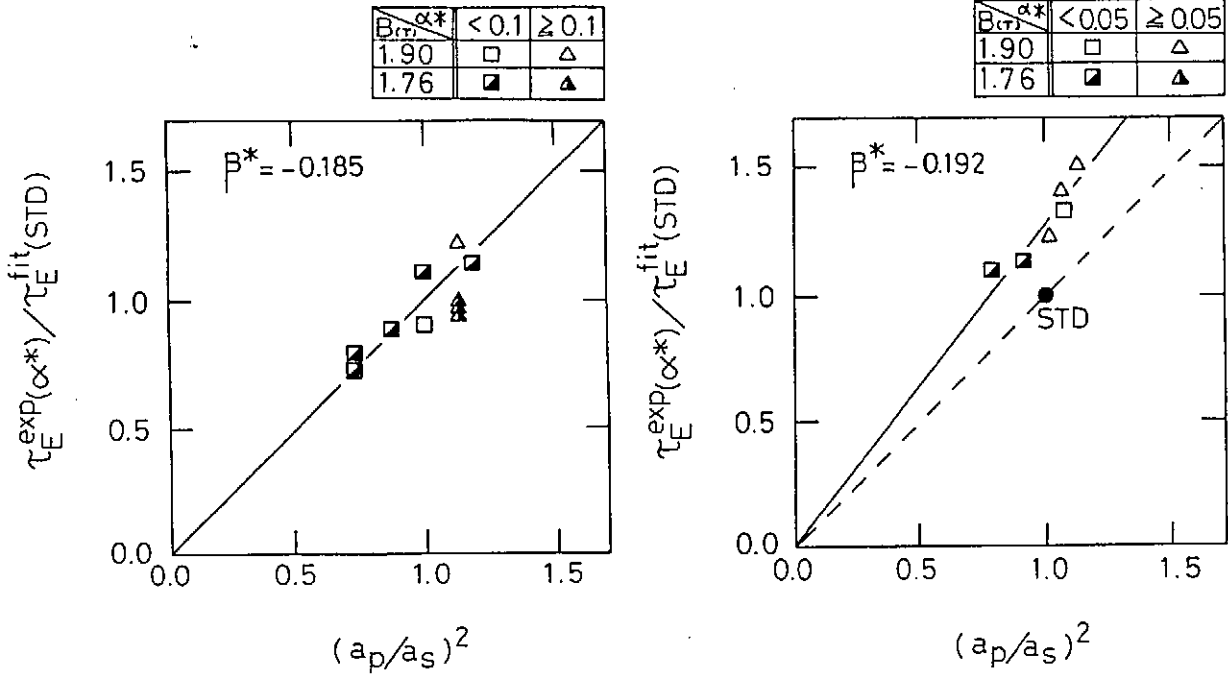


Fig.2 (a) Gross energy confinement time as a function of plasma radius at $\beta^* = -0.185$ ($\Delta v = 0$).
 (b) Gross energy confinement time as a function of plasma radius at $\beta^* = -0.192$ ($\Delta v = -2$ cm).
 (a_s ; plasma radius of STanDard configuration)

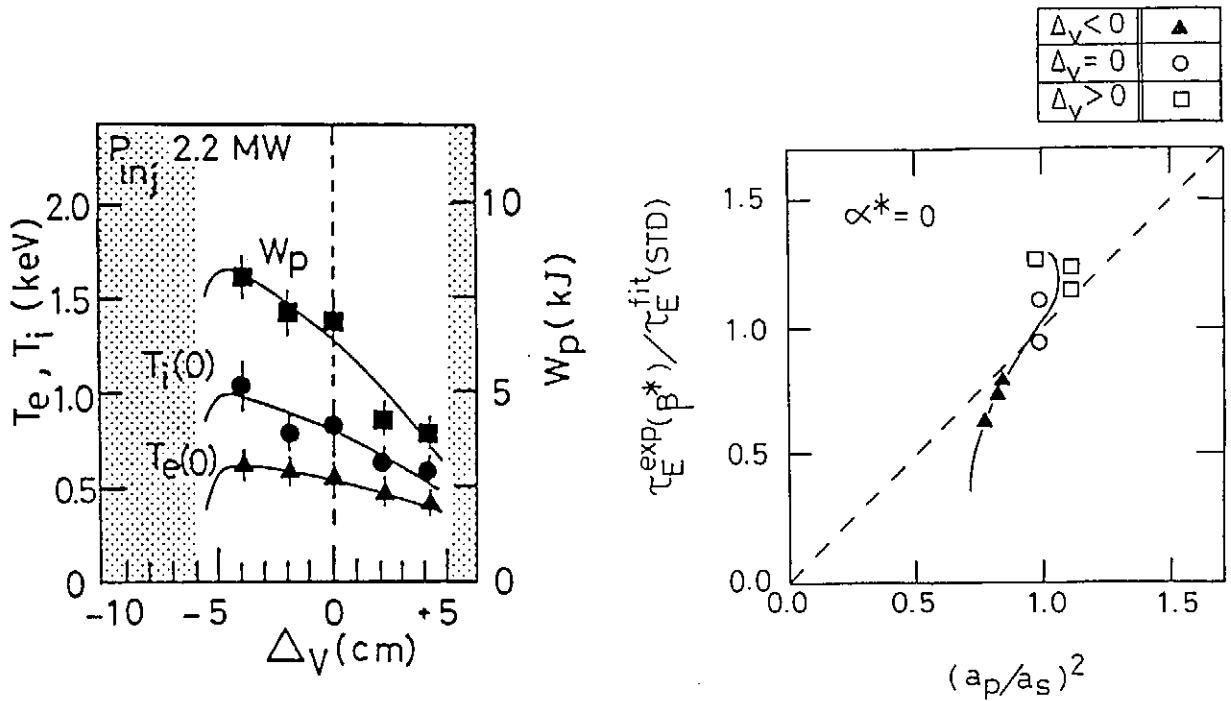


Fig.3 (a) Plasma parameter dependences ($W_p, T_i(0), T_e(0)$) as a function of magnetic axis shift Δ_V .
 (b) Gross energy confinement time as a function of plasma radius at $\alpha^* = 0$ (β^* -scan database).

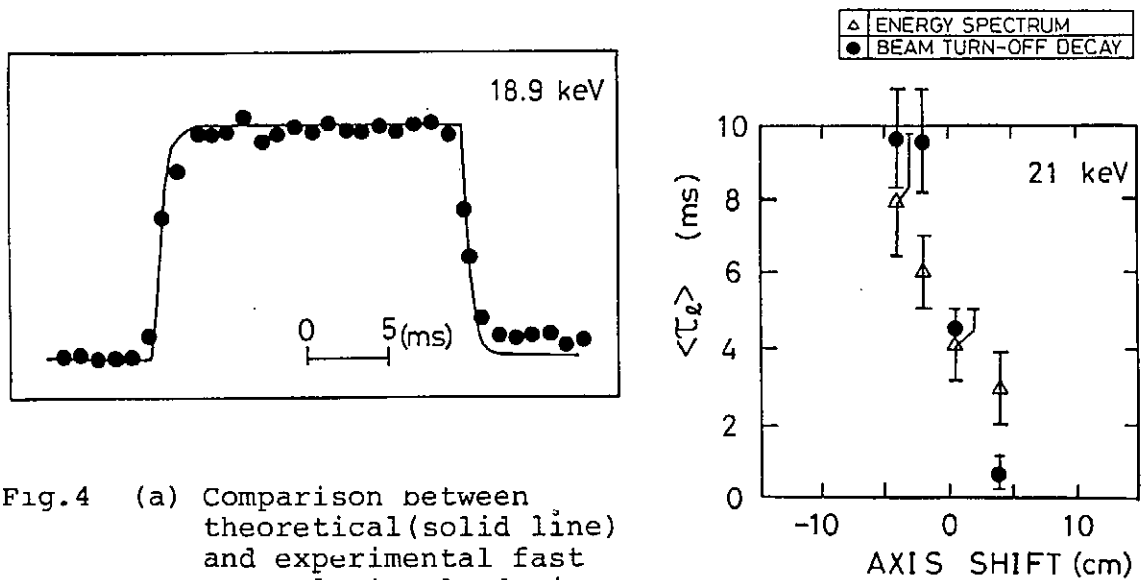


Fig.4 (a) Comparison between theoretical (solid line) and experimental fast neutral signals during perpendicular NBI.
 (b) Experimental effective confinement time $\langle \tau_E \rangle$ of the injection-energy (21.0 keV) fast ions as a function of magnetic axis shift.

Profile measurements in magnetic surface variation experiments/Multiple pellet injection experiments

S.Sudo, T.Baba, F.Sano, M.Sato, K.Kondo, H.Zushi, T.Mizuuchi,
H.Okada, S.Besshou, M.Wakatani, T.Obiki

*Plasma Physics Laboratory
Kyoto University*

Abstract: Temperature and density profile measurements by Thomson scattering method in magnetic surface variation experiments are shown in Part 1. The density profile becomes peaked when α^* ($\equiv B_{T0}/B_{H0}$) decreases, while the central electron temperature changes little. This property is common in NBI plasmas. Apart from α^* value, there is optimum when β^* ($\equiv B_{V0}/B_{H0}$) = $-0.192[\Delta_v = -2(cm)]$. When $\beta^* = -0.192$, there is optimum when $\alpha^* = 0.05 \sim 0.10$. In the case, the edge plasma is observed to expand when α^* is increased from 0 to ~ 0.10 . Density clamping of ECH plasmas ($P_{ECH} \sim 450kW$) is stopped under the condition of $\alpha^* > 0$. Optimum condition is $\alpha^* \sim 0.05$ with $\beta^* = -0.192$. A quasi-steady state plasma with density of $\bar{n}_e = 4 \times 10^{19}m^{-3}$, which is higher than cut-off density of $n_e \sim 3.5 \times 10^{19}m^{-3}$, can be produced under the condition of $T_e(0) \sim 350eV$ in case of $\alpha^* = 0.05$ and $\beta^* = -0.192$.

Multiple pellet injection experiments on Heliotron E are described in Part 2. By multiple pellet injection, regime of $n - T$ diagram is expanded in the high density region. As a result of high nT plasma production, MHD instability has appeared first in case of $B = 1.9T$ under the standard configuration. Peaked density profile with high density ($\bar{n}_e \sim 1 \times 10^{20}m^{-3}$) is achieved by pellet injection, which cannot be obtained only by gas puffing. The behavior of pellet-injected plasma is studied also under the magnetic surface variation.

Part 1. Temperature and density profile measurements in magnetic surface variation experiments.

The α^* ($\equiv B_{T0}/B_{H0}$) dependence of electron temperature and density in the inner region measured by the Thomson scattering system⁽¹⁾ is shown in Figs.1(a) and (b). The electron temperature in the inner region changes little, while the density in that region changes to some extent. The peaking factor η defined as the ratio of $n_e(B5)$ to $n_e(B8)$ is shown as a function of α^* in Fig.2, where $B5$ and $B8$ denotes the vertical positions of $Z \sim 0mm$ and $\sim 150mm$, respectively. From the figure, the density profile becomes peaked when α^* decreases. The candidates of the cause of the peaking are : (a) difference of ϵ changes particle transport (ϵ increases when α^* decreases) due to the neoclassical effect, (b) inward pinch effect depending on α^* , (c) change of particle deposition of NBI depending on α^* , (d) smaller plasma radius a_p results in increase of relative area of the outer bad confinement region (a_p decreases when α^* decreases), which may cause the peaking of the relative density profile.

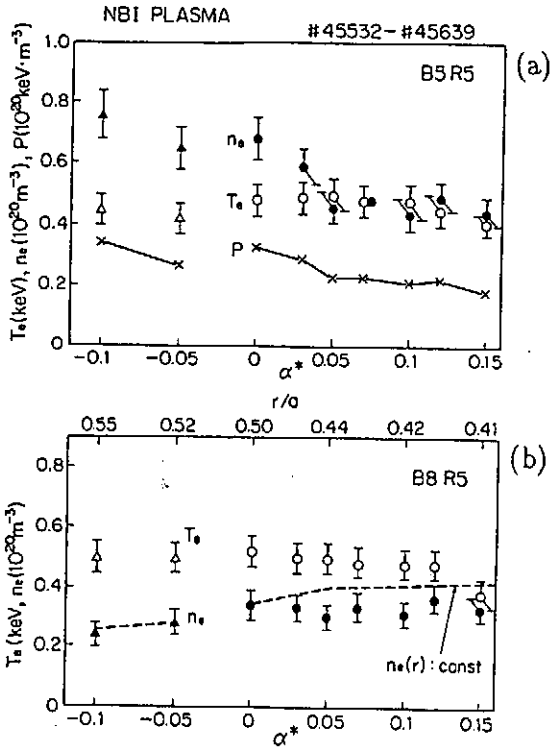


Fig.1 (a) α^* dependence of T_e and n_e at B5R5 ($r/a = 0$ for standard configuration),
 (b) α^* dependence at B8R5 ($r/a = 0.5$ for standard configuration).

In Figs.3 (a) and (b), the electron temperature and density in the outer region are shown also as a function of α^* . When α^* becomes from 0 to negative, the boundary temperature decreases. This is consistent with the change of plasma minor radius. The dotted line indicates the case when the relative electron temperature profile is kept constant with the same central electron temperature. The values of the relative position r/a are also given in the top abscissa axis in the figure. The electron temperature at the fixed position increases little, although the relative position moves inward when α^* increases. This may be attributed to the braiding of the outer magnetic surface or to the existence of effective limiter (vacuum chamber wall or several obstacles such as carbon protector, laser viewing dump).

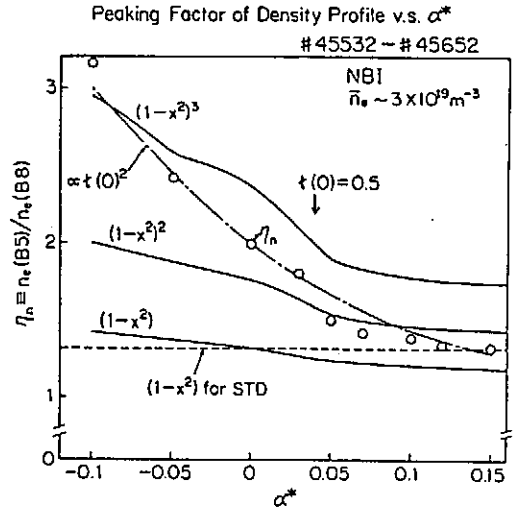


Fig.2 Peaking factor η_n versus α^* .

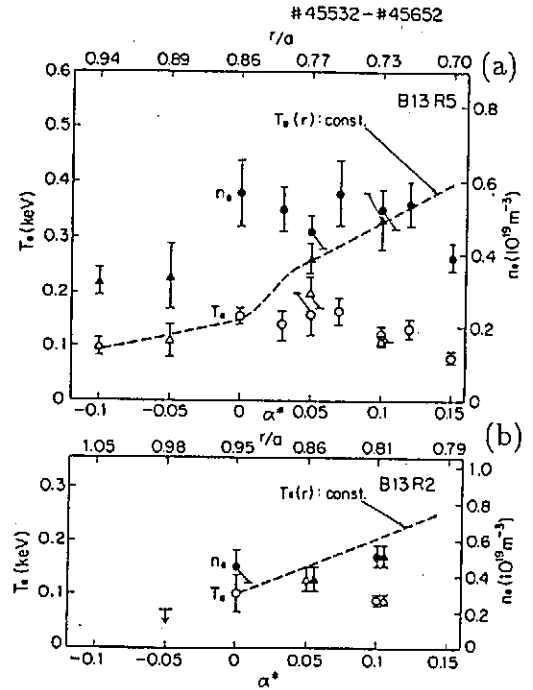


Fig.3 (a) α^* dependence of T_e and n_e and B13R5 ($r/a = 0.86$ for standard configuration).
 (b) α^* dependence at B13R2 ($r/a = 0.95$ for standard configuration).

The β^* dependence of the electron temperature, density, and pressure is studied. The optimum condition is obtained when the magnetic axis is shifted 20mm inward. This optimum condition as to β^* is independent of α^* value. Thus, α^* is varied with keeping β^* constant at $\beta^* = -0.192$ (magnetic axis is shifted 20mm inward). The optimum condition exists at $\alpha^* = 0.05 - 0.1$ with $\beta^* = -0.192$. The fact that the plasma parameters become worse in case of α^* larger than 0.15, is probably due to stronger plasma-wall interaction. From the temperature and density profile measurements, these profiles remain continuous even outside of $\epsilon = 1$, and the temperature gradient at the edge is confirmed to exist at a certain level for $\alpha^* = 0.05$ and $\beta^* = -0.192$. Under the same α^*, β^* condition, the ECH plasma is also optimum, and the density clamping is stopped. The $T_e - n_e$ diagram is shown in Fig.4. A quasi-steady state plasma with density of $n_e(0) = 4 - 5 \times 10^{19} m^{-3}$, which is higher than cut-off density of $n_e \sim 3.5 \times 10^{19} m^{-3}$, can be produced under the condition of $T_e(0) \sim 350eV$.

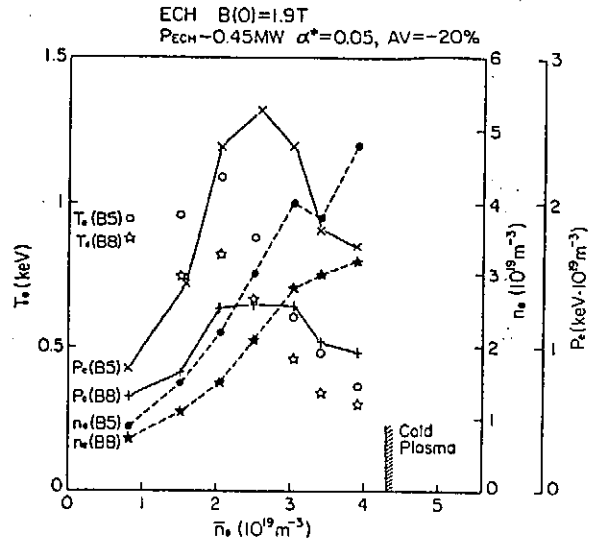


Fig.4 ECH plasma under the condition of $\alpha^* = 0.05$ and $\beta^* = -0.192$ (20mm inward shift of magnetic axis).

Part 2. Multiple pellet injection experiments on Heliotron E.

A six-pellet injector for Heliotron E⁽²⁾ is being continuously operated for one year. It is proved to be useful for refueling and for controlling a density profile.

By multiple pellet injection, regime of $n - T$ diagram is expanded in the high density region as shown in Fig.5. As a result of high nT plasma production, MHD

instability has appeared first in case of $B = 1.9T$ under the standard configuration as shown in Fig.6(a). The stable and unstable region in the flatness factor (defined as the ratio of $\bar{n}_e(CH5)$ to $\bar{n}_e(CH3)$, where CH5 and CH3 denote FIR chord for the outer and central chord, respectively) - \bar{n}_e diagram is shown in Fig.6(b). Peaked density profile with

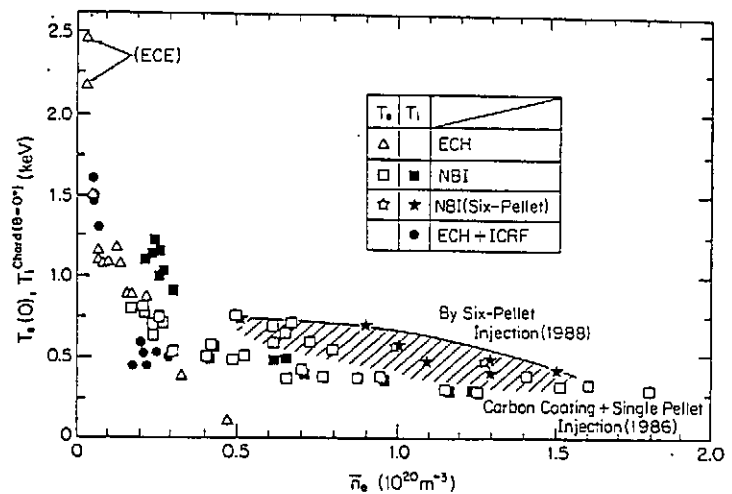


Fig.5 $\bar{n}_e - T$ diagram. Multiple pellet injection expanded nT product.

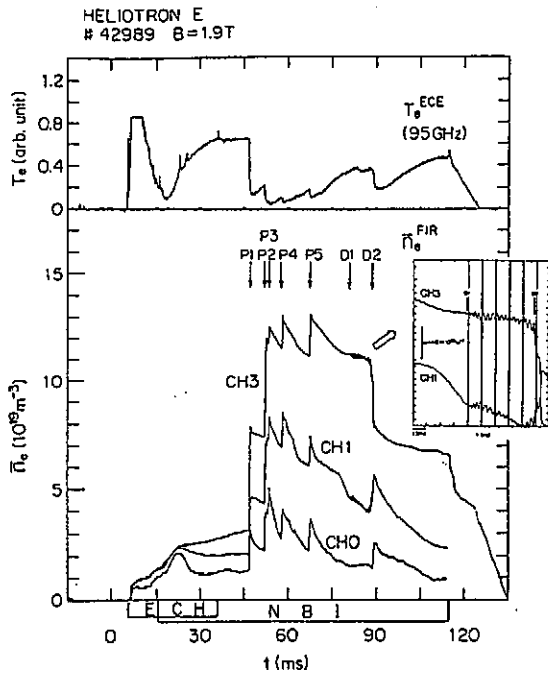


Fig.6(a) As a result of high nT plasma production, MHD instability ($m/n = 1/1$ in this case) has appeared first in case of $B = 1.9T$ under the standard magnetic configuration.

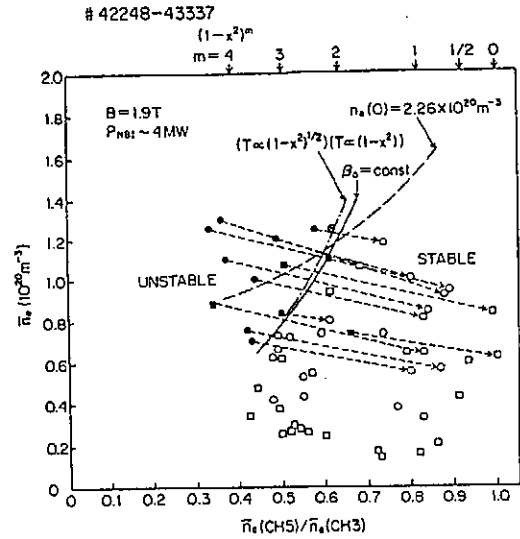


Fig.6(b) Stable and unstable regions in the flatness factor ($\equiv \bar{n}_e(CH5)/\bar{n}_e(CH3) - \bar{n}_e$) diagram.

high density ($\bar{n}_e \sim 1 \times 10^{20} m^{-3}$) is achieved by pellet injection, which cannot be obtained only by gas puffing. The behavior of pellet-injected plasma is studied also under the magnetic surface variation. The particle transport is rather sensitive to α^* and β^* values.

References

- (1) SUDO,S., KONDO,K., MUTOH,T., ZUSHI,H., IIYOSHI,A., UO,K., Jpn. J. Appl. Phys. **22** (1983) 485.
- (2) SUDO,S., *et al.*, in proceedings of IAEA Technical Committee Meeting on Pellet Injection and Toroidal Confinement (Gut Ising, FRG, Oct.24-26, 1988).

Impurity Behavior in Heliotron E

K.Kondo, T.Oda¹, K.Miyake², and Heliotron E group

Plasma Physics Laboratory, Kyoto University, Uji, Japan

1. Faculty of Engineering, Hiroshima University, Higashi-Hiroshima, Japan

2. Faculty of Engineering, Kyoto University, Kyoto, Japan

Abstract

Impurity behavior in the Heliotron E plasma was studied by a VUV spectrometer in the various magnetic configurations with or without carbon coating on the vacuum chamber wall.

§1. Introduction

Impurities in the magnetically confined plasmas have been severe restrictions to obtain high temperature plasma. It is an important task to study impurity species, sources, and production mechanisms. In Heliotron E, it is possible to vary the magnetic surface in size, and to shift its magnetic axis by superposing the toroidal and vertical fields on the helical field [1]. Thus the distance between the outermost closed magnetic surface and the vacuum chamber wall can be controlled by the ratio of the toroidal (B_t) and the vertical (B_v) field to the helical field (B_h). Impurity behavior was investigated by changing the distance between the plasma and the wall, and the surface materials from the stainless steel to carbon by carbonization.

§2. Experimental Setup

Impurity line emissions were measured by a time-resolving grazing incidence spectrometer with a 1024 channel multi-detector [2]. The available wavelength region was 50 Å to 400 Å, where the significant resonance lines from metallic ions are distributed. The dispersion was 0.23 Å/ch at 400 Å and 0.11 Å/ch at 50 Å. The minimum integration time was 10 ms and the integrated charges were digitized in 10 bit full scale. The line of sight of the spectrometer was in the plasma midplane.

§3. Experimental Results

Figures 1(a) and 1(b) show the typical spectra observed in the neutral beam heated plasma with 2.2 MW power at 1.9 T. The parameter $\alpha^*(= B_t/B_h)$ was 0.1. The average electron density was $6 \times 10^{13} \text{ cm}^{-3}$ and the central electron temperature was 450 eV, respectively. The vertical axes are intensities and they are expanded to enhance weak lines. The horizontal axes are the channel numbers corresponding to the wavelength. The prominent lines are indicated their ionic species and wavelengths in the parentheses (Å-unit). The dominant metallic impurities were iron, nickel, and chromium, which were released

from the stainless steel of the wall, and titanium which was evaporated for gettering. The residual light impurities were oxygen, carbon and chlorine. The highest ionization states were *Fe XVIII*, *Ni XVIII*, *Cr XVI*, *Ti XVI*, *O VIII*, *C VI* and *Cl XV*, respectively.

The line intensities of metallic impurities increased as α^* increased to 0.12. Figure 2 shows the dependence of the line intensity on α^* , where line intensities were normalized by the average electron density, because the electron density increased with α^* . The central electron temperatures were 500 eV at $\alpha^* = 0.0$, and slightly low at $\alpha^* = 0.1$, and the temperature profiles were almost same. The central electron densities at $\alpha^* = 0.0$ were $6 \times 10^{13} \text{cm}^{-3}$, and $9.2 \times 10^{13} \text{cm}^{-3}$ at $\alpha^* = 0.1$. Thus the increase of the metallic line intensity more than 10 times was attributed to the increase of the impurity density. Oxygen did not increased as metallic impurities. The outermost closed magnetic surface attached to the chamber wall in α^* larger than 0.05. Applying the carbonization to change wall surface to carbon [3], the metallic impurities except titanium disappeared and carbon line emissions become prominent, as shown in Figure 3. This spectrum was observed in the neutral beam heated plasma with 2.2 MW power at $\alpha^* = 0.07$. The central electron temperature and density were 500 eV and $6 \times 10^{13} \text{cm}^{-3}$, respectively. The metallic impurity lines, however, appeared as α^* increased to 0.1, where the plasma attached to the wall.

§4. Summary

Impurity behavior in the Heliotron E plasma was investigated by a vacuum-ultraviolet spectrometer. Line emissions of metallic impurities depended on α^* . As the plasma attached to the vacuum chamber wall, the enhancement of the line intensities was observed, which suggested that the impurity source rate increased due to the strong plasma-wall interaction.

References

- [1] T.Obiki, *et al.*, This conference, VI-4
- [2] K.Kondo, *et al.*, Jpn.J.Appl.Phys. 27 (1988) 1287
- [3] K.Kondo, *et al.*, Jpn.J.Appl.Phys. 27 (1988) 2368

Figure Captions

Figure 1(a) and 1(b). Impurity spectra in the neutral beam heated plasma with beam power of 2.2 MW. The α^* was 0.1.

Figure 2. The α^* dependence of impurity line intensities normalized by the average electron density.

Figure 3. The spectrum in the neutral beam heated plasma with 2.2 MW power and the wall was carbon coated. The α^* was 0.07.

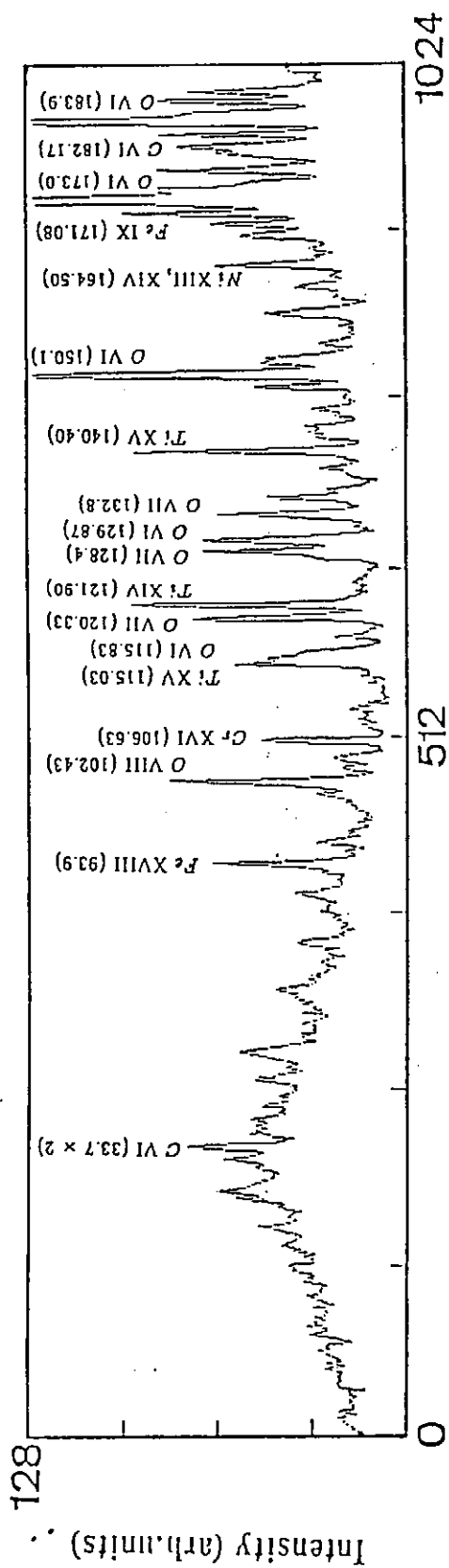


Figure 1(a)

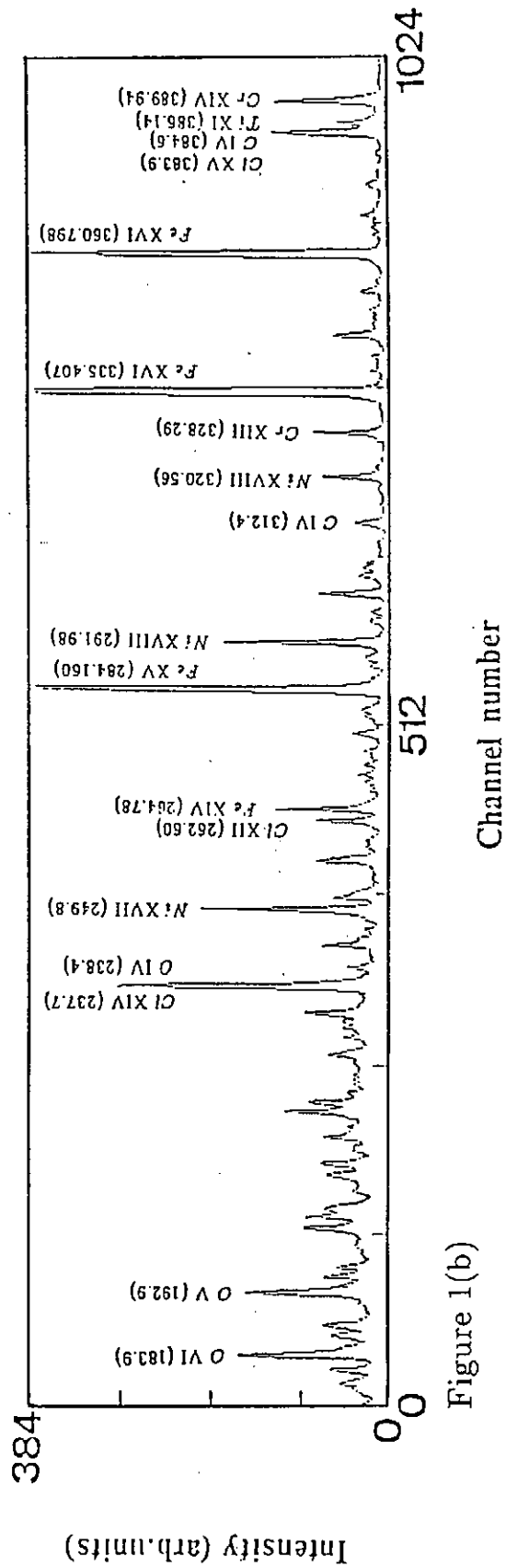


Figure 1(b)

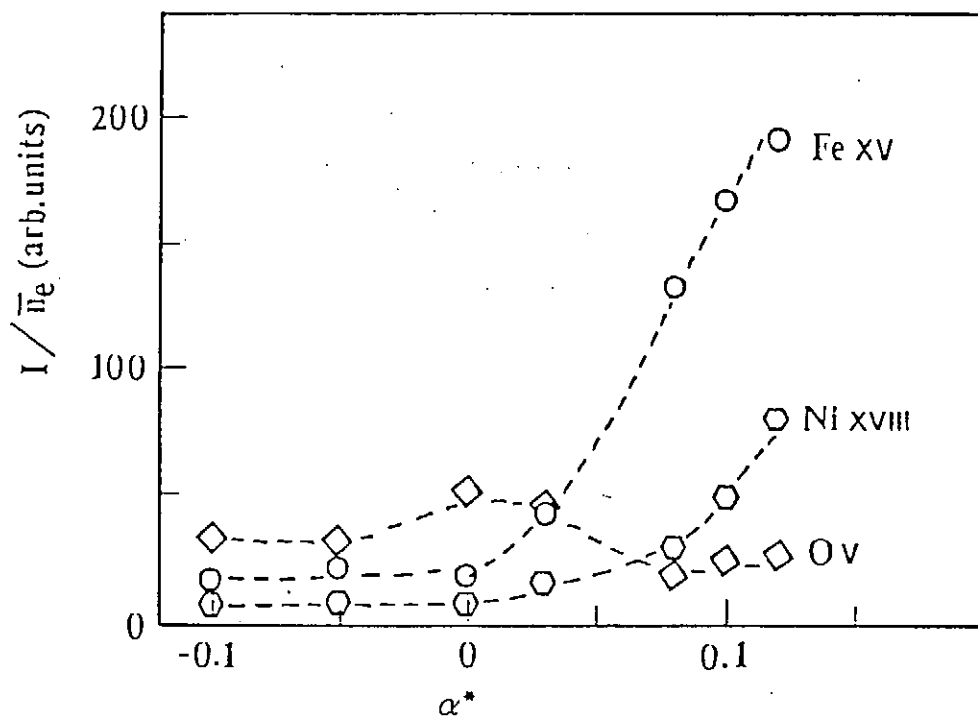


Figure 2

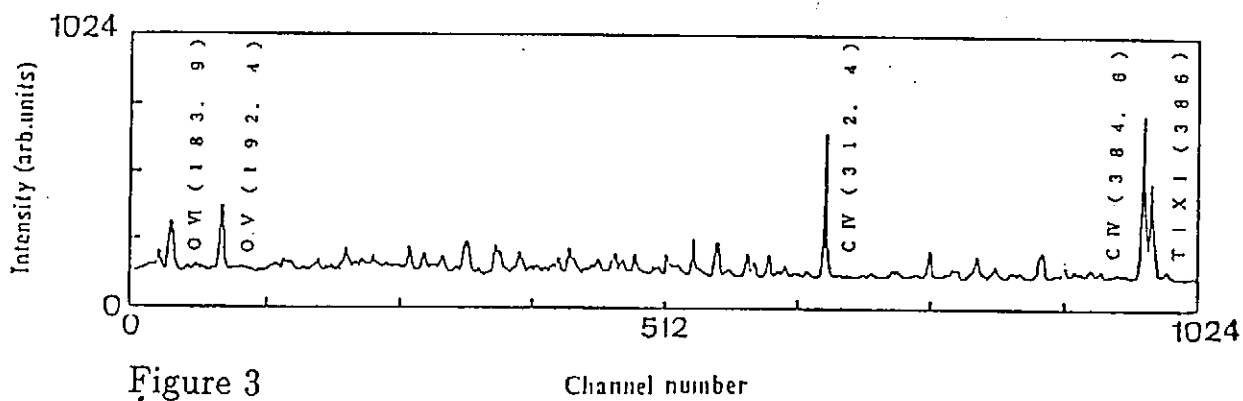


Figure 3

Edge Plasma Study in Heliotron-E

T. Mizuuchi, H. Matsuura¹, A. Komori², M. Harada,
S. Nagai², H. Zushi, F. Sano, K. Kondo, S. Sudo,
S. Sato, M. Nakasuga, Y. Kawai², T. Obiki

Plasma Physics Laboratory, Kyoto University,
Gokasho, Uji, Kyoto, 611 Japan.

¹College of Engineering, University of Osaka Prefecture.

²Interdisciplinary Graduate School of Engineering Sciences,
Kyushu University.

Abstract

Magnetic field configuration of Heliotron E can be controlled by additional toroidal field and/or vertical field. The change of the configuration, especially in the edge region, is experimentally confirmed by measurement of edge plasma profile and by measurement of the vacuum magnetic surface with the beam impedance method.

In the Heliotron E device, the magnetic surface can be produced by the $l=2$ and $m=19$ helical coil. This coil can also produce the build-in divertor geometry or "divertor trace". The numerical trace of the field line shows that these configuration is varied by modifying the strength of the toroidal and vertical field components. The distribution of edge plasma agreed well with that expected from the calculated field structure in the standard configuration.¹⁾ In this paper, we discuss the effects of the magnetic configuration on these edge property by changing the toroidal field(B_{t0}) and the vertical field(B_{av0}).

Edge plasma parameters(density, temperature, etc.) are measured with movable Langmuir probes, a thermal Li beam probe, a laser Thomson scattering system. Figure 1 shows typical profile of edge density, temperature, and floating potential along major radius for standard magnetic configuration($\alpha^*=B_{t0}/B_{h0}=0$, $\beta^*=(B_{v0}+B_{av0})/B_{h0}=-0.185$), where B_{h0} is the toroidal field component produced only by helical coil and B_{av0} is the vertical field for the standard case. In this case, the plasma is produced by ECRH only(about 450kW) and line averaged density is about $1 \times 10^{13}(\text{cm}^{-3})$. $X=0(\text{cm})$ is the center of the vacuum chamber and $X=28.4(\text{cm})$ corresponds to the outer most surface by the field line tracing calculations. Electron temperature is almost constant(about 20 eV) in the edge region. The density profile obtained from two independent methods, the Langmuir probes and the thermal Li beam probe shows good agreement except for the absolute value. As shown in the figure, the edge density shows the exponential decay with two e-holding lengths, about 3 cm for $X < 33(\text{cm})$ and 1 cm for $X > 33(\text{cm})$. The position of this inflection point is about 3 cm outside the calculated outer most surface and moves outward with

positive α^* and inward with negative one as shown in Fig. 2. For $\alpha^* > 0.1$, clear inflection point isn't found. This may be due to carbon protector of bellows of vacuum vessel, which act as material limiter for $\alpha^* > 0.1$.²⁾ This behavior agrees well with that of the point where the connection length becomes short rapidly.^{3),4)} Near the calculated outer most surface, however, no clear change in the density, temperature, or floating potential profile is observed.

The change in the "divertor trace" is examined by measuring the poloidal(θ) distribution of the heat load on the wall with calorimeter array and of the ion saturation current near the wall with probe array. The change of the vertical field(β^*) shows little effect on the distribution but the change of the toroidal field(α^*) shows clear effect on it. Figure 3 shows the poloidal distribution of heat flux and ion saturation current for the "fish-tail" part (outside of the torus). It moves toward the mid plane with positive α^* and departs from it with negative one. This change is consistent with the change of the "divertor trace" position estimated by field line tracing calculations. "Fish-mouth" part (inside of the torus) is also affected by toroidal field.

The attempt to check the change of vacuum magnetic configuration is performed by using beam impedance method.^{5),6)} In principle, the detected emission current of the electron gun under the constant bias voltage is a measure of imperfection of magnetic surface. Figure 4 shows the detected current as the function of the beam-source position along the major radius for two α^* cases. The pattern of the I-X curve shifts as α^* is changed. The distance of this shift is consistent with the change of the calculated magnetic surface and the saturation point of emission current agrees with the inflection point of density gradient. A low impedance region, however, is observed inside of the calculated outer most surface. The position of this region seems to be related with the position of higher rational surface. When we apply a error field and destroy the magnetic surface, however, emission current increases only for $X=10-20$ (cm), where impedance is very high when no error field is applied. Considering that we use isotropic electron source and that the width of banana orbit for deeply trapped particles is a few cm, we think that observed imperfection of magnetic surface may be due to loss cone effect of beam electron rather than due to the nonlinear overlapping of magnetic islands. In order to check this, 2-dimensional measurement and comparison with drift orbit of electrons with various pitch angle against field line⁷⁾ will be needed.

- ref. 1) T. Obiki et al., 12th IAEA conf. (1988)
2) k. Kondo et al., this conference
3) O. Motojima et al., J. Nucl. Mater., 128&129(1984)524
4) k. Nagasaki et al., this conference
5) A. V. Georgievskij et al., 12th European conf.(1985)
6) R. Takahasi. 6th Int. Stellarator workshop (1986)
7) k. Watanabe, this conference

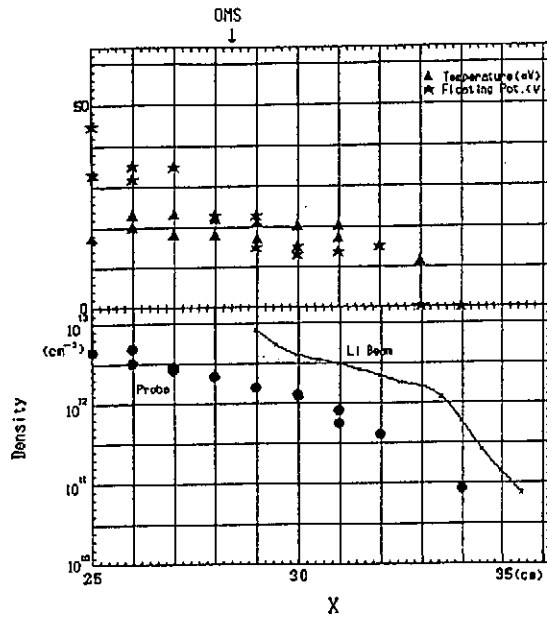


Fig.1 Typical edge plasma profile of Heliotron E for the standard magnetic configuration ($\alpha^*=0, \beta^*=-0.185$). X is the coordinate along major radius in cm unit. Outer most surface exists on $X=28.4$ (cm). \star is floating potential and \blacktriangle is electron temperature. Electron density obtained from Langmuir probes is indicated by \bullet and density from a Li beam probe is indicated by solid line.

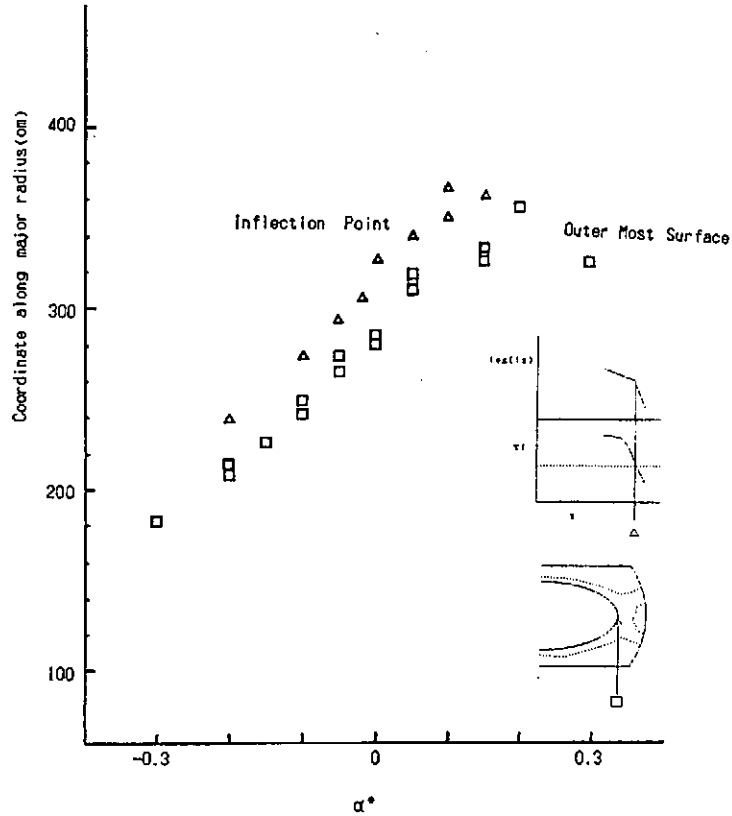


Fig.2 Effect of α^* on outer most surface or the inflection point of density profile. For $\alpha^*>0.1$, clear inflection point isn't found and magnetic surface is limited by high field side wall.

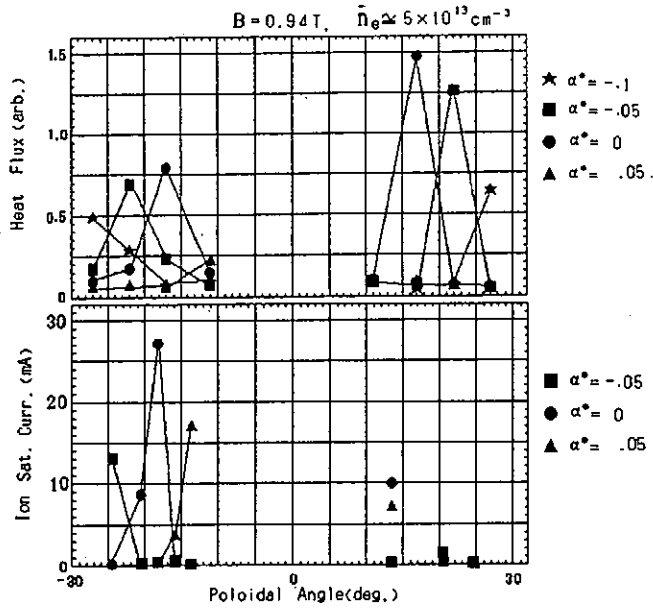


Fig.3 Poloidal distribution of heat flux on the wall and ion saturation current near the wall for various α^* -conditions in the high β experiment. θ is poloidal angle and helical coil exists at $\theta = \pm 90^\circ$ and mid plane is at $\theta = 0^\circ$. Target plasma is produced by about 450kW ECH and heated by 2.5MW NBI. Line averaged density is about $5 \times 10^{13} (\text{cm}^{-3})$.

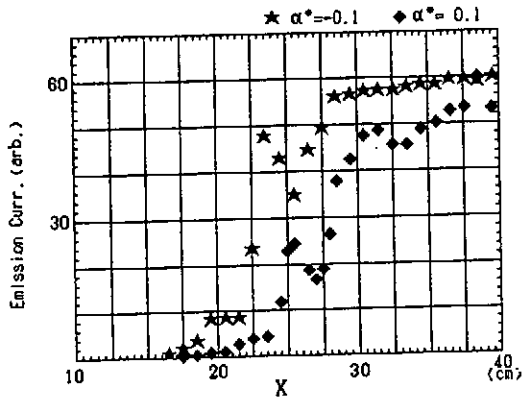


Fig.4 Effect of α^* on the vacuum magnetic surface. X is the same as in Fig.1. Emission current is the measure of the magnetic surface. Data for $\alpha^* = -0.1$ is plotted by \star and data for $\alpha^* = 0.1$ is plotted by \blacklozenge .

RECENT DIAMAGNETIC MEASUREMENTS OF TOROIDAL COIL EXPERIMENTS ON HELIOTRON E

S. Besshou and Heliotron Group*
Plasma Physics Laboratory, Kyoto University
Gokasho, Uji, Kyoto, Japan.

Abstract

This paper describes recent results (Jul.-Nov. 1989) on diamagnetic measurements of Heliotron E toroidal coil experiments. The status of the system is described, including calibration and electronic signal compensation. Recent results are presented showing the behavior of the stored plasma energy or average beta with additional toroidal field $\Delta B_T(\alpha^*)$, additional vertical field $\Delta B_v(\beta^*)$, B_0 , \bar{n}_e and heating powers.

1. Introduction

Diamagnetic measurement is one of the basic measurements to determine the stored plasma energy and average beta in toroidal devices[1-3]. Diamagnetic measurements in Heliotron E re-started since Jul. 1989 to study the effects of toroidal field and vertical field on stored energy or average beta. We have used electronic compensation method throughout this experiments.

2. Diamagnetic System

The diamagnetic system on Heliotron E uses a single turn diamagnetic coil, which is installed in a stainless steel tube in the vacuum chamber [3]. Compensation signal is derived from Rogowski coils mounted on the helical-vertical coil, the toroidal coil bus and auxiliary vertical coil bus. The compensation signals pass through passive filters with time constants $\tau_H = 10ms$ for helical coil Rogowski, $\tau_T = 5ms$ for toroidal coil Rogowski and $\tau_{AV} = 90ms$ for auxiliary vertical coil Rogowski. We add the filtered signals to diamagnetic coil signal at the input of operational amplifier of a gated integrator. Three time constants are decay times of eddy currents in a vacuum chamber, which are determined experimentally.

Figure 1 shows compensated diamagnetic signals, HF coil currents, TF coil currents, and AV(aux.-vertical) coil current. In this case total toroidal magnetic field is 0.95 Tesla. Second harmonic ECRH (53GHz) produces

DIAMAGNETIC FLUX & MAGNETIC COIL CURRENTS

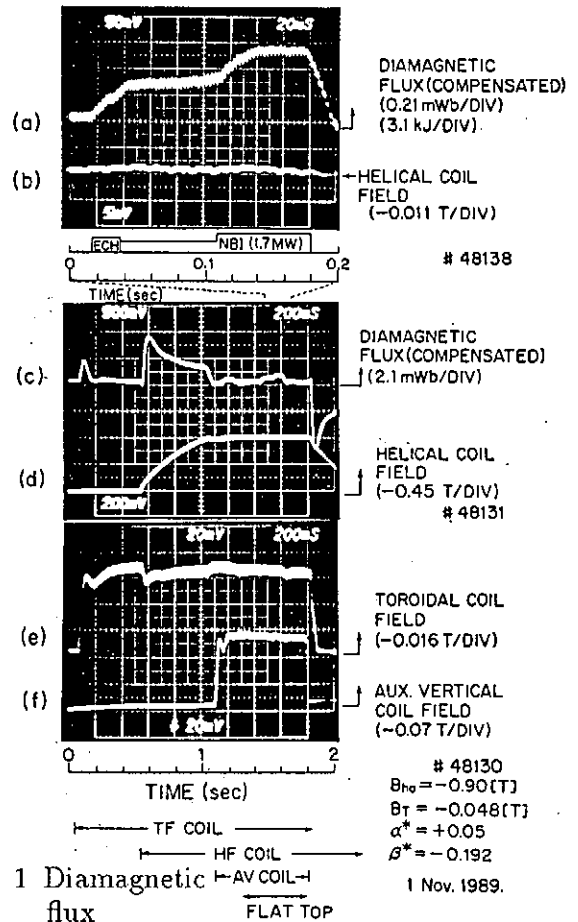


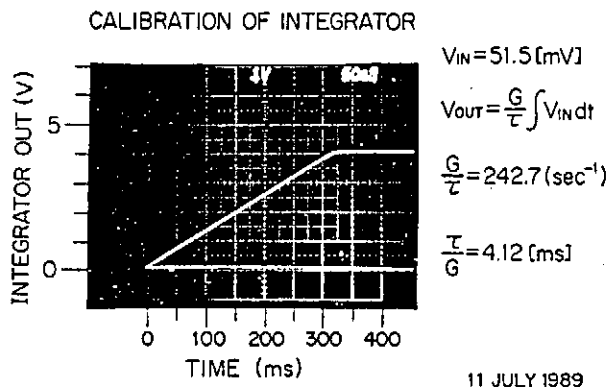
Fig. 1

Diamagnetic flux

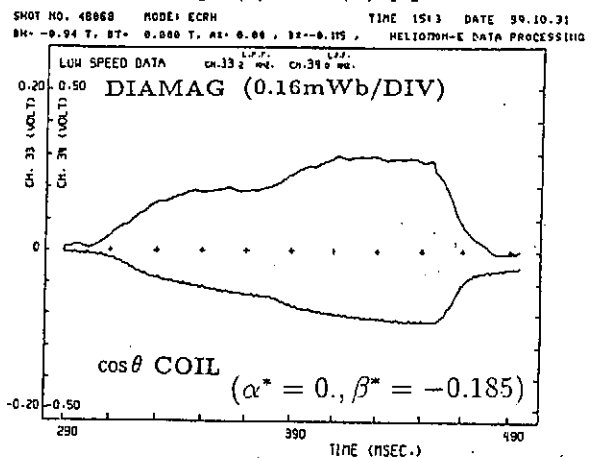
plasma and NBI heats further. Figure 1(a) indicates diamagnetic coil flux of 0.567 mWb at flat top. The observed ripple in helical coil current is 0.28 % from Fig.1(b) and (d). Figure 1(c) is also compensated diamagnetic signal in the whole field duration, showing zeroth order compensation at flat top.

3. Calibration and Raw Diamagnetic Signals.

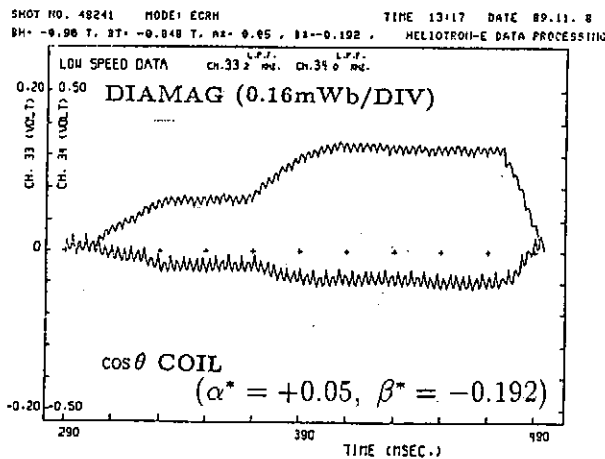
We calibrated the integrator by applying D.C. voltage, determining effective time constant 4.12ms as shown in Fig.2(a). The compensated diamagnetic coil signal is connected to "OKITAC" ADC ch33 with sensitivity 4.12 [mWb/V]. Figure 2(b) is a typical on line diamagnetic signal and $\cos\theta$ coil signal at standard configuration with $\alpha^* \equiv B_t/B_h = 0$ (without toroidal field) and $\beta^* \equiv B_v/B_h = -0.185$ (without auxiliary vertical field). The $\cos\theta$ coil is sensitive to the equilibrium dipole current and also sensitive to the pressure profile [4]. Figure 2(c) shows a raw diamagnetic signal with toroidal field ($\alpha^* = +0.05$) and auxiliary vertical field. Figure 2(d) shows toroidal current ($\leq 1.5kA$)[5], loop voltage and bolometer signals ($\leq 500kW$). Figure 3 shows calibrated diamagnetic flux ($\leq 0.55mWb$), I_p , W_p ($\leq 8.5kJ$) and average beta $\langle \beta_T \rangle^{DIA}$ ($\leq 0.7\%$). Small effect of toroidal current is included by software compensation in Fig.3(c) and (d) [3].



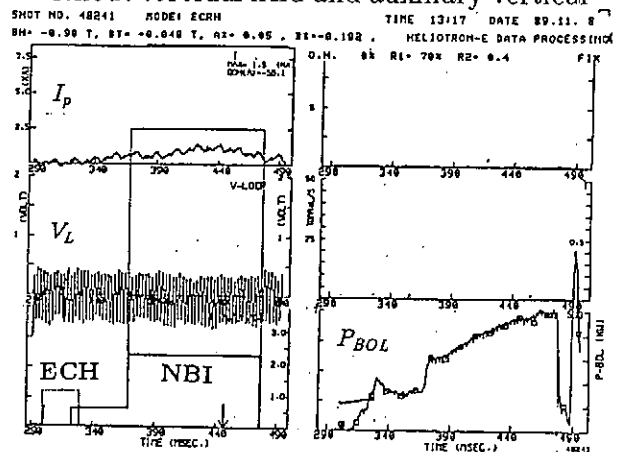
(a) calibration of integrator



(b) diamag coil signal and $\cos\theta$ coil signal without toroidal field and auxiliary vertical



(c) diamagcoil and $\cos\theta$ coil signal with toroidal field and auxiliary vertical field.



(d) I_p , V_L and bolometer

Fig. 2 Calibration and raw diamagnetic signals.

4. Diamagnetic Stored Energy W_p^{DIA} vs. Toroidal Field and Vertical Field in High β Experiments ($B = -0.94T$).

Figure 4(a) shows W_p^{DIA} as a function of additional toroidal field $\alpha^* \equiv B_t/B_h$. Stored energy W_p increases with α^* in $-0.15 \leq \alpha^* \leq 0$. However W_p^{DIA} is almost constant or decreases with α^* in $0.05 \leq \alpha^* \leq 0.15$. Considering that average plasma radius \bar{a}_p increases with α^* , the observed W_p^{DIA} ($4 \sim 10kJ$) shows $\langle \beta_T \rangle^{DIA} \leq 1\%$ for $-0.15 \leq \alpha^* \leq +0.05$. Plasma wall interaction is important for $\alpha^* \geq 0.05$ [6]. Figure 4(b) shows the effect of vertical field (horizontal shift of plasma column) on W_p^{DIA} . Inward shifted case ($\Delta_H \sim -2cm$) has an optimum for W_p^{DIA} .

We have requested NBI power scan twice during this experimental term by changing numbers of ion sources. Figure 5 shows W_p^{DIA} at $B = 0.94T$ as a function of NB port through power. Solid line (A) in Fig.5 is W_p^{DIA} with standard configuration ($\alpha^* = 0, \beta^* = -0.185$) at the line average density $5 \times 10^{13} cm^{-3}$, indicating $W_p^{DIA} \leq 8kJ, \langle \beta_T \rangle^{DIA} \leq 0.9\%$. Broken line (B) in Fig.5 is W_p^{DIA} with inward shifted case ($\alpha^* = +0.05, \beta^* = -0.192, \Delta_H \doteq -2cm$) at the line average density $(3.5 - 9) \times 10^{13} cm^{-3}$, indicating $W_p^{DIA} < 10kJ, \langle \beta_T \rangle^{DIA} < 1\%$.

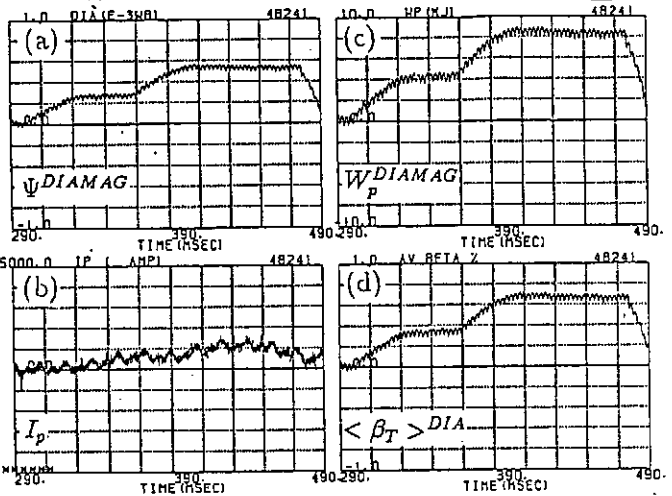
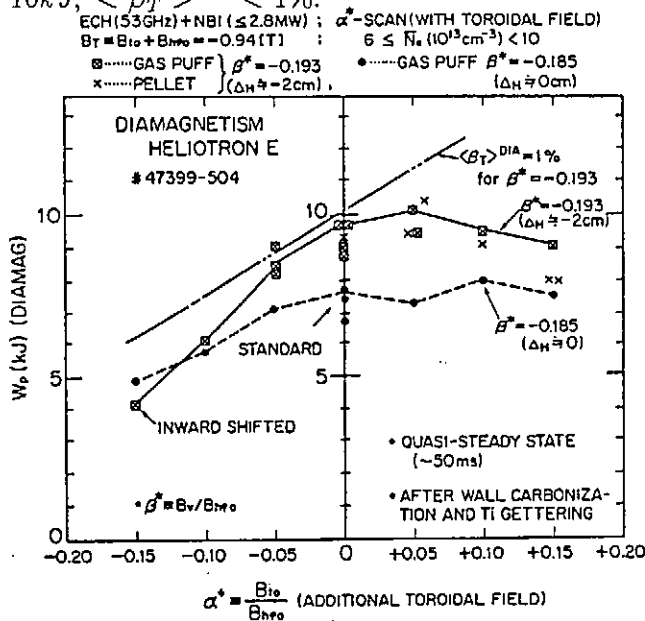
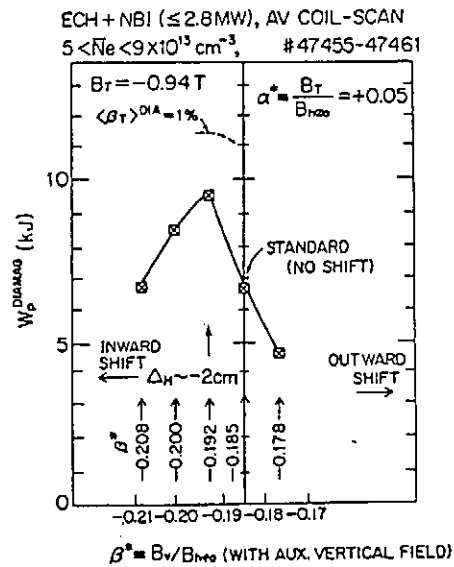


Fig. 3 Diamag flux, W_p^{DIA} , $\langle \beta_T \rangle^{DIA}$, and I_p .



(a) Toroidal field dependence



(b) Vertical field dependence

Fig. 4 Diamagnetic stored energy W_p^{DIA} at $0.94T$

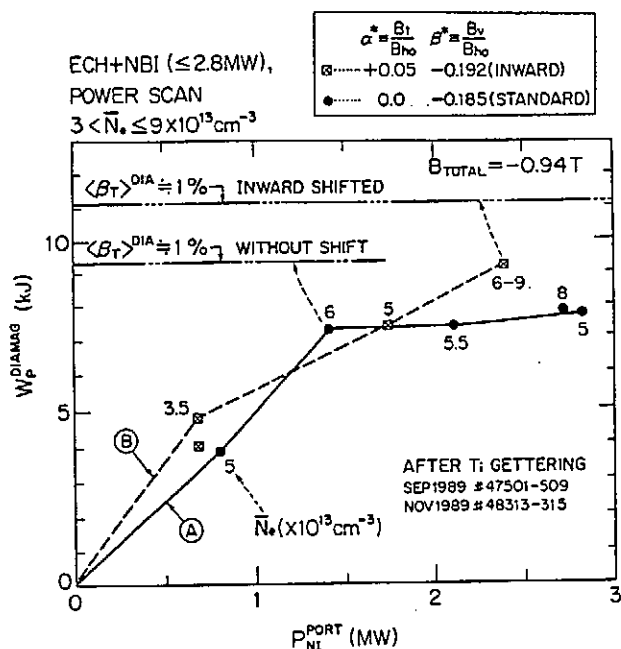


Fig. 5 W_p^{DIA} vs. NB port through power at $0.94T$.

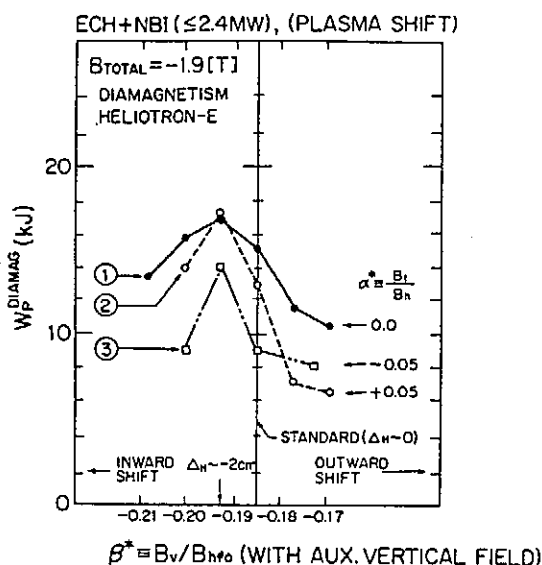


Fig. 6 W_p^{DIA} vs. vertical field (shift) at $1.9/1.76T$.

	$B_{TOTAL}(T)$	α^*	$N_e(x10^{13}cm^{-3})$	$P_{NI}(MW)$
①	-1.9	0.0	8-10	2.4
②	-1.9	+0.05	7	2.0
③	-1.76	-0.05	4	2.0

5. Diamagnetic Stored Energy W_p^{DIA} at higher fields ($-1.9T/-1.76T$).

Figure 6 shows W_p^{DIA} as a function β^* with $\alpha^* = 0, \pm 0.05$ at total magnetic field $1.9T$ or $1.76T$. The W_p^{DIA} has an optimum peak ($14 \sim 18kJ$) at $\beta^* \doteq -0.192(\Delta_H = -2cm)$. Comparing Fig. 6 with Fig. 4(b), the optimum (or largest) W_p^{DIA} is obtained at inward shifted case by $-2cm$, independent of B_0 , and α^* . Thus W_p^{DIA} is quite sensitive to the horizontal position of a plasma column. The W_p^{DIA} optimum at inward shift case seems to support the predicted increment of NB power deposition by inward shift [7].

6. Conclusion

We have studied the effects of toroidal field and vertical field on stored energy W_p^{DIA} by electronically compensated diamagnetic measurements in Heliotron E. The W_p^{DIA} increases with toroidal field $\alpha^* \equiv B_t/B_h$ and \bar{a}_p in $-0.15 \leq \alpha^* \leq 0.0$. The W_p^{DIA} is almost constant in $0 < \alpha^* \leq 0.15$. Additional vertical field realizes optimum W_p^{DIA} when a plasma column is shifted inward by $-2cm$, indicating possible optimum power deposition there. Diamagnetic data available are $W_p^{DIA} \lesssim 12kJ$, $\langle \beta_T \rangle^{DIA} \leq 1\%$ at 0.94 Tesla and $W_p^{DIA} \leq 20kJ$ at 1.9 Tesla with NB port through power $2.8MW$.

References

* see paper of T. Obiki, this meeting.

- [1] Neilson, G. H., ORNL/TM-8767(1983)
- [2] Renner, H., W7-AS Team, invited paper, the 16th European Conference, Venice(1989)
- [3] Besshou S., et al., Nuclear Fusion **26** (1986) 242
- [4] Besshou S., et al., Bull. Jap. Phys. Soc. (1986) 29p BA2
- [5] Besshou S., et al., Plasma Physics **26** (1984) 565
- [6] Kondo K., this conference.
- [7] Hanatani K., Bull. Jap. Phys. Soc. (1989) 28a Te10

Study of Resistive Interchange Mode in Heliotron E

H. Zushi and Heliotron Group

Heliotron Plasma Physics Laboratory, Kyoto University Gokasho, Uji 611, Japan

Abstract

The effects of the magnetic axis shift and the toroidal field on pressure driven instabilities are studied. It is found that the internal disruption caused by the interchange modes is sensitive to the magnetic well formation near the magnetic axis. It is also observed that the additional toroidal field ($B_t/B_h \sim 5\%$) is effective to stabilize it. Dominant instability modes are changed from the $m=2/n=1$ or $m=3/n=2$ modes ($0 < r/a < 0.3$) to the $m=1/n=1$ mode ($0.6 < r/a < 0.7$) as beta increases.

1. Introduction

In order to achieve high beta plasmas in helical systems, the stability of the pressure driven interchange mode should be ensured¹. In Heliotron E, characterized by the high rotational transform and high shear stabilized configuration, the effects of the pressure profile on stabilities of poloidal and toroidal mode numbers of $m=1/n=1$, $m=3/n=2$ and $m=2/n=3$ have been studied²⁻⁶. It was found that these modes caused internal disruptions or sawtooth oscillations depending on the pressure (especially density) profile. The density profile becomes peaked during the neutral beam injection pulse ($\lesssim 0.2$ sec), and then the $m=1/n=1$ mode is destabilized around the $\iota = 1$ surface at $r/a \sim 0.67^{3,4}$. When the beam power is increased up to 4MW, the density profile becomes more peaked. Then the $m=3/n=2$ mode is destabilized near the $\iota = 2/3$ surface at $r/a \sim 0.4^5$. With carbonization of the chamber wall these two modes are stabilized because of the resulted broad density profile, but the $m=2/n=3$ mode is destabilized due to a steep gradient near the $\iota = 3/2$ surface at $r/a \sim 0.8^6$.

In order to study the effect of magnetic configuration quantities on the stability of these modes, the effects of the vertical field B_v and the toroidal field B_t are studied. The vertical field can make the average magnetic well (hill) through the outward (inward) magnetic axis shift. Thus the rational surface near the magnetic axis is stabilized (destabilized) by the well (hill). The toroidal field has two minor effects. One is the effect on the rotational transform and shear. The rotational transform on axis can be changed by B_t as $\iota_o/(1+\alpha^*)^2$ where ι_o is the rotational transform on axis without B_t and $\alpha^* \equiv B_t/B_{ho}$ is the ratio of the toroidal field by the toroidal coils to that by the helical coils. When α^* is positive (B_t is added to B_{ho}), ι_o decreases and global shear $(\iota_a - \iota_o)/\iota_o$ increases. Thus we can adjust the radial location of the most dangerous rational surface to avoid the region where the pressure gradient ∇P is maximum. The other effect is the magnetic well/hill formation by deformation of the magnetic surface near the axis. When $\alpha^* < 0$, the shape of the magnetic surface becomes more elliptic. Since the direction of the elongation is equal to

the direction along which the magnetic field strength is decreased, the magnetic hill is formed. When $\alpha^* > 0$, the shallow well is formed by circular deformation.

In this paper, these effects are experimentally studied. The parameters are as follows; $2 < \bar{n}_e < 8 \times 10^{13} \text{cm}^{-3}$, $200 < T_e(0) < 600 \text{ eV}$, $200 < T_i < 900 \text{ eV}$; $0.94 \leq B_o \leq 1.9 \text{ T}$, $\beta(0) \lesssim 2\%$ and $P_{NBI} \leq 2.5 \text{ MW}$.

2. Experimental Results

2-1. Effects of the vertical field on stability ⁷

For the outward shift (well) case of $0 \leq \Delta_v \leq 4 \text{ cm}$ there were no visible oscillations on the soft X-ray and line density signals at the range of $0.4 < \beta(0) < 1\%$. However, for the inward shift (hill) case MHD activities were observed. The fluctuations appeared on both signals at $\Delta_v \sim -1 \text{ cm}$ and then internal disruptions with $\Delta I_{SX}/I_{SX}$ of $\sim 60\%$ occurred at $\Delta_v \sim -2 \text{ cm}$. At $\Delta_v \sim -4 \text{ cm}$, the amplitude decreased to less than 10% but the sawtooth repetition time reduced to 2–3 ms from about 10 ms at $\Delta_v \sim -2 \text{ cm}$.

2-2. Effects of the toroidal field on stability

The effects of B_t are studied under the fixed condition of B_v . At $\Delta_v \sim 0$, a plasma was stable for $\alpha^* > 0$, but for $\alpha^* < 0$ a plasma became unstable. The fluctuations with $\delta n_l/n_l$ of $\sim 5\%$ were observed on the line density, and finally a disruption occurred at $\alpha^* = -0.1$. The phase inversion radius r_{inv} of this disruption was found around the $\iota = 2/3$ surface near the magnetic axis. This was due to the magnetic hill formation by the elliptic deformation effect of B_t and the peaked density profile depending on α^* ⁸.

At $\Delta_v \sim -2 \text{ cm}$, internal disruption occurred at $\alpha^* = 0$ as was described in §2-1. The radius r_{inv} was close to the $\iota = 1/2$ surface near the axis. The $m=2/n=1$ oscillations were found during two disruptions, but these oscillations disappeared just before the subsequent disruption. For $\alpha^* < 0$ the amplitude of the internal disruption became large, and enhanced MHD activities caused the density gradient and $n_e(0)$ to be lower than that for $\alpha^* \geq 0$. On the other hand, when a small B_t is added ($0.03 \leq \alpha^* \leq 0.08$), these internal disruptions were stabilized. The line averaged density increased up to $4 \times 10^{13} \text{cm}^{-3}$ from $2.5 \times 10^{13} \text{cm}^{-3}$ ($\alpha^* \leq 0$) under the same gas puffing rate. The similar change was observed on the soft X-ray chordal profile. For $\alpha^* \geq 0.1$, however, sawtooth oscillations appeared again. Although the line averaged density increased up to $5 \times 10^{13} \text{cm}^{-3}$, the soft X-ray intensity decreased, which corresponded to the reduction of T_e (Fig.1). At $\Delta_v \sim -4 \text{ cm}$, the same stabilization effects of B_t were observed in spite of the more unstable hill configuration. At $\alpha^* \sim 0.05$ an unstable sawtooth plasma was stabilized.

2-3. Relation between the pressure gradient and the interchange instabilities

Thus it was found that the outward axis shift stabilized a plasma and the inward shift destabilized it. It was also studied that small positive B_t had a significant stabilization effect, but negative B_t and more positive B_t destabilized a plasma. In order to investigate how these instabilities affect the pressure profile a relation between a pressure gradient and MHD activities was studied by varying B_t and B_v . Here we used the gradient of the soft X-ray profile at the rational surfaces $r = r_S(\iota = 1/2 \text{ or } 2/3)$ as a measure of ∇P_e at r_S . All data were taken just before the disruption for unstable discharges and at the

maximum soft X-ray intensity for stable discharges. The profile was fitted by a gaussian profile. As is shown in Fig.2, the maximum gradient near the magnetic axis was obtained at $\alpha^* \sim 0.05$. For unstable plasmas ($\alpha^* \leq 0$ or $\alpha^* \geq 0.1$) it became difficult to obtain the steep gradient. For more unstable case of $\Delta_v \sim -4\text{cm}$, it was also found that the maximum gradient was obtained around $\alpha^* \sim 0.05$. This result indicates that even in the hill configuration the maximum attainable pressure (density) gradient is increased by small B_t through stabilization of interchange modes.

2-4. Finite beta effect on the interchange instabilities

In a heliotron/torsatron configuration, the interchange mode near the magnetic axis can be stabilized by Shafranov shift. Since the rotational transform on axis increases as beta increases, the radius of the rational surface moves towards the axis, and then the mode associated with such rational surface tends to be stabilized by the magnetic well due to the finite beta effect. On the other hand, the interchange mode from $0.5 \times a$ to $0.7 \times a$ is hardly stabilized, because the finite beta well effect (Shafranov shift) is not sufficient and finite beta shear effect is also small. These points were studied in the configuration with $\alpha^* = -0.1$ and $\Delta_v = 0\text{cm}$. In vacuum, there is no well near the axis. Figure 3(a) and (b) show two unstable discharges with different beta values. At low beta of 0.6 % the phase inversion radius for the internal disruption was around the $\iota = 2/3$ surface. The ideal $m=3/n=2$ mode is Mercier stable, but the resistive mode is unstable. At the high beta of 1.5 % the disruption by the $m=3/n=2$ mode did not occur, but the disruption by the $m=1/n=1$ mode appeared. In general, these central modes associated with the rational surfaces near the axis tended to be stabilized as the beta increased, and the modes associated with $\iota = 3/4, 4/5, 1/1$ and $3/2$ became more unstable. This observation agree well with the theoretical prediction⁹, as is seen in Fig.3(c) and (d).

3. Summary

The role of the vertical and toroidal field on stabilization of the interchange modes is studied. It is found that the magnetic axis shift by B_v stabilizes (destabilizes) interchange modes ($m=2/n=1$ or $m=3/n=2$) associated with rational surfaces near the magnetic axis through the magnetic well (hill) formation. Even for a hill configuration ($-4 < \Delta_v < 0\text{cm}$) additional small B_t is effective to stabilize the $m=2/n=1$ mode near the magnetic axis.

Reference

1. B.A.Carreras, G.Grieger, J.H.Harris, J.L.Johnson, et al., Nucl. Fusion 28 (1988) 1613.
2. M.Wakatani, IEEE Trans. Plasma Science PS-9, 243 (1981).
3. J.H.Harris, O.Motojima, H.Kaneko, et al., Phys. Rev. Lett. 53 (1984) 2242.
4. M.Wakatani, H.Shirai, M.Yamagiwa, Nucl. Fusion 24 (1984) 1407.
5. H.Zushi, et al., Nucl. Fusion 27 (1987) 835.
6. M.Wakatani, Theory of Fusion Plasmas, edited by A.Bondeson, E.Sindoni and F.Troyon, p.333, Varenna 24-28, August 1987.
7. H.Zushi, et al., 7th Int. Workshop on Stellarators, Oak Ridge Apr. 1989, 03-3.
8. S.Sudo, this conference.
9. Y.Nakamura, private communication.

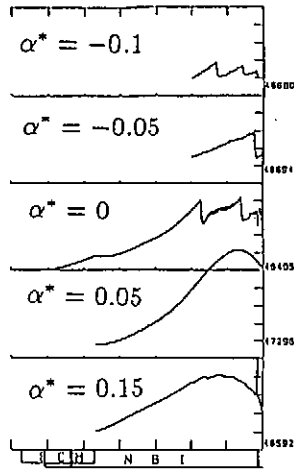


Fig.1 Temporal evolution of the soft X-ray along the central chord for different α^* at $\Delta_v \sim -2\text{cm}$.

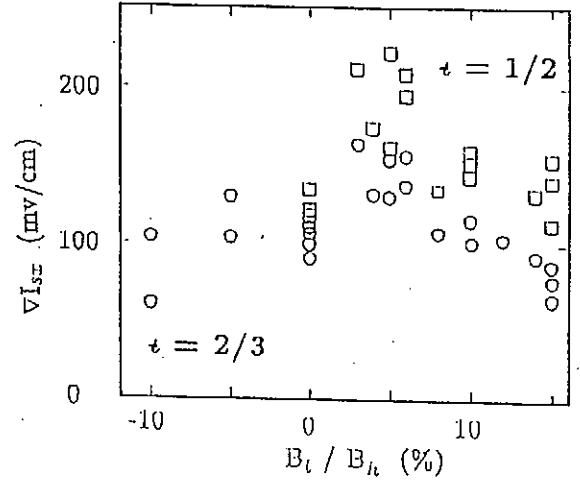


Fig.2 The gradient of the soft X-ray profile at $t = 1/2$ and $2/3$ surfaces versus α^* .

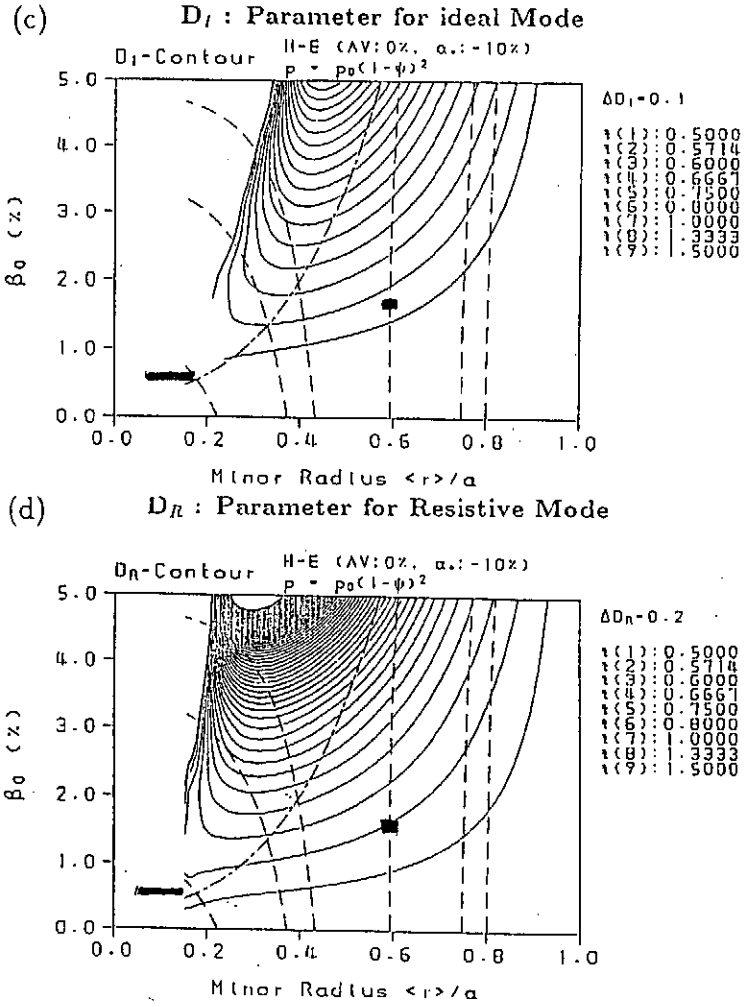
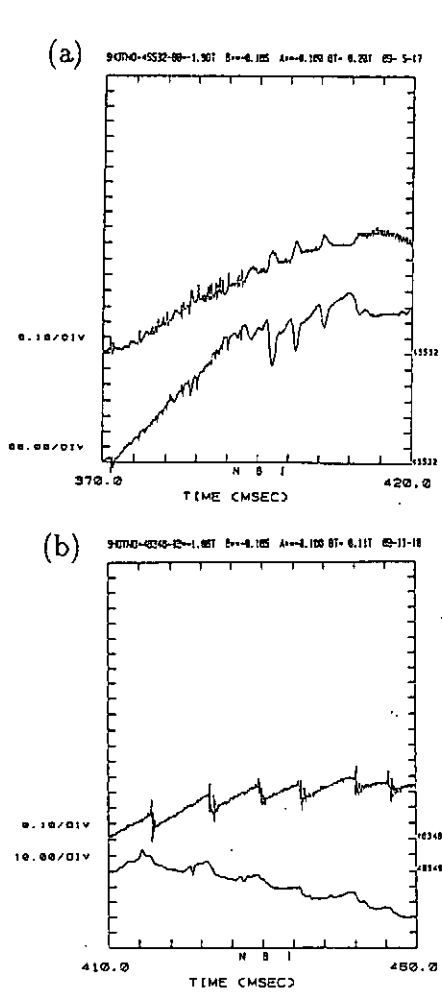


Fig.3 (a) Internal disruptions by the $m=3/n=2$ mode. (b) Internal disruptions by the $m=1/n=1$ mode. (c) Mercier stability boundary, $D_I = 0$. (Solid line) (d) Resistive mode stability boundary, D_R .

Measurement of Magnetic Fluctuations in Heliotron E

M.Harada, H.Zushi, F.Sano, T.Mizuuchi, M.Nakasuga, S.Sudo, K.Kondo, S.Besshou,
M.Sato, H.Kaneko*, O.Motojima*, M.Wakatani, T.Obiki

Plasma Physics Laboratory, Kyoto University
National Institute for Fusion Science*

1. INTRODUCTION

In Heliotron E, it has been found that pressure driven internal disruptions occur in high β plasmas[1]. Then, the burst of magnetic fluctuations has been detected at the internal disruption driven by the $M=1/N=1$ mode associated with the $\iota=1$ surface. In the inward shift cases, internal disruptions are observed near the axis[2][3], where the $\iota=0.5$ surface appears in the magnetic hill region. But in this case, there is no burst of magnetic fluctuations at the internal disruption. This difference of the two cases has been interpreted to depend on the position of the rational surface. However, further studies to analyze these magnetic fluctuations, for instance, Fourier analysis or cross-correlation analysis, have not been done yet.

Magnetic fluctuations are thought to have relation to pressure driven instabilities. Thus, it is important to study the role of magnetic fluctuations on these instabilities, and in order to understand the property of the fluctuations, it is also important to investigate the cross-correlation between \tilde{B} and the other fluctuations. On the other hand, since pressure driven interchange modes are thought to be associated with the resonant rational surface, they are expected to be affected by well and shear profile. The relation between pressure driven MHD activities and magnetic fluctuations is studied by changing the magnetic configuration by the auxiliary vertical magnetic field B_v or toroidal field B_t .

In this paper, the first report on cross-correlation analysis of magnetic fluctuations in Heliotron E is presented, and we discuss the properties of coherent magnetic oscillations related with MHD activities affected by the magnetic configurations. Correlations between \tilde{B}_θ and the other fluctuations($\tilde{n}_e, \tilde{S}X$) are also presented.

2. EXPERIMENTAL EQUIPMENT

The data discussed here are obtained with six magnetic probes located at various poloidal/toroidal positions, FIR interferometer, and soft X-ray arrays. The position of the magnetic probes is at 41cm from the geometrical center, on the chamber wall. Each probe is protected by a metal shield which produces an effective integration of the signal above about 100kHz. The frequency range discussed here is then from a few kHz to 100kHz. The signals are recorded with two different sampling rates, those are, a sampling frequency of 500kHz on a time window of 16ms(8192 samples each channel) and a sampling frequency of 12.5kHz for 320ms. In a similar way, soft X-ray and FIR interferometer signals are recorded and analyzed together. The property of the heliotron magnetic surfaces can be described by following parameters; $\alpha^* \equiv B_t/B_h$ and $\beta^* \equiv B_v/B_h$, where B_h and B_t denote

tion between two density chords cross the $\iota=1$ surface, but no correlation is found with the chord outside the $\iota=1$ surface. This result suggests that the mode of \tilde{n}_e is the $M=1/N=1$ mode, which is consistent with the $\tilde{B}_\theta(M=1/N=1)$. Generally, the $M=1/N=1$ mode seems to become unstable easily at many configurations.

There are also changes in MHD activities depending on the pressure profile. After carbonization of the wall, the density profile changes from a peaked one to a broader one, and then another coherent magnetic oscillations which is identified to be $M=2/N=3$ mode are detected in the frequency range of 15k-20kHz. The mode is consistent with that of internal disruptions in the previous report of the carbonization experiment[7].

Among 20k-100kHz, the other coherent magnetic oscillations whose modes are different from the above are observed in various magnetic configurations and even in low β plasmas which are stable for the low M/N modes discussed here. These high frequency oscillations grow at the early period of the duration of plasmas, and continue till the end. These M/N modes have not been identified though the oscillations are thought to have higher mode numbers, and have no visible coherence with the other measurement systems. Because \tilde{B}_θ has r^{-M-1} dependence, the detected high frequency (and maybe high- M) oscillations are thought to be from the edge region, and may contribute to anomalous transport. The relation between the modes destabilized in low β and the pressure driven resistive interchange mode is under study. To clarify the mode of these high frequency oscillations, we are preparing to install several arrays of magnetic probes.

4. SUMMARY

The coherent magnetic oscillations (frequency ≤ 20 kHz) are studied in currentless NBI heated plasmas by six magnetic probes. The toroidal/poloidal mode numbers (M/N) of oscillations are found to be (2/1, 1/1, 2/3). $\tilde{B}_\theta(M=2/N=1)$ is consistent with $\tilde{S}X$ detected just after the internal disruption near the $\iota=0.5$ surface. $\tilde{B}_\theta(M=1/N=1)$ has a good correlation with \tilde{n}_e , whose mode is consistent with the $M=1/N=1$ mode. $\tilde{B}_\theta(M=2/N=3)$ is observed in the case of a broad density profile by carbonization of the wall. Correlation analysis is useful to identify the mode numbers of these oscillations even if these are not clearly visible in raw signal. High frequency ($20 \leq f \leq 100$ kHz) unknown mode oscillations are detected even in low β plasmas, and are thought to be from the edge region.

REFERENCES

- [1] J.H.Harris, et al, Phys. Rev. Let. 53(1984), 2242.
- [2] H.Zushi, this conference.
- [3] H.Zushi, et al, U.S. Japan workshop on theoretical problems with non-axisymmetric toroidal configurations, Kyoto, Japan, 1989.
- [4] F.Sano, this conference.
- [5] S.Matsuda, et al, JJAP, 14(1975), 87.
- [6] B.A.Carreras, et al, Phys. Fluids. 29(1986), 3356.
- [7] K.Uo, et al, Plasma Phys. Contr. Nucl. Fusion Research, Kyoto. IAEA-CN-47/D-I-1, Vol.2(1986), 355.

toroidal magnetic field strength made by helical coil and by toroidal coils, respectively. B_v is the vertical magnetic field by main and auxiliary vertical coils. The effects of α^* and β^* on the transport will be discussed in ref.[4]. The parameter range is as follows; $2 \leq n_e \leq 8 \times 10^{13}/cm^3$, $300 \leq T_e \leq 600eV$, $0.4 \leq \beta_0 \leq 1.5\%$, $0.94 \leq B_0 \leq 1.9T$, $P_{NBI} \leq 2.5MW$.

3. RESULTS

Pressure driven internal disruptions are found near the $\iota=0.5$ surface in the inward shift case[2][3] as shown in Fig.1. Although no significant change is found in raw signal of magnetic probes at the internal disruption, the coherent magnetic oscillations($\sim 4kHz$) are observed just after the internal disruption(Fig.2b). The toroidal/poloidal mode is identified as the $M=2/N=1$ mode by phase differences of each pair of all probes. There are also oscillations of $M=2/N=1$ mode in soft X-ray signal near the $\iota=0.5$ surface. The mode structure, frequency, and time evolution of $\tilde{B}_\theta(M=2/N=1)$ agree well with $SX(M=2/N=1)$. The amplitude of $\tilde{B}_\theta(M=2/N=1)$ at the $\iota=0.5$ surface, $\tilde{B}_\theta^{2/1}$, can be estimated from the relation

$$\tilde{B}_\theta^{2/1} = \tilde{B}_\theta^{wall} \times (a_{wall}/a_{(\iota=0.5)})^{M+1}$$

, where a_{wall} and $a_{(\iota=0.5)}$ are minor radii at the position of the magnetic probe and at the $\iota=0.5$ surface, respectively. Substituting observed value of $\tilde{B}_\theta^{wall} \simeq 1mGauss$ and $M=2$ into the above relation, $\tilde{B}_\theta^{2/1}$ is estimated about $3.7Gauss$. The island width induced by the mode, W , can be derived to be $\simeq 4cm$ from the relation[5];

$$W = 4\sqrt{\tilde{B}_\theta^{2/1} R/B_0 M \iota'}$$

, and agrees well with the width($3\sim 4cm$) from the observed soft Xray profile.

In this configuration, the coherent \tilde{B}_θ ($\sim 11kHz$) with the $M=1/N=1$ mode is also detected(Fig.2a). This mode appears when the density profile starts to be peaked before the internal disruption, and continues till the end. But there is no corresponding visible oscillations in soft Xray emissions. The $M=1/N=1$ mode in the frequency range of 8k-20kHz is detected in many configurations regardless of the appearance of internal disruptions. But there are some cases in which this mode is stable. The stabilization effect of B_t on this mode is studied in the inward shift case of $\Delta_v \simeq -2cm$, as shown in Fig.3a. It is found that small $B_t(0.05 \lesssim \alpha^* \lesssim 0.10)$ can suppress the $M=1/N=1$ mode, and then the highest ∇p at the $\iota=1$ surface and the maximum stored energy are achieved. Here, we use the gradient of the soft X-ray profile ∇I_{SX} as a measure of ∇p . The magnitude in \tilde{B}_θ at the $\iota=1$ surface increases from $\sim 16mGauss(\alpha^*=0.03)$ to $\sim 170mGauss(\alpha^*=-0.10)$, which corresponds to enhancing MHD activities and results in the reduction of ∇p at the $\iota=1$ surface. It is also observed that \tilde{B}_θ grows again for $\alpha^* \gtrsim 0.1$. Since the shear ι' at $\iota=1$ in vacuum increases from $\sim 9(/m)$ at $\alpha^*=-0.1$ to $\sim 12(/m)$ at $\alpha^*=+0.15$ as shown in Fig.3b, the stabilization phenomena may not be interpreted simply by means of the shear stabilization effect[6]. The other experiment with pellet injection($\alpha^*=-0.1$, and a configuration of magnetic well near the axis), we find a strong coherence between the $\tilde{B}_\theta(M=1/N=1)$ and density fluctuation \tilde{n}_e measured by a FIR interferometer(in Fig.4) though no visible oscillations are found in raw signals of density and soft X-ray. There is significant correla-

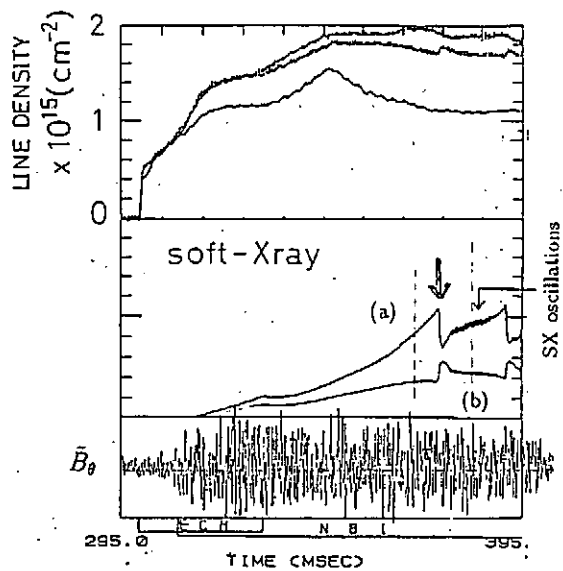
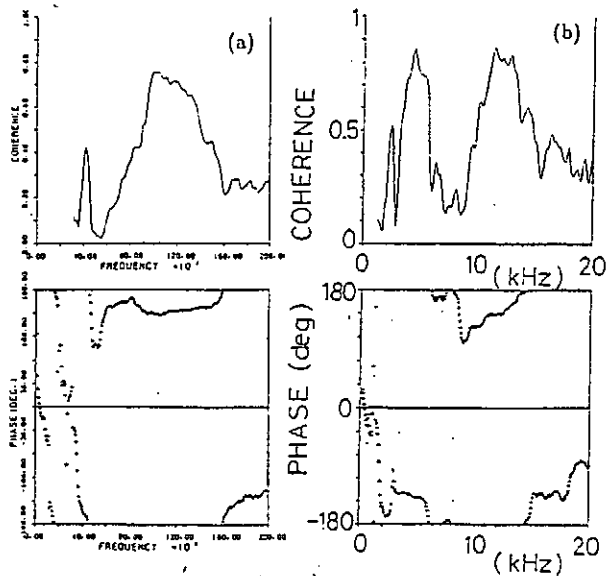


Fig.1

Time evolution of line density, soft X-ray, magnetic probe signal. Internal disruption occurs at an arrow, and SX oscillations are found just after it.



(c) magnetic probe
120°
Fig.2

Cross-coherence and phase between two magnetic probes.
(a) before disruption
(b) after disruption as shown in Fig.1
(c) position of the two probes

vacuum chamber magnetic probe

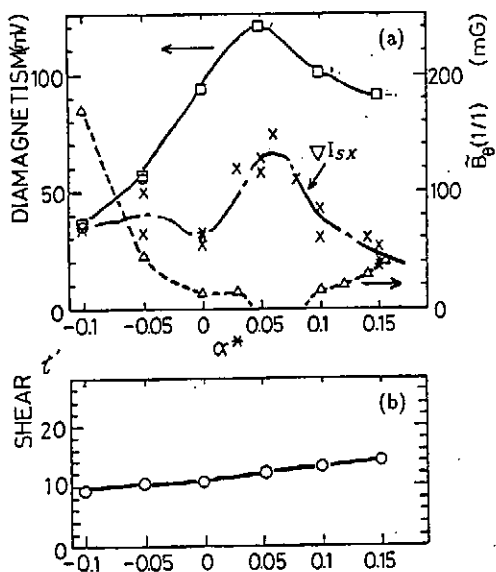


Fig.3

Stabilization effect on $\bar{B}_\theta (M=1/N=1)$ by B_z .
In (a), Δ - amplitude of $\bar{B}_\theta (M=1/N=1)$ at the $\epsilon=1$ surface, \times - ∇I_{SX} as a measure of ∇p , \square - stored energy obtained by diamagnetic loop. (b) Vacuum magnetic shear $\epsilon' (m)$ at the $\epsilon=1$ surface.

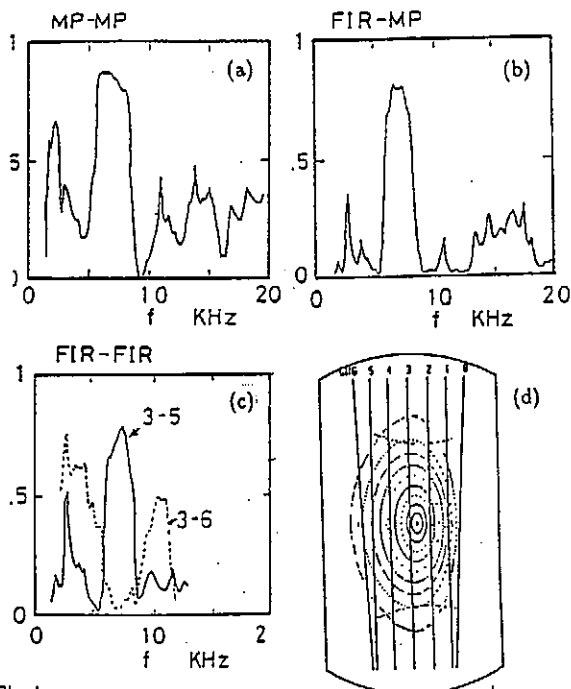


Fig.4

Coherences of $M=1/N=1$ mode between: (a) two magnetic probes, (b) magnetic probe and FIR, (c) two FIR chords, (d) chord of each channel of FIR.

Transport Study of ECH and NBI Plasmas in CHS

H.Yamada, H.Iguchi, H.C.Howe*, Y.Takeiri, S.Kubo, S.Okamura,
R.N.Morris*, D.K.Lee*, and CHS group¹⁾

National Institute for Fusion Science, Nagoya 464-01, Japan
**Oak Ridge National Laboratory, Oak Ridge, TN37831, U.S.A.*

Abstract

Power balance of ECR and NBI heated plasmas in CHS has been analysed using the time-independent transport code PROCTR-mod. The power losses in the ECH plasma are dominated by electron heat conduction which is typically larger than the prediction from the neoclassical theory by a factor of 4, while that for the NBI plasmas is several-tens times larger than the prediction from the neoclassical theory.

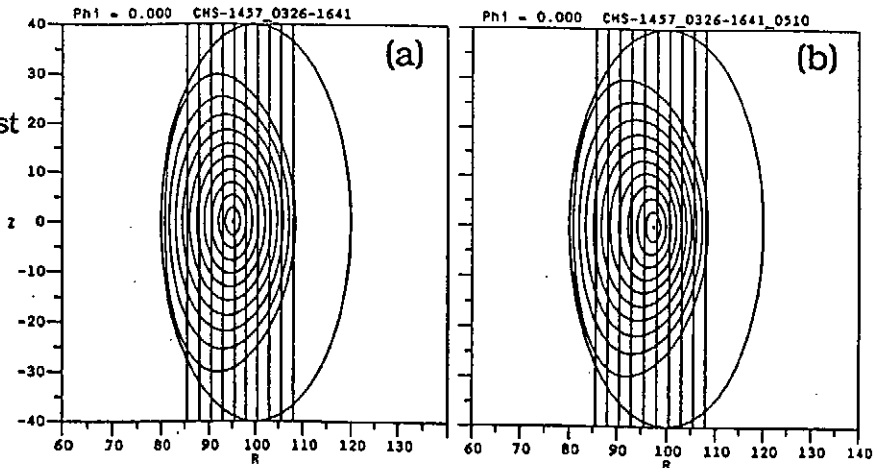
1. INTRODUCTION

Thermal transport in high-power heated plasmas is one of the key issues to be clarified for the fusion research. While the thermal transport in tokamaks is recognized anomalous in particular for electrons, plasmas confined in a helical magnetic field have been frequently discussed from the viewpoint of neoclassical transport theory involving a helical ripple transport. In the CHS, plasmas with the wide range of collisionality have been realized by the ECR and NBI heating²⁾. Comparison of the experiments and the neoclassical transport theory is of much importance and also prerequisite for the discussion about the anomalous transport.

2. MODEL

PROCTR-mod³⁾ is a 1-D time-independent transport analysis code which can describe 3-D geometry intrinsic to helical systems. Electron temperature and density profiles measured by the scannable Thomson scattering system and radiation profile measured by the 11-ch-bolometer array which is normalized by the total radiation measurement⁴⁾ have been involved in the analyses. The ion heat conduction coefficient χ_i is given by the neoclassical heat transport model including the transport due to the helical ripple⁵⁾ with an enhancement factor. Validity of the computed results is checked with the comparison with experimentally obtained stored energy and ion temperature⁶⁾. Since finite β effects on the magnetic configuration are significant for NBI heated plasmas (see Fig.1 (a) and (b)), the 3-D equilibrium code VMEC⁷⁾ is used to get a consistent geometry with the pressure profile estimated from PROCTR-mod.

Figure 1 Magnetic surface geometry described by 14 Fourier components. The value of τ of the outermost magnetic surface is 1.18. Chords of radiation measurement are also shown. (a) Vacuum geometry. (b) When $\langle \beta \rangle = 0.5\%$.



3. ECH PLASMAS

The power balance of ECR heated plasmas with Ti gettering is calculated using the model described above. Heating power deposition profile for 28 GHz ECR (fundamental) is estimated from the area of resonance layer⁸⁾ and that for 53 GHz (2nd harmonic) is assumed to be proportional to $n_e T_e^2$ assuming multi-path absorption. In the code, convection loss is determined by the balance of the global particle confinement time τ_p and neutral particle penetration from the wall. Since a direct measurement of τ_p has not been available yet, τ_p is set larger (10 ms) than the reasonable value. Therefore, a conduction term includes convection loss in part and obtained conduction loss is a pessimistic estimate. Figure 2 shows the electron temperature and density profiles to be analyzed when the plasma is heated by 28 GHz and 53 GHz ECR simultaneously. Figure 3 shows the electron and ion power balances. Power loss is dominated by the electron heat conduction (80%) and χ_e is estimated around $4.0 \text{ m}^2/\text{s}$ at $\rho = 2/3$, which is roughly 4 times larger than the prediction from the neoclassical transport model.

Figure 2 Electron temperature and density profiles of the ECH plasma measured by the scannable Thomson scattering system, where ρ is the toroidal flux averaged minor radius. Fitted functions are used in the analyses.

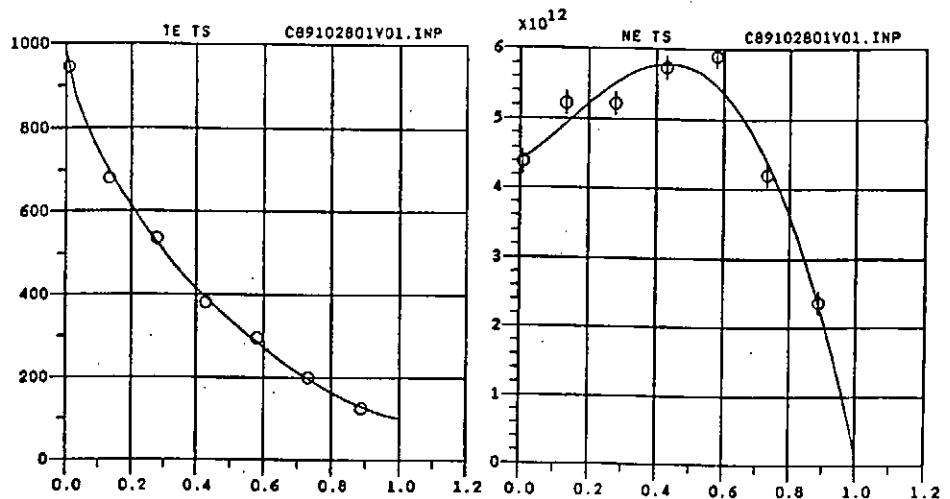
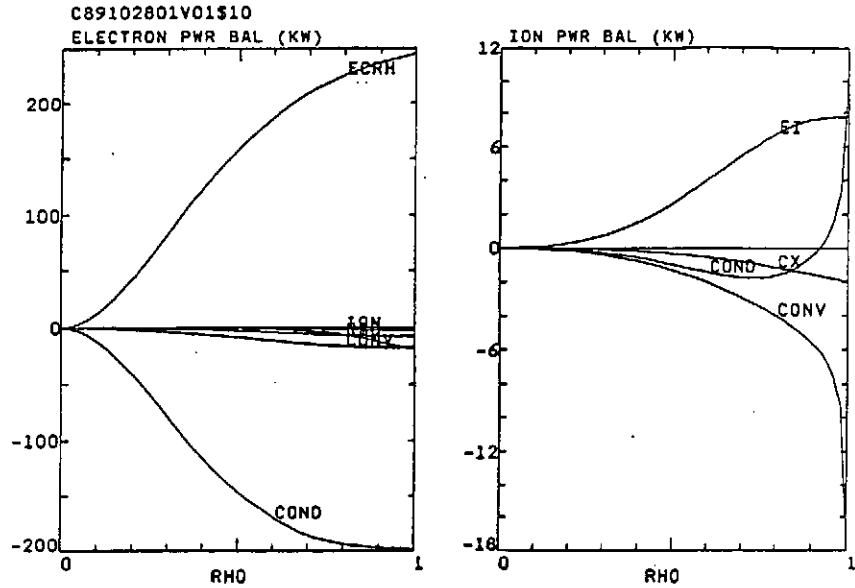


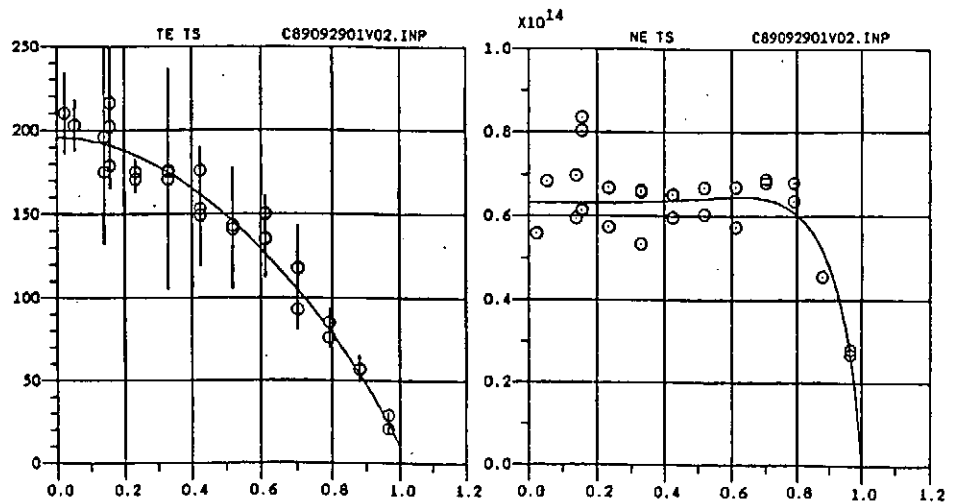
Figure 3 Power balances of electron and ion in the ECH plasma.



4. NBI HEATED PLASMAS

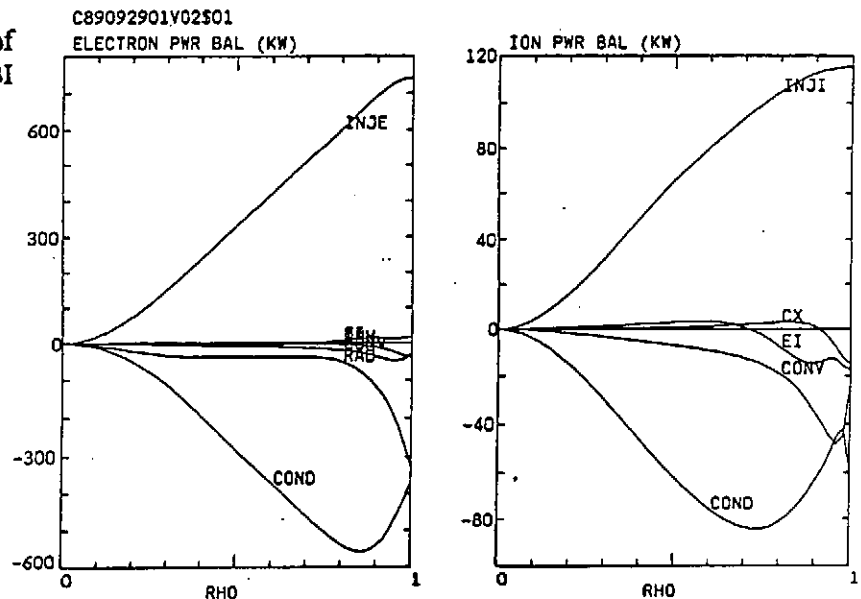
Quasi-steady state plasmas have been obtained with the NBI for up to 250 ms. Figure 4 shows the electron temperature and density profiles at 1.05 T where the target plasma is produced by the 13 MHz ICRF. The initial analysis is done using the vacuum magnetic field and then the finite β equilibrium is reconstructed from the obtained pressure profile (see Fig. 1 (b)). The volume averaged β including the beam pressure is around 0.5 % in this case which agrees with the diamagnetic measurement. Profile analysis is done again using the finite β equilibrium. The power deposition model of NBI takes account of charge exchange loss but orbit loss, which might not be negligible in such a low aspect ratio configuration as CHS and requires further investigation using a Monte-Carlo code. In high density discharges like one shown in Fig.4, more than 95 % of the port through power is deposited in the plasma. Although τ_p is set 7 ms here, the computed results are not sensitive to τ_p unlike

Figure 4 Electron temperature and density profiles of the NBI heated plasma. Fitting is done using the finite β geometry (see Fig. 1(b)).



ECH plasmas because the neutral density is much less than 10^{-5} of the electron density. Figure 5 shows the power balance of the discharge shown in Fig.4. Here χ_t is set as a neoclassical value. The dominant loss channel of energy is conduction for both electron and ion, and the reproduced ion temperature is almost same as electron's, which agrees with the experimental observation. The calculated χ_e at $\rho=2/3$ is around $5 \text{ m}^2/\text{s}$, which is several-tens times larger than the neoclassical prediction.

Figure 5 Power balances of electron and ion in the NBI heated plasma.



ACKNOWLEDGEMENT

This research was in part sponsored by the Office of Fusion Energy, U. S. Department of Energy, under contract DE-AC05-84OR21400 with Martin Marietta Energy Systems Inc.

REFERENCES

- 1)CHS group; M.Fujiwara, M.Hosokawa, K.Ida, H.Idei, H.Iguchi, O.Kaneko, S.Kubo, K.Masai^{a)}, K.Matsuoka, S.Morita, K.Nishimura, N.Noda, S.Okamura, T.Ozaki, A.Sagra, H.Sanuki, T.Shoji^{a)}, S.Sobhanian^{b)}, C.Takahashi, Y.Takeiri, Y.Takita, K.Tsuzuki, H.Yamada
 - a)Plasma Science Center, Nagoya University, Nagoya 464-01, Japan.
 - b)On leave from the University of Tabriz, Tabriz, Iran.
- 2)K.Matsuoka and *et al.*, presented in this conference.
- 3)H.C.Howe, Technical Report ORNL/TM-9537, Martin Marietta Energy Systems, Oak Ridge Natl. Lab., 1985.
- 4)S.Morita and *et al.*, presented in this conference.
- 5)D.E.Hastings, W.A.Houlberg and K.C.Shaing, Nucl. Fusion, **25** (1985) 445.
- 6)K.Ida and *et al.*, presented in this conference.
- 7)S.P.Hirshman, W.I.van Rij, P.Merkel, Comput. Phys. Comm. **43** (1986) 143.
- 8)S.Kubo and *et al.*, presented in this conference.

Effect of Magnetic Axis Shift on CHS Plasma Characteristics

S.Okamura, H.Iguchi and CHS group

National Institute for Fusion Science
Nagoya 464-01, Japan

1. Introduction

When we try to understand phenomena occurring in the laboratory, it is often very useful method to change variable parameters and to investigate the dependence of the results on these parameters. For the study of plasma transport in helical systems, the comparison of the confinement for different magnetic configurations should give us lots of useful informations for understanding the transport mechanism as well as the scaling studies for various plasma parameters.

The poloidal coil system of CHS device consists of four pairs of hoop coils. Three of them are energized by independent power supplies which make it possible to realize a wide variation of poloidal field configurations. It is possible to decompose the poloidal field structure into a sum of multipole components. We chose the values of dipole (vertical) and quadrupole components as two free parameters to determine the poloidal coil current settings. To determine the third free parameter, we set the condition of minimizing the stray field around the machine with which we can reduce the perturbing field that is brought by the magnetic material around the machine.

2. Variation of Magnetic Field Configurations

Dipole component of the poloidal field determines the horizontal position of the magnetic axis, while the quadrupole component changes the elongation of the plasma cross section. In this paper, we report the effects of the magnetic axis shift on the plasma characteristics. The quadrupole component was fixed during these experiments at the value that reduces by half the quadrupole component produced by helical coils.

The range of magnetic axis shift for which we investigated the plasma characteristics was from $\Delta = -11.2$ cm (inward shift) to $+1.6$ cm (outward shift) relative to the major radius of helical coil winding center ($R = 100$ cm). When we shift the magnetic axis out of this range, the plasma parameters fell down. The dominant reason why the operational range of magnetic axis position is shifted inward is the low aspect ratio of CHS device but it should be also noted that the helical winding of CHS has $\alpha^* = 0.3$ pitch modulation. Various characteristics of the vacuum magnetic field configuration change according to the magnetic axis shift. Some quantities have their best value at positions within the range of shift but generally they do not coincide.

First of all, the volume of confinement region which is defined by the last closed magnetic surface is maximum at $\Delta = -2.5$ cm (0.85 m³). It is reduced by 44 % at $\Delta = -11.2$ cm and by 28 % at $\Delta = +1.6$ cm (Fig.1). If the transport coefficient does not depend on any characteristics of magnetic field configurations, the volume of the plasma should determine the confinement dominantly. Secondly, when we consider the MHD activities for high β plasma, structures of magnetic well and magnetic shear are important. The magnetic well exists in the central area of confinement region for the outward shifted case. It becomes smaller as the magnetic axis position moves inward and finally disappears at $\Delta = -4$ cm. The finite β effect generally expands the magnetic well region but such effect is not significant

for the plasma parameters in the series of experiments explained in this paper. The magnetic shear is maximum at $\Delta = -3$ cm and decreases rapidly when the magnetic axis position moves outward.

The behavior of particles which are trapped in the helical ripples is very important in the transport mechanism of helical systems. For the collisionless regime, the drift orbits of such particles deviate a lot from the magnetic surfaces and enhance the transport. Because such drift orbits scarcely change when the poloidal field is varied, the inward shift of magnetic axis makes them coincide better. The position of magnetic axis at $\Delta = -11.2$ cm is for such coincidence. The concept of orbit optimization can be described in another way which discusses the structure of the magnetic field ripple along the field line. Depending on the position of the magnetic axis, the variation of helical ripple changes its pattern. When the magnetic axis is shifted inward the helical ripple has a larger amplitude at the inboard side of torus which is considered favorable in the neoclassical transport model. The structure of helical ripples along the field line is also important when we are faced to the problem of anomalous transport in helical systems. Because the distribution of trapped particles in the torus depends largely on such ripple structure, this aspect of the characteristics of magnetic field configuration must be important for the plasma in the high collisionality regime.

The $l=2$ torsatron type magnetic field generally has a natural divertor. CHS magnetic field has such a divertor structure only for the outward shifted case. For the magnetic axis position $\Delta < -2$ cm, the plasma boundary is determined by the vacuum chamber wall at the inboard side of torus. The configuration with magnetic position $\Delta = -5$ cm is distinctive by the characteristics that the field line along

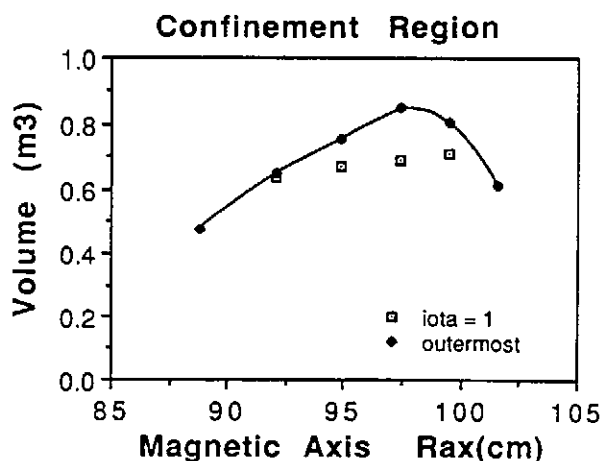


Fig.1 Confinement region

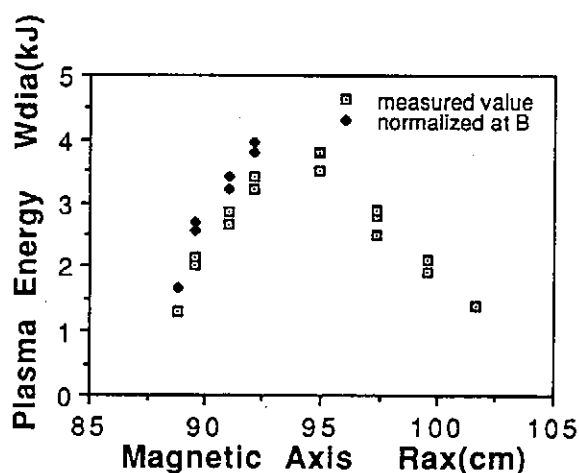


Fig.2 Total plasma energy

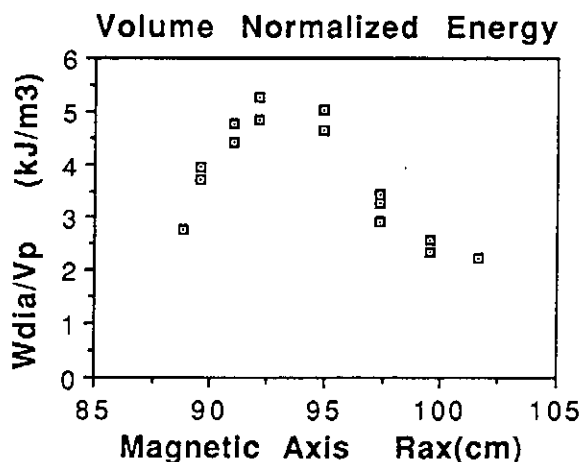


Fig.3 Volume normalized energy

the magnetic axis has no magnetic ripple. It makes the heat deposition profile localized at the center when the ECR heating is applied with the resonant condition adjusted at the magnetic axis.

3. Experimental Results

The confinement characteristics for different magnetic axis positions are investigated first by comparing the maximum energies obtained for each magnetic axis position with the same level of heating power. Figure 2 shows the plasma total energy obtained from the diamagnetic signal for the neutral beam heating of about 1 MW port-through power. The data (squares) for $\Delta > -5$ cm ($R_{ax} > 95$ cm) are all from the experiments with the magnetic field $B_t = 1.05$ T, but the data for $R_{ax} < 92$ cm are with smaller magnetic field because the ECH production of target plasma needed it. The black dots are normalized values for $B_t = 1.05$ T field where we assumed that the total energy scales in proportion to the magnetic field strength. The maximum energy is obtained for $\Delta = -8$ cm which is about 1.5 times larger than the value for $\Delta = -2.5$ cm where the volume is largest. In order to get the transport characteristics which do not depend on the plasma size, we calculated the volume normalized energy for these experiments shown in Fig.3. Though the normalization for the magnetic field strength is not made for these data, the value at $\Delta = -8$ cm is about two times larger than that at $\Delta = -2.5$ cm.

It is usually observed for NBI plasma in CHS that the higher energy plasma is obtained with the higher density. It is true for the data in Fig.2. The factor of two improvement of confinement for $\Delta = -8$ cm compared with $\Delta = -2.5$ cm includes the effects of increased density. Figure 4 shows the comparison of the discharges for different magnetic axis positions with almost same densities and same heating power. Though the electron temperatures are low because the magnetic field is low for these experiments, it is clear that the configurations with different magnetic axis positions have the different electron temperature profiles for the same heating power and the density. It is also important that the difference in temperature is mainly at plasma center which means that the transport in central region is improved by the shift of magnetic axis position.

Figure 5 shows the dependence of central elec-

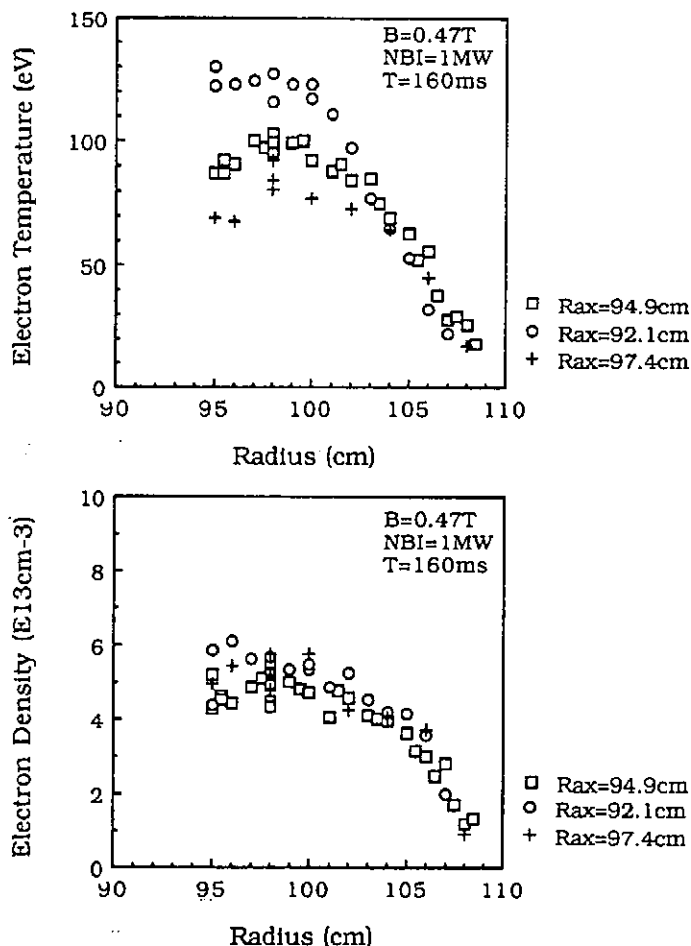


Fig.4 Temperature and density profiles

tron temperatures on the plasma density for different magnetic axis positions with $B_t = 1.05$ T. In this experiment, the port-through power of the neutral beam was kept constant at about 1 MW. When we decrease the density with the same heating power, we expect the increase of the temperature if the confinement does not change so much. But it is not the case in the experiments as shown in Fig. 5. The increase of the temperature is very slight compared with the change in the density. One reason for that is the increase of the beam shine through power. But, because the beam is injected tangentially to the torus in CHS, the shine through power is only 30-40 % even for the low density plasma : $\bar{n}_e = 2 \times 10^{13} \text{ cm}^{-3}$. The decrease of net input power can not explain the slight increase of the temperature. Another possible reason is the degradation of the confinement for the low density plasma. It is usually observed for the NBI heated plasma in helical systems that the electron temperature varies little when the plasma density changes.

When the position of the magnetic axis is shifted, the electron temperature largely changes. The difference of the temperature for two different axis positions is even larger than the difference caused by the change of the density. In Fig.5, the open circles and closed ones are for different injection angles of beams which correspond to the tangential radii of 87 cm and 94 cm, respectively. The difference for these two cases is not significant. It shows that the relation between the magnetic axis position and the beam tangential radius is not important.

Though it is difficult to find out the real mechanism for such effects of magnetic axis shift on the confinement, we can point out some candidates among the magnetic field characteristics explained above. These are the confinement of fast ions and the variations of magnetic field ripple along the field line.

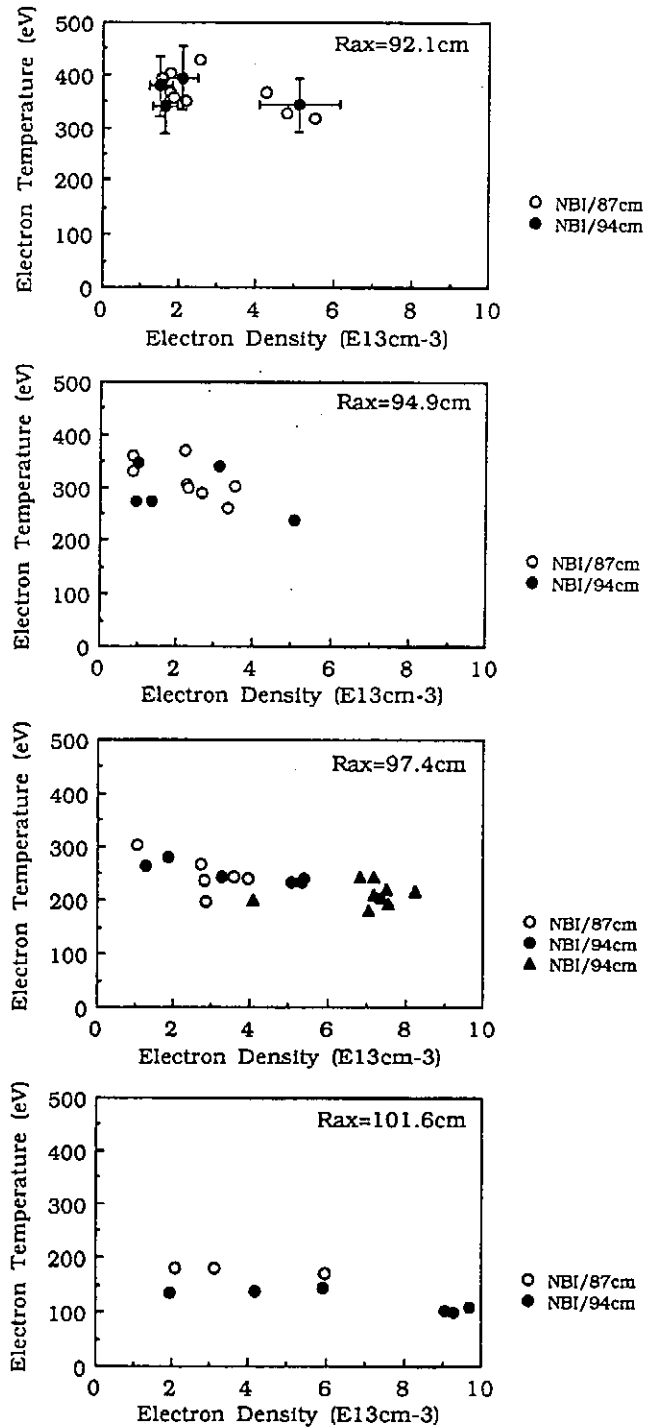


Fig.5 Central electron temperatures

A Study of Radiation Collapse in CHS Plasmas

S.MORITA and CHS group

National Institute for Fusion Science, Nagoya 464-01, Japan

It is found that ECH plasmas without Ti gettering cause radiation collapse at some magnetic configurations in which a plasma-wall distance is extremely decreasing. In NBI plasmas the radiation collapse can be observed even in the Ti-flashed discharges, when strong gas puffing is carried out. Spectroscopic results and analysis indicate that the radiation collapse is caused by the oxygen buildup reaching 10-20% and 3-5% of electron density in ECH and NBI plasmas, respectively. These critical values decrease because of a flat or hollow electron density profile of the CHS plasmas. In addition hydrocarbon pellets are injected into the NBI plasmas to make these phenomena clear. The spherical pellet injection of 0.46mm dia. corresponding to 5% carbon fraction of electron density causes the radiation collapse. However, the pellet injection of 0.32mm dia. corresponding to 2.3% of electron density does not cause the collapse. These results show good agreement with the analysis.

I. Introduction

Radiation collapse is widely known as a phenomenon of a sudden decrease of an electron temperature caused by an increase of radiation loss following impurity buildup. Helical systems are suitable to studying the radiation collapse because magnetic fields are supplied externally and a magnetic structure for the plasma confinement is fundamentally independent of the electron temperature. The radiation collapse has been studied with ECH and NBI plasmas in Compact Helical System (CHS) using spectroscopic and bolometric techniques. In addition, an impurity pellet injection which mixes a known quantity of the impurity with the plasmas is also applied for the study of the radiation collapse.

At present main impurities in CHS are oxygen in both plasmas of ECH and NBI. In following analyses the oxygen is treated as a unique impurity in the CHS plasmas.

II. Radiation collapse of ECH plasmas

Typical example of radiation collapse of ECH plasma in CHS is shown in Fig.1. We can see the radiation collapse happens at $t=22\text{ms}$. After the time emission lines from low-ionized ions such as CIII become dominant. This means the decrease of an electron temperature. The electron temperature is estimated to be less than 10eV at a time after the radiation collapse. The time behaviour of the OV line becomes a good index to observe the radiation collapse. In CHS the phenomenon of the radiation collapse strongly depends on a position of magnetic axes as shown in Fig.2. A plasma-wall distance becomes smaller according to inward shift of the magnetic axis. Most outer magnetic surface is in contact with the inner vacuum wall at a region less than R_{ax} . The large plasma-wall interactions make an oxygen influx rate increase. As a result the radiation collapse is triggered by the buildup of the oxygen level. This phenomenon can be understood also by electron density behaviours (see Fig.3). The electron densities go up with the inward shift of R_{ax} and go down with the outward shift of R_{ax} whereas the electron densities at the first rise are the same in every position of R_{ax} .

The analysis is carried out with calculations of radiation loss from the oxygen atoms as shown in Fig.4, in which the total oxygen level is fixed to 1% of the electron density. The radiation loss from the oxygen

is dominated by Li-like and Be-like stages localizing at $r=(3/4)a_p$. Therefore the total radiation loss becomes sensitive to the electron density profiles. In CHS almost all plasmas of ECH and NBI have a hollow or flat electron density profile. That is a severe condition in the view point of the radiation loss from light impurities. The radiation collapse of the ECH plasmas is described with replacement of plasma particles by the oxygen corresponding to 10-20% of the electron density.

In ECH plasmas the radiation collapse is completely disappeared by the use of Ti gettering (see Fig.5). The radiation level is suppressed within 5kW. In the figure both circles indicate discharges without the Ti gettering and solid circles mean the radiation collapse discharges. We can understand that the Ti gettering drastically makes impurity levels decrease in the case of ECH plasmas.

III. Radiation collapse of NBI plasmas

In NBI plasmas discharges can not be kept for relatively long time without Ti gettering. Then the Ti gettering has been carried out periodically before the first discharge of a day. Comparisons are done with an additional strong Ti gettering. Figure 7 shows the comparison of the NBI plasmas between periodical (solid lines) and periodical plus additional (dotted lines) Ti gettering. The strong gas puffing to raise the electron density causes the radiation collapse even in the periodically Ti-flashed discharge. In this situation the additional Ti gettering is frequently carried out. This additional gettering is useful for suppression of the radiation collapse. However, the effect of the additional gettering is not so large compared with the ECH plasmas. Because the oxygen level gradually increases in proportion to the discharge summation.

The radiation problem of the NBI plasma is relatively severe because the plasma has a high n_e with flat profile. The analysis indicates that the NBI plasmas cause the radiation collapse at oxygen level corresponding to 3-5% of the electron density.

IV. Impurity pellet injection

Plastic HC (hydrocarbon) pellets have been injected to make above mentioned phenomena clear. The impurity pellets injected are listed in Table I. The fraction of the carbon atoms to be injected is ranging over 2-5% of the electron density when the line-averaged n_e of $5 \times 10^{13} \text{cm}^{-3}$ is assumed.

The results are shown in Fig.10. The plasma behaviours are very clear depending on the size of the injected pellets. In the case of $d=0.32\text{mm}$ HC pellet the radiation collapse does not happen, although there are an increase in the radiation loss of roughly 100kW and a small dip in the stored energy. On the contrary the injection of $d=0.39\text{mm}$ HC pellet causes the small radiation collapse. However, the plasma revives after 30ms from the injection since the radiation loss decreases at the same time. The stored energy at the revival after the injection exceeds that of the NBI plasma without pellet injection shown in Fig.10(a). The revival of the plasma is related to the change of $n_e(r)$ due to the cooling of the plasma outer region. It is estimated that the realization of a peaked electron profile brings the decrease of the radiation loss and the increase of the electron temperature.

Complete radiation collapse is caused by the injection of $d=4.6\text{mm}$ HC pellet. The radiation loss observed is roughly 1MW, and it is equal to the input power of the NBI. This radiation level can be interpreted with carbon fraction of 5% of n_e from the calculations shown in Fig.9. This fraction is equal to the calculated percentage listed in Table I.

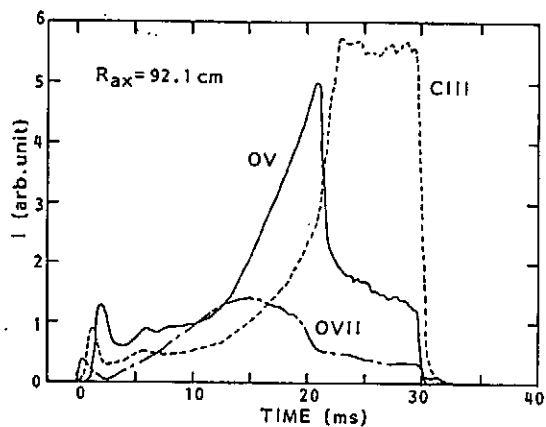


Fig.1 Radiation collapse of ECH plasma in CHS.

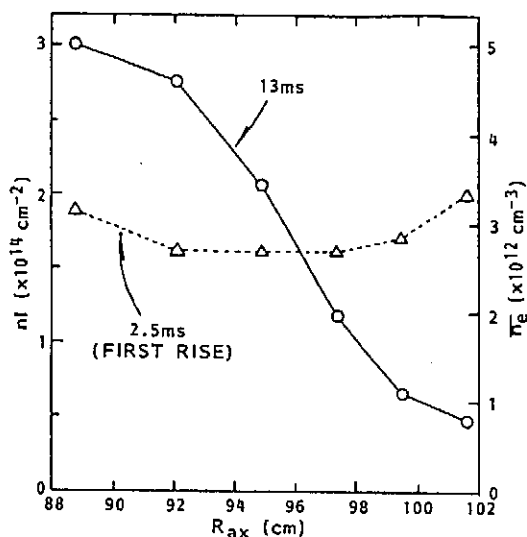


Fig.3 Density rise of ECH plasmas without Ti gettering as a function of R_{ax} .

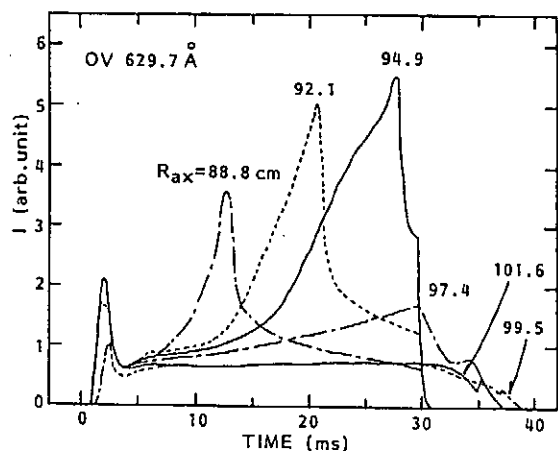


Fig.2 OV time behaviours as a function of magnetic axis R_{ax} .

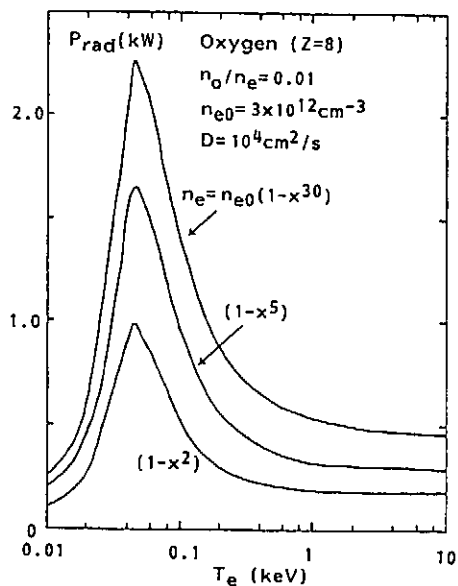


Fig.4 Calculations of radiation loss from oxygen atoms as a function of electron density profiles.

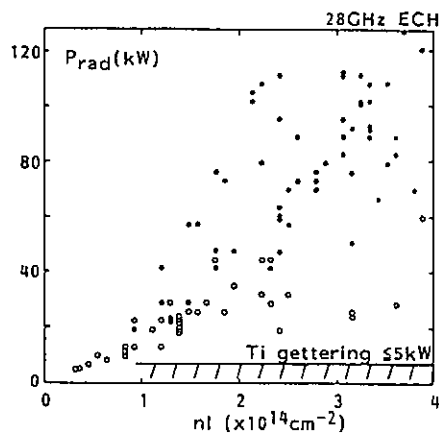


Fig.5 Radiation loss from ECH plasmas.

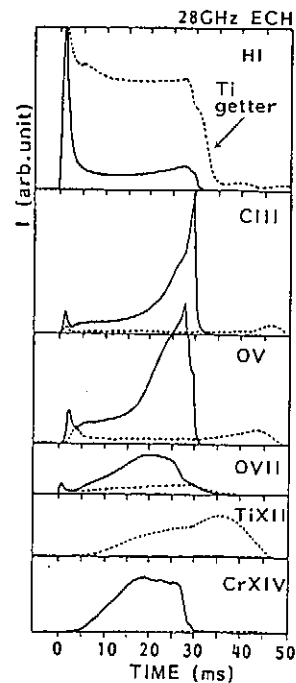


Fig.6 Comparison of impurity behaviours between ECH plasmas with and without Ti gettering.

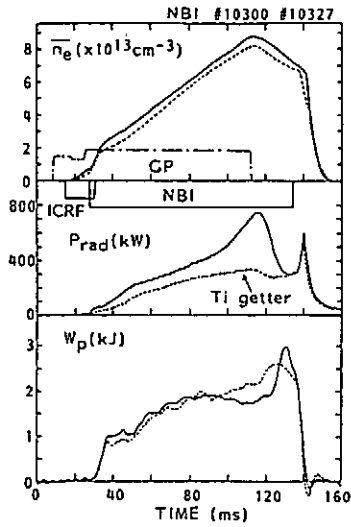


Fig.7 Effect of strong Ti gettering on NBI plasma.

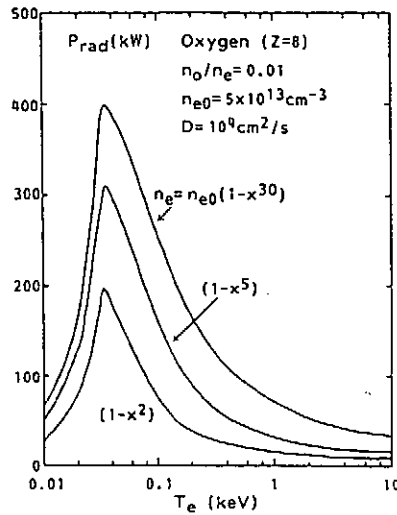


Fig.8 Calculations of radiation loss from oxygen atoms.

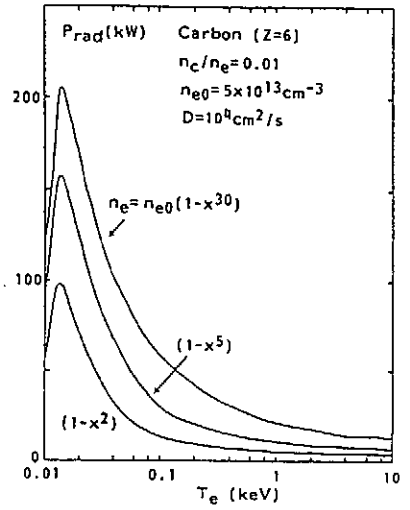


Fig.9 Calculations of radiation loss from carbon atoms.

Table I. Spherical HC (hydrocarbon) pellets.

Size	N_c	$n_c (=N_c/V_p)$	Δn_e	n_c/\bar{n}_e
0.32mm ϕ	0.9×10^{18}	$1.1 \times 10^{12} \text{ cm}^{-3}$	$0.7 \times 10^{13} \text{ cm}^{-3}$	2.3%
0.39mm ϕ	1.6×10^{18}	$2.0 \times 10^{12} \text{ cm}^{-3}$	$1.5 \times 10^{13} \text{ cm}^{-3}$	3.4%
0.46mm ϕ	2.6×10^{18}	$3.3 \times 10^{12} \text{ cm}^{-3}$	$2.1 \times 10^{13} \text{ cm}^{-3}$	5.0%

N_c : total number of carbon atoms. Δn_e : 50% C^{6+} and 50% H^+ are assumed.
 V_p : plasma volume ($=0.8m^3$). \bar{n}_e : $5 \times 10^{13} \text{ cm}^{-3}$ is assumed.

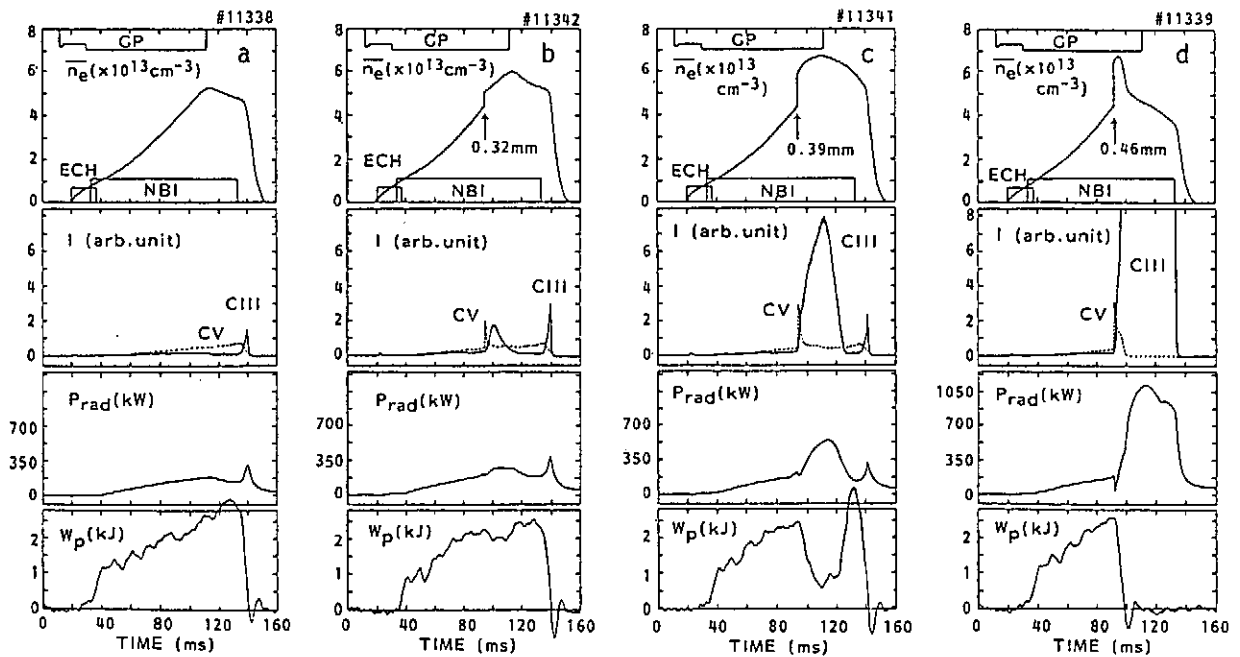


Fig.10 Experimental results of HC pellet injections in NBI plasmas.
 (a: without pellet, b; 0.32mm ϕ , c; 0.39mm ϕ , d; 0.46mm ϕ)

Ion Temperature and Poloidal Rotation Profiles for NBI heated plasma in CHS

K. Ida, S. Hidekuma and CHS group
National Institute for Fusion Science
Nagoya 464-01 Japan

ABSTRACT

Ion temperature and poloidal rotation velocity profiles are measured with 68 channel space resolved spectrometer using beam emission spectroscopy technique in CHS. The electric field near the plasma edge ($r = 0.7a$, a is averaged minor radius) derived from poloidal rotation velocity is 15V/cm for low density 28 GHz ECH plasma, and -35V/cm for high density NBI plasma. The peak of the ion temperature is shifted from the vacuum magnetic axis by up to 4 cm. This shift depends on the location of the magnetic axis and becomes larger as the magnetic axis moves toward the tangential major radius of the heating neutral beam. This shift is larger than that estimated from finite β calculation by a factor of two or less. Presumably the shift is due to a significant parallel beam pressure as well as thermal component.

1. Introduction

Ion temperature and electric field profiles are the crucial plasma parameter in helical device, since the electric field is expected to reduce helical ripple loss and improve energy confinement by Neoclassical theory. This theory also predicts centrally peaked ion thermal diffusivity which results in a flat ion temperature profile, while an anomalous transport theory predicts a more peaked ion temperature profile. Ion temperature profiles have been measured with fast neutral analyzer or spectrometer using various impurity line radiation¹⁾. However these measurements are not precise enough to distinguish whether the ion thermal diffusivity is Neoclassical or anomalous.

The electric field can be measured with heavy ion beam probe²⁾ or inferred from poloidal and toroidal rotation velocity using momentum balance equation. The poloidal rotation has been measured with CV line radiation in Heliotron-E device³⁾. The measurements are limited only at the plasma edge, since the electron temperature in the core plasma is high enough to ionize C^{4+} to higher ionized stages. No measurement for poloidal rotation velocity near the plasma center has been done in helical devices. In most of tokamak plasmas beam emission spectroscopy techniques have been used to measure ion temperature and toroidal rotation velocity even in the region where carbon or oxygen impurities are fully stripped, however they have not been well established in a helical device due to its complexity of magnetic configuration. In these techniques, the ion temperature and rotation velocity are measured respectively from the Doppler width and shift of the radiation for the high n level transition (visible region) of hydrogen-like impurities excited by the charge transfer between fully stripped impurities and the heating neutral beam.

In this paper we describe 1) multi space and wavelength spectrometer, 2) poloidal rotation velocity profile from intrinsic line radiation for ECH plasma and 3) ion temperature and poloidal rotation profiles with beam emission spectroscopy for NBI plasma.

2. Beam Emission Spectroscopy System in CHS

Compact Helical System (CHS)⁴⁾, which is an $l = 2$ heliotron/torsatron type device with the major radius of 100 cm and the averaged minor radius

of 20 cm. A 28 GHz gyrotron with the injection power of 100 kW produces ECH plasma with low density below $1 \times 10^{13} \text{ cm}^{-3}$, while tangential NBI can sustain the plasma with high density up to $1 \times 10^{14} \text{ cm}^{-3}$.

A 68 channel space resolved 1 m visible spectrometer system using CCD detector coupled with image intensifier⁵⁾ has been developed to measure spectrum in poloidal cross section as shown in Fig.1. Two set of 34 channel optical fiber arrays, one viewing a fast neutral beam and the other viewing off the neutral beamline to subtract background radiation, have been installed in CHS. These optical fibers with $100 \mu\text{m}$ diameter are led into the entrance slit of 1 m Czerny-Turner spectrometer with 2400 grooves/mm grating. At the exit plane the light from each fiber gives the spectrum from one spatial position. The light from all of the fibers is focused onto an image intensifier tube coupled with CCD TV camera. The resolution of the wavelength is $0.1 \text{ \AA}/\text{ch}$ (100 spectral channels), while its time resolution is only 16.7 ms.

The background radiation is mostly due to the reaction between fully ionized impurity and background thermal neutral in the plasma periphery. This background emitted from the cool plasma edge is proportional to the neutral density at the plasma edge and depends on the clearance between plasma edge and inner wall (the position of magnetic axis) and the amount of gas puff. The background is too high to derive ion temperature profile for the plasma with the magnetic axis of $< 92 \text{ cm}$ even without gas puff. The most measurements have been done using CVI 5292 \AA ($n = 8-7$) for low or medium density plasma with a weak or medium gas puff.

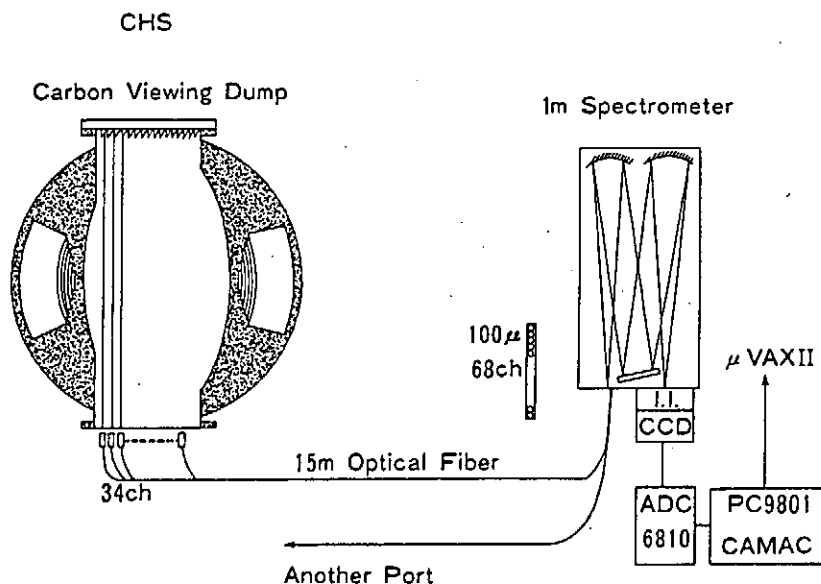


Fig.1 Schematic of the diagnostic set up on CHS for beam emission spectroscopy to measure ion temperature and poloidal rotation profiles.

3. Poloidal Rotation Profile

For ECH plasma the beam emission spectroscopy techniques can not be used due to the lack of neutral beam. The intrinsic line radiations emitted from the plasma edge are measured to derive poloidal rotation velocity. Even though the measurements of poloidal rotation cover whole plasma ($84 \text{ cm} < R < 107 \text{ cm}$) the measured velocities represent the component of poloidal rotation velocity to the line of sight and the emission is localized at $r=0.7a$. The radial electric field averaged along the magnetic surface is 15 V/cm (positive) for the low density ($\bar{n}_e = 3 \times 10^{12} \text{ cm}^{-3}$) plasma produced by 28

Although the position of the magnetic axis is sensitive to the pressure profiles, it seems obvious that the peak position of the ion temperature is shifted more outward than that from the estimate of the code. The neutral beam is injected tangentially at the tangential radius of 87 cm, while the vacuum magnetic axis R_{ax} is from 92 cm to 101 cm. The neutral beam deposits its power and momentum near center for $R_{ax} = 92$ cm, while the power deposition is off center for $R_{ax} = 101$ cm. The shift is enhanced as the neutral beam deposits the power near the plasma center as shown in Fig 4. This indicates that the parallel beam pressure which is not detected to diamagnetic loop or Thomson scattering measurements has a significant role to shift the magnetic axis. More precise analysis should be done with measured bulk pressure profile and estimate of pressure of parallel fast ion measured by fast neutral analyzer. However the significant shift of the peak of the ion temperature imply that the beam pressure is comparable to the bulk pressure near the plasma center.

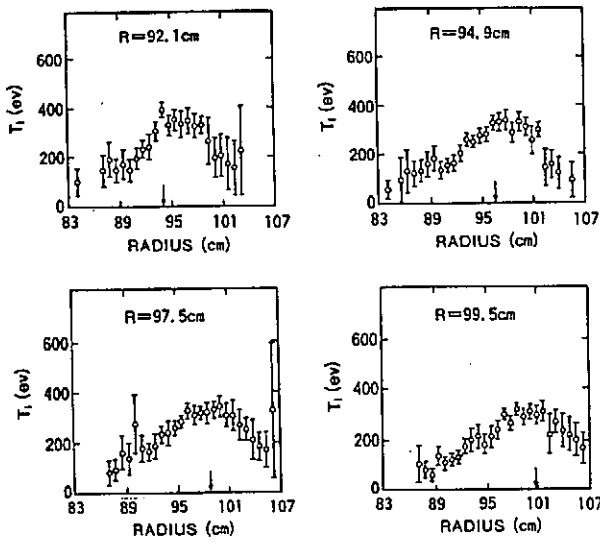


Fig.3 Ion temperature profile for the different vacuum magnetic axes. The arrows stand for the magnetic axis estimated from equilibrium code by the use of data of diamagnetic measurement.

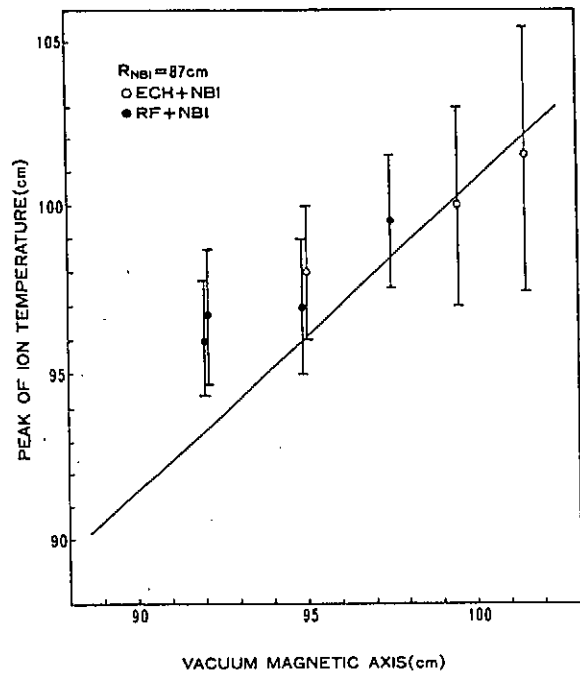


Fig.4 The peak position of the ion temperature as a function of vacuum magnetic axis.

Reference

- 1) R.S. Isler, L.D. Horton, E.C. Crume, H.C. Howe, G.S. Voronov, *in Proc. 16th European Conf. Venice* 1989.
- 2) G.A. Hallock, J. Matthew, W.C. Jennings, R.C. Hickok, A.J. Wootton and R.C. Isle, *Phy. Rev. Lett.* **56** (1986) 1248.
- 3) K. Kondo, H. Zushi, S. Nishimura, et. al., *Rev. Sci. Instrum.* **59** (1988) 1533.
- 4) K. Matsuoka et. al., *in Plasma Physics and Controlled Nuclear Fusion Research (in Proc. 12th IAEA Conf. Nice, 1988) IAEA-CN-50/I-1-3.*
- 5) K. Ida and S. Hidokuma, *Rev. Sci. Instrum.* **60** (1989) 876.

GHz ECH with the toroidal magnetic field of 0.5 T as shown in Fig. 2(a). The central electron temperature is 600 eV. This indicates that the plasma potential is positive in the collisionless regime.

On the other hand, the beam emission spectroscopy techniques can be used for the NBI plasma. The emission is more localized at the cross section of neutral beam line (midplane) and line of sight. The measured velocity is more likely poloidal rotation velocity at each point, although the space resolution becomes poor near the plasma center due to the integration effect along the neutral beam. As shown in Fig. 2(b) the poloidal rotation is reversed and indicate negative electric field (-35 V/cm at $r = 0.7a$) for NBI plasma with the toroidal field of 1 T and the electron density of $\bar{n}_e = 2 \times 10^{13} \text{ cm}^{-3}$ and electron temperature of $T_e(0) = 250 \text{ eV}$ (collisional regime). The radial electric field is roughly proportional to minor radius.

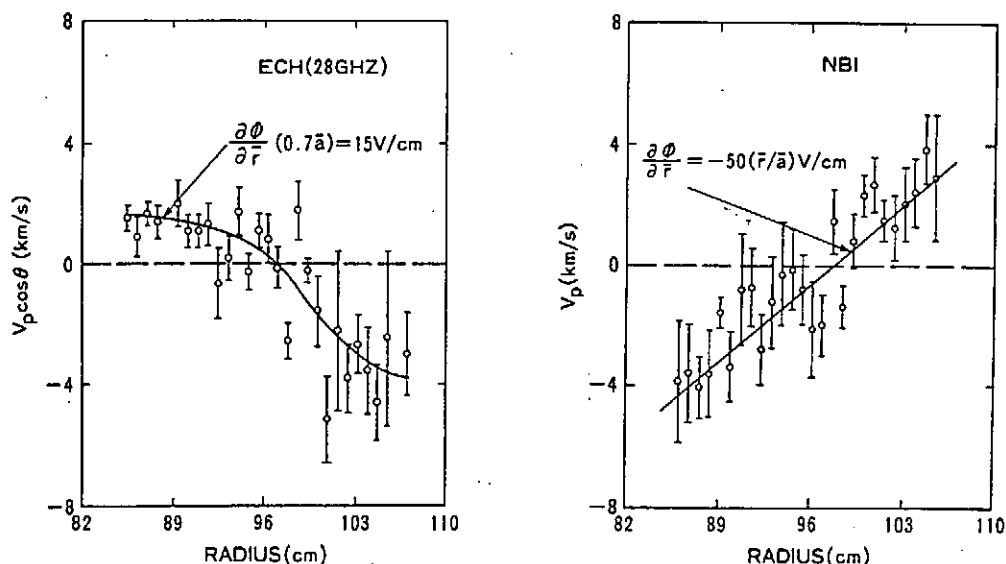


Fig.2 Poloidal rotation velocity profiles for 28 GHz ECH plasma (a) and NBI plasma (b).

4. Ion Temperature Profiles

The thermal diffusivity should be measured from ion temperature and electron density and temperature, however, it is described in an accompanying paper. In this paper we emphasize the shift of the ion temperature peak from the vacuum magnetic axis. The magnetic axis shifts outward due to the effect of finite β . It is usually estimated from pressure profile calculated with equilibrium code. It is possible to estimate the magnetic axis from the peak of electron or ion temperature profile. The electron temperature profiles are measured by Thomson scattering in CHS, however the measurements is limited only within outer half of the plasma ($R > 95 \text{ cm}$) and it is quite difficult to estimate the peak of electron temperature profile. However the peak of the ion temperature profile is measured accurately enough to compare with the position of the magnetic axis estimated from equilibrium code.

Figure 3 shows the ion temperature profile for various vacuum magnetic axis. The shift of the magnetic axis is estimated with finite β equilibrium code by the use of stored energy from diamagnetic loop and the assumption of reasonable pressure profile. The stored energy is 1 kJ for the inward shifted plasma ($R_{\alpha} = 92.1 \text{ cm}$) and the volume averaged β is 0.27 %.

DRIVEN CURRENTS IN NEUTRAL BEAM HEATED PLASMA

O.Kaneko, Y.Takeiri, H.Yamada, H.Iguchi, S.Okamura, K.Matsuoka,
NBI group and CHS group

National Institute for Fusion Science
Nagoya 464-01, JAPAN

Abstract: Plasma currents, which are observed in the tangential neutral beam heated plasma, are studied under the various plasma conditions in CHS. The plasma current is mainly driven by high energy beam when the plasma density is low, while the bootstrap current seems to be dominant in the dense plasma.

1. Introduction

Helical systems such as heliotron and stellarator are in principle to be operated in net-current-free regime. In actual situations, however, the plasma currents are induced by external driven force accompanying with auxiliary heating, or by diffusion (bootstrap current). Especially, the bootstrap current can exist in helical systems even if the system is free from externally driven currents. Therefore, experimental investigations of these currents and their effects on the confinement and stability is very important.

In CHS, we have also observed a plasma current in both ECH and NBH plasmas. Especially in NBH plasma, a large amount of current is induced because the beam is injected tangentially and is not balanced. In this paper, we will describe the behavior of plasma currents that are induced in the neutral beam heated plasma.

2. Experimental Conditions

CHS has one neutral beam line which is capable of 40keV, 1.2MW hydrogen beam through the port for one second. A peculiar feature of our NBI is that the injection angle can be changed from tangential to normal direction by rotating the whole beam line (Fig.1)[1]. In this year, however, the injection angle is limited to be tangential ($R_t=94$ or 87 cm, where R_t is the radius of inscribed circle to the beam axis.) due to the lack of wall protecting armor plates, so that the beam injection is not balanced.

Toroidal plasma currents are measured by a Rogowski coil which is located on the inner wall of vacuum chamber. The direction of the beam is usually in 'co'-direction which corresponds to the direction of effective plasma current that enlarges a rotational transform. In CHS, this direction is opposite to the toroidal magnetic field (Fig.1). Other diagnostics are: a FIR laser interferometer for line density, Thomson scattering for $T_e(r)$ and

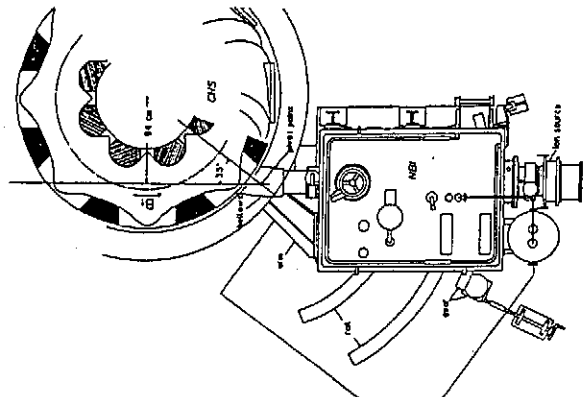


Fig.1. Schematic view of the movable beam line.

$n_e(r)$, a diamagnetic coil for stored energy, and a charge exchange recombination spectroscopy for $T_e(r)$ and rotation measurement. VUV spectroscopy is used for monitoring the impurity behavior.

A target plasma is produced by ECH or RF for 15-30ms before beam injection. NI overlaps with ECH or RF for 0-15ms, and after that the plasma can be maintained by NI alone for 200ms (so far, pulse length is limited by gas puffing system). Neutral beam heating experiments have been carried out under the conditions of $B_t=0.47-1.5T$ and the magnetic axis of 88-102cm.¹³ The plasma parameters obtained by NI are: $\bar{n}_e=1-8 \times 10^{13} \text{ cm}^{-3}$, $T_e(0)=550-200\text{eV}$, and the maximum stored energy of 5.4kJ is achieved at 1.5T.

3. Plasma Current

Figure 2 shows typical time evolutions of plasma current at $B_t=1T$. When the plasma density is low, a large amount of current is observed in the direction of neutral beam injection (Fig.2(a)), while at high density the plasma current decreases and in some cases it flows backward (Fig.2(b)). The dependence of the plasma current on the electron density is shown in Fig.3 with the magnetic field strength and the magnetic axis as parameters.

The backward current is more often found at low B_t . When $B_t=0.47T$, the plasma current flows backward through out the beam pulse even if the plasma density is not very high ($\bar{n}_e < 5 \times 10^{13} \text{ cm}^{-3}$, see Fig.2(c)).

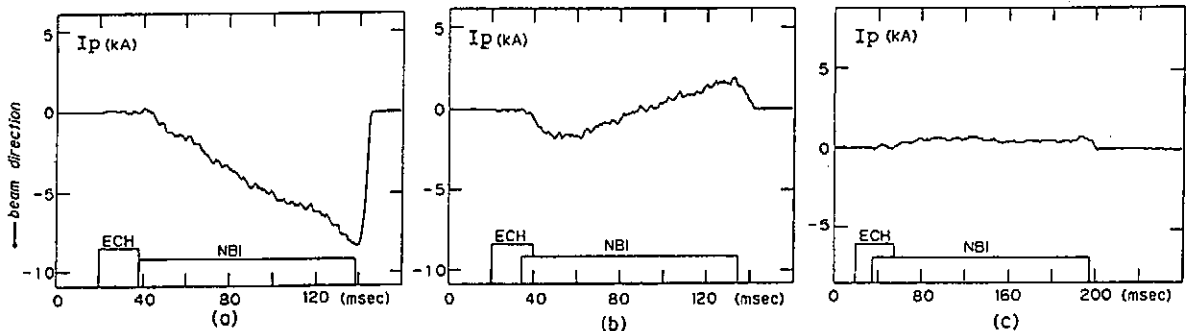


Fig.2. Time evolutions of plasma currents:

- (a) $\bar{n}_e = 1-2.9 \times 10^{13} \text{ cm}^{-3}$, $B_t = 1.05T$.
- (b) $\bar{n}_e = 1-6.6 \times 10^{13} \text{ cm}^{-3}$, $B_t = 1.05T$.
- (c) $\bar{n}_e = 1-5.0 \times 10^{13} \text{ cm}^{-3}$, $B_t = 0.47T$.

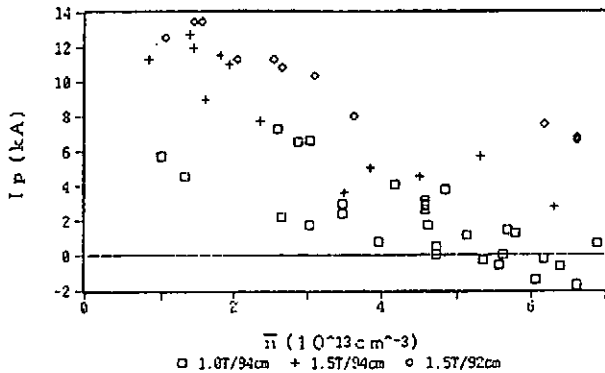


Fig.3. Dependence of plasma current on electron density.

4. Discussions

(1) Beam Driven Current

By tangential injection, the fast ions produced by NI are

passing particles and then they generate the current as in tokamaks. In tokamak, the driven current may be expressed[2]

$$J_{bd} = J_{circ} [1 - Z_p/Z_{eff}(1-G)],$$

where J_{circ} is the current due to circulating fast ions, Z_p the electric charge of the ion, Z_{eff} the effective charge of the plasma, and G is a rate of blocked electrons. In helical system, the trapped particles can also exist in both electrons and ions, but the effect of these trapped particles may be neglected because they are localised in the region of high pitch angle. Therefore eq.(1) may still hold in helical system.

The Fokker-Planck analysis shows the parameter dependence of J_{circ} roughly as $P_{in} \langle T \rangle / \bar{n} / R$, where P_{in} is the injected power, $\langle T \rangle$ the volume averaged electron temperature, \bar{n} the line averaged plasma density, and R is the major radius. Figure 4 shows the dependence of the plasma current on a trial function $P_{in} T_e(0) / \bar{n} / R$. The figure shows that the experimental data fit this scaling as far as the plasma density is not high. The line in the figure indicates the coefficient that corresponds to the result of DITE tokamak[3]. As can be seen from the figure the coefficient of our result is about a half of that of tokamaks. One reason of this discrepancy is that at low density the driven current does not reach its steady state as shown in Fig.2, while at high density the bootstrap current cancels the beam driven current. Another candidate is Z_{eff} . If Z_{eff} is close to Z_p , the driven current decreases as eq.(1) shows, but we have not evaluated Z_{eff} yet.

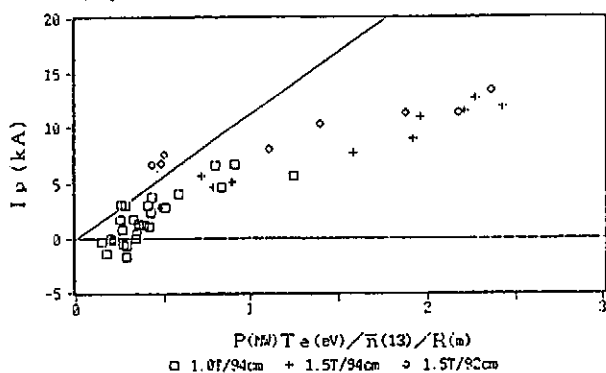


Fig.4. Dependence of plasma current on $P_{in} T_e(0) / \bar{n} / R$, where the line shows the corresponding coefficient of the result of DITE.

A large plasma current modifies the magnetic configuration of CHS. Figure 5 shows the radial profile of electron density and temperature at 70 ms after beam injection. The electron temperature has a parabolic profile while the density has a broad one. The current may have a peaked profile in this case, and changes the profile of rotational transform. The change of rotational transform by the driven current is 0.05-0.1 at the plasma surface. However, we have not observed any deleterious effect on confinement. Figure 6 shows the comparison of the experimental diamagnetic energy with 'LHD'-scaling with the plasma current as a parameter. We don't find apparent degradation from the scaling even if the plasma current is large. (note that the experimental data shown here are not always taken at their maximum and therefore they are smaller than the LHD scaling values)

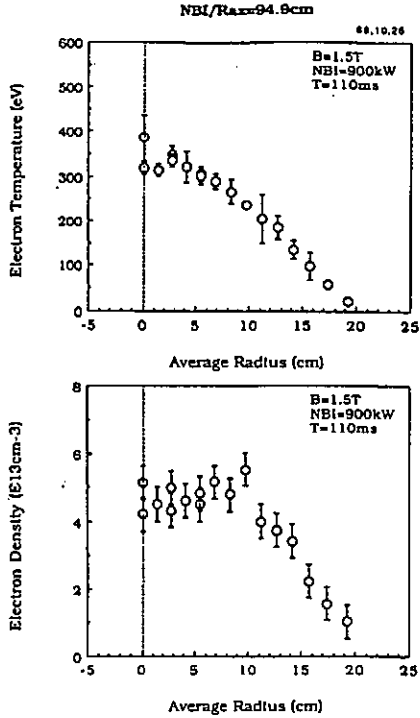
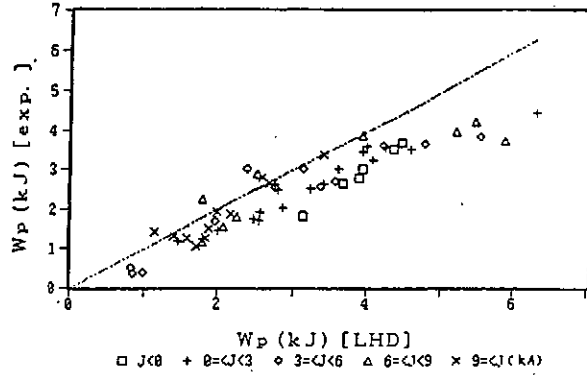


Fig.5
Typical radial profiles of electron temperature and density of NBH plasma.

Fig.6
Comparison of stored energy with LHD scaling for different plasma current.



(2) Bootstrap Current

The backward current which is observed experimentally can not be explained by the beam driven current. The bootstrap current may flow in 'counter' direction. The most part of NBH plasma is in plateau regime. The theory predicts the expression of the bootstrap current as[4]:

$$j_b = -\sqrt{\pi} \frac{v_{te}}{Rq v_{te}} \frac{1}{B_p} \left(\epsilon_i^2 - l \epsilon_h^2 - m g \frac{B_p^2}{B_i^2} \epsilon_h^2 \right) \times \left(1.16 \frac{dp}{dr} + 1.54 n_0 \frac{dT_e}{dr} + 0.58 n_0 \frac{dT_i}{dr} \right).$$

In CHS ϵ_h is usually larger than ϵ_i at $r/a > 3/4$ and in this case the current flows backward. In fact, figure 5 shows that the pressure gradient is large at the periphery of the plasma. Therefore the experimental data is qualitatively consistent with the theory.

We are still studying the bootstrap current in ECH plasma as well as NBH plasma. We have observed that the amount of current depends on the quadruple component of magnetic field. The comparison of the experimental data with the simulation is now in progress.

References

- [1] O. Kaneko, A. Ando, Y. Oka, Y. Takeiri, T. Kohmoto, A. Karita, T. Kuroda, et al., *13th Symp. on Fusion Engineering*, 29-P-26, Knoxville, (1989).
- [2] J.W. Connor and J.G. Cordey, *Nucl. Fusion* **14**, 185 (1974).
- [3] W.H.M. Clark, J.G. Cordey, M. Cox, R.D. Gill, J. Hugill, J.W. Paul, and D.F.H. Start, *Phys. Rev. Lett.* **45**, 1101 (1980).
- [4] K.C. Shaing, S.P. Hirshman, and J.D. Callen, *Phys. Fluids* **29**, 521 (1986).

Power Deposition during ECH in CHS

S. Kubo, M. Hosokawa, Y. Takita, H. Idei,
and CHS group

National Institute for Fusion Science
Nagoya 464-01, Japan

Abstract: Power deposition profile and the total absorbed power during electron cyclotron heating (ECH) in CHS are estimated from the resonance structure at each flux surface. The dependence of the central electron temperature on the magnetic field can be well accounted for by this method. Total deposited power into the plasma is estimated from the measurement of the leakage power around the torus. Using this power deposition profile, preliminary confinement analysis of the electron is done.

1. Introduction

Power deposition profile is one of the key issues for the confinement investigation. Conventionally the deposited power and its radial profile had been estimated from the ray tracing analysis, and these estimations are compared with the local electron temperature decay measurement. In contrast, during 28GHz ECH in CHS, optical depth is so thin that one can hardly include all the wall reflection effect in the ray tracing code because of the complexity of the wall structure and the input wave mode (TE_{01} , O-X mixture). Under such condition, the deposition profile is estimated from the resonance structure at each flux surface. Moreover, total absorbed power inside the confinement region is estimated from the measurement of microwave leakage power distribution around the torus. Using these results, electron energy confinement properties are analyzed.

2. Power Deposition Profile

In the ECH plasma of the CHS, the electron temperature on axis, T_{e0} , ranges from 0.1 to 0.8 keV and electron density, n_{e0} , 1.5 to $8.0 \times 10^{12} \text{ cm}^{-3}$. In such parameter range, one path absorption rate is so small (at most nearly 3%) for the 28GHz fundamental resonance of O-mode. As is well known, at the fundamental resonance, the absorption rate of X-mode is much smaller than that of O-mode. Microwave power is launched by the straight-cut waveguide antenna with TE_{01} mode, so that both O- and X-modes will be excited and 3-dB lobe extends to almost whole plasma cross section as shown in Fig. 1. The opposite side of the launcher

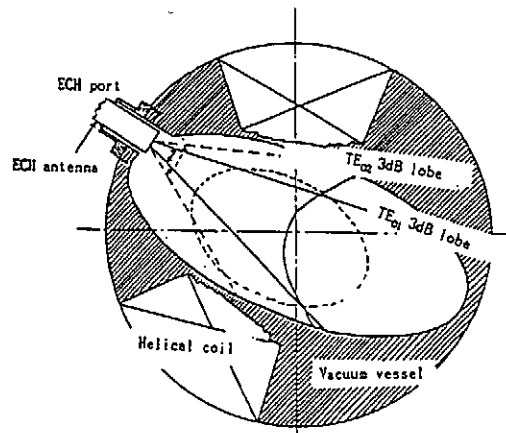
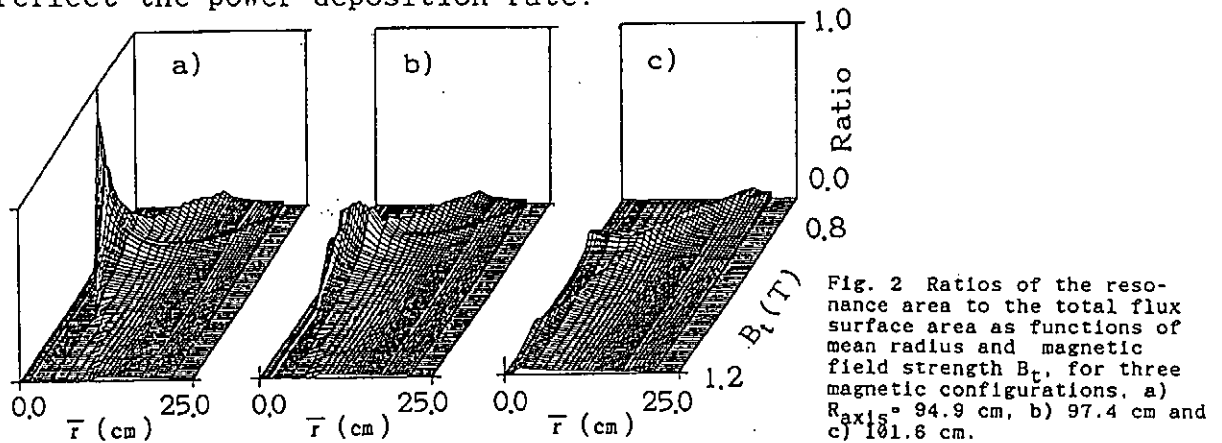


Fig. 1 Poloidal cross section at the injection port of ECH.

is geometrically complex for the presence of the vacuum vessel and ports. In consequence, in order to estimate the power deposition profile, ray tracing calculation including all wall reflection effect is not realistic, or one cannot help including many assumptions. In contrast, if the assumption that the wave is completely scattered at the wall, that is, the wave field is isotropic and constant everywhere inside the vacuum vessel holds and if we consider only the Doppler-broadened cyclotron damping as the absorption mechanism, estimation of the deposition profile from averaged treatment of the resonance structure is possible. In Fig. 2 are shown the ratios of area of the resonance band to that of the total flux surface as functions of magnetic field strength B_z at the center of the vacuum vessel for three different configurations. For the case of small field ripple on axis corresponding to Fig. 2 a), it is shown that the electron which makes excursion on the magnetic surface near the magnetic axis almost always remains within the resonance layer if B_z is set at 0.94 Tesla. In contrast, for high ripple case (Fig. 2 c)), efficiency that electrons gain energy from rf field is suggested to be very low everywhere even though B_z is scanned. Therefore, it can be considered that these area ratios directly reflect the power deposition rate.



In order to check this scheme to derive the deposition profile, electron kinetic energy on axis, W_{e0} , measured by the Thomson scattering during the B_z scan for three different magnetic configurations is compared with the calculated one. In Fig. 3 a) is shown the measured W_{e0} dependence on B_z . These dependencies cannot obviously be expected by the one path ray tracing calculation. As the radiation loss and power flow from electron to ion are negligible in the present parameter range, the following diffusion equation for only the electron kinetic energy holds ;

$$\frac{\partial W_e}{\partial t} + \frac{1}{r} \frac{\partial}{\partial r} \left(r \chi_e \frac{\partial W_e}{\partial r} \right) = P \quad (1)$$

can be numerically integrated with the power deposition profile to obtain the kinetic energy of electron on axis in the steady state, assuming the diffusion coefficient as a function of the mean radius as :

$$\chi_e(r) = \chi_{e0} 10 \frac{r}{r_c} \quad (2)$$

In Fig. 3 b) are shown the results of the above mentioned numerical calculations. The tendency of the B_z dependence of W_{e0} for each magnetic configuration could well be reproduced by the calculation. Therefore, power deposition profile estimation from the resonance band structure is shown to be effective.

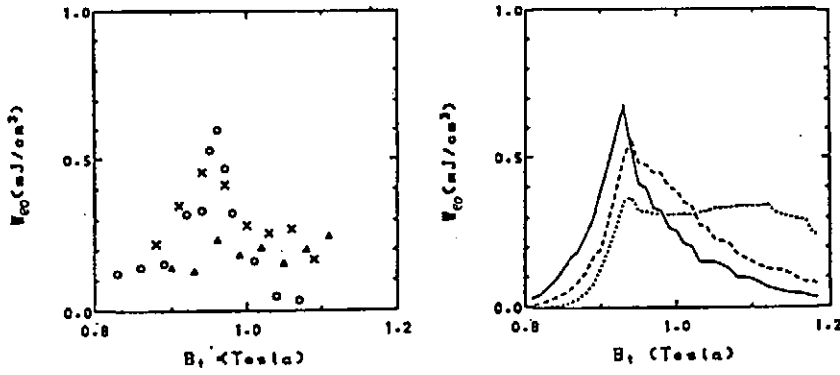


Fig. 3 a) Experimental and b) estimated dependence of the central electron kinetic energy W_{e0} on magnetic field B_t for R_{axis} = 94.9 cm (O ———), 97.4 cm (X - - - -), and 101.6 cm (Δ ·····).

3. Total Absorbed Power

In the course of the confinement analysis, total power absorbed in the plasma is an important parameter as well as the deposition profile. Total absorbed power is estimated by measuring the leakage power from the vacuum vessel. Detectors for microwave leakage power are set just outside of the quartz windows located 45 degree apart from each other along the toroidal direction. In order to formulate the power balance, vacuum vessel is divided into $2n$ toroidal sections. Input power for i - section is the summation of externally injected power $P_{in,i}$, power flow from adjacent sections $P_{i-1,i}$ and $P_{i+1,i}$. On the other hand, loss power for i - section is wall loss $P_{w,i}$, leak loss $P_{L,i}$ and power flow out to the adjacent section $P_{i,i-1}$, $P_{i,i+1}$. Assuming all waves starting from the wall or the boundary between the sections are isotropic, the power balance equation for the i - section can be expressed by

$$P_{i,i+1} = P_{in,i} \Gamma^0 + P_{i-1,i} \Gamma^+ + P_{i+1,i} \Gamma^-,$$

$$\Gamma^0 = e^{-\tau} \frac{1-\alpha}{2} \frac{1}{1-\alpha(1-f_w-f_L)e^{-\tau}}, \quad \Gamma^+ = \beta e^{-2\tau} \frac{1-f_w-f_L}{1-\alpha(1-f_w-f_L)e^{-\tau}}, \quad \Gamma^- = \Gamma^+ (1-\beta) e^{-\tau}. \quad (3)$$

Here, multi-reflection effect is taken into account. The parameters α and β represent the power flow rate to the wall from adjacent wall and boundary, respectively. The constants f_L and f_w are the leak and wall loss rate of the power reached at the wall. Effective one path optical depth τ is introduced to take plasma absorption into account at each section. By solving the equation system for the power balance of every section, leakage power distribution along the toroidal direction can be calculated with the effective optical depth as a free parameter. In Fig. 4 a) are shown the leakage power distributions for the various optical depths with α , β and f_L calculated from real geometrical configuration and f_w from empirical ohmic loss rate of SUS plate. Here, the leakage power is normalized by that at the power input section. Summing over all sections, total absorbed power, leakage power, and wall loss power can be expressed by

$$P_{abs} = \frac{P_0(1-e^{-\tau})}{1-\alpha(1-f_w-f_L)e^{-\tau}} \left(1 + \frac{2\Gamma^0}{1-\Gamma^+-\Gamma^-} \right), \quad \left[\frac{P_{leak}}{P_{wall}} \right] = \frac{P_0 e^{-\tau}}{1-\alpha(1-f_w-f_L)e^{-\tau}} \left(\alpha + \frac{2\Gamma^0\beta}{1-\Gamma^+-\Gamma^-} \right) \left[\frac{f_L}{f_w} \right].$$

The dependence of these power on effective optical depth can be calculated as shown in Fig. 4 b). In Fig. 4c) is shown the experimental leakage power dependence on the injected power. During the injection power scan, main variable parameter is the electron temperature. These data can be interpreted as the dependence of the leakage power on the effective optical depth. It is clear that leakage power at the further section from power input section saturates faster than that at the nearer one. From these results, it is concluded that at nearly 100 kW level input power, almost 80% of the input power is absorbed in the plasma.

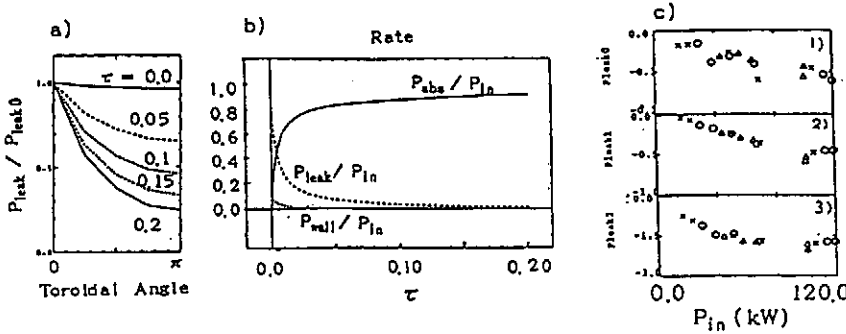


Fig. 4 a) Estimated leakage power distribution along the toroidal direction for several optical depths. b) The dependence of the absorbed, leakage, and wall loss power on effective optical depth. c) Experimental leakage power dependence on injected power for 1) 0.0, 2) 45.0 and 3) 90.0 degree toroidally apart from injection port for low (O), medium (X), and high (Δ) density case.

4. Electron Energy Confinement Analysis

In the previous sections, total absorbed power and the deposition profile are estimated. The energy flow to the ions or radiation loss is negligible in the typical plasma parameter range in interest. Taking only the electron energy balance, that is to say, solving the diffusion equation for only electrons, measured and calculated time evolution of the electron energy at ($\bar{r} = 0$ cm and $\bar{r} = 7.5$ cm) are compared in Fig. 5. Here the diffusion coefficient is set at 3.0×10^{-4} cm²/s on axis and its functional form on the radius is set the same as Eq.(2). This result indicates that the deposition profile estimation and the diffusion coefficient assumption is appropriate.

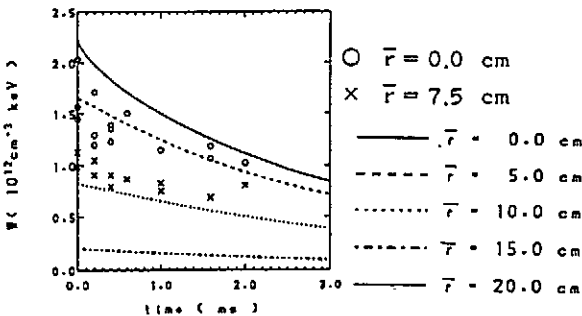


Fig. 5 Electron energy decay estimation from diffusion model (lines) and experimental measurement (o, x).

5. Conclusion

Power deposition profile during 28 GHz ECH experiment was estimated by the resonance structure. This estimation scheme was checked by the dependence of the central electron kinetic energy on the magnetic field for three different magnetic configurations. Total absorbed power into the plasma is estimated from the model which takes account of the wall loss, leak loss, and multi-reflection effects and leakage power distribution measurement. With these estimations, simple electron transport analysis is done resulting in the electron diffusion coefficient nearly 3×10^{-4} cm²/s.

A POSSIBLE MODIFICATION OF THE FT TOKAMAK INTO A COMPACT HIGH FIELD STELLARATOR WITH SEPARATRICES.

F. Alladio, P. Buratti, F. Crisanti, S. Mancuso, P. Micozzi

Associazione EURATOM-ENEA sulla Fusione, C.R.E. Frascati,
C.P.65 - 00044 - Frascati, Rome, Italy

ABSTRACT

A possible modification of the FT Tokamak could be to transform it into a compact high field stellarator experiment. The removal of the copper shell and of the secondary liner would leave space (9 cm.) between the inside of the toroidal magnet ($r=29\text{cm.}$) and possible vacuum vessel with $r=20\text{ cm.}$ This space could be used for the helical windings. As the toroidal magnet is built by 12 sectors a rather attractive possibility could be an $l=2\ m=6$ stellarator.

Since the FT Tokamak is at the present out of operation a possible idea to reuse of it is the transformation to an high field stellarator. In order to use as much as possible the present facilities a few parameter are straightforward. The major radius is given by the toroidal magnet ($R=83\text{cm.}$ in FT); however we propose to locate the magnetic axis at $R=78\text{ cm.}$ in order to have a toroidal field of 5 T on it, this would allow the use of the ECRH at 140 GHz ($\approx 1\text{ MW}$) available on FTU [1]. Actually the FT Tokamak has been designed to produce a toroidal field of 10 T and the use of it at a lower field could leave the possibility of using the steel casing to sustain the forces of the helical coils. The l,m numbers can be derived considering that the toroidal magnet is composed by 12 sectors, therefore an obvious choice is $m=6\ l=2$ with the possibility of 12 full ports. The choice to put the helical windings inside the toroidal magnet (to be as close as possible to the plasma) gives a limit to the plasma cross section. A preliminary analysis suggests a minor radius of 20 cm. for the vacuum vessel, leaving 9cm. available for the helical windings. The presence of the FT transformer, used at a really small current level, could allow plasma current control, ohmic start-up and ohmic stellarator operation; besides the present vertical field and bias coils can be used to optimize the stellarator magnetic configuration. In our proposal the four helical windings should be wound using the law of

constant pitch in toroidal coordinates [2,3]. This fact causes the cross section of the helical winding to be variable from 100cm^2 (inside) to 250cm^2 (outside) (Fig.1).

Each coil should carry about 1 MA; up to now the detailed procedure to build them has not been yet analyzed. However a possible way could be to make a separate construction for each of the 12 magnet modules (that means two geometries of construction for 6 modules each) and to join them when the modules are assembled. This could imply the construction of each coil by 6-8 windings capable of carrying 120-160 KA each. A solution like this could be useful also for the necessity to feed the coils from 6 different symmetric point in order to minimize the field errors.

In Fig.1 a preliminary $l=2$, $m=6$ vacuum field configuration is shown: it is produced by a toroidal field of 5 T at 78 cm, 4 helical field coils carrying 700 KA each and by a vertical field produced with 53 KA and 47.5 KA flowing respectively in the external and the internal coil. Fig 2 shows a more detailed view of the magnetic configuration with a circular vacuum vessel of 20 cm radius and the inside of the toroidal magnet of 29 cm radius, the average minor radius of the plasma being 15 cm, that means an aspect ratio $A=5.2$. The main characteristic of such configuration are: the strong separatrix-like features at the edge of the plasma where $\psi = 1$, the high shear in the last 2 cm of the configuration (Fig.3), the relatively broad and flat $\psi = 0.22$ profile near the magnetic axis and the presence of a small (2 % deep) magnetic well. The equilibrium and stability study has to be done but, from similar low aspect ratio stellarator/torsatron studies performed in the past [3] one could guess a quite large equilibrium β limit (of order of $\langle\beta\rangle \approx 10\%$ in the case the high shear region between $\psi = 0.5$ and $\psi = 1.0$ is not destroyed by finite β induced islands and $\langle\beta\rangle \approx 2.5\%$ in the case it gets lost). The Mercier stability should be guaranteed by the magnetic well in the central region of the plasma and by the high shear at the edge. A remarkable feature of the vacuum configuration is that within the separatrix no islands are present even at the major resonances $\psi = 1/2$, $1/3$, $1/4$, $2/3$ etc...

The vacuum chamber could have a circular cross section, however the possibility to produce diverted plasma (see the strong separatrix-like feature in Fig.1) increasing the helical current or decreasing the toroidal field suggests to protect by tiles the region of the divertor. Another peculiar feature could be the possibility to build in the vacuum vessel an ICRF helical antennas system that could fill the empty spaces present inside along two of the coils.

Apart from the existing ohmic transformer of FT the above quoted ECRH system could be used for the plasma start-up and sustainment. At full field both the possibility of first harmonic O-mode launch from the low (divertor helical coil) field side as well as first-harmonic X-mode launch from the high (other helical coil) field side by an optical or waveguide launching system should be present. At half field the second harmonics X-

mode launch is possible.

An ICRH system with 4-6 MW could be tunable from 30 to 90 MHz using the helical antennas built in the vacuum vessel; their power feed could be through the 6 ports where also the helical field coils are fed.

A simple confinement assessment can be made on the basis of the (pessimistic) LHS scaling

$$\tau_E = 0.17 P^{-0.58} n^{0.69} B^{0.84} a^2 R^{0.75}$$

(s) (MW) (10^{14}cm^{-3}) (T) (m)

by assuming that the density could be pushed up to $n_e = 3 \cdot 10^{14}\text{cm}^{-3}$ at $B_T = 5 \text{ T}$.

Confinement times from $\tau_E = 40\text{ms}$ at $P = 0.5 \text{ MW}$ down to

$\tau_E = 10\text{ms}$ at $P = 5 \text{ MW}$ are deduced; they correspond to volume averaged temperatures from $\langle T \rangle = 400\text{eV}$ up to $\langle T \rangle = 1100\text{eV}$. The volume averaged β value is at most 1% at $P = 5 \text{ MW}$.

On the other hand a scenario with $n_e = 1.5 \cdot 10^{14}\text{cm}^{-3}$ at $B_T = 5 \text{ T}$ gives τ_E from 22 ms at $P = 0.5 \text{ MW}$ down to 6 ms at 5 MW, volume averaged temperatures from 260eV up to 700 eV but β values up to 2% with $P = 5 \text{ MW}$.

A central feature of this experiment could be the study of the effects and of the resilience of the narrow high shear region at the plasma edge and of the confinement effects of the separatrices. A preliminary assessment of the effect of the rippled toroidal field (with $N=12$ and 15% empty space between the magnet modules) has been investigated with $I_{He1}=900 \text{ KA}$, $B_T=5 \text{ T}$, $I_{V1}=68.1 \text{ KA}$, $I_{V2}=61.4\text{KA}$. Fig.3(a,b,c) show that the separatrix-like feature at the plasma edge is barely affected by the ripple.

REFERENCES

- 1) Airoidi,A.,Buratti,P.,Cenacchi,G., et al. 14th EPS Conference on "Controlled Fusion and Plasma Physic",Madrid June 1987, Vol.III,pag. 976
- 2) Morse,P.M.,Fesbach,H., Methods of theoretical physic. Mac Graw-Hill, New York (1953)
- 3) Alladio,F.,Batistoni,P.,Crisanti,F.,De Marco,F.,Mancuso,S., "Analytical Field Results for Stellarator/Torsatron configuration" 7th International Workshop on Stellarator. OAK RIDGE, Tennessee, April 1989.

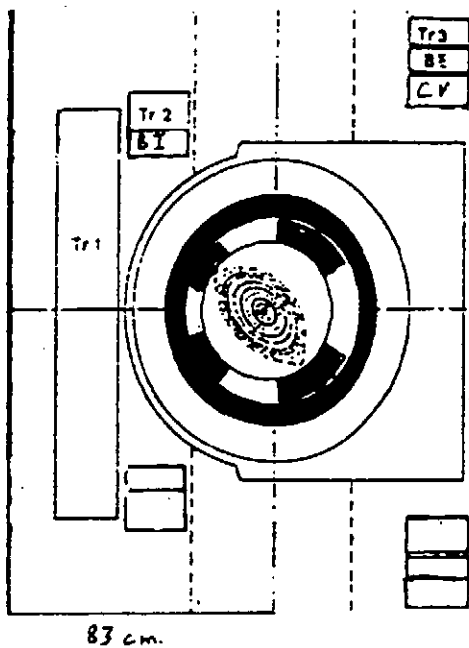


Fig. 1) The FT toroidal magnet with sketched the helical windings and the vacuum magnetic configuration

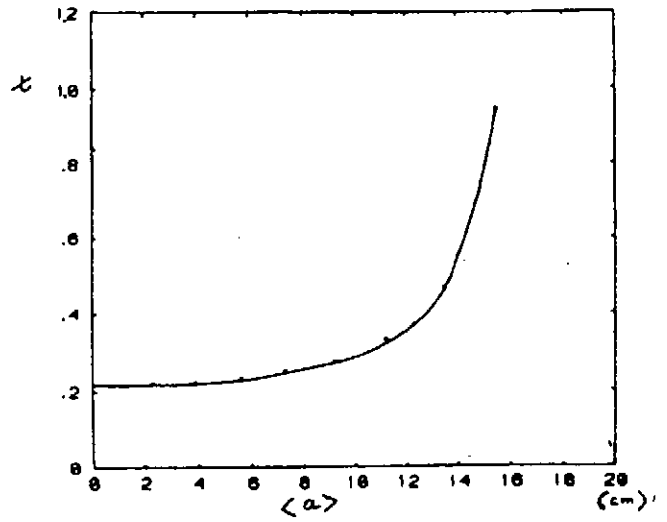


Fig. 2) χ versus the mean radius

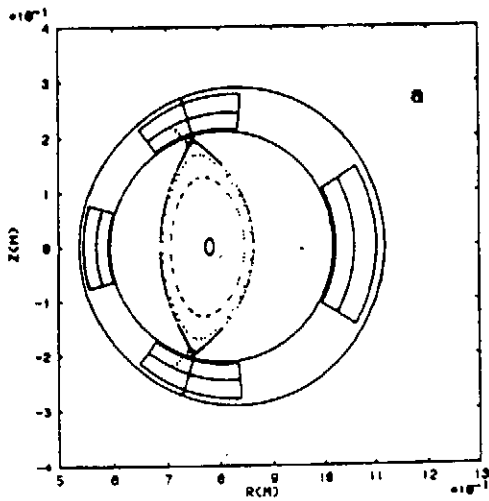
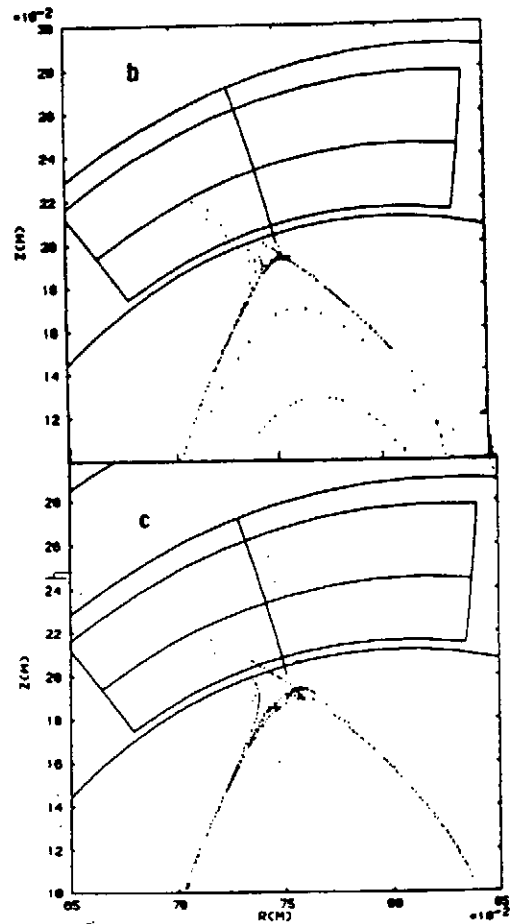


Fig. 3) a) The vacuum magnetic configuration showing the separatrix like feature
 b) detailed view of the separatrix region without the toroidal field ripple.
 c) as b) but including the toroidal field ripple



Page 4

Engineering Design of Large Helical Device

J. Yamamoto, O. Motojima, and LHD Design Group
National Institute for Fusion Science
Chikusa, Nagoya 464-01

Abstract: Engineering design of Large Helical Device and technical subject to realize the device are described. Research and development works of superconducting coil are also introduced here.

1. Introduction

Large Helical Device (LHD) is a one of the largest fusion engineering device including the largest stored energy superconducting magnet. LHD includes the number of innovative engineering items, therefore the construction of the LHD must break through a lot of technological hardness, then will contribute world wide society not only energy engineering but also all aspects.

This paper mostly covers the superconducting coils and its utility system. Force analysis and plasma vacuum vessel are introduced in other papers. Major parameter of the device is introduced in Table 1. The research and development of the superconductor is handled by another.

2. Components of LHD

LHD is mainly made from the plasma vacuum vessel, superconducting helical coils, superconducting poloidal coils, supporting structure, outer vacuum shell for thermal insulation (Bell Jar), heating and diagnostics ports. Artist's view of the device is shown in Fig. 1. The device is surrounded by liquid helium cooling system, vacuum pump system, coil current supply, plasma heating device, plasma diagnostics system as shown in Fig. 2.

3. Engineering Items to be Solved

3.1. Helical coil: winding technology, electrical insulation, cooling channel, error field, mechanical structure, force transfer from coil to coil can.

3.2. Poloidal coil: reduce AC loss, error field, mechanical structure, electrical insulation.

3.3. Among coils: Mechanical support (material selection, structure design), relative position.

3.4. Vacuum vessel: welding reliability, cooling, port.

3.5. Between helical coil and vacuum vessel: relative position in wide temperature range, support rod, thermal insulation.

3.6. Bell jar: vacuum (outgas, leak), mechanical stiffness.

3.7. Power supply: current control, voltage ripple, current breaker, bus line.

3.8. Cryogenics: heat load (radiation, conduction), coolant supply, power lead for sc coil, thermally insulated support structure, refrigerator, gas handling.

3.9. Emergency: coil quench, power supply failure,

cryogenics shut down, control system down, water supply down, heavy vacuum leak.

4. Engineering Aspects of Superconducting Coil

Important points for design of superconducting coil system are as follows: 1. selection of conductor and its cooling method. 2. mechanical and structural design of helical coil. 3. winding technology of helical coil to assure magnetic field accuracy. 4. test method of coils before combined as LHD. 5. Assurance of relative position among the vacuum vessel, coil, and Bell jar at operating temperatures. 6. Reliability, safety, and economy.

Table 2 shows the specification of poloidal coils. The coil is designed for ac operation. Due to the large diameter of the coil, the conductor of the coil will be a steel jacketed forced flow type.

The largest magnetic field in a helical coil will be experience with mode#3, its field is 8.35T, the largest electromagnetic force is over than 1000 ton/m. Figure 3 shows the empirical law of the coil current and coil energy. Therefore we choose the operation current of 20 to 30 kA for helical coil. Material of helical coil conductor is NbTi, Either pool cooling and forced cooling type are candidates of the conductor

5. R&D Items

Table 3 shows the R&D coils which is undergone by the Institute. Each coil shares the object of the LHD engineering items. Operating current and stored energy is shown in Fig. 4.

6. Conclusion

Basic design of LHD is established. Its engineering problems can be solved after R&D of vacuum vessel and superconducting coil.

The order of construction of the vacuum vessel and the superconducting helical coil will strongly affect engineering items.

Either cooling method of conductor will be possible to realize helical coil. The choice of the method may be decided by helical coil winding method and cryogenic aspects.

Most of superconducting technology to realize helical and poloidal coils will be established in these two years, as results of the R&D project undergone.

Cryogenic technology to assure the geometrical position at liquid helium temperature, thermal insulation, and refrigeration system have to be developed parallel to superconducting technology.

Table 1. Specification of Large Helical Device.

MAJOR RADIUS	4 m
COIL MINOR RADIUS	0.96m
AVERAGED PLASMA RADIUS	0.5~0.6 m
PLASMA ASPECT RATIO	7~8
β	2
m	10
$\gamma = N/2 \cdot a_0/R$	1.2
POLOIDAL COILS NUMBER	6(3 PAIRS)
MAGNETIC FIELD (CENTER)	4T
(COIL SURFACE)	~8T
HELICAL COIL CURRENT	8 MAT
COIL CURRENT DENSITY	40 A/mm ²
COIL ENERGY	2 GJ
WINDING ACCURACY	5×10^{-4}
ERROR FIELD (GLOBAL)	Less than 4 G
(LOCAL)	Less than 10 G
REFRIGERATION POWER	5~7 kW

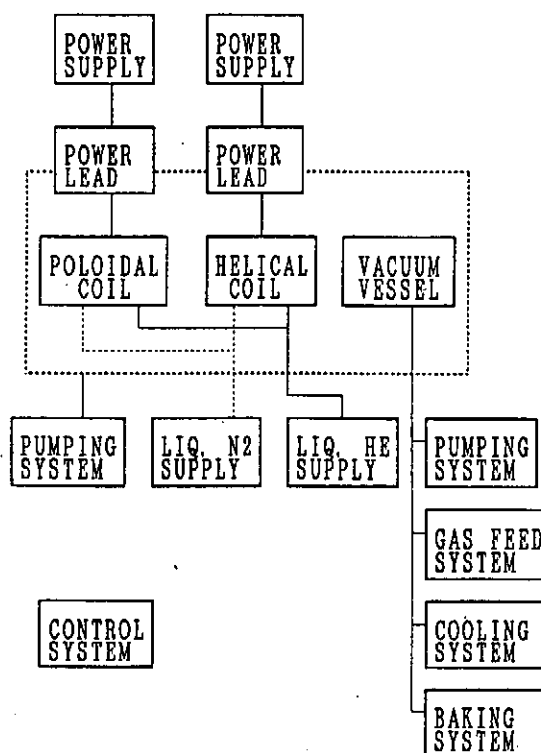


Figure 2. Composition of Large Helical Device.

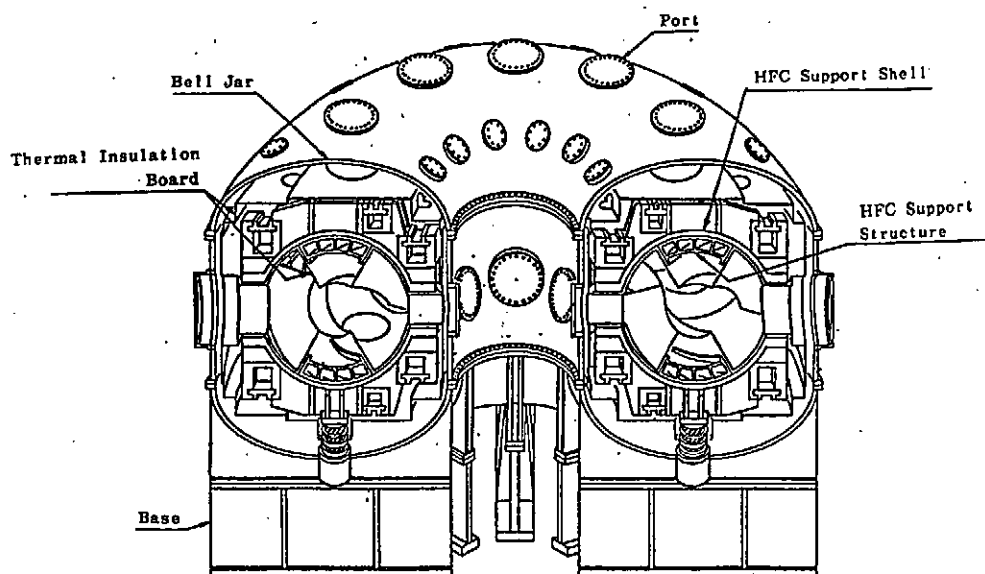


Figure 1. Schematic drawing of Large Helical Device.

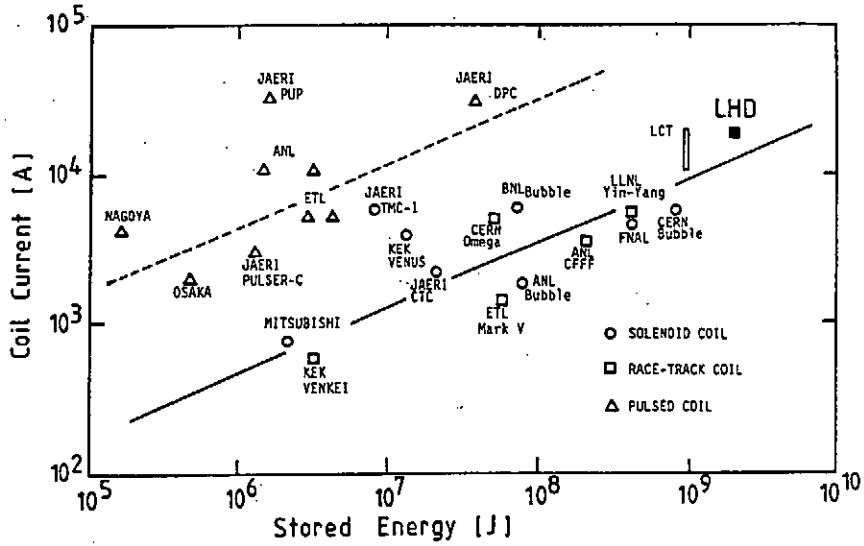


Figure 3. Relation between coil energy and current.

Table 3. Specification of R&D coils.

NAME	TYPE	COOLING	SPECIFICATIONS
KYOTO-SC	HELICAL m=16 l=2	POOL	R=0.3m r=0.063m B=2.0T I=0.775kA
TOKI-HB	HELICAL m=3 l=1	POOL	R=0.8m r=0.2m B=3.0T I=8.93kA
TOKI-TF	HELICAL m=4 l=1	FORCED-FLOW	R=0.9m r=0.25m B=2.77T I=8.08kA
TOKI-PF	POLOIDAL 2 DOUBLE PANCAKES	FORCED-FLOW	Ri=0.6m Ro=0.82m B=2.76T I=25kA
TOKI-MC	S-SHAPE	POOL	Ri=0.4m Ro=0.7m B=7.5T I=20kA
TOKI-WT	SECTIONAL LHD MODEL	NO COOLING	R=4.0m r=0.96m Cu conductor

Table 2. Specification of poloidal coils.

	OV COIL	IS COIL	IV COIL
AVERAGE RADIUS	mm 5650	3100	2130
CENTER POSITION	mm +-1550	+2030	+1250
MAGNETMOTIVE FORCE MAT	-5.02	-3.22	6.11
COIL CURRENT	kA 32.6	22.36	21.22
INDUCTANCE	H 1.44	0.57	1.26
NUMBER OF TURNS	11X14 =154	12X12 =144	18X16 =288
MAXIMUM FIELD	T 4.97	5.20	7.13
CONDUCTOR SIZE	mm 36X36	24X26	24X26
INSULATOR THICKNESS	mm 1.0	1.0	1.0
CURRENT DENSITY	A/mm ² 25.2	35.8	34.0
COIL SIZE	mm 396X504	288X312	432X416
CONDUCTOR LENGTH	m 5467	2805	3854

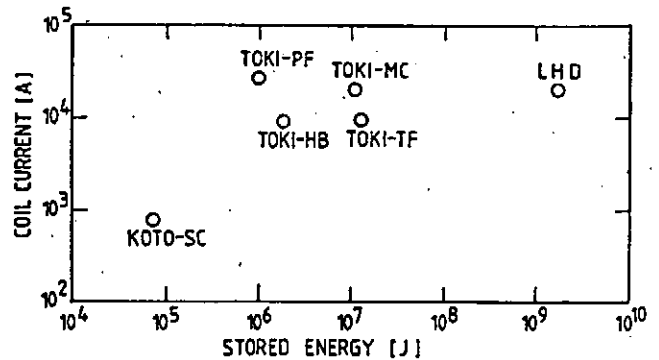


Figure 4. Stored energy and current of R&D coils.

Operation Scenario and Structural Design Analysis of LHD (Large Helical Device) Coils

Kozo YAMAZAKI, Osamu MOTOJIMA and LHD Design Group
*National Institute for Fusion Science,
Chikusa-ku, Nagoya 464-01, Japan*

Abstract

Flexible operation modes of coil system are presented for the Large Helical Device (LHD) with $m(\text{field period})=10$, 4-layer HFC (Helical Field Coil) and 3-pair PFC (Poloidal Field Coil) superconducting systems. For these operation modes, electromagnetic force and stress analyses are carried out, and it is clarified that coil supporting system within the permissible stress level is possible with adequate stiffness to keep clean magnetic surface without large magnetic islands.

1. Introduction

For the flexible currentless plasma operations of Large Helical Device, magnetic field properties such as rotational transform, plasma position/shape, plasma-wall clearance etc. should be controlled by the external coils. For one of these purposes the four-layer structure of HFC are adopted, especially to adjust the helical pitch parameter and the divertor-wall clearance. Moreover, three-pair poloidal coils are designed (Fig.1) to control the plasma axis position(Δ), plasma cross-sectional shape(κ, δ, \dots), poloidal plasma flux(ψ), the leakage magnetic field strength(B_{leak}), stored coil magnetic energy and so on. In order to avoid induction of plasma current, the poloidal flux should be designed to keep constant in time. Moreover, the leakage magnetic field should be minimized to reduce the eddy current and unfavorable magnetization of structural materials.

2. Operation Modes

The applied vertical magnetic field from HF and PF (OV,IS,IV) coils is decomposed to each multipole components:

$$B_Z(HF) = B_D(HF) + B_Q(HF) \cdot X + B_H(HF) \cdot X^2 + \dots$$

$$B_Z(PF) = b_D(i)I_i + b_Q(i)I_i \cdot X + b_H(i)I_i \cdot X^2 + \dots$$

$$B_D(PF) = \sum_{i=OV,IS,IV} b_D(i)I_i$$

$$B_Q(PF) = \sum_{i=OV,IS,IV} b_Q(i)I_i$$

$$B_H(PF) = \sum_{i=OV,IS,IV} b_H(i)I_i$$

$$X = \frac{R - R_{axis}}{R_{axis}}$$

Three pair PF coils have three degrees of freedom, required to adjust the axis position (Δ) by dipole component $B_D(PF)/B_D(HF)$, the elongation (κ) by quadrupole component $B_Q(PF)/B_Q(HF)$ and the loop voltage by poloidal flux ψ . By taking the minimization of B_{leak} at $R = 10$ m into account, four typical operation modes are defined: (1) steady state operation, (2) axis shift mode, (3) shaping mode, and (4) current drive/suppression mode. The required PF coil currents for these modes are given in Table 1. In addition to preprogrammed operations, the feedback scenarios for plasma position, cross-section and plasma current are also considered.

3. Accuracy of Coil Winding and Setting

To keep magnetic island smaller than 10 percents of the plasma minor radius, permissible global error field (toroidal mode number $n = 1 \sim 2$) should be less than 4 Gauss, and local mode ($n = 5 \sim 10$) should be within 10 Gauss at 4.0 Tesla operations. The required winding and installing accuracy of coils is within $5 \cdot 10^{-4}$ (2 mm) by the this criterion. Therefore, the mechanical stiffness of the coil support structure is necessary to hold these constraints. The displacement due to thermal shrink in the coil cooling-down phase is about a few ten millimeters, and special attention should be paid to the uniformity of this thermal shrink.

4. Electromagnetic force and Support structure Design

Figure 2(a) and (b) show the electromagnetic force on HFC without and with PF maximum current, respectively. The maximum electromagnetic force exceeds 1000 ton/m in the outward direction without PFC (Fig.2(a)) and in the inward direction with PFC (Fig.2(b)). The force of the IV (Inner Vertical) coils also exceeds 1000 ton/m. On the other hand, the electromagnetic force on the OV (Outer Vertical) and IS (Inner Shaping) coils is less than 1000 ton/m.

5. Support structure Design and FEM Analysis

As for HFC, the winding conductor and coil-can have not enough mechanical stiffness

to all three directions (F_R , F_ϕ and F_Z). Therefore, the transportation of this electromagnetic force to the 4.4°K external support is necessary. The toroidal shell or toroidal ring with reinforcing mechanical ribs is adopted to keep acceptable displacement. On the other hand, the mechanical stiffness of PFC is enough for hoop force F_R , however the F_Z force should be supported by the ribs on the structural toroidal shell. The total coil system is supported by this torus supporting shell structure.

The structural analyses of HFC and PFC supporting structure under the above-mentioned operation modes are done using several FEM (Finite Element Method) models by three engineer groups independently. The calculated maximum deformation are horizontally < 1.2 mm, toroidally < 0.8 mm and vertically < 1.7 mm. The maximum stress appears at the inboard-side support ring, and its value of 18.0 kg/mm² is tolerable.

6. Conclusion

Several operational scenarios of the Large Helical Device coils are defined and electromagnetic force and stress analyses are carried out using Finite Element Method. It is clarified that the stress level of coil can and supporting structure is about 30 kg/mm² which is allowable for the stainless steel at low temperature. The stiffness of this coil system can be adequate (less than 2 mm) to keep clean magnetic surface without large islands which are induced by the coil deformation.

Acknowledgment

The FEM analyses are carried out by engineers of Hitachi, Mitsubishi and Toshiba LTD.

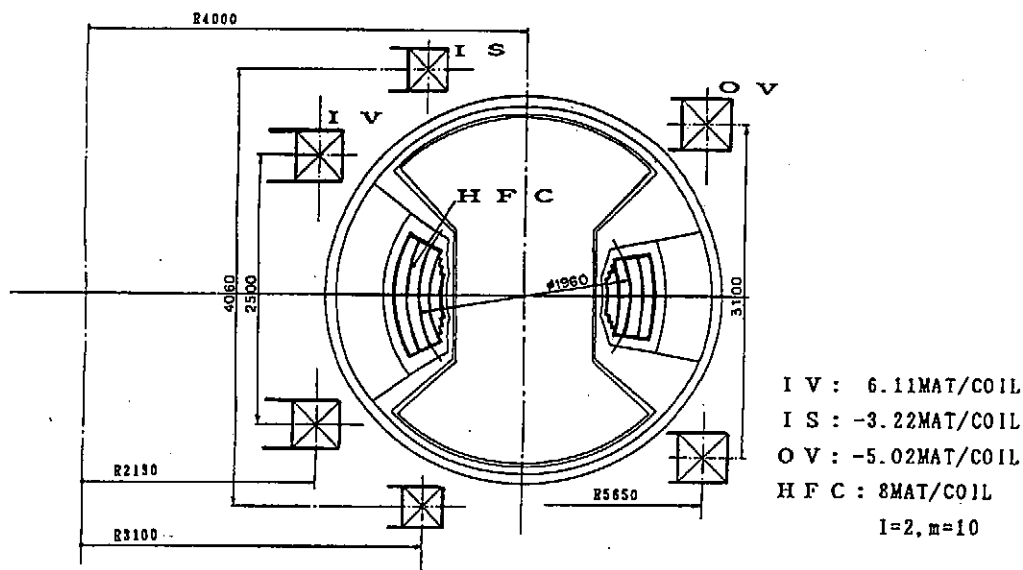


Fig. 1 Configuration and ampere-turns of LHD coil system

Table 1 Operation modes and coil currents of PFC.

Operation Mode		time = 0 s	time = 5 s
# 1 (Steady-State Operation)	$-B_D(PF)/B_D(HF)$	102%	
	$-B_0(PF)/B_0(HF)$	100%	
	$\phi(PF)+\phi(HF)$	80 Wb	
	I_{ou}	-4.51 MA	
	I_{is}	-1.88 MA	
	I_{iu}	4.77 MA	
# 2 (Axis-Shift Operation)	$-B_D(PF)/B_D(HF)$	98%	106%
	$-B_0(PF)/B_0(HF)$	100%	100%
	$\phi(PF)+\phi(HF)$	80 Wb	80 Wb
	Δ_{axis}	~-0 cm	~-20 cm
	I_{ou}	-4.34 MA	-4.67 MA
	I_{is}	-1.95 MA	-1.82 MA
	I_{iu}	4.41 MA	5.12 MA
# 3 (Shaping Operation)	$-B_D(PF)/B_D(HF)$	102%	102%
	$-B_0(PF)/B_0(HF)$	50%	150%
	$\phi(PF)+\phi(HF)$	80 Wb	80 Wb
	Δ_{axis}	~-10 cm	~-10 cm
	I_{ou}	-4.78 MA	-4.25 MA
	I_{is}	-0.55 MA	-3.22 MA
	I_{iu}	3.42 MA	6.11 MA
# 4 (Current Drive/Suppression)	Within Constraints of #1~#3 operation modes		

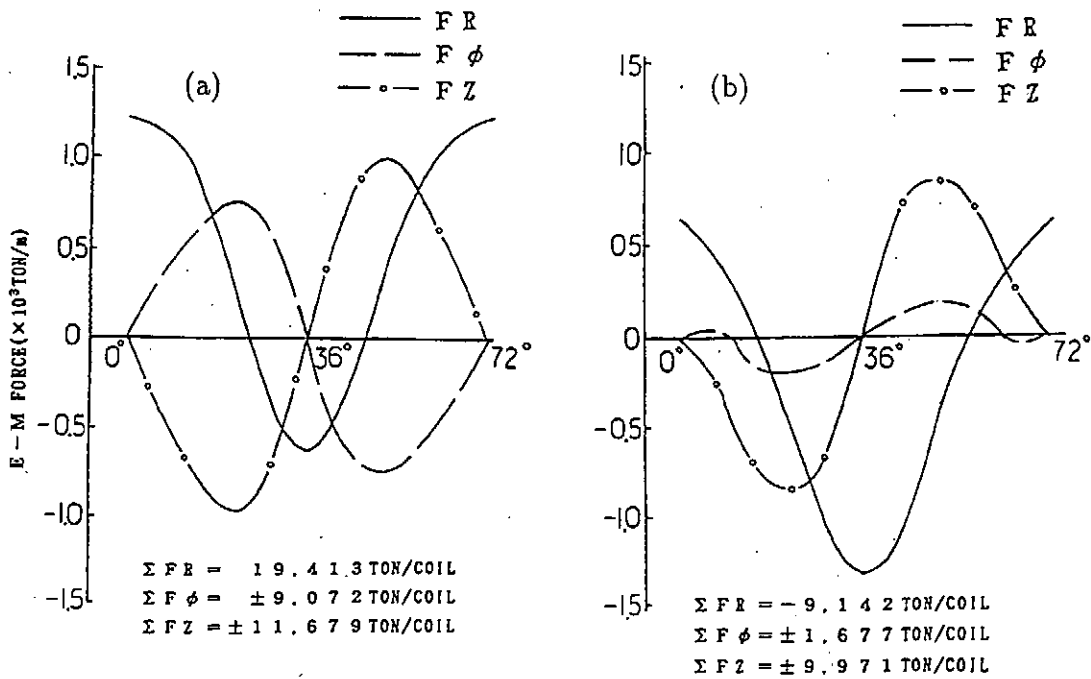


Fig. 2 Electromagnetic forces of HFC (a) without PFC and (b) with PFC.

Engineering Design of LHD Vacuum Vessel

N. Ohyabu & N. Noda

National Institute for Fusion Science

presented at Toki Conference

Toki, Japan (Dec. 1989)

Abstract - There are two key issues in designing the LHD vacuum vessel, i) how to accommodate a closed helical divertor system. The divertor is one of the major features of the LHD program. ii) how to assemble the vessel. The assembly procedure is quite different, depending on whether it is done before or after the coil winding.

The conceptual design of the LHD vacuum vessel is discussed. The vacuum vessel is helically twisted and rather complex, shown in Fig.1. The LHD vacuum vessel must be designed to satisfy physics requirements in addition to maintaining the vacuum integrity. The principal physics requirement is to accommodate a closed helical divertor system, shown in Fig.(2). Divertor is one of the major features of the LHD program and is expected to control the impurity contamination and to improve the energy confinement. The minor radius of the vessel is 1.60m, allowing divertor chambers with reasonable size. A critical point for the vessel and the helical coil designs is that gap between the coil surface and the first wall inner surface must be less than 15cm on the small major radius side of the torus in order to avoid plasma-wall interaction there, as shown in Fig.3. This necessitates an accurate fabrication and assembly of the vessel ($\pm 5\text{mm}$).

The LHD vacuum vessel must withstand various loads, requiring a certain thickness of the vessel. The LHD vessel tends to require thicker wall because of its complex shape compared with those of tokamak devices. However, thicker vessel allows higher vessel current when the axis or shape of the plasma is changed by the poloidal coil. The induced vessel current generates the error field, which may destroy the closed flux surfaces. Recent study has indicated that the main

component of the induced magnetic field is axisymmetric and thus harmless. Therefore wall (stainless steel) thickness of 3cm is found to be quite acceptable for the LHD operation. Even if the vessel shape is similar to that shown in Fig.1, the vessel with wall thickness of 3cm can withstand the atmospheric loading. The most severe loading may occur when large plasma current decays within the vessel time constant (~ 10msec). Therefore discharge must be operated carefully not to exceed a certain current level.

The vessel also must handle the heat flux from the plasma, 20MW for 10sec pulse operation and a few MW for steady state operation. In the normal discharges, the majority of the heat flux is guided to the divertor plates (carbon tiles) with water cooling. Heat fluxes on the divertor plate for the pulse operation (20MW, 10sec) and for the steady state operation (a few MW) are ~ 500W/cm² and ~ 50W/cm² respectively.

At the high density operation, the majority of the heat flux may be converted into the radiative power and the heat flux on the wall under the helical coil can be 20W/cm² for the pulse operation. The thermal stress on the wall due to the heat flux of 20W/cm² is found to be tolerable. The major engineering issue of the vessel design is how to fabricate and assemble the vessel. Fabrication and Assembly procedure will be quite different, depending on whether it is done before or after the coil winding. In the case where the vessel assembly is done before the coil winding, sectors (72°) of the vessel are fabricated at the factory and are shipped to the site. The assembly of the vessel will be easier, but it may cause difficulty in winding the coil. For the other case, many segments of the vessel wall are patched to make a vessel with complex shape, while maintaining vacuum integrity as well as accuracy of the assembly (± 5 mm). This is not an easy task. Finally specifications of the LHD vacuum vessel are summarized in Table 1.

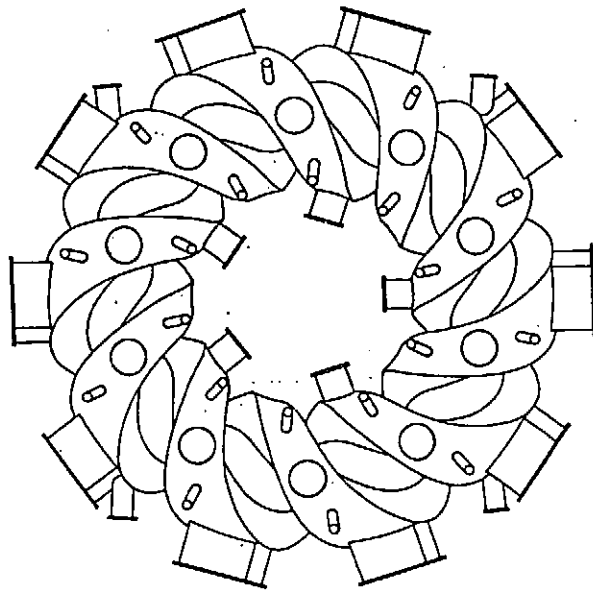


Fig.1 LHD vacuum vessel

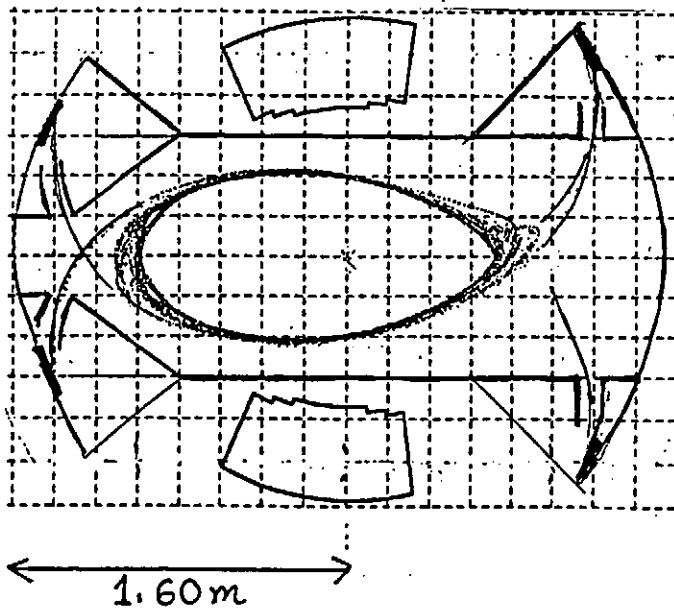


Fig.2 A design of LHD helical divertor

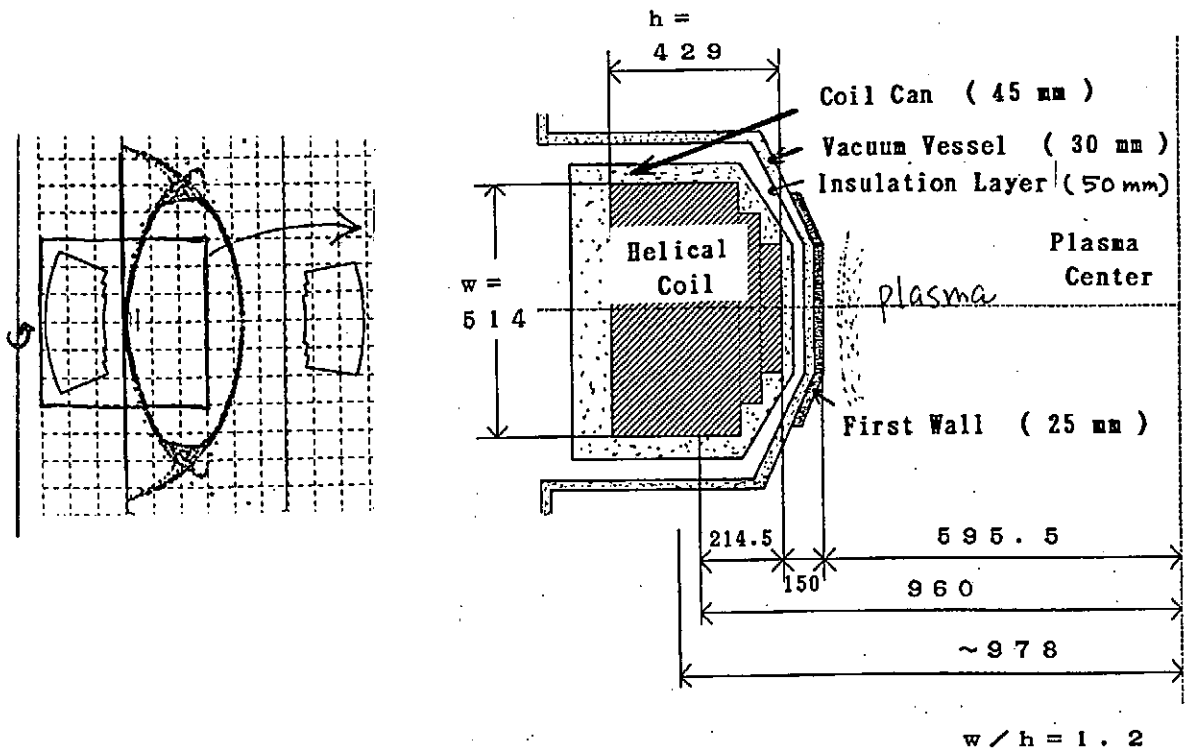
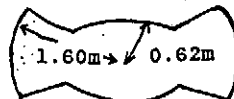


Fig.3 Small gap between the coil surface and the edge plasma region.

1) Size, Shape

- . Major radius $R=4m$
- . Shape



- . gap between coil surface and the first wall (Δ)
- $\Delta \leq 150mm$

- . Toroidal Resistance $\geq 0.05 m$

2) Baking Temperature

Vacuum Vessel	100° C
First wall (divertor tile)	350° C (550° C ?)

3) Heat Flux

Divertor plate	500w/cm ² for 20MW, 100sec
	50W/cm ² for 2MW, ∞ sec
First wall	20W/cm ² for 20MW, 10sec
	2W/cm ² for 2MW, ∞ sec

Table 1 Specifications of the LHD Vacuum Vessel (not final)

Development of Superconductor for Large Helical Device

T. Mito, J. Yamamoto, K. Takahata, O. Motojima
National Institute for Fusion Science
Furo-cho, Chikusa-ku, Nagoya-shi, 464-01, Japan

F. Sumiyoshi
Faculty of Engineering, Kagoshima University
Kagoshima-shi, 890, Japan

Abstract: The present situation of the design and construction of R&D superconducting conductors for Large Helical Device is reported. At first, the required properties for the conductor of LHD and the design criteria of the conductors are mentioned. Then the designed patterns of the cross sections of R&D conductors are shown. The test and estimation items of conductors are listed. Lastly, the R&D schedule are shown.

1. Required properties for the conductor of LHD

The required properties for the conductor of the superconducting helical coil of LHD are shown as follows.

- 1) The superconducting characteristics, thermal properties and mechanical properties are not lowered by the large electromagnetic force of the helical coil.
- 2) There are no damage of the conductor during the helical winding process.
- 3) The conductor has high current density in order to satisfy the coil average current density of 40 A/mm^2 at 8 T.
- 4) The conductor is enough stable against the quench because the superconducting coils have large magnetic stored energy about 2 GJ.
- 5) The conductor must be easy to wind because the winding process is done at the experimental site.
- 6) The AC loss due to the field change of the poloidal coils is reduced in order not to affect the stability of the helical coils.

2. Design criteria of R&D conductors

The conductor for the large helical coil must satisfy the criteria mentioned as follows.

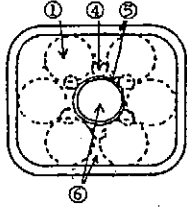
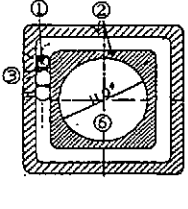
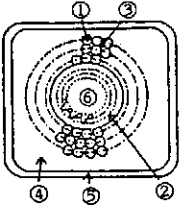
- 1) NbTi superconductor is selected considering large electromagnetic force and twisted helical winding.
- 2) The current density of the conductor is about 55 A/mm^2 at 8T in order to satisfy the coil average current density of 40 A/mm^2 .
- 3) The operational current of the conductor is about 30 kA in order to satisfy both requirements of feasibility of the winding and the coil safety after quench.
- 4) The conductors with both cooling types of the pool boiling and the forced flow are considered as a candidate for LHD.
- 5) The pool boiling conductors are aimed to study how the difference of the position of pure aluminium in the conductor affects the stability and the mechanical properties.
- 6) The forced flow conductors are aimed to study the difference of the position of helium cooling path and superconducting wire.

3. Designed patterns of R&D conductors

Table 1. Pool boiling conductors for LHD

CONDUCTOR NAME	DESIGN-H	DESIGN-M	KISO-IB	KISO-2B	KISO-3B	KISO-4B
NOMINAL CURRENT (kA)	30.3	20.0	22.0	30.0	30.0	30.0
CRITICAL CURRENT (kA) at 8T, 4.2K	60.5	34.7	40.0	60.0	60.0	60.1
OVERALL CURRENT DENSITY (A/mm ²)	58.3	55.4	56.7	55.0	50.8	55.0
NbTi CRITICAL CURRENT DENSITY (A/mm ²) at 8T, 4.2K	800	960	850	950	950	850
SIZE (mm×mm)	40.0×13.0	19.0×19.0	19.7×19.7	28.5×19.0	29.5×20.0	23.4×23.4
NUMBER OF STRANDS	26	55	30	24	24	80
DIAMETER OF NbTi/Cu STRAND (mm)	2.7	1.2	2.0	2.46	2.46	1.50
DIAMETER OF Al CLAD STRAND (mm)	-	-	-	3.80	3.80	-
Cu/SC RATIO IN STRAND	0.97	1.0	1.0	0.8	0.8	1.0
AREA OF CROSS SECTION (mm ²)	520	361	388.1	541.5	590.0	547.6
COMPOSITION (VALUE FOR 10kA)						
NbTi	75.6 (25.0)	36.1 (18.1)	47.0 (21.4)	63.2 (21.1)	63.2 (21.1)	70.7 (23.6)
Cu	258.6 (85.3)	223.8(111.9)	182.0 (82.7)	299.5 (99.8)	50.6 (16.9)	338.5(112.8)
Al	157.8 (52.1)	83.0 (41.5)	121.0 (55.0)	158.7 (52.9)	158.7 (52.9)	105.2 (35.1)
PbSn	28.0 (9.2)	18.1 (9.0)	18.1 (9.0)	20.1 (6.7)	0.0 (0.0)	33.2 (11.1)
SS	0.0 (0.0)	0.0 (0.0)	0.0 (0.0)	0.0 (0.0)	199.9 (66.3)	0.0 (0.0)
LHe	0.0 (0.0)	0.0 (0.0)	0.0 (0.0)	0.0 (0.0)	88.0 (29.6)	0.0 (0.0)
Cu(SPACER)	0.0 (0.0)	0.0 (0.0)	0.0 (0.0)	0.0 (0.0)	28.8 (9.6)	0.0 (0.0)
RESISTANCE OF CONDUCTOR (Ω/cm)	2.23×10 ⁻⁹	3.93×10 ⁻⁹	2.94×10 ⁻⁹	2.18×10 ⁻⁹	2.52×10 ⁻⁹	3.02×10 ⁻⁹
RESISTANCE OF 10kA CONDUCTOR	6.76×10 ⁻⁹	7.86×10 ⁻⁹	6.47×10 ⁻⁹	6.54×10 ⁻⁹	7.56×10 ⁻⁹	9.09×10 ⁻⁹
PRIMER (cm)	10.6	7.6	7.88	9.5	11.4	9.4
EXPOSURE RATIO	0.667	0.5	0.65	0.5 (0.667)	0.65	0.5 (0.667)
STABILITY PARAMETER	0.97	1.38	0.93	1.37(1.03)	1.02	1.94(1.45)
MANUFACTURER	HITACHI	MITSUBISHI	SUMITOMO	FURUKAWA	FURUKAWA	HITACHI CABLE
CROSS SECTION						
	① NbTi/Cu ② 1/2H Cu ③ PbSn ④ Al ⑤ SS					

Table 2. Forced flow conductors for LHD

CONDUCTOR NAME	DESIGN-T	KISO-1F	KISO-2F
NOMINAL CURRENT (kA)	34.8	22.0	30.0
CRITICAL CURRENT (kA) at 8T, 4.2K	70.0 (@ 8.4T)	40.0	59.4
OVERALL CURRENT DENSITY (A/mm ²)	54.2	56.7	52.1
NbTi CRITICAL CURRENT DENSITY (A/mm ²) at 8T, 4.2K	774 (@ 8.4T)	850	850
SIZE (mm×mm)	27.0×23.8	19.7×19.7	24.0×24.0
NUMBER OF STRANDS	486	30	137
DIAMETER OF NbTi/Cu STRAND (mm)	0.7	2.0	1.14
Cu/SC RATIO IN STRAND	1.0	1.0	1.0
INNER DIAMETER OF COOLING PIPE (mm)	7.0	11.0	10.5
AREA OF CROSS SECTION (mm ²)	642.6	388.1	576.0
COMPOSITION (VALUE FOR 10kA)			
NbTi	90.4 (26.0)	47.0 (21.4)	69.9 (23.3)
Cu	90.4 (26.0)	230.0(104.7)	69.9 (23.3)
Al	55.4 (15.9)	0.0 (0.0)	151.6 (50.5)
SS	143.4 (41.2)	0.0 (0.0)	109.4 (34.5)
CuNi	6.5 (1.9)	0.0 (0.0)	0.0 (0.0)
Pipe	11.8 (3.4)	0.0 (0.0)	39.5 (13.2)
He	244.7 (70.3)	95.0 (43.2)	103.8 (34.6)
PbSn	0.0 (0.0)	14.6 (6.6)	29.5 (9.8)
RESISTANCE OF CONDUCTOR (Ω/cm)	6.36×10 ⁻⁹	2.08×10 ⁻⁸	2.49×10 ⁻⁹
RESISTANCE OF 10kA CONDUCTOR	2.21×10 ⁻⁸	4.59×10 ⁻⁸	7.47×10 ⁻⁹
MANUFACTURER	TOSHIBA	SUMITOMO	HITACHI CABLE
CROSS SECTION ① NbTi/Cu ② 1/2H Cu ③ PbSn ④ Al ⑤ SS ⑥ SHE			

There are two types of R&D conductors. One is proposed from the LHD coil design and the farther R&D coil design in 1989 by a coil manufacturer (DESIGN-H, DESIGN-M, DESIGN-T). The other is designed in the R&D program on superconductor for LHD in collaboration with a cable manufacturer (TOKI-1B - 4B, TOKI-1F - 2F)

The parameters of the pool boiling conductors are listed in Table 1 and those of the forced flow conductors are listed in Table 2.

4. Test and estimation items of conductors

We are planning to test the 1/3 scale R&D conductors about the superconducting characteristics, the stability and the mechanical properties from February 1990. The considered test and estimation items are listed as follows. The preliminary selection of the conductor will be done according to the result of part of the following tests.

- 1) Mechanical properties at the room temperature

- <Short sample>
 - Young's modulus of the single conductor
 - Boundary condition of each materials inside the conductor with bending and twisting stress.
- <Coil pack>
 - Young's modulus of the coil pack
 - Boundary condition of each materials of the coil pack with compressive stress corresponding to the electromagnetic force
- 2) Superconducting properties at the LHe temperature
 - <Short sample>
 - Critical current
 - Current distribution in the conductor after the normal transition
 - Stability and cooling properties
 - AC loss
- 3) Mechanical properties at the LHe temperature
 - <Short sample>
 - Young's modulus of the single conductor
 - Effects of the thermal cycle
 - <Coil pack>
 - Young's modulus of the coil pack
 - Stress distribution and coil deformation
- 4) Superconducting properties under mechanical loads at the LHe temperature
 - <Short sample>
 - Stress effect of superconducting properties
 - Degradation of the conductance of pure aluminum
 - Stability against the mechanical disturbance

5. R&D schedule

- 1) We are now developing various R&D superconducting conductors with the operational current of 7 - 10 kA which are 1/3 scale of the conductor of LHD (20 - 30 kA).
- 2) We are planning to test the R&D conductors about the superconducting characteristics, the stability and the mechanical properties from February of 1990.
- 3) At first the superconducting characteristics are tested at the Plasma Physics Laboratory of Kyoto University using the superconducting coil test facility.
- 4) Then the farther tests including the mechanical tests under the liquid helium temperature will be done at new cryogenic building of NIFS in Toki site from the autumn of 1990.

Acknowledgement: The authors are indebted to Prof. A. Iiyoshi, Director General of NIFS, and Prof. M. Takeo of Kyushu Univ. for their continuous encouragements and helpful discussions. The authors are also grateful to Prof. T. Obiki, Director of PPL Kyoto Univ., and other members of PPL for helpful discussions and collaboration. We deeply thank Sumitomo Electric Industries, Furukawa Electric Co., LTD., and Hitachi Cable, Ltd. for their cooperation with us to develop the conductors. We would like to thank Hitachi, Ltd., Mitsubishi Electric Co., LTD., and Toshiba Corporation for their cooperation with us to design the superconducting helical coils and conductors.

Toki-Conference, December 1989

Overview of Engineering Design of Wendelstein VII-X J. Sapper

Max-Planck-Institut für Plasmaphysik, Euratom Association
D-8046 Garching, FRG

1) Introduction

The Experiment Wendelstein VII-X is in the final stage of preparatory studies at the Max-Planck-Institut für Plasmaphysik, Garching, (IPP). It is a large machine in that the plasma to be studied should be representative for future Stellarator reactors. The main parameters are: major radius $R_0 = 5,5$ m, magnetic induction $B_0 = 3$ T, stored magnetic energy $W = 600$ MJ. The average plasma radius will be 0.53 m. Following the Garching development line, the confinement field will be generated by one set of nonplanar coils, modularly arranged in toroidal periods. Additional planar coils will allow experimental flexibility (τ -variation), which will not be necessary later on in an optimized reactor design with fixed operating conditions.

Under the constraint of a required pulse-length of more than 10 sec. for the experiment, superconduction is the technical solution for the coil design. In a first design step the technical features of the machine were studied together with competent industrial companies.

2.) The coil set

The total arrangement of the nonplanar coils is shown in figure 1. Fifty individual coils are assembled in 5 periods. There are 5 types of coils and each period is built up with these 5 types using symmetry conditions to the mid-plane of the period. In figure 2 one field period is shown together with the 4 planar (but not circular) coils, allowing variation of the rotational transform τ of about ± 20 % referred to the standard value of 0.84 on the plasma axis. In table I characteristic technical data of the coil set are listed.

3.) Structure and Cryostat

The winding pack of each coil will be surrounded by a housing of stainless steel, 5 cm thick. A 8 cm thick toroidal shell, surrounding the coil set from outside is comprehending the confinement coils in a stiff toroidal arrangement. All of these machine components will be on LHe temperature

of 4 K, so that a cold mass of approximately 400 tons has to be cooled. This mass is in the same range as it was in the LCT project in Oak Ridge, USA, and which was practically operated during the test-runs. The cold mass of the experiment will sit in a toroidal double-walled cryostat of which the inner vessel is the plasma chamber for the experiment and the outer vessel is enveloping the whole confinement system. Ports and coil supplies are penetrating the cryostat thermally insulated. The arrangement is illustrated in figure 3.

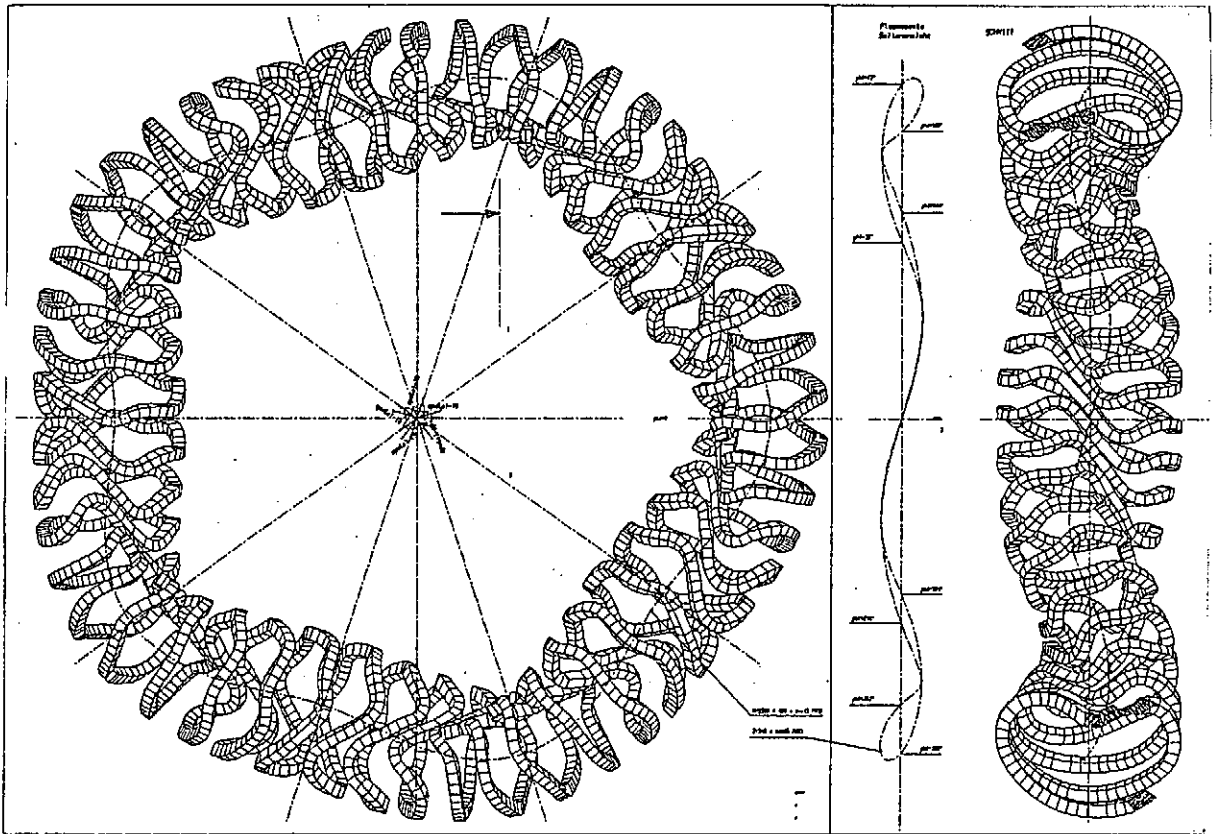


Fig. 1: Modular coil set, total arrangement.

Fig. 2: A field period with four additional planar coils.

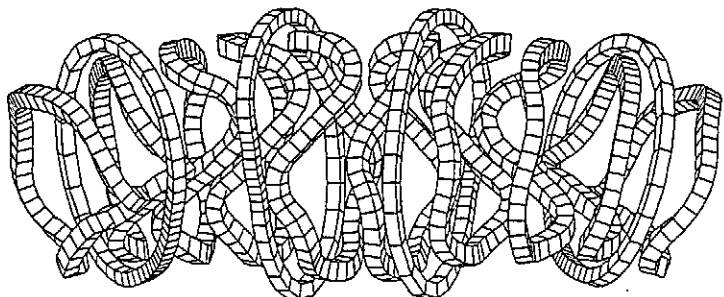


TABLE I Characteristic data of the experiment WVII-X

Average major radius	R_0	[m]	5.5
Average coil radius	r_c	[m]	1.14
Radial coil height	t	[m]	0.21
Lateral coil width	w	[m]	0.18
Total coil volume	V_c	[m ³]	15.1
Min. radius of curvature	p_c	[m]	0.23
Min. distance plasma-coils	Δ_{pc}	[m]	0.18
Total coil current	I_c	[MA]	1.82
Overall current density	j_c	[MA/m ²]	48.1
Stored magnetic energy	W	[GJ]	0.60
Induction on axis	B_0	[T]	3.0
Max. induction at coil	B_m	[T]	6.1
Rotat. transform on axis	l_0		0.84
Average plasma radius	r_p	[m]	0.53
Average force density	f	[MN/m ³]	79.
Max. net force (one coil)	F_{res}	[MN]	3.6

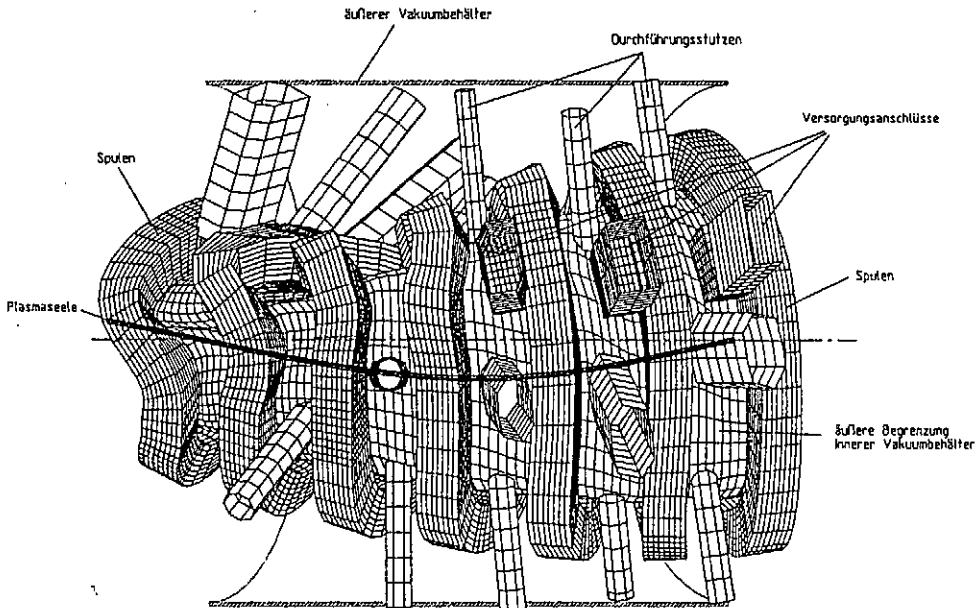


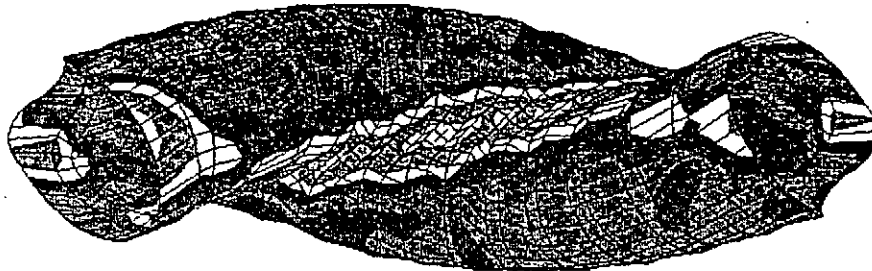
Fig. 3: Coil arrangement in the cryostat.

4.) Forces and FE-modelling

The considerable magnetic forces of the coils (see table I) are acting on the 8 cm toroidal shell. This shell is free of residual outside forces (excepted the weight) and is hanged with thermal insulators in the cryostat. In a finite element analysis stresses in the shell material have been calculated. Figure 4 demonstrates the V. Mises stress distribution on the shell surface.

LOADCASE: 101
FRAME OF REF: GLOBAL
STRESS - VON MISES MIN: 7.76E+00 MAX: 2.34E+02

SHELL SURFACE: TOP



Ident-N./No. 32.07
Seite/Page: 4 - 39

Fig. 4: Stress distribution on the surface of the toroidal cold shell

5.) Superconductor

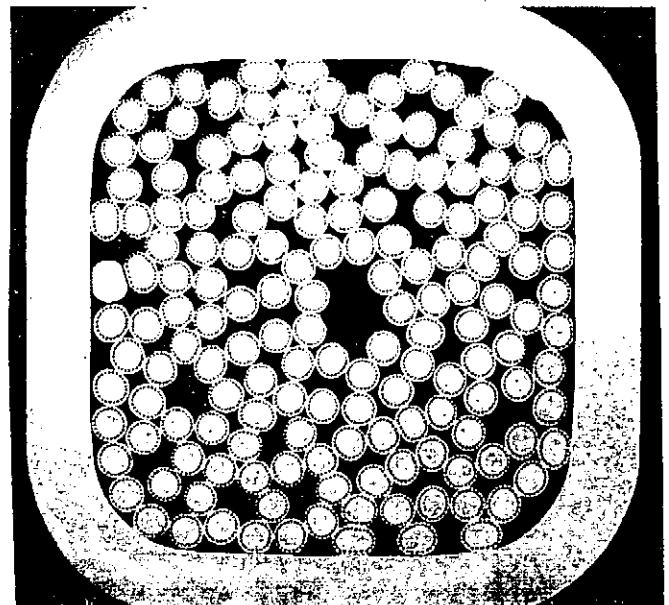
The coils for the experiment shall be wound in high precision moulds from a cable-in-conduit conductor. Copper strands with embedded NbTi-fibres are cabled and enclosed in a He-tight envelope. The volume between the strands serves for forced flow He-cooling. It is ensured that cable lengths of approx. 300 m can be manufactured, so the coils can be wound in double-layer technique. The cooling medium pressure drop along one double-layer is in the range of 10 bar. In figure 5 the cross-section of a cable with a steel jacket is shown.

6.) Realization of the Project

The project will be realized in three essential steps:

A prototyping phase of about 3 years will be followed by an industrial manufacturing period for the components of 4 years. The assembly phase on site will take another year, so that the experiment would be operational in 1998 when started immediately.

Fig. 5: Cross-section through the superconductor with steel jacket. Void fraction for cooling approx. 35 %.



100GHz Half Megawatt Microwave Transmission System Development with Whispering gallery Mode

M.Sato¹, M.Iima¹, S.Kobayashi¹, S.Sudo¹, F.sano¹, H.Zushi¹, T.Obiki¹, M.Nakajima²,
S.Kubo³, M.Hosokawa³, T.Mutoh³, K.Ohkubo³, T.Kuroda³, O.Motojima³, K.Sakamoto⁴,
T.Nagashima⁴, M.Thumm⁵, W.Kasperek⁵

1. Plasma Physics Laboratory, Kyoto University, Gokasho, Uji 611, Japan
2. Department of Electronics, Kyoto University, Kyoto 601, Japan
3. National Institute for Fusion Science, Nagoya 464-01, Japan
4. Japan Atomic Energy Research Institute, Naka, Ibaragi, Japan
5. Institut für Plasmaforschung der Universität Stuttgart, 7. Stuttgart 80, F.R.G.

Gyatron Tube

A 106 GHz half megawatt ECRH system has been developed at PPL Kyoto University since 1986. The high density ($\sim 10^{20}m^{-3}$) plasma production and heating can be expected by the system. The engineering object toward the development is a breakthrough in the two hundreds Kw system to one Mw system with the single tube at the frequency around hundred GHz.

The deferent concepts would be available for the interaction cavity of the high power gyatron. The cavity oscillating with whispering gallery mode is the most provable candidate. Because, the structure of the tube is almost as same as the conventional axsymetric mode gyatron, and the mode separation and wall loading in the cavity can be reduced lower than the conventional mode at the same power level. The design study had started for the practical tube in 1986. PPL Kyoto University ordered development of first long pulse half megawatt whispering gallery mode tube to Varian in 1987 and received it in 1988. The specifications of the tube satisfied the requirements. More over, the dynamic operation ranges are two or three times wider than that we expected from the experience of conventional 200 KW tubes.

Quasi-Optional Mode Converter Development

The whispering gallery is a rotating transverse electric ($TE_{m,n}$) mode in a cylindrical waveguide with a high azimuthal (m) and a low radial (n) mode numbers. The improved efficiency quasi-optical (Vlasov) converter has been developed to get the simple Gaussian like beam or a simple low loss waveguide mode from the whispering gallery mode. The Vlasov converter is a kind of parabolic antenna which has radiator with the function to radiate the linear polarized microwave. The conversion efficiency is less than 80 % on the original Vlasov's design, since the radiation field has a flat profile in the azimuthal directions which shall be eased to a gaussian-like peaked profile with the generation of side lobes during the propagation along the beam axis. The best way to reduce the side lobe generation is to obtain a Gaussian like radiation field directly from the radiator. The new

mirror, we call "Visor", is added to the output mouth of the radiator. The shapes of Visor and mouth are designed by the methods of geometrical optics. The cold test has been done using one inch radiator and $TE_{12,2}$, 120GHz, whispering mode generator. The measured radiation patterns are shown in Fig.1 (a) and (b) for the comparison of the original Vlasov converter and improved Q-O converter. The side lobe level can be reduced to less than 5 %. The phase front of the output beam of improved converter is almost in a flat plane in the near field of the focus reflector. It must be better to set the phase correcting mirror just after the Q.O converter to obtain the pure Gaussian like TEM_{00} mode. The mirror can be designed according to the phase measurement results.

Transmission Line

The overall transmission system is shown in Fig.2. The TEM_{00} beam transmission method is mainly employed. The beam waist radius are shown in the figure. The system consists of three parts, which are the improved Q.O. mode converter, the long distance beam transmission line and the launcher section including the polarization rotating twist reflector and the beam to waveguide coupler at the vacuum tight window. The output mode purity and the power of the desired $TE_{12,2}$ mode are monitored by the wave number spectrometer. The elliptical mirrors (6) and (9) have small arrays of holes ($\phi 0.14mm$) with bolometers to monitor the beam alignment which can be adjusted by remote control system (14). The absolute power is measured by the water load (11), if the mirror (9) swings up. The wavenumber spectrometer will be calibrated by the water load including almost all the conversion and transmission losses, since the undesired mode cannot be radiate in the main beam from the Q.O converter and absorbed SiC tiles in the cylindrical support structure, we can estimate the injection power to the plasma by the spectrometer for every shot. The transmission loss from Mirror (5) to (9) is expected about 7 %, and the mode converter loss will be 5 %. The overall efficiency will be 88 %.

Summary

1. The 106GHz, half megawatt ECRH system is now under the final stage of the development.
2. This system will be completed in 6 month.
3. The information from this system will serve for future one megawatt design.

Reference

M.Iima, M.Sato, *et al.*; Measurement of radiation field from an improved efficiency Q-O converter for whispering Gallery mode, Proc. of 14th int. Cont. on Infrared and millimeter waves, Würzburg F.R.G. 1989.

Fig.1(a) Power counter levels for conventional converter

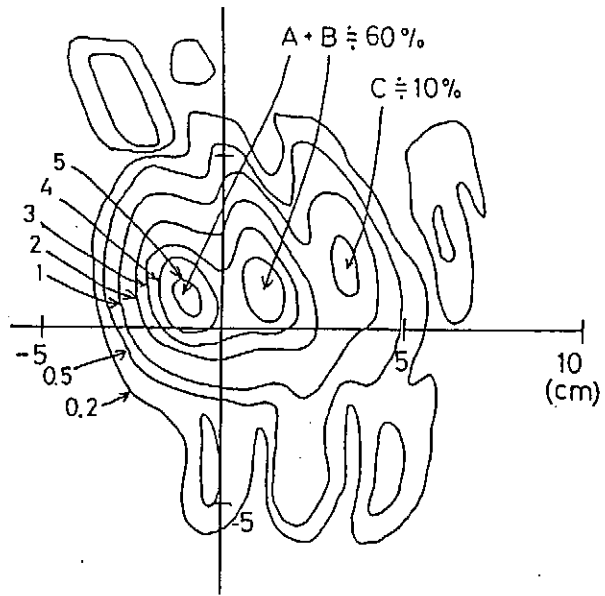
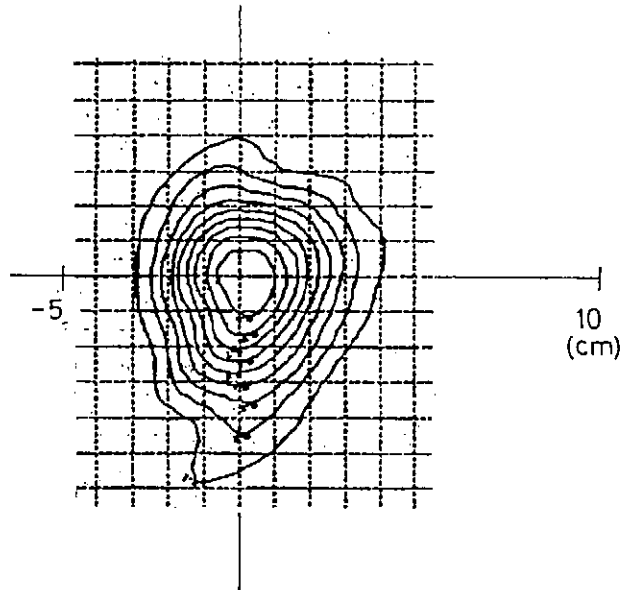


Fig.1(b) Power counter levels for Improved efficiency converter.



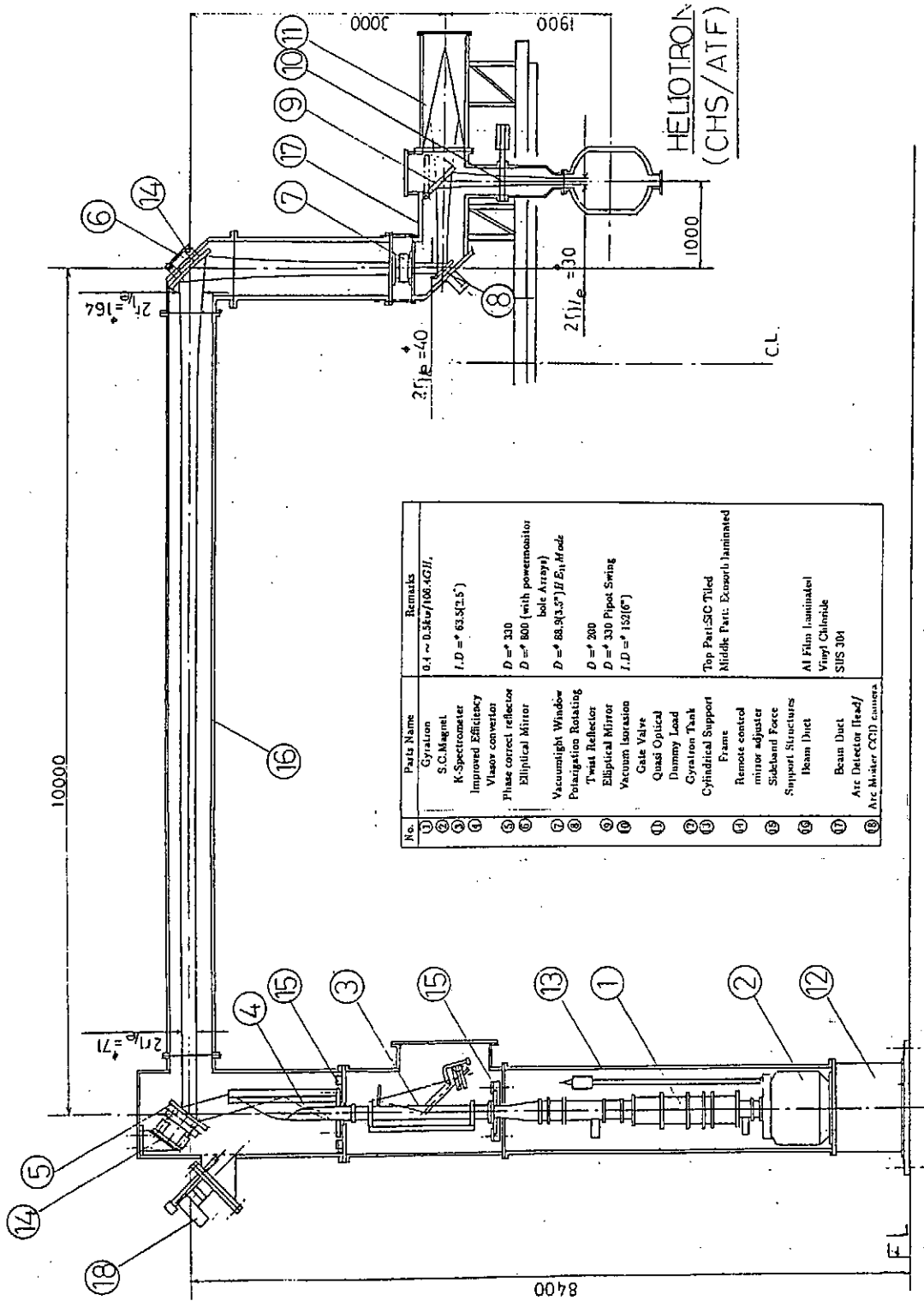


Fig.2 Overall transmission system design

NBI System with Negative Ion Source in Large Helical Device

Y.Takeiri, O.Kaneko, F.Sano*, A.Ando,
Y.Oka, K.Hanatani*, T.Obiki*, and T.Kuroda

National Institute for Fusion Science, Nagoya 464-01, Japan
**Plasma Physics Laboratory, Kyoto University, Uji 611, Japan*

Abstract: Negative-ion-based NBI system is designed for Large Helical Device. Injection energy is 125 keV for hydrogen beam and total injection power is 20 MW which is provided by four tangential injectors with two ion sources. Design concept for the system performance and hardware system design are described.

1. Introduction

NBI heating is expected to be one of the most promising heating methods in the Large Helical Device (LHD) project. Achievement of the objective plasma parameters in the LHD, which are $n_e \tau_E T_i = 0.1 \sim 1 \times 10^{20} m^{-3} sec keV$ (high $n\tau T$ mode), $T_i(0) = 10 keV$ (high T_i mode) and $\langle \beta \rangle \geq 5\%$ (high β mode), requires the injection power of 20 MW. NBI heating method is also attractive for investigation of the plasma physics issues such as current drive/suppression, transport analysis, and MHD activity.

We have proposed 125 keV(H)/20MW negative-ion-based NBI system which satisfies the experimental conditions of every mode in the LHD. In the following, basic system parameters

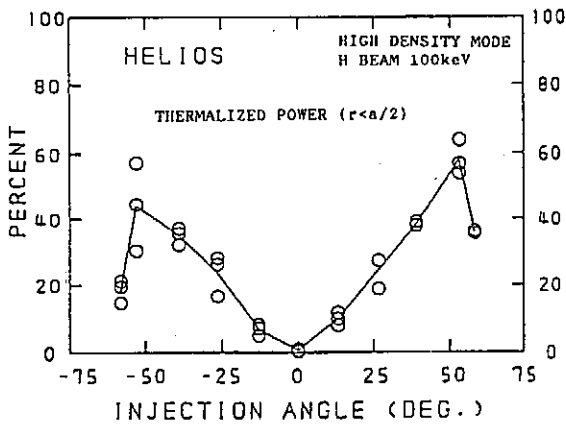


FIG. 1 Ratio of the thermalized power within a half radius to the port-through power as a function of the injection angle under the conditions where the H beam of 100keV is injected to plasma in the high-density mode.

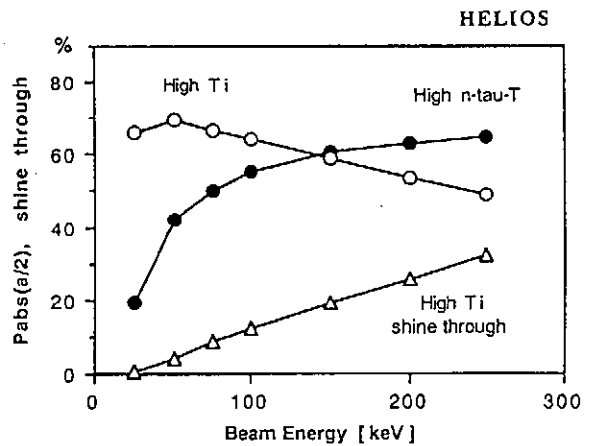


FIG. 2 Ratios of the absorption power within a half radius to the port-through power as a function of the H beam injection energy at the tangential injection. The shine-through power in the low-density mode is also shown.

determined from physics aspect and the first-phase hardware design of NBI system are described.

2. Determination of Basic System Parameters

Basic design concepts for the NBI system are as follows;

- (1) core plasma heating,
- (2) passing particle heating,
- (3) constant input power for the wide range of the plasma density.

The LHD has loss-cone in velocity space at the peripheral region. To achieve the core plasma heating without reduction of the heating power, the passing particle heating is essential. Figure 1 shows the ratio of the thermalized power within a half radius to the port-through power, which is a measure of the core plasma heating, as a function of the injection angle in the high-density mode (high $n\tau T$ mode). This result is obtained by the orbit-following Monte-Carlo code, HELIOS. It is found that the tangential injection (injection angle of about 50°) is effective to the core plasma heating. Although the loss-cone area is changed by adjusting the magnetic surface configuration, the passing particle heating, which has almost no orbit loss within a half radius, is the most reliable to every experimental mode.

Figure 2 shows the ratios of the absorption power within a half radius to the port-through power as a function of the injection energy (H beam) at the tangential injection. The shine-through power in the low-density mode (high T_i mode) is also shown in the figure. In the high-density mode the shine-through power is negligibly small. At the injection energy of 100 to 200 keV the core plasma heating above 50 % is achieved in both the low- and the high-density modes. Since the shine-through power in the low-density mode is more than 15 % of the port-through power at the beam energy above 150 keV, the appropriate injection energy is 100 to 130 keV for wide range of plasma density. Thus, we have decided that the injection energy is 125 keV for hydrogen injection.

On the other hand, 20 MW of the NBI power is injected through four ports. The tangential view of the injection port is relatively narrow for 5 MW injection, ~ 400 mm in diameter, and the injection port is long, ~ 3 m, due to the large cryostat of the LHD. Thus, the beam divergence angle should be small. Figure 3 shows the beam transport efficiency as a function of the beam divergence angle, under the conditions where two ion sources with the extraction area of $25 \times 150\text{cm}^2$ are placed at a distance of 11.5 m from the entrance of the injection port. The beam transport efficiency in the case of the 3 m-long injection port with the rectangular entrance of $40 \times 40\text{cm}^2$ is restricted to 80 % even at the beam divergence angle of 0.4° , as shown in Fig. 3(a). When the injection port is taper-shape with the entrance aperture of $80 \times 80\text{cm}^2$ and the exit aperture of $40 \times 40\text{cm}^2$, the transport efficiency is improved to more than 90 % at the beam divergence angle of 0.5° , as shown in Fig. 3(b). However, all of the loss power is deposited inside of the injection port. Even if the injection port shape is optimized, the beam divergence angle is required to be less than 0.5° .

Neutralization efficiency of negative ions are much higher than positive ions at the beam energy above 100 keV and the negative ion beam has a potential to realize the small beam divergence angle below 0.5° . Therefore, we have adopted the negative-ion-based NBI system, which satisfies the both conditions of the injection energy and the beam divergence angle.

3. Hardware Design

The performance of 125 keV/20 MW negative-ion-based NBI system for the LHD is indicated in Table I. In hydrogen injection, eight ion sources are installed at four injectors and

provide the 20 MW - 10 sec neutral beam. The tangential injectors are arranged as balanced injection is possible. In deuterium injection, since the injection energy is 250 keV, four ion sources are used for 20 MW injection. Thus, two injectors are designed as 250 keV injection system. The schematic diagram of the injector is shown in Fig. 4.

A negative ion source is large, the extraction area of which is $25 \times 150 \text{ cm}^2$, and delivers 45 A with the current density of 30 mA/cm^2 . Development of this ion source is a key issue to construct the NBI system.

The gas-load of the negative ion source is large and, thus, the injector has two chambers with large cryo-panels connected by 5m-long neutralizers. The reflection-type (180° deflection) deflection magnet is used for separating the residual ion beams in the first-phase design.

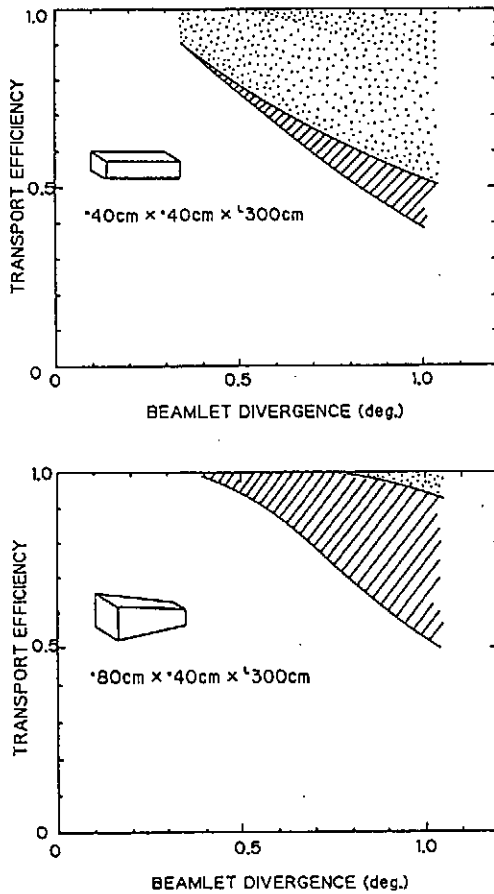


FIG. 3 Beam transport efficiency as a function of the beam divergence angle, under the conditions where two ion sources with the extraction area of $25 \times 150 \text{ cm}^2$ are placed at a distance of 11.5 m from the entrance of the injection port. The dotted area indicates the beam power lost before entering the injection port and the hatched region indicates the beam power lost inside of the injection port. The shape of the injection port is (a) rectangular of $40 \times 40 \text{ cm}^2$ and (b) taper-shape with the entrance aperture of $80 \times 80 \text{ cm}^2$ and the exit aperture of $40 \times 40 \text{ cm}^2$.

TABLE I Performance of 125keV/20MW negative-ion-based NBI system in the LHD.

Overall

Injection power	20 MW (port through)
Beam energy	125 keV (H) / 250 keV (D)
Pulse length	10 sec
Ion species	H or D
Number of injector	4 (H) / 2 (D)
Number of ion source	2 per an injector
Injection angle	Tangential injection (Balanced injection)

Ion source

Source type	Volume production
Grid size	$25 \text{ cm} \times 150 \text{ cm}$ (3750 cm^2)
Transparency	40 %
Extracted current	45 A
Current density	30 mA/cm^2
Beam divergent angle	0.5°

Neutralizer

Size	$25 \text{ cm} \times 150 \text{ cm} \times 500 \text{ cm}$
Line density	16.7 Pa cm ($4.4 \times 10^{15} \text{ molecules/cm}^2$)
Pressure	$6.5 \times 10^{-2} \text{ Pa}$ (at entrance) $1.5 \times 10^{-3} \text{ Pa}$ (at exit)

Cryo-pump

Source Chamber	$505 \text{ m}^3/\text{s}$
Beam dump chamber	$2040 \text{ m}^3/\text{s}$
Refrigerator power	$\sim 1 \text{ kW}$ (at 3.7K)

Injection port

Size	$400 \sim 500 \text{ mm}^\phi$
Length	3 m
Pressure	$1.5 \times 10^{-3} \text{ Pa}$

The injector is fairly large, which is 15 m-long, 5 m-wide and 10 m-high. Thus, in the second-phase design we should make the injector as compact as possible. For example, the deflection magnet become smaller by making the residual ion beams deflect with a smaller angle. The smaller deflection magnet is required also for reduction of error magnetic field in the LHD.

4. Summary

Basic system parameters and the first-phase hardware design of the 125 keV/20 MW negative-ion-based NBI system in the LHD are described. Intensive five year R&D program for development of the negative ion source has been started in 1989.

There is an alternative design concept of 250 keV/20MW NBI system, where 250 keV hydrogen injection in the high-density mode and 250 keV deuterium injection in the low-density mode are utilized. This concept means that objective of the NBI heating is restricted mainly in the high-density mode. Detailed design should be proceeded from physics aspect and hardware construction.

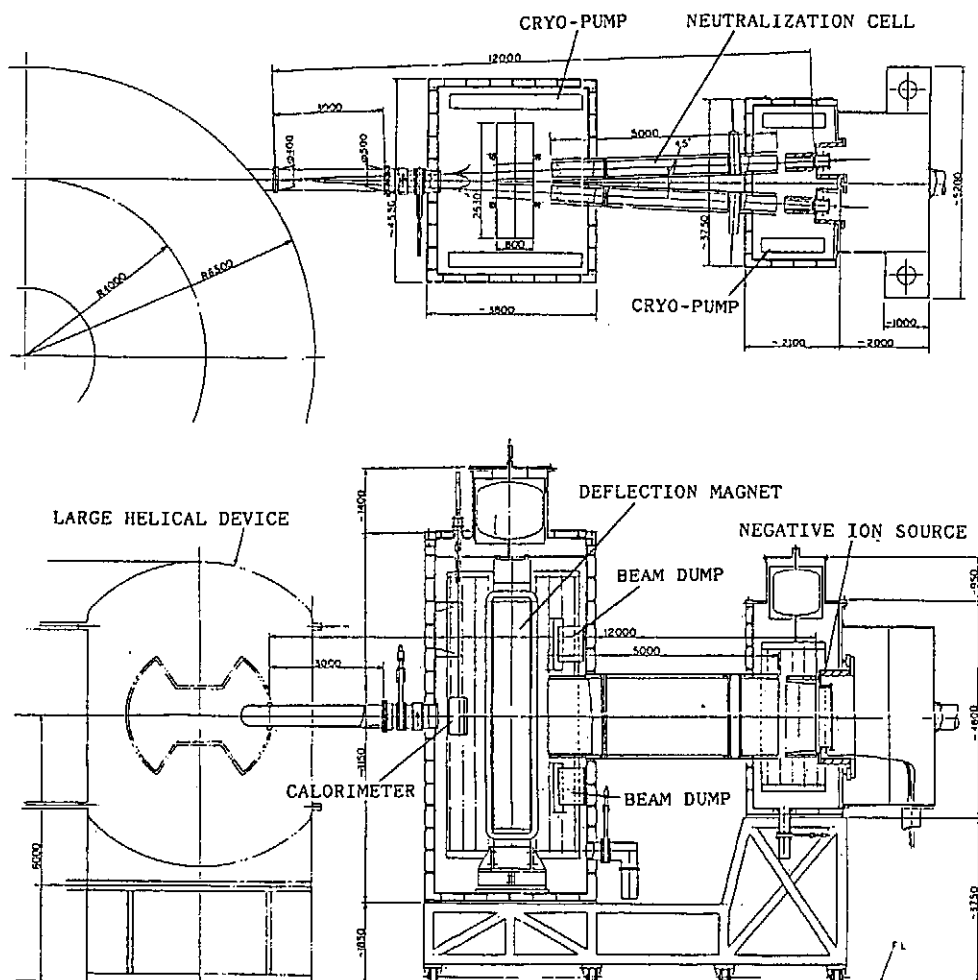


FIG. 4 Schematic diagram of negative-ion-based NBI system for the Large Helical Device.

Appendix I

PROGRAM of FIRST INTERNATIONAL TOKI CONFERENCE on
PLASMA PHYSICS and CONTROLLED NUCLEAR FUSION

NEXT GENERATION EXPERIMENTS

December 4(Monday)-7(Thursday), 1989
Tokishi Bunka Plaza, Toki City, Japan

4 Monday	5 Tuesday	6 Wednesday	7 Thursday
10:00-12:00 Registration	9:00-10:40 Session II MHD 10:55-12:10 Session III Transport	9:00-12:40 Session VI On-going Experi- ments	9:00-12:00 Session VIII Engineering 12:00-12:15 Closing
13:00-13:30 Opening A.Iiyoshi H.Wakabayashi Y.Tsukamoto J.F.Lyon G.Grieger	13:30-15:00 Session IV Special Topics 15:15-16:55 Session V Edge Physics and Confinement Im- provement	14:00-15:30 Session VII Poster Session 14:30-16:30 Open Lecture on Fusion Re- search A.Iiyoshi G.Grieger	
13:30-18:10 Session I Next Generation Experiments LHD O.Motojima WVII-X G.Grieger ATF-II J.F.Lyon TJ-II C.L.Alejaldre ANU Helic R.L.Dewar CA Torsatron R.Gandy	18:00- Banquet	16:00- Tour	

PROGRAM of FIRST INTERNATIONAL TOKI CONFERENCE on
PLASMA PHYSICS and CONTROLLED NUCLEAR FUSION

NEXT GENERATION EXPERIMENTS

December 4(Monday)-7(Thursday), 1989
Tokishi Bunka Plaza, Toki City, Japan

Monday, December 4, 1989

Opening

(Chairman; J. Fujita)

13:00-13:30

A. Iiyoshi (NIFS)
H. Wakabayashi (MOE)
Y. Tsukamoto (Toki City)
J. F. Lyon (ORNL)
G. Grieger (Max Planck Inst.)

Session I

Next Generation Experiments (Chairman; M. Fujiwara and H. Wobig)

13:30-14:30

Present Status of Large Helical Device Project
O. Motojima (NIFS)

14:30-15:30

Status of the Wendelstein VII-X Project
G. Grieger (Max Planck Inst.)

15:30-15:40

Coffee Break

15:40-16:40

Overview of the ATF-II Studies
J. F. Lyon (ORNL)

16:40-17:10

Review of the TJ-II Flexible Helic Project
C. L. Alejaldre (CIEMAT)

17:10-17:40

The ANU Helic Program
R. L. Dewar (ANU)

17:40-18:10

Design of the Compact Auburn Torsatron
R. Gandy (Auburn Univ.)

Tuesday, December 5, 1989

- Session II MHD (Chairman; M. Okamoto)**
- 9:00- 9:25 Optimization of Helias
J. Nuhrenberg (Max Planck Inst.)
- 9:25- 9:50 Second Stability Studies in a Helical Axis Device:TJ-II
C. Alejaldre (CIEMAT)
- 9:50-10:15 3D Equilibrium of Helical System: Magnetic Islands and Their Control
T. Hayashi (NIFS)
- 10:15-10:40 Resistive MHD Stability Studies for ATF Plasmas during Operation in the Second Stability Regime
L. A. Charlton (ORNL)
- 10:40-10:55 Coffee Break
- Session III Transport (Chairman; J. W. Van Dam)**
- 10:55-11:20 Drift Optimization of Helical Systems
K. Hanatani (PPL, Kyoto Univ.)
- 11:20-12:10 Plasma Transport in Advanced Stellarators
H. Wobig (Max Planck Inst.)
- 12:10-13:30 Lunch
- Session IV Special Topics (Chairman; M. Murakami)**
- 13:30-14:00 Recent Experiments in JT-60
H. Kishimoto (JAERI)
- 14:00-14:30 Graphites as Plasma Facing Material of a Large Fusion Device
T. Hino (Hokkaido Univ.)
- 14:30-15:00 The Main Fusion Activities in Institute of Plasma Physics, Academia Sinica
Wang Shao-hu (ASIPP)
- 15:00-15:15 Coffee Break
- Session V Edge Physics and Confinement Improvement (Chairman; T. Obiki)**
- 15:15-15:40 Analysis of Scrape off Layer in Toroidal Helical Systems
K. Nagasaki (PPL, Kyoto Univ.)
- 15:40-16:05 Detached Plasma and Density Limit of Tokamaks
S. Yoshikawa (PPPL)
- 16:05-16:30 Confinement Improvement by Edge Control
N. Ohyabu (NIFS)
- 16:30-16:55 Effects of Perturbing Helical Fields on Confinement of Heliotron DR Plasma
S. Morimoto (NIFS)

Wednesday, December 6, 1989

Session VI On-going Experiments (Chairman; J. L. Shohet and H. Ringler)

- 9:00- 9:45 Status of the ATF Experimental Program
M. Murakami (ORNL)
- 9:45-10:30 Status of the Wendelstein VII-AS Program
H. Ringler (Max Planck Inst.)
- 10:30-10:45 Coffee Break
- 10:45-11:15 Present status of the Torsatron/Stellarator Program at the University of Wisconsin
J. L. Shohet (Univ. of Wisconsin)
- 11:15-11:45 Review of Heliotron E Experiment
T. Obiki (PPL, Kyoto Univ.)
- 11:45-12:15 Review of CHS Experiment
K. Matsuoka (NIFS)
- 12:15-12:40 Experimental Studies of a Helical Axis Stellarator (TU-Heliac)
H. Watanabe (Tohoku Univ.)
- 12:40-14:00 Lunch

Session VII Poster Session

14:00-15:30

- 1 Diverted Particle-Flux Studies in the IMS and Proto-Cleo Stellarators
J. L. Shohet (Univ. of Wisconsin)
- 2 Pressure and Potential Measurements in IMS During Electron Cyclotron Heating
J. N. Talmadge (Univ. of Wisconsin)
- 3 Numerical and Experimental Studies of Simulated Toroidicity Effects in a Linear High-Beta Heliac
B. A. Nelson (Univ. of Washington)
- 4 Theory of Electron Cyclotron Heating in the Flexible Heliac TJ-II
C. Alejaldre (CIEMAT)
- 5 STORM : A Low Aspect Ratio Torsatron for Plasma Stability Studies
A. P. Navarro (CIEMAT, Presented by C. Alejaldre)
- 6 Dissipative Trapped Electron Modes in $\ell = 2$ Torsatrons
B. A. Carreras (ORNL, Presented by J. F. Lyon)
- 7 Low-n Stability Calculations for Three Dimensional Stellarator Configurations
L. Garcia (Universidad Complutense, Presented by C. Alejaldre)
- 8 Destruction of Magnetic Surfaces in Helical Torus
J. Todoroki (NIFS)
- 9 Ripple Diffusion and Bootstrap Current in Large Helical Device
T. Amano (NIFS)
- 10 Numerical Analysis of Temporal Development of RF-Heated Plasma

- T. Watanabe (NIFS)
- 11 Island Studies for Helias Configurations
P. Merkel (Max Planck Inst.)
 - 12 On Strong RF Plasma Turbulence
M. M. Skoric (Boris Kidric Inst.)
 - 13 Structural Design of Large Helical Device
M. Shibui (Toshiba Corp.)
 - 14 R&Ds of Forced Flow Superconducting Coil for Large Helical Device
S. Tsuruga (Toshiba Corp.)
 - 15 Pool-Cooled Superconducting Magnet Design of Large Helical Device
S. Suzuki (Hitachi Ltd.)
 - 16 Behavior of Vacuum Vessel Eddy Current in Large Helical Device
H. Fukumoto (Hitachi Ltd.)
 - 17 Fundamental Design on Large Helical Device with Bath Cooling
Method
S. Tado (Mitsubishi Fusion Center)
 - 18 A Compact Helical Device for a Superconducting Large Helical Coil
Y. Tsuda (Mitsubishi Electric Co.)
 - 19 Optimization of Design Parameters for Large Helical Device
K. Yamazaki (NIFS)
 - 20 Effect of Multi-Layer Operation of Helical Coil in Large Helical
Device
M. Asao (Kobe Steel Ltd.)
 - 21 ECH System in the Large Helical Device
K. Ohkubo (NIFS)
 - 22 ICRF Heating Program in the Large Helical Device
T. Mutoh (NIFS)
 - 23 Motion of Charged Particle in Helical Systems
M. P. Srivastava (Delhi Univ.)
 - 24 Equilibrium, Stability and Transport in $\ell = 1$ Compact Helical Axis
Configuration
H. Kikuchi (NIHON Univ.)
 - 25 Electron Cyclotron Emission Measurements on ATF
R. F. Gandy (Auburn Univ.)
 - 26 Confinement Studies of Heliotron E Plasmas in Magnetic Surface
Variation Experiments
F. Sano (PPL, Kyoto Univ.)
 - 27 Profile Measurements in Magnetic Surface Variation Experiments/
Multi Pellet Injection Experiments
S. Sudo (PPL, Kyoto Univ.)
 - 28 Impurity Behavior in Heliotron E
K. Kondo (PPL, Kyoto Univ.)
 - 29 Edge Plasma Study in Heliotron E
H. Matsuura (Univ. of Osaka Pref.)
 - 30 Recent Diamagnetic Measurement of Heliotron E Toroidal Coil
Experiments
S. Besshou (PPL, Kyoto Univ.)
 - 31 Study of Resistive Interchange Modes in Heliotron E
H. Zushi (PPL, Kyoto Univ.)

- 32 Measurement of Magnetic Fluctuations in Heliotron E
M. Harada (PPL, Kyoto Univ.)
- 33 Transport Analysis of ECH and NBI Plasmas in CHS
H. Yamada (NIFS)
- 34 Effect of Magnetic Axis Shift on CHS Plasma Characteristics
S. Okamura (NIFS)
- 35 A Study of Radiation Collapse in CHS Plasmas
S. Morita (NIFS)
- 36 Ion Temperature and Poloidal Rotation Profile Measurements in
CHS
K. Ida (NIFS)
- 37 Driven Currents in Neutral Beam Heated CHS Plasma
O. Kaneko (NIFS)
- 38 Power Deposition during ECH in CHS
S. Kubo (NIFS)

Thursday, December 7, 1989

- Session VIII Engineering** (Chairman; S. Morimoto and J. Yamamoto)
- 9:00- 9:25 Engineering Design of Large Helical Device
J. Yamamoto (NIFS)
 - 9:25- 9:50 Operation Scenario and Structural Design Analysis of LHD (Large
Helical Device) Coils
K. Yamazaki (NIFS)
 - 9:50-10:15 Engineering Design of Vacuum Vessel
N. Ohyabu (NIFS)
 - 10:15-10:40 Development of Superconductor for Large Helical Device
T. Mito (NIFS)
 - 10:40-10:45 Coffee Break
 - 10:45-11:10 Overview of Engineering Design of Wendelstein VII-X
J. Sapper (Max Planck Inst.)
 - 11:10-11:35 100GHz Half Megawatt Microwave Transmission System Development
Whispering Gallery Mode
M. Sato (PPL, Kyoto Univ.)
 - 11:35-12:00 NBI System with Negative Ion Source in Large Helical Device
Y. Takeiri (NIFS)

Closing

- 12:00-12:15 J. Fujita
A. Iiyoshi

Appendix II

LIST OF PARTICIPANTS

Erol Oktay	Division of Toroidal Confinement Systems Office of Energy Research U.S. Dept. of Energy Washington, D.C. 20545 U.S.A.
Masanori Murakami James F. Lyon Lowell A. Charlton	Oak Ridge National Laboratory P.O.Box 2009 Oak Ridge, Tennessee 37831-8072 U.S.A.
Juda L. Shohet Joseph N. Talmadge	Dept. of Electrical & Computer Engineering University of Wisconsin 1415 Johnson Drive Madison, Wisconsin 53706 U.S.A.
Shoichi Yoshikawa	Plasma Physics Laboratory Princeton University James Forrestal Campus P.O.Box 451 Princeton, New Jersey 08544 U.S.A.
Brian Nelson	Dept. of Nuclear Engineering 120 AERL FL-10 University of Washington Seattle, Washington 98195 U.S.A.
Rex Gandy	Physics Department Auburn University Alabama 36849 U.S.A.
Gunter Grieger Jurgen Nuhrenberg Horst Wobig Jorg Sapper Heinz Ringler Volker Erckmann Peter Merkel	Max-Planck-Institut fur Plasmaphysik Boltzmannstr. 2 D-8046 Garching bei Munchen Federal Republic of Germany
Carlos L. Alejaldre	EURATOM/CIEMAT Association Av. Complutense 22 - Ciudad Universitaria 28040 Madrid Spain
Robert L. Dewar	Research School of Physical Sciences Australian National University GPO Box 4 Canberra, ACT 2601 Australia

Mahesh P. Srivastava	Dept. of Physics University of Delhi Delhi - 110007 India
Wang Shao-hu Li You-yi	Institute of Plasma Physics, Academia Sinica P.O.Box 26, Hefei, Anhui P.R.China
Milos M. Skoric	Boris Kidric Institute of Nuclear Sciences P.O.Box 522 11000 Belgrade Yugoslavia
T. N. Todd	Experimental Division Culham Laboratory United Kingdom Atomic Energy Authority Abingdon, Oxon OX14 3DB United Kingdom
Faiz H. Ali Mazin A. Sultan	Iraqi Atomic Energy Commission Baghdad P.O.Box 765 Iraq
James W. Van Dam	Institute for Fusion Studies University of Texas at Austin Austin, Texas 78712-1018 U.S.A.
Toshiro Yamashina Tomoaki Hino	Engineering Department Hokkaido University Kita-13, Nishi-8, Kita-ku, Sapporo, Hokkaido, Japan 〒060
Hiroshige Watanabe Sumio Kitajima	Department of Nuclear Engineering Faculty of Engineering Tohoku University Aramaki, Aoba, Aoba-ku, Sendai, Japan 〒980
Hiroshi Takuma	Institute for Laser Science University of Electro-Communications 1-5-1, Chofugaoka, Chofu-shi, Tokyo, Japan 〒182
Takashige Tsukishima	Faculty of Engineering Nagoya University Furo-cho, Chikusa-ku, Nagoya, Japan 〒464
Shinsaku Kajita	Engineering Department Gifu University 1-1 Yanagito, Gifu, Japan 〒501-11
Yoshinosuke Terashima	Plasma Science Center Nagoya University Furo-cho, Chikusa-ku, Nagoya, Japan 〒464-01

Tokuhiro Ohbiki Shigeru Sudo Fumimichi Sano Katsumi Kondo Motoyasu Sato Sakae Bessho Hideki Zushi Kiyoshi Hanatani Mitsuru Harada Shoji Ichiguchi Kazunobu Nagasaki Masahiro Wakatani	Plasma Physics Laboratory Kyoto University Gokasho, Uji, Kyoto, Japan ̄611
Hiroto Matsuura	College of Engineering University of Osaka Prefecture 4-804 Mozuumemachi, Sakai, Osaka, Japan ̄591
Atsushi Fukuyama	Engineering Department Okayama University 3-1-1 Tsushimanaka, Okayama, Japan ̄700
Kyoji Nishikawa Motohiko Tanaka	Hiroshima Institute for Fusion Theory Hiroshima University 1-1-89 Higashisendmachi, Nakaku, Hiroshima, Japan ̄730
Katsunori Muraoka	Plasma Engineering Laboratory Kyushu University 6-1 Kasugakoen, Kasuga-shi, Fukuoka, Japan ̄816
Ichiro Kawakami Kiyomitsu Suzuki Hitoshi Kikuchi Masamitsu Aizawa	Atomic Energy Research Institute Nihon University 1-8-14 Kanda-Surugadai, Chiyoda-ku, Tokyo, Japan ̄101
Koji Uo	Future Energy Association Pasteur Bldg., 103-5 Tanaka Monzen-cho Sakyo-ku, Kyoto, Japan ̄606
Hiroshi Kishimoto	Japan Atomic Energy Research Institute 801-1 Mukoyama, Naka-machi, Naka-gun, Ibaraki Japan ̄311-02
Ryusei Saito Shohei Suzuki Yukio Ishigaki Hideshi Fukumoto Tetsu Mochizuki Sei Inomata Sho Saito Shoji Murai Taisei Uede Takeshi Kojima Satoru Ishidahara	Nuclear Fusion Project Division Hitachi Manufacturing Co., Ltd. 4-6 Surugadai, Kanda, Chiyoda-ku, Tokyo, Japan ̄100

Shigeru Ioka
Toshihiro Sasaki
Tadaaki Fujikura
Hideo Aoki
Kazushi Taoka
Shigenori Tsuruga
Keiichi Yamamoto
Hirohisa Takano
Masanao Shibui
Yoshio Sawada
Mitsugu Yamaguchi

Power & Fusion Technology Development Dept.
Toshiba Corporation
1-1-6 Uchisaiwaicho, Chiyoda-ku, Tokyo, Japan 7100

Masato Asao

Kobe Steel Ltd.
Wakihamacho, Chuo-ku, Kobe, Japan 7651

Masana Nishikawa

Mitsubishi Atomic Power Industries, Inc.
4-1, Shiba-Koen 2-chome, Minato-ku, Tokyo, Japan 7105

Hyota Fujita
Shigeru Tado
Katsuhiko Shimizu
Tadanori Tsukamoto
Masao Yamada
Yuuichi Kawazoe
Kimihiro Ioki
Yoshiyuki Tsuda
Masaru Suzuki

Mitsubishi Fusion Center
2-2-3 Marunouchi, Chiyoda-ku
Tokyo, Japan 7100

Makoto Miura
Katsuaki Tsujiyama
Kazuhiko Saka

Mitsubishi Electric Corporation
Dainagoya Bldg. 6F, 3-28-12 Meieki, Nakamura-ku
Nagoya, Japan 7450

Kazuyuki Fujii

Sakai Works, No.1 Engineering Dept.
Osaka Vacuum, Ltd.
7-7-5 Otorihigashicho, Sakai-shi, Osaka, Japan 7593

Teruhiko Tozawa
Shozo Shinoda
Satoshi Kurata
Hidetaka Ooishi

The Chubu Electric Co., Inc.
1-Banchi Toshincho, Higashi-ku, Nagoya, Japan 7461

Atsuo Iiyoshi
Masami Fujiwara
Osamu Motojima
Tsutomu Kuroda
Junji Fujita
Shigeyuki Morimoto
Kunizo Ohkubo
Kozo Yamazaki
Keisuke Matsuoka
Masao Okamoto
Koji Kamata
Yuichi Ogawa
Kiyohiko Nishimura
Yoshihide Oka

Naruyoshi Ohyabu
Takashi Mutoh
Jiro Todoroki
Kimitaka Itoh
Junya Yamamoto
Hiroshi Yamada
Shoichi Okamura
Katsumi Ida
Yasuhiko Takeiri
Osamu Kaneko
Tetsuya Sato
Tetsuo Kamimura
Shigeru Morita
Harukazu Iguchi

Chusei Namba
Haruo Ohbayashi
Yoichi Sakuma
Heiji Sanuki
Tsuneo Amano
Shin Kubo
Toshiyuki Mito
Nagato Yanagi
Tsuguhiro Watanabe
Noriyoshi Nakajima
Takaichi Kawamura
Hiroshi Kaneko
Yukio Mizuno
Takaya Hayashi

National Institute for Fusion Science
Furo-cho, Chikusa-ku, Nagoya, Japan 7464-01